

# **RIKEN Accelerator Progress Report**

1999

vol. **33**

理化学研究所  
**RIKEN (The Institute of Physical and Chemical Research)**

**RIKEN Accelerator Progress Report** 1999  
**January-December**

**vol. 33**

理化学研究所

**RIKEN (The Institute of Physical and Chemical Research)**  
**Wako, Saitama, 351-0198 JAPAN**

### **Editors**

T. Abe	A. Goto
T. Ichihara	R. Kadono
T. Kambara	Y. Kobayashi
A. Ozawa	I. Shimamura
S. Yamaji	Y. Yamazaki

All rights reserved. This report or any part thereof may not be reproduced in any form (including photostatic or microfilm form) without written permission from the publisher.

All reports are written on authors' responsibility and thus the editors are not liable for the contents of the report.

# CONTENTS

	Page
<b>I. PREFACE</b> .....	1
<b>II. OPERATION OF ACCELERATORS</b>	
The Tandem Operation .....	3
RRC and AVF Cyclotron Operations .....	4
RILAC Operation .....	6
<b>III. RESEARCH ACTIVITIES</b>	
<b>1. Nuclear Physics</b>	
Reaction Mechanism and Characteristics of $T_{20}$ in $d+{}^3\text{He}$ Backward Elastic Scattering at Intermediate Energies .....	9
Structure of Li Isotopes Studied by Gaussian Single-Particle Bases .....	10
Molecular-Orbital Structure in Be Isotopes .....	11
Model-Independent Analysis of the One-Body Density of Unstable Nuclei .....	13
Development of a New Code for Large-Scale Shell-Model Calculations Using a Parallel Computer .....	14
Monte Carlo Shell-Model Study of Unstable Nuclei around $N = 20$ .....	15
A Search for a Unified Effective Interaction for Monte Carlo Shell-Model Calculations .....	16
Monte Carlo Shell-Model Calculations for Medium-Heavy Nuclei .....	17
The Nucleon Pair Approximation of the Shell Model .....	18
Effects of the Dirac Sea on the Giant Monopole States .....	19
The Phonon Damping Model .....	20
Statistical Analysis of the Hot Giant Dipole Resonance with the Phonon Damping Model .....	21
Hot Giant Dipole Resonance in the Static Path Approximation .....	22
Damping of Multiphonon Giant Resonances .....	23
Giant Dipole Resonance in Neutron-Rich Nuclei within the Phonon Damping Model .....	24
Local Harmonic Approaches with Approximate Cranking Operators .....	25
Relativistic Tilted Axis Cranking Model and Its Application to Shears Bands in the $A = 80$ Mass Region .....	26
Wobbling Motion in the Multi-Bands Crossing Region .....	27
Relativistic Hartree-Bogoliubov Approach for Nuclear Matter with a Non-Linear Coupling Term .....	28
The r-Process Nucleosynthesis in Supernovae .....	29
Hydrodynamical Study of Neutrino-Driven Winds as r-Process Sites .....	31

$^{44}\text{Ti}$ : Its Effective Decay Rate in Young Supernova Remnants, and Its Abundance in Cassiopeia A .....	32
A New Parameterization of Polarized Parton Distribution Functions .....	33
Large $p_T$ $\Lambda_c^+$ Production in Polarized $pp$ Scattering .....	34
$\Lambda_c^+$ Productions in Polarized $ep$ Reaction and Polarized Gluons in the Proton .....	35
Behavior of Polarized Light Sea-Quarks in a Nucleon .....	36
Color-Octet Contribution to the Photoproduction of $\psi'$ .....	37
Antiquark Flavor Asymmetry in Polarized Drell-Yan Processes .....	38
Nucleon-Structure Functions in the NJL Model .....	39
$U_A(1)$ Symmetry Breaking and Eta Prime Meson in the Bethe-Salpeter Approach .....	40
Final Countdown to RHIC Spin Program .....	41
Measurement of the Charged Pion Asymmetry and Beam Polarization in AGS E925 .....	43
Sensitivities of the Gluon Polarization Measurement at PHENIX .....	44
Performance of the PHENIX Muon Reconstruction Software .....	46
Precise Measurement of the Muon Lifetime .....	48
Measurement of the Ortho-Para Effect in Muon-Catalyzed dd-Fusion .....	49
Study of Muon Catalyzed Fusion in Solid D-T Mixtures .....	51
Electron Scattering at MUSES/RIBF .....	52
Measurement of the Polarization Transfer Coefficients, $K_{ij}^{y'}$ , for $d$ - $p$ Elastic Scattering at $E_d = 270$ MeV .....	53
Measurement of the Cross Sections and Vector and Tensor Analyzing Powers for $d$ - $p$ Elastic Scattering at $E_d = 270$ MeV .....	54
The $^3\text{He}(\vec{d}, p)^4\text{He}$ Reaction at Intermediate Energies .....	55
Measurement of the Deuteron Spin-Flip Probabilities in the $^{28}\text{Si}(\vec{d}, \vec{d}')^28\text{Si}$ Reaction at $E_d = 270$ MeV .....	56
Proton Spectra from the $^{208}\text{Pb} + ^{208}\text{Pb}$ Reaction at 15 A MeV .....	57
GDR $\gamma$ -Rays from the Binary Reaction of $^{209}\text{Bi} + ^{209}\text{Bi}$ at 12 MeV/u .....	58
Search for a $Z = 118$ Superheavy Nucleus in the Reaction of $^{84}\text{Kr}$ with $^{208}\text{Pb}$ .....	59
First Measurement of the $^8\text{B}(p, \gamma)^9\text{C}$ Reaction by the Coulomb-Dissociation Method .....	60
Development of a Li-Ion Isotope Separation and Counting System for a Precise Measurement of the $^{11}\text{Li}$ Charge Radius .....	61
Coulomb Dissociation of $^{12}\text{N}$ and $^{13}\text{O}$ .....	63
Coulomb Dissociation of $^{13}\text{N}$ and $^{14}\text{O}$ .....	65
Isobaric Analog State of $^{14}\text{Be}$ .....	66

Coulomb Excitation of $^{15}\text{O}$ .....	67
Coulomb Excitation of $^{28}\text{Ne}$ and $^{32,34}\text{Mg}$ .....	68
Population of Excited States in Unstable Nuclei Produced by the Fragmentation of $^{36}\text{Si}$ .....	69
Gamma-Ray Spectroscopy of the Very Neutron-Rich Nucleus $^{34}\text{Mg}$ .....	70
Half-Life Determination of $^{44}\text{Ti}$ Using a Radioactive Beam Technique .....	72
Collective States of Neutron-Deficient Doubly Even Barium Isotopes .....	73
Production Cross Sections of Light Neutron-Rich Nuclei from $^{40}\text{Ar}$ Fragmentation ...	74
<b>2. Atomic and Solid-State Physics</b>	
Positron Scattering by Polyatomic Molecules .....	75
Total Cross Sections for Electron and Positron Collisions with $\text{CF}_3\text{I}$ Molecules .....	76
Simulation of a Diatomic Molecule Colliding with Surfaces .....	77
Radiative Electron Capture of Swift Heavy Ions into the Continuum State .....	78
Fullerene-like Fragment Ion Production in Fast Ion- $\text{C}_{60}$ Collision .....	79
Isotope Shifts between He-like $^{12}\text{C}$ and $^{13}\text{C}$ Ions .....	80
Foil Ageing Problems in Beam-Foil Spectroscopy Continued .....	81
Time Delayed Spectral Lines in Beam-Foil Spectroscopy .....	82
Spectroscopy of High Z Spin-Aligned States .....	83
High-Resolution Soft X-Ray Study of Ne Hollow Atoms Created by a Microcapillary Target .....	84
Angular Dependence of Scattering Intensity in $\text{C}^{4+} + \text{He} \rightarrow \text{C}^{2+} + \text{He}^{2+}$ at Collisional Energy of 120 eV/ $q$ .....	85
Acoustic Emission Following Fast Heavy-Ion Irradiation of Solids .....	86
Defect Production via Electronic Excitation in Oxide Superconductors Irradiated with High Energy Heavy Ions .....	87
Effects of Defect Morphology on the Vortex Dynamics in $\text{Bi}_2\text{Sr}_2\text{CaCu}_2\text{O}_{8+\delta}$ Irradiated with GeV Heavy Ions .....	88
Radiation Annealing Induced by Electronic Excitation in Iron .....	89
Infrared Spectroscopy Study on Vacancy-Oxygen Pairs in CZ-Si Irradiated by 3.5 GeV Xe Ions .....	90
Evaluation of SEB in Power MOSFETs Caused by Heavy Ions .....	91
Dynamic Behavior of a Nuclear Probe $^{57}\text{Mn}/^{57}\text{Fe}$ in Si after Projectile-Fragment Separation and Implantation .....	93
Atomic-Force-Microscopy Observations of FZ-Si after GeV- $^{57}\text{Mn}$ Implantation Using RIKEN Projectile Fragment Separator (RIPS) .....	94
A New Spin Polarimeter Proposed for Spin-Polarized Slow Positron Beams .....	95

Xe Bubble Formation in Xe-Implanted Fe as Observed by the Channelling Method ...	97
Observation of Ion Current in Superfluid Helium .....	99
Observation of a Full Dispersion Curve for the Low Energy Excitation in a Spin Ladder .....	100
$\mu$ SR Study on the 1/8 Effect in the Bi-2212 System .....	101
LF- $\mu$ SR Studies of the Vortex State in $\text{Bi}_2\text{Sr}_2\text{CaCu}_2\text{O}_x$ .....	102
Current-Induced Vortex Motion in Type-II Superconductors .....	103
$\mu$ SR Study on the Spin Dynamics of <i>Kagomé</i> Antiferromagnet, <i>m</i> -MPYNN- $\text{BF}_4$ .....	104
Radio-frequency Muon Spin Resonance of a Haldane-Gap System $\text{NiC}_2\text{O}_4 \cdot 2 \cdot (2\text{-methylimidazole})$ .....	105
Muon Spin Resonance Study on an Organic Radical TEMPO Derivative .....	106
Intra- and Inter-molecular Electron Transfer in Cytochrome c and Myoglobin Observed by the Muon Spin Relaxation Method .....	107
<b>3. Radiochemistry and Nuclear Chemistry</b>	
In-beam Mössbauer Study of $^{57}\text{Mn}/^{57}\text{Fe}$ in Si Following Projectile Fragmentation and Implantation .....	109
Biological Transport of the Various Trace Elements in the Pregnant Rats and Fetus ..	111
Uptake of Zinc and Other Trace Metals in Tumor-Bearing Murines .....	112
Biological Tissue Distribution of Vanadium in STZ-Induced Diabetic Rats: Simultaneous Tracing of V, Cr, Mn, Fe, Co, Zn, and Se Using a Radioactive Multitracer .....	113
Metabolic Study of Trace Elements in Se-Deficient Rats (IV) .....	114
Distribution of Bio-Trace Elements in Cell Fraction of Selenium-Deficient Rat Liver ..	116
Effect of Dietary Selenium Species and Doses on the Organ Distribution of Multitracer .....	117
Uptake Rates of Trace Elements in Zn-Deficient Mice .....	118
Characterization of Manganese Transport System Using Cadmium-Resistant Metallothionein-Null Cells .....	119
Biobehavior of Multitracers in the Brain and Other Organs of 1-, 3- and 8-Week-Old Mice .....	120
Effect of Oral Administration of NaFeEDTA on the Biodistribution of Trace Elements .....	121
Contribution of Arbuscular Mycorrhizal Hyphae to Acquisition of Trace Elements by Marigold .....	122
Influence of Zn on the Uptake of Various Elements into Carrot .....	123
Enhanced Uptake of Mn by <i>LeGlp1</i> -Transgenic Tobacco Plants .....	125
Selective Detection of EC-Decay Radionuclides in Multitracers: A Proposal .....	127
Evaluation of the <i>in vitro</i> Stability of Radiolabeled DTPA and DOTA and Their Conjugated Antibodies .....	128

HPLC Elution Behavior of Multitracer Metallofullerenes .....	129
Gamma-Ray Detection System for Multitracer Research .....	130
Time Course Induction of p53 in Human Cell Lines .....	131
<b>4. Radiation Chemistry and Radiation Biology</b>	
Electron-Hole Plasma Luminescence from the Ion Track of Insulator Crystals .....	133
Luminescence Spectra and Decay Curves of Diamond Crystals Irradiated by Heavy Ions .....	134
Ultrafast Luminescence and Exciton Dynamics in Ion-Irradiated RbI Single Crystal ..	135
Strontium Uptake by Yeast <i>Schizosaccharomyces pombe</i> .....	137
Influence of Endophytes on the Uptake of Radionuclides by Perennial Ryegrass .....	138
Analysis of Heavy-Ion Beam-Induced DNA Damage in <i>Saccharomyces cerevisiae</i> .....	139
Effective Plant-Mutation Method Using Heavy-Ion Beams (IV) .....	140
Effects of Heavy-Ion Beam Irradiation on Shoot Elongation in Roses .....	141
Adaptive Response of Human Cultured Cells to Heavy-Ion Irradiation .....	142
Cytogenetic Effects of Heavy-Ion Beams on Mammalian Cells .....	144
Effect of Heavy Ion Beams on Cell Cycle Progression .....	145
Recognition of Hit Sites within the Cells Exposed to Accelerated Iron Ions Using CR-39 Plastics .....	146
Oxidation Degradation of High Density Polyethylene Irradiated with Ion Beam .....	147
Heavy Ion Beams: Application to Mouse Mutagenesis (II) .....	148
<b>5. Instrumentation</b>	
Design of Liquid-He-Free Superconducting Solenoid Coils for Electron Cyclotron Resonance Ion Source .....	149
Automatic <sup>18</sup> F Supply System for a Slow Positron Beam .....	151
Design and Simulation of an Electrostatic Spin-Polarized Positron Beam System for Surface Magnetism Studies .....	152
Calibration of Beam-Line Polarimeter at $E_d = 140$ and $200$ MeV .....	153
Absolute Calibration of the Deuteron Beam Polarization at an Intermediate Energy via the <sup>12</sup> C( $d, \alpha$ ) Reaction .....	154
Calibration of <sup>3</sup> He Polarization Using Electron-Spin-Resonance Method .....	156
Response of an Imaging Plate for Heavy Particles .....	158
Development of Time-of-Flight Detector with Streak Camera .....	159
Development of a New Photon Detector System for Nuclide Identification .....	161
Development of High-Efficiency Delay-Line PPAC for High-Energy Light Ions .....	163
Construction of PHENIX Muon Tracking Chambers .....	165

Status of PHENIX Muon Identifier Mechanics .....	166
High-Energy Beam Test of PHENIX EM Calorimeter at CERN .....	168
Feasibility Test of Proton-Carbon CNI Polarimeter for RHIC .....	170
PHENIX Computing Center in Japan (CC-J) .....	172
A Workstation Farm Optimized for Monte Carlo Shell Model Calculations: Alphleet .....	174
Development of High-Rate MUSIC .....	176
Calibration of Heavy Ion Telescope on Board MDS-1 Satellite with <sup>40</sup> Ar Beam .....	177
Beam Calibration of Fiber Neutron Monitor onboard the Exposed Facility of the Japanese Experimental Module .....	178
RF Ion-Guide System for Trapping Energetic Radioactive Nuclear Ions from Fragment Separators .....	180
Development of a Polarized Solid Proton Target by Means of the Integrated Solid Effect (ISE) .....	182
<b>6. Material Analysis</b>	
Development of a Highly Sensitive High-Resolution In-Air Particle-Induced X-Ray Emission (PIXE) System: I .....	183
PIXE Analysis of Lead in the Feather of a Jungle Crow Living in Tokyo .....	185
RBS Analysis of Na-Implanted Glassy Carbon .....	186
Heavy-Ion Irradiation Effects in Bi-2223 Tapes .....	187
A New Method for Determining the Vacancy Formation Energy of Metals Using the Positron Age-Momentum Correlation Technique .....	188
<b>7. Miscellaneous</b>	
Neutrino Advanced Generation with Accelerated Muon .....	189
Light Hadron Spectrum in Quenched Lattice QCD .....	191
Monte Carlo Simulation of Supersymmetric Matrix Model .....	192
New Method for Trace Element Analysis Using the Electron Cyclotron Resonance Ion Source and Heavy-Ion Linac .....	193
<b>IV. NUCLEAR DATA</b>	
Status Report of the Nuclear Data Group .....	195
<b>V. DEVELOPMENT OF ACCELERATOR FACILITIES</b>	
Biased Electrode Method for RIKEN 18 GHz ECRIS .....	197
Present Status of 14.5 GHz Caprice in RIKEN .....	199
Development of Compact High Current Multicharged Ion Source for RIKEN RI Beam Factory .....	200
Laser-Plasma Production for Laser Ion Source at RIKEN .....	202
Generation of Heavy-Ion Pulses with Short Width and Long Interval .....	203

A Plan for a New Control System for the RIKEN Ring Cyclotron Using EPICS .....	204
Low Power Test of CSM Resonators .....	206
Construction of the IRC for RIKEN RI Beam Factory .....	208
Model Test of the RIKEN-IRC Main Resonator .....	210
Status of the SRC for the RIKEN RI Beam Factory .....	212
Development and Construction of the SRC Sector Magnets .....	214
Quench Analysis of Stagnant Normal Zone in the RIKEN Prototype Sector Magnet ..	216
Analysis of the Injection and Extraction Systems for the RIKEN Superconducting Ring Cyclotron .....	218
Superconducting Magnetic Channel for the RIKEN Superconducting Ring Cyclotron .....	220
Helium Cooling System of RIKEN Superconducting Ring Cyclotron .....	222
Design of the RIKEN-SRC RF System .....	224
Vacuum System for the RIKEN Superconducting Ring Cyclotron .....	226
Influence of External Magnetic Field on the Performance of Cold Cathode Gauges ...	228
Design Studies on Beam Transport System of RIKEN RI Beam Factory .....	230
Design Study of Beam Transport Lines from SRC to Three Big RIPSs .....	232
Design of a 2 T Room-Temperature Dipole Magnet for Beam Transport Lines of RIBF Project .....	234
Design of the BigRIPS Separator for the RIKEN RI-Beam Factory Project .....	236
Design of a Superferric Quadrupole Magnet for the RIKEN RI-Beam Factory Project .....	238
Estimation of Deposited Heat and Damage by Neutrons on the Downstream Superconducting Magnet of the Target Assembly .....	241
Shielding Design of RIKEN RI Beam Factory .....	243
Refinement of Accumulator Cooler Ring Lattice Design .....	245
Development of ACR Electron Cooler (2) .....	247
Study of Pickup for Stochastic Cooling .....	249
The Ferrite Test Cavity for MUSES (II) .....	251
Development of the Kicker Magnet for BSR .....	253
Development of a High-Intensity Slow-Positron Source for Cooling of Highly Charged Ions .....	255
Preliminary Studies on CORBA-based RIBF Control System .....	257
Spin Tracking with “Real” Siberian Snakes in Relativistic Heavy Ion Collider(RHIC) .....	259
Ion Optics Study of RHIC OPPIS .....	261
Ultraslow Muon Production Using the Resonant Ionization Method .....	263

**VI. RADIATION MONITORING**

Radiation Safety Control System for the RIKEN Ring Cyclotron ..... 265  
Routine Work for Radiation Safety in the Ring Cyclotron Facility ..... 266

**VII. LIST OF PUBLICATIONS** ..... 269

**VIII. LIST OF PREPRINTS** ..... 276

**IX. PAPERS PRESENTED AT MEETINGS** ..... 279

**X. LIST OF SYMPOSIA** ..... 292

**XI. LIST OF SEMINARS** ..... 294

**XII. LIST OF PERSONNEL** ..... 299

**AUTHOR INDEX**

## I. PREFACE

This issue of RIKEN Accelerator Progress Report reports research activities of the RIKEN Accelerator Research Facility (RARF) during the calendar year of 1999. The research programs have been coordinated in the framework of the project entitled Multidisciplinary Researches on Heavy Ion Science. The project involves a variety of fields such as: nuclear physics, atomic physics, nuclear chemistry, radiation biology, condensed matter physics in terms of accelerator or radiation application, basic studies on energy production, basic studies on accelerator cancer therapy, material characterization, application to space science, accelerator physics and engineering, laser technology, and computational technology. These activities involved 12 laboratories in RIKEN and more than 300 researchers including outside users from domestic and foreign institutions. Thirty-six universities and institutes from within Japan and 33 institutes from 10 countries are included.

Major research activities of the RARF are based on the heavy-ion accelerator complex consists of the  $K = 540$  MeV RIKEN Ring Cyclotron (RRC), the energy-variable heavy-ion linear accelerator (RILAC) and the  $K = 70$  MeV azimuthally variable field cyclotron (AVF), which have altogether provided a beam time (on the target) of more than 6500 hours through the year. The operation time is shorter than those of 1998 because of the two and half months shutdown due to the part of the construction-program of RI Beam Factory.

The three accelerators deliver heavy-ion beams of a variety of elements with energies ranging from a few  $A$  MeV to 135  $A$  MeV. The two-injector machines (AVF and RILAC) are equipped with ECR heavy ion sources. The AVF is additionally equipped with a polarized ion source for vector and tensor polarized deuterons. The three accelerators have been used in various configurations. The RRC operate with the AVF or the RILAC as the injector. The AVF has been providing beams of ions of mass number up to 60 and the RILAC has been providing beams of ions of mass number larger than that. In addition, the AVF and the RILAC were used separately, when they are not used as the injector, for low energy applications. Recently, low energy (5  $A$  MeV) beam of  $^{54}\text{Kr}$  has been accelerated for the study of superheavy elements. The beam current as high as 0.8 particle  $\mu\text{A}$  was delivered on the target.

Two new laboratories have been established. One is Applied Nuclear Physics Laboratory and the other is Beam Dynamics Laboratory. The later is the laboratory that takes care of the construction of MUSES in

RI Beam Factory.

Two third of the RRC research beam time ( $\sim 5000$  hours in total) goes to nuclear physics and one third is used by atomic physics, material science, nuclear chemistry, radiation biology and others. While the RILAC and the AVF beam time were used for fields other than nuclear physics. The research beam time at the AVF is 2100 hours and 800 hours at the RILAC.

The use of radioactive-ion (RI) beams is the main emphasis of the science at the RRC. Three different types of radioactive beams, i.e., (1) projectile-fragment (PF) radioactive beam, (2) spin-polarized radioactive beam, and (3) high-spin isomer beam, have been developed and used in a broad scope of nuclear research. The PF beams are most widely used by virtue of their versatility and prominent intensities. The spin-polarized beams are particularly useful for NMR experiments of radioactive isotopes. These beams are primarily used for the study of nuclear physics. Major subjects pursued are: (1) exotic nuclear structure and new dynamics of extremely neutron-rich nuclei (such as those with a neutron halo or skin), (2) nuclear astrophysics involving unstable-nucleus reactions, (3) synthesis of new unstable isotopes far from the valley of stability, (4) extensive measurements of nuclear moments. Characteristic features of intermediate-energy direct reactions are often exploited for such studies.

The RI beams were useful for other domains of science as well. In particular, application to condensed matter science has been developed to a large extent by exploiting on-line capability of Mössbauer and PAC spectroscopies that are feasible only with RI beams.

Intermediate-energy heavy ions from the RRC have found their own applicability. A strikingly efficient mutagenic effect has been observed when the embryo of a Tobacco plant is shot by heavy ions. High-energy heavy ions were irradiated to the plants naturally placed in the air for desirable amount of LET through sample. It has opened a new scheme of mutant production that is efficient and well controlled. The method is so efficient that it is expected to offer new possibilities of bioscience research through comparison between normal and mutagenic samples. For more detailed information such as cross talks between cells is planned to be studied by developing a micro beam.

Another remarkable development has been seen in the application field of radioactive tracer technique. High-energy heavy ion reactions facilitate production of a wide variety of isotopes simultaneously. This feature is exploited to cultivate a novel multi-tracer methodology in which a radioactive tracer source con-

taining a variety of elements is prepared to be injected into a sample. This enabled to study circulation behaviors of different elements for a common sample, drastically improving reliability and efficiency over the single-tracer experiments. Application of the method is rapidly extending to the fields of bioinorganic chemistry, dietetics, toxicology, pharmacology, environmental issues, and medical fields in general.

The RARF carries many international collaborations, among them are large-size two international-collaboration programs using overseas accelerator facilities: one is the muon science project at ISIS in collaboration with the Rutherford-Appleton Laboratory (RAL), and another is the spin physics program at RHIC in collaboration with the Brookhaven National Laboratory (BNL). The pulsed muon beam facility

at ISIS has been operated steadily. Studies of quark-gluon spin structure functions at BNL/RHIC are waiting for the commissioning of RHIC operation soon. The RIKEN/BNL Research Center is in operation and attracts physicists from all over the world. The large computer system for the analysis (CC-J) is under construction.

The RI beam factory project is going reasonably fast. The construction of the sector magnet for the booster cyclotron (ISR) has been completed and magnetic field measurements are in progress. Windings of the superconducting coil for the ring cyclotron (SRC,  $K = 2500$  MeV) is also in progress. The design work of MUSES (accumulator ring and colliding rings) has been started.

I. Tanihata

*Director*

*RIKEN Accelerator Research Facility*

## **II. OPERATION OF ACCELERATORS**



## The Tandem Operation

K. Ogiwara, E. Yagi, and T. Urai

The 1.7 MV tandem accelerator has been moved to a new experimentation hall, following the construction plan of the new accelerator facilities (RIBF), and, therefore, was shut down from March to the end of August, 1999. It was, however, operated for 40 days for experiments, except for the machine inspection and beam test, during the annual reporting period from Nov. 1, 1998 to Oct. 31, 1999.

Experimental studies on the following subjects have been performed, and some are still in progress:

- (1) Rutherford Backscattering Spectroscopy (RBS)
  - (a) Behaviour of Xe atoms implanted into iron.
  - (b) Channelling analysis of dopants in II-VI compound semiconductors.
  - (c) RBS analysis of polystyrene surfaces and glassy carbon films modified by ion implantation.
- (2) Nuclear Reaction Analysis (NRA)
  - (a) Lattice location of hydrogen in niobium alloys using the channelling method.
  - (3) Particle-Induced X-ray Emission (PIXE)
    - (a) Application of PIXE in the biomedical and materials sciences: Trace element analysis using energy-dispersive X-ray spectrometry.
    - (b) Trace element analysis of feathers to monitor environmental pollution.
    - (c) Development of an in-air high-resolution PIXE system for chemical state analysis.
    - (d) Characterization of II-VI ternary semiconducting crystals.

## RRC and AVF Cyclotron Operations

M. Kase, A. Goto, T. Kageyama, M. Nagase, S. Kohara, T. Nakagawa, K. Ikegami, J. Fujita, N. Inabe, O. Kamigaito, M. Kidera, M. Komiyama, A. Yoneda, I. Yokoyama, H. Isshiki,\* H. Akagi,\* R. Abe,\* N. Tsukiori,\* K. Takahashi,\* T. Maie,\* T. Homma,\* R. Ohta,\* K. Kobayashi,\* and Y. Yano

The operation statistics of the RIKEN Ring Cyclotron (RRC) for 1999 are listed in Table 1. The cumulative statistics since the beginning of operation in 1986 are shown in Fig. 1.

The total hours of operation in 1999 amounted to 5060 hr. This is 20% less than that in the previous year. The main reason for this decrease is the shut-down of all machines for two months due to the preparation for the RI Beam Factory (RIBF) project.

In order to clear the construction site for the new RIBF buildings, every power station, heat source and water supply for all the existing machines was moved to the west side of the Nishina Memorial Building. New

buildings for RF power supplies for RRC and RILAC were constructed on the south and north sides of the Nishina Memorial Building, respectively. Almost all cables and pipes connecting the machines to these facilities outside of the building were replaced. The renovation began in February and was finished completely in the middle of April.

The lower limit of output energy of RRC, which had been 7 MeV/nucleon, was decreased to 5.5 MeV/nucleon using a harmonic number of 13. A 5.5 MeV/nucleon  $^{84}\text{Kr}$  beam was successfully accelerated with an intensity of 1 pA in September 1999. The parameters are listed in Table 2. This beam was required in the research of superheavy elements ( $Z = 118$ ). The experiment in the Gas-filled Recoil Isotope Separator (GARIS) was carried out in October using this beam for a duration of as long as two weeks.

The operation with a harmonics of 13 is extremely inefficient, especially in RILAC. Only first three cavities of RILAC are operated with very low power levels. To make the acceleration of a low energy beam more efficient, RILAC energy will be upgraded by using acceleration cavities of Charge State Multiplier (CSM). The maximum energy will be 6 MeV/nucleon, which meets the requirements of superheavy elements research.

Six CSM cavities will be installed just after RILAC.

Table 1. Statistics of RRC Operation.

Category	Hours
Total of Operation Time	5060
(Beam Tuning)	1400
(Nucl. Phys. Experiments)	2980
(Other Field Experiments)	680
Trouble Shooting	460
Open House for Guests	40
Construction	1700
Holiday & Maintenance	1500
Total	8760

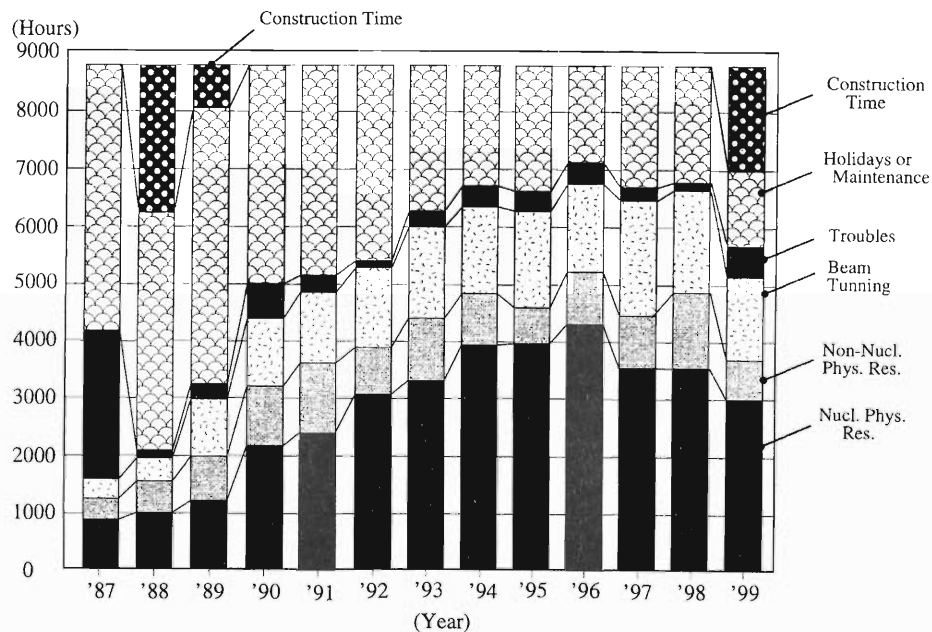


Fig. 1. Statistics of the RRC operation during the twelve years from 1987 to 1999.

\* Sumiju Accelerator Service, Ltd.

Table 2. Acceleration Conditions for 5.5 MeV/nucleon  $^{86}\text{Kr}$  beam.

RF Frequency	Cavity No. of RILAC	Harmonics of RRC	Charge-Stripper	Beam Intensities ( $\mu\text{A}$ )		
				Ion Source	Entr. of RRC	Target
18.7 MHz	3	13	No use	6*	1.96	1.2

\*18GHZ ECR  
\*Enrichment 90%

The first two of them are acceleration cavities, which were designed as the first unit of the CSM and completed in March of 1999. Their frequency tunable range is 36 to 78 MHz. On the other hand, the other four cavities, which have been fabricated, will be CSM cavities without a course frequency tuner, operated only at a frequency of 76 MHz. The entire accelerator will be installed in June of 2000 and a high-intensity low-energy beam, such as 6 MeV/nucleon  $^{84}\text{Kr}$  beam with an intensity of more than 2  $\mu\text{A}$ , will be available with stand-alone operation of RILAC in the autumn of 2000. In connection with this, GARIS will be moved from the E1 experiment room of RRC to the No. 1 target room of RILAC in June of 2000, and the RILAC-RRC operation will be stopped from May to August of 2000.

Machine troubles in 1999 were related mainly to a layer short in a main coil of the W-sector magnet of RRC. A beam became unstable periodically in February 1999. Since, at the beginning, the effect was so small and it lasted for a short duration, thus it was very difficult to identify the source of the disturbance. After the long-term precise measurement of terminal voltages of each coils as well as a magnetic field, it was discovered that a very unstable and incomplete short circuit between layers had occurred inside of the lower main coil in the W-sector magnet.

The main coil consists of eleven pancakes, each of which has a six-turn two-layer coil. Each conductor was covered with glass insulation tape, and the entire coil was molded with epoxy resin after being wound

and assembled. After a careful search on a surface of the molded coil by the thermoviewing method, the exact position where the layer short had been occurring was found in May of 1999. Fortunately, it occurred near the coil surface and also near to the coil terminal. By partially removing epoxy resin, the defective hollow conductor with a square cross-sectional shape was exposed. After the corner edge of each conductor was scraped to create enough space between them, this trouble was overcome completely.

A new ECR ion source using a super-conducting solenoid was completed in the summer of this year and a plasma test was started in the autumn. An injection beam line will be changed for two ECR ion sources, so that one can be tested while the other can be used for the AVF cyclotron.

During the shutdown period, improvement of injection system of RRC was done. Two sets of magnetic inflection channels (MIC1 & MIC2) were replaced with new ones and the size of beam pipe was enlarged slightly. Beam monitors along the injection line will be replaced with new types of monitors, preparing for the high intense beam injection in the future.

The radiation safety system has been changed to a new system using distributed function via a network. All the replacement was completed in the end of April.

In June of 2000, the spectrometers of DUMAS, which are currently installed at the beam line on RCNP, will be moved to experimental hall E7 in the cooperation with the Center of Nuclear Study of Tokyo University.

## RILAC Operation

E. Ikezawa, S. Kohara, M. Fujimaki, T. Aihara,\* T. Ohki,\* H. Hasebe,\*  
H. Yamauchi,\* and M. Kase

During this reporting period, RILAC has been in steady operation and has supplied various kinds of ion beams for various experiments. Table 1 shows the statistics of RILAC operation from January through December, 1999. The days taken for overhaul and improvement, as shown in Table 1, include two kinds of large works. First, the sub-power station for RILAC was moved to a new site in order to open space in the project for a RI Beam Factory. Second, improvement of the rf system of RILAC was carried out. Regular RILAC operation was discontinued twice, from February 13 through May 28, 1999, and from November 22 through December 10, 1999.

Table 2 summarizes the number of days allotted to different research groups. The percentage of beam time used by the RIKEN Ring Cyclotron (RRC) group was

Table 1. Statistics of RILAC operation from January 1 through December 31, 1999.

	Days	%
Beam time	121	33.2
Overhaul and improvement	134	36.7
Periodic inspection and repair	24	6.6
Machine trouble	0	0.0
Scheduled shut down	86	23.6
Total	365	100

Table 2. Beam time allocated for different research groups.

	Days	%
Atomic physics	15	12.4
Nuclear physics	2	1.7
Radiation chemistry	16	13.2
Material analysis and development	12	9.9
Instrumentation	8	6.6
Accelerator research	5	4.1
Beam transport to RRC	63	52.1
Total	121	100

Table 3. Statistics of the RILAC ion beams delivered using the Cockcroft-Walton injector.

Ion	Mass	Charge states	Days
B	11	3	2
C	12	1,4	7
C	13	1,2	2
N	14	4	4
N	15	4	2
Ne	20	4	4
Ar	40	8	2
Ti	48	5	1
Kr	84	13	6
Nb	93	12	3
Rh	103	16	1
Xe	136	15	1
Ta	181	16	2
Bi	209	16	4
Total			41

Table 4. Statistics of the RILAC ion beams delivered using the new preinjector.

Ion	Mass	Charge states	Days
O	16	4	2
Ar	40	8	9
Fe	56	8,11	3
Ni	58	9	10
Kr	78	18	2
Kr	84	10,11,17	23
Xe	136	18,20,27	31
Total			80

approximately 52% of the total. The  $^{58}\text{Ni}$ ,  $^{84}\text{Kr}$ ,  $^{136}\text{Xe}$ ,  $^{181}\text{Ta}$ , and  $^{209}\text{Bi}$  ions accelerated by RILAC were injected to RRC. Tables 3 and 4 show the statistics of the number of days of the RILAC ion beams were delivered using the Cockcroft-Walton injector with an 8 GHz ECR ion source (NEOMAFIOS) and those delivered using the new preinjector (consisting of an 18 GHz ECR ion source and a variable-frequency RFQ equipped with a folded coaxial resonator), respectively. The ion beams of 15 elements were used for the experiments and beam acceleration tests. The percentage of beam time using metallic ions amounted to approximately 21% of the total.

We carried out the following machine improvements during this reporting period.

(1) The No. 6 and No. 5 rf systems were replaced with newly designed ones in May 1999 and in De-

\* Sumijyu Accelerator Service, Ltd.

ember 1999, respectively. The power amplifier chain of the new rf system consists of a solid-state amplifier (1 kW) as the first stage, a tetrode (SIEMENS-RS2012CJ) as the second stage (15 kW), and a tetrode (SIEMENS-RS2042SK) as the final stage (300 kW). The basic design is similar to that of RRC.

(2) A PC-based control system has been adopted for the new rf system. Windows NT is used as the operating system of the personal computer. The system communicates with programmable logic controllers by InTouch software.

(3) Three sets of plate power supplies as the final stages were replaced with newly designed ones in May 1999, because they were worn out from many years of operation. Rated output power is 480 kW for the No. 1 and No. 2 rf systems, 700 kW for the No. 3 and No. 4 rf systems, and 1120 kW for the No. 5 and No. 6 rf systems. Maximum output voltages are 12 kV, 14 kV, and 16 kV, respectively. The ripple voltage at the rated full load is 0.5% peak to peak.

(4) The power supplies for the bending magnet and

quadrupole magnets of the beam transport line from the 450 kV Cockcroft-Walton injector were replaced with new ones, because they were worn out from many years of operation. Each new magnet power supply is a switching type.

(5) A PC-based control system for the new magnet power supplies was developed. This new system uses a personal computer with a Windows NT operating system and an application program (HP-VEE). Each new magnet power supply has a GPIB interface module, and is connected to Ethernet LAN through LAN/HP-IB Gateway E2050. The control system has been used since September 1999.

We experienced the following machine troubles during this reporting period. (1) A GPIB card of the computer system controlling RILAC had trouble; we replaced it with a spare one. (2) The No. 4 resonator had a small vacuum leak at the outer wall of the rf feeder. (3) A power supply for the filament (4.5 V, 1640 A) of the final vacuum tube (No. 1) had trouble.



### **III. RESEARCH ACTIVITIES**



# 1. Nuclear Physics



# Reaction Mechanism and Characteristics of $T_{20}$ in $d+{}^3\text{He}$ Backward Elastic Scattering at Intermediate Energies

M. Tanifuji,<sup>\*1</sup> S. Ishikawa,<sup>\*1</sup> Y. Iseri,<sup>\*2</sup> T. Uesaka, N. Sakamoto, Y. Satou, K. Itoh, H. Sakai, A. Tamii, T. Ohnishi, K. Sekiguchi, K. Yako, S. Sakoda, H. Okamura, K. Suda, and T. Wakasa

[NUCLEAR REACTION,  ${}^3\text{He}(d,{}^3\text{He})d$ ,  $E_d = 140, 200, 270$  MeV, PWIA with one-proton-exchange]

For the last few decades, the tensor analyzing power,  $T_{20}$ , of the backward elastic scattering of deuterons by protons ( $d+p$ ) at intermediate energies has been intensively studied as an important source of information about nuclear interactions and reaction dynamics. Since  ${}^3\text{He}$  has the same spin as proton, the spin structure of the scattering amplitude of the  $d+{}^3\text{He}$  system is similar to that of  $d+p$  when  ${}^3\text{He}$  is considered to be a single body. Thus, the backward elastic scattering of the deuteron by  ${}^3\text{He}$  has attracted our attention for investigations of probable differences as well as similarities of information when compared to  $dp$  scattering.<sup>1)</sup>

A  $d+{}^3\text{He}$  experiment was carried out at the RIKEN Accelerator Research Facility using polarized deuteron beams of  $E_d = 140\text{--}270$  MeV. The beam was provided by a high-intensity polarized ion source. Three polarization modes (unpolarized and two tensor-polarized modes) were cycled every 5 seconds. The beam polarization was measured with a polarimeter based on  $d+p$  elastic scattering. It was continuously monitored during a run, and found to typically be 60–80% of the ideal value. Scattered  ${}^3\text{He}$  particles were momentum-analyzed in the magnetic spectrograph SMART and detected by a multi-wire drift chamber and plastic scintillators placed at the focal plane. In an off-line analysis, data for  $\theta_{\text{lab}} \leq 1.4^\circ$  were used. The background spectrum from the ( $d, {}^3\text{He}$ ) reactions on Havar foils was subtracted to obtain the net yield for  $d+{}^3\text{He}$  events. The signal-to-noise ratio at the peak region was 5–25, depending on the beam energy.

In the  $d+p$  backward scattering, the assumption of a mechanism by neutron transfer from the deuteron to the proton has been fundamentally successful in explaining the energy dependence of the observables. For example, a simple PWIA calculation by the mechanism qualitatively describes the features of the measured tensor analyzing power,  $T_{20}$ , and the polarization transfer coefficient,  $K_y^y(d \rightarrow p)$ , at a few hundred MeV. In the case of a  ${}^3\text{He}$  target, the possible reaction mechanism of the backward scattering of the deuteron would be proton transfer from  ${}^3\text{He}$  to the deuteron. For the transfer assumption,

$$T_{20} = \{2\sqrt{2}R \cos \Theta - R^2 - 32R'^2 + 12RR' \cos(\Theta' - \Theta)\}/N_R,$$

<sup>\*1</sup> Department of Physics, Hosei University

<sup>\*2</sup> Department of Physics, Chiba Keizai College

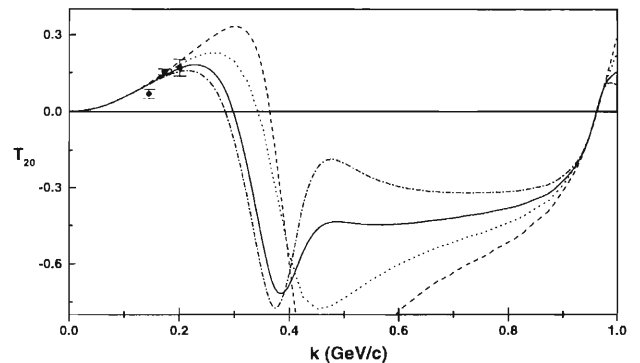


Fig. 1.  $T_{20}$  in  $d+{}^3\text{He}$  backward elastic scattering as a function of the p-d relative momentum in  ${}^3\text{He}$ ,  $k$ .

with

$$N_R = \sqrt{2} + 2\sqrt{2}R^2 + 34\sqrt{2}R'^2 - 4R' \cos \Theta',$$

where  $R$  and  $R'$  are the magnitudes of the tensor scattering amplitudes relative to the scalar one;  $\Theta$  and  $\Theta'$  are their relative phases. In PWIA,  $R$  and  $R'$  are given by

$$R = \frac{4|r|}{4+r^2}, \quad R' = \frac{r^2}{\sqrt{2}(4+r^2)} \quad \text{with} \quad r = \frac{w(k)}{u(k)},$$

where  $u(k)$  and  $w(k)$  are the  $S$ - and  $D$ -wave functions of the p-d relative motion in  ${}^3\text{He}$ , respectively. The p-d relative momentum in  ${}^3\text{He}$ ,  $k$ , is related to the incident deuteron momentum,  $k_d$ , as  $k = \frac{1}{3} k_d$ . The  ${}^3\text{He}$  wave function was obtained by solving the Faddeev equation with the AV14 nucleon-nucleon potential.  $\Theta$  and  $\Theta'$  were treated as flexible parameters which describe the effects of the virtual excitation of other reaction channels.

Figure 1 shows the calculated and measured  $T_{20}$  as a function of  $k$ , where the dashed, dotted, solid and dash-dotted lines are for  $\Theta' = 60^\circ, 120^\circ, -60^\circ$  and  $-120^\circ$ , respectively,  $\Theta$  being fixed at  $60^\circ$ . All calculations with  $\Theta = 60^\circ$  describe well the present data, suggesting the importance of deuteron breakup effects. The resonance-like structures around  $k = 0.4$  GeV/c in the solid and dash-dotted lines stimulate us to conduct an experimental examination if they are observed.

## References

- 1) M. Tanifuji et al.: Phys. Rev. C **61**, 024602 (2000).

# Structure of Li Isotopes Studied by Gaussian Single-Particle Bases

S. Haruyama, T. Otsuka, K. Varga,\* and T. Mizusaki

[Unstable nuclei, Clustering]

Each Li isotope has its own distinctive feature. For example,  ${}^7\text{Li}$  has a clustering structure and  ${}^{11}\text{Li}$  has a halo structure. We have tried to calculate the structures of Li isotopes with some Gaussian single-particle bases in order to explain these features systematically with only a few assumptions.

We have adopted a Gaussian function as a single-particle wave function,

$$\varphi_{\mathbf{s}}^{\nu}(\mathbf{r}) = \left(\frac{2\nu}{\pi}\right)^{3/4} \exp\left(-\nu(\mathbf{r}-\mathbf{s})^2\right) |\beta\rangle,$$

where  $|\beta\rangle$  is the spin-isospin wave function and  $\nu$  is the Gaussian size parameter; vector  $\mathbf{s}$  shows the center of the Gaussian. Here,  $\nu$  and  $\mathbf{s}$  are variational parameters. There was no variational parameter on the spin-isospin wave function in this work. We made a basis function of a nucleus by a Slater determinant:

$$|\Psi\rangle = \mathcal{A}\{\varphi_i(\mathbf{r}_i)\} = \det\{\varphi_i(\mathbf{r}_i)\},$$

$$(\varphi_i(\mathbf{r}_i) = \varphi_{\mathbf{s}_i}^{\nu_i}(\mathbf{r}_i)).$$

We expressed the wave function of the total system by superposing multi non-orthogonal many-body bases that have different Gaussian size parameters,

$$|\Phi\rangle = c_1|\Psi_1\rangle + c_2|\Psi_2\rangle + \dots + c_i|\Psi_i\rangle + \dots + c_N|\Psi_N\rangle.$$

Here,  $\{|\Psi_i\rangle\}$  are non-orthogonal bases. The coefficients,  $\{c_i\}$ , were determined by diagonalization of the Hamiltonian.

We selected parameters of the wave functions in a stochastic manner. We also projected wave functions onto eigenstates of the angular momentum and parity. In calculations of stochastic selections and projections, we used a parallel computing machine, called Alphleet.

In this study, we used a Modified Volkov No. 1 Force<sup>1)</sup> ( $m = 0.58$ ,  $b = 0.15$ ,  $h = 0.05$ ) as the central force and the G3RS force<sup>2)</sup> as the spin-orbit force. We used a Coulomb force approximated by the sum of seven Gaussians.

We calculated the structures of the  ${}^6\text{Li}$ ,  ${}^7\text{Li}$ ,  ${}^8\text{Li}$  and  ${}^9\text{Li}$  ground states. In the process of selecting basis wave functions, the z-component of the angular momentum and parity were projected. After we selected wave functions, we projected then onto the eigenstates

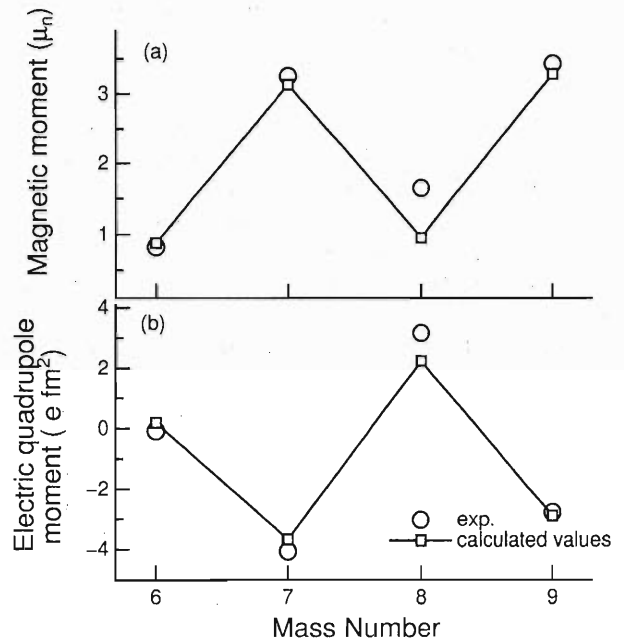


Fig. 1. Magnetic dipole (a) and electric quadrupole (b) moment of Li isotopes. The experimental data are indicated by the circles.<sup>3)</sup>

of the total angular momentum and calculated the energies and moments. We show the calculated values of the magnetic dipole moments and electric quadrupole moments in Fig. 1.

These calculated values show good agreement with the experimental values, although the calculated value of the magnetic moment of  ${}^8\text{Li}$ , 0.956, is smaller than the experimental value, 1.65. We suppose that this disagreement occurs because the spin wave function had no variational parameter in this work.

## References

- 1) A. B. Volkov: Nucl. Phys. **74**, 33 (1965); T. Ando, K. Ikeda, and A. Tohsaki-Suzuki: Prog. Theor. Phys. **64**, 1608 (1980).
- 2) N. Yamaguchi, T. Kasahara, S. Nagata, and Y. Akaishi: Prog. Theor. Phys. **62**, 1018 (1979); R. Tamagaki: Prog. Theor. Phys. **39**, 91 (1968).
- 3) P. Raghavan: At. Data Nucl. Data Tables **42**, 189 (1989).

\* Argonne National Laboratory, USA



The agreement of the experimental and the theoretical  $\log(ft)$  values suggests that the breaking of the  $N = 8$  magic number is realized in  $^{12}\text{Be}$ .

#### References

- 1) T. Suzuki and T. Otsuka: Phys. Rev. C **56**, 847 (1997).
- 2) Y. Abe, J. Hiura, and H. Tanaka: Prog. Theor. Phys. **49**, 800 (1973).
- 3) H. Furutani, H. Kanada, T. Kaneko, S. Nagata, H. Nishioka, S. Okabe, S. Saito, T. Sakuda, and M. Seya: Prog. Theor. Phys. Suppl. **68**, 193 (1980).
- 4) M. Seya, M. Kohno, and S. Nagata: Prog. Theor. Phys. **65**, 204 (1981).
- 5) N. Itagaki and S. Okabe: to be published in Phys. Rev. C.

# Model-Independent Analysis of the One-Body Density of Unstable Nuclei

A. Kohama, S. Yamaji, R. Seki,\* and A. Arima

[Unstable nuclei, Matter distribution, Proton-nucleus elastic scattering]

We have analyzed the matter distribution of unstable nuclei model-independently based on the experimental data of proton-unstable-nucleus elastic scattering. We applied the method of Friar and Negele.<sup>1)</sup> This method was originally proposed to determine the charge distributions of stable nuclei.

Since the first observation,<sup>2)</sup> the reaction cross sections of neutron-rich light nuclei have been found to be quite large. This suggests an extended structure of the neutron-rich nuclei; information concerning the one-body matter distribution is indispensable to prove this hypothesis.

In the formulation of Friar and Negele, the one-body density,  $\rho(\mathbf{r})$ , is expanded in terms of the Fourier-Bessel series. No assumption is made concerning the form of the density. The expansion coefficients are determined by minimizing  $\chi^2$ , defined as

$$\chi^2 = \sum_{\alpha=1}^N \frac{1}{\epsilon_{\alpha}^2} \left( \frac{\sigma_{\alpha}^{\text{exp}}}{d\Omega} - \frac{\sigma_{\alpha}^{\text{th}}}{d\Omega} \right)^2.$$

Here,  $N$  is the number of data points, and  $\epsilon_{\alpha}$  is the error of each data point. The superscript “exp” of the cross section implies the experimental data, and “th” implies the theoretically obtained value. We use

the expression of the first-order optical potential in the Glauber approximation for the theoretical cross section in this work. It includes the one-body density explicitly.<sup>3)</sup>

Detailed numerical calculations are in progress. We simply point out that the previous work on the determination of the matter distribution of  ${}^6\text{He}$  and  ${}^8\text{He}$ <sup>4)</sup> may still be too naive.<sup>5)</sup> The authors first assume the function form of the density, and then make a parameter-fit using the experimental data. By assuming the function form, theoretical prejudice could be brought into the analysis, which is not a good way to treat this kind of problem. Presently, the available data do not give the density with sufficient accuracy in our formulation.

## References

- 1) J. L. Friar and J. W. Negele: *Adv. Nucl. Phys.* **8**, 219 (1975).
- 2) I. Tanihata et al.: *Phys. Lett. B* **160**, 380 (1985).
- 3) A. Kohama, S. Yamaji, R. Seki, and A. Arima: in preparation.
- 4) G. D. Alkharov et al.: *Phys. Rev. Lett.* **78**, 2313 (1997).
- 5) R. Seki and I. Tanihata: preprint (1999).

---

\* Department of Physics and Astronomy, California State University, Northridge, and W. K. Kellogg Radiation Laboratory, Caltech, USA

# Development of a New Code for Large-Scale Shell-Model Calculations Using a Parallel Computer

T. Mizusaki

[Shell model, Parallel computation]

The nuclear shell model is a fundamental framework for describing interacting nucleons. Therefore, many efforts have been devoted to solve the shell-model problem. Among these efforts, a numerical approach is quite important, especially for *realistic* shell-model calculations. Due to the recent rapid progress of computer technology, several numerical methods<sup>1,2)</sup> are being advocated, and can, indeed, come over the limitation of the conventional shell-model diagonalization in many respects. However, up to now, only a shell-model diagonalization method can grant an *exact* (not approximate) solution in the case where a shell-model calculation is possible.<sup>†</sup> Therefore, shell-model diagonalization still keeps its unique value in a nuclear spectroscopic study. In addition, shell-model diagonalization, itself, can also be further developed by the use of modern computational technology.

In this paper, we present the current largest shell-model calculations based on a new shell-model code with a massively parallel computer, called Alphleet.<sup>‡</sup> Alphleet was originally designed for Monte-Carlo shell-model (MCSM)<sup>1)</sup> calculations. In the MCSM, the numerical intensive part is an angular-momentum projection, performed by three-fold integration over the Euler angles. The strategy of parallel computation is division concerning the Euler angles. This parallelization is quite easy and its efficiency is quite high. On the other hand, efficient parallelization of shell-model diagonalization is difficult because it requires a quite huge amount of numerical data. In the distributed memory system, huge data transfer among CPU's is inevitable. By developing an algorithm which minimizes the data-transfer during shell-model diagonalization, a new shell-model code on such a distributed memory system becomes efficient. For instance, by 24 CPU's, we can solve the shell-model problem with 0.1 billion dimension. In this case, one Lanczos iteration requires about 6600 seconds. Then, a converged solution can be obtained within few days. The computational time will be further shortened by using a larger number of CPU's.

In Fig. 1, we show the pf-shell calculations of

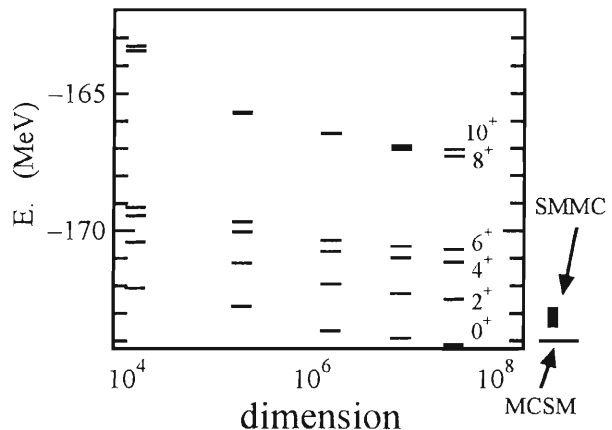


Fig. 1. Yrast energy levels in  $^{54}\text{Fe}$  as a function of the dimension.

$^{54}\text{Fe}$  with the FPD6 interaction for  $0^+ - 10^+$ , as an example. The energy eigenvalues are shown as a function of the dimension of the truncated shell-model space, defined by  $\oplus_{s \leq t} (f_{7/2})^{A-40-s} (r)^s$ , where  $r$  means the  $f_{5/2}$ ,  $p_{3/2}$  and  $p_{1/2}$  orbits and  $t$  is the maximum number of particle allowed to be excited. The dimension is counted for  $J_z = 0$  space. The results of SMMC and QMCD methods for the ground-state are also added as a reference. As the truncation space becomes larger, the eigenvalues converge. Consequently, such a large-scale shell-model calculations are shown to be quite useful for the yrast spectroscopy of the pf shell region.

In summary, a new shell-model code has been developed, which is well optimized for massively parallel computers. By this code, shell-model calculations with over 0.1 billion dimension become possible, and the realm of full pf-shell calculations becomes enlarged.

## References

- 1) M. Honma, T. Mizusaki, and T. Otsuka: Phys. Rev. Lett. **75**, 1284 (1995).
- 2) S. E. Koonin, D. J. Dean, and K. Langanke: Phys. Rep. **577**, 1 (1996).

<sup>†</sup> In the SMMC method, a notorious minus sign problem induces a large error bar for the ground-state energy, as shown in Fig. 1. In the MCSM method, its energy is quite precise, but is still variational upper limit

<sup>‡</sup> Alphleet is a customized parallel computer in the RI Beam Factory in RIKEN

# Monte Carlo Shell-Model Study of Unstable Nuclei Around $N = 20^\dagger$

Y. Utsuno, T. Otsuka, T. Mizusaki, and M. Honma

[NUCLEAR STRUCTURE shell model, Shell gap]

The  $N = 20$  closed-shell structure is known experimentally to disappear in the neutron-rich region, for instance, by the  $2_1^+$  level<sup>1)</sup> and the large  $B(E2; 0_1^+ \rightarrow 2_1^+)$  value<sup>2)</sup> of  $^{32}\text{Mg}$ . The aim of this study was to clarify the mechanism of the vanishing shell gap in terms of the shell model. Because the shell-model dimension is too large to diagonalize the shell-model Hamiltonian exactly, we adopted the Monte Carlo shell-model calculation.<sup>3)</sup> Since it is desirable to make a systematic calculation in this region to examine the mechanism, we performed shell-model calculations, in a single framework, for even-even nuclei from O to Si. The computations were carried out mainly using the Alphleet computer system at RIKEN.

Figure 1 shows the number of neutrons excited from the  $sd$  shell to the  $pf$  shell for the ground states of Ne, Mg, and Si isotopes. Particle-hole excitation occurs considerably around  $N = 20$  for Ne ( $Z = 10$ ) and Mg ( $Z = 12$ ) isotopes, while the ground state of Si ( $Z = 14$ ) primarily consists of the normal configuration. We note that the calculated states successfully reproduce the energy levels and the  $B(E2)$  values.

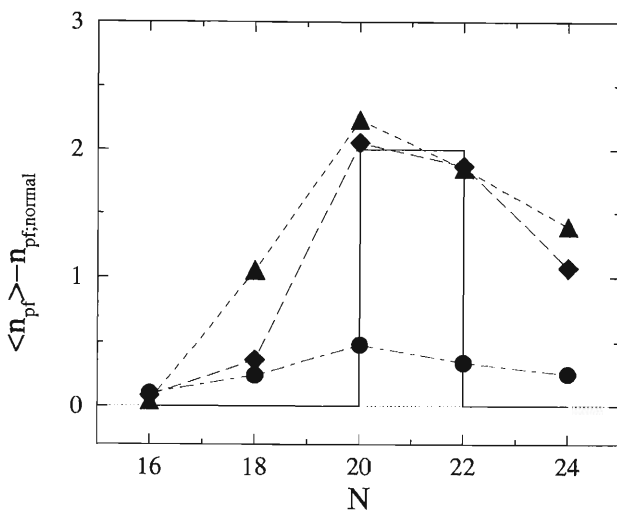


Fig. 1. Average number of neutrons in the  $pf$  shell subtracted by the corresponding number in the normal (i.e., filling) configuration. The triangles, diamonds, and circles stand for the values of the Ne, Mg, and Si isotopes, respectively. The solid line denotes the corresponding value of the Na and Mg isotopes, as predicted by the “island of inversion” of Ref. 4.

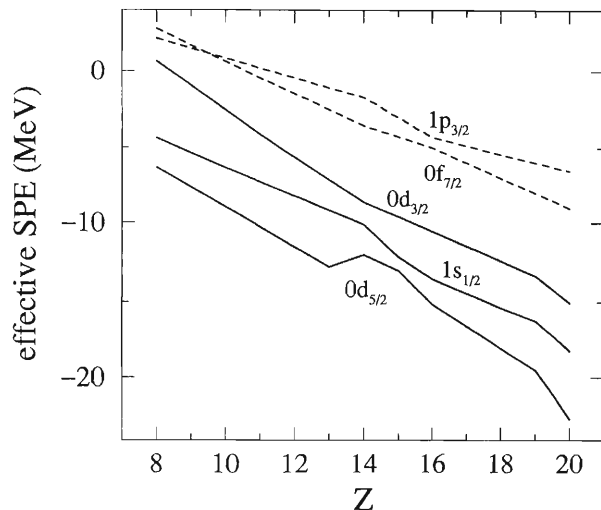


Fig. 2. Effective neutron single-particle energies for  $N = 20$  isotones as a function of the proton number.

In order to analyze the result, the effective single-particle energy (SPE) is very useful. Assuming the normal configuration for  $N = 20$  nuclei, we define the effective SPE of a given orbit as the one-neutron separation energy from this orbit, and then the energy is evaluated by the monopole interaction of the shell-model Hamiltonian. From Fig. 2, it can be seen that the shell gap between  $0d_{3/2}$  and  $0f_{7/2}$  becomes wider as  $Z$  increases, whereas the gap is quite small for Ne and Mg isotopes. This occurs because the strong proton-neutron monopole interaction within the same major shell ( $sd$  shell) stabilizes the  $N = 20$  shell closure.

We suggest that the narrow gap between the  $sd$  and  $pf$  shells is a cause of a vanishing of the closed-shell structure in the neutron-rich Ne and Mg isotopes, together with a preference for a prolate deformation of these isotopes.

## References

- 1) D. Guillemaud-Mueller et al.: Nucl. Phys. A **426**, 37 (1984).
- 2) T. Motobayashi et al.: Phys. Lett. B **346**, 9 (1995).
- 3) T. Otsuka, M. Honma, T. Mizusaki: Phys. Rev. Lett. **81**, 1588 (1998) and references therein.
- 4) E. K. Warburton, J. A. Becker, and B. A. Brown: Phys. Rev. C **41**, 1147 (1990).

<sup>†</sup> Condensed from the article in Phys. Rev. C **60**, 054315 (1999)

# A Search for a Unified Effective Interaction for Monte Carlo Shell-Model Calculations

M. Honma, B. A. Brown,\* T. Mizusaki, and T. Otsuka

[Shell model, Effective interaction]

The nuclear shell model has been successful as one of the most fundamental models of nuclei. It has been demonstrated by p- and sd-shell calculations that, once a suitable effective interaction is found, the shell model can describe various nuclear properties both accurately and systematically in the whole major shell. In such cases, the shell model acquires predictive power; one can see an indication of new physics in any possible deviation of new experimental data from shell-model predictions. For such systematic studies, it is crucially important to find a *reliable* effective interaction which can properly reproduce the variation of the nuclear structure over a wide mass-range.

On the other hand, the conventional shell-model diagonalization in a complete one-major-shell has been possible only up to the sd-shell, since the dimension of the Hamiltonian matrix becomes too large to diagonalize for larger shells. In order to overcome this difficulty, we have proposed the Monte-Carlo shell model (MCSM)<sup>1)</sup> based on the quantum Monte-Carlo diagonalization (QMCD) method. In MCSM calculations, basis states are generated stochastically, and are either adopted or discarded according to its importance for the energy gain. The Hamiltonian matrix is then diagonalized in a subspace spanned by these small number of selected basis states. By using MCSM we can carry out shell-model calculations in the pf- and larger shells with reasonable accuracy.

For the pf-shell nuclei, various effective interactions have been investigated. For example, the KB<sup>2)</sup> interaction has been constructed on the basis of the G-matrix derived from an NN-potential. However, for quantitative studies, such a realistic interaction requires sizable empirical corrections to its monopole part. The monopole-modified G-matrix interaction (KB3)<sup>3)</sup> has been found to be successful in the lighter half of the pf-shell ( $A \leq 52$ ). However, the KB3 interaction is dangerous to use beyond <sup>56</sup>Ni, because of its too-large shell gap above the  $f_{7/2}$  orbit. A different strategy is taken for the FPD6<sup>4)</sup> interaction, where an analytic form of the two-body potential, which contains several parameters, is assumed; these parameters are determined by a fit to the experimental data of  $A = 41$ – $49$  nuclei. The FPD6 interaction is quite successful for describing heavier pf-shell nuclei, such as <sup>64</sup>Ge and <sup>56</sup>Ni. The difficulty of the FPD6 interaction is found in the single-particle properties (a too-low  $f_{5/2}$  orbit),

which can typically be seen in <sup>57</sup>Ni. There are several other effective interactions for pf-shell nuclei, which have been evaluated with a certain truncation of the model space.

However, such a truncation restricts the applicability and predictive power of the shell model to several limited cases. Thus, it is a quite challenging problem to investigate whether it is possible to construct a *unified* shell-model effective interaction for pf- and larger shells which can describe various nuclear properties systematically over a wide model space, including both the beginning and the middle of the shell. MCSM enables us to study such a problem. Since MCSM utilizes general deformed bases, we can consider the whole model space without any truncation.

We can approach to this problem by a “model-independent” method, in which two-body matrix elements and single-particle energies are treated as parameters, and are determined by a least-squares fit to the experimental binding energies and the excitation energies. This technique was successfully applied to the sd-shell, leading to success concerning the USD interaction.<sup>5)</sup> In the USD interaction, 63 two-body matrix elements and 3 single-particle energies were fixed in a fit to 447 energy data with an rms deviation of 185 keV. Practically, the 47 best-determined linear combinations of parameters were determined in a fit, and for the remaining 19 linear combinations the corresponding values of the G-matrix interaction were used.

In the case of the pf-shell, 195 two-body matrix elements and 4 single-particle energies should be determined. Although the number of parameters becomes about 3-times larger than that of the sd-shell, this method is still applicable if we can take a sufficiently large number of data. The shell-model calculations were carried out by a massive parallel machine, Alphleet, at RIKEN. By taking 742 energy data we have obtained a fit with an rms deviation 254 keV. We are now searching for a better set of parameters by changing the data selection and the number of linear combinations to be determined by a fit.

## References

- 1) T. Otsuka et al.: Phys. Rev. Lett. **81**, 1588 (1998).
- 2) T. T. S. Kuo et al.: Nucl. Phys. A **114**, 241 (1968).
- 3) A. Poves et al.: Phys. Rep. **70**, 235 (1981).
- 4) W. A. Richter et al.: Nucl. Phys. A **523**, 325 (1991).
- 5) B. A. Brown et al.: Ann. Rev. Nucl. Part. Sci. **38**, 29 (1988).

---

\* Michigan State University, USA

# Monte Carlo Shell-Model Calculations for Medium-Heavy Nuclei

N. Shimizu, T. Otsuka, T. Mizusaki, and M. Honma

[Shell model, Nuclear structure, Collective motion, Computational physics]

It is known that a part of the even-even nuclei around the rare-earth region shows a shape-phase transition, which is nothing but a gradual variation in the spherical-deformed change of the nuclear shape with increasing neutron number. The properties of these nuclei have been well studied using the Interacting Boson Model (ex. see Ref. 1). The purpose of this report is to discuss this intriguing structure change by utilizing a nuclear-shell-model description involving fermions, not bosons.

We have focused on  $^{138-150}\text{Ba}$  isotopes, which are among the above-mentioned nuclei. The single-particle states of the nuclear shell model consists of  $N = 82-132$  and  $Z = 50-82$ . The effective interaction which we have used consists of the pairing-type, quadrupole-pairing-type and quadrupole-quadrupole-type interactions whose parameters were fitted for the excitation levels of semi-magic nuclei, except for the proton-neutron quadrupole-quadrupole interaction. We restricted the shell-model Hilbert space to that with an axially symmetric deformation, which is considered to be a good approximation for these nuclei. Since Hilbert space is too huge to use the conventional shell-model diagonalization method, we have used the Monte-Carlo Shell Model method, which was recently developed by M. Honma *et al.*<sup>2)</sup> in order to overcome such a difficulty. In addition, we revised the method so as to utilize pair-bases.

Figure 1 shows a comparison between the experimental values and the MCSM results for the  $2^+$ ,  $4^+$ ,  $6^+$ ,  $8^+$ ,  $10^+$  levels of Ba isotopes. The experimental

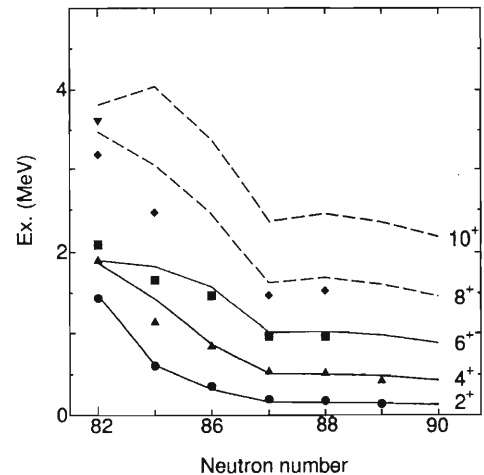


Fig. 1. Energy levels of Ba isotopes. The symbols and lines denote the experimental values and theoretical results, respectively.

energy levels show transition from vibrational nuclei (left-hand side) to rotational nuclei (right-hand side). We can see that the theoretical results reproduce such a character quite well.

These computations have been carried out mainly using the Alphleet computer system at RIKEN.

## References

- 1) O. Scholten: Phys. Rev. C **28**, 1783 (1983).
- 2) T. Otsuka, M. Honma, and T. Mizusaki: Phys. Rev. Lett. **81**, 1588 (1998) and references therein.

# The Nucleon Pair Approximation of the Shell Model

Y. M. Zhao, S. Yamaji, N. Yoshinaga, and A. Arima

[Nucleon pair approximation, Shell model, Collective excitations]

We have completed a series of studies<sup>1-4)</sup> on the nucleon pair approximation of the shell model.<sup>5)</sup>

Firstly, the validity of the *SD*-pair truncation of the shell model was tested in a single-*j* shell and many-*j* shells within the framework of the nucleon pair shell model. It has been found that *SD*-pair truncation is a good approximation of the shell model in the single-*j* case when the Hamiltonian consists of (monopole and quadrupole) pairing plus quadrupole-type interactions. The *SD*-pair truncation deteriorates if the QQ-type interaction is artificially large compared with the monopole pairing interaction. For multi-*j* shells, schematic calculations in the degenerate *sd*, *pf*, and *sdg* shells were performed for the extreme case of a pure QQ-type interaction. There is a large difference between the binding energies in the *SD*-pair truncated subspace and those calculated in the full shell-model space, as in the case of a single-*j* shell. However, it has been found that the basic properties of the band structure remain intact, and that the difference in the energy levels, i.e., moments of inertia, can be easily absorbed by adjusting the interaction strengths.

Secondly, calculations using the nucleon-pair shell model were performed in terms of the *SD* collective pairs, which were obtained in a suitable way to obtain the maximum collectivity. This method was applied to even-even Sn, Te, Xe, Ba, and Ce isotopes near the  $A = 130$  region using the (monopole and quadrupole) pairing plus quadrupole-type interactions by adjusting a very few parameters. The structure of the energy levels for the quasi gamma band as well as the ground band has been well reproduced for each nucleus. Other properties, such as  $B(E2)$ 's, agree with the experimental data very well. The calculated nuclear radii are well consistent with the relativistic mean-field calculation. The overall fit with the experimental data is superior to that of the previous calculations.

Thirdly, we investigated the role of the single-particle energies on the low-lying states of  $^{132}\text{Ba}$ , a typical  $O(6)$  nucleus in the IBM and the FDSM. It has been found that one can usually "restore" the physics of a realistic problem with non-degenerate single-particle energies using degenerate single particle levels and a slightly different parametrization of the two-body interaction. However, if the single-particle

splittings are enlarged by a factor of 1.5, the  $O(6)$  behavior of the nucleus is lost and a model that assumes degenerate levels cannot describe its collective structure. The contributions from interactions other than monopole and quadrupole pairing and quadrupole-quadrupole interactions have been found to be unimportant for the low-lying states. Although the role of the abnormal parity level depends on the details of the single-particle structure, its effects can be "compensated" by using different Hamiltonian parameters and degenerate single-particle levels in the FDSM treatment.

Fourthly, the Wick theorem for coupled Fermion clusters has been used to derive the nucleon-pair approximation for an odd nucleus. The building blocks of the model space were constructed using one unpaired valence nucleon coupled with the collective nucleon pairs stepwisely. Analytical expressions for the related commutators were derived, and formulas were given for the matrix elements of a general Hamiltonian. The formalism for an odd system was presented in a similarly recursive way as the even system. By treating the two-body interaction as an integrated operator in the re-arrangement of the operators before computing the related commutators, the computing time of a general two-body interaction matrix elements is comparable to that of the one-body interaction matrix elements, which is crucial for the nucleon pair approximation of an odd system to be realizable. This formalism unifies the analytical expressions of the Hamiltonian for an even system and an odd system (including odd-even, even-odd, and doubly odd cases). We call this "the unified formalism for even and odd systems".

## References

- 1) Y. M. Zhao, N. Yoshinaga, S. Yamaji, and A. Arima: Phys. Rev. C, to be published.
- 2) Y. M. Zhao, S. Yamaji, N. Yoshinaga, and A. Arima: Phys. Rev. C, to be published; RIKEN Accel. Prog. Rep. **32**, 18 (1999).
- 3) Y. M. Zhao, N. Yoshinaga, S. Yamaji, and A. Arima: Phys. Rev. C, to be published.
- 4) Y. M. Zhao, N. Yoshinaga, S. Yamaji, J. Q. Chen, and A. Arima: Phys. Rev. C, to be published.
- 5) J. Q. Chen: Nucl. Phys. A **626**, 686 (1997).

# Effects of the Dirac Sea on the Giant Monopole States

H. Kurasawa\* and T. Suzuki

[Relativistic model, Effects of the Dirac sea, Giant resonance states]

The relativistic mean-field approximation (RMFA) neglects the Dirac sea in describing the nuclear ground state. Recently, however, it has been numerically shown that in a relativistic random-phase approximation (RRPA) built on RMFA, the monopole states cannot be well described without Pauli blocking terms, which express transitions between the Dirac sea and the occupied Fermi sea.<sup>1)</sup> If the blocking terms are neglected, the excitation energies of the monopole states in RRPA are much lower than those in the time-dependent relativistic mean-field approximation.<sup>2)</sup>

We show in an analytic way the role of the Dirac sea in the excitation energy of the monopole states. In the relativistic model, the excitation energy of the monopole states is expressed as<sup>3)</sup>

$$E_M = \left( \frac{K}{\epsilon_F \langle r^2 \rangle} \right)^{1/2}, \quad (1)$$

where  $\epsilon_F$  denotes the Fermi energy and  $\langle r^2 \rangle$  the root-mean-square radius of the nucleus. The incompressibility coefficient,  $K$ , is expressed in terms of the relativistic Landau-Migdal parameters,  $F_0$  and  $F_1$ , as

$$K = \frac{3p_F^2}{\epsilon_F} \frac{1 + F_0}{1 + \frac{1}{3}F_1}, \quad (2)$$

$p_F$  being the Fermi momentum.

In order to see the effects of the Pauli blocking terms on the monopole states, we derive the Landau-Migdal parameters according to RRPA. We calculate the longitudinal RRPA correlation functions with and without the Pauli blocking terms.<sup>4)</sup> By comparing them with the correlation function of the Landau theory, we can obtain the expressions of the Landau-Migdal parameters in each approximation.

Including the Pauli blocking terms, we obtain

$$F_0 = F_V - \frac{1 - v_F^2}{1 + a_s F_s} F_s, \quad F_1 = -\frac{v_F^2 F_V}{1 + \frac{1}{3}v_F^2 F_V}, \quad (3)$$

where we have defined

$$F_s = N_F \left( \frac{g_s}{m_s} \right)^2, \quad F_V = N_F \left( \frac{g_V}{m_V} \right)^2, \quad (4)$$

$$N_F = \frac{2p_F E_F}{\pi^2}, \quad v_F = \frac{p_F}{E_F},$$

$$E_F = (p_F^2 + M^{*2})^{1/2}. \quad (5)$$

In the above equations,  $g_s$  and  $g_V$  stand for the Yukawa coupling constants,  $m_s$  and  $m_V$  the masses of the  $\sigma$ -

and  $\omega$ -meson, respectively, and  $M^*$  denotes the effective nucleon mass.  $N_F$  and  $v_F$  represent the relativistic density of states at the Fermi surface and the relativistic Fermi velocity. The factor  $a_s$ , in  $F_0$  of Eq. (3), is given by

$$a_s F_s = \frac{4}{(2\pi)^3} \left( \frac{g_s}{m_s} \right)^2 \int d^3p \frac{\mathbf{p}^2}{E_p^3} \theta_p, \quad (6)$$

$$E_p = (p^2 + M^{*2})^{1/2},$$

where  $\theta_p$  denotes the step function,  $\theta(p_F - |\mathbf{p}|)$ .

If we neglect the Pauli blocking terms, we obtain the Landau-Migdal parameters as

$$F_0 = F_V - (1 - v_F^2) F_s, \quad F_1 = -v_F^2 F_V. \quad (7)$$

The difference between Eqs. (3) and (7) is very clear.  $F_0$  and  $F_1$  in Eq. (7) have no denominator. In fact, we can show that the Landau-Migdal parameters in Eq. (3) are those from the second derivative of the total energy density with respect to the quasiparticle distribution. In order to obtain correct expressions of  $F_0$  and  $F_1$  within RMFA, we thus need to include the Pauli blocking terms in the configuration space of RRPA.

The values of  $K$  were calculated using the following parameters<sup>5)</sup> as an example:

$$M = 939, \quad m_s = 520, \quad m_V = 783 \text{ (MeV)},$$

$$g_s^2 = 109.626, \quad g_V^2 = 190.431, \quad (8)$$

which reproduce the nucleon binding energy,  $E_B = -15.75$  MeV, at  $p_F = 1.30 \text{ fm}^{-1}$ . In this case, we have  $K = 544$  MeV by taking the Pauli blocking terms into account, and  $K = 357$  MeV by neglecting them. Thus, the value of  $K$  is fairly reduced, if the Pauli blocking terms are neglected. In  $^{208}\text{Pb}$ , the reduction amounts to about 2.7 MeV for the present parameters. This fact may be observed in Ref. 1 by numerical calculations.

## References

- 1) N. V. Giai and Z. Ma: RIKEN Rev., No. 23, p. 69 (1999).
- 2) D. Vretenar, H. Berghammer, and P. Ring: Nucl. Phys. A **581**, 679 (1995).
- 3) S. Nishizaki, H. Kurasawa, and T. Suzuki: Nucl. Phys. A **462**, 687 (1987).
- 4) H. Kurasawa and T. Suzuki: Nucl. Phys. A **445**, 685 (1985).
- 5) C. J. Horowitz and B. D. Serot: Nucl. Phys. A **368**, 503 (1981).

\* Faculty of Science, Chiba University

## The Phonon Damping Model

N. Dinh Dang, K. Tanabe, and A. Arima

[Hot giant dipole resonance, Double and triple giant dipole resonances, Damping, Exotic nuclei]

The Phonon Damping Model (PDM) was proposed by Dinh Dang and Arima in 1998<sup>1)</sup> as PDM-1. Its further development, which includes all configuration mixings up to two-phonon configurations, has been carried out by Dinh Dang, Tanabe, and Arima (PDM-2).<sup>2)</sup> The primary purpose of PDM is to describe the damping of the giant dipole resonance (GDR) in highly excited (hot) nuclei. This model has shown that the main mechanism that causes a sharp increase in the GDR width at low temperatures,  $T \leq 3$  MeV, and its saturation at high temperatures,  $T > 3-4$  MeV, is coupling of the GDR phonon to the particle-particle ( $pp$ ) and hole-hole ( $hh$ ) configurations, which appear due to the deformation of the Fermi surface at  $T \neq 0$ . In PDM, a model Hamiltonian including coupling between the GDR phonon to all  $ph$ ,  $pp$ , and  $hh$  configurations at  $T \neq 0$  is used, and the strength function is calculated directly in the laboratory frame without any need for an explicit inclusion of the thermal fluctuations of shapes or the angular-momentum effect. The PDM has been proved to be quite successful in reproducing not only the the width, but also experimentally observed shapes of hot GDR in  $^{120}\text{Sn}$  and  $^{208}\text{Pb}$ .

Very recently, in order to test the capability of PDM, we have further developed and applied it to:

(1) A statistical analysis of the shape evolution of hot GDR in  $^{120}\text{Sn}$ ,<sup>3)</sup>

(2) A study of multiphonon GDRs, especially double and triple GDRs in heavy nuclei;<sup>4)</sup>

(3) A study of damping of GDR in neutron-rich nuclei.<sup>5)</sup>

Our analysis of numerical calculations has shown that:

(1) The GDR shapes predicted by the PDM strength functions in combination with the calculations<sup>3)</sup> are in overall reasonable agreement with the data from inelastic  $\alpha$ -scattering experiments;

(2) PDM can account reasonably well for the damping of double and triple GDRs, where a noticeable difference in the damping of the DGDRs in open-shell and double magic nuclei has been pointed out;<sup>4,6)</sup>

(3) PDM is able to describe the damping of GDR in exotic nuclei. In particular, it shows the appearance of a low-lying dipole mode in neutron-rich nuclei, like  $^{18,24}\text{O}$ ,  $^{60}\text{Ca}$ , and  $^{150}\text{Sn}$ .<sup>5)</sup>

### References

- 1) N. Dinh Dang and A. Arima: Phys. Rev. Lett. **80**, 4145 (1998); Nucl. Phys. A **636**, 427 (1998).
- 2) N. Dinh Dang, K. Tanabe, and A. Arima: Phys. Rev. C **58**, 3374 (1998); Nucl. Phys. A **645**, 536 (1999).
- 3) N. Dinh Dang, K. Eiseman, J. Seitz, and M. Thoennessen: Phys. Rev. C **61**, 027302 (2000).
- 4) N. Dinh Dang, K. Tanabe, and A. Arima: RIKEN-AF-NP-325 (1999).
- 5) N. Dinh Dang, T. Suzuki, and A. Arima: RIKEN-AF-NP-331 (1999).
- 6) N. Dinh Dang, K. Tanabe, and A. Arima: Phys. Rev. C **59**, 3128 (1999).

# Statistical Analysis of the Hot Giant Dipole Resonance with the Phonon Damping Model

N. Dinh Dang, K. Eisenman,\* J. Seitz,\* and M. Thoennessen\*

[Giant resonances, Thermal and statistical models]

The comparison between theory and experimental data of the hot GDR is not straightforward. Typically, only the parameters of a Lorentzian strength

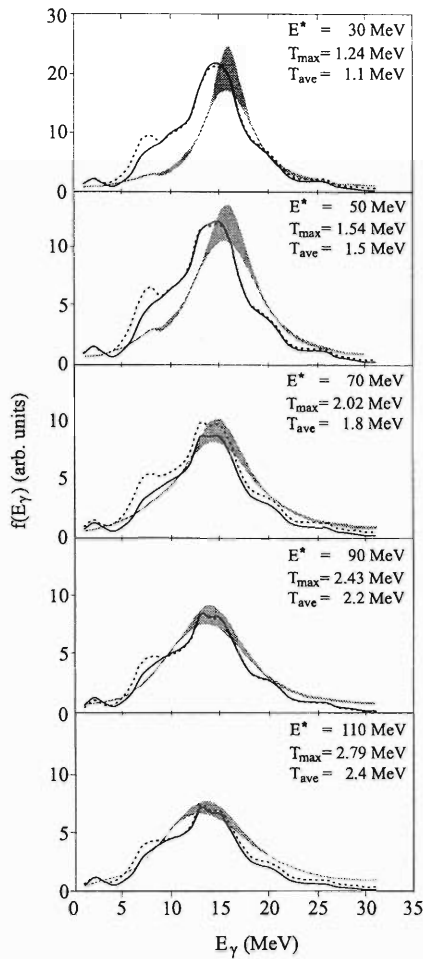


Fig. 1. Experimental (shade areas) and theoretical divided spectra calculated within the CASCADE without pairing (dashed curves) and including pairing (solid curves) at various excitation energies.

function (resonance energy, width and strength) are extracted from the data and compared to the theoretical values. In addition, the conversion of the experimentally measured excitation energy to the temperature which is calculated within theoretical models is difficult and sometimes can even be misleading as has been recently discussed.<sup>1,2)</sup> Although the importance of including the temperature dependence of the GDR parameters in the statistical model calculations was pointed out a long time ago, it was not crucial as long as the data were not compared to detailed models, but only fitted to extract a functional form of the width increase. Recently, a method has been proposed to incorporate the theoretical strength functions directly into full statistical decay calculations.<sup>2)</sup> This way, not only the GDR energy and width, but also the entire shape of the GDR strength functions, can be compared with the measured spectra. In this work, we have applied this method to the strength functions of the hot GDR obtained within the PDM.<sup>3)</sup>

The strength functions of the hot giant dipole resonance (GDR) in  $^{120}\text{Sn}$ , obtained within the phonon damping model (PDM), have been included in complete statistical CASCADE calculations and compared with their experimental divided spectra as a function of the temperature,  $T$ . The entire experimental shape of the hot GDR can be reproduced reasonably well using the PDM strength functions. The effect of superfluid pairing at  $T < 1$  MeV is important to obtain better agreement between theory and the experimental data (Fig. 1).

## References

- 1) M. P. Kelly, K. A. Snover, J. P. S. van Schagen, M. Kicinska-Habior, and Z. Trznadel: *Phys. Rev. Lett.* **82**, 3404 (1999).
- 2) G. Gervais, M. Thoennessen, and W. E. Ormand: *Phys. Rev. C* **58**, 1377R (1998).
- 3) N. Dinh Dang and A. Arima: *Phys. Rev. Lett.* **80**, 4145 (1998); *Nucl. Phys. A* **636**, 443 (1998).

\* National Superconducting Cyclotron Laboratory, Michigan State University, USA

# Hot Giant Dipole Resonance in the Static Path Approximation

A. Ansari,\* N. Dinh Dang, and A. Arima

[Static path approximation, Giant dipole resonances, Thermal fluctuations of shapes]

The effects of the thermal fluctuations of nuclear shapes on the damping of the hot giant dipole resonance (GDR) have been the subjects of a number of recent studies. These effects have usually been incorporated so far by averaging the  $\gamma$ -absorption cross section,  $\sigma(E_\gamma)$ , over all possible quadrupole shapes using a Boltzmann weight factor,  $e^{-F/T}$ , where  $F$  is the free energy, which depends on the quadrupole deformation parameters,  $\beta$  and  $\gamma$ , and temperature,  $T$ . In the calculations of Ref. 1 the dipole strength function is computed by a simple deformed harmonic-oscillator (HO) model. At the same time, for thermal averaging, a free energy is used corresponding to the macroscopic-microscopic Strutinsky shell correction approach in combination with a parametrized expansion following the macroscopic Landau theory of phase transitions. Hence, a particular specific Hamiltonian has not been employed to calculate every quantity, such as the GDR strength function. On the other hand, the thermal averaging can be performed in a consistent manner following the static path approximation (SPA)<sup>2)</sup> for the grand canonical partition function using the same Hamiltonian. The SPA allows one to include the angular-momentum effects rather easily within the standard cranking approach. Thus, thermal averaged values,  $\langle\beta\rangle$  and  $\langle\gamma\rangle$ , can also be computed at given temperature and spin.

In this work, the GDR was calculated in  $^{120}\text{Sn}$  using the linear response theory incorporating the thermal shape fluctuations within SPA. This is the first application of such an approach to the GDR in a realistic nucleus at finite temperature and angular momentum. A model Hamiltonian with a quadrupole-quadrupole interaction was used. The obtained results show that the thermal fluctuations of quadrupole shapes increase

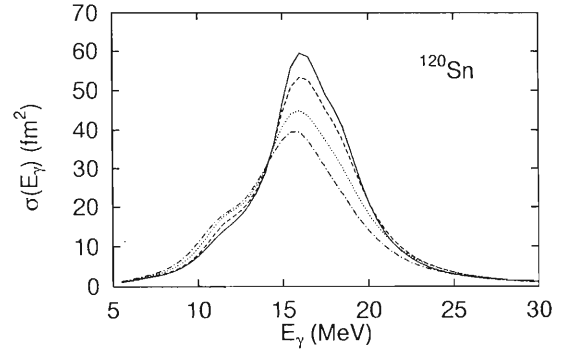


Fig. 1.  $\gamma$ -absorption cross section,  $\sigma(E_\gamma)$ , of the GDR in  $^{120}\text{Sn}$  at various angular momenta,  $J$ , and temperatures,  $T$ . The solid, dashed, dotted, and dash-dotted curves correspond to the results obtained at  $(T, J) = (0.4 \text{ MeV}, 5.24 \hbar)$ ,  $(1 \text{ MeV}, 7.1 \hbar)$ ,  $(2 \text{ MeV}, 13.5 \hbar)$ , and  $(3 \text{ MeV}, 18.9 \hbar)$ , respectively.

the GDR width by only 40% at  $T = 3 \text{ MeV}$ , compared to its value at  $T = 0$ . The effect of the angular momentum on the damping of the hot GDR is found to be negligible for this nucleus up to  $T \simeq 4 \text{ MeV}$  and  $J \simeq 80 \hbar$ . The combined effect of temperature and angular momentum leads to a GDR energy that is nearly independent of the excitation energy (Fig. 1).

## References

- 1) Y. Alhassid and B. Bush: Nucl. Phys. A **531**, 39 (1991); W. E. Ormand, P. F. Bortignon, R. A. Broglia, and A. Bracco: Nucl. Phys. A **614**, 217 (1997); D. Kuznesov, Y. Alhassid, and K. Snover: Phys. Rev. Lett. **81**, 542 (1998).
- 2) B. K. Agrawal, A. Ansari, and P. Ring: Nucl. Phys. A **615**, 183 (1997).

\* Institute of Physics, Bhubaneswar, India

# Damping of Multiphonon Giant Resonances

N. Dinh Dang, K. Tanabe, and A. Arima

[Multiphonon giant resonance, Strength function, Anharmonicity]

Recent observation of the double giant dipole resonances (DGDR) in relativistic heavy-ion reactions via the Coulomb excitation<sup>1)</sup> and pion-induced charge-exchange reactions<sup>2)</sup> has sparked intensive studies and hot debates on the issue of multiphonon excitations. The harmonic picture represents the  $n$ -phonon giant resonance as a result of folding  $n$  independent single resonances. The energy of an  $n$ -phonon dipole resonance would be exactly  $n$  times of the energy of the giant dipole resonance (GDR), each with a width  $\Gamma_{\text{GDR}}$ . Hence, the width of the  $n$ -phonon GDR would be equal to  $n\Gamma_{\text{GDR}}$ . If a Gaussian distribution is used instead of a Lorentzian to approximate the GDR, the width of the  $n$ -independent-phonon GDR becomes  $\sqrt{n}\Gamma_{\text{GDR}}$ . The data, however, have shown that there is a significant deviation from the harmonic picture of the DGDR. In a closed-shell nucleus ( $^{208}\text{Pb}$ ) this deviation is much smaller than that in an open-shell one ( $^{136}\text{Xe}$ ). In  $^{208}\text{Pb}$ , the cross section of the DGDR in the Coulomb excitation is about 33% larger than the value obtained by folding the cross sections of two independent GDRs (the folding results). In  $^{136}\text{Xe}$ , the cross section has been observed ( $215 \pm 32$  mb) to be strongly enhanced about 2–3 times compared to the folding results (70–87 mb). Since the harmonic picture neglects the coupling between the GDRs, the fundamental question is how large the anharmonicity is, or how strongly the coupling between GDR phonons makes the description of the multiphonon resonance deviate from the independent-phonon picture.

In this work, the phonon damping model (PDM)<sup>3)</sup> was applied to derive a set of equations that describe the damping of  $n$ -phonon giant resonances ( $n > 1$ ). As examples of the application of this approach, the results of numerical calculations for the double giant resonance (DGDR) ( $n = 2$ ) and triple giant dipole resonance (TGDR) ( $n = 3$ ) in  $^{90}\text{Zr}$ ,  $^{120}\text{Sn}$  and  $^{208}\text{Pb}$  are discussed and compared with the folding results. For the DGDR in the double magic nucleus  $^{208}\text{Pb}$ , we found that these results are very close to the folding results. In the open-shell nuclei  $^{90}\text{Zr}$  and  $^{120}\text{Sn}$ , a clear deviation from the folding results was obtained, in agreement with the experimental trend. The results for the integrated strength and energy of TGDR are found to be much closer to the folding results in all three nuclei

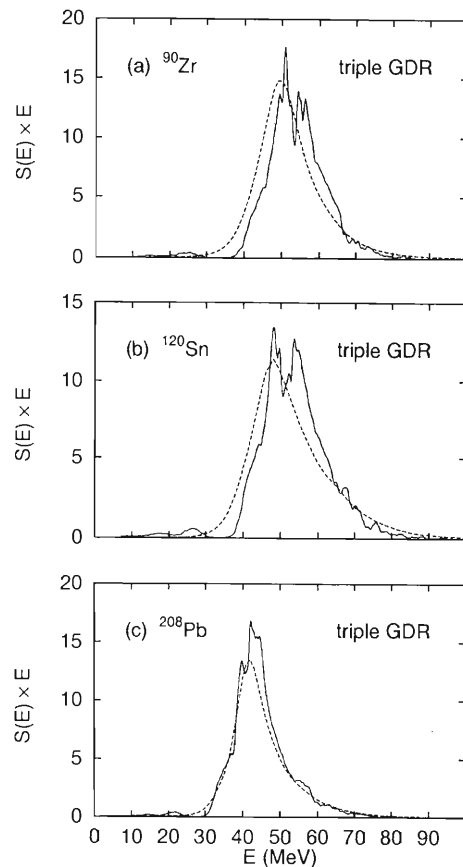


Fig. 1. Energy-weighted strength functions of the TGDR in  $^{90}\text{Zr}$  (a),  $^{120}\text{Sn}$  (b), and  $^{208}\text{Pb}$  (c). The solid curves are the results obtained within the PDM, while the dashed curves are the folding results.

(Fig. 1). The TGDR widths in the open-shell nuclei were found to be larger than the folding results. We also show that a small deviation of the two-phonon energy is sufficient to cause a noticeable change in the DGDR strength compared to the independent-phonon picture.

## References

- 1) H. Emling: Part. Prog. Nucl. Phys. **33**, 629 (1994); K. Boretzky et al.: Phys. Lett. B **384**, 30 (1996).
- 2) S. Mordechai et al.: Phys. Rev. Lett. **61**, 531 (1988).
- 3) N. Dinh Dang and A. Arima: Phys. Rev. Lett. **80**, 4145 (1998); Nucl. Phys. A **636**, 443 (1998).

## Giant Dipole Resonance in Neutron-Rich Nuclei within the Phonon Damping Model

N. Dinh Dang, T. Suzuki, and A. Arima

[Giant resonances, Pigmy resonance, Exotic nuclei, Thermal and statistical models]

When the binding energy approaches zero, coupling to the continuum becomes very important. Large gaps between the proton and neutron binding energies in exotic nuclei lead to a big difference in the neutron and proton level spacing. As a result, the distribution of the giant dipole resonance (GDR) in exotic nuclei becomes more fragmented. These are some common features of the GDR in exotic nuclei that have

been obtained in a number of theoretical calculations within the random-phase approximation,<sup>1)</sup> relativistic RPA,<sup>2)</sup> self-consistent Hartree-Fock plus RPA,<sup>3)</sup> and large-scale shell-model calculations.<sup>4)</sup> In these calculations, the damping of the GDR has not been explicitly calculated, but the strength distributions were just smeared out by a Lorentzian with a finite width. The question concerning the effect of damping of the GDR on the strength of the pigmy resonance in exotic nuclei still remains open.

In this work, the damping of the giant dipole resonance (GDR) in neutron-rich unstable nuclei  $^{18,24}\text{O}$ ,  $^{60}\text{Ca}$ , and  $^{150}\text{Sn}$  was calculated within the phonon damping model (PDM)<sup>5)</sup> and compared with those in stable isotopes:  $^{16}\text{O}$ ,  $^{40}\text{Ca}$ , and  $^{120}\text{Sn}$ . The Hartree-Fock single-particle energies obtained employing the SGII interaction were used in the calculations. The PDM parameter for the (particle-hole)-phonon interaction between the levels close to the Fermi surface in exotic nuclei was chosen to simulate the strong coupling between the GDR phonon and the dense incoherent particle-hole configurations. The results of the calculations show the appearance of a low-lying structure (pigmy resonance) in all neutron-rich nuclei under consideration. Figure 1 shows the difference between the GDRs in stable nuclei ( $^{40}\text{Ca}$  and  $^{120}\text{Sn}$ ) and those in unstable nuclei ( $^{60}\text{Ca}$  and  $^{150}\text{Sn}$ ) obtained within the PDM. The calculations at nonzero temperature show that the GDR in a hot medium and heavy neutron-rich nuclei exhibits a similar behavior to that of the hot GDR in stable nuclei. The pigmy resonance is smoothed out with increasing temperature.

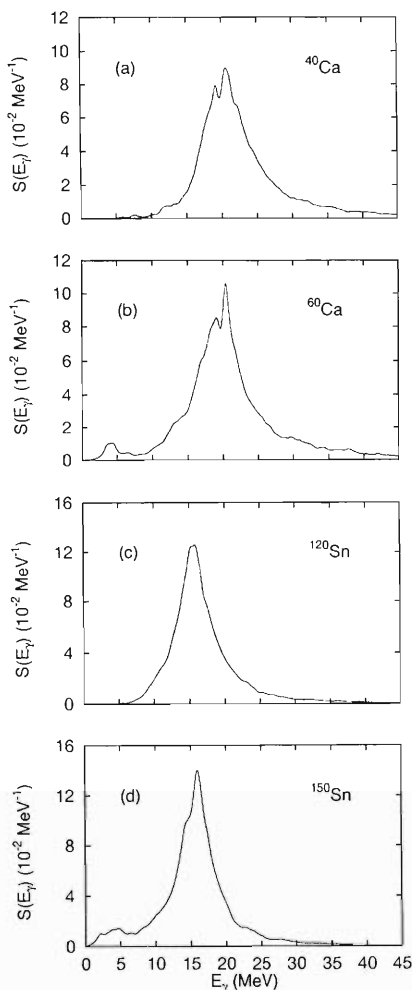


Fig. 1. GDR strength functions in  $^{40}\text{Ca}$  (a),  $^{60}\text{Ca}$  (b),  $^{120}\text{Sn}$  (c), and  $^{150}\text{Sn}$  (d).

### References

- 1) I. Hamamoto, H. Sagawa, and X. Z. Zhang: Phys. Rev. C **53**, 765 (1996); Phys. Rev. C **57**, R1064 (1998); P. G. Reinhard: Nucl. Phys. A **649**, 305c (1999).
- 2) Z. Ma, H. Toki, B. Chen, and N. Van Giai: Prog. Theor. Phys. **98**, 917 (1997).
- 3) E. G. Lanza: Nucl. Phys. A **649**, 344c (1999).
- 4) H. Sagawa and T. Suzuki: Phys. Rev. C **59**, 3116 (1999); T. Suzuki, H. Sagawa, and P. F. Bortignon: Nucl. Phys. A (2000), in press.
- 5) N. Dinh Dang and A. Arima: Phys. Rev. Lett. **80**, 4145 (1998); Nucl. Phys. A **636**, 443 (1998).

# Local Harmonic Approaches with Approximate Cranking Operators

T. Nakatsukasa, N. R. Walet,<sup>\*1</sup> and G. Do Dang<sup>\*2</sup>

[Collective models, Hartree-Fock, Random-phase approximations]

The selection of proper collective variables is an important problem in studying large-amplitude collective motion. In the usual Constrained Hartree-Fock (CHF) or Hartree-Fock-Bogoliubov (CHFB) calculations, the collective subspaces are generated by a small number of one-body constraint (also called cranking) operators, which are most commonly taken to be of the multipole form ( $r^L Y_{LK}$ ). In realistic calculations of processes such as fission, because the number of coordinates used to describe the full nuclear dynamics can easily become larger than can be dealt with in a satisfactory manner, a method to determine the optimal combination needs to be devised. Even assuming that such a method exists, there is no *a priori* reason to limit oneself to multipole operators, and the cranking operators should be determined by the nuclear collective dynamics, itself, from the set of all one-body operators. This is clearly a difficult task, and one would like to be able to select a small group of operators, and to find the optimal combination of these operators at each point of the collective surface.

In our past work, we investigated a theory of adiabatic large-amplitude collective motion as a method to generate self-consistent collective subspaces.<sup>1,2</sup> The key ingredient of the method is the self-consistent determination of the constraint operator; as such, it may provide an answer to the selection question discussed above. Using the local-harmonic version of the theory, the local-harmonic approximation (LHA), we have recently embarked on a study of the properties of large-amplitude collective motion in systems with pairing.<sup>2)</sup>

We would like to find the collective coordinate,  $q = q(\xi)$ , for a classical Hamiltonian in a large configuration space  $\{\xi^\alpha\}$ ,

$$H = \frac{1}{2} B^{\alpha\beta} \pi_\alpha \pi_\beta + V(\xi). \quad (1)$$

In LHA, the collective path (or collective surface for more than one coordinate) is determined by solving the CHFB problem with a cranking operator which is self-consistently determined by the local random-phase approximation (RPA). The usual RPA equation can be expressed by

$$V_{;\alpha\gamma} B^{\gamma\beta} q_{;\beta} = \omega^2 q_{;\alpha}, \quad (2)$$

where a comma denotes the derivative as

$$V_{;\alpha\gamma} = \frac{\partial^2 q}{\partial \xi^\alpha \partial \xi^\gamma}, \quad q_{;\alpha} = \frac{\partial q}{\partial \xi^\alpha}. \quad (3)$$

We have shown that this RPA equation should be modified as follows, when the state is not a local minimum:

$$V_{;\alpha\gamma} \tilde{B}^{\gamma\beta} q_{;\beta} = \omega^2 q_{;\alpha}, \quad (4)$$

where the covariant derivative  $V_{;\alpha\gamma}$  is defined by

$$V_{;\alpha\gamma} = V_{,\alpha\gamma} - \Gamma_{\alpha\gamma}^\beta V_{;\beta}, \quad (5)$$

$$\Gamma_{\alpha\gamma}^\beta = \xi_{,q}^\beta q_{;\alpha\gamma}. \quad (6)$$

The mass parameter,  $B^{\alpha\beta}$ , is also modified according to the terms of the second order in momentum. This modified RPA equation guarantees separation of the spurious (Nambu-Goldstone) modes.

Since the LHA procedure requires us to solve RPA at each point on the collective path, it will be very useful if the RPA eigenvectors can be approximated by taking linear combinations of a small number of one-body operators. This means that we can restrict RPA diagonalization to this small space, rather than deal with the full millions-by-millions RPA matrix. For the pairing-plus-quadrupole model, we have examined the possibility of expressing the self-consistent cranking operator in terms of a limited set of one-body operators. It seems to be very difficult to approximate the normal-mode vectors using elementary one-body operators. This difficulty disappears, however, when we use a small number of *state-dependent* one-body operators. This may reflect the importance of the self-consistent determination of the collective coordinates for large-amplitude collective motion, because the coordinates now have a state dependence as well. The best cranking operator that we have found for describing the  $\gamma$  vibration is the quadrupole operator, whose two-quasiparticle matrix elements are weighted with a factor  $E_{2qp}^{-2}$ . With the self-consistent cranking operators, LHA should provide a significant improvement over the conventional CHFB calculation based on fixed cranking operators.

## References

- 1) A. Klein, N. R. Walet, and G. Do Dang: *Ann. Phys.* **208**, 90 (1991).
- 2) T. Nakatsukasa and N. R. Walet: *Phys. Rev. C* **57**, 1192 (1998); *Phys. Rev. C* **58**, 3397 (1998).

<sup>\*1</sup> Department of Physics, UMIST, UK

<sup>\*2</sup> Laboratoire de Physique Théorique, Université de Paris-Sud, France

# Relativistic Tilted Axis Cranking Model and Its Application to Shears Bands in the $A = 80$ Mass Region

H. Madokoro, J. Meng, M. Matsuzaki, and S. Yamaji

[Relativistic mean field, Tilted axis cranking, Shears bands,  $^{84}\text{Rb}$ ]

New shears bands in  $^{82}\text{Rb}$  and  $^{84}\text{Rb}$  were discovered in a recent experiment.<sup>1)</sup> Many shears bands have been observed in several mass regions, such as the  $A \sim 200$ , 130 and 100 regions; this is the first experimental data obtained in the  $A \sim 80$  mass region. Up to now, many features of these shears bands have been well understood within the framework of Tilted Axis Cranking (TAC),<sup>2)</sup> by using the pairing+QQ model<sup>3)</sup> and the shell model.<sup>4)</sup> On the other hand, fully microscopic and self-consistent calculations have not been performed. Therefore, for the first time we have applied the Relativistic Mean Field (RMF) model, which has gratefully been successful in reproducing many properties of finite nuclei, to such tilted rotation.

For applications to rotating nuclei, the Lagrangian of the RMF model must be generalized into a uniformly rotating frame which rotates with constant rotational frequency,  $\Omega$ . From this generalized Lagrangian, the equations of motion can be derived. This can be done in the same manner as that in the Principal Axis Cranking (PAC) case. For details, see Ref. 5. The method used to solve the coupled equations of motion is, again, the same as that in the PAC case. The nucleon and meson fields are expanded in terms of 3-dimensional harmonic-oscillator eigenfunctions.

In the actual calculation, we use a parameter set called NL3. Here, we show the result for  $^{84}\text{Rb}$  as an example. The configuration is fixed to  $\pi(1g_{9/2})^2\nu(1g_{9/2})^{-3}$ . The contribution to the total angular momentum mainly comes from 2 proton particles and 3 neutron holes in the  $1g_{9/2}$  orbital. The calculated quadrupole deformation at  $\Omega = 0.1$  MeV is  $\beta_2 \sim 0.2$ . This value seems to be slightly too large compared with the typical values observed in the shears bands in other regions. In our present calculation, the pairing correlation is not taken into account. Note that including the pairing correlation may reduce the quadrupole deformation. The triaxial deformations are rather small, which can be neglected.

Figures 1 and 2 show how the direction of the total angular momentum vector changes with an increase of the rotational frequency in  $^{84}\text{Rb}$ . Also shown are the net contributions from proton particles and neutron holes individually. From Figs. 1 and 2, we can see that both the proton and neutron angular momenta align towards the total spin as the rotational frequency increases. The direction of the total angular momentum does not change very much. We thus observed that the shears mechanism does appear in this case. In the

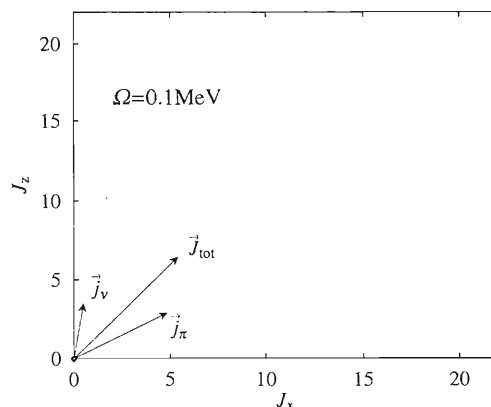


Fig. 1. Composition of the total angular momentum at  $\Omega = 0.1$  MeV.  $\vec{J}_\pi$  and  $\vec{J}_\nu$  represent the contribution from proton particles and neutron holes, respectively.  $\vec{J}_{\text{tot}}$  is the total angular momentum.

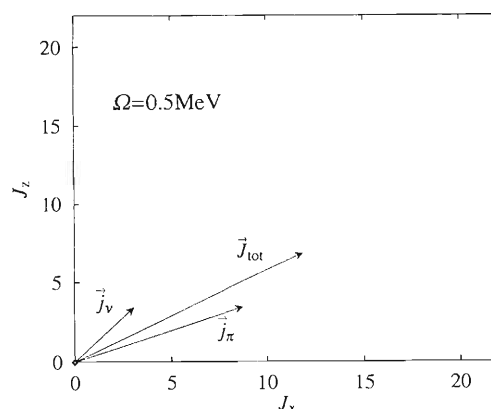


Fig. 2. Composition of the total angular momentum at  $\Omega = 0.5$  MeV.

future, we will include a pairing correlation within the framework of the cranked relativistic Hartree Bogoliubov approach.

## References

- 1) H. Schnore et al.: Phys. Rev. Lett. **82**, 4408 (1999).
- 2) S. Frauendorf, J. Meng, and J. Reif: Proc. Conf. on Physics from Large  $\gamma$ -Ray Detector Arrays, Vol. 2, p. 52 (1994).
- 3) S. Frauendorf: Nucl. Phys. A **557**, 259c (1993).
- 4) S. Frauendorf, J. Reif, and G. Winter: Nucl. Phys. A **601**, 41 (1996).
- 5) H. Madokoro and M. Matsuzaki: Phys. Rev. C **52**, R2934 (1997).

# Wobbling Motion in the Multi-Bands Crossing Region<sup>†</sup>

M. Oi, A. Ansari,\* T. Horibata, and N. Onishi

[NUCLEAR STRUCTURE; Wobbling motion, Tilted cranking, Band crossing]

The back-bending in the  $A \simeq 180$  mass region is expected to be caused by multi-bands crossing between low- $K$  (g- and s-bands) and high- $K$  bands ( $K^\pi = 8^+$ ).<sup>1,2)</sup> We have analyzed a mechanism for coupling these bands in terms of a dynamical treatment for nuclear rotations, i.e., the wobbling motion. The wobbling states are produced through the generator coordinate method after angular momentum projection, in which the intrinsic states are constructed through 2d-cranked HFB calculations.<sup>3,4)</sup>

We have investigated a mechanism of back-bending and signature inversion in  $^{182}\text{Os}$ , by means of the generator coordinate method with angular momentum projection (GCM after AMP) on the 2d-cranked HFB states. Using this method, we qualitatively reproduced the main feature of level structure showing the signature inversion in the high- $K$  band (see Fig. 1). We interpret this result from the point of view of an inter-band interaction between the low- $K$  and high- $K$  bands. We have shown that the perturbed states have characters of the wobbling

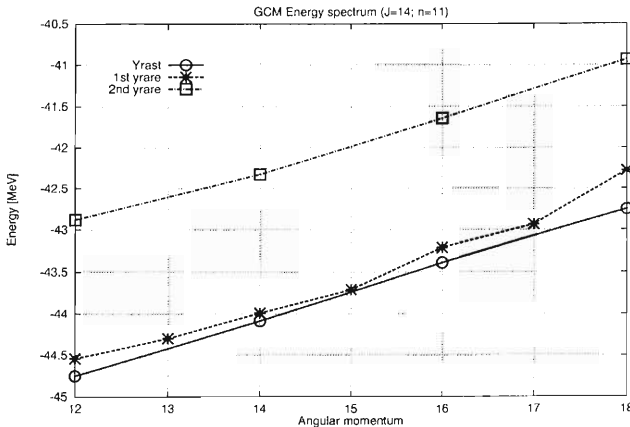


Fig. 1. Energy spectrum calculated through GCM after AMP. The angular momentum constraint for the intrinsic state is fixed to be  $J = 14 \hbar$ . From an analysis of the generator wave functions, the yrast and the second yrare bands ( $\Delta I = 2$ -bands) are of the low- $K$  characters, while the first yrare band ( $\Delta I = 1$ -band) is of the high- $K$  character. The signature inversion is seen at the region  $I > 15 \hbar$ .

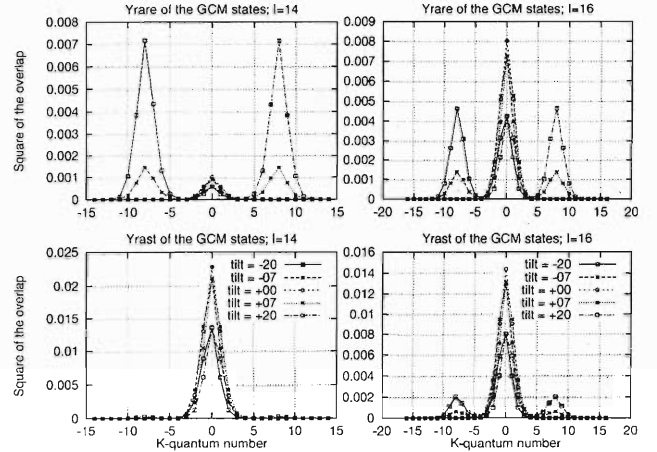


Fig. 2. Graphs for the overlaps between the GCM state and the spin-projected intrinsic states:  $g_K^I \equiv \langle \Psi(J, \theta) | \hat{P}_{MK}^{I\dagger} | \Psi_M^I \rangle$ . The left panels are for the GCM states before band crossing ( $I = 14 \hbar$ ), and the right panels are for the states after crossing ( $I = 16 \hbar$ ). The lower and upper panels show the yrast and first yrare states, respectively. In each panel, the graphs are separately drawn for each tilt angle:  $\theta = 0^\circ, \pm 7^\circ$  and  $\pm 20^\circ$ .

motion, that is, dynamical-mode coupling low- $K$  PAR and high- $K$  TAR states (see Fig. 2). In terms of this wobbling model, we have discussed an enhancement of back-bending in the  $A \simeq 180$  region, in which the typical rotation-alignment is somewhat suppressed by the location of the Fermi level. We have also shown that the solutions of the Hill-Wheeler equation have a new type of symmetry (“signature”) in the wobbling model, and that the restoration of the signature through the wobbling motion is related to coupling between high- $K$  and low- $K$  states.

## References

- 1) T. Shizuma et al.: Phys. Lett. B **442**, 53 (1998).
- 2) P. M. Walker et al.: Proc. Int. Conf. on the Future of Nuclear Spectroscopy, Crete (1993).
- 3) T. Horibata and N. Onishi: Nucl. Phys. A **596**, 251 (1996).
- 4) A. Ansari, M. Oi, T. Horibata, and N. Onishi: Nucl. Phys. A **654**, 558 (1999).

<sup>†</sup> Condensed from the article submitted to Phys. Lett. (1999)

\* Institute of Physics, Doordarshan Marg, India

# Relativistic Hartree-Bogoliubov Approach for Nuclear Matter with a Non-Linear Coupling Term

S. Sugimoto, K. Sumiyoshi, and H. Toki

[Relativistic Hartree-Bogoliubov theory, Pairing interaction]

We have developed the new method which can incorporate non-linear coupling terms of mesons into the pairing channel in the relativistic Hartree-Bogoliubov theory (RHB). RHB theory is an extended version of the relativistic mean-field theory (RMF),<sup>1)</sup> which can treat both the pairing channel and the particle-hole channel self-consistently. We have applied it to nuclear matter to see the effect of the non-linear coupling terms of mesons on the pairing channel, and found that these terms reduce the pairing gap,  $\Delta$ , by a few MeV.

Pairing interaction is a well-known residual interaction, which is especially important for open-shell nuclei. In the mean-field theory it is usually implemented by a BCS-type scheme. In this scheme, because two nucleons which are in the time-conjugate states to each other constitute a Cooper pair, the ground-state energy of the nuclei are lowered. It is known that BCS theory works well in the region around the stable line. However, the BCS scheme cannot properly incorporate the mean field of nuclei in the pairing channel. The Hartree-Fock-Bogoliubov (HFB) theory can incorporate the mean field of nuclei in the pairing channel in addition to the usual mean-field effect, which is brought by Hartree-Fock theory. The relativistic Hartree-Fock-Bogoliubov (RHFB) theory is a relativistic version of the HFB theory, which was first derived by Kucharek *et al.*<sup>2)</sup> In RHFB theory the pairing interaction is mediated by mesons. We can treat the particle-hole interaction and the pairing interaction self-consistently and simultaneously within RHFB theory. Recently, RHFB theory and RHB theory, which neglects the Fock term, have been applied to nuclear matter<sup>3)</sup> and finite nuclei,<sup>4)</sup> with satisfactory results.

However, by now the non-linear terms of mesons are being neglected in the pairing channel. In RMF theory these terms are needed to reproduce the properties of nuclear matter and the finite-nuclei properly.<sup>5,6)</sup> We can believe that these terms may have some effect on the pairing channel in RHFB and RHB theory. We have thus extended the RHFB theory to be able to incorporate non-linear meson coupling terms in the pairing channels. In our framework, meson fields are expanded around the classical mean field value, which can reproduce the RMF theory, and the residual terms mediate the pairing interaction.

For a detailed formulation we are presenting a paper.

In Fig. 1 we show the pairing gap,  $\Delta$ , at the Fermi momentum,  $k_F$ , in nuclear matter, calculated by the

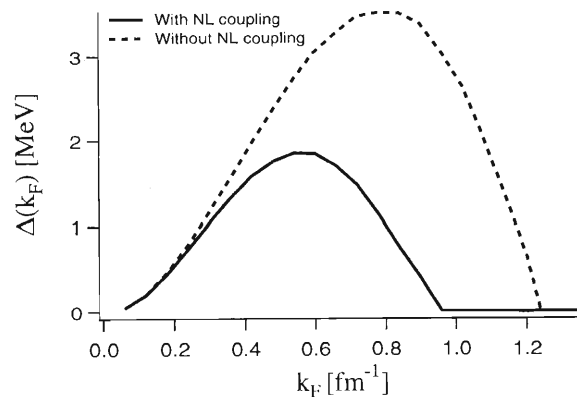


Fig. 1. Pairing gap at the Fermi surface  $\Delta(k_F)$  as a function of the density characterized by the Fermi momentum,  $k_F$ . The solid line is obtained with the non-linear term of mesons in the pairing channel. The dashed line corresponds a scheme without the non-linear term effect.

RHB theory with the non-linear terms having an effect on the pairing channel. In Fig. 1 we also show the result without the non-linear coupling term. We use the TM1 parameter set, which has non-linear  $\sigma$  and  $\omega$  meson terms.<sup>6)</sup> From Fig. 1 we can see that by including the non-linear terms the pairing gap is reduced by a few MeV. This is because the masses of the mesons increase effectively by the non-linear terms of the mesons. If we use the other parameter set, although the maximum  $\Delta(k_F)$  values somewhat change, all other tendencies are almost the same. Note that in the calculation we introduce the cut-off parameter in the pairing channel.

In summary, we extended the RHFB theory to include non-linear meson terms in the pairing channel. We have applied it to nuclear matter, and have found that the non-linear terms reduce the  $\Delta$  by a few MeV. In the future we will apply it to finite nuclei.

## References

- 1) B. D. Serot *et al.*: *Adv. Nucl. Phys.* **16**, 1 (1986); P. Ring *et al.*: *Prog. Part. Nucl. Phys.* **37**, 193 (1996).
- 2) H. Kucharek *et al.*: *Z. Phys. A* **339**, 23 (1991).
- 3) F. B. Guimarães *et al.*: *Phys. Rev. C* **54**, 2385 (1996); M. Matsuzaki: *Phys. Rev. C* **58**, 3407 (1998).
- 4) J. Meng *et al.*: *Phys. Rev. Lett.* **77**, 3963 (1996); G. A. Lalazissis *et al.*: *Phys. Rev. C* **60**, 014310 (1999).
- 5) J. Boguta *et al.*: *Nucl. Phys. A* **292**, 413 (1977).
- 6) Y. Sugahara *et al.*: *Nucl. Phys. A* **579**, 557 (1994).

# The r-Process Nucleosynthesis in Supernovae

M. Terasawa, K. Sumiyoshi, T. Kajino, and I. Tanihata

[r-Process, Supernova]

All elements up to the region of the iron peak are synthesized by the charged-particle-induced nuclear reaction in stars. If heavier elements above the iron peak had been produced by silicon burning or another charged-particle-induced fusion reaction, their abundances would drop very steeply with increasing mass. Actually, the observed solar-system abundance distribution of the heavy elements exhibits a much slower decrease with mass number and much higher abundances than expected from charged-particle-induced reactions. On the other hand, heavy elements easily capture neutrons even at extremely low energy with no coulomb barrier to overcome. Moreover, the abundances of heavy elements have characteristics correlated with neutron captures. The most important characteristic would be seen to be an enhanced stability of nuclei with magic numbers  $N = 50, 82,$  and  $126$  neutrons. We observe six peaks in the solar-system abundance distribution, three at the number of the neutron magic number, and the other three at a number smaller than the magic number. The abundances of the nuclear species seem to suggest that two different types of neutron-capture processes (s-process and r-process) have participated in the synthesis of the heavy elements.

For the s-process, neutron capture is slower than beta-decay, and closely follows the valley of beta-stability. Thus, relatively stable nuclei at the magic number are abundant. The astrophysical site where the s-process occurs is He flash of an AGB star. This has been confirmed by an observation of  $^{99}\text{Tc}$  in S-type stars.

On the contrary, if neutron capture proceeds on a rapid time scale compared with the beta-decay lifetimes, the network of reactions is called the r-process, which occurs in a very strong neutron flux. The r-process follows a path at the extreme neutron-rich side of the valley of stability. Very neutron-rich nuclei also have the property of magic nuclei. Thus, magic nuclei are abundant. Once the neutron flux ceases, neutron-rich matter produced evolves quickly by several beta-decays to the region of stability. We observe the nuclei after beta-decay. Then, the nuclei at a smaller number than the magic number are abundant. Although many studies have been devoted for clarifying the origin and evolution of those nuclei, the astrophysical site for the r-process still remains an unresolved mystery. The high neutron density and rapid expansion time scale associated with the r-process suggest core-collapse (type II or type Ib) supernovae as being the most likely setting

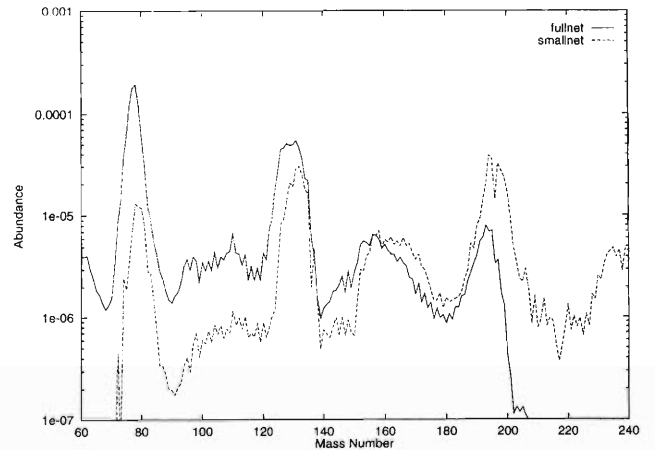


Fig. 1. Final abundances as a function of the mass number. The solid line is in the case of including light neutron-rich nuclei and the dotted line is that of including only 3-body reactions.

for explosive nucleosynthesis, though the exact environment within supernovae is unclear. Most of the focus of recent studies on the r-process has been on the stellar wind or the atmosphere of a hot neutron star to be formed as a remnant of collapsing iron cores of massive stars. This is because these models are directly relevant to SN 1987A, and most of the collapse models currently being studied are representative of this progenitor mass,  $15\text{--}20M_{\odot}$ .

Previous works in the literature have shown that 3-body reactions (for example  $3\alpha$ ) are most important to create seed nuclei for the r-process. They ignored light neutron-rich nuclei ( $Z < 10$ ). This is because at high temperature ( $T$ ) and high density ( $\rho$ ) the rate of 3-body reactions is higher than that of other reactions. However, in the r-process environment  $T$  varies from 1 to 0.1 MeV and  $\rho$  from  $10^9$  to  $10^2$  g/cc, typically. If  $T$  and  $\rho$  drop rapidly, seed nuclei must be continually created when  $T$  and  $\rho$  get low. This implies the importance of no-3-body reactions. In studies of the r-process nucleosynthesis, the r-process could occur in a low-entropy environment with a short dynamic time scale of the expansion. Thus, we included light neutron-rich nuclei reactions in our network calculation. The results are shown in Fig. 1. In this calculation, we applied a short dynamic expansion model (Sumiyoshi et al. 1999). Figure 1 shows that the light neutron-rich nuclei reactions play an important role in the r-process. We are now determining what are the most important reactions.

## References

- 1) S. E. Woosley, J. R. Wilson, G. J. Mathews, R. D. Hoffman, and B. S. Meyer: *Astrophys. J.* **433**, 229 (1994).
- 2) Y.-Z. Qian, W. C. Haxton, K. Langanke, and P. Vogel: *Phys. Rev. C* **55**, 1533 (1997).
- 3) K. Sumiyoshi, H. Suzuki, K. Otsuki, M. Terasawa, and S. Yamada: in preparation.

# Hydrodynamical Study of Neutrino-Driven Winds as r-Process Sites

K. Sumiyoshi, M. Terasawa, H. Shen,\* K. Oyamatsu, H. Toki, H. Suzuki, and S. Yamada

[EOS, Supernova, r-Process]

The rapid neutron-capture process (r-process) is believed to be the origin of heavy elements in the Universe. Although supernova explosions are most likely to be the sites, where and how the r-process can occur in supernovae has not yet been clarified. We have studied the neutrino-driven wind as an r-process site by performing hydrodynamical simulations to clarify whether the r-process nucleosynthesis can occur or not.<sup>1)</sup> We have simulated the hydrodynamics of the surface layers just above the proto-neutron star, which is born in a supernova explosion, and have performed r-process network calculations using the trajectories obtained from the simulations.

We adopted a numerical code for the general relativistic, implicit hydrodynamics in spherical symmetry.<sup>2)</sup> The heating and cooling processes due to neutrinos are added on top of the hydro code. As for the equation of state (EOS) of dense matter, we have adopted the table of the relativistic EOS, which was recently derived for supernova simulations.<sup>3)</sup> The relativistic EOS is derived by the relativistic nuclear many-body framework, which reproduces the nuclear matter saturation and the properties of stable and unstable nuclei in the nuclear chart.<sup>4)</sup> The table covers a wide range of density, electron fraction and temperature, which has enabled us to perform supernova simulations.

Figure 1 demonstrates the hydro simulations of the neutrino-driven wind. The surface layers above the proto-neutron star are heated up by neutrinos and

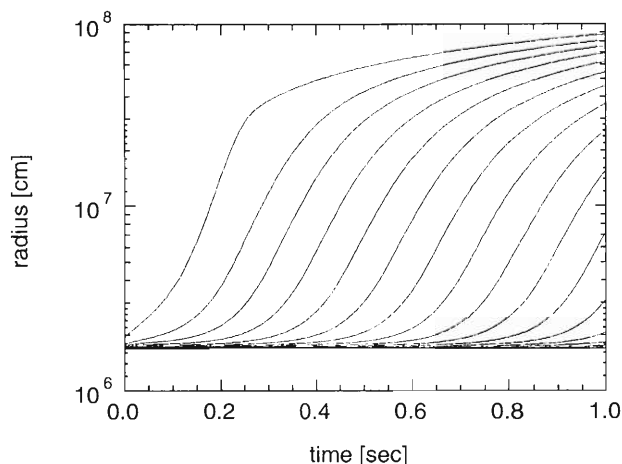


Fig. 1. Trajectories of mass elements in hydrodynamical simulations displayed as functions of time.

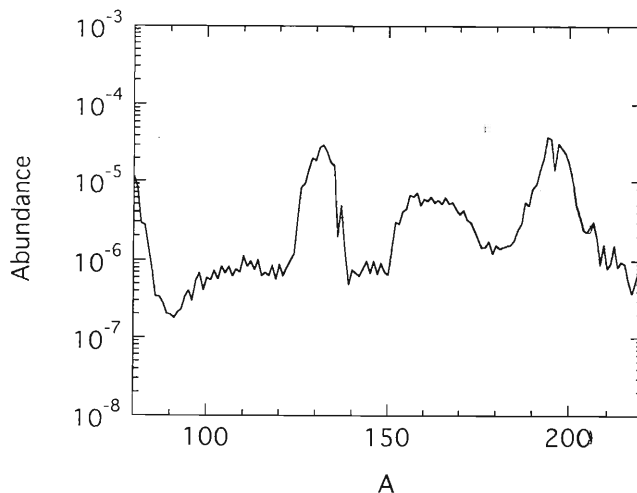


Fig. 2. Calculated abundance of the r-process elements as a function of the mass number.

ejected as expanding matter. We have examined this expansion, which leads to nucleosynthesis, to judge whether the r-process is possible from numerical simulations. We found that the expansion time scale is shorter than those in previous analytic studies. A shorter expansion time scale is favorable for the r-process, since it leaves a higher neutron-to-seed-nuclei ratio.

Using the trajectory obtained from the simulations, we performed the nuclear reaction network calculations of the r-process. Figure 2 shows the calculated abundance of the r-process elements as a function of the mass number. In this case, mass elements up to the 3rd peak ( $A = 195$ ) are successfully created. We have found that the r-process indeed occurs in the case of a short expansion time scale with a massive and compact neutron star having a high neutrino luminosity.

In summary, we have shown by hydro simulations that the neutrino-driven wind in supernova explosions is a promising site for the r-process to create heavy elements.

## References

- 1) K. Sumiyoshi, H. Suzuki, K. Otsuki, M. Terasawa, and S. Yamada: astro-ph/9912156, submitted to Publ. Astron. Soc. Jpn.
- 2) S. Yamada: *Astrophys. J.* **475**, 720 (1997).
- 3) H. Shen, H. Toki, K. Oyamatsu, and K. Sumiyoshi: *Nucl. Phys. A* **637**, 435 (1998).
- 4) D. Hirata, K. Sumiyoshi, I. Tanihata, Y. Sugahara, T. Tachibana, and H. Toki: *Nucl. Phys. A* **616**, 438c (1997).

\* Nankai University, China

## $^{44}\text{Ti}$ : Its Effective Decay Rate in Young Supernova Remnants, and Its Abundance in Cassiopeia A<sup>†</sup>

Y. Mochizuki, K. Takahashi,\*<sup>1</sup> H. T. Janka,\*<sup>1</sup> W. Hillebrandt,\*<sup>1</sup> and R. Diehl\*<sup>2</sup>

[Nucleosynthesis, Supernovae]

Radioactive isotopes such as  $^{44}\text{Ti}$  probably offer the most direct probe into nucleosynthesis environments in the interior of exploding stars, when the associated  $\gamma$ -ray activities in the explosion remnant are detected and translated back to the isotopic abundances at the time of the explosion. In this paper, we assert that the procedure may not necessarily be straightforward, at least in the case of  $^{44}\text{Ti}$ , an orbital-electron capture decay isotope.

The binding energy of the K-shell electrons of  $^{44}\text{Ti}$  was calculated to be 6.6 keV. Hence, it is obvious that  $^{44}\text{Ti}$  is fully ionized when it is synthesized in a supernova explosion. After the explosion, the temperature of the ejected material decreases rapidly due to adiabatic cooling as the ejecta freely expands. Consequently, it is expected that the freshly synthesized nuclei become neutral within about 1000 sec.

There is a possibility that  $^{44}\text{Ti}$  re-ionizes, however. This is due to reverse-shock heating. The reverse shock is produced by high pressure behind the blast-wave shock interacting with the surrounding circumstellar medium. The reverse shock goes back into the ejecta and heats up and ionizes it during the free-expansion phase on the evolutionary course of the supernova remnant.

Using the analytic model of McKee & Truelove<sup>1)</sup> for young supernova remnants, and assuming the existence of overdense  $^{56}\text{Fe}$ -dominated clumps that also contain  $^{44}\text{Ti}$ , we showed that a high degree of ionization may be caused by reverse shock, so that the electron-capture rate of  $^{44}\text{Ti}$  can be significantly reduced from its laboratory value. Note that the decay rate measured in laboratories is for neutral atoms.

The nuclear  $\gamma$ -rays from  $^{44}\text{Ti}$  decay have been detected by COMPTEL experiments on the CGRO satellite from Cassiopeia A (Cas A), a nearby supernova remnant. The  $\gamma$ -ray flux detection has a strong impact, since we can test the theories of collapse-driven supernova explosions through conversion of the flux into the initial abundance of  $^{44}\text{Ti}$  at the time of the explosion, employing the values of the decay rate, the distance, and the age of Cas A.

In order to estimate the observable consequences of the reduced  $\beta$ -decay rates, one has to recall that the

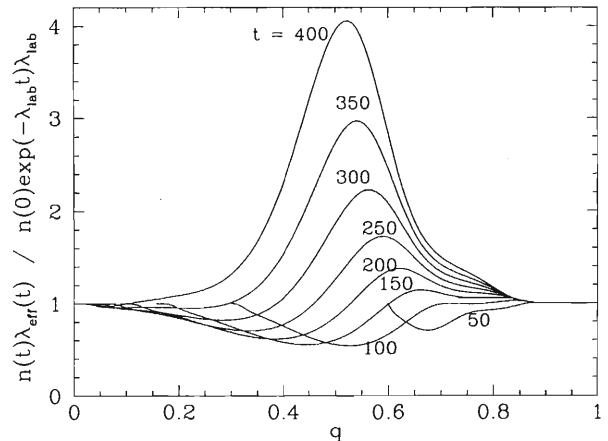


Fig. 1. The  $^{44}\text{Ti}$  radioactivity observable at time  $t$  (“age” in years) relative to the case that assumes no reduction of the  $\beta$ -decay rate, as a function of the mass coordinate,  $q$ , within the ejecta.

measurable  $\gamma$ -ray activity per (normalized) unit mass of the remnant is the product of the current  $\beta$ -decay rate and the current abundance,  $n(t)\lambda_{\text{eff}}(t)$ . Figure 1 illustrates the  $^{44}\text{Ti}$  radioactivity observable at time  $t$  (“age” in years) relative to the case that assumes no reduction of the  $\beta$ -decay rate. In the figure, the abscissa  $q$  shows the relative mass coordinate within the ejecta.

In conclusion, we found that under certain conditions the ionization of  $^{44}\text{Ti}$  and the corresponding delay of its decay can yield up to three times higher  $^{44}\text{Ti}$  activity at the present time than predicted on the grounds of the laboratory decay rate. This effect is large enough to reduce the apparent discrepancies between the  $^{44}\text{Ti}$  production in the explosion inferred from the COMPTEL  $\gamma$ -line measurements and the theoretical predictions from the current supernova nucleosynthesis models. This possibility is, however, subject to various uncertainties, and particularly to the unknown properties and radial distribution of the clumps in the ejecta.

### References

- 1) C. F. McKee and J. K. Truelove: Phys. Rep. **256**, 157 (1995).

<sup>†</sup> Condensed from the article in *Astron. Astrophys.* **346**, 831 (1999)

\*<sup>1</sup> Max-Planck-Institut für Astrophysik, Germany

\*<sup>2</sup> Max-Planck-Institut für Extraterrestrische Physik, Germany

# A New Parameterization of Polarized Parton Distribution Functions

Y. Goto, N. Hayashi, M. Hirai, H. Horikawa, S. Kumano, M. Miyama,  
T. Morii, N. Saito, T.-A. Shibata, E. Taniguchi, and T. Yamanishi

[RHIC, Spin, Asymmetry, Polarized PDF, Polarized DIS]

We started a collaboration to determine the spin contents of the parton distribution function (PDF) in a nucleon based on high-energy polarized experimental data.<sup>1)</sup> In this article, we report on our first result of a world asymmetry data analysis. See Ref. 2 for the detailed analysis and references therein.

The main sources of the PDF information are inclusive deep-inelastic-scattering (DIS) experiments. For unpolarized PDF, the Drell-Yan process, the prompt-photon process, and the jet-production process are also available to cover a wider kinematical region.

For the polarized PDF, we have only polarized DIS data to determine the distribution, although there has been progress concerning the data precision. Theoretically, there has been much progress, including a next-to-leading order (NLO) calculation. Many groups are analyzing the polarized DIS data and parameterizing the polarized PDF. Because the polarized DIS data are still limited, there are many uncertainties in the analysis. Conventional analyses show that the quark contribution to the proton spin ( $\Delta\Sigma$ ) is only 20% to 30% of the total spin. To explain other contributions to the proton spin, we need to know the gluon contribution,  $\Delta G$ .

Experimentally, in addition to the DIS data, there have been several attempts to determine the gluon contribution to the proton spin. Charm production at DESY-HERMES and CERN-COMPASS, and prompt photon, heavy flavor and jet production in polarized  $pp$  collisions at BNL-RHIC will constrain both the shape and the first moment of  $\Delta G$ .

The parameterized polarized PDF provides predictions for current and future polarized experiments to test their analyses. After new data are obtained, parameterization will be performed by including all of the new information.

In our model for the parameterization, we require two natural conditions: the positivity condition and the counting rule. Its functional form at the initial scale  $Q_0^2$  is

$$\Delta f_i(x, Q_0^2) = A_i x^{\alpha_i} (1 + \gamma_i x^{\lambda_i}) f_i(x, Q_0^2)$$

for  $i = u_v, d_v, \bar{q}, g$  (valence  $u$  quark, valence  $d$  quark, sea quark, and gluon). Functions  $f_i(x, Q_0^2)$  show the unpolarized PDFs,  $\Delta f_i(x, Q_0^2)$  show the polarized PDFs, and  $A_i$ ,  $\alpha_i$ , and  $\lambda_i$  are parameters to be determined in the analysis. This form satisfies the counting rule by requiring it on  $f_i(x, Q_0^2)$ . The positivity condition is required by  $|\Delta f_i(x, Q_0^2)| < f_i(x, Q_0^2)$ . Here, we reduce the number of free parameters by assuming the

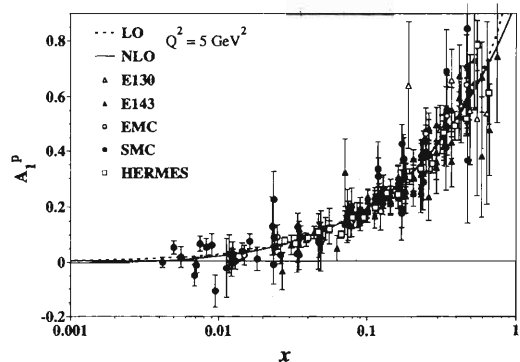


Fig. 1. Comparison of our calculations with the experimental asymmetry,  $A_1(x, Q^2)$ , data for the proton. The leading-order (LO) and the next-to-leading order (NLO) results are shown by the solid and dotted lines, respectively.

SU(3) flavor symmetry for the sea quarks.

The physical quantities to be fitted are the cross-section asymmetry,  $A_1(x, Q^2)$ , of the proton, neutron, and deuteron. The polarized PDFs are evolved to the  $(x, Q^2)$  points where the experimental data were taken to calculate  $A_1(x, Q^2)$  for a  $\chi^2$  analysis. Figure 1 shows  $A_1(x, Q^2)$  data for the proton and the fitting result of our leading-order (LO) and the next-to-leading order (NLO) calculation.

In this analysis, we did not apply any theoretical requirements to restrict the small- $x$  behavior of the PDF, *e.g.* the Regge theory or perturbative QCD. The amount of quarks carrying the nucleon spin is  $\Delta\Sigma = 0.201$  in the LO, and  $\Delta\Sigma = 0.051$  in the NLO at  $Q^2 = 1 \text{ GeV}^2$ . Although these results confirm that the quarks carry a small amount of nucleon spin, it should be noted that our  $\Delta\Sigma$  in the NLO seems to be considerably smaller than the conventional values. The difference originates mainly from the small- $x$  behavior of the antiquark distribution. The existing data cannot fix it. In order to clarify the situation, we need to have higher energy facilities.

We also obtained positive values of  $\Delta G$  in both LO and NLO. However it is difficult to determine  $\Delta G$ , particularly in the LO. We need to wait for measurements of  $\Delta G$  at DESY, CERN and RHIC.

## References

- 1) Y. Goto et al.: RIKEN Accel. Prog. Rep. **30**, 35 (1997); **31**, 44 (1998); **32**, 37 (1999).
- 2) Y. Goto et al.: RIKEN-AF-NP-342 (1999); to be published.

# Large $p_T$ $\Lambda_c^+$ Production in Polarized $pp$ Scattering

K. Ohkuma, K. Sudoh, and T. Morii

[ $pp$  interaction, Polarized gluon,  $\Lambda_c^+$  production]

The proton spin has been long considered to be given by the sum of the constituent quark spin in the naive quark model. However, recent experimental data on the polarized structure functions of nucleons,  $g_1^{p(n)}$ , have revealed that the amount of the proton spin carried by quarks is very small.<sup>1)</sup> This has been called the ‘‘proton spin puzzle’’. Actually, the proton spin is given by the sum of the spin of quarks, gluons and orbital angular momenta among them. To understand the physical ground of this spin-sum rule, it is very important to understand the behavior of the polarized partons in the nucleon. However, knowledge about the polarized gluon density,  $\Delta g(x)$ , in a nucleon is still poor, though many processes have been proposed so far to extract information about them.

Here, to extract the polarized gluon distribution,  $\Delta g(x)$ , we propose another process, large  $p_T$   $\Lambda_c^+$  productions in polarized  $pp$  scattering, in anticipation of the forthcoming RHIC experiment. The  $\Lambda_c^+$  spin is basically carried by a charm quark, which is produced by gluon-gluon fusion at the lowest order in this process. Hence, an observation of the spin of the produced  $\Lambda_c^+$  provides information about polarized gluons in the proton. To extract information about  $\Delta g(x)$ , we calculated the spin-dependent differential cross section for  $p\bar{p} \rightarrow \bar{\Lambda}_c^+ + X$  at the large- $p_T$  region and the spin-correlation asymmetry,  $A_{LL}$ , defined by

$$A_{LL} = \frac{d\sigma_{++} - d\sigma_{+-} + d\sigma_{--} - d\sigma_{-+}}{d\sigma_{++} + d\sigma_{+-} + d\sigma_{--} + d\sigma_{-+}} \\ = \frac{d\Delta\sigma/dp_T}{d\sigma/dp_T},$$

where  $d\sigma_{+-}$ , for example, denotes the spin-dependent differential cross section with the positive helicity of the target proton and the negative helicity of the produced  $\Lambda_c^+$ . Those values will be measured by the forthcoming RHIC experiment. To calculate the cross section and asymmetry,  $A_{LL}$ , we took the GS96<sup>2)</sup> and GRSV96<sup>3)</sup> parameterization models for the polarized gluon distribution function and the GRV95<sup>4)</sup> model

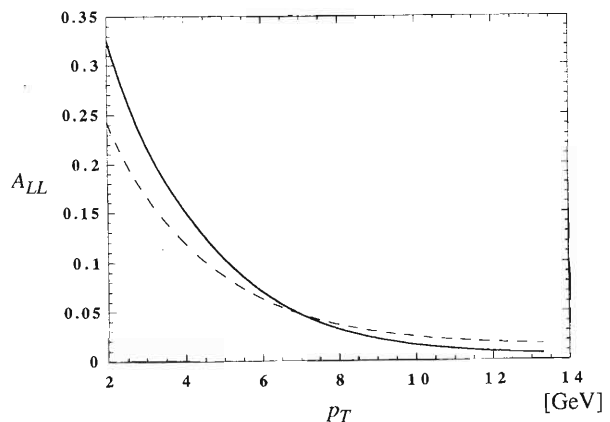


Fig. 1. Spin correlation asymmetry,  $A_{LL}$ , as a function of  $p_T$  at  $\sqrt{s} = 50$  GeV. The solid line and dotted lines indicate the GS96 and GRSV96 models, respectively.

for the unpolarized one. The GS96 and GRSV96 models can excellently reproduce the polarized structure function of nucleons, though the polarized gluon distributions for those models are quite different.

We show the numerical result of  $A_{LL}$  in Fig. 1. Here, the difference can be seen between the solid and dotted lines corresponding to the GS96 and GRSV96 models, respectively. As shown in Fig. 1,  $A_{LL}$  is sensitive to the polarized gluon distribution functions. Therefore, this process which we proposed here could provide good information about the distribution of the polarized gluons in a nucleon.

## References

- 1) D. Adeva et al., SMC Collab.: Phys. Lett. B **329**, 399 (1994); K. Abe et al., E143 Collab.: Phys. Rev. Lett. **74**, 354 (1995).
- 2) T. Gehrmann and W. J. Stirling: Phys. Rev. D **53**, 6100 (1996).
- 3) M. Glück, E. Reya, M. Stratmann, and W. Vogelsang: Phys. Rev. D **53**, 4775 (1996).
- 4) M. Glück, E. Reya, and A. Vogt: Z. Phys. C **67**, 433 (1995).

## $\Lambda_c^+$ Productions in Polarized $ep$ Reaction and Polarized Gluons in the Proton

N. I. Kochelev, T. Morii, and S. Oyama

[Polarized gluon,  $\Lambda_c^+$  production, Semi-inclusive reaction]

Over the years, the spin structure of nucleons has been one of the most challenging topics in nuclear and particle physics. To understand it deeply, it is very important to know the polarized gluon distribution. However, knowledge about the polarized gluon distribution in a nucleon is still poor. To extract such information, we propose to study the process of semi-inclusive  $\Lambda_c^+$  production in electron-polarized proton scattering,

$$e + \vec{p} \longrightarrow e + \Lambda_c^+ + X.$$

In the naive quark model, the spin of  $\Lambda_c^+$  is equal to the spin of the  $c$  quark. In addition, the  $c$  quark is produced from protons just through gluon fusion in the lowest order. Therefore, a measurement of the spin of  $\Lambda_c^+$  provides information about the polarized gluon in the proton. Furthermore, since the process directly depends on the polarized gluons in the proton, it must be effective for testing the model of polarized gluons. By using the typical parameterization models of polarized gluons, GS96<sup>1)</sup> and GRSV96,<sup>2)</sup> we calculated the spin-dependent differential cross sections,  $d\Delta\sigma/dydz$ , and their 2-spin asymmetry,  $A_{LL}$ , between the proton and  $\Lambda_c^+$  on semi-inclusive  $\Lambda_c^+$  productions in electron-proton scattering;  $y$  and  $z$  are dimensionless variables used in semi-inclusive deep inelastic scattering. The results are presented in Fig. 1.

In Fig. 1, we can see that the results largely depend on the models of the polarized gluon distribu-

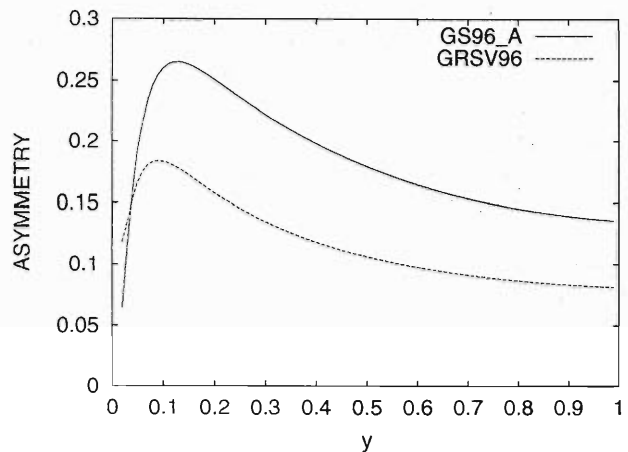


Fig. 1. 2-spin asymmetry,  $A_{LL}$ , between the proton and  $\Lambda_c^+$ .  $\sqrt{s} = 50$  GeV and  $z = 0.05$ .

tions. Therefore, the process proposed here must be promising for testing the polarized gluon distribution in the proton, though we need to know the polarized fragmentation function of the  $c$  quark to  $\Lambda_c^+$  decays to make the numerical results more accurate.

### References

- 1) T. Gehrmann and W. J. Stirling: Phys. Rev. D **53**, 6100 (1996).
- 2) M. Glück, E. Reya, M. Stratmann, and W. Vogelsang: Phys. Rev. D **53**, 4775 (1996).

# Behavior of Polarized Light Sea-Quarks in a Nucleon

T. Morii and T. Yamanishi

[Parton distribution, Sea quark, Structure function, Nucleon spin structure]

Experimental groups of NMC, E866/NuSea and HERMES observed a violation of the flavor symmetry in the unpolarized light flavor sea-quark distributions. Recently, this subject has been a challenging topic in particle and nuclear physics. In the polarized case, an important question is whether the symmetry of polarized sea-quarks of  $\Delta\bar{u}$  and  $\Delta\bar{d}$  is also violated at an initial  $Q_0^2$  in the nonperturbative region. So far, several theoretical groups have presented excellent parameterization models by analyzing high-precision data of polarized deep inelastic scatterings based on NLO of QCD.<sup>1)</sup> From these analyses, we now have a good understanding of the polarized valence of  $u$  and  $d$  quarks. However, our understanding of polarized sea-quarks and gluons is still very poor.

Here, we propose new formulas<sup>2)</sup> for extracting a difference in the polarized light sea-quark density,  $\Delta\bar{d}(x) - \Delta\bar{u}(x)$ , from the present polarized deep-inelastic semi-inclusive data. By using these formulas together with suitable unpolarized quark distributions and fragmentation functions, we have estimated the values of  $\Delta\bar{d}(x) - \Delta\bar{u}(x)$  from the data set of  $(A_{1p}^{h^\pm}, A_{1d}^{h^\pm})$  by SMC, and  $(A_{1p}^{h^\pm}, A_{1^3He}^{h^\pm})$  and  $(A_{1p}^{\pi^\pm}, A_{1^3He}^{\pi^\pm})$  by HERMES<sup>3,4)</sup> on the double spin asymmetries. The result is shown in Fig. 1. To extract some physics from this result, we parameterized the difference of the light flavor sea-quark densities as  $\Delta\bar{d}(x) - \Delta\bar{u}(x) = C x^\alpha \{\bar{d}(x) - \bar{u}(x)\}$  at  $Q^2 = 4 \text{ GeV}^2$ , and carried out a  $\chi^2$  fitting to the result presented in Fig. 1. The  $\chi^2$  fitting led to  $C = -3.40$  and  $\alpha = 0.567$  for the GRV98(LO) unpolarized parton distribution.  $C \neq 0$  is a remarkable result, suggesting an asymmetry of  $\Delta\bar{d}(x)$  and  $\Delta\bar{u}(x)$ , as shown in Fig. 1. It is interesting to note that the negative value of  $C$  is consistent with predictions from an instanton interaction or the chiral quark soliton model.<sup>5,6)</sup> However, it must be premature to emphasize this result, because the present data have

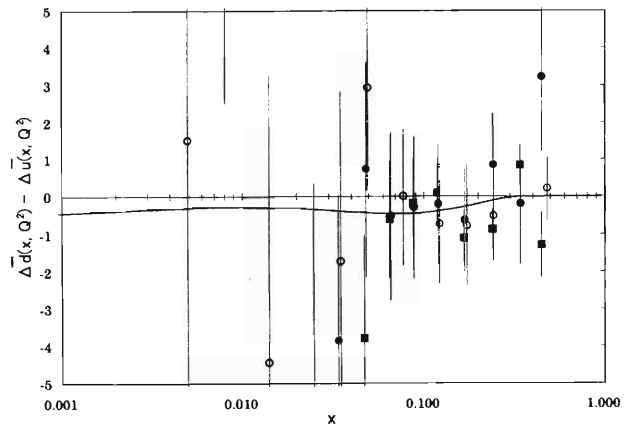


Fig. 1.  $x$  dependence of  $\Delta\bar{d}(x, Q^2) - \Delta\bar{u}(x, Q^2)$  at  $Q^2 = 4 \text{ GeV}^2$ . The marks indicated by the open circle, solid circle and solid square denote the results calculated from the set of SMC data, HERMES data for charged hadron productions and HERMES data for charged pion productions, respectively. The solid line indicates the result of a  $\chi^2$ -fit by the parameterization formula presented in the text.

errors that are too large. We urgently need to have more high-precision data to confirm this result.

## References

- 1) For examples, E. Leader, A. V. Sidorov, and D. B. Stamenov: Phys. Rev. D **58**, 114028 (1998).
- 2) T. Morii and T. Yamanishi: Phys. Rev. D **61**, 057501 (2000).
- 3) B. Adeva et al.: Phys. Lett. B **420**, 180 (1998).
- 4) A. Simon: HERMES Internal Note 98-054.
- 5) A. E. Dorokov, N. I. Kochelev, and Yu. A. Zubov: Int. J. Phys. A **8**, 603 (1993); A. E. Dorokov and N. I. Kochelev: Phys. Lett. B **304**, 167 (1993).
- 6) M. Wakamatsu and T. Kubota: Phys. Rev. D **59**, 034020 (1999).

# Color-Octet Contribution to the Photoproduction of $\psi'$

K. Sudoh and T. Morii

[Color-octet model, NRQCD, Polarized gluon]

Heavy quarkonium productions and decays have been traditionally calculated within the framework of the color-singlet model based on QCD. However, the predictions by the color-singlet model were too small to explain the recent Tevatron and HERA data.<sup>1)</sup> During these years, the color-octet model has been discussed as one of the most promising candidates that can remove such large discrepancies between the theoretical prediction and the experimental data. A rigorous formulation of the color-octet model has been introduced based on an effective field theory called nonrelativistic QCD (NRQCD).<sup>2)</sup> The cross section can be systematically calculated by the factorization approach based on NRQCD. However, the validity of the NRQCD factorization approach has not yet been confirmed with good accuracy. The discussion still seems to be controversial. It is thus important to test the model in other processes.

In this work, to test the possible color-octet contribution, we propose the following process:

$$\vec{\gamma} + \vec{p} \rightarrow \psi' + X,$$

at small- $p_T$  regions, which might be observed in the forthcoming COMPASS or polarized HERA experiment, where the arrow attached to the particles means that these particles are longitudinally polarized. The process is dominated by the color-octet subprocess,  $\gamma + g \rightarrow (c\bar{c})_{octet}$ , at small- $p_T$  regions, if the color-octet mechanism works. The conventional color-singlet subprocess,  $\gamma + g \rightarrow (c\bar{c})_{singlet} + g$ , appears only as a second order of the strong coupling constant,  $\alpha_s$ . Furthermore, since the process is dominantly produced in photon-gluon fusion, the cross section is sensitive to the gluon density in a proton. We can thus obtain good information about the polarized gluon distribution functions, if the NRQCD factorization approach is confirmed with good accuracy.

To test the color-octet mechanism and polarized gluon, we calculated the two-spin asymmetry,  $A_{LL}$ , for  $\psi'$  production in the polarized process, which is defined by

$$\begin{aligned} A_{LL} &\equiv \frac{[d\sigma_{++} - d\sigma_{+-} + d\sigma_{-} - d\sigma_{-+}]}{[d\sigma_{++} + d\sigma_{+-} + d\sigma_{-} + d\sigma_{-+}]} \\ &= \frac{d\Delta\sigma}{d\sigma} = \frac{d\Delta\sigma_8 + d\Delta\sigma_1}{d\sigma_8 + d\sigma_1}, \end{aligned}$$

where  $d\sigma_{+-}$ , for instance, denotes that the helicity of the beam particle is positive and that of the target

proton is negative. If there is only the color-octet contribution, which is the lowest-order process in  $\alpha_s$ , the asymmetry of  $A_{LL}$  can be given by a product of the ratio of gluon densities and that of the color-octet long-distance parameters,  $\Theta$  and  $\tilde{\Theta}$ , which could be determined from other experiments, as

$$A_{LL}^{\psi'}(\gamma p)_{lowest} = \frac{d\Delta\sigma_8}{d\sigma_8} = \frac{\Delta g(x, Q^2)}{g(x, Q^2)} \cdot \frac{\tilde{\Theta}}{\Theta}.$$

The factor of  $\Theta/\tilde{\Theta}$  has been extracted from recent analysis of the charmonium hadroproduction data,<sup>3)</sup> as follows:

$$\frac{\tilde{\Theta}}{\Theta} \equiv \frac{\langle \mathcal{O}_8^{\psi'}(^1S_0) \rangle - \frac{1}{m_c^2} \langle \mathcal{O}_8^{\psi'}(^3P_0) \rangle}{\langle \mathcal{O}_8^{\psi'}(^1S_0) \rangle + \frac{7}{m_c^2} \langle \mathcal{O}_8^{\psi'}(^3P_0) \rangle} \approx 3.6 \sim 8.0.$$

To calculate  $A_{LL}$ , we used the GS96 (set A and B)<sup>4)</sup> and GRSV96<sup>5)</sup> parametrizations for the polarized gluon distribution. In the GS96 or GRSV96 parametrization model, which is widely used, the maximum value of  $\Delta g(x)/g(x)$  becomes roughly 0.2–0.35. Hence, if we rely on this value for the ratio of the gluon distributions, the maximum value of the ratio of the NRQCD matrix elements should be

$$\frac{\tilde{\Theta}}{\Theta} \lesssim 5.0,$$

from the requirement that the  $A_{LL}$  should be less than 1.

In summary, to investigate possible color-octet contribution, we calculated the two-spin asymmetry,  $A_{LL}$ , for various values of  $\tilde{\Theta}/\Theta$ , and found that  $A_{LL}$  becomes quite large in the regions  $\sqrt{s} = 10\text{--}20$  GeV. Therefore, we can sufficiently test the color-octet model in this process. In addition, the measurement of  $A_{LL}$  is very effective to severely constrain the value of the NRQCD matrix elements, though it depends on the polarized gluon distribution,  $\Delta g(x)$ .

## References

- 1) CDF Collab., F. Abe et al.: Phys. Rev. Lett. **69**, 3704 (1992); Phys. Rev. Lett. **71**, 2537 (1993); H1 Collab., C. Adloff et al.: Eur. Phys. J. C **10**, 373 (1999).
- 2) G. T. Bodwin et al.: Phys. Rev. D **51**, 1125 (1995).
- 3) M. Beneke et al.: Phys. Rev. D **54**, 2005 (1996); A. K. Leibovich et al.: Phys. Rev. D **56**, 4412 (1997).
- 4) T. Gehrmann et al.: Phys. Rev. D **53**, 6100 (1996).
- 5) M. Glück et al.: Phys. Rev. D **53**, 4775 (1996).

# Antiquark Flavor Asymmetry in Polarized Drell-Yan Processes

S. Kumano and M. Miyama

[Parton distribution, Structure function]

Light antiquark flavor asymmetry has been an exciting topic after the discovery of the Gottfried-sum-rule violation in 1991.<sup>1)</sup> It is important for testing a nonperturbative aspect of the nucleon structure. In light of the RHIC-Spin project, the polarized version should become an interesting topic in the near future. In this report, we discuss the relation between the ratio of the proton-deuteron (pd) Drell-Yan cross section to the proton-proton (pp) one,  $\Delta_{(T)}\sigma_{pd}/2\Delta_{(T)}\sigma_{pp} \equiv R_{pd}$ , and the flavor asymmetry in polarized light-antiquark distributions.<sup>2)</sup>

A formalism of the polarized proton-deuteron Drell-Yan process is given in Ref. 3. The difference between the spin-parallel and anti-parallel cross sections is given by

$$\begin{aligned} \Delta_{(T)}\sigma_{pd} \propto \sum_a e_a^2 \times [\Delta_{(T)}q_a(x_1) \Delta_{(T)}\bar{q}_a^d(x_2) \\ + \Delta_{(T)}\bar{q}_a(x_1) \Delta_{(T)}q_a^d(x_2)], \end{aligned} \quad (1)$$

where  $\Delta_{(T)} = \Delta$  or  $\Delta_T$ , depending on the longitudinal or transverse case, and  $\Delta_{(T)}q_a^d$  and  $\Delta_{(T)}\bar{q}_a^d$  are the quark and antiquark distributions in the deuteron. The pp cross sections are given in the same way simply by replacing the parton distributions in Eq. (1):  $q^d \rightarrow q$  and  $\bar{q}^d \rightarrow \bar{q}$ .

We investigated the cross-section ratio,  $R_{pd}$ . If the valence-quark distributions satisfy  $\Delta_{(T)}u_v(x \rightarrow 1) \gg \Delta_{(T)}d_v(x \rightarrow 1)$ , the ratio  $R_{pd}$  at large  $x_F = x_1 - x_2$  becomes

$$R_{pd}(x_F \rightarrow 1) = \frac{1}{2} \left[ 1 + \frac{\Delta_{(T)}\bar{d}(x_2)}{\Delta_{(T)}\bar{u}(x_2)} \right]_{x_2 \rightarrow 0}. \quad (2)$$

Therefore, if the distribution  $\Delta_{(T)}\bar{u}$  is the same as  $\Delta_{(T)}\bar{d}$ , the ratio is simply given by one. The above equation suggests that the deviation from one should be related to the  $\Delta_{(T)}\bar{u}/\Delta_{(T)}\bar{d}$  asymmetry. In this way, we have found that the data in the large- $x_F$  region are especially useful for measuring the flavor asymmetry ratio,  $\Delta_{(T)}\bar{u}(x)/\Delta_{(T)}\bar{d}(x)$ . On the other hand, if another limit,  $x_F \rightarrow -1$ , is taken, the ratio becomes

$$R_{pd}(x_F \rightarrow -1) = \frac{1}{2} \left[ 1 + \frac{\Delta_{(T)}\bar{d}(x_1)}{4\Delta_{(T)}\bar{u}(x_1)} \right]_{x_1 \rightarrow 0}. \quad (3)$$

If the antiquark distributions are flavor symmetric, the ratio is given by  $R_{pd} = 5/8 = 0.625$ . Comparing the above equation with Eq. (2), we find a difference of a factor of 4. This suggests that the ratio  $R_{pd}$  for  $x_F \rightarrow -1$  should not be as sensitive as that in the large- $x_F$  region, although the  $\Delta_{(T)}\bar{u}/\Delta_{(T)}\bar{d}$  asymmetry could also be found in this region.

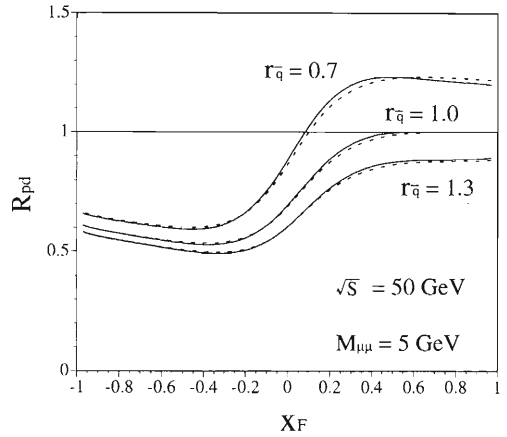


Fig. 1. Drell-Yan cross-section ratio,  $R_{pd} \equiv \Delta_{(T)}\sigma_{pd}/2\Delta_{(T)}\sigma_{pp}$ . The solid and dashed curves are for the longitudinally and transversely polarized cases, respectively.

Next, we show expected pd/pp ratios numerically. The leading-order (LO) results are shown in Fig. 1 at  $\sqrt{s} = 50$  GeV and  $M_{\mu\mu} = 5$  GeV. The Drell-Yan cross-section ratio,  $R_{pd}$ , was calculated in the longitudinally and transversely polarized cases; the results are indicated by the solid and dashed curves, respectively. For the transversity, we assumed that they are equal to the longitudinal distributions at  $Q^2 = 1$  GeV<sup>2</sup>. They are evolved to those at  $Q^2 = M_{\mu\mu}^2$  with the LO evolution equations.<sup>4)</sup> The flavor asymmetry ratio was taken to be  $r_{\bar{q}} \equiv \Delta_{(T)}\bar{u}/\Delta_{(T)}\bar{d} = 0.7, 1.0, \text{ or } 1.3$  at  $Q^2 = 1$  GeV<sup>2</sup>. As shown in Fig. 1, the flavor asymmetry effects are conspicuous especially at large  $x_F$ .

We have shown that the difference between the pp and pd cross sections is valuable for finding the flavor asymmetry. It is especially important that we point out the possibility of measuring the flavor asymmetry in the transversity distributions, because it cannot be found in  $W$ -production processes and inclusive lepton scattering due to the chiral-odd property. We hope that the experimental possibilities are seriously considered at FNAL, HERA, RHIC, and JHF.

## References

- 1) S. Kumano: Phys. Rep. **303**, 183 (1998).
- 2) S. Kumano and M. Miyama: hep-ph/9909432.
- 3) S. Hino and S. Kumano: Phys. Rev. D **59**, 094026 (1999); Phys. Rev. D **60**, 054018 (1999).
- 4) M. Hirai, S. Kumano, and M. Miyama: Comput. Phys. Commun. **108**, 38 (1998); Comput. Phys. Commun. **111**, 150 (1998).

# Nucleon-Structure Functions in the NJL Model<sup>†</sup>

H. Mineo,\* W. Bentz, and K. Yazaki

[Quark distribution function, Faddeev approach, NJL model]

Quark light-cone momentum distributions in the nucleon are calculated in a relativistic 3-body approach to the NJL model<sup>1,2)</sup> by using a simple “static approximation”<sup>3)</sup> for the Faddeev kernel, which reduces the original three-body problem to an effective two-body problem.

A method based on a straightforward Feynman-diagram evaluation is presented which automatically satisfies the number and momentum sum rules, even in the regularized theory. In order to assess the sensitivity to the regularization scheme, two schemes which can be formulated in terms of light-cone variables are discussed. One is due to Lepage and Brodsky,<sup>4)</sup> which introduces a cut-off in the two-body invariant masses. The other is due to Lenz *et al.*,<sup>5)</sup> which introduces a cut-off only in the transverse directions, while renormalizing the longitudinal direction. A comparison of the resulting distributions with the empirical ones after the  $Q^2$ -evolution<sup>6)</sup> indicates that the latter scheme is superior, which is similar to the situation found previously for the distribution in the pion.<sup>7)</sup>

The effects of the (composite) pion cloud are taken into account in a convolution approach, and the violation of the Gottfried sum rule is discussed. The effects slightly improve the agreement with the empirical distributions and enhance the violation, but are not sufficient to explain the observed asymmetry of the sea-quark distributions.

## References

- 1) Y. Nambu and G. Jona-Lasinio: Phys. Rev. **122**, 345 (1960); Phys. Rev. **124**, 246 (1961).
- 2) T. Hatsuda and T. Kunihiro: Phys. Rep. **247**, 221 (1994).
- 3) N. Ishii, W. Bentz, and K. Yazaki: Nucl. Phys. A **578**, 617 (1995).
- 4) G. P. Lepage and S. J. Brodsky: Phys. Rev. D **22**, 2157 (1980).
- 5) F. Lenz, K. Ohta, M. Thies, and K. Yazaki: to be published.
- 6) S. Kumano: Phys. Rep. **303**, 183 (1998); M. Miyama and S. Kumano: Comp. Phys. Commun. **94**, 185 (1996).
- 7) W. Bentz, T. Hama, T. Matsuki, and K. Yazaki: Nucl. Phys. A **651**, 143 (1999).

<sup>†</sup> Condensed from the article in Phys. Rev. C **60**, 065201 (1999)

\* Department of Physics, Graduate School of Science, University of Tokyo

# $U_A(1)$ Symmetry Breaking and Eta Prime Meson in the Bethe-Salpeter Approach

K. Naito, K. Yoshida,\* Y. Nemoto, M. Oka,\* and M. Takizawa

[Chiral symmetry,  $U_A(1)$  anomaly, Relativistic bound state]

Chiral symmetry and its spontaneous breakdown are key concepts in hadron physics. Eight pseudo-scalar mesons ( $\pi, K, \eta$ ) have been identified as the Nambu-Goldstone bosons. Further,  $U_A(1)$  symmetry breaking is also important, because it affects the chiral symmetry breaking and the properties of the ninth pseudo-scalar meson,  $\eta'$ . Since the chiral symmetry is closely related to the Lorentz covariance, non-relativistic approaches, such as the harmonic-oscillator model, are not suitable. We use the fully relativistic Bethe-Salpeter approach and concentrate on the pseudo-scalar mesons:  $\pi, \eta$  and  $\eta'$ .

We employ the improved ladder gluon exchange interaction<sup>1,2)</sup> and the 't Hooft-type three-flavor determinant interaction,

$$-(I_G)^5 \{ \det[\bar{\psi}(1 - \gamma_5)\psi] + \det[\bar{\psi}(1 + \gamma_5)\psi] \}, \quad (1)$$

with the Gaussian form factor. The former reproduces the asymptotic behavior of the quark propagator and the latter brings a  $U(1)_A$  symmetry breaking. The quark full propagator is obtained by the Schwinger-Dyson (SD) equation shown in Fig. 1. The bound state is obtained by the Bethe-Salpeter (BS) equation shown in Fig. 2. These coupled equations respect the chiral symmetry and its spontaneous symmetry breaking.

The results are given in Table 1 and Fig. 3. We choose the model parameters to bring out the strong chiral symmetry breaking by the gluon exchange interaction mainly. The scale parameter is fixed at  $\Lambda_{\text{QCD}} = 600$  MeV. This value is somewhat larger than the standard value. This is because the lack of the infrared enhancement of the gluon propagator we employed. In our approach, the BS amplitude is obtained

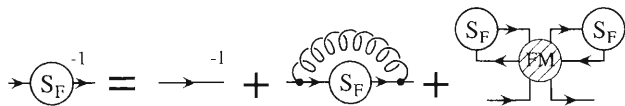


Fig. 1. SD equation.

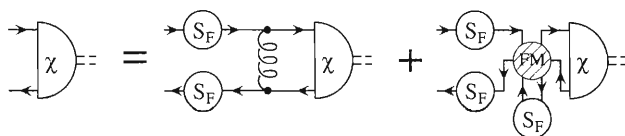


Fig. 2. BS equation.

Table 1. The  $\eta'$ -meson solutions of the BS equation.

$m_{qR}$ MeV	$m_{sR}$ MeV	$I_G$ $\text{GeV}^{-1}$	$M_{\eta'}$ MeV	$f_8^{\eta'}$ MeV	$f_0^{\eta'}$ MeV	$\theta_{\eta'}$ deg
0	0	0.0	0	0	86	0
0	0	1.6	194	0	87	0
0	0	2.0	350	0	88	0
0	0	2.4	634	0	94	0
0	100	0.0	723	-101	72	-54.7
0	100	1.6	731	-99	76	-52.5
0	100	2.0	764	-88	88	-45.0
0	100	2.4	1020	-41	118	-19.2
5	100	0.0	723	-101	72	-54.7
5	100	1.6	732	-98	77	-51.8
5	100	2.0	777	-86	90	-43.7
5	100	2.4	1060	-36	122	-16.4

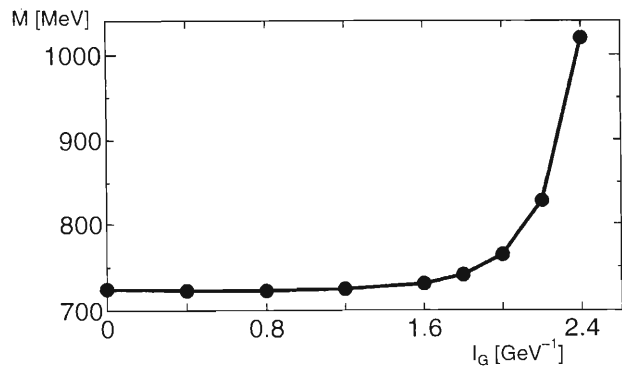


Fig. 3.  $I_G$  dependence of the mass of the  $\eta'$  meson with  $m_{qR} = 0$  and  $m_{sR} = 100$  MeV.

as a solution of the BS equation. Its flavor structure depends on both the relative and total momenta of the quark and anti-quark. We thus define the mixing angle from the decay constants,  $f_8$  and  $f_0$ . In the  $SU(3)$  symmetry limit, no flavor mixing occurs. On the other hand, in the broken  $SU(3)$  case with  $I_G = 0$ ,  $\eta$  and  $\eta'$  are in ideally mixed states, i.e.,  $\theta_{\eta'} = \arctan(-\sqrt{2}) = -54.7$ . The mixing angles,  $\theta_{\eta}$  and  $\theta_{\eta'}$ , increase as  $I_G$  becomes strong. Physically, the mixing angle for the  $\eta'$  meson,  $\theta_{\eta'}$ , is more than 5/3-times the calculated mixing angle for the  $\eta$  meson. This means that the momentum dependence of the flavor structures is not very small. In Fig. 3, the effect of the mixing of the  $u, d$  quark component seems to be negligible, and the  $\eta'$  meson mass grows rapidly from  $I_G \sim 2.0$   $\text{GeV}^{-1}$ .

## References

- 1) K. Aoki, M. Bando, T. Kugo, M. G. Mitchard, and H. Nakatani: Prog. Theor. Phys. **84**, 683 (1990).
- 2) K. Naito, K. Yoshida, Y. Nemoto, M. Oka, and M. Takizawa: Phys. Rev. C **59**, 1095 (1999).

\* Department of Physics, Tokyo Institute of Technology

## Final Countdown to RHIC Spin Program

H. En'yo, I. Alekseev,<sup>\*1</sup> T. Awes,<sup>\*2</sup> M. Bai,<sup>\*3</sup> B. Bassalleck,<sup>\*4</sup> S. Bathe,<sup>\*5</sup> A. Bazilevsky, M. L. Brooks,<sup>\*6</sup> D. Bucher,<sup>\*5</sup> H. Buesching,<sup>\*5</sup> G. Bunce, V. Cianciolo,<sup>\*2</sup> A. Deshpande,<sup>\*7</sup> J. Doskow,<sup>\*8</sup> S. Eilerts,<sup>\*4</sup> D. E. Fields,<sup>\*4</sup> Y. Goto, H. Hamagaki, N. Hayashi, H. Huang,<sup>\*3</sup> V. Hughes,<sup>\*7</sup> T. Ichihara, K. Imai, M. Ippolitov,<sup>\*9</sup> M. Ishihara, V. Kanavets,<sup>\*1</sup> D. M. Lee,<sup>\*6</sup> E. Kistenev,<sup>\*3</sup> L. Kotchenda,<sup>\*10</sup> K. Kurita, K. Kwiatkowski,<sup>\*8</sup> B. Lewis,<sup>\*4</sup> Z. Li, B. Lozowski,<sup>\*8</sup> Y. Makdisi,<sup>\*3</sup> Y. Mao, H.-O. Meyer,<sup>\*8</sup> V. Mexner,<sup>\*5</sup> J. Murata, M. Nakamura,<sup>\*3</sup> S. Pate,<sup>\*11</sup> T. Peitzman,<sup>\*5</sup> U. von Poblitzki,<sup>\*5</sup> K. Pope,<sup>\*12</sup> B. Przewoski,<sup>\*8</sup> K. Read,<sup>\*2,\*8</sup> T. Rinkel,<sup>\*8</sup> T. Roser,<sup>\*3</sup> A. Rusek,<sup>\*3</sup> N. Saito, T. Sakuma,<sup>\*13</sup> H. D. Sato, S. Sawada, T.-A. Shibata, B. Smith,<sup>\*4</sup> W. Sondheim,<sup>\*6</sup> S. Sorenson,<sup>\*12</sup> M. Sugioka, D. Svirida,<sup>\*1</sup> M. Syphers,<sup>\*3</sup> A. Taketani, E. Taniguchi, T. L. Thomas,<sup>\*4</sup> W. Tian,<sup>\*2,\*14</sup> J. Tojo, H. Torii, D. Underwood,<sup>\*15</sup> C. Velissaris,<sup>\*11</sup> Y. Watanabe, S. White,<sup>\*3</sup> D. Wolfe,<sup>\*4</sup> K. Yamamoto,<sup>\*16</sup> S. Yokkaichi, and L. Zhu

[ $pp$  interaction, Structure function, Spin, Asymmetry, Polarized beam]

The relativistic heavy-ion collider (RHIC) will undergo its first collision in the year 2000. The RIKEN collaboration of this international project has resulted in strong enhancements to the collider, one of which is the upgrade of the collider for the acceleration of polarized protons and another is the upgrade of the PHENIX detector for the study of spin physics. The RHIC has become the machine with which to explore "The creation of quark gluon plasma" which has been a dream of physicists for over 20 years, as well as to solve "The spin puzzle of the nucleon" which relates to the fundamentals of quantum chromodynamics (QCD).

The superspectrometer, PHENIX, which we are working on, will play an important role in exploring such physics at RHIC. The collaboration includes 41 institutes and about 400 physicists and engineers. The spectrometer consists of two arms for electron and photon detection and another two for muon detection (see the figure below). The second muon arm was added to increase the spin physics capability of PHENIX. These probes (leptons and photons) are essential for the investigation of the state of nuclear matter in heavy-ion collisions, and also for the detection of possible spin carriers (gluons and antiquarks) to reconstruct the missing spin in a nucleon from individual constituents of a nucleon. The polarized proton collider will enable us, for the first time, to directly

measure those spin carriers which remain unidentified in former experiments using polarized lepton scattering.

In 1999 we passed a very important milestone with the onset of RHIC operation with the successful storage of beam particles in the rings. The development of the RHIC polarimeter is one of our major contributions this year to the spin acceleration project at RHIC. Our recent work has established a novel technique using proton-carbon nuclear interference for the beam polarization measurements.<sup>1)</sup> The RHIC polarimeter design is now in progress based on this method.

The successful completion of the muon identifier construction, which was carried out in Japan and the USA,<sup>2,3)</sup> is now followed by efforts to make the detector operational in the collision hall.<sup>4)</sup> Since May 1999 we have been contributing to the muon tracking-chamber construction,<sup>5)</sup> another of the key detectors in the muon arms to be installed in the summer of 2000. The quality assurance of the produced chambers is the one of our major responsibilities.

For the detections of electromagnetic probes it is essential to understand the calorimeter response for high-energy particles. A test experiment was carried out at CERN in 1998<sup>6)</sup> and the analysis is essentially finalized.<sup>7)</sup> The outcome is very promising for the direct  $\gamma$  and the  $W \rightarrow e + \nu$  measurements which are the key channels of the spin program. The measured energy resolution of the calorimeter was  $d\sigma/E = 1.9\% + 8.2\%/\sqrt{E}$  with a linearity better than 2% up to the energy of 80 GeV.

The new project of constructing a computing complex containing 300 Linux-based PCs at Wako was begun in 1999,<sup>8)</sup> and is the key project in the analyses of the data. The goal of the project is to reach 10 k SPECint95 by the end of 2001. Even in the preliminary stages of development in 1999, the simulation works have progressed significantly owing to this new computing project. A possible new probe, the coincidence signal of electron and muon, to detect gluon polarization was recently studied with the sim-

---

\*1 Institute of Theoretical and Experimental Physics, Russia  
 \*2 Oak Ridge National Laboratory, USA  
 \*3 Brookhaven National Laboratory, USA  
 \*4 Department of Physics and Astronomy, University of New Mexico, USA  
 \*5 University of Muenster, Germany  
 \*6 Los Alamos National Laboratory, USA  
 \*7 Department of Physics, Yale University, USA  
 \*8 Indiana University Cyclotron Facility, USA  
 \*9 Kurchatov Institute, Russia  
 \*10 Interphysica, Russia  
 \*11 New Mexico State University, USA  
 \*12 University of Tennessee, USA  
 \*13 Tokyo Institute of Technology  
 \*14 CIAE, China  
 \*15 Argonne National Laboratory, USA  
 \*16 Department of Physics, Kyoto University



Fig. 1. The PHENIX detector. Two magnets with a flowerpot shape on the left- and right-hand sides are the muon magnets (the left one is fabricated in Kobe, Japan). Adjacent to these, one can see the panels of the muon identifiers. The central magnet and the frames of the central arms are seen at the center, pending the installation of the detectors for electrons and photons. [Photograph by R. Stoutenburgh (BNL)]

ulation, and proved to be sensitive to the gluon-gluon scattering which produces a heavy quark pair with an excellent signal-to-background ratio.<sup>9)</sup> Progress is has also been made in the muon identification and muon tracking software<sup>10)</sup> through the full simulation of the detector response in the muon arms.

The final countdown to the first collision has begun. Although a lot of work remains to be accomplished by then, we enjoy marching towards the promised land of spin physics (Fig. 1).

#### References

- 1) J. Tojo et al.: RIKEN Accel. Prog. Rep. **33**, 170 (2000).
- 2) K. Kurita et al.: RIKEN Accel. Prog. Rep. **32**, 48

- (1999).
- 3) A. Taketani et al.: RIKEN Accel. Prog. Rep. **32**, 50 (1999).
- 4) A. Taketani et al.: RIKEN Accel. Prog. Rep. **33**, 166 (2000).
- 5) J. Murata et al.: RIKEN Accel. Prog. Rep. **33**, 165 (2000).
- 6) Y. Goto et al.: RIKEN Accel. Prog. Rep. **32**, 47 (1999).
- 7) H. Torii et al.: RIKEN Accel. Prog. Rep. **33**, 168 (2000).
- 8) T. Ichihara et al.: RIKEN Accel. Prog. Rep. **33**, 172 (2000).
- 9) H. D. Sato et al.: RIKEN Accel. Prog. Rep. **33**, 44 (2000).
- 10) Y. Mao et al.: RIKEN Accel. Prog. Rep. **33**, 46 (2000).

# Measurement of the Charged Pion Asymmetry and Beam Polarization in AGS E925

N. Hayashi, C. Allgower,<sup>\*1</sup> M. Bai,<sup>\*2</sup> V. Baturine,<sup>\*3</sup> N. Belikov,<sup>\*4</sup> G. Bunce,<sup>\*2</sup> A. Derevschikov,<sup>\*4</sup> H. En'yo, V. Ghazikhanian,<sup>\*5</sup> Y. Goto, M. Grosse Perdekamp, T. Ichihara, G. Igo,<sup>\*5</sup> T. Kasprzyk,<sup>\*4</sup> Y. Kondo,<sup>\*6</sup> K. Krueger,<sup>\*1</sup> H. Huang,<sup>\*2</sup> S.-Y. Lee,<sup>\*7</sup> Y. Matulenko,<sup>\*4</sup> Y. Makdisi,<sup>\*2</sup> Y. Nakada, M. Nakamura,<sup>\*6</sup> L. Nogach,<sup>\*4</sup> S. Nurushev,<sup>\*4</sup> N. Saito, H. Sakai, H. Sato, A. Taketani, A. Ogawa,<sup>\*3</sup> M. Okamura, A. Pavlinov,<sup>\*4</sup> T. Roser,<sup>\*2</sup> H. Spinka,<sup>\*1</sup> M. Syphers,<sup>\*2</sup> S. Trentalange,<sup>\*5</sup> D. Underwood,<sup>\*1</sup> A. Vasiliev,<sup>\*4</sup> T. Wakasa, C. Whitten,<sup>\*5</sup> K. Yako, A. Yokosawa,<sup>\*1</sup> and L. Zhu

[RHIC, AGS, Spin, Asymmetry, Polarized beam, Polarimeter]

We have measured the inclusive charged pion asymmetry at the large- $x_F$  and high- $p_T$  region for 22-GeV/ $c$  transversely polarized protons scattered from carbon or liquid-hydrogen targets.<sup>1)</sup> This phenomenon has been considered in relation to such phenomena as hyperon polarization from unpolarized beams and the proton spin crisis. The mechanism may be studied via inclusive hadron production in polarized proton interactions.

The experiments were performed in November, 1997, with a carbon target and in March, 1999, with a hydrogen target. This paper presents the results of the carbon target; an analysis of hydrogen data using the same procedure is under way.

The polarized proton beam was extracted from the BNL AGS and its polarization,  $P$ , was measured by  $pp$  elastic scattering with a  $\text{CH}_2$  target. In 1997 the polarization  $P$  was determined to be  $P = 0.271 \pm 0.059(\text{stat.}) \pm 0.028(\text{syst.})$ . A detailed description can be found in a previous report.<sup>2)</sup>

Inclusive measurements were carried out using an independent set of counters (BL1-4, BR1-4, FLA(B) and FRA(B)) for the elastic arm (see Fig. 1). Pion triggers from a 4.0-cm thick carbon target were defined as the combination of three counter hits (S1, S2 and S3) and three out of four hodoscopes (H1-4). The spectrometer magnet gave a transverse momentum kick,  $p_T$ , of about 1 GeV/ $c$ . Its magnetic field was reversed periodically to accept both positive and negative pions. From the position information in each hodoscope, the particle momentum as well as Feynman's  $x_F$  and  $p_T$  were extracted. A threshold-type Cerenkov counter filled with about 2 bar of  $\text{CO}_2$  was used to separate pions from other hadrons.

The asymmetry,  $A_N$ , of inclusive pions was measured as a function of  $x_F$  using

$$A_N = \frac{N^\downarrow - N^\uparrow}{P[N^\downarrow + N^\uparrow - 2N_B]}, \quad (1)$$

<sup>\*1</sup> Argonne National Laboratory, USA

<sup>\*2</sup> Brookhaven National Laboratory, USA

<sup>\*3</sup> Pennsylvania State University, USA

<sup>\*4</sup> Institute of High Energy Physics, Russia

<sup>\*5</sup> UCLA, USA

<sup>\*6</sup> Kyoto University

<sup>\*7</sup> Indiana University, USA

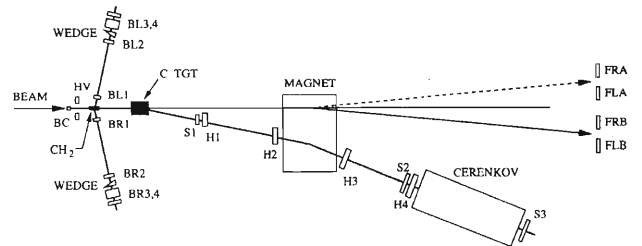


Fig. 1. Schematic drawing of the E925 setup.

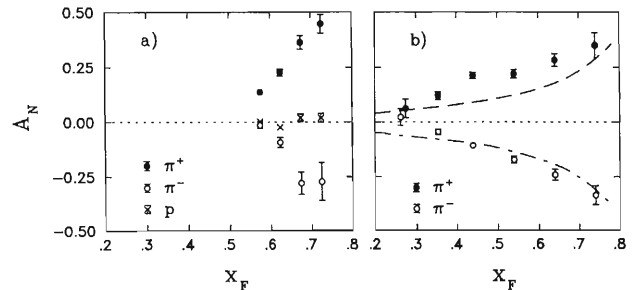


Fig. 2. Inclusive asymmetry,  $A_N$ , measured as a function of  $x_F$  at a) 22 GeV/ $c$  and b) 200 GeV/ $c$ .

where  $N^\downarrow$  ( $N^\uparrow$ ) is the normalized number of produced particles going to the right when the polarization of the beam is pointing up (down).  $N_B$  is the normalized number of estimated background events.

The obtained value of  $A_N$  is shown in Fig. 2 a). Here, they are compared with the results from experiment FNAL-E704 (Fig. 2 b)) (200 GeV/ $c$  polarized proton beam on a hydrogen target).<sup>3)</sup> It should be noted that the asymmetry is large and the  $x_F$  dependence similar to the E704 results in the large- $x_F$  region, despite the large difference in the beam momenta and production targets. This feature could be exploited as a high-energy proton beam polarimeter for accelerators, such as RHIC or HERA.

## References

- 1) K. Krueger et al.: Phys. Lett. B **459**, 412 (1999).
- 2) N. Hayashi et al.: RIKEN Accel. Prog. Rep. **32**, 46 (1999).
- 3) D. L. Adams et al.: Phys. Lett. B **264**, 462 (1991).

# Sensitivities of the Gluon Polarization Measurement at PHENIX

A. Bazilevsky, H. En'yo, Y. Goto, N. Hayashi, K. Imai, K. Kurita, Y. Mao, N. Saito,  
H. D. Sato, T. Sakuma, T.-A. Shibata, and A. Taketani

[RHIC, PHENIX, Spin, Asymmetry, Gluon polarization]

Polarized deep inelastic scattering experiments show that the fraction of the quark polarization in the proton is only about 30% of the proton spin. The remaining fraction needs to be explained by other sources. We plan to directly measure the gluon polarization in the proton at PHENIX using RHIC polarized-proton collisions. This will be carried out by utilizing gluon+quark and gluon+gluon reactions. At PHENIX, we have two kinds of detector systems to detect many channels of physics signals from these reactions. Two Muon Arms detect muons in the forward pseudo-rapidity region,  $1.2 < |\eta| < 2.4$ . Two Central Arms detect photons, hadrons, and electrons in the central pseudo-rapidity region,  $|\eta| < 0.35$ . Each of these channels covers different kinematical range complementally. The range of the momentum fraction of the gluon in the proton,  $x_g$ , extends from 0.005 to 0.3 totally.

The open and bound-state heavy-flavor production are to be identified by detecting lepton(s) using the Muon Arms and the Central Arms. Since these reactions are dominated by the gluon fusion process at RHIC energy, a measurement of the double-longitudinal spin asymmetry,  $A_{LL}$ , is sensitive to the gluon polarization,  $\Delta G(x)/G(x)$ , in the proton. We show three channels used to probe the heavy-flavor production: di-muon, high- $p_T$  single electron, and electron-muon pair. We have estimated the ratios of the signal and background events, and have investigated the sensitivities to the gluon polarization measurement in each channel.

Prompt photons and  $\pi^0$ s are detected in the Central Arms. The prompt photon production is theoretically a clean channel, because it is dominated by the gluon Compton process. By measuring  $A_{LL}$ , we can determine the gluon polarization by using knowledge of the quark polarization from the polarized deep-inelastic-scattering experiments and the calculable asymmetry of the gluon Compton process. A measurement of  $\pi^0$  serves both as a background estimation of a prompt photon measurement, and as a measurement of the gluon polarization by itself.

We studied the sensitivities of our measurements using the PYTHIA event generator and the GRV-94LO parton distribution function for  $pp$  collisions. To evaluate  $A_{LL}$ , three models of the polarized parton distribution function (GS-A, GS-B, and GS-C) with different gluon polarization are used.<sup>1)</sup>

Table 1 summarizes the estimated statistical errors

Table 1. Summary of the estimated statistical errors and predicted values of the  $A_{LL}$  and the  $x_g$  range to be covered by each channel. The statistical errors show the absolute values for 10% luminosity  $32pb^{-1}$  for channels indicated by,\*<sup>)</sup> and full luminosity  $320pb^{-1}$  for other channels.

Probes	$A_{LL}$	$A_{LL}$ Predictions			$x_g$ Range
	Errors	GS-A	GS-B	GS-C	
$J/\psi \rightarrow \mu\mu$	0.006	0.01	0.01	0.002	0.005 - 0.01
$c\bar{c} \rightarrow eX$	0.001* <sup>)</sup>	-0.02	-0.01	-0.0003	0.005 - 0.2
$c\bar{c} \rightarrow e\mu X$	0.006	-0.05	-0.02	-0.0001	0.005 - 0.2
$b\bar{b} \rightarrow e\mu X$	0.006	0.01	0.01	-0.0004	0.01 - 0.3
prompt $\gamma$	0.006	0.05	0.03	0.001	0.1 - 0.3
$\pi^0$	0.001* <sup>)</sup>	0.02	0.01	0.0001	0.05 - 0.3

and predicted values of the  $A_{LL}$  and the  $x_g$  range to be covered by each channel. We encountered systematic errors from a background subtraction procedure and beam-polarization and -luminosity measurements.

We can clearly identify  $J/\psi$ s by reconstructing the invariant mass of di-muons with a mass resolution of  $100 \text{ MeV}/c^2$ . We also plan to measure the polarization of  $J/\psi$  to investigate its production mechanism. We have a large yield of single electrons with  $p_T > 1 \text{ GeV}/c$  from open charm quarks and have good sensitivity with only 10% of the full luminosity to distinguish the three models. We can perform this measurement in the first year of the RHIC polarized-proton run (2000-). We can reduce the major background from  $\pi^0$  Dalitz decays and  $\gamma$  conversions effectively by detecting charged tracks. An electron-muon pair is also a useful probe for open heavy-flavor production because of the low background event rate. The background from hadrons can be estimated and subtracted by comparing like-sign and unlike-sign pairs.

We can detect prompt photons in the  $p_T$  range of more than  $10 \text{ GeV}/c$  using a background-reduction technique, like an isolation cut. For a  $\pi^0$  measurement, we have a large yield at  $p_T > 5 \text{ GeV}/c$ . Identification of  $\pi^0$ s can be achieved by mass reconstruction of 2 photons with a small background in this  $p_T$  range. The

measurement can be performed from 2000.

In summary, we can start the gluon polarization measurement from the first year of the RHIC polarized-proton run with many feasible channels.

#### References

- 1) T. Sakuma et al.: RIKEN Accel. Prog. Rep. **32**, 45 (1999); Y. Goto et al.: RIKEN Accel. Prog. Rep. **31**, 54 (1998) and references therein.

## Performance of the PHENIX Muon Reconstruction Software

Y. Mao, M. L. Brooks,<sup>\*1</sup> N. Hayashi, K. Kurita, J. Murata, K. Pope,<sup>\*2</sup> K. Read,<sup>\*2</sup> N. Saito, H. Sato, S. Sorenson,<sup>\*2</sup> and A. Taketani

[Reconstruction efficiency, Road finding, Track finding]

We have been developing and testing offline software to reconstruct muon events for the PHENIX experiment. The integrated muon offline software has been established, and has been used for various studies, such as Mock Data Challenge(MDC)<sup>1)</sup> and a study of the beam pipe shielding for south muon arm. Single-muon events were simulated and reconstructed to check the reconstruction efficiency of the software; single-pion events were simulated and passed to the whole analysis chain to see the hadron rejection capability as well. The performance of the software to analyze data in high multiplicity was also investigated by mixing J/ $\Psi$  signal events with central Au-Au background events.

The complete data-simulation procedure is as follows: Generate events with a event generator, for example a PYTHIA event generator; pass the events to PHENIX Integrated Simulation Application (PISA) to simulate the detector response; convert the PISA output to PHENIX Raw Data Format (PRDF); reconstruct the PRDF events and save them as Data Summary Tape (DST). The PHENIX muon detector comprises two arms with a tracking part (MuTr) and an identification part (MuID) in each arm. The reconstruction of an event can be briefly described as: (1) find the clusters in each gap of the MuID; (2) find roads in the MuID based on the clusters; (3) pass the found roads to MuTr track finding; (4) apply a particle-identification algorithm with such information as the momentum and the depth in MuID of a found track.

We improved our road-finding algorithm<sup>2)</sup> during a study for beam shielding for the south muon arm. A new version of the road finder was optimized in order to satisfy the following requirements: a higher reconstruction efficiency and a smaller number of ghost roads by allowing a smaller cluster size and a larger search window and implementing a share-hit method to drop ghost roads. It is possible to study specific physics by setting the control parameters; for example, one can choose a narrow search window and a deeper depth if a high-momentum muon is interesting. One can also use a looser cut for p-p and a tighter cut for the Au-Au collision to drop ghost roads for the multiplicity is much less in the former case.

We analyzed 3000 single muon events and 30000 single pion events to check the muon software performance. The muons and/or pions were launched from the collision point with an emission angle of  $135^\circ \pm 2^\circ$

and an azimuthal angle of  $155^\circ$ . The results had, as shown in Table 1, a road-finding efficiency of about 99% and a track-finding efficiency of about 96–98% for muons in 2.5–5.0 GeV/c momentum region, while the pion-reduction rate was about  $3.1 \times 10^{-3}$  in the same momentum region. The efficiency loss was only a few percent after applying muon identification.

To check the performance in high multiplicity, we analyzed 2000 J/ $\Psi$  mixed with Au-Au central events. Figure 1 shows the mass spectrum of the mixed events. The J/ $\Psi$  resonance was clearly seen, even mixed with such strong background, the multiplicity being about 3000/event in a muon arm. The signal/noise ratio was about 15 : 1 in the J/ $\Psi$  mass region. The number of reconstructed J/ $\Psi$  muon pairs in Fig. 1 was consistent with the numbers in Table 1 after considering the efficiency loss due to the chamber framework of MuTr and the absorber of MuID.

As a result from our evaluation work as well as from our MDC1 and MDC2, we have confirmed that the muon offline software is in good shape, and is satisfactory for our current requirement. Some more refinements are necessary in the muon-identification module

Table 1. The performance of muon software.

Momentum GeV/c	Road finder	Track finder	Identi- fication
Muon reconstruction efficiency			
2.5	99.2%	95.7%	98.7%
3.0	99.7%	96.5%	99.8%
5.0	99.9%	98.2%	99.9%
Pions reduction rate			
2.5	$3.5 \times 10^{-3}$	$2.5 \times 10^{-3}$	$2.2 \times 10^{-3}$
3.0	$5.1 \times 10^{-3}$	$3.9 \times 10^{-3}$	$3.2 \times 10^{-3}$
5.0	$8.5 \times 10^{-3}$	$5.8 \times 10^{-3}$	$3.8 \times 10^{-3}$

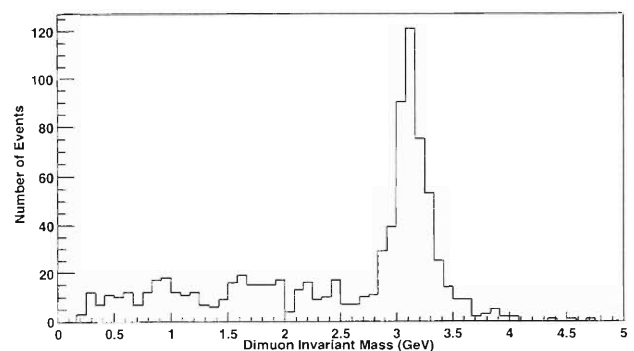


Fig. 1. The reconstructed dimuon mass spectrum.

<sup>\*1</sup> Physics Division, LANL, USA

<sup>\*2</sup> Physics Department, University of Tennessee, USA

to reject more hadrons and in the ghost track drop module to throw away more ghost tracks while keeping a relatively high muon reconstruction efficiency.

Shimane.

- 2) Y. Mao: <http://www.phenix.bnl.gov/phenix/WWW/publish/mao/roadfinder/algorithm/>

#### References

- 1) H. Sato et al.: Japan Physics Society Meet., 1999 Fall,

## Precise Measurement of the Muon Lifetime

S. N. Nakamura, D. Tomono,\*<sup>1</sup> Y. Matsuda, K. Ishida, T. Matsuzaki, I. Watanabe,  
K. Nagamine, M. Iwasaki, S. Sakamoto, and G. Mason\*<sup>2</sup>

[Standard model, Fermi coupling constant, Muon lifetime]

The Fermi coupling constant ( $G_F$ ) is one of the most basic parameters of the standard model. The standard model requires at least three electroweak parameters from the experimental measurements; usually  $\alpha$  (the fine structure constant),  $M_Z$  (the mass of  $Z$ ) and  $G_F$  are used. The uncertainty of  $\alpha$ ,  $M_Z$  and  $G_F$  are, respectively, 0.045 ppm, 77 ppm and 17 ppm;<sup>1)</sup> thus, the  $M_Z$  uncertainty dominated until now. However, the recent preliminary LEP results yield an uncertainty of the  $Z$  mass of 20 ppm or less;<sup>2)</sup> the situation is changing.

The muon lifetime is directly associated with  $G_F$  by the muon lifetime formula.<sup>3)</sup> The input uncertainty of  $G_F$  is dominated by the muon lifetime ( $\tau_\mu$ ) uncertainty (PDG average 18 ppm). The uncertainty of the 2-loop electroweak calculation (10–15 ppm) has also been limiting the accuracy of the theoretical application with  $G_F$  defined by the muon lifetime formula in the standard model. However, a precise 2-loop electroweak calculation was recently carried out<sup>4)</sup> with an accuracy of better than 1 ppm; thus, the accuracy of  $G_F$  is now limited by the uncertainty of the experimentally measured muon lifetime.

The last  $\mu^+$  lifetime measurements ( $\sim 30$  ppm accuracy) were performed more than 10 years ago at TRIUMF<sup>5)</sup> and Saclay,<sup>6)</sup> and no improvement has been made so far (Fig. 1). These experiments observed one muon decay in an observation time window to avoid any pileup detection of positrons which distorts the muon decay-time spectrum. With this method, because the data-acquisition rate is simply limited by the

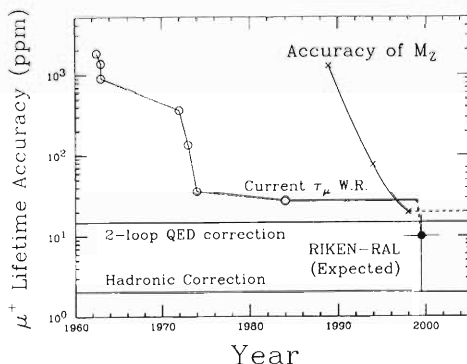


Fig. 1. History of the  $\mu^+$  lifetime accuracy. The accuracy of the  $Z$  mass is also plotted as a reference.

\*<sup>1</sup> Department of Physics, Tokyo Institute of Technology

\*<sup>2</sup> Department of Physics and Astronomy, University of Victoria, Canada

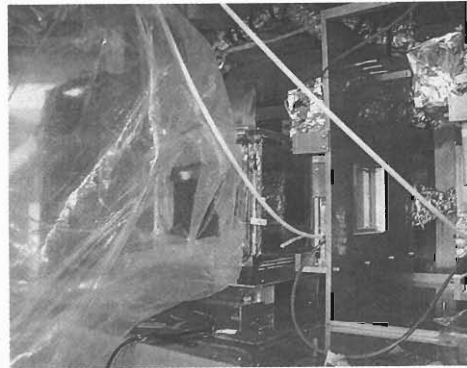


Fig. 2. Setup of the  $\mu^+$  lifetime experiment placed at the port 2 beamline of the RIKEN-RAL Muon Facility. One set of the MWPCs for positron detection can be seen in front of the target, and the other set is hidden by the target and the helium bag.

width of the time window, there exists a practical accuracy limit with a realistic beamtime. It is essential to develop a multi-decay per one time window method for more accurate muon lifetime measurements. We designed a new experimental setup<sup>7)</sup> (Fig. 2) and started to observe  $10^9$ – $10^{10}$  muon decays at the RIKEN-RAL Muon Facility. We used a holmium plate as a muon stopping target to minimize the effect of the muon polarization. The target was placed in a helium bag to reduce the number of the muons stopped around the target. Multiwire proportional chambers (MWPC) were used as a positron timing and tracking device to realize a fine segmentation which reduces the pileup effect. A clock system with GPS (global positioning system) was newly developed to achieve very good differential and integral linearity. We will finish the first-stage data acquisition ( $\sim 5 \times 10^9$  muon decays = 10–20 ppm) by the end of 1999; a preliminary analysis of the acquired data is now in progress.

### References

- 1) C. Caso et al.: Review of Particle Physics, European Physical Journal C **3**, 1 (1998).
- 2) The LEP Collaborations: CERN-PPE/96-183 (1996).
- 3) W. J. Marciano and A. Sirlin: Phys. Rev. Lett. **61**, 1815 (1988).
- 4) T. van Rmmbergen and R. G. Stuart: hep-ph/9904240 (1999).
- 5) K. L. Giovanetti et al.: Phys. Rev. D **29**, 343 (1984).
- 6) G. Bardin: Phys. Lett. B **137**, 135 (1984).
- 7) S. N. Nakamura et al.: RIKEN Rev., No. 20, p. 58 (1999); RIKEN Accel. Prog. Rep. **32**, 173 (1999).

## Measurement of the Ortho-Para Effect in Muon-Catalyzed dd-Fusion

A. Toyoda, K. Ishida, K. Shimomura, Y. Matsuda, W. Higemoto, S. N. Nakamura, T. Matsuzaki, and K. Nagamine

[Keyword  $\mu$ CF, Ortho-para effect]

This measurement will provide a new test of one of the most important theories in muon-catalyzed fusion ( $\mu$ CF), namely the resonant formation of a muonic molecule. It will also provide a critical test on the puzzling "solid state" effect in  $\mu$ CF.

The muon acts as a catalyst in the fusion process through forming a  $dd\mu$  muonic molecule. Here, resonant formation of  $dd\mu$ ,  $d\mu + D_2 \rightarrow [(dd\mu)dee]$  plays an important role. Because of the finite muon lifetime ( $2.2 \mu\text{sec}$ ), the  $dd\mu$  formation rate is quite important in achieving a high fusion yield. By artificially changing the initial molecular state, we expect to increase the formation rate, and thus enhance the overall fusion cycling rate. So far, there have been three parameters

used to change the  $D_2$  state: (1) the temperature, (2) the phase, and (3) the density. This experiment aims to control the fourth parameter, namely the rotational state, which can be achieved by changing the ortho and para ratio of the deuterium.

Furthermore, some theories predicted that the  $dd\mu$  formation rate decreases rapidly with reducing the temperature below 20 K, although the experiments measured no formation rate change below 20 K.<sup>1,2)</sup> At present, there are several possible explanations.<sup>3-5)</sup> The para deuterium plays an essential role in the current explanations for this discrepancy. Our measurement will test these mechanisms by reducing the para concentration.

In the experiment, we measured fusion protons,  $\mu$ -decay electrons, and various muonic X-rays. We formed a solid deuterium target in a vacuum so as to minimize the material between the target and the proton detector.<sup>6)</sup> For fusion proton detection, we use a pair of silicon surface barrier (SSB) detectors. The 3 MeV proton passes the first SSB detector for  $\Delta E$  ( $25 \mu\text{m}^t$ ) and stops in the second one for  $E - \Delta E$  ( $150 \mu\text{m}^t$ ).

The experiment is being carried out at the RIKEN-RAL Muon Facility in the UK. Figure 1 shows a scatter

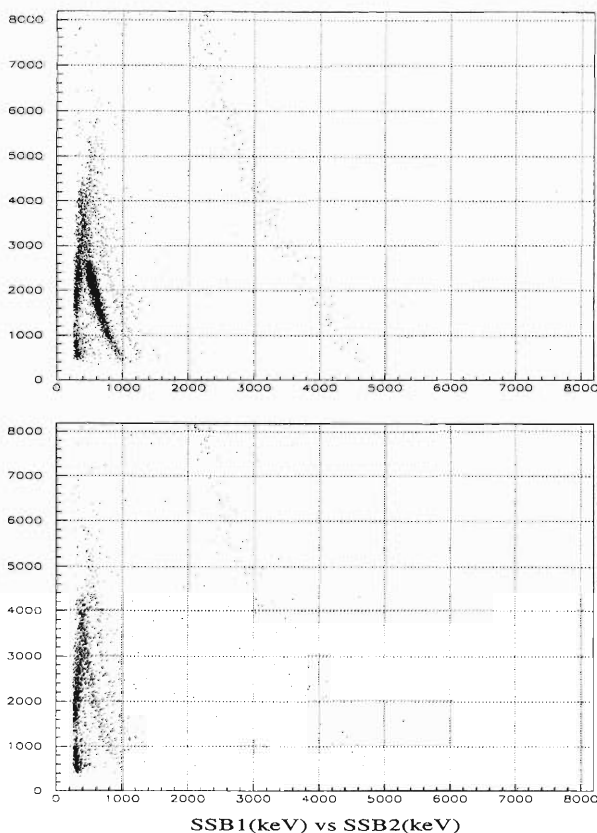


Fig. 1. Scatter plots for the proton detectors. The top figure is for a normal deuterium target and the bottom figure is for an empty target. The horizontal axis is for the energy deposited in the first SSB (in keV) and the vertical is for the second SSB.

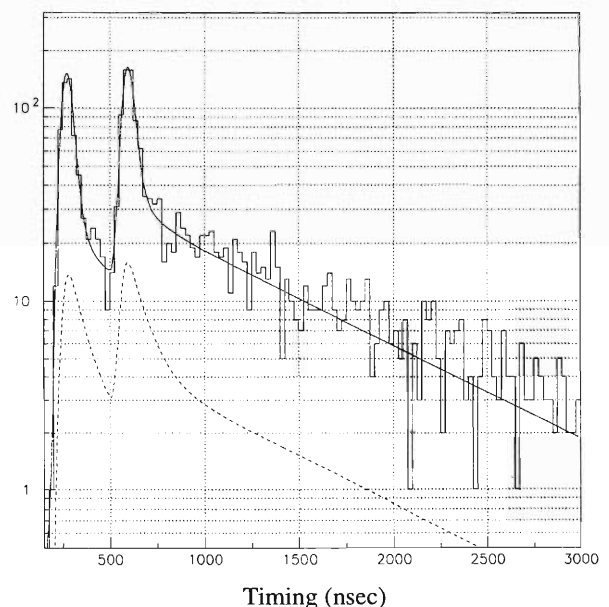


Fig. 2. Fitting result of the fusion proton time spectrum.

plot of the two SSB detector's output pulse height. The fusion protons are clearly seen in the region around  $\text{ADC1}(\Delta E) = 0.6 \text{ MeV}$  and  $\text{ADC2}(E-\Delta E) = 2.4 \text{ MeV}$ . The  $\Delta E$ - $E$  particle-identification method greatly suppressed the background noise, such as by scattered muons and  $\mu e$ -decay electrons to achieve a sufficiently high S/N ratio ( $\sim 5$ ) of fusion protons; nevertheless, we placed the proton detectors near to the muon beam. Figure 2 shows a typical fusion proton time spectrum with fast and slow components. This spectrum also reflects the double-pulsed muon beam structure of the ISIS synchrotron. The dotted line corresponds to the background level, which was estimated from the data without the deuterium target. It is theoretically predicted that the slow component is less dependent on the ortho-para state of deuterium than the fast component; therefore, we compared 33% para(normal) data, 5% para data, and 0.8% para data by observing

the fusion proton yield from the fast component. The detected fusion protons with a fast component normalized by detected electrons from  $\mu$ - $e$  decay in the deuterium target was  $6.4(13) \times 10^{-3}$  for normal deuterium,  $5.6(16) \times 10^{-3}$  for the 5% para case, and  $5.8(24) \times 10^{-3}$  for the 0.8% para case. We are planning further experiments under more sophisticated conditions to improve the statistics.

#### References

- 1) D. L. Demin et al.: *Hyperfine Interact.* **101/102**, 13 (1996).
- 2) P. E. Knowles et al.: *Hyperfine Interact.* **101/102**, 21 (1996).
- 3) L. I. Menshikov et al.: *Hyperfine Interact.* **101/102**, 207 (1996).
- 4) A. Adamczak: *Hyperfine Interact.* **101/102**, 113 (1996).
- 5) G. L. Gurin et al.: *Hyperfine Interact.* **118**, 147 (1999).
- 6) P. Strasser et al.: *Phys. Lett. B* **368**, 32 (1996).

## Study of Muon Catalyzed Fusion in Solid D-T Mixtures

N. Kawamura, K. Nagamine, T. Matsuzaki, K. Ishida, S. N. Nakamura, Y. Matsuda, S. Sakamoto, M. Tanase, M. Kato, K. Kurosawa, H. Sugai, K. Kudo,\*<sup>1</sup> N. Takeda,\*<sup>1</sup> and G. H. Eaton\*<sup>2</sup>

[Muon catalyzed fusion]

Through the muon catalyzed fusion ( $\mu$ CF) studies at the RIKEN-RAL Muon Facility since 1995, we have obtained the muon cycling rate ( $\lambda_c$ ) in solid/liquid deuterium and tritium (D-T) mixtures with various tritium concentration ( $C_t$ ).<sup>1)</sup>

According to Vesman's mechanism, which is based on resonant  $dt\mu$  formation through a two-body collision, i.e.  $t\mu + D_2 \rightarrow [(dt\mu)dee]$ ,  $\lambda_c$  was expected as constant to the D-T mixture density. In order to remove any trivial density dependence,  $\lambda_c$  is already normalized by the target density. However, Jones *et al.* found an unexpected density dependence<sup>2)</sup> (Fig. 1). Our data also showed such a tendency,<sup>1)</sup> and they were comparable to data at above 100 K, although they were obtained at much lower temperatures, 20 K (liquid) and 16 K (solid). On the other hand, a theoretical calculation based on Vesman's mechanism indicated a steep decrease of  $\lambda_c$  with the temperature decreasing below about 100 K.<sup>3)</sup>

Menshikov and Ponomarev introduced the idea of three-body collision<sup>4)</sup>;  $t\mu + D_2 + D_2' \rightarrow [(dt\mu)dee] + D_2'$ , where the third particle,  $D_2'$ , absorbs any excess energy in  $dt\mu$  formation. This explains the high molecular-formation rate at low temperature; also, the density dependence is explained by the contribution

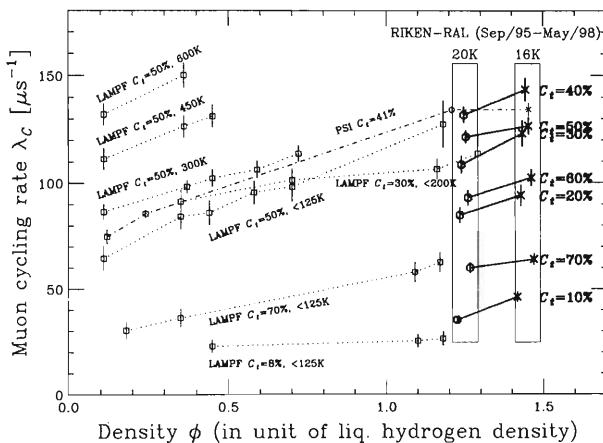


Fig. 1. Density dependence of the muon cycling rate. The liquid and solid data are shown around  $\phi = 1.2-1.3$  (circle) and  $\phi = 1.4-1.5$  (cross), respectively. The reference data are taken from the following articles: "S. E. Jones *et al.*, Phys. Rev. Lett. **56**, 588 (1986)" (LAMPF), and "W. H. Breunlich *et al.*, Phys. Rev. Lett. **58**, 329 (1987)" (PSI).

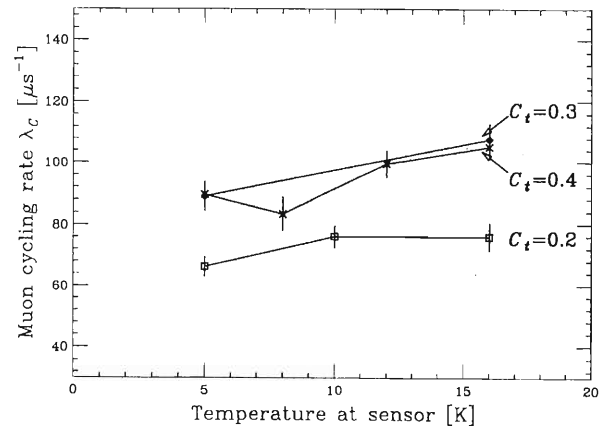


Fig. 2. Observed temperature dependence of the muon cycling rate.

of  $D_2'$ . Fukushima takes into account the effect of phonons in a solid, which play the role of a third particle.<sup>5)</sup> However, still, no theory can provide a quantitative understanding of the unexpected high  $\lambda_c$  at low temperature. Observing the temperature dependence of  $\lambda_c$  can supply new important information to the theory of  $dt\mu$  formation.

In order to investigate this problem, we started a  $\mu$ CF study in a cryo-solid from 16 K to 5 K, and a preliminary analysis was performed. Figure 2 shows the temperature dependence of  $\lambda_c$ . For each  $C_t$ ,  $\lambda_c$  decreases by about 15% with decreasing temperature. This can be explained by a decrease of the  $dt\mu$ -molecule formation rate in collision between  $(t\mu)^{F=0}$  and  $D_2$  ( $\lambda_{dt\mu}^{F=0,D_2}$ ):  $420 \mu s^{-1}$  (16 K)  $\rightarrow$   $300 \mu s^{-1}$  (5 K), where  $F$  denotes the hyperfine level. However, there is a slight possibility that the change of a different parameter, such as the muon transfer rate from  $(d\mu)_{1s}$  to  $(t\mu)_{1s}$  ( $\lambda_{dt}$ ), would cause a decrease of  $\lambda_c$ . By analyzing the  $C_t$  dependence of  $\lambda_c$ ,  $\lambda_c$  can be dissolved into  $\lambda_{dt\mu}^{F=0,D_2}$  and  $\lambda_{dt}$  terms. In the coming experiment, we will use a high- $C_t$  target and determine the cause of the decrease of  $\lambda_c$ .

### References

- 1) K. Nagamine *et al.*: Hyperfine Interact. **119**, 273 (1999).
- 2) S. E. Jones *et al.*: Phys. Rev. Lett. **56**, 588 (1986).
- 3) M. P. Faifman *et al.*: Phys. Lett. B **265**, 201 (1991).
- 4) L. I. Menshikov and L. I. Ponomarev: Phys. Lett. B **167**, 141 (1986).
- 5) K. Fukushima: Phys. Rev. A **48**, 4130 (1993).

\*<sup>1</sup> Electrotechnical Laboratory (ETL)

\*<sup>2</sup> Rutherford-Appleton Laboratory (RAL), UK

## Electron Scattering at MUSES/RIBF

T. Suda, K. Maruyama, and I. Tanihata

[Electron scattering, Charge form factor, Unstable nuclei]

The working group for the electron-nucleus (eA) collider of MUSES has been working to design an electron spectrometer. The main efforts have so far been paid to clarify the necessary performances which an electron spectrometer must have for measuring the elastic electron scattering cross section from unstable nuclei.

As is well known, the charge form factor of a nucleus is deduced from the elastic electron-scattering cross section. The charge distributions, such as radii and shapes, of many unstable nuclei will be determined by elastic electron scattering at MUSES. Simulations have shown that the charge radii can be determined for unstable nuclei whose luminosities ( $L$ ) are greater than  $10^{25} \text{ cm}^{-2} \text{ s}^{-1}$ , and that the shape of the charge distribution will be studied for  $L \geq 10^{27} \text{ cm}^{-2} \text{ s}^{-1}$ . Many unstable nuclei, whose life time is longer than about 1 minute, are expected to be studied at MUSES.

To determine the shape of the charge distribution in unstable nuclei, the charge form factor must be measured over a wide momentum transfer ( $q_{NR}$ ) range by the elastic electron scattering. Here,  $q_{NR}$  is defined in the nucleus-rest (NR) frame. Since the elastic cross section changes rapidly as a function of  $q_{NR}$ , it is important to determine  $q_{NR}$  with high precision. In addition, a good energy-transfer resolution,  $\Delta\omega_{NR}$ , is also necessary to identify the elastic-scattering process.

We set our goal concerning the charge form factor measurements at MUSES as follows:

- (1)  $q_{NR}$  range :  $q_{NR} = 100\text{--}400 \text{ MeV}/c$
- (2)  $q_{NR}$  resolution :  $\Delta q_{NR}/q_{NR} \sim 10^{-3}$
- (3)  $\omega_{NR}$  resolution :  $\Delta\omega_{NR} \leq 1 \text{ MeV}$

The difficulties to design an electron spectrometer to carry out such measurements are related to the limited luminosities for unstable nuclei. Because the conventional electron spectrometers which have good momentum resolution (typically  $10^{-4}$ ) but a small solid angle ( $\sim 30 \text{ msr}$ ), can not be our solution, a large-acceptance spectrometer must be necessarily employed.

The performances that such a large acceptance electron spectrometer must have can be summarized as follows:

- (1) High momentum resolution:  $\Delta p/p \leq 10^{-3}$
- (2) Accurate determination of the scattering angle:  $\Delta\theta \sim 10^{-3} \text{ rad}$ .

Here, let us discuss an optimum electron beam energy ( $E_e$ ) for the charge form-factor measurements at MUSES. From the point of view of luminosity, a higher  $E_e$  is favorable. Higher energy is also better to suppress any multiple scattering effects of electrons in the materials of the spectrometer, such as trackers. In fact, suppressing the multiple-scattering effect is a key to achieving good momentum and angular resolution for scattered electrons.

On the other hand, the minimum electron scattering angle, corresponding to  $q_{NR} = 100 \text{ MeV}/c$ , becomes large for lower  $E_e$ . For example, they are  $12^\circ$ ,  $8^\circ$  and  $6^\circ$  for electron-beam energies of  $E_e = 500, 750$  and  $1000 \text{ MeV}$ , respectively, which are almost independent of the mass number,  $A$ , and the energy of nuclear beam. A lower  $E_e$  frees us from serious interference between the spectrometer and the MUSES rings.

Simulations assuming a large acceptance magnetic spectrometer with tracking devices have shown that the optimum electron beam energy will be in the range of  $E_e = 500\text{--}750 \text{ MeV}$ , and that the necessary performances of an electron spectrometer for this energy range are:

- (1) coverage of a polar angle of  $\theta = 8\text{--}40^\circ$
- (2) coverage of an azimuthal angle of  $\phi = 2\pi$
- (3) field integral greater than  $2 \text{ Tm}$
- (4) total thickness of material,  $X \leq 0.3\%$  of radiation length

Currently, two types of magnetic spectrometers are being intensively discussed. They are spectrometers with a solenoid- and toroidal-magnetic field. Detailed simulations including various effects, such as beam emittance, and multiple scattering, are now under way.

In addition to the simulation, the detection of recoiled nuclei in the storage ring to identify the elastic scattering is also being discussed simultaneously with the design group of MUSES.

In summary, the eA working group has been focusing on designing an electron spectrometer, which will be used for elastic electron-scattering experiments at MUSES to determine the charge distribution of many unstable nuclei. The performances required of the spectrometer have been clarified, and detailed simulations for two types of large-acceptance magnetic spectrometers are in progress.

## Measurement of the Polarization Transfer Coefficients, $K_{ij}^{y'}$ , for $d$ - $p$ Elastic Scattering at $E_d = 270$ MeV

H. Kato, H. Sakai, A. Tamii, T. Ohnishi, K. Sekiguchi, K. Yakou, S. Fukusaka, S. Sakoda, M. Hatano, Y. Maeda, N. Sakamoto, T. Uesaka, Y. Satou, K. S. Itoh, H. Okamura, K. Suda, and T. Wakasa

[NUCLEAR REACTIONS,  ${}^1\text{H}(\vec{d}, \vec{p}){}^2\text{H}$ ,  $E_d = 270$  MeV measured:  $K_{xx}^{y'}$ ,  $K_{yy}^{y'}$ ,  $K_{zz}^{y'}$  and  $P_{y'}$ ]

Measurements of the cross sections as well as the vector- and tensor-analyzing powers for deuteron-proton ( $d$ - $p$ ) elastic scattering at 270 MeV have been reported by Sakamoto *et al.*<sup>1)</sup> and Sekiguchi.<sup>2)</sup> The results are interesting because the observables are sensitive to the effect of the three-nucleon force (3NF).<sup>3,4)</sup> The differential cross sections are in excellent agreement with calculations including 3NF by Witala *et al.*<sup>3)</sup> Although the vector-analyzing powers are also in good agreement, that at the tensor-analyzing powers is rather poor.

As new research on 3NF, we measured the polarization transfer coefficients ( $K_{xx}^{y'}$ ,  $K_{yy}^{y'}$ ,  $K_{zz}^{y'}$ ) and the induced polarization ( $P_{y'}$ ) for  $d$ - $p$  elastic scattering at 270 MeV. The measurement was performed using the spectrometer SMART and polarized deuteron beams. First, polarized deuterons were bombarded onto a polyethylene ( $\text{CH}_2$ ) target. Secondly, the emitted protons were scattered by a carbon target at the second focal plane of SMART. Finally, the scattered protons were detected by a focal-plane polarimeter DPOL, by which the polarizations of the emitted protons were measured.

The relation between the polarizations and the observables can be represented by

$$p_{y'} \frac{d\sigma}{d\Omega} = \frac{d\sigma_0}{d\Omega} \left( P_{y'} + \frac{3}{2} p_y K_y^{y'} + \frac{2}{3} p_{xz} K_{xz}^{y'} + \frac{1}{3} (p_{xx} K_{xx}^{y'} + p_{yy} K_{yy}^{y'} + p_{zz} K_{zz}^{y'}) \right),$$

where  $x$ ,  $y$  and  $z$  are the coordinates of the incident deuterons;  $x'$ ,  $y'$  and  $z'$  are those of the emitted protons; and  $\frac{d\sigma_0}{d\Omega}$  means the differential cross section with unpolarized beams.

The results of the measurement are plotted in Fig. 1. by the solid circles with statistical errors. The solid curves are theoretical predictions with 3NF and the dashed curves are those without 3NF. Both predictions were calculated by Witala *et al.*<sup>3)</sup> The horizontal axis ( $\theta_{cm}$ ) is defined as the angle between the incident and

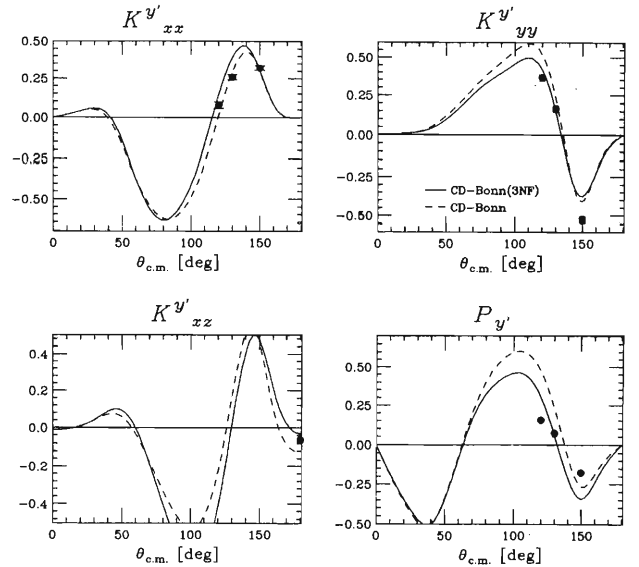


Fig. 1.  $K_{xx}^{y'}$ ,  $K_{yy}^{y'}$ ,  $K_{zz}^{y'}$  and  $P_{y'}$  for the  $d$ - $p$  elastic scattering at  $E_d = 270$  MeV. The solid circles are the experimental results. The dashed curves are theoretical predictions of the Faddeev calculation using the  $NN$  CD-Bonn potential without 3NF. The solid curves are those of a calculation which included the effect of 3NF.

outgoing deuterons in the center-of-mass system.

As a result,  $K_{yy}^{y'}$  and  $K_{zz}^{y'}$  are rather consistent with the predictions with 3NF. However,  $K_{xx}^{y'}$  is rather consistent with the predictions without 3NF.

It cannot be concluded from only this experiment whether the effect of 3NF was observed or not. Clear evidence may be obtained by an additional study at more forward angles, where the discrepancy between those with and without 3NF is much larger.

### References

- 1) N. Sakamoto *et al.*: Phys. Lett. B **367**, 60 (1996).
- 2) K. Sekiguchi: Master thesis, University of Tokyo (1999).
- 3) H. Witala *et al.*: Phys. Rev. Lett. **81**, 1183 (1998).
- 4) S. Nemoto *et al.*: Phys. Rev. C **58**, 2599 (1998).

# Measurement of the Cross Sections and Vector and Tensor Analyzing Powers for $d$ - $p$ Elastic Scattering at $E_d = 270$ MeV

K. Sekiguchi, H. Sakai, N. Sakamoto, H. Okamura, A. Tamii, T. Uesaka, Y. Satou, T. Ohnishi, T. Wakasa, K. Yakou, S. Fukusaka, S. Sakoda, K. Suda, H. Kato, Y. Maeda, K. S. Itoh, and T. Niizeki

[NUCLEAR REACTIONS,  ${}^1\text{H}(\vec{d}, d)$ ,  $E_d = 270$  MeV measured:  $\sigma(\theta)$ ,  $A_y(\theta)$ ,  $A_{yy}(\theta)$ ,  $A_{xx}(\theta)$ ,  $A_{xz}(\theta)$ ]

A study of the nucleon-deuteron system has made substantial progress both experimentally and theoretically. We have shown in Ref. 1 that there is a discrepancy in the cross section minimum between the data and the Faddeev calculations without the three nucleon force (3NF) at an intermediate energy. It was recently shown that this discrepancy can be explained by 3NF.<sup>2,3)</sup>

We have made precise measurements of the cross sections and vector and tensor analyzing powers for  $d$ - $p$  elastic scattering at  $E_d = 270$  MeV. The angular range was  $\theta_{c.m.} = 10^\circ$ – $180^\circ$ . A  $\text{CH}_2$  target with a thickness of  $46.7$  mg/cm<sup>2</sup> was bombarded by a polarized deuteron beam, and either scattered deuterons or protons were momentum analyzed by the spectrograph SMART and detected at the focal plane, depending on the scattering angle.

The experimental results are shown with solid circles in Figs. 1 and 2. The errors are only statistical ones. The open circles are the measurement by Sakamoto *et al.*<sup>1)</sup> Since the two independent measurements provide almost the same values in the overlapping region,

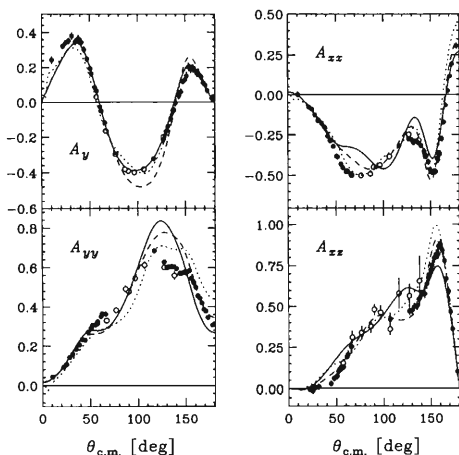


Fig. 1.  $A_y$ ,  $A_{yy}$ ,  $A_{xx}$ ,  $A_{xz}$  for the  $d$ - $p$  elastic scattering at  $E_d^{lab} = 270$  MeV. The solid circles are the results of this experiment and the open squares are those of Ref. 1. The solid curves and dashed curves are the Faddeev calculations with and without 3NF, respectively. CD BONN potential is taken as  $NN$  interactions. Coulomb force is not included. The dotted curves are the Faddeev calculations without 3NF. The Argonne  $v_{14}$  potential is used as  $NN$  interactions.

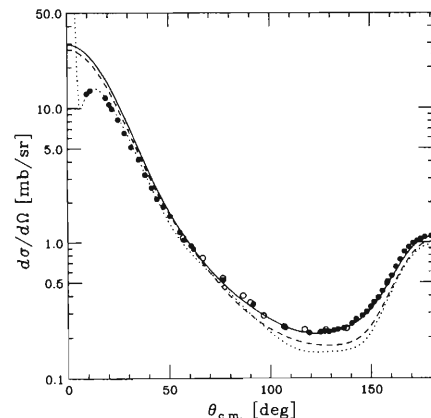


Fig. 2. The cross section for the  $d$ - $p$  elastic scattering at  $E_d^{lab} = 270$  MeV. The solid circles are the results of this experiment and the open squares are those of Ref. 1. The solid dashed and dotted curves are the same as Fig. 1.

the systematic errors seem to be small. The dashed and solid curves in Figs. 1 and 2 are results of the calculations with and without 3NF by Witała *et al.*<sup>2,4)</sup> The CD BONN potential<sup>5)</sup> is taken as  $NN$  interactions. Note that the Coulomb interaction is not included. The dotted curves are the Faddeev calculations without 3NF in which the Argonne  $v_{14}$ <sup>6)</sup> potential is used.<sup>1)</sup> For the cross sections, the calculation with 3NF shows an excellent fit almost over all angles. Thus, the discrepancy in the cross section minimum is indeed reproduced by including 3NF. The observed vector analyzing power,  $A_y$ , is also in good agreement with the calculations with 3NF. However, none of the calculations shows superiority in describing the tensor analyzing powers ( $A_{yy}$ ,  $A_{xx}$  and  $A_{xz}$ ). It should be noted that the agreement is deteriorated when 3NF is included. These results indicate that there seems to be ambiguity of the spin-dependent parts of 3NF as well as  $NN$  interactions.

## References

- 1) N. Sakamoto *et al.*: Phys. Lett. B **367**, 60 (1996).
- 2) H. Witała *et al.*: Phys. Rev. Lett. **81**, 1183 (1998).
- 3) S. Nemoto *et al.*: Phys. Rev. C **58**, 2599 (1998).
- 4) H. Kamada: private communications.
- 5) R. Machleidt *et al.*: Phys. Rev. C **53**, R1483 (1996).
- 6) R. B. Wiringa *et al.*: Phys. Rev. C **29**, 1207 (1984).

## The ${}^3\text{He}(\vec{d}, p){}^4\text{He}$ Reaction at Intermediate Energies

T. Uesaka, H. Sakai, H. Okamura, A. Tamii, Y. Satou, T. Ohnishi, K. Sekiguchi, K. Yako, S. Sakoda, N. Sakamoto, T. Wakasa, K. Itoh, and K. Suda

[ ${}^3\text{He}(d, p){}^4\text{He}$ ,  $E_d = 140, 200,$  and  $270$  MeV, Measured analyzing powers]

The high-momentum component of the deuteron wave function provides a unique opportunity to reveal the short-range behavior of the nucleon-nucleon (NN) interaction.<sup>1,2)</sup> Especially, the D-state wave function, which arises from the existence of the tensor component in NN interaction, manifests its importance in the short-range ( $r < 1$  fm) or high-momentum ( $k > 1$  fm<sup>-1</sup>) region.

The  ${}^3\text{He}(\vec{d}, p){}^4\text{He}$  reaction can be an effective probe to the deuteron D-state wave function because of its strong spin-selectivity.<sup>3)</sup> We measured, for the first time at  $E_d = 270$  MeV and  $\theta_{\text{lab}} = 4^\circ$ , the polarization correlation coefficient,  $C_{//}$ , which is proportional to the D-state density within the framework of one-nucleon-exchange (ONE) approximation. The result of  $C_{//}$  was found to be more than a factor of 2 smaller than the expected value calculated with the ONE approximation and the realistic NN potential model. It is important to investigate the relevance of the reaction mechanism in order to assess the deuteron D-state wave function by using the polarization observables.

Following this line, we have recently measured the cross sections and analyzing powers ( $A_y$ ,  $A_{yy}$ , and  $A_{xx}$ ) for the  ${}^3\text{He}(\vec{d}, p){}^4\text{He}$  reaction in the angular range of  $\theta_{\text{lab}} = 0^\circ$ – $25^\circ$  and at  $E_d = 140, 200,$  and  $270$  MeV. Details of the experimental procedure are described in Ref. 4.

In Fig. 1, polarization observables at three energies are plotted as a function of the scattering angle in the

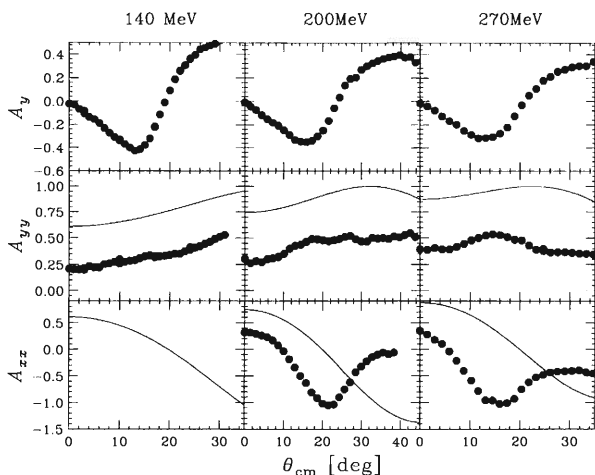


Fig. 1. Polarization observables at  $E_d = 140, 200,$  and  $270$  MeV. The solid lines are the result of ONE calculations.

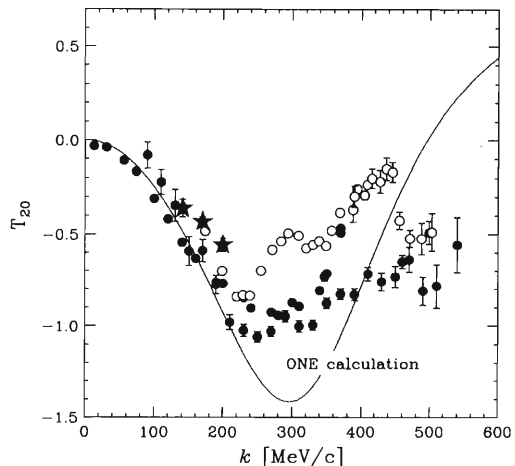


Fig. 2.  $T_{20}$  at zero degree for the  ${}^3\text{He}(\vec{d}, p){}^4\text{He}$  ( $\star$ ), the  $d+p$  backward scattering ( $\circ$ ), and the deuteron inclusive breakup ( $\bullet$ ).

center-of-mass system. The solid lines represent the result of ONE calculations. The vector analyzing power, which is expected to be identical to zero in the ONE approximation, takes large negative values ( $-0.3$ – $-0.6$ ) at forward angles. It is also clearly seen that the magnitude of the tensor-analyzing powers is much smaller than the prediction of the ONE calculation. Thus, it is concluded that the ONE approximation is insufficient to describe the  ${}^3\text{He}(\vec{d}, p){}^4\text{He}$  reaction in these energy regions.

The tensor-analyzing power,  $T_{20} [= -\frac{1}{\sqrt{2}}(A_{yy} + A_{xx})]$ , at zero degree is also compared with those for the  $d+p$  backward scattering and the deuteron inclusive breakup data (Fig. 2). The comparison exhibits the similarity among these reactions. This result indicates that the reaction mechanism of the  ${}^3\text{He}(d, p){}^4\text{He}$  reaction is similar to those of the  $d+p$  backward scattering and the deuteron inclusive breakup, and therefore the reaction models which have been developed to describe the latter reactions can also be applicable to the  ${}^3\text{He}(d, p){}^4\text{He}$  reaction.

### References

- 1) A. P. Kobushkin: Phys. Lett. B **421**, 53 (1998) and references therein.
- 2) L. S. Azhgirey et al.: Phys. Lett. B **391**, 22 (1997) and references therein.
- 3) T. Uesaka et al.: Phys. Lett. B **467**, 199 (1999).
- 4) T. Uesaka et al.: RIKEN Accel. Prog. Rep. **32**, 63 (1999).

## Measurement of the Deuteron Spin-Flip Probabilities in the $^{28}\text{Si}(\vec{d}, \vec{d}')$ Reaction at $E_d = 270$ MeV

Y. Satou, S. Ishida, H. Sakai, H. Okamura, N. Sakamoto, H. Otsu, T. Uesaka, T. Wakasa, T. Nonaka, T. Ohnishi, G. Yokoyama, K. Sekiguchi, K. Yakou, S. Fukusaka, K. Itoh, T. Ichihara, T. Niizeki, and K. Hatanaka

[NUCLEAR REACTION,  $^{28}\text{Si}(\text{polarized } d, \text{polarized } d')$   $E_d = 270$  MeV; deuteron spin-flip] probabilities  $S_1$  and  $S_2$

Inelastic scattering of polarized deuterons provides a unique tool to study nuclear spin responses. Since it is able to transfer spin  $\Delta S = 1$  without transferring isospin  $\Delta T = 0$ , the  $(d, d')$  reaction is an efficient probe of isoscalar spin excitations.<sup>1)</sup> In addition, being a probe with spin equal to one, the  $(d, d')$  reaction provides an opportunity to search for the possible existence of  $\Delta S = 2$  excitations, such as the Double Gamow-Teller states.<sup>2)</sup>

We report here on a  $^{28}\text{Si}(\vec{d}, \vec{d}')$  forward-angle measurement of the cross section and eight polarization observables ( $A_y$ ,  $A_{yy}$ ,  $P^{y'}$ ,  $P^{y'y'}$ ,  $K_y^{y'}$ ,  $K_{yy}^{y'}$ ,  $K_y^{y'y'}$  and  $K_{yy}^{y'y'}$ ), which aims to understand the isoscalar spin strengths in  $^{28}\text{Si}$ . For the deuteron two spin-flip probabilities (SFPs),  $S_1$  and  $S_2$ , can be defined corresponding to a change of 1 and 2 units in the component of the deuteron's spin perpendicular to the scattering plane. The SFPs,  $S_1$  and  $S_2$ , are expected to be useful signatures of the  $\Delta S = 1$  and  $\Delta S = 2$  excitations, respectively. These are expressed in terms of the polarization observables, as follows:

$$S_1 = \frac{1}{9}(4 - P^{y'y'} - A_{yy} - 2K_{yy}^{y'y'}), \quad (1)$$

$$S_2 = \frac{1}{18}(4 + 2P^{y'y'} + 2A_{yy} - 9K_y^{y'} + K_{yy}^{y'y'}). \quad (2)$$

The experiment was carried out using SMART. The 270 MeV vector and tensor polarized deuteron beams from the RIKEN Ring Cyclotron were focused on a 58.1 mg/cm<sup>2</sup>-thick  $^{nat}\text{Si}$  target ( $^{28}\text{Si}$ : 92.2%). The beam swinger magnet was set at 5°, covering an angular range of  $2.5^\circ < \theta_{lab} < 7.5^\circ$ . The scattered deuterons were detected at the focal plane of SMART with a multiwire drift chamber backed with two plastic scintillation counters. The polarizations of the scattered deuterons were determined by a focal-plane deuteron polarimeter, DPOL. DPOL had a 2.5 cm-thick polyethylene block as the second scatterer, and made use of the  $^{12}\text{C}(d, d)$  and  $^1\text{H}(d, pp)$  reactions for the vector and tensor polarization measurements, respectively.<sup>3)</sup>

Figure 1 (a) shows the excitation energy ( $E_x$ ) spectrum of the cross section. A known spin-flip  $1^+$  state at 9.50 MeV is clearly excited as well as non-spin-flip collective states, such as  $4^+$  at 4.62 MeV,  $0^+$  at 4.98 MeV,  $2^+$  at 7.40 MeV and 7.93 MeV and  $3^-$  at 6.88 MeV

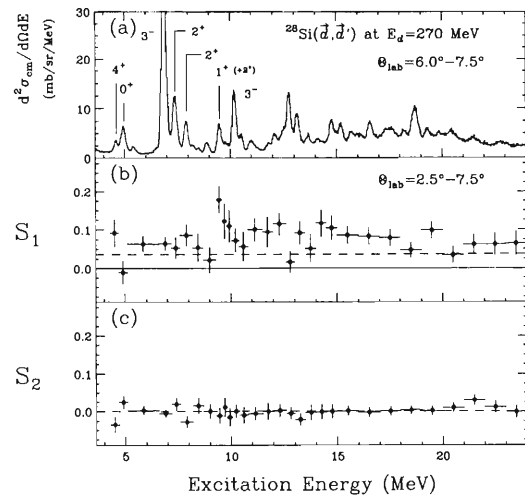


Fig. 1. Measured  $(d, d')$  spectra on  $^{28}\text{Si}$  at  $E_d = 270$  MeV. (a) Double-differential cross section. (b) Spin-flip probability,  $S_1$ . (c) Double-spin-flip probability,  $S_2$ .

and 10.18 MeV. Figure 1 (b) shows the spectrum of  $S_1$ . The isoscalar  $1^+$  state at 9.50 MeV is enhanced in this spectrum, while other non-spin-flip states are all suppressed, in accordance with spin-flip nature of these states. One may also see slightly enhanced  $S_1$  values relative to those for free deuteron-nucleon ( $d$ - $N$ ) scattering (shown by the dashed line) over the excitation energy  $E_x \approx 11$ –18 MeV region. It would be interesting to note that several  $T = 0$ ,  $1^+$  states have recently been reported over the  $E_x$  region of 9.7–15.8 MeV.<sup>4)</sup> Figure 1 (c) shows the  $S_2$  spectrum. The  $S_2$  values are found to be close to zero for all of the measured  $E_x$  region. Within the framework of PWIA, it is necessary to have  $S_2 = 0$  if we assume a one-step reaction process without any contribution from the tensor terms in the  $d$ - $N$   $t$ -matrix.<sup>5)</sup> Such an assumption is expected to be valid in the low-momentum transfer kinematics of the present experiment.

### References

- 1) M. Morlet et al.: Phys. Lett. B **247**, 228 (1990).
- 2) P. Vogel et al.: Phys. Lett. B **212**, 259 (1988); N. Auerbach et al.: Ann. Phys. **192**, 77 (1989).
- 3) S. Ishida et al.: AIP Conf. Proc. **343**, 182 (1995).
- 4) Y. Fujita et al.: Phys. Rev. C **55**, 1137 (1997).
- 5) T. Suzuki: Prog. Theor. Phys. **86**, 1129 (1991).

# Proton Spectra from the $^{208}\text{Pb}+^{208}\text{Pb}$ Reaction at 15 A MeV

K. Yoshida, M. Shimooka, R. Wada, T. Nakagawa, K. Nakagawa,  
I. Tanihata, Y. Aoki, J. Kasagi, and W. Q. Shen\*

[ $^{208}\text{Pb}+^{208}\text{Pb}$  15 A MeV, Fission]

The proton energy spectra have been measured for the  $^{208}\text{Pb}+^{208}\text{Pb}$  reaction at 15 A MeV to investigate the formation of a very heavy compound nucleus. Due to the strong Coulomb repulsion, it has been thought that the formation of a compound nucleus is strongly hindered in collisions between heavy nuclei, such as  $^{208}\text{Pb}+^{208}\text{Pb}$ . However, recent theoretical calculations suggest that a heavy compound nucleus can be formed in heavy nucleus-nucleus collisions at sufficiently high incident energies to overcome the strong Coulomb repulsion. The proton energy spectrum is expected to be a good measure of the formation of the compound nucleus, since the large Coulomb barrier strongly affects the protons evaporated from the compound nucleus. In order to minimize the strong contribution from the deep inelastic scattering, protons were detected in coincidence with three large fragments, which were produced from the compound nucleus through ternary fission.

The experiment was performed at the RIKEN Ring Cyclotron.  $^{208}\text{Pb}$  beams with an energy of 15 A MeV and an intensity of 0.1 pnA were bombarded onto a 99.9%-enriched  $^{208}\text{Pb}$  foil of 1 mg/cm<sup>2</sup> in thickness backed with 20  $\mu\text{g}/\text{cm}^2$  collodion. Protons were detected with BaF<sub>2</sub> phoswich detectors,<sup>1)</sup> which covered 130–165° laboratory angles around the beam axis. A large PPAC/IC chamber<sup>2)</sup> was placed at 25–75° laboratory angles in order to measure the energies and velocities of the fission fragments.

The proton spectra have been deduced for two types of the spatial distributions of three detected fragments. One is the asymmetric one: one of the folding angles of the fragments is about 60°, and the others are about 150°. The other is a symmetric one: all three folding angles are nearly 120°. The correlation among the velocities of the fragments suggests that the former events come from the fission of the projectile or target nuclei after deep inelastic scattering, and the latter is associated with a simultaneous breakup of three fragments.

The proton spectra observed at two different laboratory angles are shown in Fig. 1 for two types of fragment distributions. As can be seen, the spectra for both cases are similar except for  $E_p < 10$  MeV. Yields of the protons decreased exponentially with increasing their energies. Below 8 MeV, the yield decreased along with a decrease in the proton energy for the symmetric

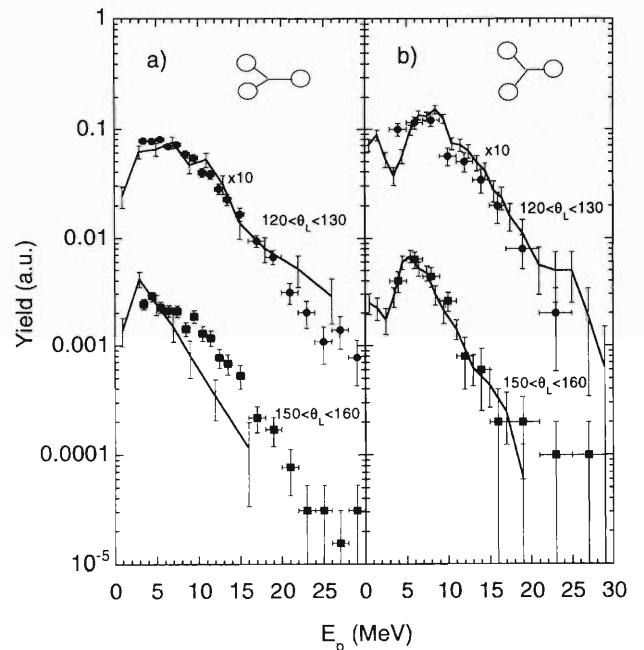


Fig. 1. Proton energy spectra in coincidence with three fragments from the  $^{208}\text{Pb}+^{208}\text{Pb}$  reaction at 15 A MeV. a) Protons coincidence with the asymmetric distribution of the three fragments. b) Protons for the symmetric distribution of the fragments. Lines are results of the Monte Carlo simulation.

distribution, whereas the spectra for the asymmetric distribution remain almost constant.

Monte Carlo simulations were performed to investigate the proton spectrum expected from the statistical decay of the fragments. The code SIMON<sup>3)</sup> was employed to simulate the fission of the nuclei from the deep inelastic scattering; the results were compared with the spectrum for the asymmetric distributions. For symmetric distributions, a special code was developed to simulate the ternary fission following the complete fusion. The results are shown by the lines in Fig. 1. The observed spectra were reasonably reproduced by those simulations.

## References

- 1) Y. Futami et al.: Nucl. Instrum. Methods Phys. Res. A **329**, 513 (1993).
- 2) K. Yoshida et al.: RIKEN Accel. Prog. Rep. **31**, 165 (1998).
- 3) D. Durand: Nucl. Phys. A **541**, 266 (1992).

\* Shanghai Institute of Nuclear Research, Chinese Academy of Science, China

# GDR $\gamma$ -rays from the Binary Reaction of $^{209}\text{Bi} + ^{209}\text{Bi}$ at 12 MeV/u

Y. Aoki, J. Kasagi, K. Yoshida, T. Nakagawa, and K. Nakagawa

[NUCLEAR REACTION,  $^{209}\text{Bi}+^{209}\text{Bi}$  E/A = 12 MeV/u; Inelastic scattering; Measured]  
 [high energy  $\gamma$  rays, protons, and residues; Deduced GDR response]

A study of the GDR built on highly excited nuclei is one of the interesting subjects to understand the properties of hot nuclei. There have been many studies concerning on the GDR of hot nuclei in the Sn region. These studies show that the width of the GDR increases with an increase in the nuclear temperature up to 3 MeV, and then saturates at higher temperature. For heavier nuclei, the experimental data are scarce. The GDR of hot  $^{208}\text{Pb}$  excited up to the nuclear temperature  $T = 2$  MeV by  $\alpha$  inelastic scattering<sup>1)</sup> shows that the width of GDR increases rapidly along with an increase of the temperature. In order to study the GDR of heavy nuclei at higher temperature, we measured GDR  $\gamma$ -rays from the  $^{209}\text{Bi} + ^{209}\text{Bi}$  inelastic scattering.

The experiment was carried out at the ASCHRA chamber in the RIKEN RING Cyclotron. An accelerated  $^{209}\text{Bi}$  beam with an energy of 12 MeV/u and an intensity of 0.1 pA irradiated a 1 mg/cm<sup>2</sup>  $^{209}\text{Bi}$  self-support target. The residual nuclei of the reaction were detected by 3 large PPAC+Ionization chambers. The Tof and position of the residues were measured by PPACs, and their energy was measured by ionization chambers. The masses of the residues were deduced from these information. The high-energy  $\gamma$  rays were measured by 2 sets of high-energy  $\gamma$ -ray detectors consisting of 7 BaF<sub>2</sub> scintillators. The multiplicities of the  $\gamma$  rays and the charged particles were also measured by a crystal ball consisting of 65 BaF<sub>2</sub>-plastic phoswich detectors.

The  $\gamma$  ray spectra were obtained for the four excitation bins by selecting the observed masses larger than 175. The excitation energies were calculated from the angles and velocities of the detected residues by assuming 2-body kinematics. The excitation energies of the residues were ensured by the shape of the energy spectra of protons detected with the crystal ball. The observed spectra were well reproduced by statistical model simulations with the excitation energies being deduced from 2-body kinematics.

The  $\gamma$ -ray spectra were compared with statistical-

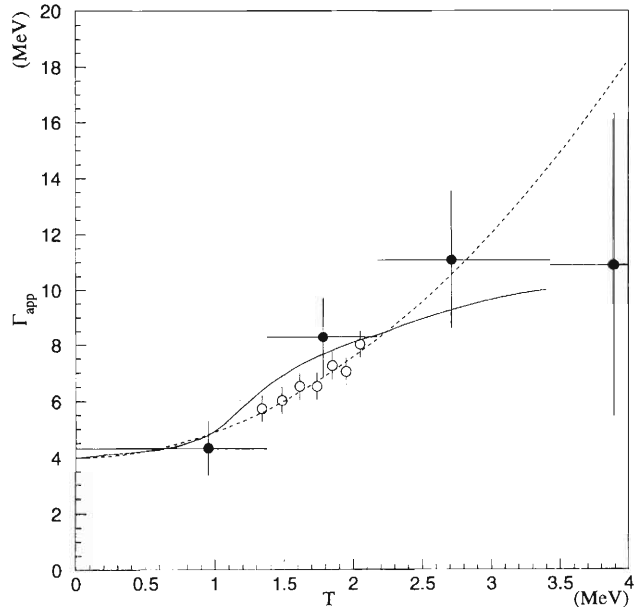


Fig. 1. GDR width plotted against the nuclear temperature. The closed circles are the present results and the open circles are from Ref. 1. The solid line represents the calculation of Ormand *et al.*<sup>2)</sup> The dashed line is the relation  $\Gamma_{GDR} = 4.0 + 0.89 T^2$ .

model calculations using the code CASCADE. The GDR energies and widths were deduced from a  $\chi^2$  fitting of the calculated spectra and experimental spectra. In Fig. 1, the deduced GDR widths are plotted versus temperature along with the data from Ref. 1. As can be seen, the present result agrees with the data from Ref. 1. The GDR widths increase in proportion to  $T^2$  in low excitation energies. At higher temperatures, however, the widths saturate at  $\Gamma_G = 11$  MeV. The result agrees well with the theoretical work of Ormand *et al.*<sup>2)</sup> in all temperature regions.

### References

- 1) E. Ramakrishnan et al.: Phys. Lett. B **383**, 252 (1996).
- 2) W. E. Ormand et al.: Phys. Rev. Lett. **77**, 607 (1996).

## Search for a $Z = 118$ Superheavy Nucleus in the Reaction of $^{84}\text{Kr}$ with $^{208}\text{Pb}$

K. Morimoto, I. Tanihata, N. Iwasa, R. Kanungo, T. Kato, K. Katori, H. Kudo, K. Morita, T. Suda,  
S. Takeuchi, F. Tokanai, K. Uchiyama, Y. Wakasaya, T. Yamaguchi, A. Yoneda, and A. Yoshida

[NUCLEAR REACTION, Gas-filled recoil separator, Alpha-decays]

Recently, three decay chains for a reaction of  $^{86}\text{Kr}$  with  $^{208}\text{Pb}$  were reported by a Lawrence Berkeley Laboratory group.<sup>1)</sup> The observed chains are consistent with the formation of  $^{293}118$  and its sequential  $\alpha$  decays. However, the decay chains are not connected to any known nuclei. The observed production cross section is 2.2 (+2.6, -0.8) pb. This experiment was performed following a recent prediction of Smolanczuk,<sup>2)</sup> which indicates that the cross section of a cold-fusion reaction of  $^{86}\text{Kr}$  with  $^{208}\text{Pb}$  is 670 pb. This is a drastically larger value than scientists have thought.

In a private communication, T. Wada, M. Ohta, Y. Aritomo, and Y. Abe suggest that the cross section of a cold-fusion reaction of  $^{84}\text{Kr}$  with  $^{208}\text{Pb}$  should be almost the same as that of  $^{86}\text{Kr}$  with  $^{208}\text{Pb}$ . If the cross section of  $^{86}\text{Kr}$  with  $^{208}\text{Pb}$  is confident, we have a chance to observe  $^{291}118$  with decay chains connected to the known nuclei. From that view, we conducted an experiment to observe the superheavy nucleus  $^{291}118$  produced in the reaction of  $^{84}\text{Kr}$  with  $^{208}\text{Pb}$ .

The experimental set up is shown in Fig. 1. The target thickness was  $300\ \mu\text{g}/\text{cm}^2$ ; it was evaporated onto the downstream side of a  $100\ \mu\text{g}/\text{cm}^2$  carbon foil. Six segments of it were mounted on a wheel that rotated at 600 rpm. The beam energy was 446 MeV, and the maximum beam current was 1000 particle nanoamperes. The incident beam energy at the center of the target was 442.2 MeV. To avoid the primary beam from

impinging on the silicon detector in the event of a broken target, a carbon foil of  $30\ \mu\text{g}/\text{cm}^2$  thick was mounted as a charge stripper of primary beams. The beam intensity was monitored through elastic scattering by a silicon detector installed at 45 degrees with respect to the incident beam.

The reaction products recoiling out of the target were separated from the primary beam by using a gas-filled recoil separator, GARIS.<sup>3)</sup> The separator was filled with He gas at one torr. The optimal magnetic field setting was obtained by scaling the value from the measured focal plane evaporation residue distribution of  $^{84}\text{Kr}+^{107}\text{Ag}$ . We have estimated the magnetic rigidity ( $B\rho$ ) to be 2.2 Tm. After the separator the recoil particles were implanted in a position-sensitive silicon detector (PSD), which had an active area of  $60 \times 60$  mm with a depth of  $300\ \mu\text{m}$ . Passing-through light particles were anti-coincided with veto SSD mounted after the PSD. Total counting rate of the PSD was several counts/sec under the condition with 1000 particle nanoamperes beam intensity. The time-of-flight measurement was additionally performed using a micro-channel plate assembly (MCP) and the PSD.

We had two experimental machine times. The first experiment (4 days) was performed for a test of targets, an estimation of the magnetic rigidity ( $B\rho$ ), calibrations of detectors and a check of the data-acquisition system. The second experiment (10 days) was performed to accumulate a dose of  $2 \times 10^{18}$  ions, but no candidate of the evaporation residue was found.

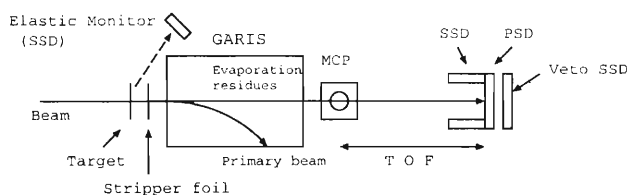


Fig. 1. Schematic drawing of the setup.

### References

- 1) V. Ninov et al.: Phys. Rev. Lett. **83**, 1104 (1999).
- 2) R. Smolanczuk: Phys. Rev. C **59**, 2634 (1999).
- 3) K. Morita et al.: Nucl. Instrum. Methods Phys. Res. B **70**, 220 (1992).

## First Measurement of the ${}^8\text{B}(p,\gamma){}^9\text{C}$ Reaction by the Coulomb-Dissociation Method

T. Motobayashi, I. Hisanaga, H. Akiyoshi, Y. Ando, H. Fujiwara,\*<sup>1</sup> N. Fukuda, Zs. Fülöp, T. Gomi, K. I. Hahn,\*<sup>2</sup> Y. Higurashi, M. Hirai, M. Ishihara, N. Iwasa, H. Iwasaki, Y. Iwata,\*<sup>3</sup> T. Kijima,\*<sup>4</sup> S. Kubono, T. Minemura, T. Nakamura, M. Notani, S. Ozawa, S. Shimoura, S. Takeuchi, T. Teranishi, and Y. Yanagisawa

[ $\text{Pb}({}^9\text{C}, {}^8\text{B} p)\text{Pb}$ , Coulomb dissociation, Astrophysical  $S$ -factor for  ${}^8\text{B}(p,\gamma){}^9\text{C}$ ]

The first experimental study of the  ${}^8\text{B}(p,\gamma){}^9\text{C}$  reaction was performed with the Coulomb-dissociation method. This reaction at low energies is one of the key processes in the hot pp mode nuclear burning.<sup>1)</sup> At very high temperatures of around  $10^8$  K and high densities of  $\rho > 10^5$  g/cm<sup>3</sup> in a hydrogen-rich circumstance, the proton capture of  ${}^8\text{B}$  becomes faster than the  $\beta^+$  decay of  ${}^8\text{B}$ . The reaction is also related to the  ${}^7\text{Li}$  production in novae.<sup>2)</sup> No experimental information is available so far for the  ${}^8\text{B}(p,\gamma){}^9\text{C}$  reaction, because its direct-capture experiment is very difficult due to the short half life of 770 ms for  ${}^8\text{B}$ . Though experiments in inverse kinematics, where a radioactive  ${}^8\text{B}$  beam bombards a hydrogen target, is in principle possible, the Coulomb-dissociation method has an advantage of high experimental efficiency caused by the larger cross section and the allowance of using a much thicker target.

The RIPS system provided radioactive  ${}^9\text{C}$  beams at 65 A MeV using the projectile fragmentation of a 135 A MeV  ${}^{12}\text{C}$  beam with a 1.64 g/cm<sup>2</sup>  ${}^9\text{Be}$  target. The secondary  ${}^9\text{C}$  beam bombarded a 100 mg/cm<sup>2</sup> lead target set at the final focal point of the RIPS. The outgoing proton and  ${}^8\text{B}$  were detected in coincidence by a plastic-scintillator hodoscope of  $1 \times 1$  m<sup>2</sup> area in a vacuum chamber, the details of which have been reported elsewhere.<sup>3)</sup> From the measured time-of-flight and hit positions of the two fragments, their relative energy, which corresponds to the center-of-mass energy for the  ${}^8\text{B}(p,\gamma){}^9\text{C}$  reaction, was obtained. The extracted Coulomb-dissociation yield is plotted in Fig. 1 as a function of the p- ${}^8\text{B}$  relative energy. The histogram represents the result of a simulation calculation that accounts for the detector response, which is affected by the angle- and energy-determination in the hodoscope and the coincidence efficiency for the pair of fragments. A constant astrophysical  $S$ -factor of 100 eV-b was assumed for the  ${}^8\text{B}(p,\gamma){}^9\text{C}$  reaction in the simulation. The data were reasonably well reproduced by the simulation,

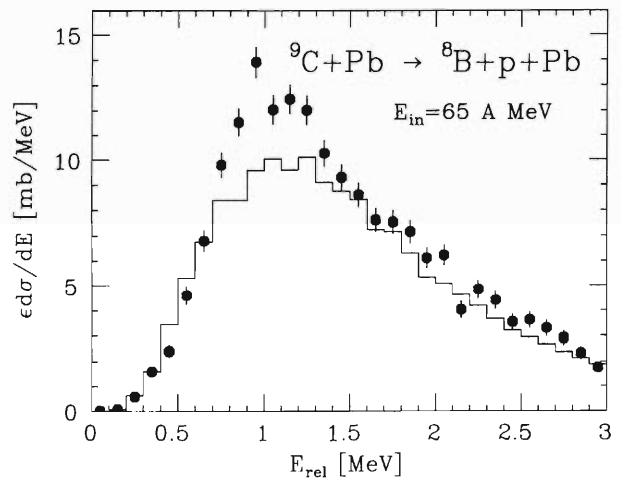


Fig. 1. Relative energy spectrum obtained for the proton and  ${}^8\text{B}$  produced by the Coulomb dissociation of  ${}^9\text{C}$ .

except for the excess of the yield at around 1 MeV, originating from the first excited state in  ${}^9\text{C}$  at  $E_x = 2.218$  MeV, corresponding to the relative energy  $E_{rel} = 0.922$  MeV.

The present result suggests that the  $S$  factor for the  ${}^8\text{B}(p,\gamma){}^9\text{C}$  reaction for the continuum region is approximately 100 eV-b. This value is closer to a prediction of Descouvemont<sup>4)</sup> of about 70 eV-b than that of Wiescher *et al.*,<sup>1)</sup> who estimate an averaged  $S$  factor of 210 eV-b for  $E_{cm} < 0.8$  MeV. Further analysis including an evaluation of the nuclear contribution is in progress.

### References

- 1) M. Wiescher *et al.*: *Astrophys. J.* **343**, 352 (1989).
- 2) H. M. J. Boffin *et al.*: *Astron. Astrophys.* **279**, 173 (1993).
- 3) N. Iwasa *et al.*: *J. Phys. Soc. Jpn.* **65** 1256 (1996); I. Hisanaga *et al.*: *RIKEN Accel. Prog. Rep.* **31**, 162 (1998).
- 4) P. Descouvemont: *Astrophys. J.* **405**, 518 (1993).

\*<sup>1</sup> Accelerator Engineering Corporation

\*<sup>2</sup> Department of Physics Ewha Womens University, Korea

\*<sup>3</sup> National Institute of Radiological Sciences

\*<sup>4</sup> Faculty of Engineering, Yokohama National University

# Development of a Li-Ion Isotope Separation and Counting System for a Precise Measurement of the $^{11}\text{Li}$ Charge Radius

T. Onishi, H. Wang, M. Wakasugi, K. Katori, and I. Tanihata

[Neutron halo, Isotope shift]

In collaboration with GSI,<sup>†</sup> we are planning an experiment for a precise measurement of the charge radius of the halo nucleus  $^{11}\text{Li}$  and two other unstable lithium isotopes by means of an “isotope shift” observation. To determine the charge radius of  $^{11}\text{Li}$  with 0.1 fm accuracy, the  $2^2\text{S}_{1/2} \rightarrow 3^2\text{S}_{1/2}$  atomic transition energies of lithium isotopes within the range of  $10^{-9}$  eV is needed. The experimental requirements for this purpose are:

- (1) high production efficiency ( $> 1000$  particle/s) of  $^{11}\text{Li}$  nuclei;
- (2) high stability and Doppler-free measurement of the transition energies by exciting lasers within a range of 0.1 MHz in frequency of a laser; and
- (3) high-signal-to-noise counting of  $^{11}\text{Li}$  ions ionized by the laser.

In this report, we present the development of Li-ion isotope separation and detection systems, which represents our work concerning the third part of these

requirements.

To perform a charge radius measurement, the following three parts are necessary in an experimental setup. The functions of the first and second parts are to produce a neutral  $^{11}\text{Li}$  atom thermal beam and to ionize the  $^{11}\text{Li}$  atom with lasers. The third part, which is the main part of this report, is used to detect ionized  $^{11}\text{Li}$ , which is extracted from the laser ion source, separating them from background nuclei and counting by  $\beta$ -ray detectors.

For the ion separation and counting systems, the following conditions are indispensable:

- (1) The system be sufficiently compact to easily settle at the final focal point of RIPS;
- (2) High transport efficiency from the ion source to a beam catcher; and
- (3) High efficiency and low background  $\beta$ -ray counting at the final catcher.

To meet these requirements, we designed and con-

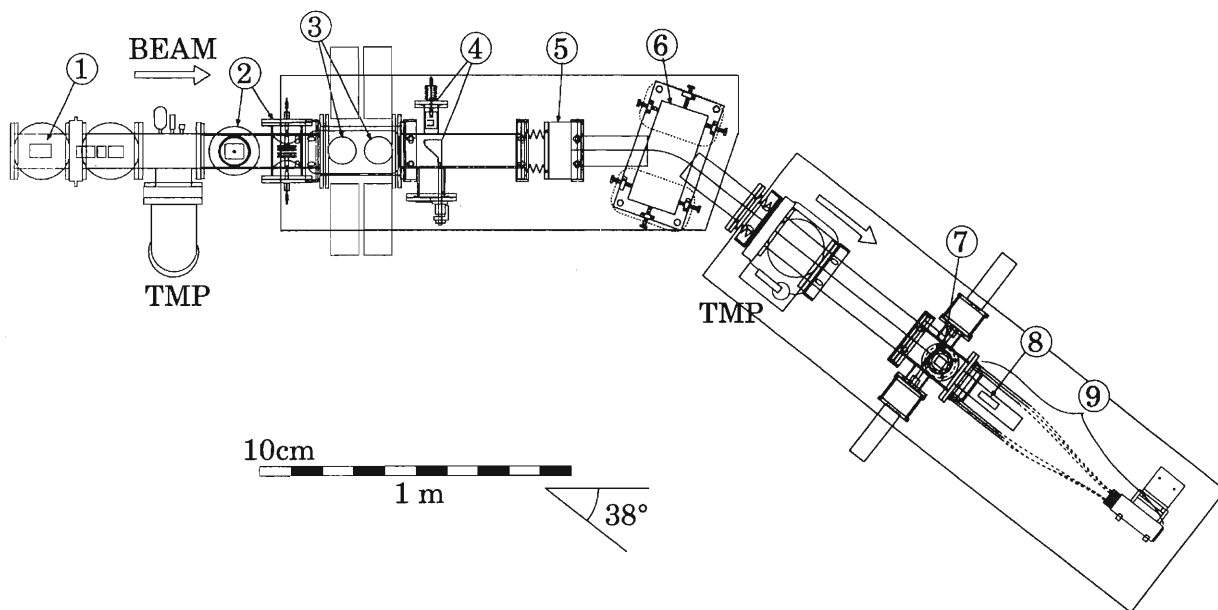


Fig. 1. Schematic view of Li ion separation and the counting systems. The beam-transport line consists of ① a Li (stable) ion source for tests, ② one set of electrostatic deflectors, ③ an electrostatic Q doublet, ④ a beam viewer and a Faraday cup as beam monitors at the first focal point, ⑤ an electrostatic Q singlet, ⑥ a 38-degree bending dipole magnet, ⑦ a collimator with a Faraday cup, ⑧ an electron multiplier as a beam catcher at the second (final) focal point and ⑨ a plastic scintillation counter telescope for  $\beta$ -ray counting.

<sup>†</sup> Collaborators in GSI for the final experiment are Reinhard Kirchner, Andreas Dax, Frank Schmitt, Thomas Kuehl, and H. -Juergen Kluge

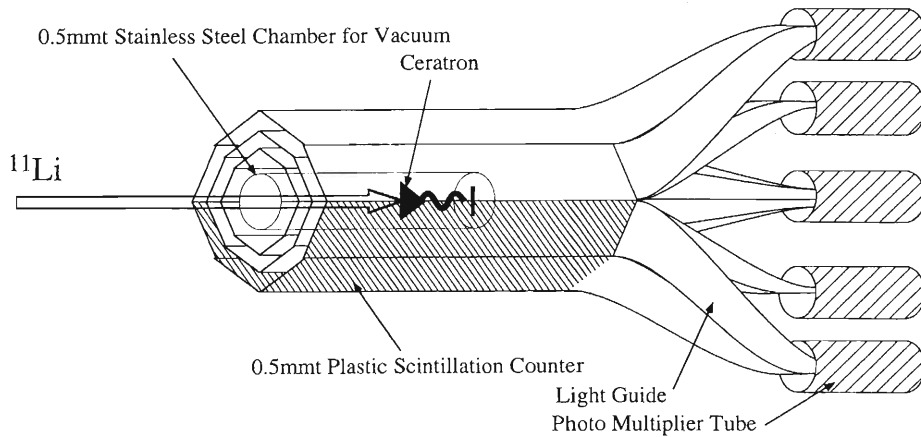


Fig. 2. A schematic layout of plastic scintillation counters for  $\beta$ -ray counting around the ceratron as a beam catcher. The  $\beta$ -ray counter telescope can be separated into 5 plastic scintillation counters. Each scintillation counter has a photomultiplier tube. Eight or four twisted light guides connect between the photomultiplier tube and scintillators.

structed an ion separator and a set of  $\beta$ -ray counters.

A schematic drawing of the separation and counting systems is shown in Fig. 1. This beam line has two foci. One dipole magnet is used to separate  $^{11}\text{Li}$  (or other lithium isotopes) from other species of ions. The Li-ion counting system around the final focus (⑧ in Fig. 1) is shown in Fig. 2. A ceratron (channel type electron multiplier) is placed in a plastic scintillation counter telescope as a beam catcher. The plastic scintillation counters are suitable for one-by-one counting of the  $\beta$  rays emitted from  $^8\text{Li}$ ,  $^9\text{Li}$  or  $^{11}\text{Li}$  nuclei, which stop in the catcher, while the ceratron is used as well for the detection of Li isotope ions through the current of secondary electrons which they produce. The plastic scintillation counter telescope consists of three layers, i.e., inner, middle and outer layer, which cover about  $2\pi$  of the solid angle around the catcher. The

inner counter is made with 8 scintillator plates combined as an octagon prism. The middle counter consists of two parts, which covers the upper and lower half ( $\pi$  solid angle) of the catcher. Both parts are made with 4 plastic scintillator plates, and are constructed with the same configuration as the inner counter. The outer counter has the same structure as the middle counter. The signals from two middle (and the outer) counters are used to produce anticoincided logic signals to reduce the background from cosmic rays.

At present, the construction of this system has been completed, and its beam-transport efficiency is to be measured by using stable Li ions. The stable Li beam had been introduced to the first focal point until November, 1999; the lithium beam for this test will be transported to the final catcher soon.

## Coulomb Dissociation of $^{12}\text{N}$ and $^{13}\text{O}$

T. Minemura, T. Motobayashi, S. Shimoura, H. Murakami, Y. Ando, T. Teranishi, N. Aoi, Zs. Fülöp, M. Hirai, H. Iwasaki, N. Imai, N. Iwasa, M. Kurokawa, H. Akiyoshi, Y. Yanagisawa, Y. Iwata, S. Ozawa, S. Takeuchi, Y. Higurashi, M. Serata, H. Kobayashi, K. Yamada, T. Gomi, H. Sakurai, K. Yoshida, Z. Liu, and M. Ishihara

$[^{208}\text{Pb}(^{12}\text{N}, ^{11}\text{C} p)^{208}\text{Pb}, ^{208}\text{Pb}(^{13}\text{O}, ^{12}\text{N} p)^{208}\text{Pb}, \text{Coulomb dissociation, Relative energy}]$   
spectra

The Coulomb breakup technique was employed to determine the radiative width of excited levels in  $^{12}\text{N}$  and  $^{13}\text{O}$ , which dominate the low-energy cross sections of the  $^{11}\text{C}(p,\gamma)^{12}\text{N}$  and  $^{12}\text{N}(p,\gamma)^{13}\text{O}$  reactions. These reactions are important in the hot pp mode nuclear burning in hydrogen-rich massive objects.<sup>1)</sup> Under a high-temperature and high-density condition, these capture reactions become faster than the  $\beta^+$  decay of  $^{11}\text{C}$  and  $^{12}\text{N}$ . However, these  $^{11}\text{C}(p,\gamma)^{12}\text{N}$  and  $^{12}\text{N}(p,\gamma)^{13}\text{O}$  reactions are difficult to study experimentally because the life times of  $^{11}\text{C}$  and  $^{12}\text{N}$  are too short to prepare them as targets.

For the present  $^{12}\text{N}$ -dissociation experiment, the relative-energy resolution is better than that in the experiment at GANIL,<sup>2)</sup> and a lower background was realized compared with our previous measurement at RIKEN.<sup>3)</sup> The latter improvement was achieved by installing the entire detector in a vacuum chamber. In the energy region of astrophysical interest, two resonant states are known for  $^{12}\text{N}$ ,  $2^+$  at  $E_{\text{ex}} = 0.960$  MeV and  $2^-$  at  $E_{\text{ex}} = 1.19$  MeV, corresponding to the  $p$ - $^{11}\text{C}$  center-of-mass energy,  $E_{\text{cm}} = 0.359$  MeV and  $0.589$  MeV, respectively. For  $^{13}\text{O}$ , only one resonant state is known at the  $p$ - $^{12}\text{N}$  center-of-mass energy  $E_{\text{cm}} = 1.23$  MeV, corresponding to the excited state at  $E_{\text{ex}} = 2.75$  MeV, whose spin has not been confirmed.

The experiments have been performed at RIKEN using the secondary beam line, RIPS. A  $77.0$  MeV/nucleon  $^{12}\text{N}$  beam and a  $83.5$  MeV/nucleon  $^{13}\text{O}$  radioactive beam were produced through fragmentation reactions of a primary  $135$  MeV/nucleon  $^{16}\text{O}$  beam. A  $30$  mg/cm<sup>2</sup>  $^{208}\text{Pb}$  target was bombarded by a secondary  $^{12}\text{N}$  beam, and a  $55$  mg/cm<sup>2</sup>  $^{208}\text{Pb}$  target was bombarded by a secondary  $^{13}\text{O}$  beam. The breakup fragments,  $^{11}\text{C}$  and a proton or  $^{12}\text{N}$  and a proton, were detected in coincidence after traveling through a  $5.1$  m flight-path by a plastic scintillator hodoscope. From the fragments' velocities, measured by their time-of-flight and their hit positions in the hodoscope, we could reconstruct the  $p$ - $^{11}\text{C}$  and the  $p$ - $^{12}\text{N}$  relative energies.

The  $p$ - $^{11}\text{C}$  relative-energy spectrum obtained in the  $^{12}\text{N}$ -dissociation experiment is shown in Fig. 1 (a). The open circles represent the data obtained in this work. The solid curve shows the result of a Monte Carlo simulation assuming three contributions, two resonances at

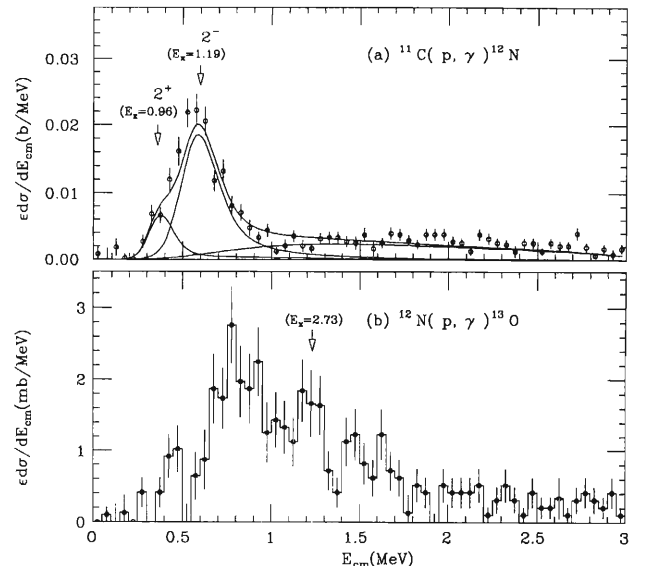


Fig. 1. (a) Relative energy spectrum obtained for the  $^{208}\text{Pb}(^{12}\text{N}, ^{11}\text{C} p)^{208}\text{Pb}$  reaction. The solid curve represents the results of a Monte-Carlo simulation, comprising the three components shown by the dashed curves. (b) Relative energy spectrum obtained for the  $^{208}\text{Pb}(^{13}\text{O}, ^{12}\text{N} p)^{208}\text{Pb}$  reaction.

$E_{\text{cm}} = 0.359$  MeV and  $0.589$  MeV, and a direct proton capture, whose magnitudes were treated as fitting parameters. As can be seen in Fig. 1, the bump observed at around  $0.6$  MeV is found to be mainly due to the E1 transition from the  $1^+$  ground state to the  $2^-$  state at  $E_{\text{ex}} = 1.19$  MeV. The  $\gamma$ -width of the  $2^-$  state is extracted from the fit to be  $\Gamma_{\gamma} \approx 20$  MeV, which is in between the two different predictions by Wiescher *et al.*<sup>4)</sup> ( $2$  MeV) and Descouvemont and Baraffe<sup>5)</sup> ( $140$  MeV), and disagrees with the results of the GANIL experiment ( $6_{-3.5}^{+7}$  MeV).

For  $^{13}\text{O}$  dissociation, the experimental relative-energy spectrum shown in Fig. 1(b) exhibits a bump. It might contain some extra strength in addition to the E1 strength to the resonance at  $E_{\text{ex}} = 2.75$  MeV. The sum of these strengths corresponds to  $\Gamma_{\gamma} \approx 3$  eV, which is much higher than expected in Ref. 4 (Wiescher).

A more complete analysis of the data, including a correction due to the  $^{12}\text{N} \rightarrow p + ^{11}\text{C}^*$  and  $^{13}\text{O} \rightarrow p + ^{12}\text{N}^*$  channels, is under way.

## References

- 1) A. Jorissen and M. Arnould: *Astron. Astrophys.* **221**, 116 (1989).
- 2) A. Lefebvre et al.: *Nucl. Phys. A* **592**, 69 (1995).
- 3) T. Minemura et al.: *RIKEN. Accel. Prog. Rep.* **31**, 69 (1998).
- 4) M. Wiescher, J. Görres, S. Graff, L. Buchmann, and F. K. Thielemann: *Astrophys. J.* **343**, 352 (1989).
- 5) P. Descouvemont and I. Baraffe: *Nucl. Phys. A* **514**, 66 (1990).

Coulomb Dissociation of  $^{13}\text{N}$  and  $^{14}\text{O}$ 

M. Serata, T. Motobayashi, S. Shimoura, H. Akiyoshi, Y. Ando, N. Aoi, Zs. Fülöp, T. Gomi, Y. Higurashi, M. Hirai, K. Ieki, N. Imai, N. Iwasa, H. Iwasaki, Y. Iwata, H. Kobayashi, M. Kurokawa, T. Minemura, H. Murakami, S. Ozawa, H. Sakurai, S. Takeuchi, T. Teranishi, K. Yamada, Y. Yanagisawa, K. Yoshida, Z. Liu, and M. Ishihara

[NUCLEAR REACTIONS:  $^{208}\text{Pb}(^{14}\text{O},\text{p})^{13}\text{N}$   $^{208}\text{Pb}$ , 85 A MeV;  $^{208}\text{Pb}(^{13}\text{N},\text{p})^{12}\text{C}$   $^{208}\text{Pb}$ , 76 A MeV]

The Coulomb dissociation method<sup>1)</sup> has been successfully applied to various astrophysical  $(\text{p},\gamma)$  reactions. However, the validity of the method has not been tested to high precision. For that purpose, we studied the Coulomb dissociation of  $^{13}\text{N}$  and  $^{14}\text{O}$ . The  $^{12}\text{C}(\text{p},\gamma)^{13}\text{N}$  reaction, which corresponds to  $^{13}\text{N}$  dissociation, has been well studied, and its cross section is known to good accuracy. Experiments concerning  $^{13}\text{N}$  and  $^{14}\text{O}$  dissociation have already been performed at RIKEN.<sup>2)</sup> Dissociation of  $^{14}\text{O}$  has also been studied at GANIL.<sup>3)</sup> The results of these experiments agree with a direct measurement performed at Louvain-La-Neuve<sup>4)</sup> within the errors. However, these agreements are confirmed at accuracies of around 30%. The present experiment is aimed at improving the experimental accuracy by reducing the systematic uncertainties with a lower background and a higher relative energy resolution.

Beams of  $^{13}\text{N}$  and  $^{14}\text{O}$  were produced by using the projectile fragmentation of a 135 MeV/nucleon  $^{16}\text{O}$  beam on a 1480 mg/cm<sup>2</sup>  $^9\text{Be}$  target. These beams were separated by the RIPS from other fragments, and were focused on a Pb or a C target with the thickness of 55 or 37 mg/cm<sup>2</sup>, respectively. The thickness of the Pb target was about seven-times as thin as that used in a previous experiment.<sup>2)</sup> This reduced multiple scattering of the products, and hence improved the angular resolution. The averaged energies were 76 MeV/nucleon and 85 MeV/nucleon, respectively, for  $^{13}\text{N}$  and  $^{14}\text{O}$  at the middle of the target. Outgoing charged particles were detected by a  $\Delta\text{E}$ -E hodoscopes.<sup>5)</sup> The velocities of the particles were determined by their time-of-flight (TOF) for a path length of 5 m. The momentum vectors of the particles were determined by combining their velocities with the hit positions on the hodoscope, and were used to calculate the relative energies of the breakup fragments measured in coincidence. Together with an improved energy resolution, resulting from the TOF measurement, a better relative-energy resolution was possible compared with that in a previous experiment.<sup>2)</sup>

Figure 1 shows the relative energy spectra for the correlated  $\text{p}-^{12}\text{C}$  and  $\text{p}-^{13}\text{N}$  pairs generating,

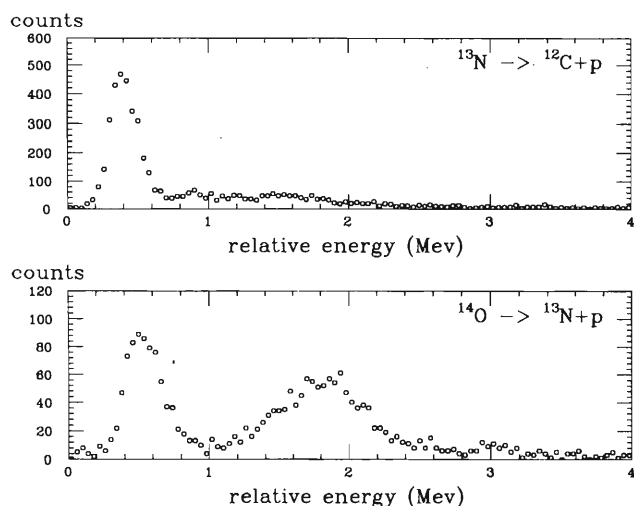


Fig. 1. Relative energy spectrum for the Coulomb dissociation of  $^{13}\text{N}$  and  $^{14}\text{O}$ .

respectively, from the Coulomb dissociation of  $^{13}\text{N}$  and  $^{14}\text{O}$ . The prominent peaks around at 500 keV correspond to the lowest E1 resonances in  $^{13}\text{N}$  and  $^{14}\text{O}$ . It is known that the  $(\text{p},\gamma)$  processes through these resonances dominate in stellar burning. Therefore, any comparison to the direct-capture data should be made concerning their yield. The widths (FWHM) of the peaks in the observed spectra were 310 keV ( $^{14}\text{O}$ ) and 250 keV ( $^{13}\text{N}$ ). These resolutions are better by a factor of two than those in the previous experiment at RIKEN.<sup>2)</sup> This is because of the better angular and energy resolutions of the present measurement.

An accurate determination of the  $\Gamma_\gamma$  values of the E1 transitions, which determine the  $(\text{p},\gamma)$  reaction rates, is now in progress.

## References

- 1) G. Baur et al.: Nucl. Phys. A **458**, 188 (1986).
- 2) T. Motobayashi et al.: Phys. Lett. B **264**, 259 (1991).
- 3) J. Kiener et al.: Nucl. Phys. A **552**, 66 (1993).
- 4) P. Decroock et al.: Phys. Rev. Lett. **67**, 808 (1991).
- 5) I. Hisanaga et al.: RIKEN. Accel. Prog. Rep. **31**, 162 (1998).

## Isobaric Analog State of $^{14}\text{Be}$

S. Takeuchi, S. Shimoura, T. Motobayashi, H. Akiyoshi, Y. Ando, N. Aoi, Zs. Fülöp, T. Gomi, Y. Higurashi, M. Hirai, N. Iwasa, H. Iwasaki, Y. Iwata, H. Kobayashi, M. Kurokawa, T. Minemura, S. Ozawa, H. Sakurai, M. Serata, T. Teranishi, K. Yamada, Y. Yanagisawa, Z. Liu, and M. Ishihara

[NUCLEAR REACTIONS:  $^1\text{H}(^{14}\text{Be}, ^{14}\text{B}^*)$ , 74 A MeV; Charge exchange reaction; Isobaric analog state; Neutron halo]

The Isobaric Analog State (IAS) of the neutron halo nucleus,  $^{14}\text{Be}$ , has been investigated using the charge-exchange reaction  $^{14}\text{Be}(p,n)^{14}\text{B}^*$  in inverse kinematics at  $E(^{14}\text{Be}) = 74$  A MeV. The present study was aimed at determining the energy of IAS( $^{14}\text{B}^*$ ), and understanding the neutron halo structure of  $^{14}\text{Be}$ . The charge-exchange reaction is useful to study IAS, and was successfully applied in a recent study on the neutron halo nucleus  $^{11}\text{Li}$ .<sup>1,2)</sup> The IAS of  $^{14}\text{Be}$  is characterised by its isospin of  $T = 3$ , while other populated states are mostly of  $T = 2$ , and it decays to the  $^{12}\text{Be}+p+n$  channel ( $T = 3$  and 2) because of isospin conservation. Thus, the IAS can be revealed by detecting a  $^{12}\text{Be}$ , proton and neutron in coincidence.

A secondary  $^{14}\text{Be}$  beam was produced by using the projectile fragmentation of a 100 A MeV  $^{18}\text{O}$  beam at a 1110 mg/cm<sup>2</sup>  $^9\text{Be}$  target and focused on  $(\text{CH}_2)_n$  and C targets. The decay particles from  $^{14}\text{B}^*$  were detected by  $\Delta E$  and  $E$  hodoscopes, which were located 492 cm downstream of the target; the time-of-flight (TOF) from the target to the hodoscopes and the hit position were measured. The momentum vectors of the decaying particles were determined by combining their velocities and hit positions on the hodoscope.

The extracted momentum vectors were used to construct the decay energy spectrum of the  $^{12}\text{Be}+p+n$  system, which is the difference between the invariant mass and the threshold energy,  $\Sigma_i M_i$  (total rest mass of all decay particles):

$$E_d = M(^{14}\text{B}^*) - \Sigma_i M_i. \quad (1)$$

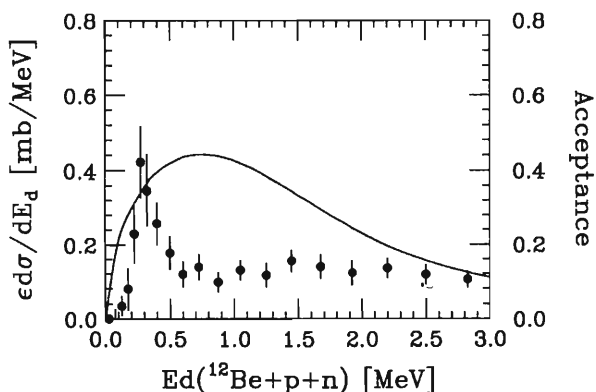


Fig. 1. Decay-energy spectrum of the  $^{12}\text{Be}+p+n$  system. The solid line shows the detector acceptance.

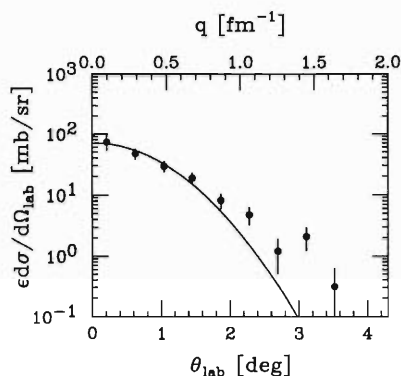


Fig. 2. Angular distribution of  $^{14}\text{B}^*$ . The solid line represents a Gaussian distribution.

Figure 1 shows the decay energy spectrum of the  $^{12}\text{Be}+p+n$  system for the  $(p,n)$  reaction, which was obtained by subtracting the spectrum of the C target from that of the  $(\text{CH}_2)_n$  target. A sharp peak is observed at  $E_d \simeq 0.3$  MeV, which is not observed in the C target spectrum. Most of the events consisting of the peak were derived from the Fermi transition which was suppressed in a reaction using a C target. The peak was fitted with a Gaussian function; the effects of the  $E_d$  resolution and the detector acceptance were taken into account in the fitting procedure. The energy of the IAS was deduced to be  $0.29 \pm 0.03$  MeV, where the error was derived from the uncertainty in the absolute magnitude of the TOF. Using a threshold energy of 16.77 MeV for  $^{12}\text{Be}+p+n$  channel, the excitation energy of the IAS was determined to be  $17.06 \pm 0.03$  MeV with respect to the ground state of  $^{14}\text{B}$ .

The angular distribution of  $^{14}\text{B}^*$ (IAS) is shown in Fig. 2, where the events in the IAS peak are plotted as a function of the angle of the center-of-mass for the  $^{12}\text{Be}+p+n$  system. The distribution is forward peaking and can be approximated by a Gaussian function centered at 0 degree. Such an angular distribution is characteristic of the  $\Delta L = 0$  angular momentum transfer, which is required for Fermi transitions. Thus, the observed forward peaking angular distribution supports the assignment of the peak in Fig. 1 to the IAS of  $^{14}\text{Be}$  populated by the Fermi transition.

### References

- 1) S. Shimoura et al.: Nucl. Phys. A **630**, 387c (1997).
- 2) T. Teranishi et al.: Phys. Lett. B **407**, 110 (1997).

Coulomb Excitation of  $^{15}\text{O}$ 

K. Yamada, T. Motobayashi, S. Shimoura, Y. Iwata, S. Ozawa, H. Kobayashi, T. Gomi, M. Serata, S. Takeuchi, Y. Higurashi, T. Minemura, Y. Yanagisawa, N. Aoi, H. Iwasaki, N. Imai, H. Sakurai, T. Teranishi, K. Yoshida, H. Akiyoshi, N. Iwasa, M. Kurokawa, Z. Liu, Zs. Fülöp, and M. Ishihara

[NUCLEAR REACTIONS:  $^{208}\text{Pb}(^{15}\text{O}, ^{15}\text{O}^*)$ , 100 MeV/u; Coulomb excitation reaction, Nu-]  
clear astrophysics

The CNO cycle has a certain effect on the rate of nuclear burning in the sun. At solar temperatures, the reaction  $^{14}\text{N}(p,\gamma)^{15}\text{O}$  determines the rate of the main CNO cycle, because its reaction rate is almost 100-times slower than the other CNO reactions. The behavior of the  $^{14}\text{N}(p,\gamma)^{15}\text{O}$  cross section at energies close to the threshold is not fully understood. Especially, a significant contribution to the ground-state capture from the subthreshold resonance at 504 keV below the  $p + ^{14}\text{N}$  threshold, which corresponds to the  $3/2^+$  state at 6.79 MeV in  $^{15}\text{O}$ , has been pointed out,<sup>1)</sup> but has not been studied experimentally. The present study was aimed at measuring  $\Gamma_\gamma$  of  $^{15}\text{O}$  in order to clarify the role of this subthreshold state by the Coulomb excitation method.

A beam of  $^{15}\text{O}$  was produced by using the projectile fragmentation of a 135 MeV/u  $^{16}\text{O}$  beam incident on a  $^9\text{Be}$  target, and selected by the RIKEN projectile-fragment separator (RIPS). The  $^{15}\text{O}$  beam was focused onto a 1480 mg/cm<sup>2</sup>  $^{208}\text{Pb}$  target at 300–400 kcps. The average beam energy was 85 MeV/u at the middle of the target. A 1.0 mm thick plastic scintillator was located at the first achromatic focal plane of RIPS (F2). Particle-identification of the  $^{15}\text{O}$  beam was carried out by a time-of-flight measured between F2 and the cyclotron RF signals. A plastic scintillator hodoscope<sup>2)</sup> consisting of  $\Delta E$  and E walls was placed 499 cm downstream from the target to detect the scattered  $^{15}\text{O}$ , which was identified by measuring the energies deposited in the  $\Delta E$  and E detectors together with the time-of-flight. An array of 64 NaI(Tl) scintillators set around the target was used to detect  $\gamma$ -rays with an efficiency of 20% for 6.79 MeV photons from  $^{15}\text{O}$  nuclei in flight with  $\beta = v/c \approx 0.4$ . The Doppler effects were corrected by the  $\gamma$ -ray emission angle determined for each crystal.

The histograms in Fig. 1 show the Doppler-corrected  $\gamma$ -ray spectra measured in coincidence with inelastically scattered  $^{15}\text{O}$  at  $\theta = 63^\circ$  and  $86^\circ$ , respectively. No distinct peak can be observed at 6.79 MeV, suffered by the background photons originating from the target excitation. The distributions exhibiting peaks in Fig. 1 represent the spectra expected for two different

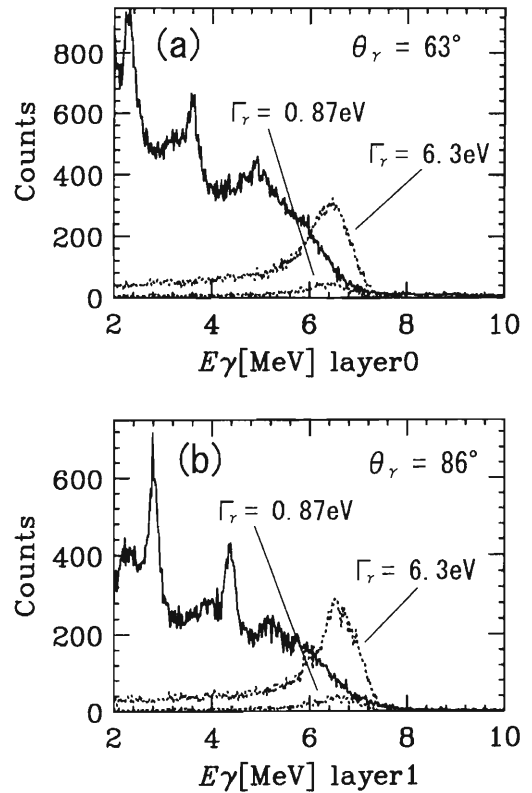


Fig. 1. Doppler-corrected  $\gamma$ -ray spectrum measured at the detector angles  $\theta = 63^\circ$  (a) and  $\theta = 86^\circ$  (b).

$\Gamma_\gamma$  values, 0.87 eV<sup>3)</sup> and 6.3 eV.<sup>1)</sup> The detector response was calculated by a Monte-Carlo simulation. Apparently, the larger value of 6.3 eV can be excluded by a comparison with the data, whereas the lower estimate,  $\Gamma_\gamma = 0.87$  eV, is compatible with the data. Thus, the present results suggest that  $\Gamma_\gamma \leq 1$  eV, pointing to only a minor effect of the 6.79 MeV state in  $^{15}\text{O}$  on the low-energy  $^{14}\text{N}(p,\gamma)^{15}\text{O}$  cross section.

## References

- 1) U. Schröder et al.: Nucl. Phys. A **467**, 240 (1987).
- 2) I. Hisanaga et al.: RIKEN Accel. Prog. Rep. **31**, 162 (1998).
- 3) R. Moreh et al.: Phys. Rev. C **23**, 988 (1981).

## Coulomb Excitation of $^{28}\text{Ne}$ and $^{32,34}\text{Mg}$

H. Iwasaki, T. Motobayashi, K. Yoneda, T. Gomi, H. Sakurai, N. Aoi, N. Fukuda, Zs. Fülöp, U. Futakami,  
Z. Gacsi, Y. Higurashi, N. Imai, N. Iwasa, T. Kubo, M. Kunibu, M. Kurokawa, Z. Liu, T. Minemura,  
A. Saito, M. Serata, S. Shimoura, S. Takeuchi, Y. X. Watanabe, K. Yamada,  
Y. Yanagisawa, and M. Ishihara

[NUCLEAR REACTIONS: Pb, C ( $^{28}\text{Ne}, ^{28}\text{Ne}\gamma$ ), ( $^{32}\text{Mg}, ^{32}\text{Mg}\gamma$ ), ( $^{34}\text{Mg}, ^{34}\text{Mg}\gamma$ ), Coulomb]  
excitation, Deduced  $B(E2)$ ]

The first experiment involving the Coulomb excitation of  $^{32}\text{Mg}$  has demonstrated the usefulness of the intermediate-energy Coulomb excitation technique for studies of low-lying states in nuclei far from the stability line.<sup>1)</sup> Experimental studies with this technique have revealed that some neutron-rich nuclei, such as  $^{32}\text{Mg}$  and  $^{44}\text{S}$ , have large quadrupole collectivity in spite of the neutron-shell closures at  $N = 20$  and  $N = 28$ .<sup>1,2)</sup>

We performed measurements of the excitation energies and  $B(E2)$  values for the  $2_1^+$  states of the neutron-rich nuclei  $^{28}\text{Ne}$  and  $^{32,34}\text{Mg}$  via intermediate-energy Coulomb excitation. Here, we report on the experimental arrangement.

The nuclei studied in the present work were produced by fragmentation of a 95 MeV/u  $^{40}\text{Ar}$  beam impinging on a 463 mg/cm<sup>3</sup>  $^9\text{Be}$  target. The reaction fragments were collected and analysed by the RIKEN projectile-fragment separator (RIPS)<sup>3)</sup> operated at the maximum values of the momentum acceptance and solid angle. A thick aluminum wedge was used to allow a unique isotopic identification of the fragments. The obtained intensities for secondary beams were typically 100 s<sup>-1</sup> ( $^{28}\text{Ne}$ ), 1000 s<sup>-1</sup> ( $^{32}\text{Mg}$ ), and 4 s<sup>-1</sup> ( $^{34}\text{Mg}$ ). Particle identification of the incident beam was carried out event-by-event using the time-of-flight (TOF)- $\Delta E$  method. The TOF was determined by two 0.3 mm thick plastic scintillators placed 5.2 m apart in the beam line. The  $\Delta E$  information was measured by a 0.35 mm thick silicon detector placed at the first achromatic focal plane (F2) of RIPS. The horizontal and vertical positions of the fragments at F2 were measured by a parallel-plate avalanche counter (PPAC). The horizontal position at F2 was incorporated in the particle identification. Lead targets were placed at the final focal plane (F3) and used to excite the projectiles. The thicknesses of the lead targets were 693 mg/cm<sup>3</sup> for the  $^{28}\text{Ne}$  and  $^{34}\text{Mg}$  measurements and 573 mg/cm<sup>3</sup> for the  $^{32}\text{Mg}$  measurement. In addition, measurements with carbon targets were performed in order to study any possible contributions of nuclear excitations. The position and incident angles of the beam at the target were measured by two sets of PPAC's placed at F3.

The number of the incident beam was counted by a 0.3 mm thick plastic scintillator placed 40 cm downstream of the target.

Scattered particles were detected by a counter telescope located 43 cm downstream of the target. The telescope comprised 4 layers of ion-implanted silicon detectors. The thicknesses of the silicon detectors were 0.5, 1.0, 1.0, 0.5 mm, respectively. The first silicon detector was a double-sided type, which divided into 16 strips both horizontally and vertically. The positions of scattered particles were determined by the 16 × 16 segments of the detector. The scattered particles of interest stopped in the second or the third detector. Each silicon detector provided independent energy-loss information, while the whole telescope provided total energy deposit information. An isotopic identification of scattered particles was achieved by the  $\Delta E$ - $E$  method. The counter telescope with an active diameter of 92 mm covered the scattering angle up to about 6 degrees. The scattering angle was determined by the hit positions in the two PPAC's at F3 and the first silicon detector.

De-excitation  $\gamma$  rays were measured in coincidence with the scattered particles. A granular array of 66 NaI(Tl) scintillators was placed around the target and used for  $\gamma$ -ray detection. Each scintillator crystal had a rectangular shape with a size of 6 × 6 × 12 cm<sup>3</sup> coupled with a 5.1 cm  $\phi$  photomultiplier tube. The energy and efficiency calibrations of each NaI(Tl) detector were made by using standard  $^{22}\text{Na}$ ,  $^{60}\text{Co}$ ,  $^{88}\text{Y}$ , and  $^{137}\text{Cs}$  sources.

Our data include the first measurement of the  $B(E2)$  value for the  $2_1^+$  state in  $^{34}\text{Mg}$ . The number of accumulated events for the  $^{28}\text{Ne}$  and  $^{32}\text{Mg}$  measurements in the present experiment was 3–10 times more than those in previous experiments;<sup>1,4)</sup> more detailed information on the collective behaviour in these nuclei is to be obtained. An analysis of the data is now in progress.

### References

- 1) T. Motobayashi et al.: Phys. Lett. B **346**, 9 (1995).
- 2) T. Glasmacher et al.: Phys. Lett. B **395**, 163 (1997).
- 3) T. Kubo et al.: Nucl. Instrum. Methods Phys. Res. B **70**, 309 (1992).
- 4) B. V. Pritychenko et al.: Phys. Lett. B **461**, 322 (1999).

# Population of Excited States in Unstable Nuclei Produced by the Fragmentation of $^{36}\text{Si}$

T. Gomi, K. Yoneda, H. Sakurai, S. Shimoura, T. Motobayashi, N. Aoi, N. Fukuda, U. Futakami, Z. Gacsi, Y. Higurashi, N. Imai, N. Iwasa, H. Iwasaki, T. Kubo, M. Kunibu, M. Kurokawa, Z. Liu, T. Minemura, A. Saito, M. Serata, S. Takeuchi, Y. X. Watanabe, K. Yamada, Y. Yanagisawa, K. Yogo, A. Yoshida, and M. Ishihara

[NUCLEAR REACTION:  $^9\text{Be}(^{36}\text{Si}, X)$ ,  $E(^{36}\text{Si}) = 50 A \text{ MeV}$ ; Measured(fragment)gamma-coin

We measured  $\gamma$  rays in coincidence with fragments produced by the  $^{36}\text{Si}+^9\text{Be}$  reaction at 50 A MeV. From the measured yield of  $\gamma$ -ray lines we extracted the population ratios of excited states in several unstable nuclei. They are related to the reaction mechanism of the projectile fragmentation, and provide useful information for exploring the possibility of spectroscopic studies of unstable nuclei.

The experiment was performed in the RIPS beam line. The setup is described in Ref. 1. Figure 1 shows typical  $\gamma$ -ray energy spectra with a Doppler-shift correction obtained for  $^{18}\text{O}$ ,  $^{22}\text{Ne}$ , and  $^{28}\text{Mg}$ . Two lines are observed in each spectrum. They correspond to the known  $2^+ \rightarrow 0^+$  and  $4^+ \rightarrow 2^+$  transitions.

The population ratio for an excited state can be expressed as

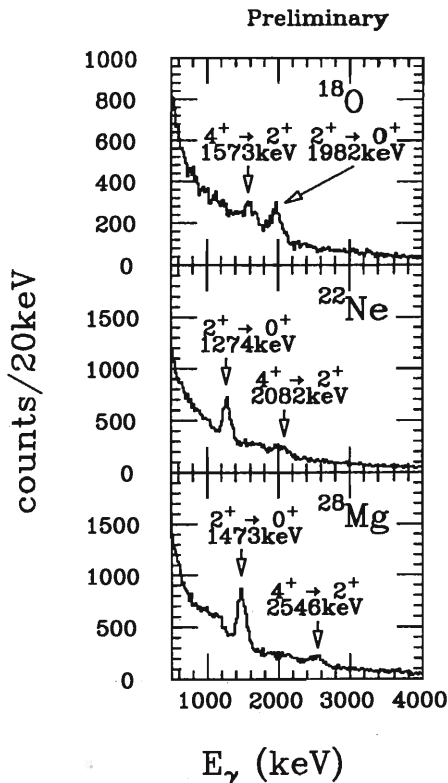


Fig. 1. Doppler-corrected  $\gamma$ -ray energy spectra associated with  $^{18}\text{O}$ ,  $^{22}\text{Ne}$ , and  $^{28}\text{Mg}$ .

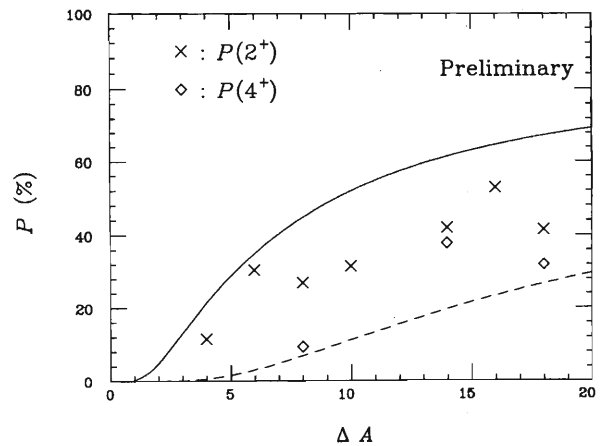


Fig. 2. Plots of the population ratios,  $P(2^+)$  and  $P(4^+)$ , as a function of  $\Delta A$ . The solid curve represents predictions for  $P(2^+)$  within the framework of the abrasion-ablation model, and the dashed curve for  $P(4^+)$ .

$$P = \frac{N_\gamma / \varepsilon(E_\gamma)}{N_f}$$

where  $N_\gamma$  represents the peak yield of the  $\gamma$ -ray;  $\varepsilon(E_\gamma)$  the photo peak efficiency as a function of the  $\gamma$ -ray energy, and  $N_f$ , the number of identified fragments. We obtained  $P(2^+)$  when we counted the peak yield corresponding to the  $2^+ \rightarrow 0^+$  transition, and  $P(4^+)$  for the  $4^+ \rightarrow 2^+$  transition.

In Fig. 2, the preliminary results of  $P(2^+)$  and  $P(4^+)$  obtained for even-even isotopes with  $Z = 8-12$  are plotted as a function of the number of nucleons removed from the projectile ( $\Delta A$ ). The solid curve represents predictions for  $P(2^+)$  based on a theoretical calculation within the framework of the abrasion-ablation model,<sup>2)</sup> and the dashed curve for  $P(4^+)$ . From the experimental data, we found that the population ratios increase when  $\Delta A$  increases; this tendency is in accord with the theoretical one. As can be seen in Fig. 2, the population ratio reaches 10% at  $\Delta A \approx 5$  for  $2^+$  and  $\Delta A \approx 10$  for  $4^+$ .

## References

- 1) K. Yoneda et al.: RIKEN Accel. Prog. Rep. 33, 70 (2000).
- 2) M. de Jong et al.: Nucl. Phys. A 613, 435 (1997).

## Gamma-Ray Spectroscopy of the Very Neutron-Rich Nucleus $^{34}\text{Mg}$

K. Yoneda, H. Sakurai, T. Gomi, T. Motobayashi, N. Aoi, N. Fukuda, U. Futakami, Z. Gacsi, Y. Higurashi, N. Imai, N. Iwasa, H. Iwasaki, T. Kubo, M. Kunibu, M. Kurokawa, Z. Liu, T. Minemura, A. Saito, M. Serata, S. Shimoura, S. Takeuchi, Y. X. Watanabe, K. Yamada, Y. Yanagisawa, K. Yogo, A. Yoshida, and M. Ishihara

[NUCLEAR REACTION:  $^9\text{Be}(^{36}\text{Si}, X)$ ,  $E = 50$  MeV/nucleon; Measured fragment $\gamma$ -coin;]  
Deduced  $Ex$  of  $^{34}\text{Mg}$

We have observed the  $\gamma$ -ray transitions in the very neutron-rich nucleus  $^{34}\text{Mg}$  for the first time. The excited  $^{34}\text{Mg}$  nuclei were created by the projectile fragmentation reaction induced by a 50 MeV/nucleon radioactive beam of  $^{36}\text{Si}$ .

The experiment was carried out at RIPS. A primary  $^{40}\text{Ar}$  beam of 95 MeV/nucleon with a typical intensity of 60 pA bombarded a  $^9\text{Be}$  production target with 462.5 mg/cm<sup>2</sup> thickness to obtain a radioactive beam of  $^{36}\text{Si}$ . The  $^{36}\text{Si}$  nuclei in the beam were separated event by event from the main contaminant  $^{37}\text{P}$  using time-of-flight (TOF) information between two plastic scintillators. The purity of the  $^{36}\text{Si}$  beam was approximately 80% and the intensity was around  $2 \times 10^4$  s<sup>-1</sup>.

A secondary target of 385 mg/cm<sup>2</sup>  $^9\text{Be}$  was placed at the focal plane of RIPS. The beam lost its energy in the target from 50 MeV/nucleon to 30 MeV/nucleon. The reaction products from the  $^{36}\text{Si} + ^9\text{Be}$  fragmentation were detected by four sets of counter telescopes in a  $2 \times 2$  matrix placed 56 cm away from the target. Each telescope consisted of three layers of ion-implanted silicon detectors of  $50 \times 50$  mm<sup>2</sup> effective area and 350  $\mu\text{m}$  thickness, followed by a 1 mm thick Si(Li) detector with the same size to identify unwanted light particles that punched through the three ion-implanted detectors. Particle identification was achieved by the  $\Delta E$ - $E$  information from the the first three detectors, combined with the TOF information between the secondary target and a parallel-plate avalanche counter (PPAC) located 48 cm downstream of the target. A good resolving power of the detectors enabled us to identify  $A$  and  $Z$  for reaction products with  $Z = 8$ -12.

Sixty-six NaI(Tl) scintillators surrounded the target to detect  $\gamma$  rays emitted from the excited fragments. Each scintillator crystal was of rectangular shape with a size of  $6 \times 6 \times 12$  cm<sup>3</sup> coupled with a 5.1 cm  $\phi$  photomultiplier tube. Their energy resolution was typically 7.5% for a 662 keV  $\gamma$  ray. The high granularity of the setup allowed us to measure the angle of the  $\gamma$  ray emission with approximately 20° accuracy, enabling us to correct for the large Doppler shift of  $v/c \approx 0.3$  according to the detector angle with respect to the beam direction. The total full-energy peak efficiency was calculated to be 18% for a 1 MeV  $\gamma$  ray. A lead shield with 5 cm thickness surrounded the NaI(Tl) for background reduction.

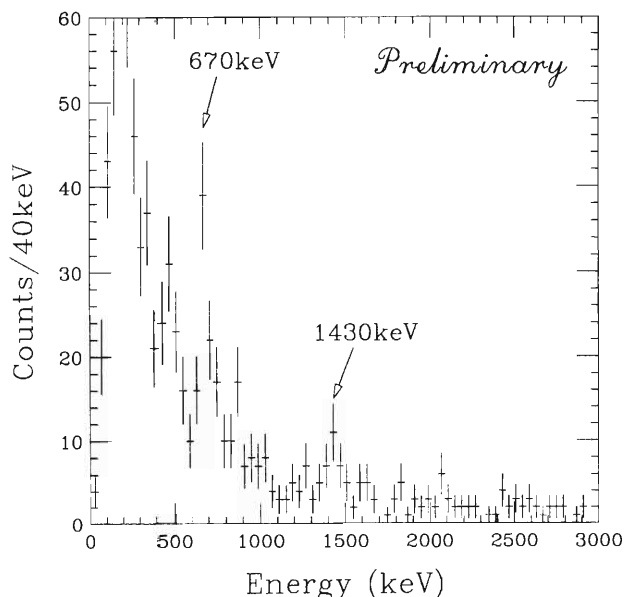


Fig. 1. Doppler-corrected  $\gamma$ -ray spectrum in coincidence with  $^{34}\text{Mg}$ , produced by the  $^{40}\text{Ar} + ^9\text{Be}$  fragmentation reaction.

Figure 1 shows the  $\gamma$  ray energy spectrum associated with  $^{34}\text{Mg}$  identified in the detectors. It was obtained as a sum of each Doppler-corrected spectrum of all the NaI(Tl) scintillators. As one can see in Fig. 1, two full-energy peaks were observed. The energies were preliminarily determined to be 670 keV and 1430 keV. The first peak can be tentatively assigned to be corresponding to the  $2_1^+ \rightarrow 0_{g.s.}^+$  transition, since it is the strongest and its energy is the lowest in the spectrum. The energy resolution deduced by fitting the first peak is 80 keV (FWHM), which is mainly due to Doppler broadening with the finite angular resolution of each NaI(Tl) crystal.

The energy 670 keV is very low compared with those of the first  $2^+$  states in the neighbouring nuclei. Using an empirical formula for the relation between the excitation energy and the deformation parameter,<sup>1)</sup>

$$E(2^+) = 1224(\langle\beta^2\rangle A^{7/3})^{-1},$$

the energy of 670 keV leads to a large deformation of  $^{34}\text{Mg}$  with  $\beta \approx 0.7$ . Within the framework of the shell model, the excitation energies of the

first  $2^+$  and the first  $4^+$  state were recently calculated to be 620 keV and 2460 keV, respectively,<sup>2)</sup> which agree well with the energies extracted in the present work (670 keV and 2100 keV), if one assumes that the second  $\gamma$ -ray peak corresponds to deexcitation from the first  $4^+$  state to the first  $2^+$  state. Furthermore, the energy ratio  $E(4^+)/E(2^+)$  is deduced to be 3.1, which is close to the 3.3

expected for the rotational band of deformed nuclei.

#### References

- 1) D. Guillemaud-Mueller et al.: Nucl. Phys. A **426**, 37 (1984).
- 2) Y. Utsuno, T. Otsuka, T. Mizusaki, and M. Honma: Phys. Rev. C **60**, 054315 (1999).

# Half-Life Determination of $^{44}\text{Ti}$ Using a Radioactive Beam Technique

Zs. Fülöp, Y. Wakasaya, C. Bordeanu, M. Golovkov, R. Goswami, T. Kato, K. Kimura, H. Kudo,\*<sup>1</sup>  
 Y. Mochizuki, H. Otsu, A. Ozawa, H. Petrascu, H. Sakurai, T. Suzuki, I. Tanihata, K. Yoshida,  
 R. N. Boyd, A. Krasznahorkay,\*<sup>2</sup> and E. Somorjai\*<sup>2</sup>

[Half-life, Nucleosynthesis]

In addition to studies of exotic nuclei, radioactive ion beam (RIB) technique also proved to be a useful tool to determine the half-life of  $^{44}\text{Ti}$  when a relative method is used.<sup>1)</sup> Here, we propose a novel method to the fast and reliable absolute half-life determination and apply it to the same isotope. In order to perform a meaningful analysis of the observed results of the  $E_\gamma = 1157$  keV line—characteristic to the decay of  $^{44}\text{Ti}$ —in the Cassiopeia A<sup>2)</sup> supernova and the recently discovered RX J0852.0-4622/GRO J0852-4642 supernova remnant,<sup>3)</sup> an accurate determination of the half-life of  $^{44}\text{Ti}$  is necessary.

Because of the relatively long half-life of  $^{44}\text{Ti}$  ( $\sim 60$  y), several years are needed to follow its decay until the desired accuracy in half-life can be reached. According to recent measurements,<sup>4,5)</sup> 2–5 years of data-taking resulted in 1–3% relative errors when the  $^{44}\text{Ti}$  half-life was determined relative to that of sources as  $^{60}\text{Co}$ ,  $^{22}\text{Na}$ , and  $^{207}\text{Bi}$ . However, for an absolute measurement,<sup>6)</sup> where the absolute activity of a sample has been determined several times, a period of 20 years was needed to reach a similar error level. The availability of  $^{44}\text{Ti}$  as RIB offers an alternative method to determine the half-lives via implanting a known amount of  $^{44}\text{Ti}$  into a stopper, and to measure the activity relevant to the decay of  $^{44}\text{Ti}$ . Görres *et al.*<sup>1)</sup> measured the half-life of  $^{44}\text{Ti}$  relative to that of  $^{22}\text{Na}$ , emphasizing that it is questionable to apply the RIB technique to absolute half-life determination because of the low expected count-rates and the systematic errors.

Our aim was to establish a method that allows an absolute half-life determination with minimum systematic error and maximum versatility. It is also desirable that the measurement should give a reasonable error without years of data-taking. In our approach, the secondary beam is optimized not for the highest available intensity, but to reach an isotopic ratio where the time-of-flight (TOF) technique is enough for the separation. Since plastic scintillators can be used for TOF, the isotopic ratio can also be monitored under high-intensity irradiation. Details about the preliminary tests, secondary beam production, the irradiation and the off-line activity measurement setup have already been published elsewhere.<sup>8)</sup> The  $^{44}\text{Ti}$  was produced by fragmentation of 90 A MeV  $^{46}\text{Ti}$  on a beryllium target.

Through appropriate settings of the fragment separator we achieved a secondary beam intensity of  $2 \cdot 10^5$ /s without implanting isotopes contributing to the gamma activity of the stopper. Also, we kept the content of  $^{42}\text{Sc}$  (same A/Z as  $^{44}\text{Ti}$ , i.e. TOF determination is not enough to separate this isotope from  $^{44}\text{Ti}$ ) to a minimum ( $< 0.5\%$ ).

The separated fragments were implanted into a 1 mm thick plastic scintillator stopper, allowing a loss-free determination of the number of implanted ions. Behind the stopper, an additional plastic scintillator served to check the presence of ions penetrating the stopper. We also investigated the effect of the breakup of the already separated  $^{44}\text{Ti}$  ions.

The  $\gamma$ -activity of the implanted sample has been investigated by a well-shielded high-efficiency HPGE gamma detector. There is no contamination observed in the gamma spectra of the irradiated sample. The efficiency determination has been carried out by using  $^{65}\text{Zn}$  and  $^{60}\text{Co}$  sources, and the effect of extended sources has also been investigated.

In summary, we have implanted  $2.7 \times 10^9$   $^{44}\text{Ti}$  ions into the stopper, and during the off-line measurement the count-rate in the detector relevant to the 1157 keV ( $^{44}\text{Ti}$ -related) peak was 50 counts/hour. On the other hand, the measured photopeak efficiency is  $1.3 \times 10^{-2}$  in the used source-detector geometry. Our preliminary half-life value for the  $^{44}\text{Ti}$  is  $62.1 \pm 1.6$  y. The relative error of this method is comparable to the previous measurements, although only one day of irradiation and two weeks of activity measurement were necessary. Preliminary studies showed that the presented method can be applied to isotopes  $^{39}\text{Ar}$  and  $^{32}\text{Si}$ .

## References

- 1) J. Görres *et al.*: Phys. Rev. Lett. **80**, 2554 (1998).
- 2) A. F. Iyudin *et al.*: Astron. Astrophys. **284**, L1 (1994).
- 3) B. Aschenbach *et al.*: Astron. Astrophys. **350**, 997 (1999).
- 4) E. B. Norman *et al.*: Phys. Rev. C **57**, 2010 (1998).
- 5) I. Ahmad *et al.*: Phys. Rev. Lett. **80**, 2550 (1998).
- 6) F. E. Wietfeldt *et al.*: Phys. Rev. C **59**, 528 (1999).
- 7) Y. Chen *et al.*: Phys. Rev. C **47**, 1462 (1993).
- 8) Zs. Fülöp *et al.*: Proc. 'Nuclei in the Cosmos V', edited by N. Prantzos and S. Harissopulos, p. 281 (1998).

\*<sup>1</sup> Niigata University

\*<sup>2</sup> ATOMKI, Hungary

## Collective States of Neutron-Deficient Doubly Even Barium Isotopes

K. Uchiyama, H. Sakamoto,\* and K. Furuno

[B(E2), Ba isotopes, Boson expansion theory]

The experimental  $B(E2; 0_1^+ \rightarrow 2_1^+)$  values in the neutron-deficient doubly even Xe and Ba isotopes show significant increase in the midshell region without any concomitant change in the energies of the low-lying states.<sup>1,2)</sup> Recently, for Ba isotopes, improved experimental results have been reported, and an old compilation of experimental data<sup>3)</sup> includes a questionable result, which is described below. To provide the systematic behavior correctly, we recompiled the experimental  $B(E2; 0_1^+ \rightarrow 2_1^+)$  values of Ba isotopes, and then compared these experimental data with new results from a microscopical calculation using the normal-ordered linked-cluster boson expansion theory.<sup>4)</sup>

All available experimental data and our adopted values are given in Table 1. We should mention that the value 0.504(71)  $e^2b^2$  reported by Towsley *et al.* in Ref. 5 has been ignored, because the description in

Table 1. Experimental  $B(E2; 0_1^+ \rightarrow 2_1^+)$  values in Ba isotopes.

Nuclide	$B(E2)$ [ $e^2b^2$ ]	Method	Reference <sup>†</sup>
<sup>122</sup> Ba	2.77(25)	Delayed Coincidence	PRC46(1992)R6
	2.77(25)	Adopted value	
<sup>124</sup> Ba	1.34(12)	Delayed Coincidence	PRC46(1992)R6
	1.99(8)	Recoil Distance	PRC52(1995)1380
	2.09(9)	Recoil Distance	EPJA2(1998)13
	2.09(9)	Adopted value	
<sup>126</sup> Ba	1.28(24)	Recoil Distance	NPA93(1967)272
	1.99(32)	Recoil Distance	PRC5(1972)1658
	1.83 <sup>+0.10</sup> <sub>-0.29</sub>	Recoil Distance	PLB80(1979)345
	2.03(15)	Recoil Distance	JPG15(1989)L85
	1.69(17)	Delayed Coincidence	PRC46(1992)R6
	1.69(5)	Recoil Distance	PRC54(1996)R2119
	1.72(5)	Adopted value	
<sup>128</sup> Ba	1.50(32)	Recoil Distance	PRC5(1972)1658
	1.46(8)	Recoil Distance	NPA543(1992)589
	1.38(9)	Recoil Distance	PRC53(1996)1606
	1.46(8)	Adopted value	
<sup>130</sup> Ba	0.75(19)	Coulomb Excitation	PR109(1958)100
	1.36(14)	Coulomb Excitation	NPA94(1967)177
	1.21(38)	Coulomb Excitation	JPSJ34(1973)442
	1.163(13)	Coulomb Excitation	NPA494(1989)102
	1.17(2)	Adopted value	
<sup>132</sup> Ba	0.73(18)	Coulomb Excitation	PR109(1958)100
	0.859(41)	Coulomb Excitation	NPA432(1985)514
	0.859(41)	Adopted value	
<sup>134</sup> Ba	0.75(25)	Coulomb Excitation	ADNDT36(1987)1
	0.672(16)	Coulomb Excitation	PRC6(1972)1016
	0.700(15)	Coulomb Excitation	NPA283(1977)526
	0.672(15)	Coulomb Excitation	NPA432(1985)514
	0.665(6)	Coulomb Excitation	NPA494(1989)102
	0.669(5)	Adopted value	
<sup>136</sup> Ba	0.53(16)	Coulomb Excitation	ADNDT36(1987)1
	0.418(11)	Coulomb Excitation	PRC6(1972)1016
	0.353(49)	Doppler Shift Attenuation	ADNDT36(1987)1
	0.399(3)	Coulomb Excitation	PRC29(1984)1672
	0.394(13)	Coulomb Excitation	NPA432(1985)514
	0.418(4)	Coulomb Excitation	PRC34(1986)732
	0.406(5)	Adopted value	

<sup>†</sup> PRC, EPJA, NPA, PLB, JPG, PR, JPSJ and ADNDT mean Physical Review C, European Physical Journal A, Nuclear Physics A, Physics Letters B, Journal of Physics G, Physical Review, Journal of the Physical Society of Japan and Atomic Data and Nuclear Data Tables, respectively.

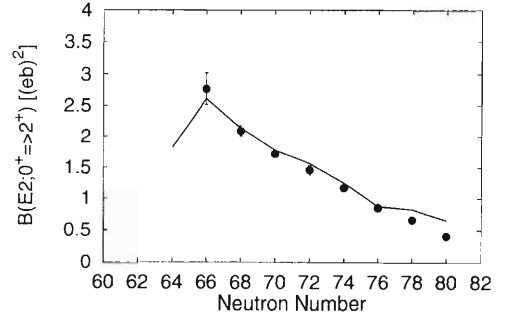


Fig. 1. Experimental and theoretical  $B(E2; 0_1^+ \rightarrow 2_1^+)$  values in Ba isotopes. The solid circles express the experimental data and the solid line denotes calculations of the boson expansion theory.

Ref. 5 contradicts itself; it is thus impossible to judge whether this value is the result for either <sup>134</sup>Ba or for <sup>136</sup>Ba. Indeed, this value had been referred to as the result for <sup>134</sup>Ba in Ref. 3; on the other hand, it had been used as the result for <sup>136</sup>Ba in Ref. 6. Although our newly adopted value of <sup>130</sup>Ba is about 9% smaller than our previous one,<sup>2,7)</sup> the new value is more desirable from systematic point of view. The difference between the newly adopted values and the previous ones is less than 2%, except for <sup>130</sup>Ba, as mentioned above.

The experimental data and calculations based on the boson expansion theory are shown in Fig. 1. The interaction strengths were changed for each nuclide, but a common effective charge of 0.550 was adopted for all of the Ba isotopes considered. The calculations are in fairly good agreement with the experimental data without any serious problems which had appeared in other calculations.<sup>1,7)</sup> In addition, it is worth noticing that the experimental  $B(E2)$  values of the  $4_1^+ \rightarrow 2_1^+$  and  $6_1^+ \rightarrow 4_1^+$  transitions for <sup>124</sup>–<sup>128</sup>Ba could be reproduced with same parameters. The detailed results of these new calculations will be described elsewhere.

## References

- 1) S. Raman *et al.*: Phys. Rev. C **52**, 1380 (1995).
- 2) K. Uchiyama *et al.*: Eur. Phys. J. A **2**, 13 (1998).
- 3) S. Raman *et al.*: At. Data Nucl. Data Tables **36**, 1 (1987).
- 4) H. Sakamoto: Phys. Rev. C **52**, 177 (1995).
- 5) C. W. Towsley *et al.*: J. Phys. Soc. Jpn. **34**, Suppl. p. 442 (1973).
- 6) M. J. Bechara *et al.*: Phys. Rev. C **29**, 1672 (1984).
- 7) M. Sugita *et al.*: Phys. Lett. B **440**, 239 (1998).

\* Faculty of Engineering, Gifu University

# Production Cross Sections of Light Neutron-Rich Nuclei from $^{40}\text{Ar}$ Fragmentation

A. Ozawa, O. Bochkarev,<sup>\*1</sup> L. Chulkov,<sup>\*1</sup> D. Cortina,<sup>\*2</sup> H. Geissel, M. Hellström,<sup>\*2</sup> M. Ivanov,<sup>\*3</sup> R. Janik,<sup>\*3</sup>  
K. Kimura, T. Kobayashi, A. A. Korshennikov, G. Münzenberg,<sup>\*2</sup> F. Nickel,<sup>\*2</sup> A. A. Ogloblin,  
M. Pfützner,<sup>\*2</sup> V. Pribora,<sup>\*1</sup> H. Simon,<sup>\*2</sup> B. Sitar,<sup>\*3</sup> P. Strmen,<sup>\*3</sup> K. Sümmerer,  
T. Suzuki, I. Tanihata, M. Winkler, and K. Yoshida

[NUCLEAR REACTIONS;  $^{40}\text{Ar} + \text{Be}$ ,  $E \sim 1 \text{ A GeV}$ ; Secondary beams; Production cross-sections]

Since the pioneering experiments at Berkeley,<sup>1)</sup> projectile fragmentation has been widely used to produce radioactive isotopes far from stability. Measurements of the production cross sections ( $\sigma_F$ ) are important to assess the feasibility of secondary-beam experiments with them. This work represents the first measurements of  $\sigma_F$  from  $^{40}\text{Ar}$  fragmentation at relativistic energies which extend far into the region of neutron-rich isotopes.

We measured  $\sigma_F$  from  $^{40}\text{Ar}$  fragmentation by using the FRagment Separator (FRS) facility at GSI. A primary beam of  $^{40}\text{Ar}$  with an energy of  $\sim 1 \text{ A GeV}$  impinged on a Be target with typically  $4.0 \text{ g/cm}^2$  thickness. A secondary electron transmission monitor was used to determine the primary-beam intensity. At the first focus at FRS, we placed a scintillation counter to start the TOF. This detector was also used as an active momentum slit ( $\Delta p/p = \pm 0.6\%$ ). At the intermediate focus, we placed a scintillation counter stack comprising five scintillation counters. One of them served as a stop signal of the TOF. The corrected pulse-height data of the counters gave  $\Delta E$  for the fragments. The magnetic field in the second dipole gave  $B\rho$  for the fragments. Thus, we applied the  $B\rho$ - $\Delta E$ -TOF method in order to identify the fragments.

In order to determine  $\sigma_F$ , the counting rates of different isotopes obtained from the particle identification spectra were corrected for any transmission losses in the FRS, for losses due to secondary interactions in the target as well as in the detectors and for the dead time of the data acquisition. The transmission losses and secondary interaction losses were estimated from a Monte-Carlo type calculation, a code called MOCADI,<sup>2)</sup> where we assumed a Gaussian curve for the momentum distributions of the fragments. The obtained  $\sigma_F$  are shown in Fig. 1.

In Fig. 1, the experimental results are compared to those previously measured with a C target at relativistic energies at LBL.<sup>3,4)</sup> Both results are very consistent. In Fig. 1, our experimental results are also compared with those from the empirical parametrization EPAX.<sup>5)</sup> For nuclei near the line of beta-

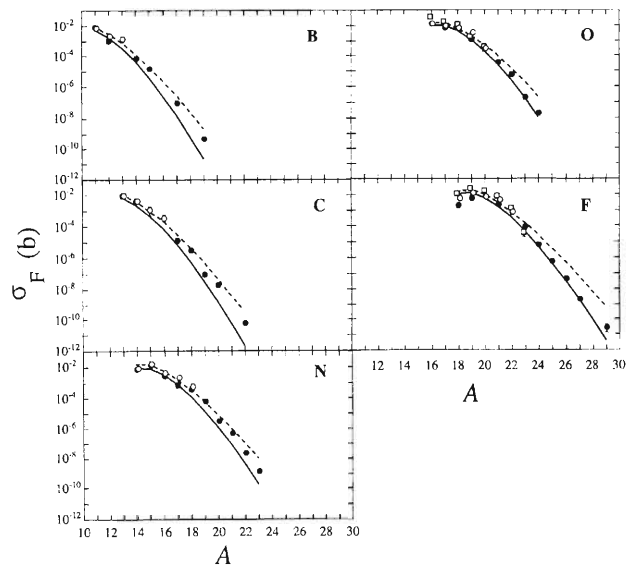


Fig. 1. Experimental production cross sections ( $\sigma_F$ ) for B to F isotopes produced with an  $^{40}\text{Ar}$  primary beam at  $1 \text{ A GeV}$  in a Be target. The closed circles show the present data. The open circles (squares) show the experimental data previously measured with a C target at  $213 \text{ A MeV}$  ( $1.6 \text{ A GeV}$ ), respectively. The  $\sigma_F$  are compared to the previous version of the EPAX formula (dashed line) and to the modified version (solid line).

stability, these quantities are in good agreement. However, for more neutron-rich nuclei, the measured  $\sigma_F$  are smaller than those from the EPAX prediction. Very recently, K. Sümmerer and B. Blank have suggested a modified EPAX formula.<sup>6)</sup> The modified version predicts the measured  $\sigma_F$  with better accuracy than the original version.

## References

- 1) D. E. Greiner et al.: Phys. Rev. Lett. **35**, 152 (1975).
- 2) N. Iwasa et al.: Nucl. Instrum. Methods Phys. Res. B **126**, 284 (1997).
- 3) Y. P. Vioggi et al.: Phys. Rev. Lett. **42**, 33 (1979).
- 4) C. Tull: Ph. D. thesis, LBL (1990).
- 5) K. Sümmerer et al.: Phys. Rev. C **42**, 2546 (1990).
- 6) K. Sümmerer and B. Blank: Phys. Rev. C, in press.

<sup>\*1</sup> Kurchatov Institute, Moscow, Russia

<sup>\*2</sup> GSI, Darmstadt, Germany

<sup>\*3</sup> Comenius University, Bratislava, Slovak Republic

## 2. Atomic and Solid-State Physics



# Positron Scattering by Polyatomic Molecules

T. Nishimura and I. Shimamura

Theoretical cross sections for elastic scattering of positrons from Ne, Ar, CH<sub>4</sub>, and SiH<sub>4</sub> targets are reported. The latter two molecules belong to the Td point group, and the effects of molecular anisotropy in these collision systems are minimal. The present work was inspired partly by the experimental elastic differential cross sections (DCSs) recently reported for CH<sub>4</sub><sup>1)</sup> and Ar<sup>2)</sup> over a large range of scattering angles of 30°–135°. The present work is based on the fixed-nuclei approximation. The interaction potential between a positron and a target is represented in the form of a local potential that consists of electrostatic and polarization components. For the latter component, a parameter-free model potential is adopted for the small values of the positron-target distance (say, less than several a.u.). This model potential is associated with the asymptotic form of the dipole polarization potential at the position where the two kinds of potentials first cross. The wave function of the scattered positron satisfies a set of coupled differential equations derived from the Schrödinger equation for the total collision system. By solving these equations, the scattering matrix is obtained from the asymptotic form of the wave function, and is transformed into the cross sections. Throughout the present calculation, no positronium (Ps) formation channel is taken into account. Therefore, the present calculations are only carried out below the Ps formation threshold energy ( $E_{Ps}$ ).

The theoretical elastic integrated cross section (ICS) from the present calculation for Ne is in very good agreement with the measured total cross section (TCS)<sup>3)</sup> (see Fig. 1). As the quantity  $E_{Ps}$  of each system becomes smaller, however, a disagreement between the theoretical elastic ICS and the experimental TCS<sup>3)</sup> becomes larger. The result suggests that the effect of the Ps formation channels on the cross sections is strong, particularly when the  $E_{Ps}$  is small. As for Ne, a minimal ICS called the Ramsauer-Townsend minimum, is seen at around 0.8 eV, and is caused by a phase shift for a dominant partial wave component being close to an integral multiple of  $\pi$ . The minimum disappears as the absolute value of the dipole polarizability of the target becomes larger, i.e., in the order of Ne, Ar, CH<sub>4</sub>, and SiH<sub>4</sub>, because the effect of the dominant partial wave component becomes more ambiguous due to a superposition of higher partial wave components. The present elastic DCS for each target has a notable minimum at around 40°–50° (see Fig. 2). For Ar and CH<sub>4</sub>, the shapes of the theoretical DCSs are generally in good agreement with the measured ones<sup>1,2)</sup> which are normalized to the elastic DCSs from the present calculations at a scattering angle of 90°.

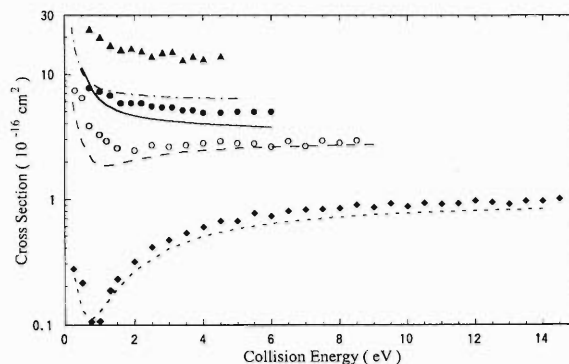


Fig. 1. Elastic ICSs of positrons from Ne, Ar, CH<sub>4</sub>, and SiH<sub>4</sub> below the  $E_{Ps}$  (14.8, 9.0, 5.8, and 4.8 eV, respectively). The present calculations for Ne (short dashes), Ar (long dashes), CH<sub>4</sub> (full), and SiH<sub>4</sub> (chain) are compared with the respective experimental TCSs<sup>3)</sup> (diamonds, open circles, full circles, and triangles, respectively).

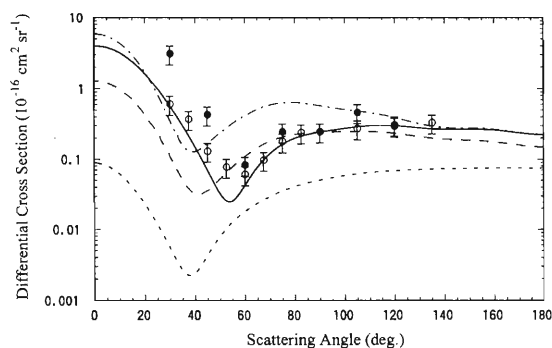


Fig. 2. Elastic DCSs for Ne (short dashes) and Ar (long dashes) at 5 eV, and those for CH<sub>4</sub> (full) and SiH<sub>4</sub> (chain) at 4 eV. Comparisons are made with the experimental DCSs for Ar (open circles)<sup>2)</sup> at 5 eV and CH<sub>4</sub> (full ones)<sup>1)</sup> at 4 eV.

We have also found a similarity between the theoretical DCSs for CH<sub>4</sub> and Ar not only in terms of shape but also magnitude. This may be attributed to a quantitative similarity between the interaction potentials for the two systems at intermediate and asymptotic values of the positron-target distance. A theoretical study on the positron-hydrogen molecule collision taking Ps formation channels into account is under way.

## References

- 1) D. A. Przybyla et al.: Phys. Rev. A **55**, 4244 (1997).
- 2) S. J. Smith et al.: Phys. Rev. Lett. **64**, 1227 (1990).
- 3) W. E. Kauppila and T. S. Stein: Adv. At. Mol. Opt. Phys. **26**, 1 (1989).

## Total Cross Sections for Electron and Positron Collisions with CF<sub>3</sub>I Molecules

O. Sueoka,\* A. Hamada,\* M. Kimura, and I. Shimamura

Because of the basic importance of the fundamental understanding of electronic and molecular structures, and scattering processes, for applications in various fields, particularly to plasma processing, a study on the total, elastic and inelastic processes of electron scattering from CF<sub>3</sub>I has attracted much interest in recent years. Due to its short lifetime in the stratosphere, this molecule has potential for application in plasma processing as a next-generation process gas.<sup>1)</sup> Therefore, it is essential to establish all cross-section data for the electron scattering of this molecule by compiling the existing experimental and theoretical results. Furthermore, a comparative study of electron and positron scattering is expected to provide deeper insight to the fundamental aspects of atomic and molecular dynamics in hydrocarbons and the interaction mechanisms. To the best of our knowledge, no complete study of total cross sections (TCSs) based on both electron and positron scattering has yet been carried out. Hence, we have initiated the present joint experimental and theoretical investigations on these processes for CF<sub>3</sub>I to provide comprehensive TCSs for assessing the magnitudes of other weak inelastic channels, as well as dynamical information to derive a guiding principle for applications to other plasma etching gases. The experimental apparatus and the measurement method of TCSs have been reported earlier.<sup>2,3)</sup> In brief, a <sup>22</sup>Na radioisotope of 90  $\mu$ Ci and baked tungsten ribbons were used as the positron source and the positron moderator for low-energy positrons, respectively. For the electron source, slow electron beams were produced after secondary electrons were moderated by multiple scattering in the tungsten ribbons. A retarding potential unit was combined with the TOF system for elimination of elastically and inelastically scattered projectiles. The theoretical approach employed is the continuum multiple-scattering (CMS) method, which is a simple but efficient model for treating electron scattering from polyatomic molecules.<sup>4)</sup> Figure 1 presents

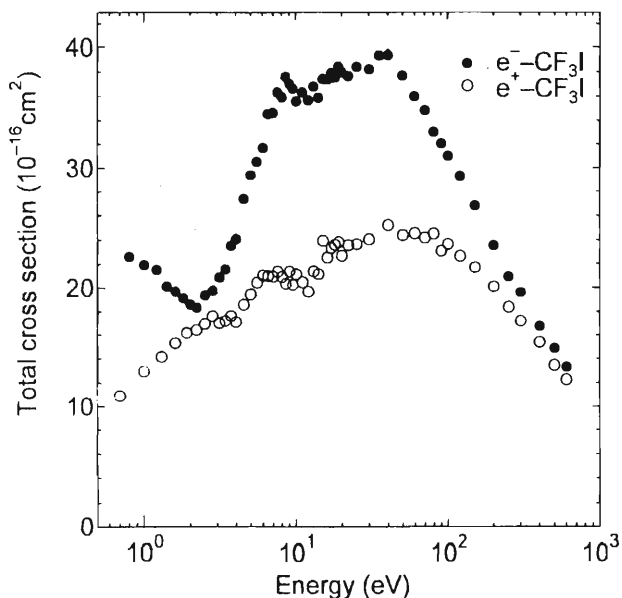


Fig. 1. Total cross sections of the CF<sub>3</sub>I molecule following positron (○) and electron (●) impacts.

the TCSs for both electron and positron impacts with CF<sub>3</sub>I, from 0.7 eV to 600 eV. Novel results can be summarized as follows: (1) The cross section following electron impact has two small, conspicuous peaks at 8 and 40 eV due to shape resonances, while that of positron impact shows clear structures above 6 eV due to positronium formation, followed by direct ionization. (2) Neither cross sections appear to merge, even beyond 500 eV.

### References

- 1) L. G. Christophorou et al.: *J. Phys. Chem. Ref. Data* **25**, 1341 (1996).
- 2) O. Sueoka and S. Mori: *J. Phys. B* **19**, 4035 (1986).
- 3) O. Sueoka et al.: *J. Phys. B* **27**, 1453 (1994).
- 4) M. Kimura and H. Sato: *Comments At. Mol. Phys.* **26**, 333 (1991).

\* Faculty of Engineering, Yamaguchi University

## Simulation of a Diatomic Molecule Colliding with Surfaces

M. Kimura and I. Shimamura

Collisions of an  $O_2$  molecule with a Ni surface are studied using a simulation based on the classical motion of equations. Taking the Morse potentials among all the colliding particles, i.e., atom-atom in the molecule, molecule-surface, and surface atom-surface atom, the simulation is carried out by changing the parameters of the surface temperature, kinetic energy, and rovibrational state of the molecule. It is clearly seen for various cases that: (1) the incoming molecule collides with the surface and bounces back, (2) the molecule collides and is adsorbed on the surface by giving off its kinetic energy and creating surface phonons, (3) the molecule fragments on the surface upon collision, (4) the molecule penetrates inside the solid, and (5) upon collision, the quantum state (rovibrational state) of the incoming molecule changes. Study of the vibrational excitation dynamics on surfaces has been an area of active research in the field of surface

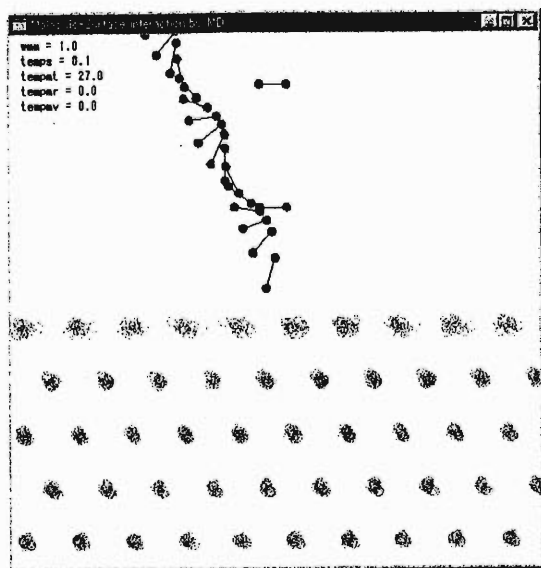


Fig. 1. Simulation of an  $O_2$  molecule colliding with an Ni surface in which the  $O_2$  molecule has a collision energy of 1 eV. The incident  $O_2$  molecule is reflected from the surface and leaves the field.

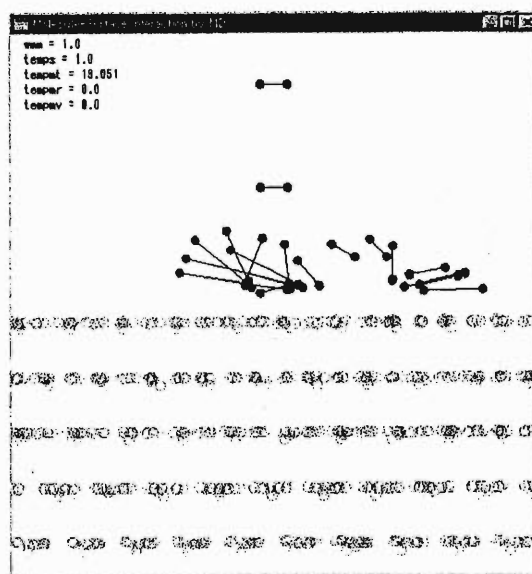


Fig. 2. The same as in Fig. 1, but the incident energy of the  $O_2$  molecule is 0.1 eV. The  $O_2$  molecule is adsorbed on the surface giving off its kinetic energy and creating surface phonons.

sciences as well as in applied fields. Vibrational excitation is governed sensitively by the characteristics of the potential energy surface and by the energy transfer between the electronic and vibrational degrees of freedom. Since the quantum of the internal vibrational excitation of  $O_2$  is approximately threefold the Debye energy of Ni, the scattering of  $O_2$  of the Ni surface is akin to the scattering of a hard ball on a soft wall. This leads to phonon creation at the surface in the scattering event, but not to  $O_2$  stretch vibrations. The experimental results indicate that vibrational heating occurs: The ratio of the excitation intensity for  $v = 1$  to that for  $v = 0$  is approximately a factor of three above the simple Boltzmann factor. We present representative examples of the simulation for this collision system. (Figs. 1 and 2)

## Radiative Electron Capture of Swift Heavy Ions into the Continuum State

T. Azuma, T. Ito, Y. Takabayashi, K. Komaki, T. Kambara,  
Y. Kanai, Y. Nakai, T. Kojima, and Y. Yamazaki

In heavy-ion-solid collisions, target bound electrons have a chance of being captured into the continuum state of projectiles satisfying energy and momentum conservation by emitting photons. This process is called “radiative electron capture into the continuum state (RECC)” as an analogy to radiative electron capture into the discrete bound state (REC), where discrete X-rays are emitted. The RECC process is accompanied by the emission of continuum X-rays with a maximum edge energy corresponding to the energy of electrons of the same velocity as the projectiles. The resultant electrons in the continuum state travel in the forward direction, and a portion of them are expected to emerge as “convoy” electrons with a cusp-shaped energy peak after passing through the solid target. Understanding of the convoy electron formation following the RECC process is very limited, although it is a fundamental process. We investigate it through the coincidence measurement of the spectra of emitted X-rays and cusp electrons.

Bare  $\text{Kr}^{36+}$  ions of 36 and 70 MeV/nucleon passed through a carbon foil tilted by  $45^\circ$  from the beam direction. Emitted X-rays at the collisions were observed either by a HPGe or Si(Li) detector located at an angle of  $90^\circ$  from the beam direction. Secondary electrons were measured using a compact magnetic analyzer coupled with a channeltron-type electron detector. The charge distribution of emerged projectiles was measured using a combination of a magnetic analyzer and position sensitive detectors at the downstream end of the beam. The signals from the charge distribution of the projectiles, X-rays, and secondary electrons were accumulated in a list mode.

The X-rays emitted from REC into the K- and L-shell, the continuum X-rays from RECC, and the characteristic X-rays of the projectiles on the shoulder of the curve for the RECC component were observed as shown in Fig. 1. The characteristic X-rays are emitted following capture of target electrons into the L or higher states of the projectiles. Although the cross sections of all processes decrease with higher projectile energy,  $V_p$ , the intensities of REC and RECC decrease more slowly ( $\propto V_p^{-5}$  and  $\propto V_p^{-2}$ ) than those for non-REC processes ( $\propto V_p^{-11}$ ). Therefore, X-rays emitted from REC and RECC are more clearly observed in the spectra for higher projectile energies. Concerning the secondary electron spectra, we clearly observed a binary encounter electron peak for both projectile energies. A cusp peak at the equivelocity of the projectiles is noticeable only for 36 MeV/nucleon  $\text{Kr}^{36+}$  ions, as

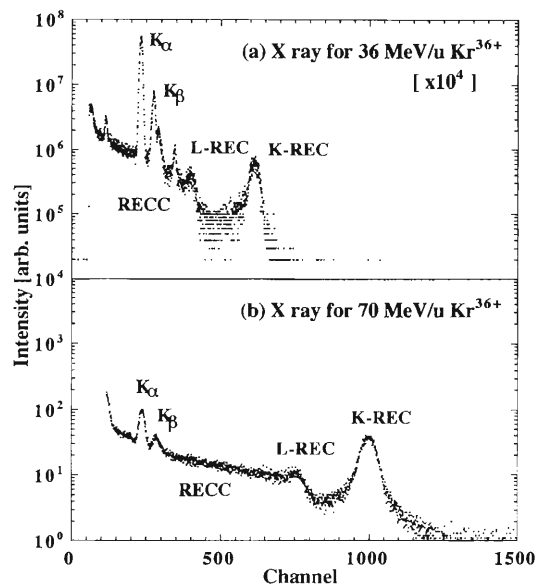


Fig. 1. X-ray energy spectra for  $\text{Kr}^{36+}$  ions of (a) 36 and (b) 70 MeV/nucleon passing through a  $85 \mu\text{g}/\text{cm}^2$  carbon foil. Detector efficiency is not taken into account.

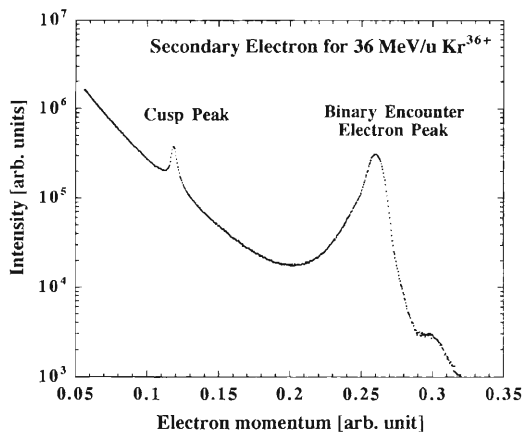


Fig. 2. A secondary electron energy spectrum for  $\text{Kr}^{36+}$  ions of 36 MeV/nucleon passing through a  $85 \mu\text{g}/\text{cm}^2$  carbon foil.

shown in Fig. 2, due to the larger capture cross section.

Considering the projectile energy dependence for X-rays and cusp electrons, the coincidence experiments are suitable at the projectile energy of 36 MeV/nucleon. We are now preparing to carry out coincidence measurements by applying a large acceptance angle Si(Li) detector to obtain a higher coincidence rate.

Fullerene-like Fragment Ion Production in Fast Ion-C<sub>60</sub> Collision

Y. Nakai, T. Kambara, A. Itoh, H. Tsuchida, and Y. Yamazaki

A number of studies of C<sub>60</sub> fragmentation have been performed with various excitation probes.<sup>1-7)</sup> The distribution of product ions strongly depends on the energy deposit, that is the internal energy of the precursor of fragmentation. We reported that high-energy deposition by fast heavy ion impact causes only multifragmentation.<sup>1)</sup> On the other hand, in low-energy deposition by electrons, atoms and collisions with the surface, C<sub>60</sub> emits small neutral clusters in a few microsecond or longer time scale after excitation.<sup>2-5)</sup> In the latter case, the activation energy and the kinetic energy release associated with C<sub>2</sub> evaporation were estimated.

The time-of-flight (TOF) peak profile for each product ion contains information of fragmentation, that is, the kinetic energy release and lifetime. However, a part of such information is often lost due to poor experimental resolution. We have developed a high-resolution TOF mass spectrometer under the Wiley-McLaren spatial-focusing condition to obtain information on the fragmentation mechanism. A beam of 10 MeV He<sup>2+</sup> and 25 MeV C<sup>6+</sup>, provided by the RILAC, passed through a C<sub>60</sub> vapor target. The electrons extracted from the collision region were used as the start signal of the TOF measurement. The TOF spectra were obtained using a multi-hit time-to-digital converter. We can separate the peaks of C<sub>60</sub><sup>q+</sup> ( $q = 1, 2, 3$ ) which contain different amounts of <sup>13</sup>C as shown in Fig. 1.

In Fig. 1, TOF peaks of C<sub>58</sub><sup>q+</sup> ( $q = 1, 2, 3$ ) generated in the collision with the He<sup>2+</sup> beam are shown. These peaks are asymmetric. We also show the TOF spectra obtained by Monte Carlo simulation for C<sub>60</sub><sup>q+</sup> → C<sub>58</sub><sup>q+</sup> + C<sub>2</sub> ( $q = 1, 2, 3$ ) with a lifetime of fragmentation and a 0.4 eV kinetic energy release.<sup>7)</sup> These tails at longer TOF are reproduced by simulation with a fragment lifetime of 2.0 μsec, 1.75 μsec, and 1.1 μsec, respectively. This indicates that the internal energy of delayed-fragment precursors increases with increase of the charge state because the activation energies of the emission of C<sub>2</sub> from C<sub>60</sub><sup>q+</sup> ( $q = 1, 2, 3$ ) do not depend on the charge state within the experimental uncertainty.<sup>4)</sup> However, the peak shape in the shorter TOF region can not be reproduced by simulations with a single lifetime component.

The peak intensities for doubly and triply ionized fragment ions decrease more rapidly towards a smaller fragment ion in the collision with He<sup>2+</sup> than C<sup>6+</sup> whereas the intensity ratios for singly ionized fullerene-

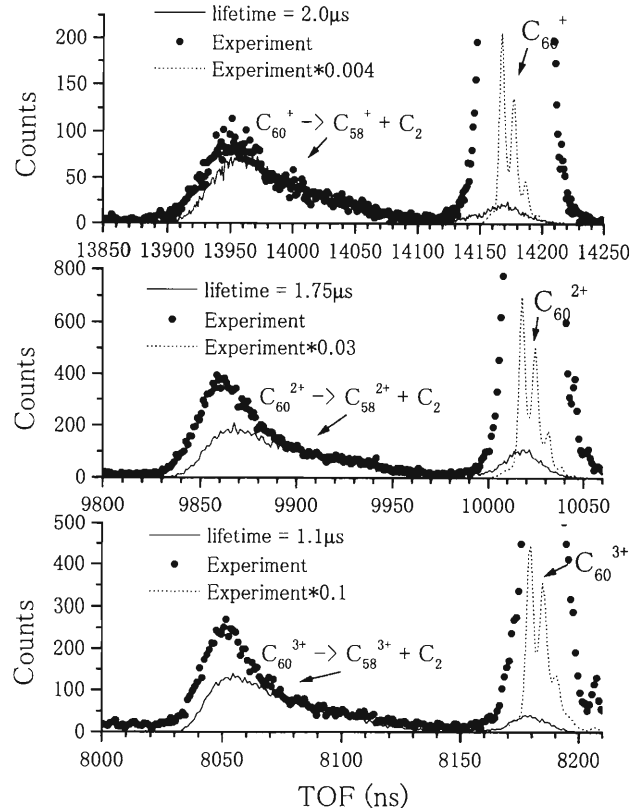


Fig. 1. TOF peaks for C<sub>58</sub><sup>1+,2+,3+</sup> generated in the collision with He<sup>2+</sup> are shown. The solid circles represents experimental data. The solid lines represents the result of Monte Carlo simulation. The dotted lines represents experimental data showing TOF resolution.

like fragment ions are almost constant. The asymmetric peak shape of fullerene-like fragment ions are observed in both cases. These results indicate that the internal energy distributions of the parent C<sub>60</sub> ion of multiply ionized fullerene-like fragments are different between He<sup>2+</sup> impact and C<sup>6+</sup> impact, but that their production mechanisms are similar.

## References

- 1) Y. Nakai et al.: J. Phys. B: At. Mol. Opt. Phys. **30**, 3049 (1997).
- 2) M. Foltin et al.: J. Chem. Phys. **107**, 6246 (1997).
- 3) P. Weis et al.: J. Chem. Phys. **104**, 6246 (1996).
- 4) R. Woergoetter et al.: J. Chem. Phys. **101**, 8674 (1994).
- 5) M. Foltin et al.: J. Chem. Phys. **98**, 9624 (1993).
- 6) R. K. Yoo et al.: J. Chem. Phys. **96**, 911 (1992).
- 7) J. Laskin et al.: Chem. Phys. Lett. **242**, 249 (1995).

# Isotope Shifts between He-like $^{12}\text{C}$ and $^{13}\text{C}$ Ions

S. Ozawa, T. Ariga, N. Inabe, M. Kase, I. Tanihata, M. Wakasugi, and Y. Yano

With the ultralow-background photon detection system which we previously designed,<sup>1,2)</sup> we measured the isotope shifts between He-like  $^{12}\text{C}$  and  $^{13}\text{C}$  ions in the  $1s2s\ ^3S_1$ - $1s2p\ ^3P_{0,1,2}$  transitions.

A NEOMAFIOS 8 GHz ECR ion source which was placed in the RILAC terminal produced positive carbon ions.  $^{12}\text{C}$  ions were accelerated to 0.9 MeV/nucleon by RILAC and stripped by a carbon foil with a thickness of  $10\ \mu\text{g}/\text{cm}^2$ .  $^{13}\text{C}$  ions were accelerated to 0.6 MeV/nucleon before being stripped by the carbon foil. Then 4+ charge state ions were directed to the experimental area. One percent of all

Table 1. Transition energies from  $^3S_1$  to each level of  $^{12}\text{C}$  and  $^{13}\text{C}$ . Values in parentheses indicate  $1\sigma$ .

Isotope	Transition J	Energy ( $\text{cm}^{-1}$ )	Reference <sup>3)</sup> ( $\text{cm}^{-1}$ )
$^{12}\text{C}^{4+}$	0	43899.749(30)	43899
	1	43887.173(19)	43886
	2	44023.404(13)	44022
$^{13}\text{C}^{4+}$	0	43901.556(41)	
	1	43889.133(26)	
	2	44025.207(18)	
Isotope shift $^{12}\text{C}$ - $^{13}\text{C}$	0	-1.807(51)	
	1	-1.960(32)	
	2	-1.803(22)	

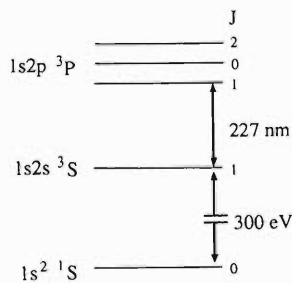


Fig. 1. Level scheme of He-like carbon ions.

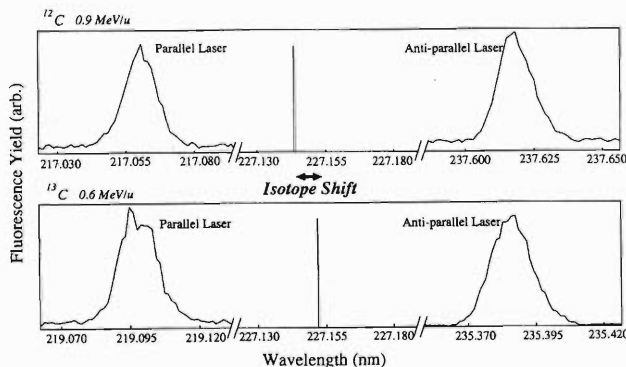


Fig. 2. Fluorescence spectra of the transition from  $^3S_1$  to  $^3P_2$ . These four resonance spectra were measured separately.

He-like ions are in the  $^3S_1$  metastable state and have a 200 ms lifetime. The level scheme of He-like carbon ions is shown in Fig. 1. A laser beam excites ions in the  $^3S_1$  state and induces fluorescence from the  $^3P_{0,1,2}$  states. To reduce the uncertainty in the absolute ion beam velocity, each transition energy was measured by two laser beams which propagate in the directions parallel and anti-parallel to the ion beam. For the wavelength calibration of the laser beam, the absorption lines in  $\text{Te}_2$  were measured simultaneously.

According to the Doppler-shift formula, the absolute energies  $E_0$  for each transition are determined as  $E_0 = \sqrt{E_p E_{ap}}$ , where  $E_p$  and  $E_{ap}$  are the resonance energies for the parallel and anti-parallel laser beams, respectively. The relationships between the resonance wavelength by the parallel and anti-parallel laser beams are shown in Fig. 2. Figure 2 also illustrates the isotope shift. The measured absolute energies and the isotope shifts in each transition are shown in Table 1.

## References

- 1) M. Wakasugi et al.: Phys. Scr. T **73**, 70 (1997).
- 2) M. Wakasugi et al.: Nucl. Instrum. Methods Phys. Res. A **419**, 50 (1998).
- 3) C. E. Moor: Atomic Energy Levels, NBS, Washington D.C., p. 30 (1949).

## Foil Ageing Problems in Beam-Foil Spectroscopy Continued

R. Hutton, Y. Zou, S. Huldt, I. Martinson, K. Ando, and H. Oyama

In a previous article<sup>1)</sup> we discussed an effect which seems to have overlooked detailed study but, however, which is very important to the methods of beam-foil spectroscopy. The effect is the change in light intensity in a given spectral line as a function of the exposure time of the foil. This effect had been discussed previously by Soerensen.<sup>2)</sup> It has been long known that the charge state fraction after the foil interaction changes as function of time, due to foil thickening for example. However we observe that the light intensity in certain spectral lines changes at a rate much faster than the change in the charge state balance, see Fig. 1. This has been found to depend on the particular ion and energy being stripped/excited by the foil. In the previous report we discussed a limited amount of data, i.e. 0.4 MeV/u Ne and 0.4 and 2.5 MeV/u Mg. In this report we will discuss new data showing the foil ageing effect to be more difficult to deal with than previously thought. The number of elements for which data is available has been increased to cover Ne, Mg, Al, Fe, Kr and Nb. In Fig. 1 the effects of foil ageing on lines from 0.8 and 2.5 MeV/u Al are illustrated. The Li-like resonance lines, ( $2s^2S_{1/2}-2p^2P_{1/2,3/2}$ ), decrease in intensity at both beam energies, however the decrease is slower for the lower energy beam. This is opposite to what one may expect, for example the foil will break quicker at the lower beam energy. Also shown in Fig. 1 is the line resulting from 5–6 transitions in the He-like ion. This is only seen for the 2.5 MeV/u beam as there is a very small fraction of He-like ions at the lower energies. Here a slight increase in line intensity is observed. Similar, but on a much weaker scale, was seen for 2.5 MeV/u Mg. For the heavier beams studies so far, (Fe, Kr and Nb), there has been little or no noticeable effect of the foil age on the light intensity. The effect of light intensity changing as a function of foil exposure time has been confirmed by data obtained at the university of Lund using much lower energy beams and thinner foils.<sup>3)</sup> Thus with the existing amount of data it is not possible to know in what experiments foil ageing will be a problem, much more data is needed.

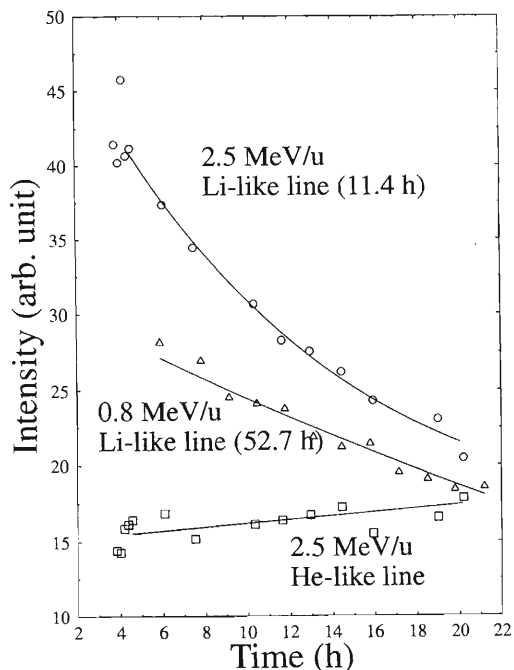


Fig. 1. This figure shows that although the Li-like  $2s-2p$  resonance line intensity decays as a function of the foil exposure time the intensity of the  $5g-6h$  He-like transition increases (at least at 2.5 MeV/u). Also seen is that the  $2s-2p$  intensity decays slower for the lower energy beam, maybe in contradiction to what one may imagine as foils usually last longer for higher beam energies. The “h” refers to hours of foil expose to the beam and comes from a single exponential fit to the data, this fit is done only for purposes of comparing numbers and has no physical significance as far as we know. The light intensity has been normalised to charge collected in a given time.

### References

- 1) R. Hutton et al.: RIKEN Accel. Prog. Rep. **32**, 95 (1999).
- 2) G. Soerensen: 1975 Beam Foil Conf., Tenn., USA, Plenum Press, p. 165 (1976).
- 3) I. Kink: private communication.

## Time Delayed Spectral Lines in Beam-Foil Spectroscopy

R. Hutton, Y. Zou, S. Huldt, I. Martinson, K. Ando, and H. Oyama

It has long been known that spectral lines can be observed at large distances behind the exciter foil used in beam-foil spectroscopy. This has been observed most drastically for Li- and Na-like ions. However, the limit as to how far spectral lines could be followed has been set by the noise of the detector. This is still true in the spectra to be discussed here, except we are now using a low noise CCD detector system and have been able to follow spectral lines over a time scale of 100 lifetimes, or more, of the radiating level. Of course the fact that radiation can still be observed is due to cascade re-population of the upper levels. This illustrates the already known fact that very high  $n$ ,  $l$  states are populated by the beam-foil interaction mechanism. In Fig. 1 we compare data taken for a beam of 2 MeV/u Nb after ionisation/excitation by a thin carbon foil. The spectra are recorded with 0 and 200 mm separations between the spectrometer entrance slit and the foil position. These separations correspond to time delays of 0 and 10 ns respectively. We should point out here that the lifetime of the  $3p\ ^2P_{3/2}$  level for Na-like Nb is only 0.029 ns.<sup>1)</sup> For the  $^2P_{3/2}$  level 10 ns represents a time delay of 340 lifetimes, however, it is clear that it is still possible to observe this line, at 135.14 Å, of course this is because of cascade re-population of the upper level from the high  $n$ ,  $l$  states. Also seen is the  $3p\ ^2P_{3/2}-3d\ ^2D_{5/2}$  line at 131.7 Å. However, the interesting thing now is that lots more lines are seen in the delayed spectra and not all of these can be assigned to allowed transitions. It may now be possible to identify slow decaying lines like E2 and M1 transitions in beam-foil spectra due to the low noise offered by the CCD detector. Moreover the well known allowed transitions can be used to calibrate the spectrometer.

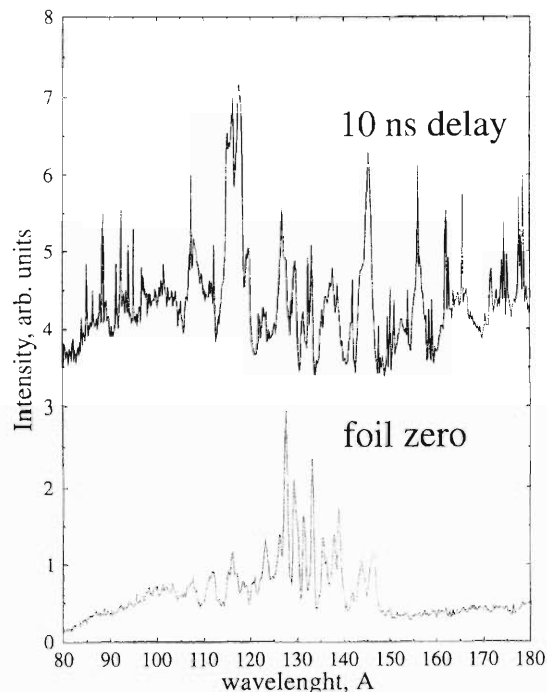


Fig. 1. Beam-foil spectra for 2 MeV/u Nb ions take with two different time delays, 0 (foil zero) and 10 ns. It is seen that lines beyond around 150 Å are much more prominent in the delayed spectra. The 10 ns delayed spectrum was recorded with a much longer time integration (4 hours) than the foil zero spectrum (1 minute), and the data intensity normalized for display purposes, hence different intensity scales.

### References

- 1) R. Hutton et al.: Phys. Rev. A **51**, 143 (1995).

## Spectroscopy of High Z Spin-Aligned States

R. Hutton, Y. Zou, S. Huldt, I. Martinson, K. Ando, and H. Oyama

The structure of spin-aligned states is best known for fairly low Z Li-like ions where the  $1s2s2p\ ^4P_{5/2}$  level is metastable against X ray decay and Coulomb auto-ionisation. However, there is a Breit induced part to the autoionisation which is quite strong even for moderately charged ions in the Li I sequence.<sup>1)</sup> There is a similar situation in Na-like ions where the  $2p^53s3p\ ^4D_{7/2}$  level is also metastable. In this case the Breit induced autoionisation is not so dominate as in the Li-like case and the  $2p^53s3p\ ^4D_{7/2}$  level remains long lived even for very highly charged ions,<sup>2)</sup> e.g. the  $^4D_{7/2}$  lifetime for Na-like Xe is predicted to be 2.32 ns.<sup>2)</sup> The metastability of this level was demonstrated using electron spectroscopy<sup>3)</sup> however as yet no lifetime measurement exists. In a recent work the  $2p^53s3d\ ^4F_{9/2}$ <sup>4)</sup> level was studied for a number of elements in the Na I sequence using VUV photon spectroscopy. This level is also metastable with regards to X-ray and auger decay but it has an allowed E1 transition to the metastable  $2p^53s3p\ ^4D_{7/2}$  level. After the identification of the  $2p^53s3p\ ^4D_{7/2}$ - $2p^53s3d\ ^4F_{9/2}$  transition a

number of other VUV transitions within the core-excited complex were identified for Na-like S and Cl.<sup>5)</sup> In this work a few transitions within the core-excited configurations of Mg-like ions will be examined for a number of elements in the Mg I sequence. The ions investigated here are S V, Cl VI, Ar VII, Ti XI, Mn XIV, Fe XV, Co XVI, Ni XVII and Cu XVIII. The data for Ti, Fe and Ni have been recorded at RIKEN using the RILAC accelerator. The other data come from various other beam-foil laboratories (Lund, Bochum and Argonne National Lab.) and a fuller report is being prepared for publication.<sup>6)</sup> The transitions of interest are between the  $2p^53s3p^2$  and  $2p^53s3p3d$  configurations, where again the maximum j level is the one giving rise to a VUV decay channel.

### References

- 1) M. H. Chen et al.: Phys. Rev. A **26**, 1441 (1982).
- 2) M. H. Chen: Phys. Rev. A **40**, 2365 (1989).
- 3) D. Schneider et al.: Phys. Rev. A **40**, 4313 (1989).
- 4) C. Jupen et al.: J. Phys. B **21**, L347 (1988).
- 5) C. Jupen et al.: Phys. Scr. **42**, 44 (1990).
- 6) R. Hutton et al.: Manuscript in preparation.

# High-resolution Soft X-ray Study of Ne Hollow Atoms Created by a Microcapillary Target

S. Thuriez, Y. Iwai, Y. Kanai, H. Oyama, R. Hutton, H. Masuda,\* and Y. Yamazaki

This work presents the first high-resolution soft X-ray study of the interaction of highly charged ions with microcapillary targets. A micro-capillary target consists of many 100-nm-diameter and 700-nm-long capillaries. For this experiment we used a beam of 5 keV/q  $\text{Ne}^{9+}$  ions from a 14.5 GHz ECR ion source (Caprice). Figure 1 shows the spectrum obtained after 0.2 ns from the capillary target as compared with a typical spectrum obtained when  $\text{Ne}^{9+}$  ions impinge on a flat surface. When we changed the target from a flat surface to a bundle of capillaries, a drastic change in the X-ray spectra and thus in the electronic population of the excited state is observed. Such a shift toward high energies for the microcapillary target is consistent with an interaction above the surface.<sup>1)</sup>

Figure 1 shows three peaks which are observed in the energy range of our spectrometer, after the beam has interacted with the microcapillary target. The maximum of the main peak between channels 48 and 49 has an energy of  $913.3 \pm 1.3$  eV. It may correspond to the pure helium-like  $1^1\text{S}_0$ - $3^1\text{P}_1$  transition at 914.9 eV, which may be shifted in energy by the effect of spectator electrons.

The peak maximum at channel 46 (Fig. 1) of energy

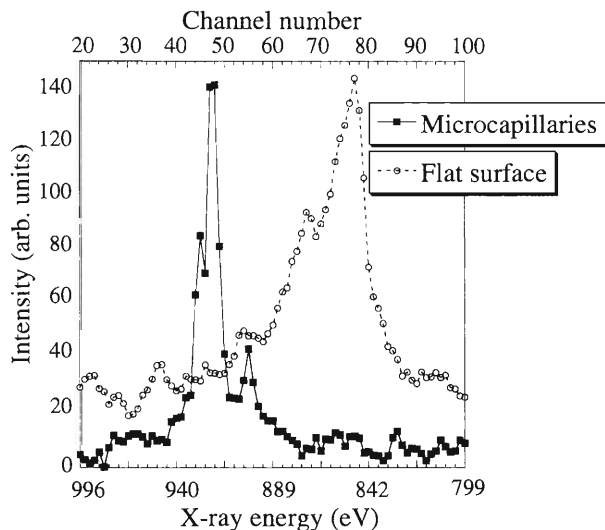


Fig. 1. Typical spectra emitted from microcapillary and flat surface targets.

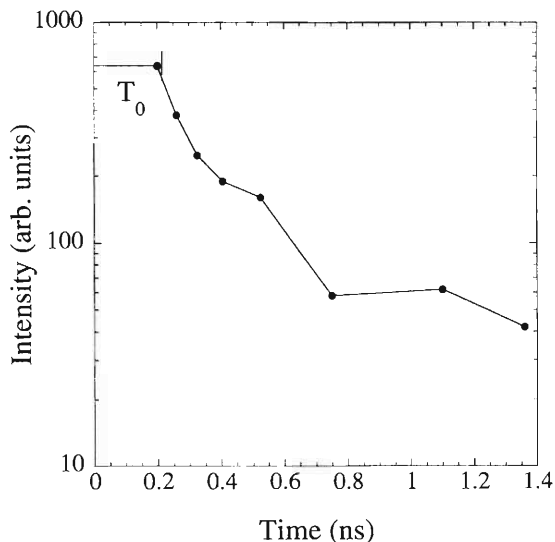


Fig. 2. Total photon emission after the passage of  $\text{Ne}^{9+}$  ions through the microcapillary as a function of the time after passing through the target.

$919 \pm 1.3$  eV may correspond to the He-like  $1^1\text{S}_0$ - $1^1\text{P}_1$  (922.1 eV), again possibly shifted by the effect of spectator electrons.

The peak maximum at channel 56 corresponds to an energy of  $894.4 \pm 1.3$  eV. For  $\text{Ne}^{7+}$ ,  $1s^22s^2$   $4^1\text{P}$  states have a long lifetime: 0.4 ns for  $4^1\text{P}_{1/2}$ , 0.6 ns for  $4^1\text{P}_{3/2}$  and 12 ns for  $4^1\text{P}_{5/2}$ . The dominant decay channels are  $4^1\text{P}_{1/2} \rightarrow 1s^22s^2$   $2^1\text{S}_{1/2}$  and  $4^1\text{P}_{3/2} \rightarrow 1s^22s^2$   $2^1\text{S}_{1/2}$  with the emission of a 895.0 eV photon.<sup>2)</sup> The line that we measured may originate from this decaying scheme. It is also consistent with the fact that the observation point is within 0.2 ns of the target end.

We have also measured the total photon emission as a function of the distance from the target (Fig. 2). The time resolution,  $T_0$  (Fig. 2) of the spectrometer is  $0.2 \pm 0.01$  ns. We observe different lifetime components, one of which is very long (longer than about 1.4 ns). This is consistent with previous measurements performed at low resolution.<sup>2)</sup>

## References

- 1) J. P. Briand et al.: Phys. Rev. A **53**, R2925 (1996).
- 2) Y. Yamazaki et al.: J. Phys. Soc. Jpn. **65**, 1199 (1996).

\* School of Engineering, Tokyo Metropolitan University

## Angular Dependence of Scattering Intensity in $C^{4+} + He \rightarrow C^{2+} + He^{2+}$ at Collisional Energy of 120 eV/ $q$

M. Hoshino, M. Kitajima, Y. Nakai, Y. Kanai, and Y. Yamazaki

Very slow collisions in ion-atom and ion-molecule systems are interesting because the angular differential cross sections are more sensitive to the shapes of active potential curves at lower collision energies. Since it is difficult to produce a very slow and well-collimated highly charged ion beam below about 200 eV/ $q$ , where  $q$  is the charge state of the projectile ion, experimental studies in this energy range have been fairly limited. Recently, we have developed a crossed-beam experimental setup for angle resolved energy gain spectroscopy in very slow collisions between highly charged ions and atoms or molecules. We utilize the ion beam from the 14.5 GHz Caprice electron cyclotron resonance (ECR) ion source at RIKEN.<sup>1)</sup>

Figure 1 shows the angle-dependent scattering intensity for double electron capture for 120 eV/ $q$   $C^{4+}(1s^2) + He \rightarrow C^{2+}(1s^2 2s^2) + He^{2+}$ . Only small contributions from other final states of  $C^{2+} + He^{2+}$  have been observed in the energy gain spectrum. Energy and angular resolutions are estimated to be 0.75 eV/ $q$  and 0.5°, respectively. It is estimated that the statistical uncertainty for each scattering intensity is less than 10%. Weak Stueckelberg angular oscillations, which result from interference between several outgoing waves with different scattering paths, are seen in the experimental data.

Charge exchange processes in  $C^{4+} + He$  collisions have been widely studied above 200 eV/ $q$ . All of the experimental and theoretical studies have shown that the most dominant process above 200 eV/ $q$  is the  $C^{4+}(1s^2) + He \rightarrow C^{2+}(1s^2 2s^2) + He^{2+}$  process, which was explained by a two-state curve crossing model. Barany et al. have measured differential cross sections for  $C^{4+}(1s^2) + He \rightarrow C^{2+}(1s^2 2s^2) + He^{2+}$  at a collision energy of 380 eV/ $q$ ,<sup>2)</sup> which enabled Boyd et al. to determine the diabatic coupling potential for the double electron capture process in this system.<sup>3)</sup> We have applied this two-state diabatic coupling potential for our experimental condition and calculated the differential cross section. The results are shown in Fig. 1 by curves. It is found that the results of calculations derived from the potential estimated at 380 eV/ $q$  do not reproduce the present experimental results at 120 eV/ $q$ . This

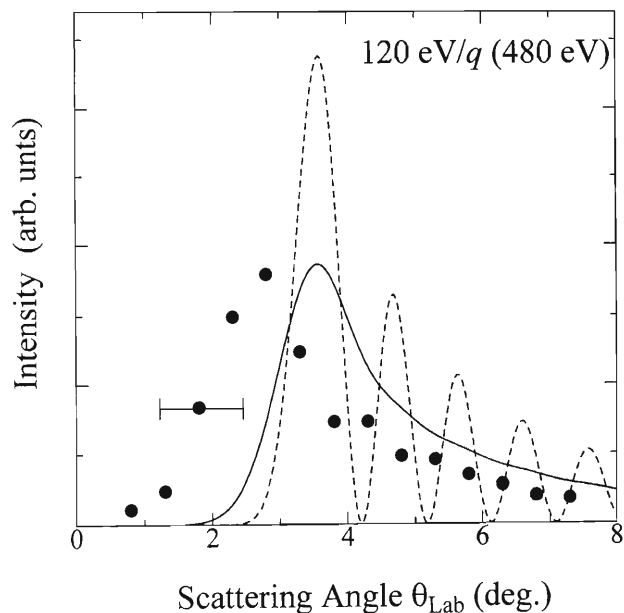


Fig. 1. The angular dependence of the scattering intensity for the  $C^{4+}(1s^2) + He \rightarrow C^{2+}(1s^2 2s^2) + He^{2+}$  collision obtained at a collision energy of 120 eV/ $q$  ( $\bullet$ ). Calculated cross sections using the diabatic coupling potential for the  $C^{4+} + He$  system (---) and those convoluted with the angular resolution of  $\pm 0.5^\circ$  (—) are shown together.

shows that potential curves derived from experimental data at higher energies are not accurate enough. It should be noted that not enough is known about interaction potentials between highly charged ions and atoms even in the case of extensively studied systems, such as the  $C^{4+} + He$  system. Experimental studies over a wide collisional energy region, especially at very low energies, are expected to reveal further information on collisions between highly charged ions and atoms or molecules.

### References

- 1) M. Kitajima, Y. Nakai, Y. Kanai, Y. Yamazaki, and Y. Itoh: Phys. Scr. T **80**, 377 (1999).
- 2) A. Barany et al.: J. Phys. B **19**, L427 (1986).
- 3) R. Boyd et al.: J. Chem. Phys. **106**, 6548 (1997).

# Acoustic Emission Following Fast Heavy-Ion Irradiation of Solids

T. Kambara, Y. Kanai, T. M. Kojima, Y. Nakai, Y. Yamazaki, and K. Kageyama

We observed, for the first time, acoustic emission up to about 2 MHz from solid materials (metal, oxide and alkali-halide) after short pulses of high-energy heavy ions. The objective of this work was to study in real time the transient deformation caused by fast heavy ions, which deposit kinetic energy in the material by electronic stopping. A Xe-ion beam was accelerated by the RILAC and the RIKEN Ring Cyclotron up to 26 MeV/u and was guided to an experimental beam line. The beam was chopped after being extracted from the 18-GHz Electron Cyclotron Resonance (ECR) ion source to short pulses whose width was shorter than 1  $\mu$ s. Since the elastic vibrations in our samples lasted as long as a few milliseconds, the interval between the beam pulses was chosen to be longer than 10 ms. The shortest pulse which we obtained consisted nearly of a single bunch with a length of about 3 ns. The number of ions in each pulse was  $10^4$ – $10^5$  depending on the pulse width. Details about the short-pulse generation are described elsewhere.<sup>1)</sup>

The beam was then guided to a vacuum chamber where the irradiated sample was mounted. The beam spot size on the sample was about 4 mm  $\times$  4 mm. The sample materials were single crystals of Al<sub>2</sub>O<sub>3</sub>, KCl, and metallic polycrystalline Al with a common dimension; 40 mm long, 10 mm wide and 5 mm thick. According to calculations with the TRIM code,<sup>2)</sup> the range of the ions in the samples is between 170  $\mu$ m and 380  $\mu$ m, which is much smaller than the sample size. Therefore all of the ions were stopped in the material near the incidence surface.

The ultrasonic signals were detected by two piezoelectric ultrasonic sensors equipped with head amplifiers (Fuji Ceramics, M304A). The sensor<sup>3)</sup> is highly sensitive to longitudinal waves up to about 2 MHz and exhibits the highest sensitivity at about 300 kHz. The ion beam was incident perpendicularly to the 40 mm  $\times$  10 mm face of the sample, and two sensors at both ends of the sample detected the acoustic signals propagating perpendicularly to the beam direction. A digital oscilloscope recorded the waveform of the acoustic signals for each pulse of the incident beam.

Figure 1 shows the acoustic signals from a single crystal of Al<sub>2</sub>O<sub>3</sub>. The acoustic signals have oscillatory structures whose frequencies distribute up to about 1.3 MHz. The frequency distribution is affected by the resonant vibration frequencies of the sample and the characteristics of the sensors. The acoustic signals of the Al<sub>2</sub>O<sub>3</sub> have an amplitude lower than that of metallic Al, while those of KCl have the highest amplitude. The signal-propagation velocity in the sample was estimated from the arrival-time difference between

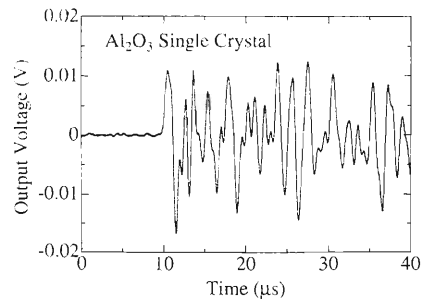


Fig. 1. Acoustic waveform of a single-crystal Al<sub>2</sub>O<sub>3</sub> sample irradiated by a nearly single-bunch pulse of the ion beam. The displayed waveform is an average over 100 pulses.

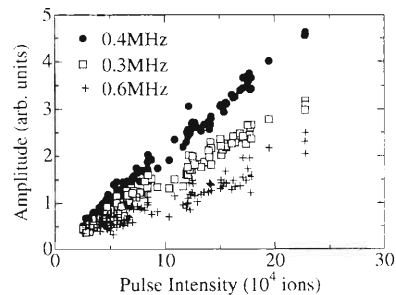


Fig. 2. Amplitudes of the Fourier components of the acoustic signals observed for an Al<sub>2</sub>O<sub>3</sub> single crystal plotted as a function of the intensity of the ion pulse.

the two sensors as a function of the irradiation position. The result for Al<sub>2</sub>O<sub>3</sub> single crystal was about  $10^4$  m/s which was in good agreement with the speed of the longitudinal wave estimated from the modulus of elasticity.

We have studied the frequency spectra of the acoustic signals from the Al<sub>2</sub>O<sub>3</sub> sample as a function of the ion-pulse intensity. The amplitude spectrum has peaks around 0.3, 0.4 and 0.6 MHz. The amplitude of the Fourier component is plotted in Fig. 2 as a function of the ion-pulse intensity. The amplitudes of the Fourier components are found to be nearly proportional to the ion-pulse intensity, indicating a linear increase with the total energy deposited in the material.

## References

- 1) A. Yoneda and T. Kambara: RIKEN Accel. Prog. Rep. **33**, 203 (2000).
- 2) J. F. Ziegler, J. P. Biersack, and U. Littmark: *The Stopping and Range of Ions in Solids*, (Pergamon Press, New York, 1985).
- 3) M. Shiwa, H. Inaba, and T. Kishi: J. JSNDI **39**, 374 (1990).

# Defect Production via Electronic Excitation in Oxide Superconductors Irradiated with High Energy Heavy Ions

N. Ishikawa, Y. Chimi, A. Iwase, N. Kuroda, O. Michikami,\* H. Wakana,\* and T. Kambara

When oxide superconductors are irradiated with high-energy heavy ions, and the energy transferred to the electrons of the target is high enough, columnar defects are created along the ion paths. The creation of such defects results in an increase in electrical resistivity, and this increase strongly depends on the size of the columnar defects and the inside resistivity (resistivity inside the columnar defects).<sup>1)</sup> In order to investigate the defect production mechanism, the resistivity has been measured for ion-irradiated oxide superconductors. Oxide superconductor  $\text{EuBa}_2\text{Cu}_3\text{O}_y$  (EBCO) thin films were prepared by the rf magnetron sputtering method and were irradiated with various ions in the energy range from 125 MeV to 3.8 GeV. The irradiating ions were 125 MeV  $^{79}\text{Br}^{10+}$  produced from a tandem accelerator at JAERI-Tokai (Japan Atomic Energy Research Institute, Tokai Establishment), and 0.7 GeV  $^{84}\text{Kr}^{11+}$ , 3.5 GeV  $^{136}\text{Xe}^{31+}$ , and 3.8 GeV  $^{181}\text{Ta}^{37+}$  from the RIKEN Ring Cyclotron. All irradiations were performed at a fixed temperature of 100 K. The values of  $\Delta\rho/\rho_0$  were measured *in situ* as a function of ion fluence,  $\Phi$ , at 100 K by the standard four-probe method, where  $\Delta\rho$  is the change in resistivity and  $\rho_0$  the resistivity before irradiation. Generally the electronic stopping power,  $S_e$ , which is defined as the energy transferred from the irradiating ion to the target electrons per unit path length, is accepted as one of the characterization parameters of the defect production process. However, in the previous study, ion-velocity dependence in defect production has been observed even for the same  $S_e$  value.<sup>2,3)</sup> In this report, we propose an alternative parameter for describing defect production; the primary ionization rate is represented by  $dJ/dx$ , where  $J$  is the number of target atoms primarily ionized by the irradiating ion and  $x$  is the path length of the irradiating ion.<sup>4,5)</sup> Figure 1 shows the change in resistivity as a function of ion fluence in EBCO irradiated with ions with the same  $dJ/dx$  value. Irradiation with the same  $dJ/dx$  value results in almost the same resistivity-fluence curve. Therefore, the primary ionization rate,  $dJ/dx$ , is a much better parameter than the electronic stopping power,

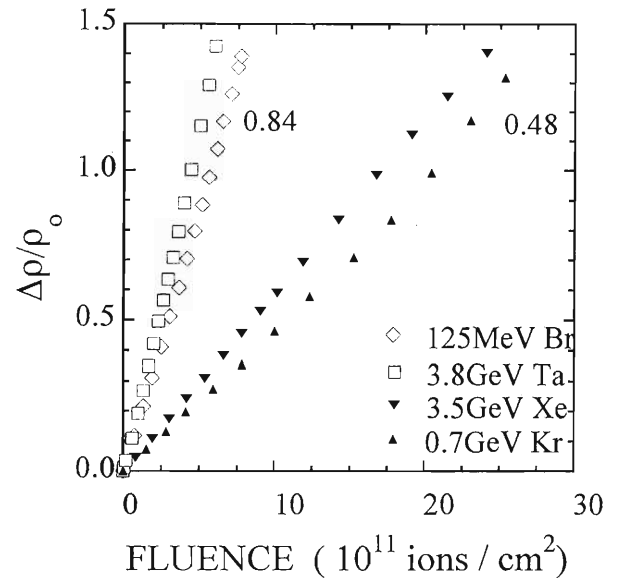


Fig. 1. The value of  $\Delta\rho/\rho_0$  plotted as a function of fluence for irradiations with 125 MeV Br and 3.8 GeV Ta. These two irradiations have the same  $dJ/dx$  value,  $0.84 \pm 0.01$  (arbitrary units). The data for irradiations with 3.5 GeV Xe and 0.7 GeV Kr are also plotted. These two irradiations have the same  $dJ/dx$  value, 0.48 (arbitrary units).

$S_e$ , for describing the defect production process. This result is consistent with the results of a previous study of lattice parameter change in ion-irradiated EBCO.<sup>6)</sup> These results suggest that the atomic displacements are triggered by Coulomb repulsion between primarily ionized atoms.

## References

- 1) N. Ishikawa et al.: Mat. Res. Soc. Symp. Proc. **504**, 171 (1998).
- 2) N. Ishikawa et al.: RIKEN Accel. Prog. Rep. **32**, 99 (1999).
- 3) N. Ishikawa et al.: Phys. Scr. T **80**, 559 (1999).
- 4) H. A. Bethe: Ann. Phys. **5**, 325 (1930).
- 5) R. L. Fleischer et al.: Phys. Rev. **156**, 353 (1967).
- 6) N. Ishikawa et al.: Nucl. Instrum. Methods Phys. Res. B **135**, 184 (1998).

\* Faculty of Engineering, Iwate University

## Effects of Defect Morphology on the Vortex Dynamics in $\text{Bi}_2\text{Sr}_2\text{CaCu}_2\text{O}_{8+\delta}$ Irradiated with GeV Heavy Ions

N. Kuroda, N. Ishikawa, S. Okayasu, A. Iwase, H. Ikeda, R. Yoshizaki,\* and T. Kambara

Previous experiments on swift heavy-ion irradiation of high- $T_c$  superconductors show that the morphology of defects depends strongly on electronic stopping power  $S_e$ .<sup>1)</sup> When  $S_e$  is less than about 2 keV/Å, elliptical defects are formed at intervals along an ion path, whereas, when  $S_e$  greater than about 2 keV/Å, a continuous columnar defect (CD) is formed. We have studied the effects of defect morphology on the vortex dynamics in a  $\text{Bi}_2\text{Sr}_2\text{CaCu}_2\text{O}_{8+\delta}$  (Bi-2212) high- $T_c$  superconductor.

Bi-2212 single crystals ( $T_c \approx 90$  K) were irradiated with the heavy ions 0.7 GeV  $^{84}\text{Kr}$ , 3.5 GeV  $^{136}\text{Xe}$ , 3.8 GeV  $^{181}\text{Ta}$ , and 3.1 GeV  $^{209}\text{Bi}$ , at the RIKEN Ring Cyclotron. In order to characterize the morphology of irradiation-induced defects, transmission electron microscopy (TEM) observations were carried out parallel to the ion path which was also parallel to the  $c$ -axis of the samples. The TEM micrographs were taken at the Foundation for Promotion of Material Science and Technology of Japan (MST). Figure 1 shows the statistical distribution of the radii of defects in the  $ab$ -plane for 0.7 GeV  $^{84}\text{Kr}$  ( $S_e \approx 1.4$  keV/Å), 3.5 GeV  $^{136}\text{Xe}$  ( $S_e \approx 1.7$  keV/Å), 3.8 GeV  $^{181}\text{Ta}$  ( $S_e \approx 3.1$  keV/Å), and 3.1 GeV  $^{209}\text{Bi}$  ( $S_e \approx 4.1$  keV/Å). The defect radius increases with increasing  $S_e$  of the irradiating ion. For Kr irradiation with the smallest  $S_e$ , the radii of defects in an  $ab$ -plane are more widely distribute than for Bi irradiation with the largest  $S_e$ . This shows that the defect radius strongly fluctuates along the ion path for Kr irradiation.

The vortex dynamics was investigated from the ac susceptibility. We obtained the relation between the frequency  $f$  and the loss-peak temperature  $T_p$ , at which the imaginary part of the ac susceptibility showed a maximum. The ac susceptibility was measured under the ac field of 0.5 Oe and the dc field of 0.3 T. Both magnetic fields were applied along the  $c$ -axis of the sample and were much lower than the dose-equivalent field  $B_\Phi$  of 0.8 T (fluence =  $4 \times 10^{10}/\text{cm}^2$ ). As is expected for a glass transition, the power law behavior  $f \sim (T_p - T_g)^n$  can be observed, where  $T_g$  is the glass temperature. The exponent  $n$  is  $3.2 \pm 0.3$  ( $T_g = 67.0 \pm 0.4$  K) for Xe irradiation,  $3.9 \pm 0.4$  ( $T_g = 67.5 \pm 0.4$  K) for Ta irradiation, and  $4.3 \pm 0.3$  ( $T_g = 68.7 \pm 0.3$  K) for Bi irradiation, showing a univer-

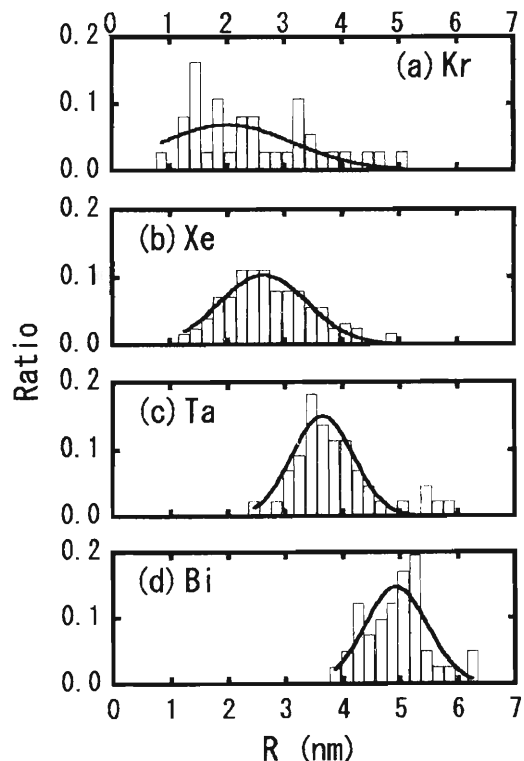


Fig. 1. Distribution of the radii of irradiation-induced defects for (a) 0.7 GeV  $^{84}\text{Kr}$ , (b) 3.5 GeV  $^{136}\text{Xe}$ , (c) 3.8 GeV  $^{181}\text{Ta}$ , and (d) 3.1 GeV  $^{209}\text{Bi}$ . The lines show the Gaussian fits.

sal power law of the Bose-glass transition which results from the production of CDs. For the Bose-glass transition, the value of the exponent  $n$  is expected to be 3.5–4.5.<sup>2)</sup> For Kr irradiation with low stopping power, however, a much larger exponent than for other irradiations,  $n = 9.6 \pm 1.9$  ( $T_g = 60.2 \pm 1.8$  K), was obtained. In the Kr irradiation with  $S_e \approx 1.4$  keV/Å, complete CDs are not produced, thus the vortex dynamics is different from that in Xe, Ta, and Bi irradiations.

### References

- 1) Y. Zhu, Z. X. Cai, R. C. Budhani, M. Suenaga, and D. O. Welch: Phys. Rev. B **48**, 6436 (1993).
- 2) M. Wallin and S. M. Girvin: Phys. Rev. B **47**, 14642 (1993).

\* Cryogenics Center, University of Tsukuba

# Radiation Annealing Induced by Electronic Excitation in Iron<sup>†</sup>

Y. Chimi, A. Iwase, N. Ishikawa, N. Kuroda, and T. Kambara

The interactions between energetic particles and an iron target have been studied. Polycrystalline iron thin films (~200 nm thick) were irradiated at a low temperature (~77 K) with 0.5–2.0 MeV ions using a 2 MV Van de Graaff accelerator,<sup>1)</sup> with 84–200 MeV heavy ions using a 20 MV tandem accelerator,<sup>2)</sup> both at JAERI-Tokai (Japan Atomic Energy Research Institute, Tokai Establishment) and with 3.1–3.8 GeV heavy ions using the RIKEN Ring Cyclotron. Defect accumulation behavior during irradiation was observed by measuring the increment in electrical resistivity of the specimen as a function of ion fluence. The defect annihilation cross section,  $\sigma_r$ , for each irradiation was derived from the defect accumulation behavior. In the present report, we mention the effects of electronic excitation in iron, focussing on radiation annealing, i.e., annihilation of defects during irradiation.

Compared with ~1 MeV ion irradiation, we have observed strong radiation annealing for ~100 MeV and GeV heavy-ion irradiations. In these cases, the elastic collision not only is not dominant for defect annihilation, but is negligible. We plotted  $\sigma_r$  for ~100 MeV and GeV ion irradiations in Fig. 1 against the electronic stopping power,  $S_e$ , which is the energy transferred through electronic excitation per unit length along the ion path. The value of  $\sigma_r$  is nonlinearly correlated with  $S_e$  ( $\sigma_r \sim S_e^{2-3}$ ). However,  $\sigma_r$ 's for some ions are different even at the same  $S_e$ . This result shows what is called the velocity effect. The slower ions are more efficient for defect annihilation. The velocity effect indicates that  $S_e$  is not the most appropriate parameter for describing this phenomenon. The excited state of secondary electrons and the energy spectrum of excited electrons are different for different ion velocities even at the same  $S_e$ . A similar ion velocity effect on damage creation has also been observed in bismuth.<sup>3)</sup> It is insisted that the experimental track radii agree with the theoretical ones estimated in the framework of the thermal spike mechanism.<sup>4)</sup> It is noted that in an oxide superconductor a primary ionization rate,  $dJ/dx$ , is the dominant parameter for describing atomic displacements.<sup>5,6)</sup> The value of  $dJ/dx$  indicates the number of atoms ionized by an incident ion per unit length along the ion path. Therefore, the result of irradiation experiments in the oxide superconductor implies that defect production, especially track formation, can be explained by the ion explosion mechanism proposed by Fleischer *et al.*<sup>7)</sup> In the case

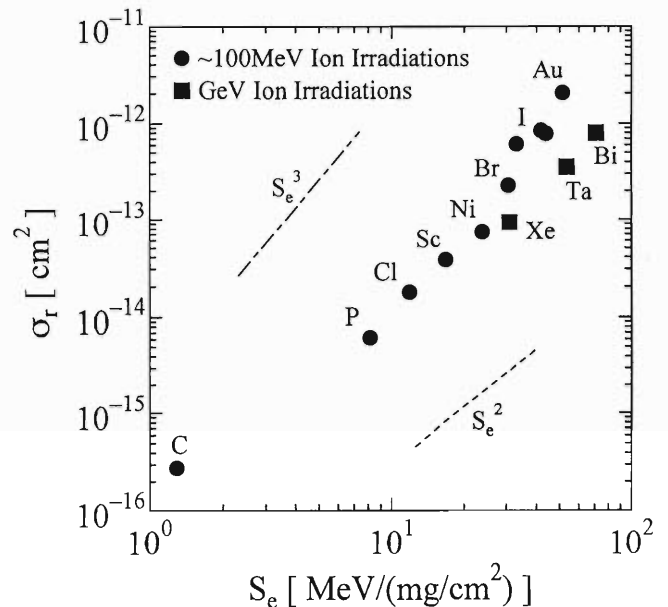


Fig. 1. Defect annihilation cross section,  $\sigma_r$ , for ~100 MeV and GeV ion irradiations plotted against the electronic stopping power,  $S_e$ .

of iron, we also have to find a pertinent parameter, other than  $S_e$ , for describing this phenomenon. For defect production in iron irradiated with GeV heavy ions, Dunlop *et al.* suggest the parameter  $\eta = Z_1^* v_0/v$ , where  $Z_1^*$  is the ion effective charge,  $v_0$  the Bohr velocity and  $v$  the ion velocity.<sup>8)</sup> They claimed that the Coulomb explosion causes defect production in iron. However, it remains uncertain whether or not the parameters  $dJ/dx$  and  $\eta$  can be applied to the radiation annealing process.

## References

- 1) Y. Chimi *et al.*: J. Nucl. Mater. **271/272**, 236 (1999).
- 2) Y. Chimi *et al.*: Mat. Res. Soc. Symp. Proc. **504**, 221 (1998).
- 3) Z. G. Wang *et al.*: Nucl. Instrum. Methods Phys. Res. B **107**, 175 (1996).
- 4) Z. G. Wang *et al.*: J. Phys.: Condens. Matter **6**, 6733 (1994); J. Phys.: Condens. Matter **7**, 2525 (1995).
- 5) N. Ishikawa *et al.*: Nucl. Instrum. Methods Phys. Res. B **135**, 184 (1998).
- 6) A. Iwase *et al.*: Nucl. Instrum. Methods Phys. Res. B **146**, 557 (1998).
- 7) R. L. Fleischer *et al.*: Phys. Rev. **156**, 353 (1967).
- 8) A. Dunlop *et al.*: Nucl. Instrum. Methods Phys. Res. B **90**, 330 (1994).

<sup>†</sup> Condensed from the article in Nucl. Instrum. Methods Phys. Res. B (2000), in press

# Infrared Spectroscopy Study on Vacancy-Oxygen Pairs in CZ-Si Irradiated by 3.5 GeV Xe Ions

X. Diao, Y. Yoshida, K. Hayakawa,\* F. Shimura,\* T. Kambara, A. Iwase, and Y. Yano

Irradiation effects have been extensively studied for decades, especially for electrons, neutrons and low-energy ions.<sup>1-3)</sup> Defects are always produced and electronic properties are modified by irradiations or deliberate implantations. However, little is known so far about the irradiation effects of high-energy GeV heavy ions in Si.

In the present investigation, Czochralski-grown (CZ) silicon was chosen as a target because it contains a rather high concentration of oxygen, i.e., around  $10^{18}$  atoms/cm<sup>3</sup>, and therefore, the oxygen atoms can act as sensitive probes to detect defects in infrared spectroscopy of Si. In addition, a conventional micro-FT-IR spectrometer would make it possible to observe the defect distribution directly along the ion tracks with a resolution of 20  $\mu\text{m}$ , since the ion range reaches up to several hundreds of  $\mu\text{m}$  in GeV ion irradiation.

Both CZ-Si and floating zone (FZ)-Si samples were irradiated with 3.5 GeV Xe ions at total doses of  $1.0 \times 10^{13}$  Xe/cm<sup>2</sup> and  $1.0 \times 10^{12}$  Xe/cm<sup>2</sup>. The irradiations were performed from the (100) direction of the Si crystal at room temperature. After the irradiation, the sample irradiated with the higher Xe dose was prepared for micro-FT-IR measurements. All IR spectra were measured at room temperature.

The infrared spectra of both nonirradiated and irradiated CZ-Si are shown for the different Xe doses in Fig. 1. After irradiation, clear bands were found at 830 and 1107 cm<sup>-1</sup>, which can be assigned to vacancy-oxygen (VO) pairs and interstitial oxygen, respectively. The VO pairs were first observed in electron-irradiated CZ-Si.<sup>1)</sup> In FZ-Si, on the other hand, we did not find these oxygen bands. By comparing the interstitial oxygen concentration before and after the irradiation, the production rate of VO pairs was determined to be  $\eta = 2.9 \times 10^2$  pairs/ion.

The depth dependence of the infrared spectra in the ion incident direction was obtained using a micro-FT-IR spectrometer with a  $20 \times 600 \mu\text{m}$  aperture, and the results are shown in Fig. 2. The 830 cm<sup>-1</sup> band is clearly detected in the depth range between 0 and 350  $\mu\text{m}$ . The intensity of the band varies depending on the depth. In the shallow region near the surface, the band shows a broad tail, possibly due to other defects, which may be produced by a primary reaction between Xe ions and the Si surface. In the region deeper than 350  $\mu\text{m}$ , the band at 830 cm<sup>-1</sup> completely disappears. This indicates that the ions did not penetrate beyond a depth of about 350  $\mu\text{m}$ , which is in good

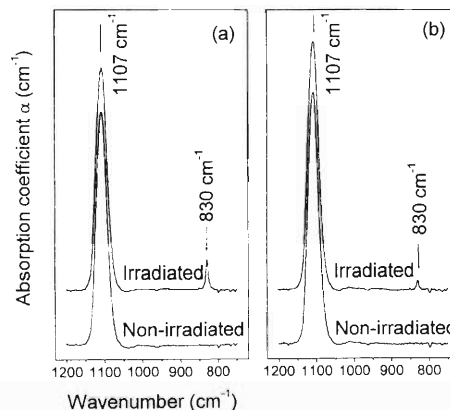


Fig. 1. IR spectra of CZ-Si irradiated with 3.5 GeV Xe at total doses of (a)  $1.0 \times 10^{13}$  Xe/cm<sup>2</sup>, and (b)  $1.0 \times 10^{12}$  Xe/cm<sup>2</sup>.

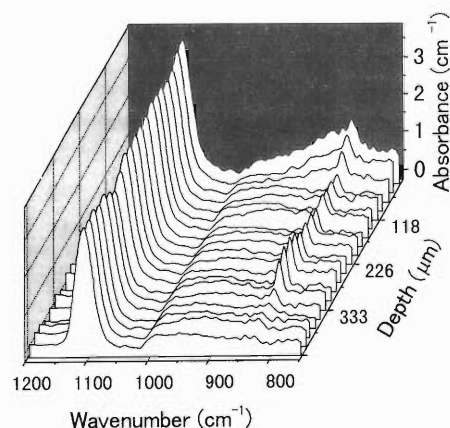


Fig. 2. Depth dependence of the IR spectra of CZ-Si irradiated at the dose of  $1.0 \times 10^{13}$  Xe/cm<sup>2</sup>.

agreement with the ion penetration range evaluated by the "TRIM" calculation. Because the electronic stopping power dominates the slowing down process for the GeV region, the nuclear collisions are thought to contribute to the energy loss only at the ends of the ion tracks. Accordingly, the present results strongly suggest that the VO defect was created by the energy loss due to electronic excitation processes.

## References

- 1) J. W. Corbert, G. D. Watkins, R. M. Chrenko, and R. S. McDonald: Phys. Rev. **121**, 1015 (1961).
- 2) P. C. Newman and D. H. J. Totterdell: J. Phys. C: Solid State Phys. **8**, 3944 (1975).
- 3) H. J. W. Zandvliet, H. B. Elswijk, E. J. van Loenen, I. S. T. Tsong: Phys. Rev. B **46**, 7581 (1992).

\* Shizuoka Institute of Science and Technology

## Evaluation of SEB in Power MOSFETs Caused by Heavy Ions

S. Matsuda, S. Kuboyama, T. Takahashi, T. Suzuki, T. Hirose, H. Ohira, Y. Nagai, and M. Kase

Semiconductor devices used for artificial satellites and spacecrafts are affected by radiation in space. It is well known that the incidence of high-energy heavy ions into semiconductor devices causes four kinds of anomalies: single-event upset (SEU), single-event latchup (SEL), single-event burnout (SEB) and single-event gate rupture (SEGR). Among them, SEB was identified as a possible catastrophic failure mode for power MOSFETs with a double-diffused MOS (DMOS) structure. To date, numerous tests on SEB of power MOSFETs have been performed, and its mechanism is becoming clear. SEB is triggered when a heavy ion passes through a power MOSFET biased in the OFF state. Transient currents generated by the heavy ion turn on a parasitic bipolar transistor (BJT) inherent to the device structure. Due to a regenerative feedback mechanism, a second breakdown sets in, creating a short circuit between the source and drain, which destroys the device.<sup>1)</sup> Therefore, it is necessary to increase SEB tolerance in power MOSFETs to enable space application. National Space Development Agency of Japan (NASDA) has studied SEB in power MOSFETs caused by heavy ions from the RIKEN Ring Cyclotron.<sup>2)</sup>

Previously, the 250V-class power MOSFET, 2SK3041, for space application was developed. Currently, we are trying to improve SEB tolerance in power MOSFETs using new methods. We have performed irradiation tests with a beam of Ni<sup>25+</sup> at 25 MeV/u (total energy of 1450 MeV) on several types of samples and have studied the breakdown voltage data associated with SEB. Because the Ni-ion beam passes through the atmosphere, the energy of the ion at the sample was degraded to approximately 286 MeV. Therefore, the linear energy transfer (LET) of the ions at the sample surface (Si) was about 26.7 MeV/(mg/cm<sup>2</sup>) and the range was about 44.7  $\mu$ m.

First, we study the effect of the diffused self-alignment (DSA) process on SEB tolerance. Generally the DSA process has been used for commercial devices. Usually, many different lithography processes are needed to form IC patterns, but the DSA process makes it possible to reduce the number of processes. The advantage of the DSA process is to make the channel length short, thus it can be expected to improve the electrical characteristics.

Four types of samples of 250V-class power MOSFETs were prepared. Three types of samples were fabricated using different DSA processes (DSA-1,2,3) and one sample was the reference sample (non-DSA process). We performed irradiation tests for these sam-

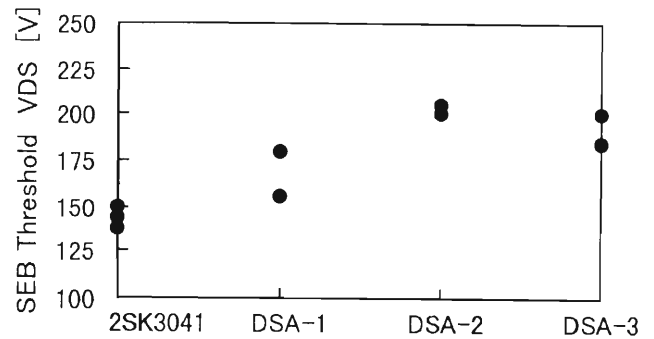


Fig. 1. DSA dependence on SEB threshold.

ples. Figure 1 shows the test results of the DSA process effect on the SEB threshold. In Fig. 1, the SEB threshold of the DSA sample is higher than that of the reference sample (non-DSA process). It is clear that the DSA process is effective in improving SEB tolerance. Among the three DSA processes, the DSA-2 process is the most effective, however, its mechanism is not yet clear.

Second, we study the effect of the lifetime of carriers in power MOSFETs on SEB tolerance. It is known that the voltage drop generated by the current along the body layer cause the activation of the parasitic BJT as a trigger of SEB.<sup>2)</sup> Thus it can be expected that SEB tolerance increases as the number of holes injected into parasitic BJT (decreasing the lifetime of carriers) decreases. To control the lifetime of the carriers, we performed electron irradiation for power MOSFET, called "Lifetime Control" (LTC). The lifetime of carriers is governed by the electron dose and the annealing conditions.

Many LTC samples were prepared. These samples were based on 2SK3041 (250V-class power MOSFET) which NASDA had developed previously. To evaluate the lifetime of the carriers, the reverse recovery time

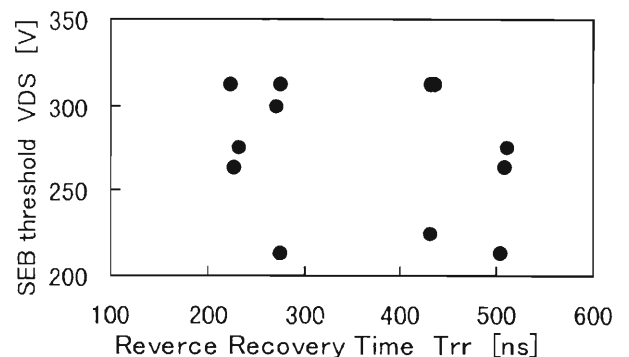


Fig. 2. Trr dependence on SEB threshold.

( $t_{rr}$ ) of these samples was measured. A short  $t_{rr}$  means a short lifetime of carriers. It is expected that the SEB tolerance increases as  $t_{rr}$  decreases. Irradiation test results are shown in Fig. 2.

In Fig. 2, the SEB threshold  $V_{DS}$  does not depend on  $t_{rr}$ , contrary to our expectation. The reason is not yet clear, but it is apparent that LTC has no effect on SEB tolerance. We expect that such test results

will be applicable to improve SEB tolerance in power MOSFETs.

#### References

- 1) M. Allenspach et al.: IEEE Trans. Nucl. Sci. **NS-43**, 2927 (1996).
- 2) S. Kuboyama et al.: IEEE Trans. Nuc. Sci. **NS-39**, 1698 (1992).

## Dynamic Behavior of a Nuclear Probe $^{57}\text{Mn}/^{57}\text{Fe}$ in Si after Projectile-fragment Separation and Implantation

Y. Yoshida, Y. Kobayashi, X. Diao, K. Hayakawa,\* K. Yukihiro,\* F. Shimura,\* A. Yoshida, Y. Watanabe, F. Ambe, and Y. Yano

An on-line isotope separator after projectile nuclear fragmentation (RIPS) can be applied to produce a radioactive isotope for  $^{57}\text{Fe}$  Mössbauer spectroscopy, that is,  $^{57}\text{Mn}$  decaying to  $^{57}\text{Fe}$  with a half-life of 1.45 min. The highly energetic particles with several GeV from the separator can be implanted even in the depth range of several hundreds  $\mu\text{m}$  from the surface, providing atomistic information on both the local surroundings and the dynamics of the probe atoms at the final lattice sites through hyperfine interactions. It is therefore appealing that this method opens a new possibility for nanometer-scale materials science particularly in bulk materials, which would be complementary to high-resolution electron microscopy for thin samples, or scanning probe microscopy for surface.

The  $^{57}\text{Mn}$  beam was separated using RIPS after the projectile fragmentation of  $^{59}\text{Co}$  nuclei with a Be target with a thickness of  $185\text{ mg/cm}^2$ . The energy and intensity of the primary  $^{59}\text{Co}$  beam were  $80\text{ MeV/nucleon}$  and approximately  $300\text{ enA}$  ( $\sim 12\text{ pA}$ ), respectively. In order to stop all the  $^{57}\text{Mn}$  nuclei in the sample, the beam energy had to be suppressed by using a  $470\text{-}\mu\text{m}$ -thick Al plate as a degrader. Finally, the implantation energy was several MeV/nucleon, leading to the implantation depth of  $100 \pm 10\ \mu\text{m}$ . The intensity of the  $^{57}\text{Mn}$  secondary beam was typically  $2 \times 10^5$  particles/s.

In order to investigate the dynamical behavior of  $^{57}\text{Fe}$  atoms in the Si matrix, we used two different floating-zone (FZ) Si wafers for two different experimental periods; a  $\langle 100 \rangle$  oriented Si wafer and a  $\langle 111 \rangle$  oriented Si wafer with thicknesses of  $530\ \mu\text{m}$  and  $525\ \mu\text{m}$ , respectively. These samples enabled us to measure Mössbauer spectra from different orientations. The resistivities of the samples were  $100$  and  $10\ \Omega\text{cm}$ , respectively, corresponding to boron concentrations of  $2 \times 10^{16}$  and  $2 \times 10^{15}/\text{cm}^3$ . The  $14.4\text{-keV}$   $\gamma$ -rays from  $^{57}\text{Fe}/^{57}\text{Mn}$  were monitored by a CdZnTe detector. Mössbauer spectra were measured by a parallel-plate avalanche counter with a stainless-steel absorber, which was 95% enriched by  $^{57}\text{Fe}$ . This counter was mounted on the velocity transducer. The measuring time and the total implantation dose of  $^{57}\text{Mn}$  necessary for one spectrum were approximately 10 hours and  $10^{10}$   $^{57}\text{Mn}$ , respectively.

Figure 1 shows the Mössbauer spectra of  $^{57}\text{Mn}/^{57}\text{Fe}$  in FZ- $\langle 111 \rangle$  oriented Si, which were measured between 350 and 650 K. The spectrum at 350 K can be fitted

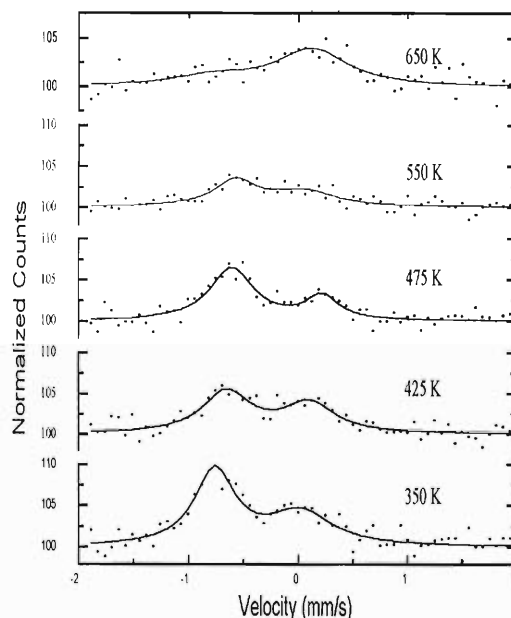


Fig. 1.  $^{57}\text{Fe}$  Mössbauer spectra in FZ-Si following projectile fragmentation and implantation of  $^{57}\text{Mn}$ .

by two components corresponding to interstitial Fe on the left-hand side ( $\delta = -0.76(2)\text{ mm/s}$ ) and substitutional Fe on the right-hand side ( $\delta = 0.02(5)\text{ mm/s}$ ), which are in good agreement with those obtained at 300 K in the first experiment on FZ- $\langle 100 \rangle$ Si.<sup>1)</sup> As the temperature is elevated, the area intensity of the interstitial line decreases, while the substitutional line increases and is accompanied by broadening in both lines. In addition, the interstitial fraction decreases above 500 K.

In order to interpret the dynamical behavior observed in the present study, we must consider two characteristic times, namely 100 s and 100 ns due to the lifetime of  $^{57}\text{Mn}$  and  $^{57}\text{Fe}$ , respectively. It is expected from the tracer diffusivity of Fe in Si that the jump frequency of interstitial Fe atoms reaches  $2 \times 10^3$  and  $2 \times 10^6$  at around 400 K and 600 K, respectively. This would lead to a kinetic reaction, on one hand, between Fe interstitials and vacancies produced by the slowing-down process of  $^{57}\text{Mn}$ , and on the other hand, diffusional line broadening accompanied by a relaxation effect on the isomer shift. Details will be discussed elsewhere.

### References

- 1) Y. Kobayashi et al.: RIKEN Accel. Prog. Rep. 33, 109 (2000).

\* Shizuoka Institute of Science and Technology

# Atomic-Force-Microscopy Observations of FZ-Si after GeV-<sup>57</sup>Mn Implantation Using RIKEN Projectile Fragment Separator (RIPS)

X. Diao, Y. Yoshida, Y. Kobayashi, A. Yoshida, Y. Yano, K. Hayakawa,\* and F. Shimura\*

It is known that ion tracks can be introduced in the wake of high-energy ions passing through solid materials, and to date they have been found in mica, graphite, some metal alloys and most insulators.<sup>1,2)</sup> However in Si, no one has observed the ion tracks after monoatomic GeV-heavy-ion irradiation. In the present investigation, atomic force microscopy (AFM) is used to search for ion tracks in a cleaved Si surface.

Two floating-zone (FZ) Si (100) samples were obtained after in-beam Mössbauer-spectroscopic experiments, which achieved the implantation of 3.2-GeV-<sup>57</sup>Mn into FZ-Si using an on-line isotope separator of projectile fragments (RIPS) and simultaneously, Mössbauer measurements were made of <sup>57</sup>Fe decayed from <sup>57</sup>Mn. The results are also presented in this report.<sup>3)</sup> The first sample was obtained from low-temperature measurements at 30, 100, 150, 250 and 300 K, and the second sample from high-temperature measurements at 300, 500, 600 and 700 K. The total implantation dose of <sup>57</sup>Mn ions for both samples was around  $5.0 \times 10^{10}$  Mn/cm<sup>2</sup>. In order to observe the ion tracks, the implanted sample was cleaved in the (110) plane and was immediately placed in the AFM vacuum chamber. Pumping to  $1.0 \times 10^{-6}$  mbar requires around 15 minutes.

Typical AFM micrographs of the first sample are shown in Fig. 1. The implantation was performed from the (110) direction of the Si crystal, i.e., incident at 45° to the (100) Si surface. The present geometry enables us to observe the region from the surface to the ion range, which is also illustrated in Fig. 1. Two types of swellings are clearly observed on the cleaved surface with diameters of approximately 100 μm and 20 nm. The larger mountainlike bumps are distributed among the smaller bumps with monodispersed sizes. The number of smaller bumps is approximately  $1.5 \times 10^{10}$  cm<sup>-2</sup>, which is close to the total implantation dose. The swellings disappear around the ion range with a sharp boundary. Figure 2 shows an AFM micrograph observed in the second sample. Only pin-shape bumps can be seen with a diameter of approximately 30 nm, but the number of the bumps is about  $1.5 \times 10^9$  cm<sup>-2</sup>, one order of magnitude lower than the total implantation dose. This suggests that the swellings are annihilated considerably at high temperatures.

The swellings observed in the present investigation are believed to be related to the ion tracks. However, the formation mechanism of the swellings from the ion

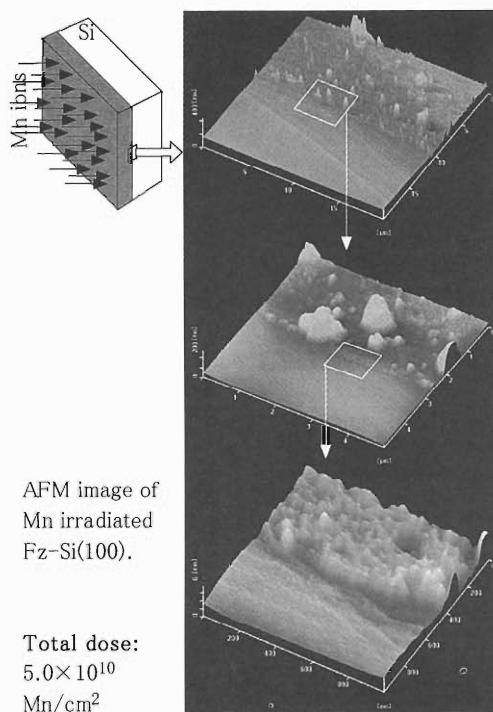


Fig. 1. AFM micrographs of cleaved FZ-Si implanted with <sup>57</sup>Mn/<sup>57</sup>Fe at low temperatures from 30 K to 300 K.

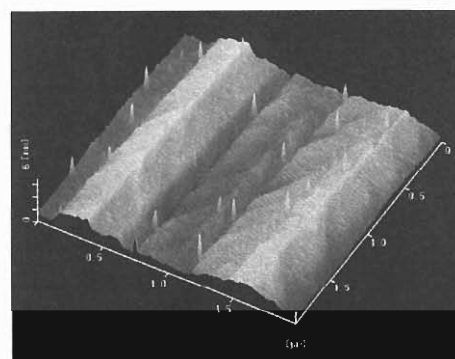


Fig. 2. AFM micrograph of cleaved FZ-Si implanted with <sup>57</sup>Mn/<sup>57</sup>Fe at high temperatures from 300 K to 700 K.

tracks is still not clear after the samples were cleaved, and further experiments are necessary.

## References

- 1) F. Thibaudau, J. Cousty, E. Balanzat, and S. Bouffard: Phys. Rev. Lett. **67**, 1582 (1991).
- 2) G. Szenes: Phys. Rev. B **51**, 8026 (1995).
- 3) Y. Yoshida et al.: RIKEN Accel. Prog. Rep. **33**, 93 (2000).

\* Shizuoka Institute of Science and Technology

## A New Spin Polarimeter Proposed for Spin-Polarized Slow Positron Beams

Y. Nagai,\* J. Kim, Y. Nagashima, Y. Itoh, and T. Hyodo

A new spin polarimeter for the spin-polarized slow positron beam<sup>1)</sup> is proposed. The Doppler broadening method with an a-SiO<sub>2</sub> sample is utilized. The polarization is determined from the magnetic field dependence of the S-parameter, i.e., the ratio of counts in the central portion of the annihilation photopeak of the Doppler broadening spectra to the total counts in the peak.

The S-parameter is related to the fraction of the positronium (Ps) which self-annihilates into  $2\gamma$   $I_{Ps}$  as  $S = \alpha I_{Ps} + \beta$ , where  $\alpha$  and  $\beta$  are constants.  $I_{Ps}$  is represented by

$$I_{Ps} = \frac{\kappa\gamma_p}{\Gamma_{o'}} \frac{y^2}{1+y^2} F_{o'} + \frac{\kappa\gamma_p}{\Gamma_{p'}} \frac{1}{1+y^2} F_{p'}, \quad (1)$$

where  $F_{o'}$  and  $F_{p'}$  are the fractions of the perturbed ortho-Ps and the perturbed para-Ps formed in a magnetic field  $B$ ;

$$F_{o'} = \frac{1}{8(1+y^2)} [(1+y)^2(1-P) + (1-y)^2(1+P)] \quad (2)$$

and

$$F_{p'} = \frac{1}{8(1+y^2)} [(1-y)^2(1-P) + (1+y)^2(1+P)]. \quad (3)$$

$y$  is given by  $y = x/[(1+x^2)^{1/2} + 1]$  with  $x = 4\mu B/\kappa\hbar\omega_0$ , and  $P$  is the positron spin polarization along  $B$  at the instant of the Ps formation.  $\mu$  is the magnetic moment of the electron and  $\hbar\omega_0$  is the hyperfine structure splitting between the ortho-Ps and the para-Ps in vacuum.  $\kappa$  is the electron-positron contact density of Ps in the sample relative to that in vacuum.  $\Gamma_{o'}$  and  $\Gamma_{p'}$  are the annihilation rates of the perturbed ortho-Ps and the perturbed para-Ps in the sample and are given as follows

$$\Gamma_{o'} = \kappa \frac{\gamma_o + y^2\gamma_p}{1+y^2} + \gamma_{pickoff} \quad (4)$$

and

$$\Gamma_{p'} = \kappa \frac{y^2\gamma_o + \gamma_p}{1+y^2} + \gamma_{pickoff}. \quad (5)$$

$\gamma_o$  and  $\gamma_p$  are the self-annihilation rates of ortho-Ps and para-Ps in vacuum, respectively, and  $\gamma_{pickoff}$  is the Ps pickoff annihilation rate in the sample. Figure 1 shows the dependence of  $I_{Ps}$  on  $B$ . The asymmetry around  $B = 0$  is ascribed to the positron spin

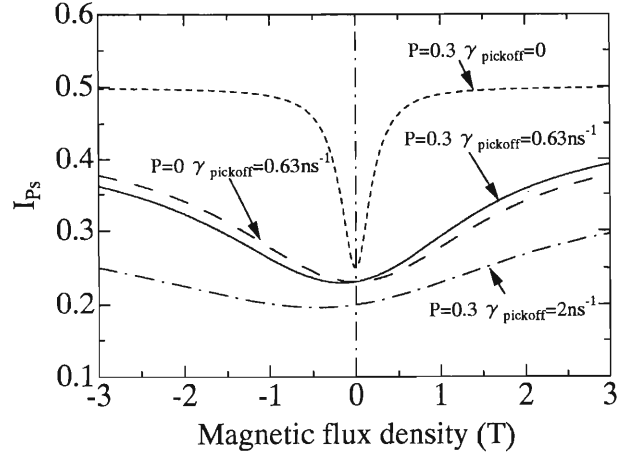


Fig. 1. Theoretical values of  $I_{Ps}$  for samples with  $\kappa = 1$  as functions of the magnetic flux density.

polarization along the magnetic field. The polarization can be determined if the magnetic field dependence of  $I_{Ps}$  or S-parameter is measured for materials with a suitable pickoff rate. One of the best materials for this purpose is a-SiO<sub>2</sub>, not only because the pickoff rate is suitable but also because the Ps formation efficiency is very high ( $\sim 80\%$ ).

The polarization of the spin-polarized slow positron beam has so far only been measured using the lifetime method using a channel electron multiplier array.<sup>2,3)</sup> The data analysis of the lifetime spectra is complicated because Ps thermalizes slowly. The method proposed here provides a much simpler way to measure the polarization of the beam.

In order to examine the sensitivity of this method, we have measured the polarization of the positrons from <sup>22</sup>Na.<sup>4)</sup> An <sup>22</sup>Na source of 8  $\mu$ Ci was deposited between two identical Kapton foils of 7.5  $\mu$ m thickness. The source was held between an a-SiO<sub>2</sub> sample and a stack of 15 Kapton foils of 0.125 mm thickness. Positronium is not formed in Kapton. Magnetic fields up to 20 kG were applied using an electromagnet.  $\gamma_{pickoff}$  was determined using the conventional positron lifetime method. The optimized value of polarization is  $0.327 \pm 0.015$ .

If we assume that the reflection of positrons from a stack of Kapton foils and the absorption of positrons in the Kapton foil holding the source are negligible, the theoretical value of the polarization is  $0.5(\bar{v}/c)$ , where  $(\bar{v}/c) = 0.67$  is the longitudinal polarization averaged over the  $\beta^+$  spectrum of <sup>22</sup>Na. The polarization determined above is consistent with this value within the

\* Institute of Materials Research, Tohoku University

range of statistical error.

#### References

- 1) J. Kim et al.: RIKEN Accel. Prog. Rep. **33**, 216 (2000).
- 2) A. Rich et al.: Appl. Phys. A **43**, 275 (1987).
- 3) T. Kumita et al.: Appl. Surf. Sci. **116**, 1 (1997).
- 4) Y. Nagai et al.: submitted to Nucl. Instrum. Methods Phys. Res. B.

## Xe Bubble Formation in Xe-Implanted Fe as Observed by the Channelling Method<sup>†</sup>

E. Yagi, T. Sasahara,<sup>\*1</sup> T. Joh,<sup>\*2</sup> M. Hacke,<sup>\*3</sup> T. Urai, T. Sasamoto,  
N. Tajima, T. Watanabe, and S. T. Nakagawa<sup>\*2</sup>

It has been demonstrated that heavier inert gas atoms (Ar, Kr and Xe) implanted into metals at room temperature precipitate into a solid phase at high implantation doses.<sup>1-3)</sup> These are often referred to as solid inert gas bubbles or solid inert gas inclusions. In fcc metals, they have an fcc structure which is crystallographically well aligned with the matrices. Although the growth of such bubbles has been extensively studied by transmission electron microscopy (TEM), there have been only a few studies on their nucleation and formation processes. For studies such as that of the nucleation of bubbles in the initial stage of implantation, which is unobservable by conventional TEM, the channelling method is very useful because it gives information on the lattice locations of implanted atoms.

In previous channelling studies on Kr-implanted Al (fcc), the nucleation of Kr bubbles and their solidification processes have been extensively studied.<sup>4-9)</sup> In the present study, to observe the difference in the state of heavier inert gas atoms in the initial stage of implantation between fcc and bcc metals, channelling experiments are performed on Xe-implanted  $\alpha$ -Fe (bcc) and the initial stage of Xe bubble formation is discussed.

Xe<sup>+</sup> ions were implanted into Fe single crystals at room temperature at an energy of 150 keV at four different doses  $10^{14}$ ,  $4 \times 10^{14}$ ,  $10^{15}$  and  $10^{16}$  Xe ions/cm<sup>2</sup>. Channelling angular scans were performed at room temperature for  $\langle 100 \rangle$ ,  $\langle 110 \rangle$ ,  $\langle 111 \rangle$  and  $\{100\}$  channels by means of the Rutherford-backscattering method with a 1.5 MeV He<sup>+</sup> beam provided by a tandem accelerator.

The channelling angular profiles of the yields of He ions backscattered by Fe atoms (the Fe angular profile) and those by Xe atoms (the Xe angular profile) for the  $10^{14}$  and  $4 \times 10^{14}$  Xe ions/cm<sup>2</sup>-implanted specimens are shown in Fig. 1. In the  $10^{14}$  Xe ions/cm<sup>2</sup>-implanted specimen, the Xe angular profile exhibits a shallow dip, which has a fine structure, with a relative depth of about 50% of that of the Fe angular profile (the Fe dip) and with approximately the same angular half-width as that of the Fe dip for all the channels investigated. On the Xe dip, a small central peak is superimposed for the  $\langle 100 \rangle$  and  $\langle 110 \rangle$  channels and small double peaks around  $\pm 0.15^\circ$  for the

$\langle 111 \rangle$  channel. In the  $4 \times 10^{14}$  Xe ions/cm<sup>2</sup>-implanted specimen, the Xe dips become shallower. On the Xe dip, small off-centre peaks are superimposed around  $\pm 0.2^\circ$  for the  $\langle 100 \rangle$  channel and a small narrow dip for the  $\langle 111 \rangle$  channel. For the  $\langle 110 \rangle$  channel a fine structure is not clearly observed. With increasing implantation dose, the Xe dips become much shallower and the fine structures are no longer clearly observed.

These results suggest that the majority of the Xe atoms are distributed over substitutional (*S*) sites and random (*R*) sites. The remainder are located at the sites responsible for the fine structures, which are considered to be tetrahedral (*T*) interstitial sites in the  $10^{14}$  Xe ions/cm<sup>2</sup>-implanted specimen and the  $\langle 111 \rangle$ -displaced (*D*) site, i.e., the site displaced from an *S* site in the  $\langle 111 \rangle$  direction in the  $4 \times 10^{14}$  Xe ions/cm<sup>2</sup>-implanted specimen.

The lattice locations of the Xe atoms and their distribution were determined by comparing the observed Xe angular profiles with those calculated taking into account the four kinds of sites, i.e., the *S*, *R*, *T* and *D* sites, for various distributions and various magnitudes of displacement of the *D* site. For the  $4 \times 10^{14}$  Xe ions/cm<sup>2</sup>-implanted specimen the Xe angular profiles can be successfully reproduced by taking the magnitude of displacement of the *D* site to be 0.085 nm from the *S* site and for a distribution of Xe atoms of 40–43% at *S*, 50–53% at *R* and 5–10% at *D* sites. For the  $10^{14}$  Xe ions/cm<sup>2</sup>-implanted specimen, they can be reproduced for the distribution of 47–50% at *S*, 35–38% at *R*, 9–12% at *T* and 3–6% at *D* sites. With increasing implantation dose, the *S*-site occupancy decreases, whereas the *R*-site occupancy increases. The changes of *T*- and *D*-site occupancies are more complex, but generally tend to decrease with increasing dose.

The *S*, *D*, *T* and *R* site occupancies are ascribed to isolated Xe atoms at *S* sites, Xe atoms associated with one vacancy (XeV) at one of their nearest neighbour sites as a result of a strong interaction between Xe atoms and the vacancies (*V*) introduced during Xe implantation, Xe atoms associated with four vacancies (XeV<sub>4</sub>) and Xe atoms associated with a much larger number of vacancies, respectively.

From the above discussion, it is concluded that at the initial stage of Xe implantation in Fe, Xe-vacancy complexes, i.e., XeV, XeV<sub>4</sub> and Xe atoms associated with a larger number of vacancies are formed, and they act as nucleation centres for the subsequent growth of Xe inclusions (bubbles). For the sake of comparison,

<sup>†</sup> Condensed from the article in J. Phys. Soc. Jpn. **68**, 4037 (1999)

<sup>\*1</sup> Department of Physics, Chuo University

<sup>\*2</sup> Department of Applied Physics, Okayama University of Science

<sup>\*3</sup> Institut für Schicht- und Ionen-technik, Forschungszentrum Jülich GmbH, Germany

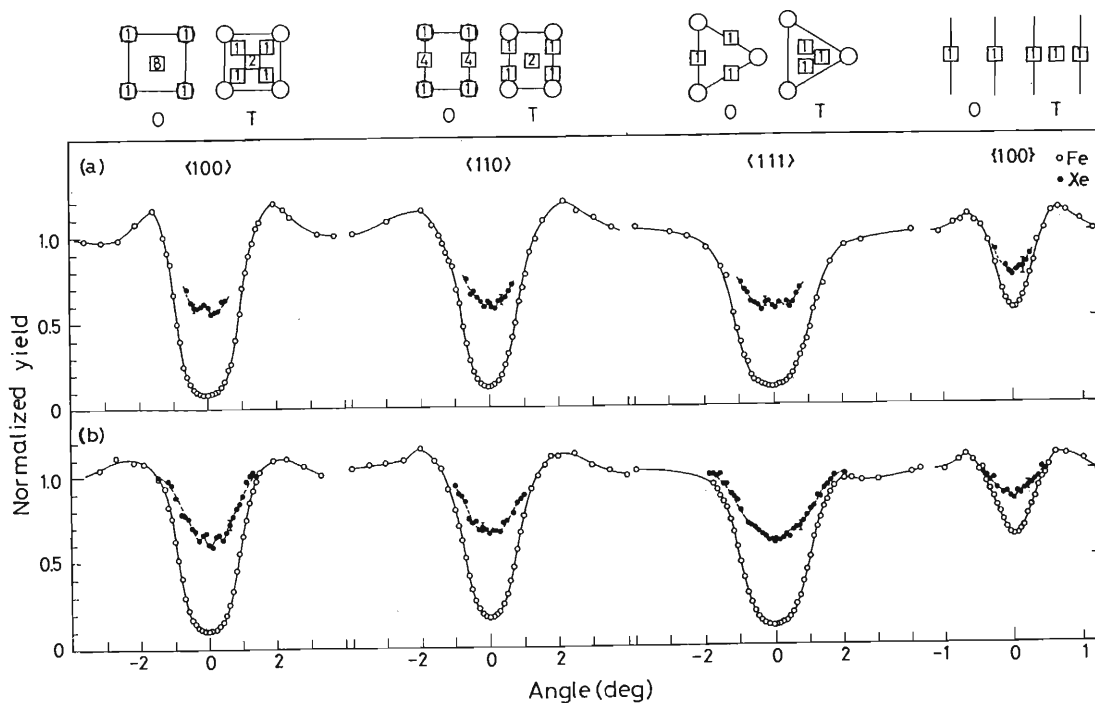


Fig. 1. Channelling angular profiles obtained at room temperature for (a) the  $10^{14}$  and (b)  $4 \times 10^{14}$  Xe ions/cm<sup>2</sup>-implanted specimens. Solid curves and dotted curves have been drawn to guide the eye. In the upper part, the projections of the *O* and *T* sites onto the plane perpendicular to the channel in question are shown by open squares with the relative weights. The open circles and lines represent the projections of the atomic rows and planes, respectively.

it should be noted that in the case of Kr in Al (fcc) also, the Kr-vacancy complexes, i.e., KrV<sub>4</sub>, KrV<sub>6</sub> and Kr atoms associated with a larger number of vacancies act as nucleation centres. A more detailed description is given in Ref. 10.

#### References

- 1) A vom Felde, J. Fink, Th. Müller-Heinzerling, J. Pfüger, B. Scheerer, G. Linker, and D. Kaletta: *Phys. Rev. Lett.* **53**, 922 (1984).
- 2) C. Templier, C. Jaouen, J. P. Rivière, J. Delafond, and J. Grilhé: *C. R. Acad. Sci., Ser. 2* **299**, 613 (1984).
- 3) J. H. Evans and D. J. Mazey: *J. Phys. F* **15**, L1 (1985).
- 4) I. Hashimoto, H. Yorikawa, H. Mitsuya, H. Yamaguchi, K. Takaishi, K. Kikuchi, K. Furuya, E. Yagi, and M. Iwaki: *J. Nucl. Mater.* **149**, 69 (1987).
- 5) E. Yagi, M. Iwaki, K. Tanaka, I. Hashimoto, and H. Yamaguchi: *Nucl. Instrum. Methods Phys. Res. B* **33**, 724 (1988).
- 6) E. Yagi: *Nucl. Instrum. Methods Phys. Res. B* **39**, 68 (1988).
- 7) E. Yagi, I. Hashimoto, and H. Yamaguchi: *J. Nucl. Mater.* **169**, 158 (1989).
- 8) M. Hacke and E. Yagi: *J. Phys. Soc. Jpn.* **64**, 800 (1995).
- 9) E. Yagi: *Phys. Rev. Lett.* **67**, 3804 (1991).
- 10) E. Yagi, T. Sasahara, T. Joh, M. Hacke, T. Urai, T. Sasamoto, N. Tajima, T. Watanabe, and S. T. Nakagawa: *J. Phys. Soc. Jpn.* **68**, 4037 (1999).

## Observation of Ion Current in Superfluid Helium

Q. Hui and Y. Matsuo

During the past two decades, laser spectroscopic studies of impurities trapped in liquid helium have provided much insight into the quantum liquid. Although the first experiment of this kind was performed with  $\text{Ba}^+$  trapped in superfluid helium in 1986 by the Heidelberg group,<sup>1)</sup> later studies were carried out exclusively on neutral species. Recently, in our experimental and theoretical studies on neutral Ag and light alkaline earth atoms such as Be and Mg, we have found that a stronger attractive force between the excited state of these atoms and helium atoms results in dynamics totally different than those of other atoms which have a weaker attraction to helium. Metal-helium exciplexes have been found to be formed when the Ag, Be and Mg atoms were excited to a p-orbital.<sup>2)</sup> Singly charged alkaline earth ions have a strong attraction to helium atoms and suitable transitions in UV and visible regions, and are very good candidates for studying dynamics of the exciplex formation process. We are currently preparing experiments with  $\text{Ca}^+$  and  $\text{Sr}^+$  in superfluid helium. In this paper we will report our recent progress.

The experimental setup is illustrated in Fig. 1. A metal cryostat (Oxford) with quartz windows was filled with He II. A quartz cell was placed above the liquid and the cell itself was also filled with He II. A metal sample was suspended about 1 cm above the quartz cell. An ablation laser beam (532 nm,  $\sim 20$  mJ/pulse) was focused onto the sample through one of the windows. Three electrodes were immersed in the liquid in such a way that the upper one remained just 1–2 mm below the liquid surface. The upper electrode (extractor) was typically at +100 V and the middle one at about +20 V. The third electrode (collector) was grounded through the impedance of a digital oscilloscope. The sample was at about +200 V. The distance between the extractor and collector was 1–2 cm. The positively charged ions produced via the laser ablation were extracted into He II by the electric field and the ion current was monitored on the digital

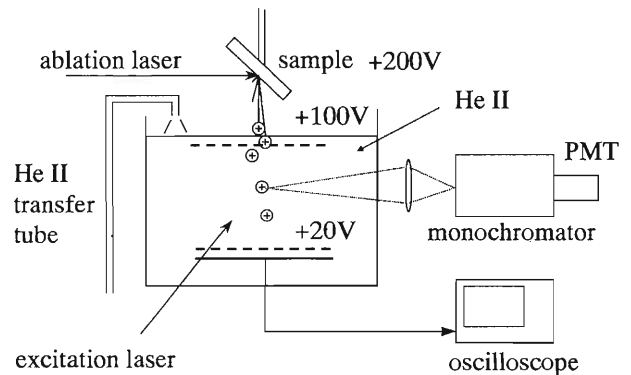


Fig. 1. Experimental setup.

oscilloscope. When the setup is complete, a CW laser beam (under preparation) will be used to intersect the ions below the extractor and excites the ions. The laser induced fluorescence (LIF) emitted by the ions will be detected at a right angle by a photomultiplier (PMT) through a monochromator.

We have observed the ion current produced by laser ablation on a Sr sample. To increase sensitivity, the impedance of the digital oscilloscope was set to  $1\text{ M}\Omega$ . The pulsed current signal was composed of two parts. Immediately after the laser pulse, a relatively sharp peak appeared which was assigned to electrons. The current signal corresponding to positively charged  $\text{Sr}^+$  ions appeared about  $1\ \mu\text{sec}$  after the laser pulse and extended to about 1 msec. The intensity of the signal was found to depend sensitively on the laser power and the surface condition of the sample. A rough estimation showed that about  $10^6$  to  $10^8$   $\text{Sr}^+$  ions were produced in the liquid by each laser pulse. An LIF experiment using a CW laser and a photon-counting method will be performed very soon.

### References

- 1) H. J. Reyher et al.: Phys. Lett. **115**, 238 (1986).
- 2) J. L. Persson et al.: Phys. Rev. Lett. **76**, 1501 (1996).

# Observation of a Full Dispersion Curve for the Low Energy Excitation in a Spin Ladder

M. Matsuda, K. Katsumata, R. S. Eccleston,<sup>\*1</sup> S. Brehmer,<sup>\*2</sup> and H.-J. Mikeska<sup>\*2</sup>

Low-dimensional antiferromagnets show novel phenomena originating from quantum fluctuations. The spin ladder system is interesting as a system between one- and two-dimensions. Extensive theoretical and experimental studies have been performed on spin ladder systems.<sup>1)</sup>  $\text{La}_6\text{Ca}_8\text{Cu}_{24}\text{O}_{41}$  consists of both chains and two-leg ladders of copper ions. The structure of the  $\text{Cu}_2\text{O}_3$  ladder is shown in Fig. 1. The  $\text{Cu}_2\text{O}_3$  ladder is a good example of an  $S = \frac{1}{2}$  Heisenberg two-leg ladder.

Neutron scattering experiments were carried out in single crystals of  $\text{La}_6\text{Ca}_8\text{Cu}_{24}\text{O}_{41}$  on the high energy transfer (HET) chopper spectrometer on the ISIS pulsed neutron source at the Rutherford Appleton Laboratory.

Figure 2 shows the experimental  $\omega$ - $Q$  dispersion relation for the two-leg spin ladder in  $\text{La}_6\text{Ca}_8\text{Cu}_{24}\text{O}_{41}$ . As is evident from this figure, we were successful in observing a full dispersion curve from the spin-ladder. As far as we are aware, this is the first experimental observation of a full dispersion curve. The standard analysis of experimental data for spin ladders uses only the two parameters  $J_{\text{leg}}$  and  $J_{\text{rung}}$ , assuming the simplest symmetric structure of the two legged ladder. For this model we have calculated the dispersion of the lowest triplet excitation using the Lanczos method for ladders with 12 rungs (i.e. 24 spins) and periodic boundary conditions. We obtained the best fit to our data for  $J_{\text{rung}} = 65$  meV and  $J_{\text{leg}} = 111$  meV ( $J_{\text{leg}}/J_{\text{rung}} = 1.7$ ). These values are not consistent (1) with the expectation from a geometrical consideration that the Cu-O-Cu exchange on legs and rungs should be approximately equal and (2) with the results of an exact diagonalization calculation for the

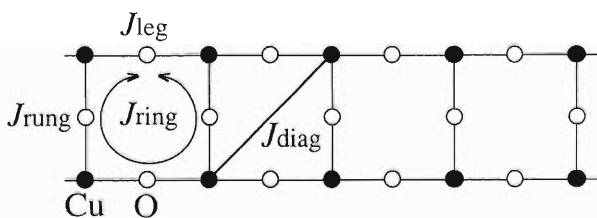


Fig. 1. Structure of the  $\text{Cu}_2\text{O}_3$  ladder. Various interactions between copper ions are also shown.

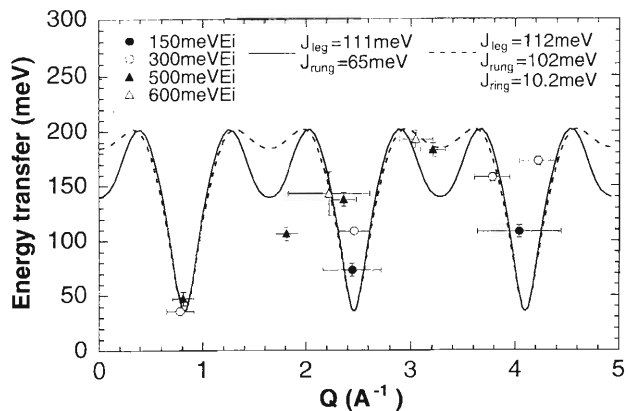


Fig. 2.  $\omega$ - $Q$  dispersion relation for the two-leg spin ladder. The solid and dotted curves are the theoretical ones with  $J_{\text{leg}} = 111$  meV and  $J_{\text{rung}} = 65$  meV and with  $J_{\text{leg}} = 112$  meV,  $J_{\text{rung}} = 102$  meV, and  $J_{\text{ring}} = 10.2$  meV, respectively. These theoretical curves are drawn through the points calculated for  $Q = \frac{n}{6}\pi$  ( $n = 0, 1, \dots, 6$ ).

electronic state of cuprates performed by Mizuno *et al.*, which gives  $J_{\text{leg}}/J_{\text{rung}} = 1.1$ .<sup>2)</sup>

We then calculated the dispersion with an additional ring exchange  $J_{\text{ring}}$ , which was recently proposed by Brehmer *et al.*<sup>3)</sup> It was shown that the ring exchange reduces the gap energy at  $Q = \pi$  considerably, thereby requiring larger values for  $J_{\text{rung}}$  and  $J_{\text{leg}}$ . The dotted curve in Fig. 2 is the theoretical one with  $J_{\text{rung}} = 102$  meV,  $J_{\text{leg}} = 112$  meV, and  $J_{\text{ring}} = 10.2$  meV. These results suggest that a moderate amount of ring exchange around the basic ladder plaquettes (about 10% of the main Cu-O-Cu bilinear exchange) should be included into the Hamiltonian of the two leg ladder, which is quite consistent with recent theoretical calculations.<sup>4)</sup>

## References

- 1) For a review, see E. Dagotto and T. M. Rice: *Science* **271**, 618 (1996).
- 2) Y. Mizuno, T. Tohyama, and S. Maekawa: *Phys. Rev. B* **58**, R14713 (1998).
- 3) S. Brehmer *et al.*: *Phys. Rev. B* **60**, 329 (1999).
- 4) Y. Mizuno, T. Tohyama, and S. Maekawa: *J. Low Temp. Phys.*, in press.

<sup>\*1</sup> ISIS Facility, Rutherford Appleton Laboratory, UK

<sup>\*2</sup> Institut für Theoretische Physik, Universität Hannover, Germany

## $\mu$ SR Study on the $1/8$ Effect in the Bi-2212 System

I. Watanabe, M. Akoshima,\* Y. Koike, and K. Nagamine

The " $1/8$  effect"<sup>1-4</sup>) is now one of the most important problems in the study of the mechanism of high- $T_c$  superconductivity (SC). Recently, anomalous suppression of the SC around the hole concentration  $p = 1/8$  per Cu was observed in a Zn-substituted Bi-2212 system by Akoshima *et al.*<sup>5</sup>) We carried out muon spin relaxation ( $\mu$ SR) measurements of Zn-substituted  $\text{Bi}_2\text{Sr}_2\text{Ca}_{1-x}\text{Y}_x(\text{Cu}_{1-y}\text{Zn}_y)_2\text{O}_{8+\delta}$  in order to examine the existence of the  $1/8$  effect in the Bi-2212 system.<sup>6,7</sup>)

Samples of  $\text{Bi}_2\text{Sr}_2\text{Ca}_{1-x}\text{Y}_x(\text{Cu}_{1-y}\text{Zn}_y)_2\text{O}_{8+\delta}$  were prepared by the conventional solid-state reaction method.<sup>5</sup>)  $\mu$ SR measurements were carried out at the RIKEN-RAL Muon Facility in the UK. A spin-polarized pulsed surface muon beam with a momentum of 27 MeV/c was used.

Figure 1 shows the temperature dependence of the zero-field (ZF)  $\mu$ SR time spectrum of the Zn-substituted sample with  $x = 0.3125$  ( $p \sim 1/8$  per Cu) and  $y = 0.025$  in which the high- $T_c$  SC is anomalously suppressed.<sup>5</sup>) The absence of the statically ordered state of the Cu spins in the Bi-2212 system is contrary to the case of the La-124 systems in which long-range magnetically ordered states have been observed.<sup>2-4</sup>)

Figure 2 shows the  $x$  dependence, namely,  $p$  dependence of the depolarization rate of the Zn-substituted samples at 0.30 and 1.8 K. Large depolarization rates at  $x \geq 0.5$  are due to the appearance of a magnetically ordered state of the Cu spins in the underdoped

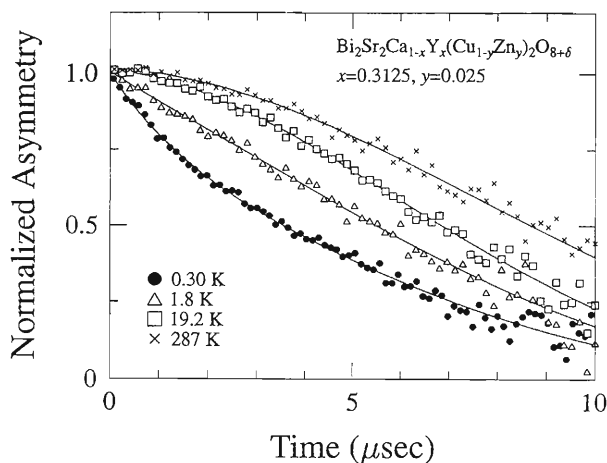


Fig. 1. Temperature dependence of the zero-field  $\mu$ SR time spectrum of  $\text{Bi}_2\text{Sr}_2\text{Ca}_{1-x}\text{Y}_x(\text{Cu}_{1-y}\text{Zn}_y)_2\text{O}_{8+\delta}$  with  $x = 0.3125$  and  $y = 0.025$  where the high- $T_c$  superconductivity is anomalously suppressed.<sup>5,7</sup>)

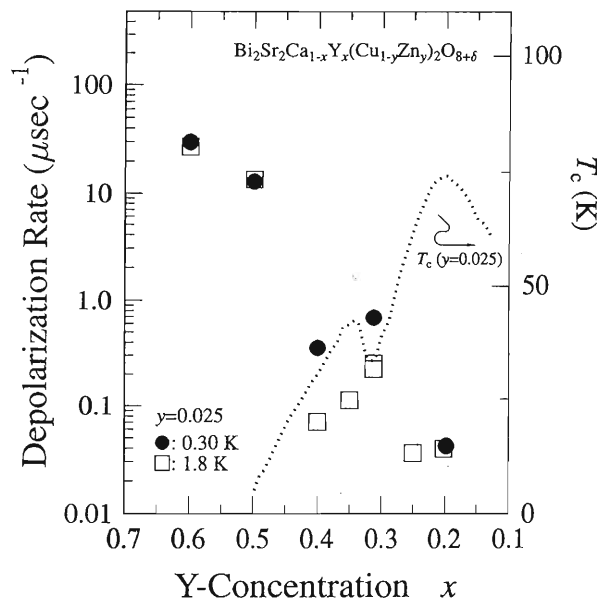


Fig. 2.  $x$  dependence of the zero-field muon spin depolarization rate of  $\text{Bi}_2\text{Sr}_2\text{Ca}_{1-x}\text{Y}_x(\text{Cu}_{1-y}\text{Zn}_y)_2\text{O}_{8+\delta}$  with  $y = 0.025$  at 0.30 and 1.8 K. Dotted lines show the  $x$  dependence of  $T_c$  with  $y = 0.025$  determined by Akoshima *et al.* from the transport measurements.<sup>5</sup>)

region. The depolarization rate decreases rapidly with increasing  $p$  and increases anomalously around  $p = 1/8$  per Cu. This result indicates that the Cu-spin fluctuations slow down around  $p = 1/8$  per Cu. This relationship between the slowing-down behavior of the Cu spins and the suppression of SC is analogous to that of the  $1/8$  effect established in the La-124 systems.<sup>3,4</sup>) Therefore, in conjunction with the results of the transport measurements,<sup>5</sup>) we can conclude that the  $1/8$  effect is likely to exist in the Bi-2212 system as well. This conclusion supports the suggestion that the  $1/8$  effect is a common feature in the high- $T_c$  SC oxides which have a  $\text{CuO}_2$  plane.

### References

- 1) A. R. Moodenbaugh *et al.*: Phys. Rev. B **38**, 4596 (1988); K. Kumagai *et al.*: J. Mag. Mag. Mater. **76/77**, 601 (1988).
- 2) G. M. Luke *et al.*: Physica C **185/189**, 1175 (1991).
- 3) I. Watanabe *et al.*: J. Phys. Soc. Jpn. **61**, 3058 (1992).
- 4) I. Watanabe *et al.*: Hyperfine Interact. **86**, 603 (1994).
- 5) M. Akoshima *et al.*: Phys. Rev. B **57**, 7491 (1998).
- 6) I. Watanabe *et al.*: Physica B **259/261**, 557 (1999).
- 7) I. Watanabe *et al.*: Phys. Rev. B **60**, R9955 (1999).

\* Graduate School of Engineering, Tohoku University

## LF- $\mu$ SR Studies of the Vortex State in $\text{Bi}_2\text{Sr}_2\text{CaCu}_2\text{O}_x$

N. Nishida, W. Higemoto, I. Watanabe, R. Kadono, K. Nagamine,  
T. Mochiku, K. Hirata,\*<sup>1</sup> R. Sugano,\*<sup>2</sup> and T. Onogi\*<sup>2</sup>

The behavior of flux and vortex lines in high-temperature copper-oxide superconductors (HTSC's) have been intensively studied from both academic points of view and the viewpoint of practical application purposes. In HTSC's, due to their short coherence length, the two-dimensional nature of their superconductivity and the high superconducting transition temperature, thermal fluctuation effects are remarkable and  $H_{c2}(T)$  cannot be well defined, unlike conventional type-II superconductors. In  $\text{Bi}_2\text{Sr}_2\text{CaCu}_2\text{O}_x$  (Bi-2212), the Josephson coupling between superconducting  $\text{CuO}_2$  layers is so weak that in magnetic fields higher than 0.03–0.05 T, the interlayer Josephson coupling is destroyed and a “pancake” vortex is formed in each layer, as schematically illustrated in Fig. 1. The pancake vortices attempt to find stable places in each  $\text{CuO}_2$  layer, interacting magnetically with each other. As a result, the flux lines tend to bend in Bi-2212. The Josephson plasma resonance experiments have revealed the degree of this bending of flux lines.<sup>1)</sup> Below 20–30 K, the pancake vortices are static and exhibit a vortex glass state. At higher temperatures, the vortices become mobile and a vortex liquid state has been proposed on the basis of transport and magnetization measurements. This behavior has been studied by the transverse magnetic field  $\mu^+$  spin rotation methods (TF- $\mu^+$ SR) by Lee *et al.*<sup>2)</sup> It is important and interesting to measure the characteristic time of flux line motion in the vortex liquid state. However, the TF- $\mu^+$ SR method is not able to determine whether the origin of transverse  $\mu^+$  spin depolarization is due to the static inhomogeneity of internal magnetic fields or due to the dynamic fluctuations. We have calculated the transverse component,  $B_{ab}$ , of the internal magnetic fields in Bi-2212 in the vortex state, as depicted in Fig. 1 in the magnetic fields of 0.03 T and 0.05 T applied perpendicular to the c-plane at various temperatures by computer simulation. The average  $B_{ab}$  values have been calculated as  $4 \sim 9 \times 10^{-4}$  T with increasing temperature from 4.2 K to 80 K. If this magnitude of  $B_{ab}$  exists and fluctuates dynamically, then the characteristic fluctuating time can be determined by the longitudinal magnetic field  $\mu^+$  spin relaxation method (LF- $\mu^+$ SR) from an exponential damping of the  $\mu^+$ -e decay asymmetry. Thus, we performed LF- $\mu^+$ SR on single crystals of underdoped Bi-2212 ( $T_c = 83$  K) with high statistics ( $\sim 10^8$  events in each  $\mu^+$ SR spectrum) at the RIKEN-RAL Muon Facility. Figure 2 shows the time evolution of the muon spin polarization under a LF of

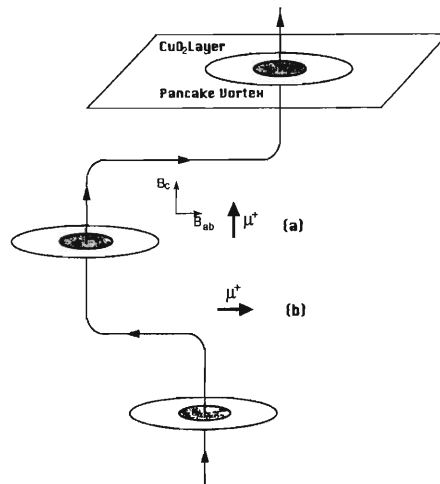


Fig. 1. Pancake vortices are schematically depicted. Small arrows indicate the initial muon spin direction for (a) LF- $\mu$ SR and (b) TF- $\mu$ SR.

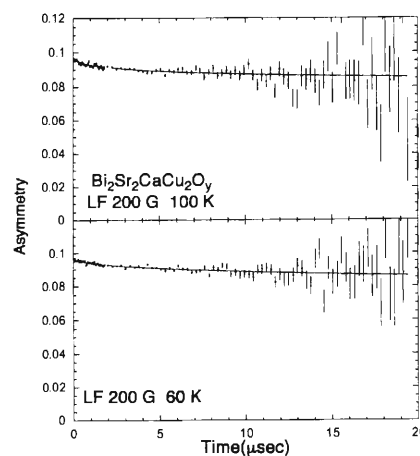


Fig. 2. Time evolution of muon spin polarization under a LF of 0.02 T at 100 K and 60 K.

0.02 T at 100 K (normal phase) and 60 K (superconducting phase and immediately above the vortex lattice melting temperature,  $T_m$ ). The  $T_m$  is determined to be 55 K at 0.02 T by the magnetization measurement. We observed no significant differences between the data. This implies that the timescale of the vortex dynamics is beyond the time range of the LF- $\mu^+$  measurements, that is, the fluctuating time is either fast or static. A detailed analysis is now in progress.

### References

- 1) S. L. Lee *et al.*: Phys. Rev. Lett. **75**, 922 (1995).
- 2) Y. Matsuda *et al.*: Phys. Rev. Lett. **78**, 1972 (1997).

\*<sup>1</sup> NRM

\*<sup>2</sup> Advanced Research Laboratory, Hitachi Ltd.

# Current-Induced Vortex Motion in Type-II Superconductors

W. Higemoto, I. Watanabe, K. Nagamine, S. Kuroda,\* and K. Takita\*

One of the central issues with regard to type-II superconductors is the structure and dynamics of the flux-line lattice (FLL). In the mixed state of type-II superconductors, an external applied electric current imposes the Lorentz force on flux lines, and the motion of the FLL is inhibited by the randomly distributed pinning potential of material defects. Beyond a critical current density, FLL can become free of its pins and flow. This process is complex and its microscopic nature is not well understood. In particular, little is known about the detailed structure and dynamics of FLL as it becomes depinned and flows in response to applied current. Theoretically, the moving glass state is predicted under an external driving force. For example, Koshelev and Vinokur predict the existence of a dynamic phase transition at a characteristic current  $j = j_t$  from the motion of the amorphous vortex configuration (“plastic flow”) at  $j < j_t$  to the motion of the vortex crystal at  $j > j_t$  (“elastic flow”).<sup>1)</sup>

We report the muon spin rotation experiment on high-quality single crystals of  $2H-NbSe_2$ . The  $\mu^+$ SR experiment was carried out at Port 2 of the RIKEN-RAL Muon Facility in the UK. Current flow was synchronized to the pulsed muon beam to prevent an excess Joule heating.

Under the current of 500 A/cm<sup>2</sup>, we did not observe any significant effect of the current in  $\mu$ SR spectra for the normal phase of  $2H-NbSe_2$ . Thus, we consider that the magnetic field induced by a current of 500 A/cm<sup>2</sup> is negligibly small for our measurements of  $2H-NbSe_2$ .

Figure 1 (a) and (b) show the  $\mu$ SR spectra under a field of 100 G of  $2H-NbSe_2$  in the absence of current. As shown in Fig. 1 (a) (normal phase) and (b) (superconducting phase), fast dumping of the muon spin rotation amplitude was observed only in the superconducting phase due to a field distribution in the vortex state. We have fitted the data by the following simple muon spin relaxation function:

$$P(t) = (A \exp(-\sigma^2 t^2) + B) \cos(\omega t + \phi). \quad (1)$$

The solid lines in Fig. 1 are fitting results. By fitting the data, we obtained an asymmetry value of sample A  $\sim 0.013$  and one of background B  $\sim 0.010$ . In the superconducting phase, we found that the relaxation rate under a current of 500 A/cm<sup>2</sup>,  $\sigma_{ON} = 0.78(5) \mu s^{-1}$ , did not differ from that without current,  $\sigma_{OFF} = 0.80(5) \mu s^{-1}$ , within the error. This result indicates that the structures of FLL are nearly the same and the flow velocities of FLL are slower than 1 m/s.<sup>2)</sup> Elastic flows of FLL have been observed under a current

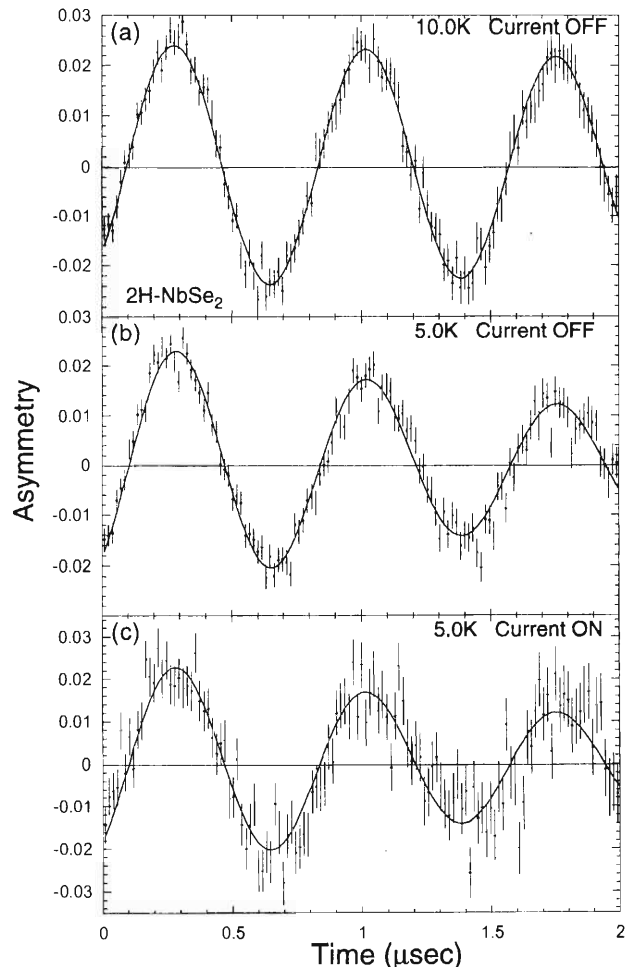


Fig. 1.  $\mu$ SR spectra of  $2H-NbSe_2$  under a magnetic field of 100 G (a) at 10.0 K (normal phase) and  $I = 0$ , (b) at 5.0 K and  $I = 0$ , and (c) at 5.0 K and  $I \sim 500$  A/cm<sup>2</sup>.

greater than  $\sim 30$  A/cm<sup>2</sup> in  $2H-NbSe_2$  by Yaron *et al.*<sup>3)</sup> If we assume that our experiment is also in the elastic flow region and that the velocity of FLL is slow, the structure of FLL under the current was not significantly different from that without current.

In conclusion, our result shows no significant difference in the structure and dynamic behavior of FLL between the presence and absence of an external current in the time window of  $\mu$ SR in  $2H-NbSe_2$ .

## References

- 1) A. E. Koshelev and V. M. Vinokur: Phys. Rev. Lett. **73**, 3580 (1994).
- 2) W. Higemoto et al.: Physica B, in press.
- 3) U. Yaron et al.: Nature **376**, 753 (1995).

\* Institute of Materials Science, University of Tsukuba

# $\mu$ SR Study on the Spin Dynamics of *Kagomé* Antiferromagnet, *m*-MPYNN·BF<sub>4</sub>

I. Watanabe, N. Wada, K. Awaga,\* S. Ohira, and K. Nagamine

The two-dimensional organic antiferromagnet, *m*-MPYNN·BF<sub>4</sub>, has a radical with  $S = \frac{1}{2}$  on each unit molecule which forms the *Kagomé* lattice.<sup>1)</sup> Two radicals form a dimer spin state with  $S = 1$  through the intradimer ferromagnetic interaction  $2J_0/k_B = 23.3$  K and two dimer spins couple through the interdimer antiferromagnet interaction  $2J_0/k_B = -3.1$  K.<sup>2)</sup> Wada *et al.* suggested, based on a susceptibility measurement, that the dimer spin system showed a spin-gap state with a nonmagnetic ground state.<sup>3)</sup> We have carried out  $\mu$ SR measurements at the RIKEN-RAL Muon Facility in the UK using an intense pulsed muon beam in order to investigate the magnetic properties of the dimer spins.

Figure 1 shows the zero-field  $\mu$ SR time spectrum of *m*-MPYNN·BF<sub>4</sub> obtained at 0.30, 165 and 270 K. The total number of muon events was 100 million. The recovery of the asymmetry parameter is clearly observed at around  $t = 8 \mu\text{s}$  at low temperatures. This indicates that the muon spin mainly depolarizes due to randomly distributed static internal fields.

The time spectrum was analyzed using the function  $e^{-\lambda t} \times G_Z(t, \Delta)$ . The first term represents the influence of the dynamically fluctuating dimer spin. The second term is the static Kubo-Toyabe function which represents the muon-spin depolarization due to nuclear dipole fields.<sup>4)</sup>

Figure 2 shows the temperature dependence of the dynamic muon spin depolarization time,  $\frac{1}{\lambda}$ . The de-

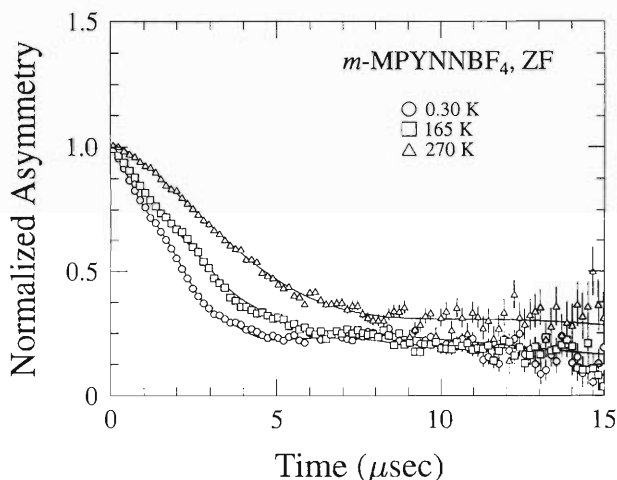


Fig. 1. ZF- $\mu$ SR time spectrum of *m*-MPYNN·BF<sub>4</sub> at 0.30, 165 and 270 K. The total number of muon events was 100 million.

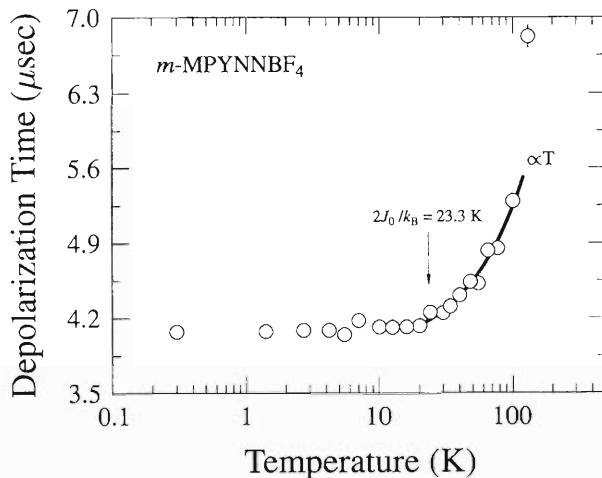


Fig. 2. Temperature dependence of the dynamic muon spin depolarization time which correlates with the dimer spin fluctuations. The dimer spin fluctuations are constant below about 20 K ( $\sim$ dimerization temperature).

polarization time is constant below about 20 K where two radicals form a dimer spin state, showing that the dimer spin fluctuation frequency becomes also constant below this dimerization temperature. The depolarization time exhibits an almost linear temperature dependence above 20 K.

After the dimer spin state is formed, quantum spin fluctuation due to the intradimer ferromagnetic interaction between two radicals is expected. This fluctuation frequency depends upon the exchange energy  $2J_0$ , according to the wave function of quantum mechanics. Since the ferromagnetic exchange energy is  $2J_0/k_B = 23.3$  K,<sup>2)</sup> the quantum fluctuation overcomes the thermal fluctuation of the radical spins below the dimerization temperature. When the ferromagnetic quantum exchange fluctuation is dominant, the fluctuation frequency of the dimer spin is ruled by this quantum fluctuation and is expected to be independent of temperature. Therefore, the constant fluctuation frequency observed below about 20 K indicates that the dimer spin fluctuation is dominated by the intra-dimer ferromagnetic quantum fluctuation.

## References

- 1) K. Awaga *et al.*: Chem. Phys. Lett. **195**, 21 (1992).
- 2) N. Wada *et al.*: Phys. Rev. B **49**, 3975 (1993).
- 3) N. Wada *et al.*: J. Phys. Soc. Jpn. **66**, 961 (1997)
- 4) Y. J. Uemura *et al.*: Phys. Rev. B **31**, 546 (1985).

\* Graduate School of Arts and Sciences, University of Tokyo

# Radio-frequency Muon Spin Resonance of a Haldane-gap System NiC<sub>2</sub>O<sub>4</sub> 2·(2-methylimidazole)

A. Fukaya, I. Watanabe, S. Ohira, and K. Nagamine

Low-dimensional quantum spin systems with anti-ferromagnetic interactions, *e.g.*, the Haldane-gap and spin ladder systems, have attracted much attention. Since these systems possess a nonmagnetic singlet ground state with an energy gap, it is expected that muon spin relaxation cannot be observed at low temperatures. In many compounds, however, an enhancement of muon spin relaxation was observed at low temperatures. In order to clarify the origin of this anomalous enhancement, it is important to examine the spin susceptibility at the muon stopping site. If implanted muons do not affect the magnetic property of a sample, the spin susceptibility at the muon site should follow the bulk susceptibility. We have measured the muon spin resonance with a radio-frequency field (RF- $\mu$ SR) for a Haldane gap system NiC<sub>2</sub>O<sub>4</sub> 2·(2-methylimidazole) in which the anomalous enhancement of muon spin relaxation was observed at low temperatures.<sup>1)</sup>

We used the powder sample of NiC<sub>2</sub>O<sub>4</sub> 2·(2-methylimidazole). RF- $\mu$ SR measurements were performed using a pulsed surface muon beam at the RIKEN-RAL Muon Facility in the UK. We fixed the frequency at 52.800 MHz and swept the longitudinal field (LF). The resonance amplitude is defined as  $A^{\text{on}}/A^{\text{off}}$ , where  $A^{\text{on,off}} \equiv (N_{\text{F}}^{\text{on,off}} - N_{\text{B}}^{\text{on,off}})/(N_{\text{F}}^{\text{on,off}} + N_{\text{B}}^{\text{on,off}})$ .  $N_{\text{F}}^{\text{on,off}}$  and  $N_{\text{B}}^{\text{on,off}}$  denote the integrated-positron-count rate in forward and backward directions, respectively, with the RF power on or off.

The LF dependence of the resonance amplitude (resonance curve) is shown in Fig. 1 (a). As a reference, the temperature dependence of the bulk susceptibility,  $\chi$ , is shown in the inset.  $\chi$  includes the Curie-Weiss term due to impurities; the bulk susceptibility corrected by the Curie-Weiss term,  $\chi_{\text{corr}}$ , is shown by the solid curve. The width of the resonance curve increases and the amplitude decreases with decreasing temperature. It is known that the presence of longitudinal or transverse relaxation increases the width and reduces the amplitude of the resonance curve. The change of the width and amplitude at low temperatures suggests that the longitudinal or transverse relaxation is enhanced with decreasing temperature, which is consistent with the previous results of muon spin relaxation measurements.<sup>1)</sup> We fitted the LF dependence of the resonance amplitude by a Lorentzian function. The shift of the resonance field,  $K$ , obtained by fitting, is shown in Fig. 1 (b).  $K$  is negative. With decreasing temperature,  $K$  increases and shows a peak at

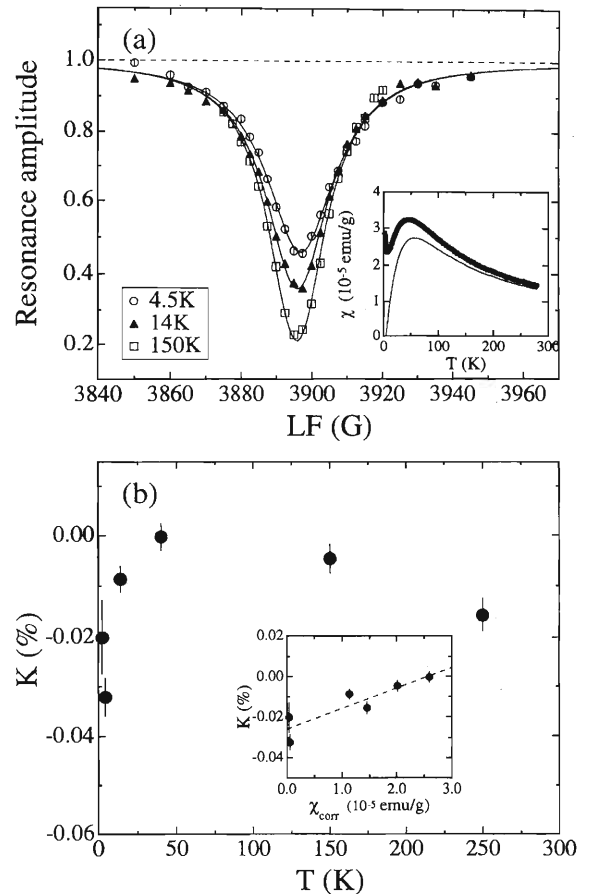


Fig. 1. (a) Longitudinal field dependence of the resonance amplitude. The inset shows bulk susceptibility,  $\chi$ . The solid curve shows  $\chi_{\text{corr}}$ . (b) Temperature dependence of  $K$ . The inset shows  $K$  as a function of  $\chi_{\text{corr}}$ .

around 50 K.

If we assume the existence of a temperature-independent shift of  $\sim -0.025\%$ ,  $K$  seems to show a linear relation with  $\chi_{\text{corr}}$ , as shown in the inset of Fig. 1 (b). This means that  $K$  follows the bulk susceptibility. However, the temperature independent shift of  $\sim -0.025\%$  is much higher than the well-known chemical shift. The origin of the shift has not yet been clarified.

In order to clarify the whole picture of the anomalous enhancement of muon spin relaxation of quantum systems, further study is necessary.

## References

- 1) A. Fukaya et al.: *Hyperfine Interact.* **120/121**, 619 (1999).

## Muon Spin Resonance Study on an Organic Radical TEMPO Derivative

S. Ohira, T. Ishida,\* T. Nogami,\* I. Watanabe, and K. Nagamine

Organic radical magnets with a 2,2,6,6-tetramethylpiperidin-1-yloxy (TEMPO) group have been developed, and their magnetic properties have been studied by various methods.<sup>1,2)</sup> The crystal structures of these systems are known to have a strongly two-dimensional (2D) arrangement of nitronyl radicals, which are localized on each N-O site and contribute to the magnetism.

We have previously carried out muon spin relaxation ( $\mu$ SR) studies on some TEMPO derivatives in order to microscopically observe magnetic transition and critical phenomena.<sup>3,4)</sup> However, the  $\mu$ SR time spectra of organic materials are sometimes difficult to interpret because it is suggested in general that a muonium or muonium-like radical state tends to form in molecular-based materials, namely, muons experiencing large hyperfine fields exist. These components are the so-called *paramagnetic* muons. In order to clarify the muon sites in the TEMPO derivatives and to observe behavior for just a *diamagnetic* muon by distinguishing it from the paramagnetic one, a muon spin resonance study with a radio-frequency field (RF- $\mu$ SR) was carried out on 4-(*p*-chlorobenzylideneamino)-TEMPO (Fig. 1).

The experiment was carried out at the RIKEN-RAL Muon Facility in the UK. Single crystals were prepared and mounted on a mylar sheet so that the *a*-axis was perpendicular to the longitudinal field,  $H_0$ , which was applied along the initial spin direction of the muon. The RF field was applied perpendicular both to  $H_0$  and to the *a*-axis with a frequency of 52.8 MHz.

The muon spin resonance in a diamagnetic environment was observed in the time evolution of the muon spin polarization. Figure 2 shows the resonance curves at 2.5 K, 5 K and 270 K. The double ratio is defined as  $A^{\text{on}}/A^{\text{off}}$ , where  $A^{\text{on}}$  and  $A^{\text{off}}$  are the asymmetries under the conditions where the RF power is on and off, respectively. One resonance peak was observed at each temperature, and a shift of the peak position was observed. The shift provides information about the hyperfine field at the muon site,  $A_{h.f.}^{\mu}$ . Although some possible positions of the diamagnetic muon are suggested from theoretical calculations,<sup>5)</sup> no fine structures were observed in the resonance curves. The observed shift is expected to be a paramagnetic shift. The hyperfine

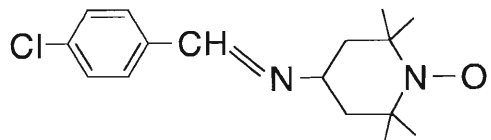


Fig. 1. Molecular structure of 4-(*p*-chlorobenzylideneamino)-TEMPO.

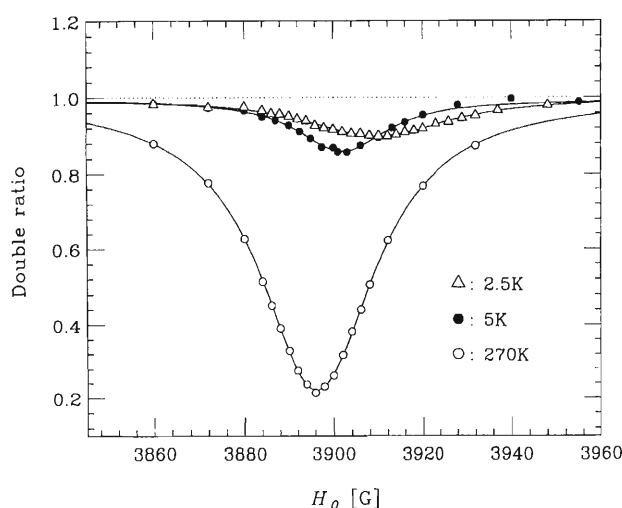


Fig. 2. Resonance curves at 2.5 K, 5 K and 270 K. The muon spin resonance in a diamagnetic environment was observed.

field at the muon site was found to be approximately  $115 \text{ G}/\mu_B$  from the plot of the shift against the susceptibility ( $K$ - $\chi$  plot). The order of the hyperfine field is comparable with the internal magnetic field observed in our previous ZF- $\mu$ SR ( $\sim 230 \text{ G}$ ),<sup>3)</sup> though the hyperfine field value is half that of the internal field value.

### References

- 1) M. Yasui et al.: Mol. Cryst. Liq. Cryst. **279**, 77 (1996).
- 2) T. Nogami et al.: Chem. Lett. **1995**, 635.
- 3) R. Imachi et al.: Chem. Lett. **1997**, 233.
- 4) S. Ohira et al.: RIKEN Rev., No. 20, p. 48 (1999).
- 5) J. Jeong et al.: Physica B, in press.

\* University of Electro-Communications

# Intra- and Inter-molecular Electron Transfer in Cytochrome c and Myoglobin Observed by the Muon Spin Relaxation Method

K. Nagamine, F. L. Pratt, S. Ohira, I. Watanabe, K. Ishida, S. N. Nakamura, and T. Matsuzaki

Electron transfer processes in macromolecules, such as the transfer in proteins, are an important part of many biological phenomena. In order to understand the details of electron transport it is very important to use methods that provide information at a microscopic level.

Among various types of proteins, cytochrome c has attracted much attention, since it plays an essential role in the respiratory electron transport chain in mitochondria, occupying a position next to the final process of the cycle, in which it transfers electrons to the surrounding oxidase complexes. Also, myoglobin is known to serve an important role in oxygen transport and it has a basic molecular structure similar to an electron-transfer protein.

In order to obtain microscopic information on electron transfer in the macromolecule, the muon spin relaxation ( $\mu$ SR) method offers great potential. During the slowing process, the injected  $\mu^+$  picks up one electron to form a neutral atomic state called muonium, which is in many ways analogous to a hydrogen atom. The muonium is then thermalized followed by chemical bonding to a reactive site on the molecule. Then, depending upon the nature of the molecule, the electron brought-in by the  $\mu^+$  can take on several characteristic behaviors, including localization to form a radical state and/or a linear motion along the molecular chain. These behaviors, by setting a time origin of electron movement, can be detected most sensitively by measuring the spin relaxation process of the  $\mu^+$ , which occurs through a magnetic interaction between the  $\mu^+$  and the moving electron produced by the  $\mu^+$  itself, using the  $\mu$ SR method.

Progress has been made in the theoretical understanding of this paramagnetic relaxation process by Risch and Kehr who considered the direct stochastic treatment of the random walk process of a spin which is rapidly diffusing along a topologically one-dimensional chain.<sup>1)</sup> An error-function-type longitudinal relaxation function (hereafter called the R-K function),  $G(t) = \exp(\Gamma t) \operatorname{erfc}(\Gamma t)^{1/2}$ , was proposed for  $\lambda t_{\max} \gg 1$ , where  $\lambda$  is the electron spin flip rate,  $t_{\max}$  the experimental time scale and  $\Gamma$  a relaxation parameter. In this theoretical treatment,  $\Gamma$  is proportional to  $1/B_{\text{ext}}$ .

Experiments on the  $\mu^+$  relaxation in cytochrome c and myoglobin have been conducted using an intense pulsed beam (70 ns pulses at 50 Hz repetition rate) of 4 MeV  $\mu^+$  at the RIKEN-RAL Muon Facility at the Rutherford Appleton Laboratory, UK. The cytochrome c used here is Fe(3+) type in a poly-

crystalline powder form extracted from horse heart (Wako Chemical product), while myoglobin was extracted from horse muscle (Sigma Co., Ltd.).

At each of the measurement temperatures, the  $\mu^+$  relaxation function was found to have an external field dependence in the cases of cytochrome c with Fe(3+) and myoglobin. The observed relaxation functions  $G(t)$  were fitted with the R-K function,<sup>1)</sup> and the longitudinal relaxation parameter  $\Gamma$  obtained at various temperatures were seen to decrease monotonically with increasing  $B_{\text{ext}}$ . On closer inspection of the  $B_{\text{ext}}$  dependence of  $\Gamma$ , there were two components: (1) a region of weak field dependence (lower field) and (2) a  $(B_{\text{ext}})^{-1}$ -dependent region (higher field). The latter region exhibits the characteristic  $\mu^+$  spin relaxation behavior due to the linear motion of a paramagnetic electron. The critical field (hereafter, we refer to this as the cutoff field) where the second region takes over from the first region has a significant temperature dependence; the cutoff field is seen to reduce with decreasing temperature.

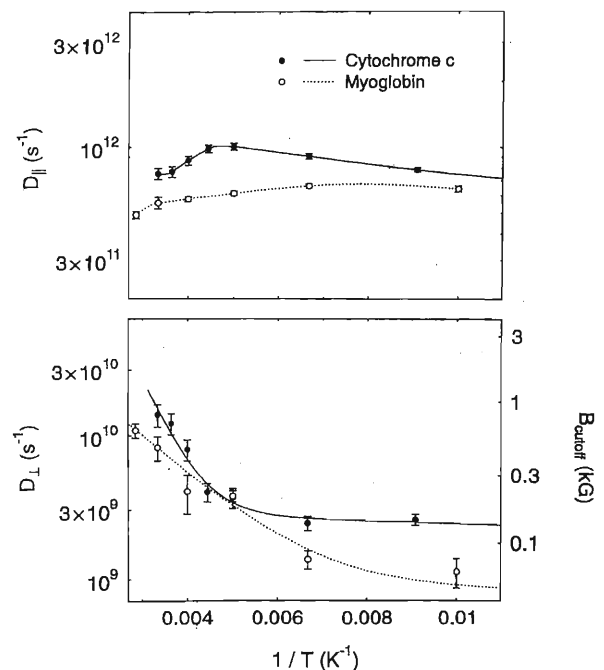


Fig. 1. The upper plot shows the temperature dependence of the parallel diffusion rate of an electron in cytochrome c and myoglobin derived from the  $B^{-1}$ -dependent part of the relaxation parameter. The lower plot shows the perpendicular diffusion rate, derived from the cutoff field, plotted against inverse temperature.

All of these results lead to the following microscopic picture of the electron transfer process for the muon-injected electron in cytochrome *c* and myoglobin.

(1) Topologically linear motion exists along the chain of the cytochrome *c*.

(2) The intersite diffusion rate along chain  $D_{\parallel}$ , which can be obtained from the measured  $\Gamma$  and the hyperfine coupling constant (500 MHz) estimated from the recovery curve of the initial asymmetry, becomes of the order of  $10^{12}$  rad/s and almost temperature independent (Fig. 1).

(3) The cutoff process represents departure on a long time scale from the topologically one-dimensional diffusion which occurs on a short time scale. Depending upon the temperature region, the obtained  $D_{\perp}$  in cytochrome *c* is dominated by two different processes, as seen in the temperature dependence

(Fig. 1); the characteristic change at 200 K of the  $D_{\perp}$  seems to be related to the well-known structural change of some proteins, which has been suggested to be a glass-like transition. On the other hand,  $D_{\perp}$  in myoglobin shows only one component, reflecting the different protein dynamics of this molecule for inter chain electron transfer.

The most important unknown pieces of information are the distribution of the locations of the  $\mu^+$  bonding sites and the corresponding electronic structure around the  $\mu^+$  at the site where the electron begins its linear motion. For this purpose, as reported later, muon spin RF resonance has been conducted on the  $\mu^+$  in both cytochrome *c* and myoglobin.

#### References

- 1) R. Risch and K. W. Kehr: Phys. Rev. B **46**, 5246 (1992).

### 3. Radiochemistry and Nuclear Chemistry



## In-beam Mössbauer Study of $^{57}\text{Mn}/^{57}\text{Fe}$ in Si Following Projectile Fragmentation and Implantation

Y. Kobayashi, Y. Yoshida, A. Yoshida, Y. Watanabe, K. Hayakawa,\* K. Yukihiro,\* F. Shimura,\* and F. Ambe

A radioactive isotope beam (RI beam) produced as a secondary beam after projectile fragmentation of nuclei is becoming very attractive in materials science research. The combined on-line technique of ion implantation using an energetic RI-beam and Mössbauer spectroscopy provides unique features in contrast to conventional-implantation Mössbauer-effect studies and in-beam Mössbauer spectroscopy. The implantation energy of the secondary RI-beam reaches GeV levels, i.e., several orders of magnitude higher than those used in conventional implantation. Thus, it is possible to implant Mössbauer probes into hundreds of  $\mu\text{m}$  depth with a straggling range of a few  $\mu\text{m}$ . In addition, we may be able to vary the range of the measuring time after implantation using different nuclear probes. In the case of  $^{57}\text{Mn}$ , for instance, which decays to  $^{57}\text{Fe}$  with a half-life of 1.45 min, a Mössbauer measurement can be started about 2 minutes after implantation.

In the present study,  $^{57}\text{Mn}$  ions were implanted into a lightly B-doped FZ-Si crystal. We have succeeded in obtaining well-resolved Mössbauer spectra of  $^{57}\text{Fe}$  in Si following the decay of  $^{57}\text{Mn}$  between 30 and 296 K.

A secondary RI-beam of  $^{57}\text{Mn}$  was produced by a projectile-fragmentation reaction between a  $^{59}\text{Co}$  primary beam and a 1-mm-thick Be production target. The energy and intensity of the primary beam were 80 MeV/nucleon and about 200 enA, respectively. The  $^{57}\text{Mn}$  beam was directly implanted into the Si sample after passing through an Al degrader. The total dose was about  $2 \times 10^{10}$   $^{57}\text{Mn}$  ions. Two parallel-plate avalanche counters (PPAC) with  $^{57}\text{Fe}$ -enriched stainless-steel foil, which were mounted on the Mössbauer transducers, were used for  $\gamma$ -ray detection.

According to TRIM<sup>1)</sup> calculation, the projected range of  $^{57}\text{Mn}$  nuclei was estimated to be 150  $\mu\text{m}$  from the surface. The vacancy concentration was  $6.7 \times 10^{-4}$  / $\text{\AA}$ /ion, which was much lower than that in the case of the low-energy implantation.  $^{57}\text{Fe}$  Mössbauer spectra in Si were measured at different temperatures between 30 and 296 K, as shown in Fig. 1. All spectra could be fitted by two singlets of components (A) and (B). The component (A) at 296 K, which has an isomer shift of 0.86(2) mm/s and an area fraction of 0.59, can be assigned to interstitial Fe atoms in Si. The same component was also observed in an in-beam experiment using Coulomb excitation and recoil implantation.<sup>2)</sup> On the other hand, the component (B) has an isomer shift of  $-0.05(4)$  mm/s, which can be attributed to Fe atoms at the substitutional sites in Si by the calculation of

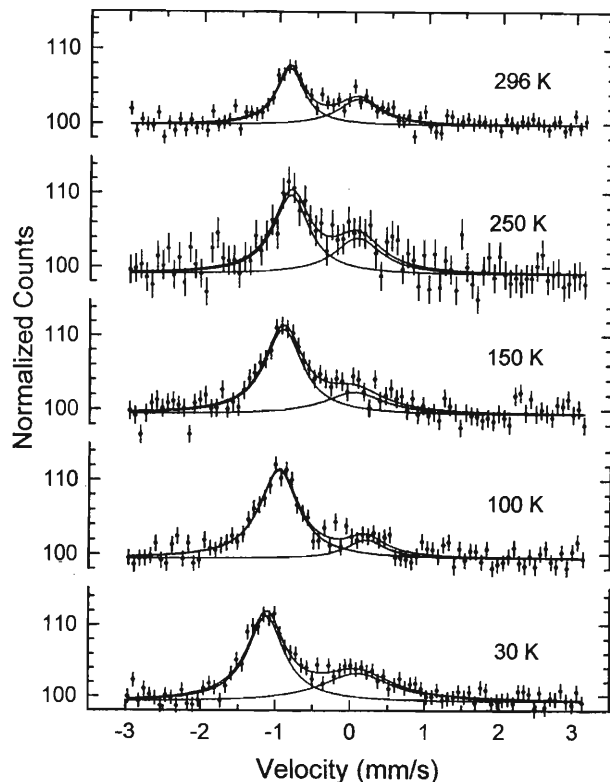


Fig. 1. Mössbauer spectra of  $^{57}\text{Fe}/^{57}\text{Mn}$  implanted into the Si sample, obtained between 296 K and 30 K.

$\delta(\text{Fe}_{\text{sub.}}) = -0.064$  mm/s.<sup>3)</sup> The area fraction of the component (A) did not change at temperatures below 296 K. This means that 60% of the  $^{57}\text{Fe}$  atoms were ultimately at the interstitial sites in Si and 40% at the substitutional sites.

The FWHM of component (B) increased with decreasing temperature below 150 K, so it was considered to have a tendency to be a doublet at low temperatures due to the interaction with vacancies introduced by irradiation with  $^{57}\text{Mn}$  ions. It is interesting to note that none of the spectra measured in the present study contain the doublet corresponding to an “amorphous” state observed in a former study<sup>2)</sup> ( $\delta = 0.23(1)$  mm/s,  $\Gamma = 0.74(2)$ ,  $E_Q = 0.83(1)$  mm/s at 300 K). The difference seems to be either due to the different time range of measurement after the implantation or due to different defect structures around the probes.

Since a secondary RI beam produced via a projectile-fragmentation reaction still maintains a large momentum from the energetic primary beam, one might think that the measured spectrum would be strongly affected by the radiation damage produced

\* Shizuoka Institute of Science and Technology

during the slowing process of such energetic ions in the probes. However, we observed well-resolved spectra, which can be analyzed in terms of two components corresponding to the Fe atoms at the interstitial and substitutional sites. Accordingly, this method offers easy analysis to a wide variety of Mössbauer spectroscopic probes, which provide atomistic information regarding physical quantities at different types of sites

of the probe atoms in a lattice immediately after implantation.

#### References

- 1) J. P. Biersack and L. Haggmark: Nucl. Instrum. Methods **174**, 257 (1980).
- 2) P. Schwalbach et al.: Phys. Rev. Lett. **64**, 1274 (1990).
- 3) G. Langouche: Hyp. Interact. **72**, 217 (1992).

## Biological Transport of the Various Trace Elements in the Pregnant Rats and Fetus

S. Enomoto, R. Hirunuma, H. Tamano, and Y. Kawamura

The placenta functions as a barrier between fetus and mother, providing regulation of heat exchange, respiration, nutrition, and excretion for the fetus. There is limited information on the transport of trace elements from the mother to the fetus.

The multitracer technique is a useful tool for metabolic studies of trace elements and can contain many isotopes simultaneously. In this paper, the multitracer technique was applied to study the maternal transfer of trace elements via the placenta to the fetus.

The radioactive multitracer solution was prepared from an Ag target irradiated with a 135 MeV/nucleon  $^{12}\text{C}$ ,  $^{14}\text{N}$ , or  $^{16}\text{O}$  beam accelerated in the RIKEN Ring Cyclotron. After chemical separation, the multitracer-physiological saline was injected to 17 days pregnant Wistar rats. The pregnant rats were sacrificed under ether anesthesia at 3, 12, 24 and 48 hours after injection. The maternal bloods, placentas, fetuses, fetus brains, and amniotic fluids were taken out from the rats and collected. The radioactivities were determined by  $\gamma$ -ray spectrometry using pure Ge detectors.

In this experiment, the multitracer solution contained the following nuclides:  $^7\text{Be}$ ,  $^{22}\text{Na}$ ,  $^{46}\text{Sc}$ ,  $^{48}\text{V}$ ,  $^{52}\text{Mn}$ ,  $^{59}\text{Fe}$ ,  $^{56}\text{Co}$ ,  $^{65}\text{Zn}$ ,  $^{67}\text{Ga}$ ,  $^{74}\text{As}$ ,  $^{75}\text{Se}$ ,  $^{84}\text{Rb}$ ,  $^{85}\text{Sr}$ ,  $^{87}\text{Y}$ ,  $^{88}\text{Zr}$ ,  $^{96}\text{Tc}$  and  $^{103}\text{Ru}$ . We examined the time dependence of the uptake of various elements. From these results, we observed a significant difference in time dependency between each element. The elements were divided into three groups (Fig. 1). In the first group, Be, V, As, Ru, Y, Zr and Tc were transported to the placenta from the maternal blood and only accumulate in the placenta. In the second group, Na, Sc, Co,

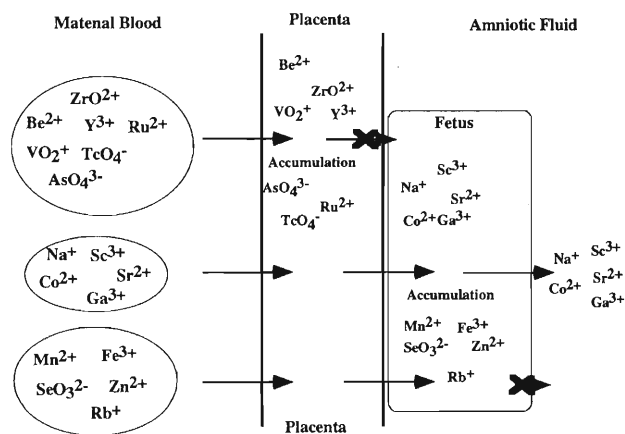


Fig. 1. Transport of trace elements from the maternal blood to the placenta and fetus. Chemical forms of various tracers in saline are indicated.

Ga, and Sr were transported to the placenta from the maternal blood and accumulates in the placenta, fetus, and amniotic fluid. In the third group elements, Mn, Fe, Se, Zn, and Rb were transported to the placenta from the maternal blood and mainly accumulates in the fetus. Based on the above results, it was considered that the placenta is highly selective because essential elements such as those in the third group are readily transported across placenta/membranes to the growing fetus, whereas nonessential metals such as those in the first group hardly penetrated the placental barrier that protects the fetus from toxic effects.

## Uptake of Zinc and Other Trace Metals in Tumor-bearing Murines

H. Tamano, S. Enomoto, and A. Takeda

Zinc is an important nutrient for both normal and malignant tissues.<sup>1)</sup> The growth of malignant tissue is effectively inhibited by zinc deprivation.<sup>2,3)</sup> Therefore, a host response of zinc mobilization might influence the proliferation of malignant tissue, and a competition for zinc might occur between host and malignant tissue. Clarification of the zinc mobilization pattern after tumor transplantation is important for an understanding of zinc homeostasis. In the present study, the zinc uptake in tumor-bearing murines was examined. Furthermore, uptakes of other trace elements in tumor-bearing mice were also examined by the multi-tracer technique.

Male rats of the Donryu strain (160–180 g) were subcutaneously (s.c.) transplanted with ascitic fluid from rats with hepatoma ( $1 \times 10^7$ /ml, 0.2 ml/rat) and male mice of the ddY strain (25–30 g) were s.c. transplanted with Ehrlich carcinoma cells ( $1 \times 10^7$ /ml, 0.2 ml/mice). Ten days after the tumor transplantation, radiolabeled zinc chloride ( $^{65}\text{ZnCl}_2$  purchased from Du Pont/NEN Research products, Boston, MA) in 0.1 M acetate buffer (pH 4.0) was intravenously (i.v.) injected into the control and tumor-bearing murines. One hour after the injection, blood was drawn and the tissues to be studied were excised. The radioactivity level of the specimens was determined using a  $\gamma$ -counter. As shown by the data in Fig. 1, one hour after the i.v. injection, the  $^{65}\text{Zn}$  uptake by the tumor was lower than that by liver, kidney and pancreas. On the other hand, the hepatic  $^{65}\text{Zn}$  level in tumor-bearing rats was significantly higher than that in control rats, while the blood  $^{65}\text{Zn}$  level in the former was significantly lower than that in the latter. Similar results were also observed in tumor-bearing mice.

The uptake of other radioactive metals, which were prepared as a multitracer solution, was determined in Ehrlich carcinoma-bearing and control mice (7 days after transplantation) 3, 24 and 48 hours after the injection. The multitracer solution contained radioactive

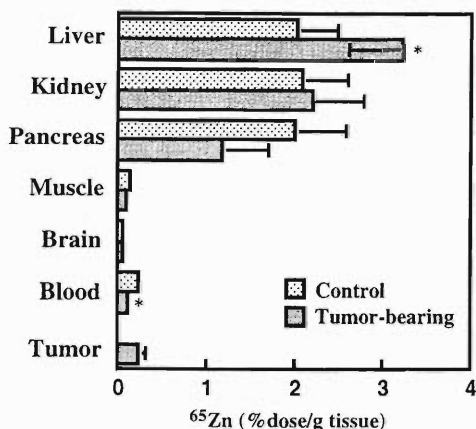


Fig. 1.  $^{65}\text{Zn}$  uptake by tissues in rats 10 days after the transplantation of AH7974F (\*,  $P < 0.05$ ).

Be, Sc, Zn, Rb, Y, Zr, Te, Ba, Hf, Ir, Pt, Ce, Eu, Gd, Yb and Lu. The  $\gamma$ -ray spectra in excised tissues were measured using a germanium detector. At 48 hours after the injection, the uptake of some radionuclides, e.g., Sc and Y, by the tumor was relatively high compared to that in normal tissues such as the liver, muscle and blood.

In conclusion, these results suggest that, in tumor-bearing murines, the Zn uptake is preferentially increased in the liver. Moreover, using the multitracer technique, some rare earth elements were observed to accumulate more in tumor tissue than in normal tissues.

### References

- 1) B. L. Vallee and K. H. Falchuk: *Physiol. Rev.* **73**, 79 (1993).
- 2) D. T. Minkel, P. J. Dolhun, B. L. Calhoun, L. A. Saryan, and D. H. Petering: *Cancer Res.* **39**, 2451 (1979).
- 3) L. A. Saryan, D. T. Minkel, P. J. Dolhun, B. L. Calhoun, S. Wielgus, M. Schaller, and D. H. Petering: *Cancer Res.* **39**, 2457 (1979).

## Biological Tissue Distribution of Vanadium in STZ-Induced Diabetic Rats: Simultaneous Tracing of V, Cr, Mn, Fe, Co, Zn, and Se Using a Radioactive Multitracer

H. Yasui, T. Takino, J. Fugono, R. Hirunuma, S. Enomoto, and H. Sakurai

The biological actions of vanadium have been investigated by many researchers. The insulin-mimetic effect of vanadium is the most remarkable among its several biological actions. Recently, vanadyl ions (+4 oxidation state of vanadium) and its complexes have been shown to normalize the blood glucose levels in streptozotocin-induced diabetic rats (STZ-induced diabetic rats). We have carried out experiments to find vanadyl complexes with more effective insulin-mimetic activity and prepare less toxic complexes using various types of coordination modes.<sup>1)</sup> Vanadyl-methylpicolinate complex (VO-MPA) containing VO(N<sub>2</sub>O<sub>2</sub>) exhibited more effective and longer lasting insulin-mimetic activities and less toxicity after oral administration than other complexes in the *in vivo* experiments.<sup>2)</sup>

In the present investigation of the metabolism of trace elements, we studied the biological tissue distribution of vanadium as well as other trace elements in normal, STZ-induced diabetic, and vanadyl sulfate (VS)-administered rats, to elucidate the relationship between the blood glucose normalizing effects and global disposition of trace elements including vanadium. In this experiment, we used VS as a positive control compound to examine the effects of vanadium on the tissue distribution of trace elements before testing VO-MPA.

A multitracer solution containing the radioisotopes of 20 elements was prepared from an Ag target irradiated by a heavy-ion beam of 135 MeV/nucleon accelerated by the RIKEN Ring Cyclotron. Vanadyl sulfate (VOSO<sub>4</sub> · 4H<sub>2</sub>O) was purchased and used as the positive control compound. Male Wistar rats (body wt. ~250 g) were divided in three groups, that is, normal, STZ-induced diabetic, and VS-administered groups. Rats treated with VS were administered three intraperitoneal (*i.p.*) injections of VOSO<sub>4</sub> at doses of 10 mgV/kg body weight once a day for three days. The multitracer solution was injected intraperitoneally (1.0 ml/rat). The rats were sacrificed at 12, 24 and 72 hrs after the administration, and blood samples were collected and selected organs (liver, kidney, muscle, and bone) were removed from the rats in each

group (n = 4). The radioactivity levels in their blood, liver, kidney, muscle, and bone was determined by  $\gamma$ -ray spectrometry. The observed  $\gamma$ -rays were analyzed in terms of their energies and half-lives. The individual behavior of Be, Na, Ca, Sc, V, Cr, Mn, Fe, Co, Zn, Ga, As, Se, Rb, Sr, Y, Zr, Tc, Ru, and Rh was examined. The obtained time courses of amount of each of the trace element in each organ were evaluated by noncompartmental analysis (moment analysis). Furthermore, we developed a novel evaluation method to directly compare the biodistribution of trace elements in normal rats with that in STZ-induced diabetic rats, using the ratio plots of tissue uptake (% of dose) of every trace element.

The mean tissue uptake rates of <sup>48</sup>V by the four tissues and blood of the rats were determined. The highest uptake of <sup>48</sup>V was observed in the kidney of all groups. The uptake rates of <sup>48</sup>V were observed to decrease with time except for that by the bone, which was increased at 72 hr in comparison with that at 12 and 24 hrs. These results are in good agreement with our previous pharmacokinetic analyses of the tissue distribution of vanadyl compounds by means of neutron activation analysis (NAA).

In addition, the amounts of other trace elements accumulated in the tissues were simultaneously determined by the radioactive multitracer technique. The effect of preadministered VS on the accumulation of trace elements in the tissues was most significant in the bone. These results suggest that the accumulation of vanadium in the body may alter the global disposition and tissue distribution processes of several trace elements. Therefore the relationship between the antidiabetic activity of the vanadyl compounds and the biobehavior of other essential trace elements must be clarified in detail.

### References

- 1) H. Sakurai, H. Watanabe, H. Tamura, H. Yasui, R. Matsushita, and J. Takada: *Inorg. Chim. Acta* **283**, 175 (1998).
- 2) S. Fujimoto, K. Fujii, H. Yasui, R. Matsushita, J. Takada, and H. Sakurai: *J. Clin. Biochem. Nutr.* **23**, 113 (1997).

## Metabolic Study of Trace Elements in Se-Deficient Rats (IV)

R. Hirunuma, K. Endo, and S. Enomoto

Selenium is an essential element to mammals but poisonous at high doses.<sup>1)</sup> It was reported that Se exhibits a competitive or synergetic relationship with several elements such as Hg and Cd.<sup>2,3)</sup> Therefore, the distribution of other trace elements in various organs is expected to be influenced by the amount of Se fed to mammals. However, no systematic study has been reported on the behavior of trace elements in Se-deficient rats. This paper describes the uptake and distribution of trace elements in Se-deficient rats by the multitracer technique and instrumental neutron activation analysis (INAA).

Wistar male rats bred from fetal stage on a Se-deficient diet (produced by Oriental Yeast Co., Ltd.) were used in these experiments as Se-deficient rats. Control rats were fed with the Se-deficient diet supplemented with 0.2 ppm of Se (adequate level of Se for normal growth).

In the first experiment, a multitracer solution containing various kinds of radionuclides was prepared from an Ag target irradiated with <sup>14</sup>N beam of 135 MeV/nucleon accelerated in the RIKEN Ring Cyclotron. The multitracer solution was injected intravenously into each rat. The Se-deficient and control rats were sacrificed at 3, 12, 24, and 72 hours after injection, and the radioactivities in the brain, liver, kidney, spleen, and testicles were measured using high-purity Ge detectors. The distribution of Se, Fe, and Zn in various organs of the rats was evaluated.

In the second experiment, the 12-week-old Se-deficient and control rats were sacrificed and the organs were obtained. Each organ was lyophilized, pulverized, and then irradiated with the thermal neutron flux of

$1.5 \times 10^{12} \text{ n cm}^{-2} \text{ s}^{-1}$  at F-24C in TRIGA II nuclear reactor of Rikkyo University.

Table 1 shows the Se, Fe, and Zn concentration in various organs of each rat determined by INAA. As for the Se-deficient rats, only a small amount of Se was found in all organs. Iron concentration in the liver and spleen of Se-deficient rats was higher than that of control ones. However, no difference in the concentration of Zn between Se-deficient and control rats was observed.

Figure 1 shows the uptake of Se, Fe, and Zn in various organs of the Se-deficient and control rats, as determined by the multitracer technique. Influences due to Se-deficiency were observed on the distribution pattern of Se and Fe in various organs. The uptake of Se was higher in the brain of the Se-deficient rats than in that of the control ones. In the liver, the uptake of Se in the control rats was higher than that in the Se-deficient ones. In the case of control rats, the uptake of Se in the liver was much higher than that in the brain. However, the uptake in the liver was

Table 1. Concentration (ppm) of Se, Fe, and Zn in various organs of Se-deficient and control rats.

Se	Brain	Kidney	Liver	Spleen	Testicles
Se-deficient	0.6±0.1	0.6±0.1	0.07±0.03	0.3±0.1	2.4±0.2
Control	1.0±0.1	7.9±1.0	3.1±0.3	2.3±0.2	10.3±1.4
Fe	Brain	Kidney	Liver	Spleen	Testicles
Se-deficient	130±20	300±35	654±41	2434±247	157±10
Control	160±24	258±26	452±45	1431±241	150±13
Zn	Brain	Kidney	Liver	Spleen	Testicles
Se-deficient	61±3	124±23	97±9	86±4	202±10
Control	59±4	100±17	87±6	90±6	215±19

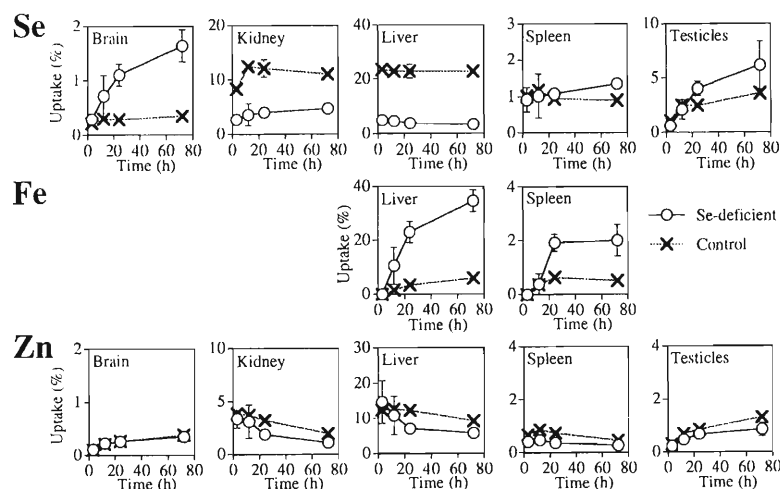


Fig. 1. Uptake of Se, Fe, and Zn in various organs of the Se-deficient and control rats.

almost comparative to that in the brain of Se-deficient rats. It is reported that a small quantity of Se fed to Se-deficient rats is absorbed preferentially in the brain over the liver.<sup>1)</sup> It is considered that the results described above are attributed to this reason. No difference was detected in the uptake of Zn between Se-deficient and control rats. On the other hand, uptake of Fe in Se-deficient rats was higher than that in control ones. The uptake of Fe in the liver of Se-deficient rats increased with time. The increase in Fe uptake by Se-deficient rats suggests an increase in Fe-containing proteins. The concentration of Fe-containing proteins, such as hemoglobin, transferrin, and ferritin was measured in the serum of Se-deficient

and control rats. The concentration of ferritin in Se-deficient rats was found to be high. The increase in Fe uptake by Se-deficient rats caused an increase in the concentration of Fe-binding proteins, such as ferritin. We suggest that ferritin in excessive amounts promotes peroxidation of cell membranes that results in cell damage.

#### References

- 1) D. Behne et al.: *Biochim. Biophys. Acta* **966**, 12 (1988).
- 2) T. Urano et al.: *Biochem. Biophys. Res. Commun.* **239**, 862 (1997).
- 3) J. Gambhir and R. Nath: *Indian J. Exp. Biol.* **30**, 597 (1992).

## Distribution of Bio-Trace Elements in Cell Fraction of Selenium-Deficient Rat Liver

K. Matsumoto, Y. Ueda,\* K. Endo, R. Hirunuma, and S. Enomoto

Selenium (Se) is the essential trace element that constitutes the active center of glutathione peroxidase (GSH-Px). It is believed that Se plays a protective role against oxidative stress in living organisms. On the other hand, it is known that Se interacts with other metal ions in biological systems. For example, the accumulation of iron (Fe) in Se-deficient rat liver, kidney, and spleen has already been reported in a previous paper, and we observed that Fe uptake increased in Se-deficient rat liver.<sup>1)</sup> However, the mechanism of Fe accumulation in the liver of Se-deficient rats has not yet been clarified. In living organisms, Fe constitutes the active center of catalase, cytochrome P-450, and xanthine oxidase, and is related to the digestion and synthesis of reactive oxygen species. Therefore, the change of *in vivo* redox reaction valence due to decreased GSH-Px activity is expected to cause the change of the Fe dynamics in Se-deficient rats.

In this experiment, using instrumental neutron activation analysis (INAA) and multitracer analysis (MTA), we examined the dynamics of metal ions which are related to *in vivo* redox regulation systems such as Se, Fe, manganese (Mn), cobalt (Co), and zinc (Zn) in liver cell fractions of Se-deficient rats.

Se-deficient and normal male Wistar rats (8 weeks old) were sacrificed by bleeding from the abdominal aorta under anesthesia. Subsequently, the liver was perfused with 0.9% NaCl. The liver was removed and homogenized with a threefold volume of 1.15% KCl. Then, nuclear (NU), mitochondrial (MT), microsomal (MC), and cytosolic (CS) fractions were separated by centrifugation. In the INAA experiment, each fraction was lyophilized. Then, an aliquot of each powdered fraction was weighed and sealed in polyethylene. Neutron irradiation was carried out in the TRIGA II nuclear reactor of Rikkyo University. Bovine liver (NBS SRM 1577) was used as a standard sample. In the MTA experiment, each cell fraction was prepared 2 days after intravenous administration of the multitracer. An aliquot of each wet fraction was put into a plastic tube. The  $\gamma$ -ray spectra of the INAA and MTA samples were measured with a high-purity Ge semiconductor detector equipped with a multichannel analyzer. In the present study, we focused our spectral analysis only on Se, Co, Mn, Zn, and Fe.

The Se contents of the separated fractions of the normal rats obtained by INAA were 2.5 ppm in MT, 1.5 ppm in MC, and 3.1 ppm in CS, respectively. In contrast, the Se contents in all the separated fractions

of the liver homogenates of Se-deficient rats were below the detection limit, which was estimated to be 0.04 ppm in the dried sample as the upper limit for Se under the present experimental conditions. The peak identification of  $\gamma$ -ray spectra was based on a criterion of greater than  $3\sigma$  (three times the standard deviation of the background counts).

The uptake of Se was determined using MTA. The results indicated that the uptake (percentage to the standard) of Se into each fraction of rat liver homogenates was not significantly different. This is believed to be due to the absence of a specific transportation system for Se.

The content of Co also decreased in Se-deficient rats compared with the normal ones, and this was believed to be due to the low content of Co in the diet. However, MTA data indicated that the uptake of Co increased in cell fractions other than CS, suggesting that the enhancement of the uptake was due to the supplement effect because of the insufficient content of Co in the Se-deficient diet.

The uptake of Mn into the MT, MC, and CS fractions of Se-deficient rats was lower than that of normal rats except for increased uptake into the NU fraction. The uptake of Zn into the CS fraction of Se-deficient rats decreased, although the uptake of Zn into the other fractions increased. The INAA data indicate that the contents of Mn and Zn in the MT and CS fractions of liver were lower in Se-deficient rats than normal rats. These two elements are known to be the active centers of Mn-SOD and Cu,Zn-SOD, and are located mainly in MT and CS fractions, respectively. The lower uptake and contents of Mn in the MT fraction and Zn in the CS fraction of Se-deficient rat liver may be responsible for the decrease of the SOD activity in these cell fractions.

The content of Fe significantly increased in Se-deficient rats, especially in the MC fraction. This is believed to be due to the change of activity of cytochrome P-450 which exists in the MC fraction. On the other hand, if the Fe existed as free-ion form (or could be coordinated by easily exchangeable ligand molecules), an increase of hydroxyl radical synthesis through the Fenton reaction and peroxidation of the lipid membrane could be expected. Although Fe uptake increased in the MC fraction of Se-deficient rat liver, its increment was not large (less than 0.2%).

### References

- 1) R. Hirunuma et al.: J. Radioanal. Nucl. Chem. **239**, 213 (1999).

\* Showa College of Pharmaceutical Sciences

## Effect of Dietary Selenium Species and Doses on the Organ Distribution of Multitracer

Y. Shiobara, Y. Ogra, R. Hirunuma, S. Enomoto, and K. T. Suzuki

Selenium (Se) is an essential trace element for mammals, and both inorganic and organic Se can be utilized as a nutritional source by the body. Inorganic Se in the form of selenite and selenate and organic Se in the form of selenocysteine (SeCys) are reduced by glutathione and glutathione reductase and metabolized by  $\beta$ -lyase, respectively, to the assumed key compound, selenide ( $H_2Se$ ). Selenide is, then, utilized for the synthesis of selenoproteins or excreted in urine and/or by respiration after being methylated. On the other hand, selenomethionine (SeMet) taken up by the body is incorporated either into general proteins without being distinguished from methionine or metabolized to selenide.

Our previous study showed that the chemical species and concentration of Se in the diet influence the concentration of Se in hair, blood,<sup>1)</sup> liver and kidneys. In particular, the Se concentration in hair, blood, liver and kidneys of rats fed with a SeMet-excessive diet was higher than that of rats fed with a selenite-excessive diet. Selenium has been known to interact with toxic heavy metals (*e.g.*, Hg and Cd) and to decrease the toxicity of Se and other metals.

In the present study, effects of the chemical species and concentration of Se in the diet on the uptake, distribution and excretion of other metals (Mn, Co, Zn, Se and Hg) administered intravenously (iv) at a low dose, were examined by the multitracer technique.

A multitracer solution containing radioisotopes of 17 elements (Be, Na, Ca, Sc, V, Cr, Mn, Fe, Co, Zn, Ga, As, Se, Rb, Y, Zr and Tc) was prepared from an Ag target irradiated with a heavy-ion beam of 135 MeV/nucleon accelerated by the RIKEN Ring Cyclotron. Then, the multitracer solution was mixed with a  $^{203}Hg$  solution, and administered iv to rats at a dose of 0.2 ml/rat.

Male rats of the Wistar strain (4 weeks old) were fed a Se-deficient (concentration of Se, less than 0.03 mg Se/kg diet), selenite-adequate (0.2 mg Se/kg diet), selenite-excessive (2.0 mg Se/kg diet), SeMet-adequate (0.2 mg Se/kg diet) or SeMet-excessive (2.0 mg Se/kg diet) diet for 2 weeks. At 6 weeks of age, all groups of rats were administered a multitracer solution containing  $^{203}Hg$ , and sacrificed 96 hr after the injection. The radio/activities in the organs (liver, kidneys, testes, spleen and brain), whole blood, plasma, hair, urine and feces were determined by  $\gamma$ -ray spectrometry and the observed  $\gamma$  rays were assigned in terms of their energies and half-lives to the individual behavior of Mn, Co, Zn, Se and Hg.

Table 1. Effect of dietary Se on uptake of tracers (Mn and Se) in the liver and kidneys.

group	liver (% of recovery)		kidney (% of recovery)	
	Mn	Se	Mn	Se
Se-deficient	6.45 $\pm$ 0.07	5.16 $\pm$ 0.13	3.38 $\pm$ 0.13	5.08 $\pm$ 0.25
Selenite-adequate	7.99 $\pm$ 0.43*	8.12 $\pm$ 0.26*	3.15 $\pm$ 0.25	3.38 $\pm$ 0.17*
Selenite-excessive	5.74 $\pm$ 0.22*	2.41 $\pm$ 0.20*	2.24 $\pm$ 0.37*	0.94 $\pm$ 0.07*
SeMet-adequate	7.31 $\pm$ 0.47	7.52 $\pm$ 0.05*	2.86 $\pm$ 0.17*	2.91 $\pm$ 0.11*
SeMet-excessive	5.58 $\pm$ 1.15	2.30 $\pm$ 0.19*	2.38 $\pm$ 0.35*	0.90 $\pm$ 0.10*

\*Significant difference from the Se-deficient group at  $p < 0.05$  ( $n=3$ ).

The behavior of radioisotope Se in each group showed that the  $^{75}Se$  distribution levels in the plasma, kidneys, testes, spleen and brain were inversely proportional to the dietary Se concentration. However, in the liver and blood, the  $^{75}Se$  recovery of the adequate groups were higher than that of the deficient group. These results were assumed to be caused by the dilution of  $^{75}Se$  with dietary Se. The behavior of the radioisotope Hg in each group showed that the  $^{203}Hg$  distribution level in the liver was inversely proportional to the dietary Se concentration.

With respect to Zn and Co, there was almost no influence on the uptake, distribution and excretion by the chemical species or concentrations of the dietary Se.

In the liver, kidneys, testes, spleen, plasma and feces, the distribution of Mn was similar to that of  $^{75}Se$  (Table 1). In other words, the Mn distribution level in the kidneys, testes, spleen, plasma and feces was inversely proportional to the dietary Se concentration. The mechanism underlying the similarity of the Mn uptake to that of  $^{75}Se$  is not clear at present because of the diverse biological functions of Mn in the body. However, the accelerated uptake of Mn may be related to oxidative stress under Se-deficient conditions.

Statistical analysis was performed by two-way ANOVA to compare the mean values between excessive or adequate and deficient groups.

In conclusion, although the effects of chemical species of dietary Se on the distributions of Zn, Co, Mn, Se and Hg were not observed, the effects of differing concentrations of dietary Se on the distributions of Se, Hg and Mn were demonstrated.

### References

- 1) Y. Shiobara et al.: *Toxicol. Appl. Pharmacol.* **152**, 309 (1998).

## Uptake Rates of Trace Elements in Zn-Deficient Mice

T. Ohyama, T. Yoshida, M. Iwama, M. Yanaga, M. Noguchi,<sup>\*1</sup> T. Omori,<sup>\*2</sup> R. Hirunuma, and S. Enomoto

Zinc is one of the most essential trace elements in living organisms, and is second only to iron in abundance. More than 300 Zn-proteins have been identified, and deficiency of this element leads to various symptoms, such as growth retardation, hypogonadism, immunodeficiency and alopecia.

The concentrations of Zn and other trace elements in various organs and tissues of Zn-deficient and control mice were determined by instrumental neutron activation analysis (INAA).<sup>1,2)</sup> Zinc concentrations in the bone and pancreas of Zn-deficient mice were significantly lower than those in control mice, although those in the other organs and tissues of Zn-deficient mice were not. It is believed that Zn is supplied from the bone to other organs, where it supports various functions. The Co concentrations in Zn-deficient mice, in however, were significantly increased in all organs and tissues.

The multitracer technique is a suitable method to investigate the behavior of these trace elements *in vivo*. This technique enables us to trace various elements simultaneously under identical conditions. In this study, the uptake rates of trace elements in Zn-deficient mice were examined using the multitracer technique and compared with the results obtained previously using INAA.

Seven-week-old male mice of the ICR strain were purchased and fed with a commercial diet and tap water. After one week, they were divided into two groups. The Zn-deficient group was fed Zn-deficient diet and distilled water (Zn-deficient mice), and the control group was fed control diet (the control diet consisted of the raw materials for the Zn-deficient diet and Zn in the form of zinc carbonate) and distilled water (control mice). After three weeks, a multitracer physiological saline solution, which was prepared from Ag foil by a previously reported method,<sup>3)</sup> was injected intraperitoneally into each mouse (0.2 ml/mouse). Six, 24 or 72 hours after the injection, they were sacrificed under diethyl ether anesthesia. Then, the brain, liver, kidney, pancreas, spleen, testis, skeletal muscle, bone and skin were removed. These organs and tissues were weighed immediately and their radioactivity levels were measured with HP Ge detectors.

The uptake rates of various trace elements by the bone are shown in Fig. 1. The uptake rate of Zn 24 and 72 hours after the injection of Zn in Zn-deficient mice decreased significantly compared with that in control mice. On the other hand, the uptake rates of Zn in

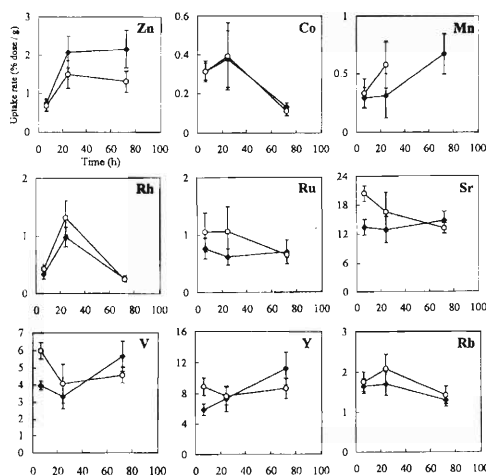


Fig. 1. Uptake rates of trace elements by the bone of Zn-deficient mice (○) and control mice (◆) 6–72 hours after intraperitoneally injection of a multitracer saline solution.

the liver, kidney and spleen in Zn-deficient mice were higher than those in control mice (data not shown), although the Zn concentrations determined by INAA in these organs of Zn-deficient mice were similar to those in control mice. These findings suggest that Zn is not only transferred from the bone to the liver, kidney and spleen, but is also taken up by these organs preferentially. Our previous works have shown that the Co concentrations in all the organs and tissues of Zn-deficient mice were higher than those in control mice.<sup>1,2)</sup> However, there were no significant differences in the uptake rates of Co in most of the organs and tissues between Zn-deficient mice and control mice. Our experiments using the INAA method showed that the accumulation of Co in Zn-deficient mice was saturated within a three-week treatment period. This might be one of reasons why no significant differences were recognized in the uptake rates of Co. It was found, furthermore, that the behavior of Sr was similar to that of V and Y in both Zn-deficient and control mice, as shown in Fig. 1. However, the uptake rate of the typical bone-seeking element, Sr, was decreased in Zn-deficient mice with the passage of time after injection.

### References

- 1) M. Yanaga, M. Iwama, K. Takiguchi, M. Noguchi, and T. Omori: *J. Radioanal. Nucl. Chem.* **231**, 187 (1998).
- 2) M. Yanaga, M. Iwama, K. Shinotsuka, K. Takiguchi, M. Noguchi, and T. Omori: *J. Radioanal. Nucl. Chem.*, in press.
- 3) M. Yanaga, T. Ohyama, M. Iwama, T. Yoshida, M. Noguchi, T. Omori, R. Hirunuma, and S. Enomoto: *RIKEN Accel. Prog. Rep.* **32**, 127 (1999).

<sup>\*1</sup> Department of Biology and Geosciences, Shizuoka University

<sup>\*2</sup> Radiochemistry Research Laboratory, Shizuoka University

## Characterization of Manganese Transport System Using Cadmium-Resistant Metallothionein-Null Cells

T. Yanagiya, N. Imura,\*<sup>1</sup> S. Enomoto, Y. Kondo,\*<sup>2</sup> and S. Himeno

Cadmium (Cd) is an environmental pollutant that has adverse effects on cells and animals. Despite the toxic effects of Cd in animals being well documented, the transport mechanisms of Cd are poorly understood. Previously, we reported that a Cd-resistant cell line (Cd-rB5) derived from immortalized metallothionein (MT)-null fibroblasts exhibited a marked decrease in cadmium uptake as compared with that by the parental MT-null cells, suggesting that changes in the cadmium transport mechanism are responsible for resistance to cadmium.<sup>1)</sup> Furthermore, when a multitracer solution was added to the medium of Cd-rB5 and parental cells, only Mn uptake was reduced in Cd-rB5.<sup>2)</sup> However, the reduced uptake of Mn was observed only at low concentrations, suggesting that a high-affinity component of the Mn transport system is down regulated in Cd-rB5 cells.<sup>2)</sup>

In the present study, to investigate the substrate specificity of the high-affinity Cd-Mn transporter, we examined the inhibitory effects of metal ions such as Zn, Co, Ni, Fe and Cu on the cellular uptake of Cd and Mn in parental cells. As shown in Fig. 1, the uptake of Cd was inhibited by Zn as well as Mn, but not by Co, Ni, Fe and Cu. Similarly, cellular uptake of Mn

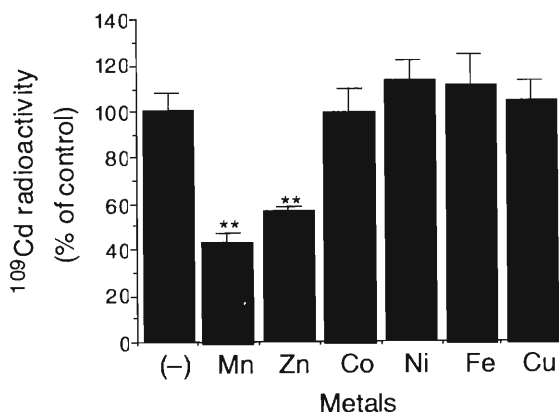


Fig. 1. Effects of various metals on the uptake of Cd by parental cells. Parental cells were exposed to 0.03  $\mu$ M [<sup>109</sup>Cd]-CdCl<sub>2</sub> in the presence of 5-fold excess amounts of MnCl<sub>2</sub>, ZnCl<sub>2</sub>, CoCl<sub>2</sub>, NiCl<sub>2</sub>, FeSO<sub>4</sub> or CuCl<sub>2</sub> for 15 min. Significantly different values were obtained in the absence of metal inhibitors (\*\*,  $p < 0.01$ ).

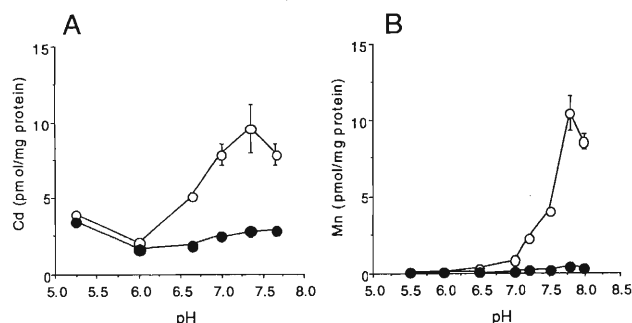


Fig. 2. pH-dependency of Cd and Mn uptake by Cd-rB5 and parental cells. A: Cd-rB5 (closed circles) and parental cells (open circles) were exposed to 0.03  $\mu$ M [<sup>109</sup>Cd]-CdCl<sub>2</sub> for 15 min in the medium adjusted to a specific pH. B: Cd-rB5 (closed circles) and parental cells (open circles) were exposed to 0.03  $\mu$ M [<sup>54</sup>Mn]-MnCl<sub>2</sub> for 15 min in the medium adjusted to a specific pH.

was inhibited by Zn and Cd, but not by Co, Ni, Fe and Cu (data not shown). These results suggest that the high-affinity Cd-Mn transport system may, at least in part, involve the mechanism for Zn transport.

Recently, Gunshin et al. reported that a divalent metal transporter 1 (DMT1), a proton symporter, is involved in Fe, Zn, Mn, Cd, Co, Ni, Cu and Pb incorporation into the intestinal mucosa.<sup>3)</sup> Since DMT1 can transport metal ions only at acidic pH, we examined the pH dependency of Cd and Mn uptake by Cd-rB5 and parental cells. As shown in Fig. 2, maximal uptake of Cd and Mn was observed at neutral pH in parental cells, but no uptake of either metal was observed at physiological pH in Cd-rB5. These findings suggest that the high-affinity Cd-Mn transporter that is suppressed in Cd-rB5 cells is not DMT1.

Application of the multitracer technique has enabled us to detect the transport system for both Mn and Cd. Further study is needed to elucidate the molecular mechanisms of Cd and Mn transport.

### References

- 1) T. Yanagiya et al.: *Life Sci.* **65**, PL177 (1999).
- 2) T. Yanagiya et al.: *J. Pharmacol. Exp. Therap.*, in press.
- 3) H. Gunshin et al.: *Nature* **388**, 482 (1997).

\*<sup>1</sup> School of Pharmaceutical Sciences, Kitasato University

\*<sup>2</sup> Department of Urology, Nippon Medical School

# Biobehavior of Multitracers in the Brain and Other Organs of 1-, 3- and 8-Week-Old Mice

T. Tarohda,\*<sup>1</sup> R. Amano, K. Sakamoto,\*<sup>2</sup> and S. Enomoto

Manganese, copper and zinc are known for their nutritional roles in animals; Mn definitely and possibly Cu and Zn have important biological functions in various metabolic processes.<sup>1)</sup> Homeostasis and interactions among these microessential elements during growth and developmental processes remain to be thoroughly studied. In this study, we focused on the transportation and retention of Mn, Zn, Se and Rb trace elements in the brain, liver, pancreas, spleen and kidney, utilizing a radioactive multitracer technique developed by us.

A carrier-free multitracer was obtained from an Ag (purity: more than 99.99%) target irradiated by the <sup>12</sup>C-ion 135 MeV/nucleon beam from RIKEN Ring Cyclotron. The multitracer solution, which was prepared according to the method of Ambe *et al.*<sup>2-4)</sup> at the Radioisotope Center of Kanazawa University, contained 17 radioisotopes of 14 elements. The physiological saline solution (0.9% NaCl in 0.001N HCl, pH 2-3) containing the multitracer was prepared for intraperitoneal (ip) injection. Table 1 lists the radioisotope specifications of a 0.1-ml multitracer solution injected into a 5-g mouse.

Sixty normal ICR mice used in this experiment were divided into three groups according to the age (1-, 3- and 8-week-old mice) An appropriate amount of the multitracer solution (0.1 ml/5-g weight of mouse) was injected intraperitoneally into each mouse. At 6, 12, 24 and 48 hr after ip injection, the mice were dissected and perfused with 0.9% NaCl solution under ether anesthesia. The brain, liver, pancreas, spleen and kidney samples were excised, and then weighed immediately and

Table 1. Specifications of a 0.1 ml multitracer solution injected into a 5-g mouse.

Radioactive tracer	Half life (d)	Radioactivity (kBq)	Estimated mass (μg)	Chemical form
<sup>7</sup> Be	53.29	3.669	0.28	Be <sup>2+</sup>
<sup>46</sup> Sc	83.81	0.061	0.05	Sc <sup>3+</sup>
<sup>48</sup> V	15.97	0.523	0.08	(?)
<sup>51</sup> Cr	27.70	1.721	0.50	Cr <sup>3+</sup>
<sup>52</sup> Mn	5.59	0.356	0.02	Mn <sup>2+</sup>
<sup>54</sup> Mn	312.12	0.445	1.55	Mn <sup>2+</sup>
<sup>58</sup> Co	70.92	0.792	0.67	Co <sup>2+</sup>
<sup>59</sup> Fe	44.50	0.130	0.06	Fe <sup>3+</sup>
<sup>65</sup> Zn	244.26	0.432	1.42	Zn <sup>2+</sup>
<sup>75</sup> Se	119.77	1.167	2.17	SeO <sub>3</sub> <sup>2-</sup>
<sup>83</sup> Rb	86.20	2.345	3.47	Rb <sup>+</sup>
<sup>84</sup> Rb	32.77	0.367	0.21	Rb <sup>+</sup>
<sup>85</sup> Sr	64.84	3.574	4.08	Sr <sup>2+</sup>
<sup>88</sup> Zr	83.40	3.703	5.63	ZrO <sub>2</sub> <sup>(?)</sup>
<sup>89</sup> Zr	3.27	4.040	0.24	ZrO <sub>2</sub> <sup>(?)</sup>
<sup>97</sup> Ru	2.90	2.625	0.15	(?)
<sup>101m</sup> Rh	4.34	5.677	0.52	Rh <sup>3+</sup>

\*<sup>1</sup> Graduate School of Natural Science and Technology, Kanazawa University

\*<sup>2</sup> Faculty of Science, Kanazawa University

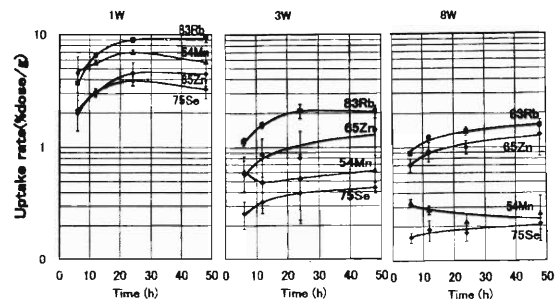


Fig. 1. Brain uptake rates for Se, Mn, Zn and Rb in normal mice at 6, 12, 24 and 48 hr after ip injection of the multitracer solution.

then freeze-dried. The dried samples were subjected to  $\gamma$ -ray spectrometry using pure Ge detectors with reference to an appropriate standard. The uptake behavior was evaluated in terms of organ uptake rate (the radioactivity percentage of injected dose per gram of the organ of interest, % dose/g). Data are expressed as the mean  $\pm$  SD (standard deviation) for five animals.

Figure 1 compares the brain uptake rates for <sup>54</sup>Mn, <sup>65</sup>Zn, <sup>75</sup>Se and <sup>83</sup>Rb tracers in mice at 6, 12, 24 and 48 hr after ip injection. The multitracer technique enabled simultaneous tracing of the elements Mn, Se, Zn and Rb in the identical brain samples and an accurate comparison of their biobehavior. The results reveal that the brain uptake rate increased with time in 1-, 3- and 8-week-old mice. On the other hand, the uptake rates for the four tracers in the other organs decreased with time. Moreover, the uptake rates for all four tracers in the brain of 1-week-old mice were found to be much higher than those of 3- and 8-week-old ones. The uptake rate in the brain of 1-week-old mice was in the following order: <sup>83</sup>Rb > <sup>54</sup>Mn > <sup>65</sup>Zn > <sup>75</sup>Se. However, in the case of 3- and 8-week-old mice, the rates were in the following order: <sup>83</sup>Rb > <sup>65</sup>Zn > <sup>54</sup>Mn > <sup>75</sup>Se. This observed higher uptake and retention of Mn in younger mice suggest some active involvement of this element in important brain functions during the growth period.<sup>5)</sup>

## References

- 1) R. M. Leach, Jr. and E. D. Harris: in *Handbook of Nutritionally Essential Mineral Elements*, edited by B. L. O'Dell and R. A. Sunde, (Marcel Dekker, New York, 1997), p. 335.
- 2) S. Ambe *et al.*: Chem. Lett. **1991**, 149.
- 3) S. Ambe *et al.*: Anal. Sci. **7**, Suppl., p. 317 (1991).
- 4) S. Ambe *et al.*: J. Radioanal. Nucl. Chem. **195**, 297 (1995).
- 5) S. Oishi *et al.*: J. Radioanal. Nucl. Chem. **239**, 411 (1999).

## Effect of Oral Administration of NaFeEDTA on the Biodistribution of Trace Elements

K. Igarashi, Y. Nakanishi, R. Hirunuma, S. Enomoto, and S. Kimura\*

Iron deficiency anemia is one of the major micronutrient deficiencies in the world, particularly in developing countries. Recent research has shown an association between iron deficiency anemia and adverse effects on the intelligence quotient in infants and children. One of the method to prevent iron deficiency anemia in developing countries may be the fortification of food products with iron. Iron bioavailability depends on the chemical formula of iron and also the on food component. In developing countries, available foodstuff consists mainly of plant foods.<sup>1)</sup> The use of NaFe-ethylenediaminetetraacetic acid (EDTA) as a food additive has recently been reviewed by the International Nutritional Anemia Consultative Group and was strongly recommended as the most suitable iron fortificant for use in developing countries. However, EDTA is a chelating agent.<sup>2)</sup> Thus it may possibly react with other minerals. We considered the influence of NaFeEDTA on the biodistribution of other trace elements as examined by the multitracer technique. This is a part of the previous study of the examination.

As the experimental animal, male wistar rats were purchased (Charles River Japan, Inc.) and were housed in stainless steel cages. The cages were placed in an air-conditioned room and subjected to 12 h of light. They were fed a standard laboratory diet and had free access to drinking water prior to the tracer experiment. A multitracer solution was obtained from an Ag target irradiated by the heavy-ion beam from the RIKEN Ring Cyclotron. To elucidate the effect of oral administration of NaFeEDTA on the biodistribution of trace elements, two type of solutions containing ferrous sulfate and NaFeEDTA were prepared. An equivalent molar solution of EDTA was also prepared to examine the effect of EDTA itself. Saline was used a control. Finally four groups were arranged. The solutions of ferrous sulfate and NaFeEDTA were orally administrated to each rat (3 mg Fe/kg B.W.). EDTA solution and saline was also orally administrated to the rats. An amount (0.2 ml) of the multitracer solution was continuously orally administrated into rats of each group. The rats were sacrificed at 7 hours after administration of the multitracer solution. The radioactivity levels of their organs were determined by  $\gamma$ -ray spectrometry.

The uptake of radioactive Fe in organs of the control rats was the highest among the four groups (Fig. 1). It is believed that the uptake of radioactive Fe was

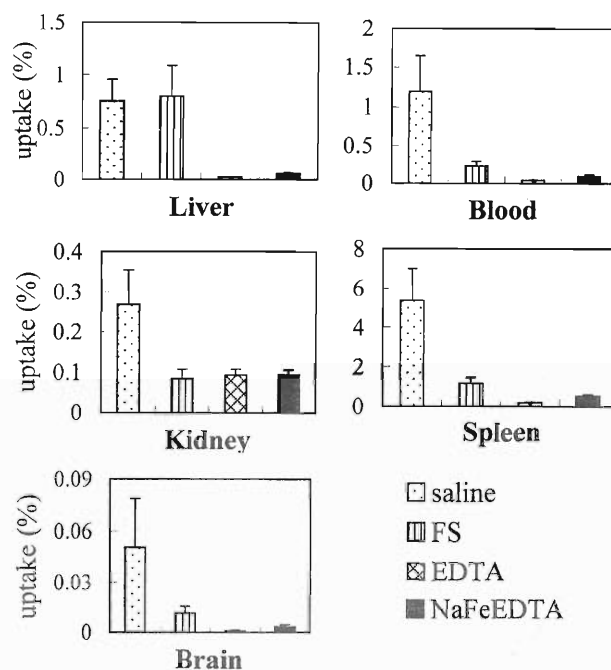


Fig. 1. Uptake of Fe in the liver, blood, kidney, spleen and brain of group I, II, III and control rats.

influenced by presupplied cold Fe such as ferrous sulfate or NaFeEDTA. The uptake of radioactive Fe was higher in organs of group I (ferrous sulfate) than in those of group II (NaFeEDTA). In addition, the uptake of radioactive Fe in organs of group II (EDTA) was lower than that in organs of the control group. The uptakes of radioactive Zn in organs of groups II and III were lower than those in the organs of control and group I. The behavior of Co was similar to that of Zn. The results in this experiment showed the adverse effects of NaFeEDTA on the biodistribution of various elements. Thus, it is difficult to evaluate the effect of NaFeEDTA in this study. However, this experiment was carried out using a system of Fe-containing solutions and multitracer solutions in the absence of food, that is without an inhibitors condition. We require more experiments to determine the role of the mechanism of NaFeEDTA in the absorption study and the biodistributions of other minerals.

### References

- 1) L. Davidsson et al.: *J. Nutr.* **128**, 1139 (1998).
- 2) L. Davidsson et al.: *Am. J. Clin. Nutr.* **60**, 231 (1994).

\* Graduate School, Showa Women's University

## Contribution of Arbuscular Mycorrhizal Hyphae to Acquisition of Trace Elements by Marigold

H. Suzuki, H. Kumagai,\*<sup>1</sup> K. Oohashi,\*<sup>2</sup> and S. Enomoto

The plant roots infected with the arbuscular mycorrhizal fungi (AMF) are known to have higher phosphorus (P) absorption capacities compared to those of non-mycorrhizal roots. Difference in this capacity between mycorrhizal and non-mycorrhizal roots was based on the increase in P absorption by the arbuscular mycorrhizal hyphae (AMH).<sup>1</sup> Similar results are obtained in experiments involving N, Zn, and Cu.<sup>2</sup> In the present study, we have examined the absorption of other trace elements by AMH in the symbiotic system of marigold plants (*Tagetes patula* L. cv. Bonanza spray) and AMF (*Glomus etunicatum*) using a multi-tracer technique, because the absorption of trace elements by AMH is still rather obscure.

Preparation of a multitracer is described in the literature.<sup>3,4</sup> A plant container (240 ml pot) was divided into the "root compartment" (RC), for the growth of the roots and AMH, and the "hyphal compartment" (HC), for the growth of AMH, by a 20  $\mu$ m nylon mesh as shown in Fig. 1. The HC contained 120 g of river sand with a multitracer solution containing the radionuclides of <sup>7</sup>Be, <sup>22</sup>Na, <sup>46</sup>Sc, <sup>51</sup>Cr, <sup>54</sup>Mn, <sup>59</sup>Fe, <sup>56</sup>Co, <sup>65</sup>Zn, <sup>75</sup>Se, <sup>83</sup>Rb, <sup>85</sup>Sr, <sup>88</sup>Y, <sup>88</sup>Zr, and <sup>95m</sup>Tc. The chemical forms of the tracers on application were assumed to be Be<sup>2+</sup>, Na<sup>+</sup>, Sc<sup>3+</sup>, Cr<sup>3+</sup>, Mn<sup>2+</sup>, Fe<sup>3+</sup>, Co<sup>2+</sup>, Zn<sup>2+</sup>, SeO<sub>3</sub><sup>2-</sup>, Rb<sup>+</sup>, Sr<sup>2+</sup>, Y<sup>3+</sup>, Zr<sup>4+</sup>, and TcO<sub>4</sub><sup>-</sup>, respectively.<sup>3</sup> The RC was filled with 280 g of river sand. A marigold seed was sown in the RC. In the mycorrhizal plant, the spore of *Glomus etunicatum* (Becker and Gerdemann) was added to the center of the RC. A non-mycorrhizal marigold was used as the control plant. The plants were grown in the biotron with a 16/8 hr day/night regime, at 15000 lux, 65% relative humidity, and 25°C. The experiment was carried out at 35% of the water holding capacity of the growth medium. The plants were harvested at 40 and 60 days after sowing (DAS). The radioactivity levels in the plants were measured with Ge semiconductor detectors.

Figure 2 shows the relative uptake (% of dose) of radionuclides in the entire plant. The relative uptake of <sup>22</sup>Na, <sup>65</sup>Zn, <sup>75</sup>Se, <sup>83</sup>Rb, and <sup>85</sup>Sr in the mycorrhizal plant was higher than that in the control plant. Although the relative uptake of <sup>54</sup>Mn and <sup>88</sup>Y was less than 0.2%, that of <sup>88</sup>Y in the mycorrhizal plant was approximately two times higher than that in the control plant at 60 DAS. In the case of <sup>95m</sup>Tc, the uptake in the mycorrhizal plant was similar to that in the control plant. The radioactivities of <sup>7</sup>Be, <sup>46</sup>Sc, <sup>51</sup>Cr, <sup>59</sup>Fe,

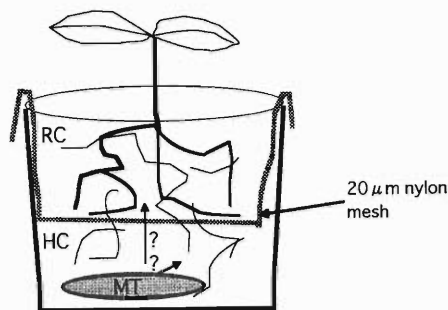


Fig. 1. The experimental system. RC, root compartment; HC, hyphal compartment; MT, multitracer.

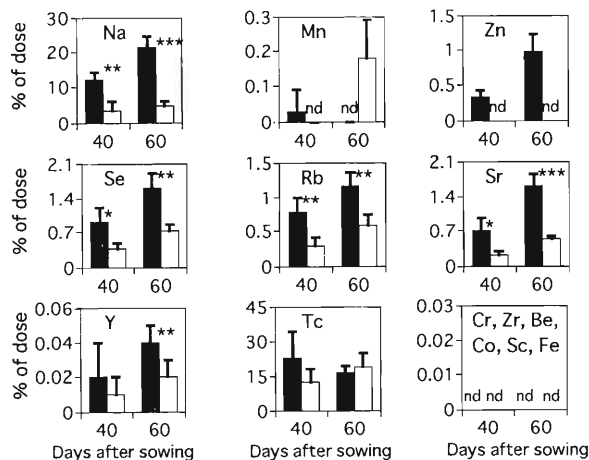


Fig. 2. Relative uptake (% of dose) of trace elements in the mycorrhizal (black bars) and control plants (white bars) at two cultivation periods. Each value in the figure represents the mean value  $\pm$  standard deviation obtained from four preparations (\* $P$  < 0.05; \*\* $P$  < 0.01; \*\*\* $P$  < 0.001).

<sup>56</sup>Co, and <sup>88</sup>Zr could not be detected in any plant.

The results show that AMH can absorb Na, Zn, Se, Rb, Sr, and Y from the soil and translocate these elements to the plant.

### References

- 1) L. H. Rhodes and J. W. Gerdemann: *New Phytol.* **75**, 555 (1975).
- 2) H. Marschner and B. Dell: in *Management of Mycorrhizas in Agriculture, Horticulture and Forestry*, edited by A. D. Robson, L. K. Abbott, and N. Malajczuk, (Kluwer Acad. Publ., Dordrecht, 1994), p. 89.
- 3) RIKEN Rev., No. 13, edited by F. Ambe (1996).
- 4) H. Suzuki et al.: RIKEN Accel. Prog. Rep. **32**, 131 (1999).

\*<sup>1</sup> Radioisotope Research Center, Chiba University

\*<sup>2</sup> Faculty of Pharmaceutical Sciences, Chiba University

## Influence of Zn on the Uptake of Various Elements into Carrot

T. Ozaki, Y. Kawamura, and S. Enomoto

To satisfy their growth requirements, plants absorb cations and anions from their surroundings. The generally accepted theory of ion uptake by plant cells is that specific molecular carriers transfer the ions through cell membranes which are otherwise almost impermeable. Zinc is one of the essential elements for all plants, and it is involved in a number of proteins and biochemical reactions.<sup>1,2)</sup> At the same time, too much Zn is known to be deleterious to plants.<sup>3)</sup> Thus, the effect of Zn on the behavior of other elements merits investigation, particularly for acquiring information about the interaction between Zn and other elements around carriers on the surface of cell membranes. In the present paper, we report the effect of ZnCl<sub>2</sub> on the uptake of various elements (Be, Na, Mn, Co, Zn, Se, Rb, Sr, Rh, Ce, Pm, Gd) by carrot, using the multi-tracer technique developed at RIKEN.<sup>4)</sup>

Carrot (*Daucus carota* cv. U. S. harumakigosun) seeds were rinsed with distilled water and then allowed to germinate on filter paper. Germinated seeds were grown on Kureha horticulture soil, and kept in a growth chamber at  $23 \pm 2^\circ\text{C}$  under supplemental lighting of  $150 \mu\text{mol}\cdot\text{m}^{-2}\cdot\text{s}^{-1}$  with a 12 h photoperiod. Twenty days after germination, when the length of plant bodies and roots was approximately 7 cm, the carrots were transplanted into ultrapurified water and kept for three days with constant bubbling of air under the same photoperiod and temperature as above. Just prior to the uptake experiment, all roots were again washed with ultrapurified water.

An uptake experiment was conducted over two days with roots of samples maintained in 50 mL ZnCl<sub>2</sub>-multitracer solutions (pH  $4.5 \pm 0.2$ ). After the uptake period, the roots were thoroughly washed with distilled water and 0.1 mol·L<sup>-1</sup> HCl, then wiped with filter paper. The plant bodies were divided into roots and upper parts. The uptake ratio for each part was

defined as: uptake ratio (%/g) =  $100 \times (\text{radioactivity in each part}/\text{total amount of radioactivity added to the uptake solution})/\text{fresh weight of the corresponding part}$ . Each datum point in the figures was given as the mean  $\pm$  standard deviation of five replications.

The portion adsorbed on the surface of roots is considered to be desorbed by washing with 0.1 mol·L<sup>-1</sup> HCl. On the other hand, the portion that has permeated the cytoplasm or the unexchangeable fraction in the so-called apoplast, which is a cell wall continuum in roots where carboxylic groups act as cation exchangers, cannot be washed out. Based on the above assumption, we discuss the effect of ZnCl<sub>2</sub> on the uptake of other elements.

The uptake ratios of Co, Rb, and Se for roots are shown in Fig. 1 (a)–(c). The uptake of Co decreased with the increase of ZnCl<sub>2</sub> concentration (Fig. 1 (a)). Two ppm of ZnCl<sub>2</sub> suppressed the uptake of Co to approximately 0.2-fold compared to that in the absence of ZnCl<sub>2</sub>. To be transported to the cytoplasm via carriers, ions must be adsorbed onto the transport sites of the carriers in the plasma membrane. Competition between ions with the same electrical charge can thus be expected. Therefore, the decreases observed in the uptake of Co are suggested to be due to the competition with Zn for the transport sites of Co.

Interestingly, the uptake of Rb was also suppressed by the addition of ZnCl<sub>2</sub> (Fig. 1 (b)). The decrease observed in the uptake of Rb<sup>+</sup> suggests that Zn<sup>2+</sup> has an affinity for the binding sites of transporting compounds by which Rb<sup>+</sup> is transported.

Interactions between anions are also reported, such as between Cl<sup>-</sup> and NO<sub>3</sub><sup>-</sup> or between SO<sub>4</sub><sup>2-</sup> and MoO<sub>4</sub><sup>2-</sup>. In the present study, the concentration of Cl<sup>-</sup> was also changed, along with the change of Zn<sup>2+</sup> concentration. As shown in Fig. 1 (c), however, no influence was observed on the uptake of Se. Considering

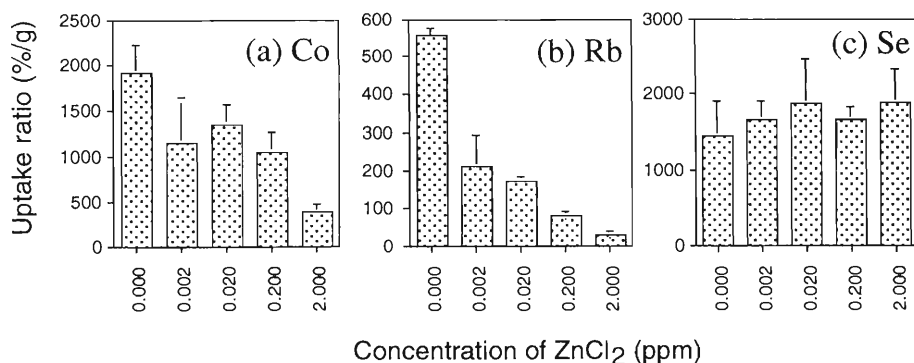


Fig. 1. Uptake of Co, Rb, and Se into roots.

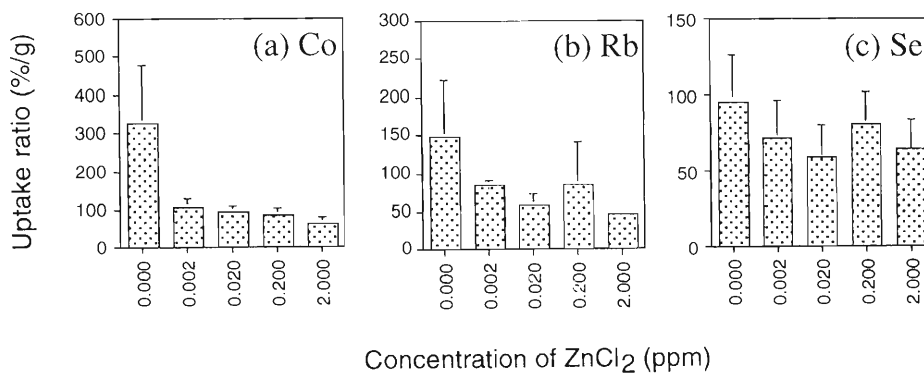


Fig. 2. Uptake of Co, Rb, and Se into leaves.

the preparation procedure of the multitracer solution, the chemical form of Se in the multitracer solution is considered to be  $\text{SeO}_3^{2-}$ . The result obtained in this investigation suggests that Se is distinguished from Cl during the uptake into roots, and they are recognized as different ion species with low physicochemical similarities.

The uptake of Co, Rb, and Se by leaves is shown in Fig. 2 (a)–(c). Apparent decreases in the uptake by leaves were also observed for Na, Sr, Mn, and Zn with increasing  $\text{ZnCl}_2$  concentration (data not shown). For the elements which exhibited a decrease in uptake

by the leaves, the degree of the decrease was almost proportional to the decrease in the uptake by the roots. This indicates that the competition of these elements with Zn for the binding sites occurred mainly outside the cytoplasm in the process of entering it, and not inside it.

#### References

- 1) B. L. Vallee and D. S. Auld: *Biochemistry* **29**, 5647 (1990).
- 2) J. E. Coleman: *Annu. Rev. Biochem.* **61**, 897 (1992).
- 3) G. D. Jessica and M. S. Larry: *Soil Sci.* **155**, 376 (1993).
- 4) S. Ambe et al.: *Chem. Lett.* **1991**, 149.

## Enhanced Uptake of Mn by *LeGlp1*-Transgenic Tobacco Plants

M. Takahashi, K. Sasaki,\* T. Kitano,\* Y. Kawamura, and S. Enomoto

Plants require sources of the inorganic nutrients C, N, P, and S to synthesize organic cell constituents. Eleven other inorganic ions have been proven essential for plant growth. Soil is the storehouse of all of these nutrients, except CO<sub>2</sub>. Nutrient uptake by plant roots involves an ion-protein interaction in which transporter molecules in the root plasma membrane recognize specific ions in the soil solution and absorb them against a concentration gradient at the expense of membrane potential,  $\Delta\text{pH}$  or ATP.<sup>1)</sup> It is believed that the transporter molecule has a site that is essential for the binding to the ions to be transferred. ABC-type transporters contain a membrane-peripheral substrate-binding subunit.

Metal ions toxic or inadventagous to plant metabolism might be inevitably absorbed through the transporters, mistaken for essential ions with similar chemical characteristics, such as ionic radius and electronic charge. These ions should be detoxicated by inclusion in stable chelating molecules or by exudation after being absorbed. Metal-protein interaction may be the most important process involved in metal homeostasis. Metal-binding proteins may be involved in individual metal-ion-requiring functions. Transition metals coordinate with the N in the amino, the S in the thiol, the O in the carboxyl and hydroxyl side chains of the protein molecule. Four to six ligands form an array with an interval adequate for forming a metal-binding pocket. Although some ligands are localized with a long interval so that they are distributed over different strands, some are within the same strand. We developed a screening method for metal-binding proteins, especially for the membrane protein and the protein with metal binding sites unexposed to the solvent. Using this screening method, a metal binding site was isolated from tomato roots and cDNA was cloned. A full-length cDNA (*LeGlp1*) of 828 bp was shown to encode a precursor protein of 23797 Da having a 27-amino-acid leader sequence at the NH<sub>2</sub> terminus. The metal-binding site is located in the NH<sub>2</sub>-terminal region of the 197-amino acid-long mature protein, however, the specificity of metals bound to this site is not yet clear. Tobacco plants (*Nicotiana tabacum* SR1) were transformed with *LeGlp1* cDNA to express the metal-binding protein in whole tissues. In this study, the uptake, by *LeGlp1*-transgenic plants, of the metal ions in a multitracer was compared with those by non-transformed control plants and *GUS* (a control gene)-transformed plants to identify the metal which predominantly accumulates in the plant expressing the

protein with the metal-binding site.

The aforementioned three lines of tobacco plants were hydroponically grown at 25°C under 18-h-light/6-h-dark cycle with Hyponex for two months followed by distilled water supplemented with a multitracer for 2 days. Multitracers were extracted from irradiated Ag targets as described,<sup>2)</sup> mixed with <sup>59</sup>Fe, and subjected to the growth medium. Plants were further chased with Murashige-Skoog's medium for 3 days. With a 1-day interval, the radioactivity of Mn, Fe, Co, Zn, and Rb in the roots and leaves of the subject plants were determined by a Ge detector (EG & G). Figure 1 shows the bioaccumulation (% of dose (g of dry wt.)<sup>-1</sup>) of Mn in the roots and leaves of the three lines of tobacco plant. Newly absorbed Mn was transferred to aerial parts of tobacco plants 3 days after the addition of <sup>54</sup>Mn into the growth medium. Metal-binding *LeGlp1*-expressing transgenic tobacco accumulated most in the leaves of the plants, although the amount of Mn in roots was comparable irrespective of the expression of *LeGlp1*. The time course of bioaccumulation of other transition metals, such as Fe, Co, and Zn, was similar to that of Mn, with Fe being most rapidly absorbed, however, the amounts of Fe, Co, and Zn, as well as Rb did not differ between the three lines of tobacco plants (data not shown).

*LeGlp1* has a binding site, presumably composed of two cysteines, for transition metal ions. *LeGlp1* itself is localized in tomato roots, not in the leaves. The

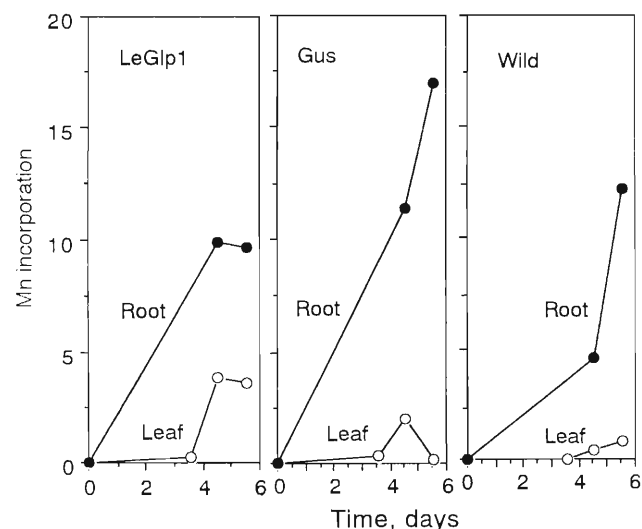


Fig. 1. Bioaccumulation of Mn in the leaf (open circles) and root (closed circles) of *LeGlp1*-transformed (left), *GUS*-transformed (middle), and untransformed control (right) tobacco plants.

\* Department of Applied Biological Chemistry, Osaka Prefecture University

multitracer experiment indicates that accumulation of Mn in leaves is enhanced in the transgenic plant that expresses LeGlp1 without any tissue specificity, suggesting that Mn is the intrinsic bound metal ion in the LeGlp1 molecule.

#### References

1) L. V. Kochian: in *Micronutrients in Agriculture*, 2nd

ed., edited by J. J. Mortvedt, F. R. Cox, L. M. Shuman, and R. M. Welch, (Soil Science Society of America, Madison, 1991), p. 229.

2) M. Yanaga, T. Ohyama, M. Iwama, Y. Yoshida, M. Noguchi, T. Ohmori, R. Hirunuma, and S. Enomoto: RIKEN Accel. Prog. Rep. **32**, 127 (1999).

## Selective Detection of EC-Decay Radionuclides in Multitracers: A Proposal

Y. Minai and S. Enomoto

The multitracer technique has been recognized as an innovative radioanalytical method to study the behavior of trace elements in biological, analytical, and environmental systems. Usually, the behavior of each element in the system is estimated from its distribution determined by  $\gamma$ -ray spectrometry. The high resolution of germanium semiconductor detector is responsible for deconvoluting the  $\gamma$ -ray spectrum to obtain the distribution of the elements applied as multitracers.

Such use of the germanium semiconductor detector has been very popular in activation analysis for determining trace elements. The high resolution of the detector changed activation analysis from a monoelemental analytical technique accompanied by tedious radiochemical separation procedures to an instrumental technique for simultaneous determination of multiple elements. Accuracy of instrumental activation analysis largely depends on the degree of overlap of the photopeaks from different radionuclides. Careful examination of each photopeak must be carried out to avoid overestimation of peak intensity due to the overlap of the photopeak from another radionuclide. Such a situation also occurs in the radioassay of the multitracer solution or of systems containing the multitracer. Extremely complex structure of the spectra, which are sometimes encountered in studies using the multitracer, may influence the accuracy of distribution data on each element. Radiochemical separation of particular group of elements has been applied to reduce the frequency of photopeak overlap in the  $\gamma$ -ray spectra.<sup>1)</sup>

As an alternative to the radiochemical methods for separation of particular elements, detection of another radiation from the corresponding radionuclides other than  $\gamma$ -rays is proposed. Preparation of the multitracer at RIKEN starts from production of radionuclides in the target material by heavy-ion bombardment. Nuclear spallation reaction accompanied with bombardment can generate neutron-deficient

radionuclides. Those nuclides tend to decay via EC processes. Utilizing the intense nature of the characteristic X-rays emitted after electron capture, detection of this radiation may be used to evaluate distribution of the EC-decay radionuclides, such as  $^{64}\text{Cu}$ ,  $^{69m}\text{Zn}$ ,  $^{109}\text{Pd}$ ,  $^{107}\text{Cd}$ , and  $^{122}\text{Sb}$ .

In earlier studies on use of Si(Li) detectors for neutron activation analysis, great improvement was shown in analytical performance for the determination of many EC-decay radionuclides.<sup>2)</sup> A relatively simple structure of the X-ray spectra can reduce ambiguity in deducing the spectral data. The potential factor affecting the accuracy of the peak intensity for a particular radioelement with an atomic number  $Z$  is the production of other radionuclides emitting the same X-ray:  $\beta$ -decay radionuclides with  $Z-2$  and IT-decay radionuclides with  $Z-1$ . As EC-decay involves the ionization of the inner sphere of an electron shell, it was found that the intensity of the characteristic X-rays is much more intense for those nuclides than for the  $\beta$ - or IT-decay nuclides in analytical condition.<sup>2)</sup>

It is noteworthy that the X-ray spectral structure, even as indicated by a simple parameter like the  $K_{\alpha}/K_{\beta}$  ratio, is a function of the oxidation state and the nature of chemical bonding.<sup>3,4)</sup> In an application study, the dissolved species of radionuclides in the multitracer solution are not well recognized. The spectral feature of the emitted X-ray may be a clue in the evaluation of the species in the solution even if the amount of the radionuclide is extremely low relative to the amounts of nonradioactive components in the system.

### References

- 1) S. Ambe et al.: RIKEN Rev., No. 13, p. 3 (1996).
- 2) M. Mantel et al.: Anal. Chem. **44**, 548 (1972).
- 3) K. E. Collins et al.: Radiochim. Acta **28**, 7 (1981).
- 4) Y. Tamaki et al.: Radiochem. Radioanal. Chem. Lett. **37**, 39 (1979).

## Evaluation of the *in vitro* Stability of Radiolabeled DTPA and DOTA and Their Conjugated Antibodies

Y. Kawamura, S. Enomoto, and R. Amano

In the field of radiopharmaceutical science, radioactive metal ions chelated to small molecules, peptides, or proteins, such as monoclonal antibodies, have been used clinically for the diagnosis of cancers and for fundamental studies on the function of various organs.<sup>1)</sup> For example, monoclonal antibodies labeled with radioisotopes such as <sup>67</sup>Ga, <sup>111</sup>In or <sup>90</sup>Y are used in radioimmunomaging and radioimmunotherapy. In the selection of suitable isotopes for radiopharmaceutical uses, we usually compare the *in vitro* and *in vivo* behavior for each labeled compound, which is time work. Moreover, slight changes in the conditions are inevitable in experiments for each radionuclide. With the multitracer technique, we can obtain much information at one time under identical experimental conditions.

In this work, labeling of antibodies, immunoglobulin G (IgG), with a multitracer was investigated using Diethylenetriamine-pentaacetic acid (DTPA) and 1,4,7,10-Tetraazacyclododecane-1,4,7,10-tetraacetic acid (DOTA),<sup>2)</sup> which is a strong chelating agent for many metal ions. We attempted to establish a procedure to evaluate the *in vitro* stability of the chelate with various metals and the efficiency and selectivity of DTPA and DOTA with metals.

A carrier- and salt-free multitracer solution was prepared from Au foil irradiated with a 135 MeV/nucleon <sup>14</sup>N beam at the RIKEN Ring Cyclotron. Details of the procedure for multitracer preparation was reported previously.<sup>3)</sup> The multitracer solution containing radioisotopes of Na, Sc, Mn, Fe, Co, Zn, Se, Rb, Sr, Rh, Ag, Ir and lanthanide was evaporated to dryness and the radioisotopes were dissolved in water.

The efficiency of the radiolabeled chelate was confirmed by paper chromatography (saline), using Whatman No. 1 paper strips pretreated with 2.5% albumin. In the paper-chromatographic system, radiocolloids remain at the origin, and the labeled and the free chelate move with the solvent front.

The spectra of the chromatographed fractions obtained using a high purity germanium gamma (HPGe) detector were quantitatively analyzed.

The radioisotopes of Zr, Hf, Y and lanthanide were found to combine with DTPA and DOTA to make stable complexes, while the other radioisotopes, such as those of the nonmetallic element Se, the alkali metals Na and Rb and the alkaline earth metal Sr, did not combine with these ligands. The other metals of Co, Ga, Mn, Sc also did not form stable complexes.

Conjugation of DTPA cyclic dianhydride to IgG was performed by the addition of 0.2 ml DTPA cyclic

dianhydride in dimethyl sulfoxide (DMSO) solution (5 mg/ml) to 200  $\mu$ l of the IgG (ChromPure) solution 11.3 mg/ml containing 0.5 M of NaCl and 0.01 M of sodium phosphate buffer to ensure a pH of 7.6. After standing at room temperature for 5 min, the mixture was loaded into a Sephadex G-50 (fine) column (of 20 cm height and 1.5 cm I.D.). The column was eluted with 0.05 M sodium citrate (pH = 5.6). The fractions showing absorbance at 280 nm (corresponding to IgG-DTPA) were collected. The multitracer solution was added to the IgG-DTPA fraction. After standing for two hours at room temperature, an IgG-DTPA-multitracer fraction was separated from the free multitracer ions using a molecular cut filter. The radioactivity remaining in the dialysis bag was measured with a HPGe detector. As a control, the same labeling procedure was performed with another IgG solution in the absence of DTPA.

In our experiment, the conjugation efficiency was determined to be 40%. Radioisotopes of Sc, Fe, Co, Zn, Ag and lanthanide were found to combine with IgG-DTPA. The radioisotopes of Se, Na and Rb did not combine with the conjugating species. Only a small fraction of the Mn, Rh and Ir radioisotopes combined with IgG-DTPA. These results suggest that the stability of the metal DTPA complex was the main factor determining the labeling efficiency. For the control sample without DTPA, the amounts of radioisotopes combined with IgG were below the detection limit.

This indicates that once metal ions combine with IgG-DTPA, the chelate is stable under the conditions studied. The DTPA and DOTA were recognized as ligand chelates for particular cations. The conjugated ligands with IgG had an affinity with these cations. This indicates that steric factors relating to the formation of conjugates with IgG were not a major factor controlling the affinity with the radioisotopes studied. These results were confirmed by both ion size chromatography and the adsorption method. This implies that the simple method applied in this work efficiently evaluated the efficiency and purity of the labeled compounds. A detailed study of *in vitro* and *in vivo* properties of IgG labeling by the multitracer technique is under way and is expected to provide important information for further radiopharmaceutical studies.

### References

- 1) L. Yuanfang et al.: Pure Appl. Chem. **63**, 427 (1991).
- 2) O. A. Gansow et al.: Int. J. Rad. Appl. Instrum. B. **18**, 369 (1991).
- 3) S. Ambe et al.: Chem. Lett. **1991**, 149.

## HPLC Elution Behavior of Multitracer Metallofullerenes

K. Sueki, K. Akiyama,\* H. Nakahara, K. Kikuchi,\* S. Ambe, F. Ambe, and S. Enomoto

The formation of metallofullerenes has been reported for the group 2 elements (Ca, Sr and Ba), for the group 3 elements (Sc, Y and lanthanoids), and for the group 4 and 5 elements (Zr, Hf and Nb).<sup>1)</sup> In this study, the elution behavior of radiotracer metallofullerenes was examined in two types of stationary phases for high performance liquid chromatography (HPLC). A Buckyprep column has a nonpolar stationary phase, but a Buckyclutcher I column has a polar stationary phase. By combining these two columns of different characters, it was expected that isomers of  $M@C_{82}$  could be identified by their subtle differences during the retention time.

Crude with multitracer metallofullerenes dissolved in toluene was passed through a Buckyprep column (Cosmosil, Nacalai Tesque Inc.) of the size i.d. 10 mm  $\times$  250 mm with a flow rate of 3.2 mL/min. Fractions of the eluant were collected every three minutes, and the radioactivity of a specific nuclide in each fraction was assigned and determined by  $\gamma$ -ray spectrometry using an HPGe detector. In the second ex-

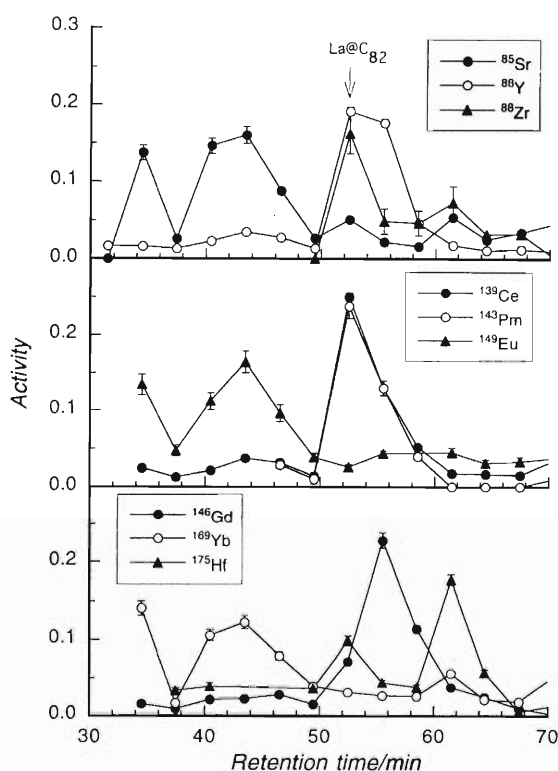


Fig. 1. HPLC elution curves of multitracer metallofullerenes obtained by  $\gamma$ -ray measurements. HPLC column: Buckyprep, i.d. 10 mm  $\times$  250 mm. Flow rate: 3.2 mL/min. Eluent solvent: toluene.

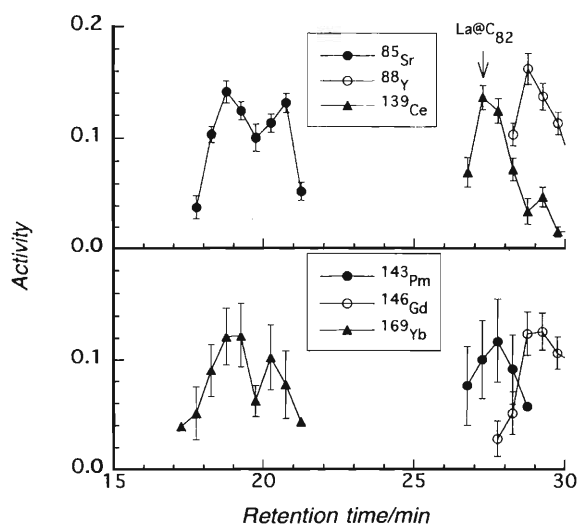


Fig. 2. HPLC elution curves of  $M@C_{82}$  obtained by  $\gamma$ -ray measurements. HPLC column: Buckyclutcher I, i.d. 10 mm  $\times$  250 mm. Flow rate: 2.0 mL/min. Eluent solvent: toluene and hexane (7 : 3).

periment, the  $M@C_{82}$  fractions eluted from the Buckyprep column were submitted to the Buckyclutcher I column (Regis Chemicals Corp., the size of i.d. 10 mm  $\times$  250 mm, a flow rate of 2.0 mL/min) for separation with a mixture of toluene and hexane (7 : 3) as solvent. Elution was monitored using a UV on-line monitor, and by  $\gamma$ -ray off-line measurements of the eluted fractions (0.5 min) using an HPGe detector.

The elution curves for an HPLC Buckyprep column obtained by  $\gamma$ -ray measurements are summarized in Fig. 1 for  $^{85}\text{Sr}$ ,  $^{88}\text{Y}$ ,  $^{88}\text{Zr}$ ,  $^{139}\text{Ce}$ ,  $^{143}\text{Pm}$ ,  $^{149}\text{Eu}$ ,  $^{146}\text{Gd}$ ,  $^{169}\text{Yb}$  and  $^{175}\text{Hf}$ . The result shows that these curves can be classified into three groups: group I ( $^{85}\text{Sr}$ ,  $^{149}\text{Eu}$  and  $^{169}\text{Yb}$ ), group II ( $^{88}\text{Y}$ ,  $^{139}\text{Ce}$ ,  $^{143}\text{Pm}$  and  $^{146}\text{Gd}$ ), and group III ( $^{88}\text{Zr}$  and  $^{175}\text{Hf}$ ).

The elution curves of  $M@C_{82}$  for an HPLC Buckyclutcher I column obtained by  $\gamma$ -ray measurements are summarized in Fig. 2 for  $^{85}\text{Sr}$ ,  $^{88}\text{Y}$ ,  $^{139}\text{Ce}$ ,  $^{143}\text{Pm}$ ,  $^{146}\text{Gd}$  and  $^{169}\text{Yb}$ . The result shows that the retention time at the point of maximum activity depends on the radionuclide detected; being around 20 min for  $^{85}\text{Sr}$  and  $^{169}\text{Yb}$ , 27 min for  $^{139}\text{Ce}$  and  $^{143}\text{Pm}$ , and 29 min for  $^{88}\text{Y}$  and  $^{146}\text{Gd}$ .

These results indicate that the distributions of the radionuclides in the metallofullerene species differ, and that the retention time of  $M@C_{82}$  for the second column depends on which radionuclide is examined.

## References

- 1) K. Sueki et al.: Chem. Phys. Lett. **300**, 140 (1999).

\* Graduate School of Science, Tokyo Metropolitan University

# Gamma-ray Detection System for Multitracer Research

Y. Yang, Y. Gono, S. Motomura, S. Enomoto, and Y. Yano

Multitracer research is a rapidly developing field since it improves the reliability and efficiency comparing with those of single-tracer research. Multitracer in an aqueous solution can be prepared by chemical separation from a target irradiated by intermediate-energy heavy ion beams. To study the dynamic behavior of nuclides in a sample, their positions in the sample must be measured. Here we propose a detector system called a Multitracer Gamma Emission Imaging System (MT-GEI), which can be used to assign the  $\gamma$ -rays of different nuclides and measure the positions of different nuclides without sacrificing the sample.

The proposed detector system consists of two segmented HPGe detector arrays and is shown in Fig. 1. The  $\gamma$ -rays emitted from samples are measured directly at two consecutive interaction positions  $x_1$  and  $x_2$  of two segmented detector arrays. The total  $\gamma$ -ray energy is then obtained by adding the energies deposited in two detector arrays once the scattered  $\gamma$ -rays have been fully absorbed in the second detector array. Nuclides can be identified based on the total  $\gamma$  energy because of the very good energy resolution of HPGe detectors. The Compton scattering angle  $\theta$  is then calculated from total  $\gamma$  energy and  $\gamma$  energy loss in the first detector array using Compton scattering kinematics. Therefore the emission point must lie on the surface of a cone defined by lines with angle  $\theta$  to the vector  $x_1-x_2$  through  $x_1$ . For a point source, a succession of emissions generates a number of cones which have a common point of intersection, thereby defining the source position.

Monte-Carlo simulations were performed for the proposed detector system, and a point  $\gamma$  source with an energy of 1.332 MeV using the GEANT program.<sup>1)</sup> The efficiency of the detector system is defined by the number of  $\gamma$ -rays that undergo Compton scattering in the first detector array and then are absorbed in the second detector array divided by the number of  $\gamma$ -rays emitted from the source. The detector system consists of two square arrays, each containing 25 segments of 1 cm  $\times$  1 cm  $\times$  2 cm. When the source is situated in the center of the surface of the first array and the distance between the centers of the two arrays is 2 cm, the efficiency is estimated to be  $5 \times 10^{-3}$ . If the distance from the source to the first array and between the two arrays is 10 cm, the efficiency is  $3 \times 10^{-5}$ . In the Monte-Carlo simulations, the centers of the segments are considered to be the interaction positions. A three-dimensional histogram can be obtained by summing a number of cones generated by a successive emissions of  $\gamma$ -rays.

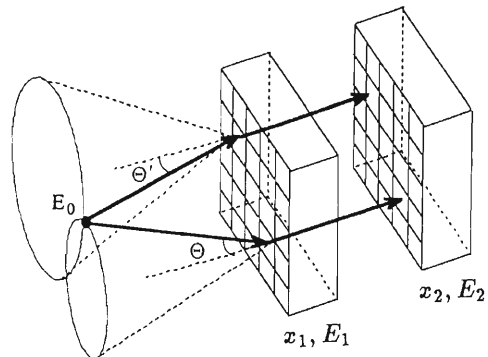


Fig. 1. The principle of MT-GEI.

Each cone consists of a number of points that are uniformly distributed on its surface. A one-dimensional position spectrum in each direction can be obtained from the projection of the three-dimensional histogram by zooming a region near the source position in the other two directions. The width of the position spectrum decreases as decreasing the size of the segment and the distance from the source to the first array, and increasing the distance between the two arrays. The coordinates of the source position are obtained by fitting the one-dimensional spectra in three directions. The positional accuracy is defined by the difference between the actual source position and the source position determined by the simulations. The positional accuracy is improved by decreasing the width of the position spectrum and increasing the number of cones which form the histogram. Simulations were carried out under the conditions of a 1 cm  $\times$  1 cm  $\times$  2 cm segment size in both arrays, and 6 cm distances between both the source and the first detector and the two detectors. When the number of cones was 8000, a positional accuracy of  $\pm 0.5$  mm in the x and y directions (parallel to the detector array plane) and  $\pm 1$  mm in the z direction was obtained. Further simulations to optimize the detector system are still ongoing, and based on the simulations, a detector system will be developed in the next two years. We are also doing research to determine  $\gamma$  interaction positions with a higher accuracy than the size of segments using the induced signals in the neighbouring segments. A much better source-position accuracy is expected with this method.

## References

- 1) R. Brun et al.: GEANT3 Users' Guide, DD/EE/84-1, CERN 1987.

## Time Course Induction of p53 in Human Cell Lines

A. Gordon, S. Morimoto, N. Fukunishi, T. Kurobe, T. Mizuno, F. Hanaoka, and F. Yatagai

To assess the influence of mutant p53 gene on mutagenesis, we are characterising the nature of the mutations induced by heavy ions of various LET (Linear Energy Transfer) in the human lymphoblastoid cell lines WI-L2-NS (mutant p53) and TK6 (wildtype p53) which are derived from the same spleen.<sup>1)</sup> We are also monitoring the time course of p53 induction in these cell lines, and how heavy ions of various LET affect the cell cycle.

Cell cycle analysis is achieved by the analysis of DNA content by laser-scanning cytometry of propidium iodide-stained cells at various times after heavy-ion treatment. At various times after heavy-ion treatment, whole cell extracts are made and used in western blotting analyses using anti-bodies against p53, p53-phosphorylated at Ser15, p21 and actin. Mutation studies involve the generation and characterisation of hypoxanthine phosphoribosyltransferase gene (*hprt*) mutations induced by heavy ions in the two cell line backgrounds.

*hprt* mutations were induced in TK6 and WI-L2-NS cells by irradiation at a LET of 23, 67, and 1000 keV/ $\mu\text{m}$  for C-, Ne- and Fe-ions, respectively. WI-L2-NS cells were more radio-resistant than TK6 cells after such exposure to these heavy-ions, as they were to X-ray exposure. *hprt* mutation induction under these exposures was also higher in WI-L2-NS cells.<sup>2)</sup> Two hours after 3 Gy irradiation (C-ion of 22 keV/ $\mu\text{m}$ , Fe-ion of 1000 keV/ $\mu\text{m}$  and X-ray irradiation), both p53 and p21 proteins are induced in the TK6 cell line. However, p53 and p21 are not induced in the WI-L2-NS cell line after any type of irradiation;

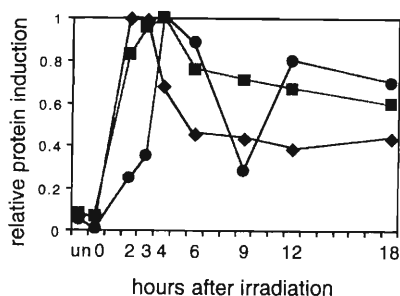


Fig. 1. Time course of p53 induction after heavy ion and X-ray irradiation. The protein was extracted at the times indicated after 3 Gy irradiation of  $2 \times 10^7$  cells. Equal amounts of protein (60  $\mu\text{g}$ ) were loaded into each lane in a 15% SDS-PAGE mini-gel, electrophoresed, and blotted onto a PVDF membrane and probed with monoclonal antibodies against p53 (DO-1, Santa Cruz Biotech). X-rays (average of two experiments), diamonds; C-ion (average of two experiments), squares; Fe-ion (one experiment), circles.

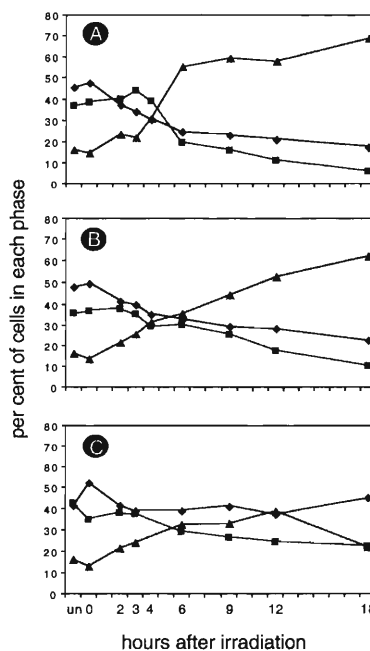


Fig. 2. Cell cycle distribution after heavy ion and X-ray irradiation. At appropriate times after treatment, cells were washed with PBS and fixed in 100% ethanol. Propidium iodide and RNase were added and the cells incubated at 37°C for 30 min. Cells were centrifuged and resuspended in PBS and concentrated onto the glass slide surface by a centrifugation step and then analysed for DNA content by microscopy. A, X-ray (average of two experiments); B, C-ion (average of three experiments); C, Fe-ion (one experiment). G1 phase, diamonds; S phase, squares; G2 phase, triangles.

in WI-L2-NS p53 is constitutively expressed and p21 is not produced (due to the mutant nature of p53). The type of irradiation did not alter the p53/p21 response of each cell line as monitored at 2 h. However, the time course of p53 induction appears to be different after the three irradiation treatments, with X-rays and C-ions producing an earlier maximal level of p53 induction compared to that induction produced by Fe-ion irradiation (Fig. 1).<sup>3)</sup> Cell cycle analysis suggests that X-ray irradiation produces the strongest G2 block, Fe-ion irradiation produces the weakest G2 block and C-ion irradiation produces a G2 block intermediate between X-rays and Fe-ions. No G1 block was seen in these lymphoblastoid cell lines (Fig. 2).<sup>3)</sup>

### References

- 1) Y. Kagawa et al.: *Mutagenesis* **14**, 199 (1999).
- 2) S. Morimoto et al.: submitted for publication.
- 3) A. Gordon et al.: manuscript in preparation.



## 4. Radiation Chemistry and Radiation Biology



## Electron-Hole Plasma Luminescence from the Ion Track of Insulator Crystals

K. Kimura, S. Sharma, and J. Kaneko

Recently, we found a new extremely fast luminescence band by measuring time-resolved luminescence spectra (its time resolution of 100 ps) of heavy-ion-irradiated  $\alpha$ -alumina, and proposed that the origin is the electron-hole plasma (e-h plasma) or the free exciton complex,<sup>1)</sup> hereafter, referred to as the e-h plasma. If this proposal is valid, the corresponding luminescence should be observed not only for alumina but also for other insulator crystals. We have examined this for single crystals of LiF, NaF, NaCl, KCl, KBr, KI, RbI, CsCl, CsBr, CsI, MgO, SiO<sub>2</sub>, and diamond, and observed the corresponding luminescence in all crystals except for SiO<sub>2</sub> and diamond. Figure 1 a and b (for KCl) and c and d (for MgO) show decay curves at various wavelengths and time-resolved spectra of luminescence, respectively. The luminescence showed the following common characteristics of these samples. (1) The lifetimes were 100 ps or shorter. (2) The band widths were unusually broad and the wavelength positions were different from all known bands. (3) The efficiency increased superlinearly with an increase in the excitation density. (4) The decay rate temperature and the efficiency were almost invariant to temperature changes. These results imply that the origin of the luminescence concerned is not self-trapped excitons, free excitons, excited defects, and excited impurity centers which have been reported so far, and also that it is not due to a localized excited state but a multiply bound state among short-lived (at most 100 ps) excited states. The state which suits these characteristics may be the e-h plasma or the free exciton complex, considering that almost all energy deposited by ions (as large as a few hundred eV/Å) is given to electronic systems to produce e-h pairs. The e-h plasma may decompose stepwise with emissions of photons of which energy is less by binding energy than that of the free exciton, analogous to excitonic molecules in semiconductors. This is expressed schematically as follows.

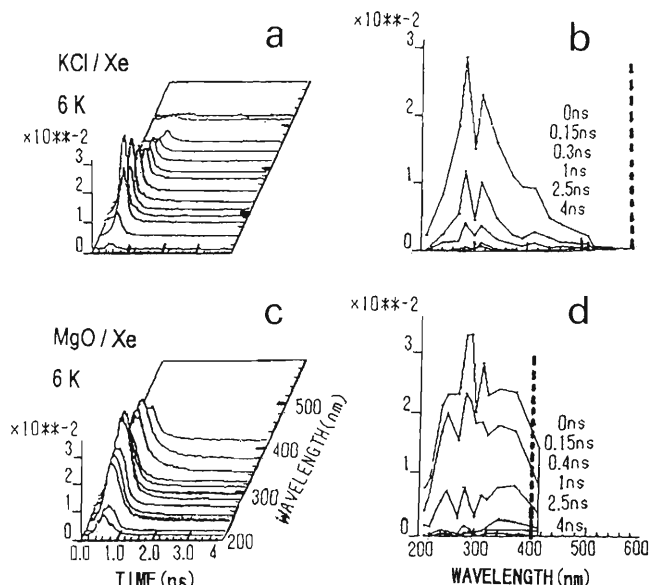
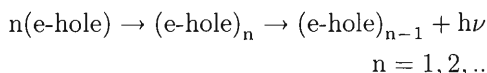


Fig. 1. Figures a and b, decay curves at various wavelengths and time-resolved spectra of luminescence from KCl irradiated by Xe ion at 6 K; c and d, similar figures for MgO. The dotted lines represent the peak positions of the known bands.

$$h\nu \doteq E_{\text{free exciton}} - E_{\text{binding}} - K^2/4M (\doteq 0).$$

Other emission processes induced by direct electromagnetic interaction between ion beams and substances, e.g., transition radiation, Bremsstrahlung and Cherenkov radiation, were ruled out by the estimation of luminescence yield and the measurement of light polarization and its spatial pattern.

### References

- 1) K. Kimura, J. Kaneko, S. Sharma, W. Hong, and N. Itoh: Phys. Rev. B **60**, 12626 (1999); K. Kimura, J. Kaneko, S. Sharma, and N. Itoh: Nucl. Instrum. Methods Phys. Res. B **154**, 318 (1999).

# Luminescence Spectra and Decay Curves of Diamond Crystals Irradiated by Heavy Ions

J. Kaneko, K. Kimura, and S. Sharma

Cathode luminescence analysis is a standard method for the characterization of diamond crystals, because it is possible to extract information about band-gap energy, centers of impurities and vacancies. Synthetic diamond crystals were irradiated by several kinds of ions from the RIKEN Linear Accelerator for purposes of characterization and study of luminescence caused by high-density excitation. Luminescence spectra from the synthetic diamond crystals were measured at 77 K. Time-resolved spectra were measured by using a single-ion-hitting and single-photon-counting (SISP) system<sup>1)</sup> whose time resolution was better than 100 ps. In this paper, experimental results using heavy ions, i.e., Xe, were described.

A high-purity type IIa single diamond crystal grown by a high-pressure and high-temperature (HP-HT) synthesis and a high-purity chemical vapor deposition (CVD) diamond polycrystal were used in this experiment. The type IIa diamond that had almost ideal crystallinity was estimated to contain less than two ppm of impurities. The CVD diamond polycrystal whose grains had a size of several  $\mu\text{m}$  was estimated to contain fewer impurities than that of the type IIa diamond crystal.

In general, a luminescence band, called band A, is predominant in cathode luminescence spectra of diamond crystals. When the type IIa and the CVD diamond crystals were irradiated by light ions, *e.g.*, He and Ar, at 77 K, the luminescence spectra had the centers of band A at 520<sup>2)</sup> and 360 nm<sup>3)</sup> respectively. Figure 1 shows luminescence spectra from the type IIa and CVD diamond crystals irradiated by Xe<sup>27+</sup> at 77 K. There are peaks of free-exciton recombination luminescence at 235 nm in each spectrum. Sensitivity dependence on wavelength was not calibrated for these spectra; thus it should be kept in mind that the luminescence yield in the short-wavelength region was higher than that in long-wavelength region. The luminescence peak located around 520 nm is still predominant in the luminescence spectrum of the type IIa diamond, though there are several peaks at 300 nm that were not observed in luminescence caused by light-ion irradiation. On the other hand, the fine structure of peaks around 360 nm became clear in the luminescence spectrum of the CVD diamond; there are peaks around 520 nm that were not observed in luminescence caused by light-ion irradiation. A peak located at 270 nm is unique to the luminescence spectrum of the CVD diamond. This peak is probably related to grain boundaries.

Figure 2 shows a time-resolved luminescence spec-

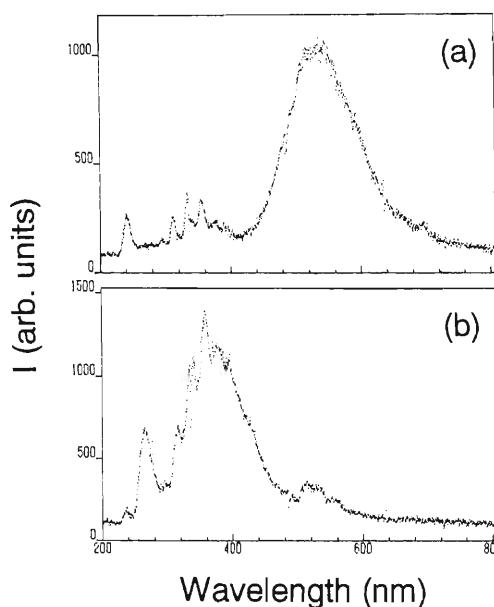


Fig. 1. Luminescence spectra of (a) HP-HT type IIa and (b) CVD diamond crystals irradiated by Xe<sup>27+</sup> ions at 77 K.

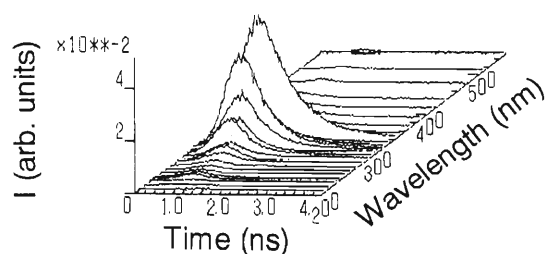


Fig. 2. Time-resolved spectrum of the CVD diamond crystal irradiated by Xe<sup>27+</sup> at 77 K.

trum up to 4 ns of the CVD diamond crystal irradiated by Xe<sup>27+</sup>. Although the free-exciton recombination luminescence was predominant in a time-resolved luminescence spectrum of the CVD diamond irradiated by Ar<sup>8+</sup>, luminescence peaks around 360 nm became predominant in the time-resolved spectrum caused by Xe<sup>27+</sup>. Additionally, there is no peak around 270 nm in the time range; thus the peak at 270 nm had a slow decay time.

## References

- 1) K. Kimura and J. Wada: Phys. Rev. B **48**, 15535 (1993).
- 2) J. Kaneko and K. Kimura: RIKEN Accel. Prog. Rep. **31**, 153 (1998).
- 3) J. Kaneko and K. Kimura: RIKEN Accel. Prog. Rep. **32**, 139 (1999).

## Ultrafast Luminescence and Exciton Dynamics in Ion-Irradiated RbI Single Crystal

S. Sharma, J. Kaneko, and K. Kimura

We are conducting a study of the luminescence and its decay of ion-irradiated wide-band-gap crystals, using a fast decay measurement technique. Heavy-ion irradiation is a useful method for high-density excitation of such crystals. Our recent studies of ion irradiated  $\alpha$ -alumina<sup>1)</sup> and alkali halides revealed the formation of a new 100-ps-lived band. This new finding prompted us to investigate in detail the luminescence and exciton dynamics in RbI. Many spectroscopic studies of RbI irradiated with electrons and photons have been carried out in the recent past.<sup>2,3)</sup> The three self-trapped exciton (STE) luminescence bands at 320 ( $\sigma$ ), 400 ( $E_x$ ) and 540 nm ( $\pi$ ) have been well identified. RbI appears to be a unique material in which all the three types of STE luminescence bands coexist.

The luminescence decay was measured using the single-ion-hitting single-photon-counting (SISP) technique with a time resolution of 100 ps.<sup>4)</sup> The projectile ions He<sup>1+</sup>, Ar<sup>8+</sup>, Kr<sup>18+</sup>, and Xe<sup>20+</sup> accelerated by the RILAC were used and the ion energies were 2.0 MeV/nucleon. The time-integrated luminescence

spectra obtained by ion irradiation, composed of bands at 320, 400, and 540 nm, were similar to those obtained by electron and photon irradiation.<sup>2,3)</sup> In contrast, the time-resolved luminescence spectra showed only the  $\sigma$  band and a new short-lived luminescence component. Figure 1 (a) shows the wavelength-dependent decay curves obtained by Xe ion irradiation of RbI, while Fig. 1 (b) shows the time-resolved spectrum. In these figures, a fast decaying component spread over both sides of the 320 nm band can be easily noticed. The half lifetime of this component was estimated to be about 100 ps, which is the time resolution of our equipment. The intense band due to the  $\sigma$  excitons at 320 nm masks the peak of the 100 ps component, however the shape of this peak may be similar to that shown in Fig. 1 (c) which was obtained by subtracting a suitably enlarged spectrum at 4 ns from the spectrum at 0 ns.

The excitation density (ED) dependence of the 100 ps component at 400 nm, where the new band is almost free from the superposition of the 320 nm band, is shown in Fig. 2. It is evident from the equiheight decay curves (Fig. 2 (a)) that the decay rate constant is scarcely influenced by the ED. This suggests that the decay rate of the 100 ps component once it is formed, is no longer influenced by the ED. The luminescence efficiency however, was largely enhanced with increasing ED (Fig. 2 (b)). The ratio of the efficiencies at  $t = 0$  (actually in a period of 20 ps) for Ar, Kr, and Xe ion irradiation was 1 : 7.6 : 53. The intensity by He ion irradiation was too weak to be evaluated. The intensity ratio for Ar, Kr, and Xe ion irradiation is much larger than the corresponding ratio of ED (1 : 1.8 : 2.4) and also its square (1 : 3.2 : 5.9), which suggests that the 100 ps component originates from multiple bindings among the primary excited states, i.e., an ex-

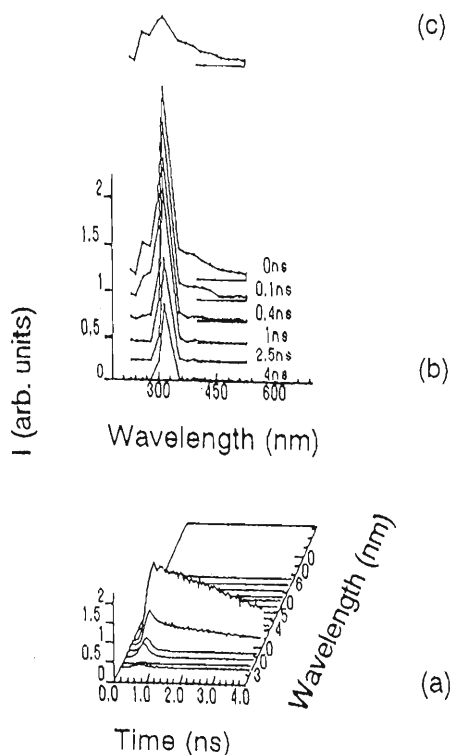


Fig. 1. Luminescence spectra obtained by Xe ion irradiation of RbI at 5 K. (a) 3-D plot of the wavelength-dependent decay curves; (b) time-resolved spectrum; (c) shape of the 100 ps component.

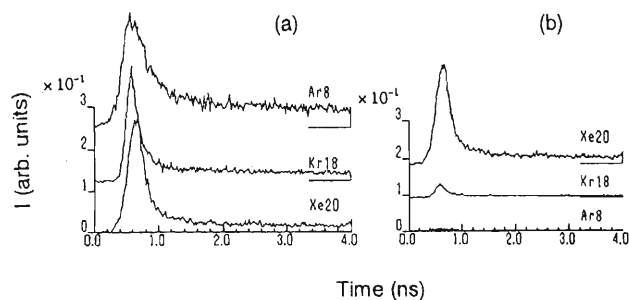


Fig. 2. Ion dependent decay curves of the 100 ps component of RbI measured at 400 nm. (a) Equi-height decay curves; (b) intensity normalized for the ion count.

citon complex. This complex may be formed by the binding among the electron-hole pairs that are formed at extremely high densities in the ion track.

The ratio of the luminescence efficiencies of the  $\sigma$  band (320 nm) for Ar, Kr, and Xe ion irradiation, 1 : 2.1 : 12, is much greater than even the corresponding ratio of  $(ED)^2$ , which suggests not only distant radiative interaction between the excited states, but also stimulated emission.

Further studies related to the exciton reaction in

wide-band-gap crystals are in progress.

#### References

- 1) K. Kimura, J. Kaneko, S. Sharma, W. Hong, and N. Itoh: Phys. Rev. B **60**, 12626 (1999).
- 2) K. S. Song and R. T. Williams: in *Self-Trapped Excitons*, edited by M. Cardona, (Springer, Berlin, 1995), p. 123.
- 3) R. T. Williams, H. Liu, G. P. Williams, Jr., and K. J. Platt: Phys. Rev. Lett. **66**, 2140 (1991).
- 4) K. Kimura and W. Hong: Phys. Rev. B **58**, 6081 (1998).

Strontium Uptake by Yeast *Schizosaccharomyces pombe*

Y. Nose and I. Yamaguchi

The disposal of radioactive wastes and nuclear facility accidents are serious social problems. For nuclear safety assessment, we have been researching the uptake of various radionuclides by living organisms, particularly yeast. Recently, we demonstrated by using the multitracer technique<sup>1,2)</sup> that the yeast *Saccharomyces cerevisiae* JCM7255 took up various radionuclides, including strontium-85. Radioactive strontium has been regarded as one of the most hazardous elements because of its high yields in <sup>235</sup>U-fission products in nuclear facilities. Therefore, we planned a series of studies viz. (1) the characterization of Sr uptake by yeast and (2) identification of the genes and proteins related to Sr uptake. In this article, we report the properties of Sr uptake by yeast.

In the experiment, the yeast *Schizosaccharomyces pombe* was used. The nuclear phase of the strain of *S. pombe* was one, whereas that of *S. cerevisiae* JCM7255 was four. Therefore, *S. pombe* was considered to be more suitable for genetic experiments. First, we studied the radionuclides uptake activity of *S. pombe*. The yeast was cultured in 10 ml of YEL medium (0.5% (w/v) Bacto Yeast Extract, 3% (w/v) glucose) at 25°C, on a shaker. Cells were collected by centrifugation at 1000 × *g*, for 5 min. To remove the YEL medium, the cell pellets were suspended in D.W. and recentrifuged under the same conditions three times. Then, the cells were suspended in 3.5 ml of 10 mM MES buffer (pH 6.0) with 3% glucose. One ml of the cell suspension was transferred into a 1.5-ml tube, and shaken at 25°C. After 30 min, 10 μl of the multitracer solution containing 1362.2 Bq of <sup>7</sup>Be, 18.6 Bq of <sup>22</sup>Na, 95.2 Bq of <sup>46</sup>Sc, 313.2 Bq of <sup>54</sup>Mn, 83.1 Bq of <sup>56</sup>Co, 1063.2 Bq of <sup>65</sup>Zn, 205.5 Bq of <sup>75</sup>Se, 3372.8 Bq of <sup>83</sup>Rb, 3024.0 Bq of <sup>85</sup>Sr, 1886.4 Bq of <sup>88</sup>Y, 1318.8 Bq of <sup>88</sup>Zr and 14.1 Bq of <sup>95m</sup>Tc, was added to the suspension, and which was then incubated at 25°C for 30 min on a shaker. The cells were collected by centrifugation and washed with D.W. three times. The cell pellets were subjected to γ-ray measurement and protein assay. Table 1 shows that the yeast *S. pombe* had the ability to take up various radionuclides, including <sup>85</sup>Sr. In the next step, a single tracer, <sup>85</sup>SrCl<sub>2</sub>, was used instead of the multitracer solution. The yeast cells were cultured in 1.5 ml of YEL medium, and washed and collected in the same manner described above. The cells were suspended in 1.5 ml of 10 mM MES buffer (pH 6.0) with or without 3% glucose, and shaken at 25°C. After 30 min, <sup>85</sup>SrCl<sub>2</sub> was added, and the cells were incubated at 25°C for 30 min. Then the cells were washed, collected and subjected to γ-ray measurement and protein assay by the same procedure described above. Figure 1 shows that

Table 1. Uptake of various radionuclides by *Schizosaccharomyces pombe*. Data represent the the γ-ray activity (Bq) of each radionuclide per microgram of cell protein. N.D.: not detectable.

Nuclides	Bq/μg protein (× 10 <sup>-1</sup> )		
	Ave.	±	SD
Be- 7	4.32		0.46
Na- 22	N.D.		—
Sc- 46	0.04		0.01
Mn- 54	2.93		0.29
Co- 56	0.70		0.09
Zn- 65	9.13		0.92
Se- 75	0.11		0.02
Rb- 83	21.04		2.27
Sr- 85	8.75		1.02
Y - 88	8.25		1.02
Zr- 88	0.27		0.08
Tc- 95m	N.D.		—

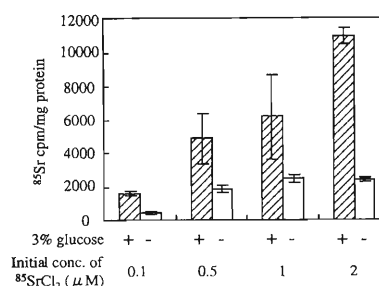


Fig. 1. <sup>85</sup>Sr uptake by *Schizosaccharomyces pombe*. Data represent the γ-ray activity (cpm) per milligram of cell protein.

the amount of <sup>85</sup>Sr taken up by *S. pombe* in the buffer with glucose (+glucose) was significantly larger than that in the buffer without it (-glucose). In +glucose, the amount of <sup>85</sup>Sr taken up increased depending on the amount of <sup>85</sup>Sr added to the cell suspension. However, in -glucose, the amount taken up remained at a low level over the entire <sup>85</sup>Sr concentration range examined (0.5–2 μM).

To identify the gene(s) related to the Sr uptake, we are planning to produce transformants of *S. pombe* by restriction-enzyme-mediated integration (REMI). The transformants will be tested for the Sr uptake, in order to select the cells with low or high Sr uptake ability. The genes disrupted by REMI event will be identified; and further more, the uptake of various metals by the transformants will be studied by the multitracer technique.

## References

- 1) Y. Nose et al.: RIKEN Accel. Prog. Rep. 31, 141 (1998).
- 2) Y. Nose and I. Yamaguchi: RIKEN Accel. Prog. Rep. 32, 128 (1999).

## Influence of Endophytes on the Uptake of Radionuclides by Perennial Ryegrass

T. Soshi, T. Arie, Y. Nose, and I. Yamaguchi

Radionuclides released by nuclear power plants into the environment are a potential risk to human health. Consumption of food contaminated with radionuclides, due to their transfer from soil to plants and then to livestock, is a significant pathway for human exposure to radionuclides. To decrease such exposure doses of humans, it is desired to eliminate radionuclides from the soil. Phytoremediation is a good method to remove radionuclides from the soil. We have shown that several factors influence the uptake of radionuclides by plants, including soil profile, pH and microorganisms in the soil.<sup>1,2)</sup> But the influence of microorganisms on the uptake of radionuclides by plants remain unclear.

Endophytes are fungi that live inside grass, for example, in tall fescue (*Festuca arundinacea*) and perennial ryegrass (*Lolium perenne*). The relationship between grasses and endophytes is symbiotic. The endophytes do not harm the grasses, but they sometimes produce toxins that are harmful to livestock.<sup>3)</sup> Infected plants can grow better and show higher drought tolerance and resistance to insects than noninfected ones. In this paper, we report the influence of an endophyte on the uptake of radionuclides by perennial ryegrass using a multitracer.

Genetically identical strains of perennial ryegrass that were infected with an endophyte (*Neotyphodium lolii*) and noninfected strains were kindly supplied by Dr. Shimanuki (National Grassland Research Institute, MAFF, Tochigi). Five plants were used in each treatment, and grasses were grown in five plastic pots containing 150 g of sterilized horticulture soil (Kureha engei baido, Kureha Chemical Industry Co. Tokyo). A solution of diluted multitracer and radioactive cesium was administered to each pot. The same amounts of solution were absorbed by filter paper for comparison. Plants were cultivated in a green house at 25–30°C and under 15000 to 17000 lux light for 12 hrs a day. After 4 weeks, aerial parts of plants were collected and dried at 50°C. Then the radioactivity was measured using hyper pure Ge detector and the results were expressed as the uptake percentage compared to the control per gram dry weight of the plant.

Figures 1 and 2 show the uptake rate of several elements (Sc, Mn, Co, Zn, Se, Rb, Sr, Cs in Fig. 1, Na and Tc in Fig. 2). In the noninfected strain, the uptake

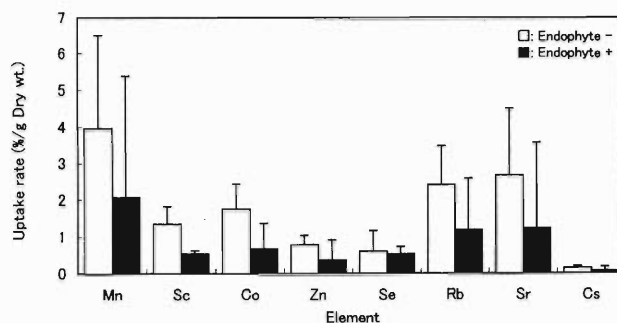


Fig. 1. Influence of endophyte presence on the uptake rate of eight elements by perennial ryegrass.

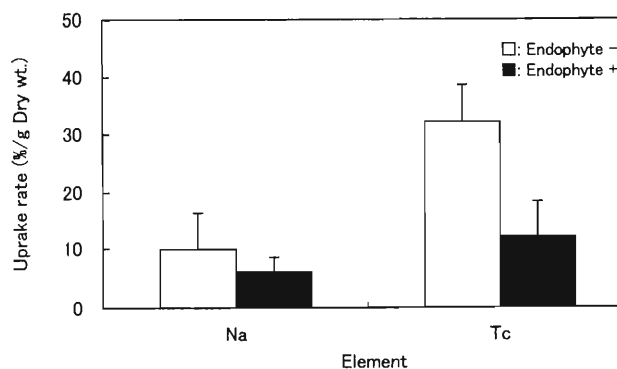


Fig. 2. Influence of endophyte presence on the uptake rate of Na and Tc by perennial ryegrass.

rates of Na and Tc were high, about 10% for Na and 32% for Tc. For other nuclides, such as Sc, Mn, Co, Se, Rb and Sr, the uptake rates were relatively low (1% to 8%). The uptake rate of Cs and Zn was less than 1% (0.14% Cs and 0.77% Zn). In the endophyte infected strain, almost all of the element's uptake rates were reduced.

### References

- 1) S. Gouthu et al.: RIKEN Accel. Prog. Rep. **30**, 117 (1997).
- 2) S. Gouthu et al.: RIKEN Accel. Prog. Rep. **31**, 146 (1998).
- 3) M. R. Seigel et al.: Ann. Rev. Phytopathol. **25**, 293 (1987).

# Analysis of Heavy-Ion Beam-Induced DNA Damage in *Saccharomyces cerevisiae*

M. Yoshimasu, T. Abe, S. Yoshida, F. Ling, and T. Shibata

It has been reported that a heavy-ion beam induced DNA double-strand breaks in the diploid cells of *Saccharomyces cerevisiae* and caused both point mutations and deletions of genomic DNA in a human cell line.<sup>1,2)</sup> In this study, we reported that the nuclear mutations were induced in the haploid cells of *S. cerevisiae* by accelerated heavy-ion beam irradiation. To identify these mutations, the sequence alternations in an open reading frame (ORF) of the *URA3* gene were examined.

We used the haploid cells of IL166-187 ( $\alpha$ , *leu2*, *trp1*, [ $\rho^+$ ])<sup>3)</sup> to induce the damage by a heavy-ion beam into the genomes. The cells, grown in a glucose medium at 30°C for 3 days were spread on 1% agar plates without the amino acids required for cellular growth. The plates were exposed to irradiation with 5 to 200 Gy of the <sup>20</sup>Ne-ion beam (135 MeV/u) accelerated by the RIKEN Ring Cyclotron. The linear energy transfer of the <sup>20</sup>Ne-ion corresponded to 63.4 keV/ $\mu$ m. After the irradiation, the cells were suspended in sterilized water and then spread on glucose plates. After incubation at 30°C for 4 days, the survival rates at various doses of the <sup>20</sup>Ne-ion beam were calculated.<sup>4)</sup> Then, the cells irradiated at 50 Gy with 32% of survival rate were spread on 5-fluoroorotic acid (FOA) containing plates to select the cells required for uracil (*ura*<sup>-</sup>). After that, the whole cellular genomes were purified from the *ura*<sup>-</sup> cells and used for amplification of the ORF of the *URA3* gene by PCR. The PCR products were digested by *Apa* I and the sizes of the PCR products were compared with that of the *URA3* gene amplified from wild-type cells through acrylamide gel electrophoresis. As shown in Fig. 1, all PCR-amplified DNA fragments from 20 mutant clones had the same length. Since it has been reported that heavy-ion beams caused deletions of genomic DNA with eighty base pairs in animal cells,<sup>2)</sup> if any deletions occurred, different sizes of PCR products would be observed. Finally, we examined the sequences of the PCR-amplified *ura3* gene in 6 clones (Table 1). Among the sequenced fragments, only point mutations with base transition from C to T or G to A were detected.

The heavy-ion beam induced DNA deletions in animal and plant cells, but we could not detect deletions on the genomes in our experiment. It is likely that there are different cellular systems corresponding to the biological effects of a heavy-ion beam on the

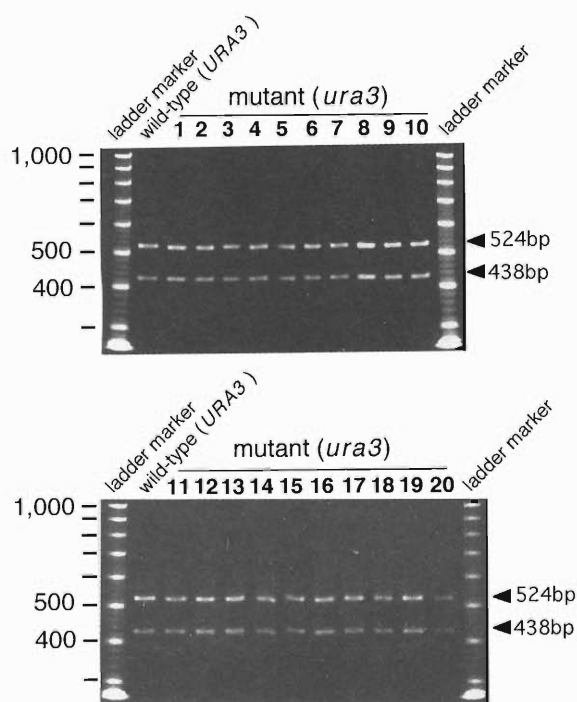


Fig. 1. Electrophoresis in acrylamide gel of DNA fragments of the *ura3* gene mutated by the heavy-ion beam.

Table 1. Ne-ion beam-induced point mutations.

Clone number	Mutation point	Transition of bases	Replacement of amino acids
1	<i>ura3</i> -134	403 C→T	134 Gln→stop
4	<i>ura3</i> -202	608 C→T	202 Pro→Leu
1	<i>ura3</i> -203	611 G→A	203 Gly→Asp

genomes between yeast and animal or plant cells.

## References

- 1) S. Ikpeme et al.: Radiat. Environ. Biophys. **34**, 95 (1995).
- 2) Y. Kagawa et al.: J. Radiat. Res. **36**, 185 (1995).
- 3) F. Ling et al.: EMBO J. **14**, 4090 (1995).
- 4) M. Yoshimasu et al.: RIKEN Accel. Prog. Rep. **32**, 148 (1999).

## Effective Plant-Mutation Method Using Heavy-Ion Beams (IV)

T. Abe, M. Miyagai, and S. Yoshida

In the previous paper<sup>1)</sup> we have reported that tobacco is quite sensitive to the irradiation with heavy-ion beams during the stage of fertilization. However, it is difficult to apply this method at this particular stage for plants that have several seeds per flower. In this paper we report the effect of heavy-ion beams on dry seeds, imbibition seeds and calli of tobacco.

Tobacco seeds (*Nicotiana tabacum* cv. Xanthi and BY-4) were incubated in 1/2MS agar medium for 24 hrs before irradiation. The imbibition seeds and dry seeds were irradiated with N or Ne-ion beams (135 MeV/u) within a dose range of 5 to 200 Gy. The linear energy transfer of the N and Ne ion corresponded to 30 and 63 keV/ $\mu$ m, respectively. One month after the irradiation, we determined their germination percentage, growth rate and morphological abnormalities. Calli (BY-4) were irradiated with N or Ne-ion beams (135 MeV/u) within a dose range of 5 to 50 Gy. After irradiation, calli were cultured on MS medium containing 1mg/L 2,4-D at 25°C under continuous light. Callus growth was measured after two weeks. The growth rate was calculated by dividing the increment in the fresh weight by the initial weight.

The germination and survival rates were not affected by ion beam irradiation in the case of dry seeds (Table 1). In the case of imbibition seeds, the germination rate was reduced when irradiated at 100 and 200 Gy, and the germinated plants produced no leaves and died at doses higher than 20 Gy (Fig. 1). The irradiation of

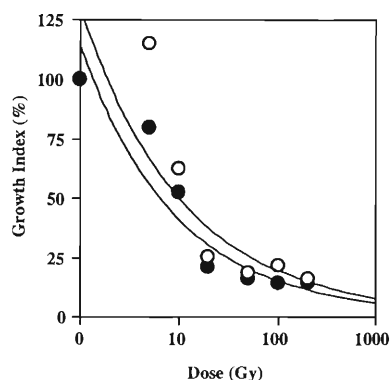


Fig. 1. Effects of irradiation of imbibition seeds with Ne-ion beams on the growth rate.  $\circ$ : Xanthi and  $\bullet$ : BY-4.

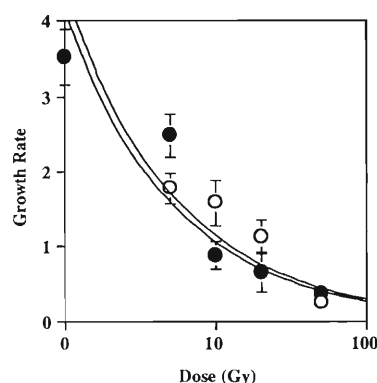


Fig. 2. Effects of irradiation of the callus with ion beams on growth.  $\circ$ : N ion and  $\bullet$ : Ne ion.

Table 1. Effect of heavy-ion beams on seed germination.

Ion	Gray	Germination (%)			
		Xanthi		BY-4	
		Dry	Imbibition	Dry	Imbibition
Control	0	98.8	98.8	99.0	99.0
N	5	98.7	96.9	98.4	91.7
	10	98.9	95.6	97.2	97.5
	20	97.2	94.7	96.3	98.0
	50	99.5	96.0	98.8	98.2
	100	98.6	93.8	100.0	38.7
	200	98.8	73.6	98.8	7.7
Ne	5	99.6	93.3	100.0	99.0
	10	100.0	96.9	100.0	98.3
	20	98.8	97.4	99.6	98.5
	50	99.6	97.9	99.4	95.6
	100	99.6	97.1	100.0	75.9
	200	99.2	ND	99.5	ND

dry seeds with N ions resulted in variegation in Xanthi (1 plant/1239 germinated plants) and formation of pale green leaves in one plant of BY-4 (1/1010) of the M<sub>1</sub> progeny. The frequencies of morphologically abnormal plants, obtained following N-ion irradiation of embryos during fertilization cycle, were 18.1 and 0.82% for Xanthi and BY-4, respectively,<sup>2)</sup> whereas the frequencies were 0.08% for Xanthi and 0.1% for BY-4 of dry seeds. Callus growth was inhibited at doses higher than 10 Gy (Fig. 2). The results indicate that there is a difference in sensitivity to ion beams between organs of tobacco. The sensitivity of these organs decreased in the following order: calli, embryos during fertilization cycle, imbibition seeds, dry seeds.

### References

- 1) T. Abe et al.: in *Modification of Gene Expression and Non-Mendelian Inheritance*, edited by K. Oono and F. Takaiwa, (NIAR, 1995), p. 469.
- 2) T. Abe et al.: RIKEN Accel. Prog. Rep. 30, 127 (1997).

## Effects of Heavy-ion Beam Irradiation on Shoot Elongation in Roses

T. Kitaura, Y. Hara, T. Abe, K. Miyoshi, and S. Yoshida

Breeding programs of roses through conventional crossing methods have proven difficult for its genetic improvement due to the variation in ploidy levels, high sterility and genetic heterozygosity. The spontaneous as well as artificial mutations in a crop, which can be easily propagated vegetatively, will accelerate its genetic improvement. Mutants of rose have been successfully induced yielding alteration of growth habit and flower color by treatment with chemical mutagen and radiation. Heavy-ion beam irradiation, which is considered to result in new variations in phenotype of induced mutants, has recently been reported as an alternative method of inducing mutation in some crops. The objective in the present study is to determine the effect of heavy-ion beam irradiation with  $^{20}\text{Ne}$  and  $^{14}\text{N}$  on rose mutation breeding, particularly the effect of exposure dose on shoot elongation of spray type roses.

Two spray type rose cultivars, namely 'Love me tender' (pink flower) and 'Bridal Fantasy' (white flower) were used. Ten offshoots (ca. 70 mm long) were used for each treatment. The explant contained one winter bud. Irradiation treatments were conducted in the dose range of 5, 10, 20, and 50 Gy for  $^{20}\text{Ne}$  ions and 5, 10, 20, 50, and 100 Gy for  $^{14}\text{N}$  ions with control (0 Gy) at an energy of 135 MeV/u. The buds were grafted on the rose stock one day after irradiation. Survival of bud and length of shoots from the grafted bud were recorded one and two months after grafting, respectively.

Survival rates of buds and length of shoots decreased with the increase in exposure dose. Survival rates and shoot length were lower after  $^{20}\text{Ne}$  beam treatment than that of  $^{14}\text{N}$  of the same exposure dose. No clear-cut genotypic difference was found in the response to irradiation. The values of  $\text{LD}_{50}$  for the two varieties were found to be 10–20 Gy of the  $^{20}\text{Ne}$  ion and 20–50 Gy of the  $^{14}\text{N}$  ion, respectively (Tables 1

Table 1. Effect of  $^{20}\text{Ne}$  heavy-ion beam irradiation on growth of roses.

Cultivar	Dose (Gy)	No. plants	Survival (%)	Shoot length (cm)
Love me tender	0	10	90	24.9
	5	10	80	24.1
	10	10	80	20.5
	20	10	50	1.9
	50	10	10	0.0
Bridal fantasy	0	10	100	46.4
	5	10	70	9.1
	10	10	50	12.6
	20	10	50	1.1
	50	10	0	0.0

Table 2. Effect of  $^{14}\text{N}$  heavy-ion beam irradiation on growth of roses.

Cultivar	Dose (Gy)	No. plants	Survival (%)	Shoot length (cm)
Love me tender	0	10	90	24.9
	5	10	100	34.2
	10	10	90	22.5
	20	10	90	35.6
	50	9	56	0.6
	100	10	30	0.0
Bridal fantasy	0	10	100	46.4
	5	10	100	39.5
	10	10	100	22.3
	20	10	100	36.6
	50	10	40	0.4
	100	9	44	0.0

and 2). Some chimeric tissues, such as the red sector in the petals of the pink flower, from irradiated buds were observed. Further experiments to induce more shoots from the putatively mutated sections should be conducted to obtain the mutants of roses.

## Adaptive Response of Human Cultured Cells to Heavy-ion Irradiation

S. Morimoto, A. Gordon, N. Fukunishi, T. Kurobe, F. Hanaoka, and F. Yatagai

Cells can become resistant to cytotoxic treatment after a low-dose exposure to various physical and chemical agents. This phenomenon is observed not only in prokaryotic cells but also in fish, plant and mammalian cells, and is defined as adaptive response. The basic mechanism of this adaptive response is not yet well understood but is regarded as an important index to estimate the risk of low-dose radiation.

The reaction kinetics of the radioadaptive response to low-dose X-ray exposure have been studied in quiescent cultured mouse cells.<sup>1)</sup> Mouse m5S cells pre-exposed in the G1 phase to low doses of X-rays became insensitive to the induction of chromosomal aberrations, mutations causing 6-thioguanine resistance and cell killing.<sup>2)</sup> In this study, we focused on such a response to heavy-ions since this subject has not been thoroughly studied.

Human lymphoblastoid TK6 cells were incubated for 2 hours at 37°C after pre-exposure to 5, 10 or 20 cGy of C-ions (22 keV/μm) or Fe-ions

(1000 keV/μm). The cells were then challenged by X-ray irradiation and the survival, mutation induction and protein induction were determined (Fig. 1). Under

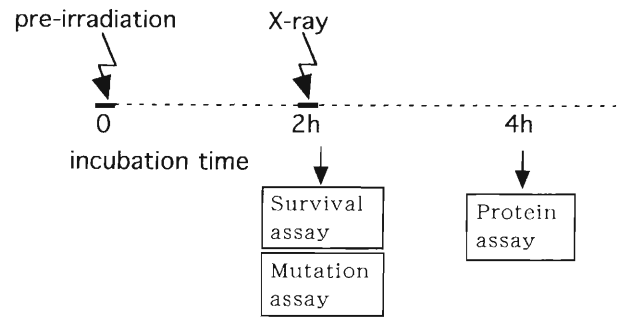


Fig. 1. Time schedule of the survival, mutation and protein assays. After 5, 10 and 20 cGy X-rays, 22 keV/μm C-ion and 1000 keV/μm Fe-ion pre-irradiation, cells were incubated for 2 hours at 37°C in 5% CO<sub>2</sub> and then challenged with X-rays.

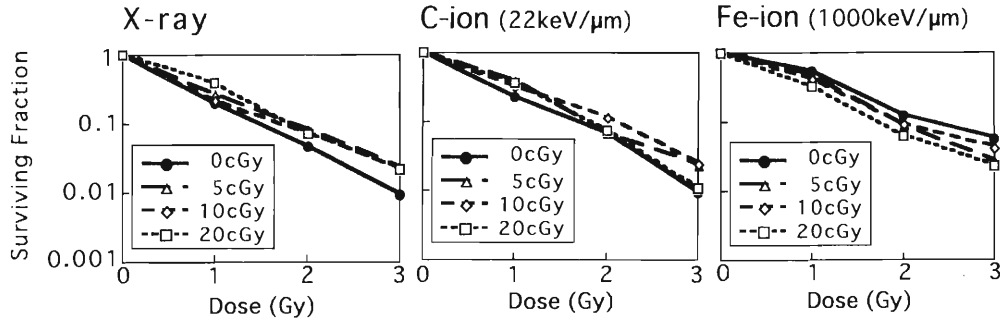


Fig. 2. Survival curves against X-ray dose after 5, 10, and 20 cGy X-rays, 22 keV/μm C-ion and 1000 keV/μm Fe-ion pre-irradiation.

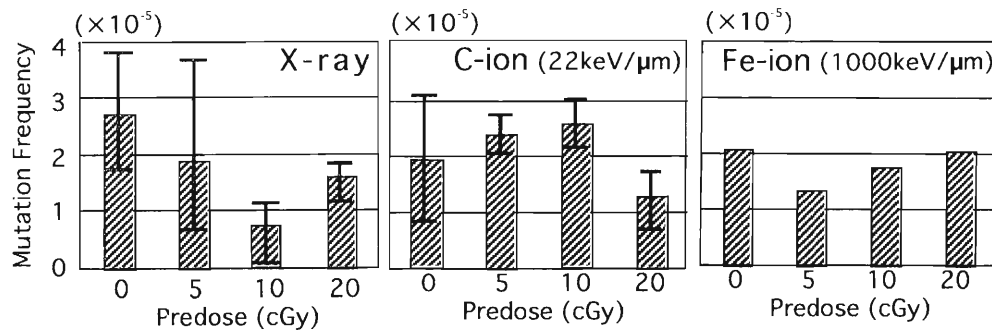


Fig. 3. *Hprt* mutation frequency after exposure to 1 Gy X-rays. 2 hours before the challenge, cells were pre-irradiated by 5 cGy X-rays, 22 keV/μm C-ions and 1000 keV/μm Fe-ions. There are no standard error bars for Fe-ions due to the results of a single experiment.

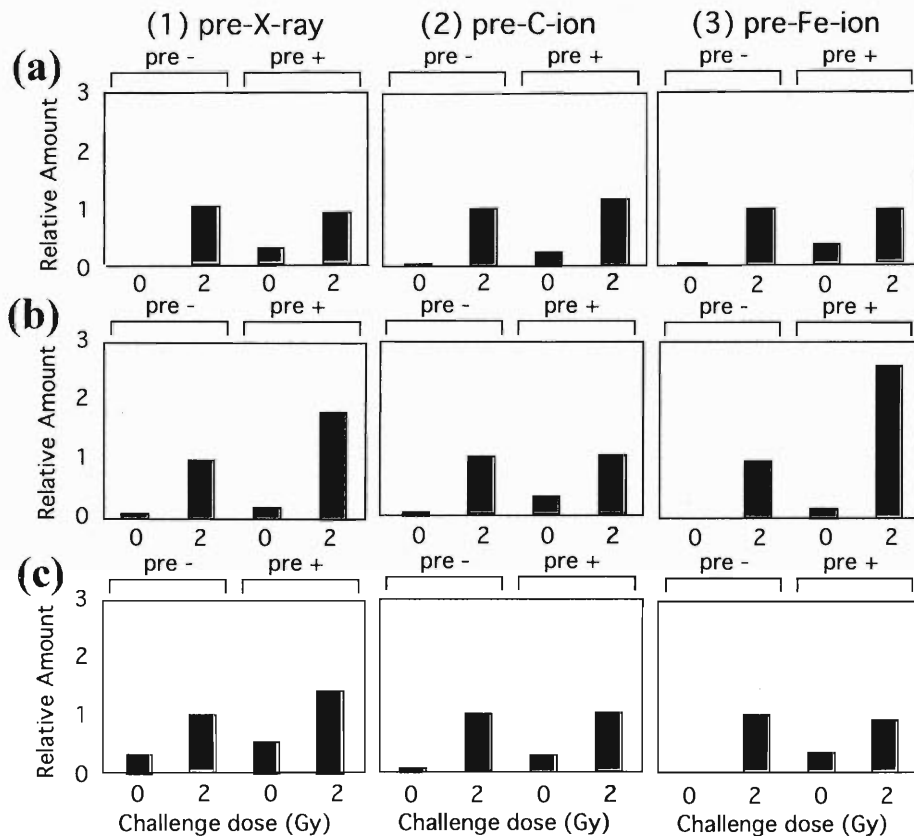


Fig. 4. Western blot analysis of (a) p53, (b) p53-Ser15-P and (c) p21 protein induction after 2 Gy X-ray irradiation with and without 5 cGy pre-irradiation. The same amount of protein was loaded in each lane and the blots were probed with DO-1 (Santa Cruz Biotechnology), Ab-1 (Oncogene Research Products) and phospho-p53 antibody (BioLabs). The amounts of protein were corrected using actin and the amount of protein induced after 2 Gy X-ray irradiation with no pre-irradiation was arbitrarily set to a value of 1.

the present condition of pre-irradiation and subsequent radiation treatment, the cells did not acquire any significant radioresistance (Fig. 2). Similarly almost no reduction in *hprt* mutation induction was observed following these heavy-ion irradiations (Fig. 3). To determine the survival fraction and the mutation frequency, we followed the procedure described by Kagawa *et al.*<sup>3)</sup>

Since such an adaptive response was not clearly detected even with pre-X-ray irradiation (Figs. 2 and 3), we would like to consider the possibility that this lymphoblastoid cell line exhibits poor adaptive responses, unlike the aforementioned mouse cells. Consistent with these results, the induction patterns of p53, p53-ser15-phosphorylated and p21 were similar between the X-ray- and the heavy-ion-irradiated groups (Fig. 4). Here, we would like to emphasize the relatively high level of induction of the above protein following

exposure to a very small dose of 5 cGy for all tested types of radiation. It is thus important to study the cellular responses to low-dose radiation, including that to heavy-ions. Furthermore, the adaptive response must be evaluated not only in terms of the survival and mutation rate but also in terms of the characteristics of the mutations. Toward this end, we are now analyzing the induction of the TK mutation using the same cell line. Furthermore, we plan to use a fibroblast cell line to carry out a similar study.

#### References

- 1) M. Sasaki: *Int. J. Radiat. Biol.* **68**, 281 (1995).
- 2) M. Sasaki: Radiation Biology Center of Kyoto University, personal communication.
- 3) Y. Kagawa, T. Shimazu, A. J. Gordon, N. Fukunishi, N. Inabe, M. Suzuki, M. Hirano, T. Kato, M. Watanabe, F. Hanaoka, and F. Yatagai: *Mutagenesis* **14**, 199 (1999).

## Cytogenetic Effects of Heavy-Ion Beams on Mammalian Cells

N. Shigematsu,\* S. Yamashita,\* N. Ihara,\* T. Kawata,\* O. Kawaguchi,\* A. Kubo,\*  
H. Ito,\* T. Kanai, Y. Furusawa, and F. Yatagai

Previous studies have shown that heavy particles are more lethal to mammalian cells than sparsely ionizing radiation such as  $\gamma$  or X-rays.<sup>1-5)</sup> Induction of mutations by high-LET ions was investigated in rodent and human cells using the well-known HPRT-locus and TK-locus models, and the results revealed higher levels of mutation than that induced by low-LET radiation.<sup>3-5)</sup> Transformations caused by heavy ions are dose- and LET-dependent and are more frequent than those induced by X-rays. It has also been shown that high-LET particles induce high rates of DNA strand breaks and chromosomal breakage and rearrangement.<sup>6-9)</sup> Chromosomal rearrangements induced by sparsely ionizing radiations are well known, and cytogenetic analyses of irradiated human lymphocytes have been widely applied to biological dosimetry. However, much less is known about chromosome aberrations induced by high-LET particles.

Most of the studies on chromosomal aberrations induced by heavy-ion radiation reported thus far have been performed using Giemsa-stained or R-banded chromosomes and have dealt with dicentric, fragment and ring formation as indicators of chromosomal changes. However, other types of aberrations such as translocations and insertions cannot be detected using these techniques. Chromosome staining by the FISH technique will facilitate simple and accurate analysis, particularly of translocations in metaphase chromosomes.

To investigate (1) whether the energized-charged particles have a more efficient effect than sparsely ionizing radiations in inducing chromosomal aberrations, (2) whether the chromosomal aberrations is dose- and LET-dependent, and (3) whether the different effects are observed in different types of particles as we showed by HPRT-locus mutations caused by carbon and neon

particles used at the same LET level,<sup>3-5)</sup> we will carry out the experiment with the following plan.

The cultured cell samples and blood samples collected from human donors are irradiated at room temperature. Heavy-ion irradiation will be performed in the plateau region of the Bragg curve with various shielding, using carbon, neon and argon. One to three hours after irradiation (samples on ice in the interim), the samples will be distributed in culture tubes, and cells in metaphase will be harvested after a colchicine block to score chromosome aberrations using the FISH technique with chromosome #1 and #2 paint probes.

### References

- 1) E. A. Blkely, F. Q. H. Ngo, S. B. Curtis, and C. A. Tobias: *Adv. Rad. Biol.* **10**, 191 (1983).
- 2) P. L. Petti and A. J. Lennox: *Ann. Rev. Nucl. Part Sci.* **44**, 155 (1994).
- 3) K. Toya, N. Shigematsu, H. Ito, S. Yamashita, A. Kubo, and T. Kanai: *Nippon Acta Radiol.* **56**, 736 (1996).
- 4) T. Kawada, N. Shigematsu, H. Ito, S. Yamashita, K. Toya, A. T. Yida-Sakate, A. Kubo, and T. Kanai: *RIKEN Accel. Prog. Rep.* **30**, 134 (1997).
- 5) T. Kawada, N. Shigematsu, H. Ito, S. Yamashita, A. Takeda, K. Toya, R. Ishibashi, A. Kubo, T. Kanai, Y. Furusawa, and F. Yatagai: *RIKEN Accel. Prog. Rep.* **31**, 149 (1998).
- 6) R. Roots, W. Holley, A. Chatterjee, M. Irizarry, and G. Kraft: *Int. J. Radiat. Biol.* **58**, 55 (1990).
- 7) J. A. Stanton, G. Taucher-Scholz, M. Schneider, J. Heilmann, and G. Kraft: *Radiat. Environ. Biophys.* **32**, 21 (1993).
- 8) G. Taucher-Scholz, J. A. Stanton, M. Schneider, and G. Kraft: *Adv. Space Res.* **12**, 73 (1992).
- 9) T. Kanai, Y. Furusawa, K. Fukutsu, H. Itsukaichi, K. Eguchi-Kasai, and H. Ohara: *Radiat. Res.* **147**, 78 (1997).

\* Department of Radiology, Keio University School of Medicine

## Effect of Heavy Ion Beams on Cell Cycle Progression

K. Eguchi-Kasai, H. Itsukaichi, M. Murakami, T. Kanai, and F. Yatagai

The analysis of chromosome aberration is an effective method to estimate the radiation dose during a space mission or at an accident at an atomic power station. Since mitotic delay is dependent on radiation dose and radiation quality, it is important to study cell cycle disturbance after irradiation with various types of radiations and at various doses using different types of cells. We studied the cell cycle progression in normal human fibroblasts (NB1RGB) or rodent cells (V79) after irradiation with carbon-ion beams.

The cells were irradiated with carbon-ion beams from the Ring Cyclotron at RIKEN, the Heavy Ion Medical Accelerator in Chiba (HIMAC) and the Cyclotron Facility at NIRS. Initial accelerated energies of carbon ions were 135 MeV/nucleon at RIKEN, 135 and 290 MeV/nucleon at the HIMAC and 12 MeV/nucleon at the Cyclotron Facility. Linear energy transfer (LET) of the beams on the target was changed by inserting a plastic plate in front of the target. The LET range was 30–250 keV/ $\mu\text{m}$  at the sample center. The radiation dose rate ranged from about 1–5 Gy/m. The reference radiation was 200 kVp X-rays filtered through 0.5 mm Al and 0.5 mm Cu with a dose rate of 0.9 Gy/m. After irradiation, the cells were incubated with 5  $\mu\text{M}$  bromodeoxyuridine (BrdU) if necessary, and the cells were then trypsinized and fixed with 70% ethanol. The cells were stained both with propidium iodide to measure the total DNA contents in a cell and anti-BrdU-fluorescein for the newly synthesized DNA, and analyzed with a flow cytometer. Cell cycle distribution was analyzed using the Modifit LT (Becton Dickinson).

For the asynchronous V79, more than 80% of the cells were in the G2/M phase from 4 to 12 h after irradiation, with a peak at around 6 h. The maximum value and the width of the peak increased with both

increasing LET and radiation dose. The relative biological effectiveness (RBE) of G2 arrest was calculated using the width of the peak at the half values. RBE increased with LET up to 180 keV/ $\mu\text{m}$ . RBE values for G2 arrest above 30 keV/ $\mu\text{m}$  were greater than those for the cell inactivation in which the RBE-LET curve had a peak around the LET of about 100 keV/ $\mu\text{m}$ . More precise analyses were carried out using BrdU. Because the cells were continuously labeled with BrdU after irradiation, cells in the G1 and the S phases at the time of irradiation incorporated BrdU. Labeled cells exhibited G2 arrest from 6 to 16 h after irradiation, depending on LET and radiation dose. In contrast, unlabeled cells exhibited little G2 arrest. Therefore, the high percentage of V79 cells exhibiting G2 arrest was due to the populations in the G1 and the S phases at the time of irradiation. There was no G1 arrest for V79 cells. This is natural because p53 gene of the V79 cells was mutated in a presumed DNA binding domain.<sup>1)</sup> In contrast, there was a high percentage of NB1RGB cells exhibiting G1 arrest, and a low percentage of those exhibiting G2/M arrest; these cells have the normal p53 gene.<sup>2)</sup>

In our first experiment of cell cycle analysis of V79 cells at the RIKEN Ring Cyclotron, a low percentage of cells in the G2/M phase was observed after 8 h incubation following the C-ion irradiation with LET of 153 keV/ $\mu\text{m}$ . The cells may have been synchronized during the time they were transported from NIRS to RIKEN. More carefully prepared samples are necessary.

### References

- 1) W. Chaung et al.: Nucl. Acids Res. **25**, 992 (1997).
- 2) K. Tsuboi et al.: Int. J. Radiat. Biol. **74**, 71 (1998).

## Recognition of Hit Sites within the Cells Exposed to Accelerated Iron Ions Using CR-39 Plastics

H. Sasaki, P. Mehnati,\* F. Yatagai, and F. Hanaoka

Since the distribution of ionization is sparse and homogeneous for low-LET radiations but it is dense and inhomogeneous for high-LET radiations, the probability that no ionization occurs within the cell target is much higher for the latter than for the former radiation when compared at the same dose level. Assuming a Poisson distribution of hit-events, the fraction of cells whose nuclei are not transversed by iron ions (4 Gy, 2000 keV/ $\mu$ ) was calculated to be about 20%. Previously, we observed CHO cells by time-lapse photography for three to five generations after exposure to the same dose of iron ions and found that about 20% of the cells (18%: 25/136) showed no division delay at the irradiated generation and continued dividing with a cell cycle time similar to that of nonirradiated cells. This suggests that a single hit by an iron ion to a cell nucleus induces an early cellular response such as division delay. In order to verify this possibility, we have to identify cellular sites (nucleus or cytoplasm) through which the iron ions transversed and then determine whether growth arrest did or did not occur for individual cells.

In this study, we used a CR-39 plastic (solid state nuclear track detector: Harzlas/TNF-1) as the detector of hit sites. First, the optimum etching condition was examined using the plastics which had already been exposed to iron ions (1-4 Gy: 2000 keV/ $\mu$ m).

When the plastics were etched following a generally adopted procedure (7N NaOH at 60°C), it took about 30 minutes to produce a microscopically recognizable pit size ( $\phi$ :  $>1 \mu\text{m}$ ). However, we could treat the plastics under very mild conditions (10 min at 37°C) using PEW (KOH : Ethanol : Water = 3D 15wt% : 65% : 20wt%, recommended by Dr. N. Yasuda: NIRS, Chiba) as an etching solution. Next, CR-39 plastics were attached to the bottom outside face of a culture flask in which Mongolian gerbil fetal (MGF) cells

were grown and treated with PEW solution at 37°C for 10 min. Two micrographs were taken under a phase-contrast microscope within the same area, one focused on the cells and the other focussed on the pits on the CR-39 plastic surface, and then they were superimposed using a computer. An example of such superimposed microphotographs is shown in Fig. 1 where CR-39 plastics were exposed to 1 Gy of iron ions. Thus, we can recognize hit sites within the cells exposed to accelerated very high LET heavy ions (Fe or Ar ions). This study is in progress to elucidate whether early-responding gene products (p53, poly(ADP-ribose)polymerase) are expressed within the cells whose distinct sites (nucleus or cytoplasm) have been transversed by accelerated iron ion.

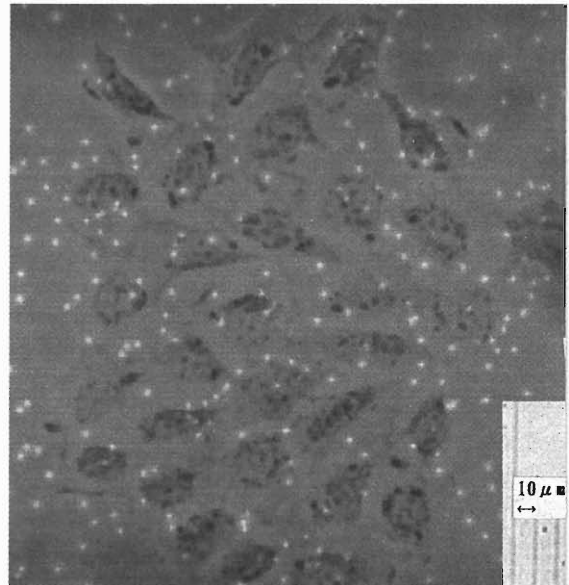


Fig. 1. A superimposed photograph showing MGF cells and tracks of transversed iron ions.

\* Faculty of Medicine, Kyushu University

## Oxidation Degradation of High Density Polyethylene Irradiated with Ion Beam

T. Oka, F. Yatagai, and Y. Hama

The transformation proceeding over a very long term was investigated in the inner region of a high density polyethylene (HDPE) slab (2 mm thick). A block of twelve piled samples, the length of which is longer than the range of the ion, was irradiated at room temperature in air with ion beams. We could not observe such a phenomenon for low density polyethylene (LDPE) in our other experiment. Figure 1 shows the depth profiles of carbonyl group measured at different dates after irradiation with 135 MeV/u  $\text{Ne}^{10+}$  in air. These profiles were obtained by micro-fourier transform infrared spectroscopy (micro-FT-IR) measurement. The carbonyl group yield in the inner region is found to increase significantly by a long storage in air. We have found that it was more marked for the sample stored for about 3 years. This suggests that the oxidation reaction has been taking place very slowly in the inner region over a long period. We have confirmed by electron spin resonance (ESR) measurement that there are no radicals remaining in HDPE irradiated in air. On the other hand, the increase in carbonyl group concentration was observed even when the same sample was irradiated in vacuum with 10 MeV/u  $\text{O}^{6+}$  and then exposed to air. The radicals produced in HDPE by irradiation under vacuum are stable at room temperature, but they disappear immediately when the sample is exposed to air. This finding suggests that the disappearance of the radicals could be caused by any

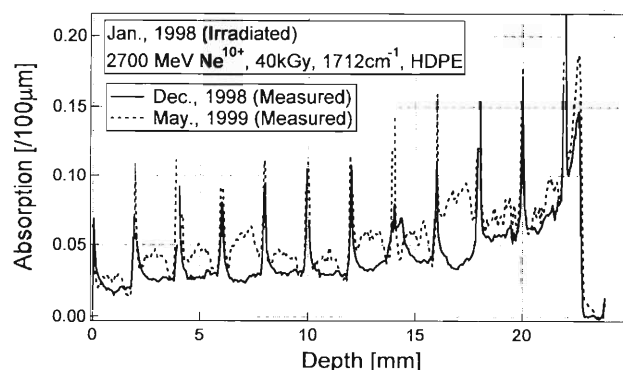


Fig. 1. Depth profiles of the carbonyl group content measured at different dates after irradiation.

oxidation reaction. This oxidation reaction, however, does not immediately produce carbonyl groups. Therefore, any group which does not include a carbonyl group may be produced, *e.g.*, hydroperoxide  $-\text{OOH}$ . It is also known that the degradation reaction in HDPE proceeds very slowly through the photo- or thermally induced cyclic chain reaction. This observation leads us to the conclusion that there are many initiators that do not include a carbonyl group, such as the  $-\text{OOH}$  group, but which can induce the chain reaction and they transform very gradually into the structures that include the carbonyl group by photo- or thermally induced chain reaction.

## Heavy Ion Beams: Application to Mouse Mutagenesis (II)

A. Yoshiki, N. Hiraiwa, F. Ike, T. Tsukada, N. Fukunishi, M. Kase, Y. Yano, and M. Kusakabe

Mouse mutants are useful animal models for human diseases. We have attempted to use heavy ion beams to induce germline mutations in mice. We used two strategies to induce germline mutations, one is the irradiation of sperm solution followed by sperm injection into the egg cytoplasm to produce G1 founders, and another is the irradiation of male testes followed by conventional mating to produce G1 founders. These G1 founders can be directly analyzed for dominant mutations which exhibit the phenotype in a heterozygous state. However, a number of abnormalities in humans and mice are known to be caused by recessive mutations, and can be detected only in the homozygous state.

In this report, we focused on the screening of recessive mutations with morphological phenotypes during early embryogenesis. Males of C57BL/6J (B6) strain mice were anesthetized, held on a plastic board and irradiated with  $^{12}\text{C}$ , and  $^{14}\text{N}$  ion beams at dosages of 3 Gy and 5 Gy, respectively. The exposure to the heavy ion beams was restricted to the inguinal region of the body. Six weeks later successful irradiation of the testes was indicated by coat color changes in the ventral and dorsal skin. These irradiated G0 males were crossed with nonirradiated B6 or BALB/c females to create G1 founders. Subsequently, the G1 founders were crossed with BALB/c females to produce G2 females, half of which were heterozygous for the newly induced mutations inherited from the G1 founders. Then, G2 females were backcrossed with their fathers, and sacrificed on day 10 of gestation for the screening of G3 embryos. Morphological abnormalities were observed under a dissecting microscope. If the phenotypes are caused by one or two recessive mutations with high penetrance, similar phenotypes should be observed repeatedly. Therefore, a G1 founder which produced two or more embryos with a similar phenotype was considered as a potential carrier of recessive mutations.

To date, we have examined 26 G1 males, and determined that 23 were fertile and 3 were sterile. With the 23 fertile G1 males, 110 G2 females became pregnant, and had 985 morphologically normal embryos, 50 morphologically abnormal ones, and 54 absorption sites. Six G1 males out of 23 ( $6/23 = 26.1\%$ ) produced two or more embryos with the similar phenotypes, and thus were selected as potential mutant carriers (lines B117, B170, B171, B25, B92, and B134), as summarized in Table 1. Samples of morphologically abnormal embryos are shown in Fig. 1 A and B. These six G1 founders have been kept for further breeding to confirm the phenotype heritability and to establish new mutant lines.

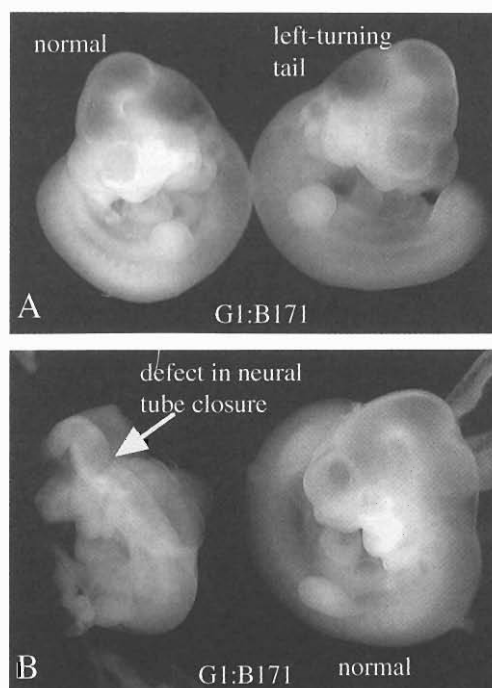


Fig. 1. Morphologically abnormal embryos found in G3.

Table 1. Potential mutant lines and their phenotypes.

Mutant lines	Beam	Dose (Gy)	Phenotypes on embryonic day 10
B117	$^{12}\text{C}$	5	developmental retardation at E9
B170	$^{12}\text{C}$	5	developmental retardation at E8
B170	$^{12}\text{C}$	5	yolk-sac-like structure without a proper embryo
B171	$^{12}\text{C}$	5	left-turning tail
B171	$^{12}\text{C}$	5	defect in neural tube closure
B25	$^{12}\text{C}$	5	left-turning tail
B25	$^{12}\text{C}$	5	developmental retardation at E9
B92	$^{14}\text{N}$	3	developmental retardation at E8
B134	$^{14}\text{N}$	3	developmental retardation at E8

Mutant lines of B170, B171, and B25 produced two different types of abnormal embryos, indicating that each G1 may carry multiple mutations.

## 5. Instrumentation



# Design of Liquid-He-Free Superconducting Solenoid Coils for Electron Cyclotron Resonance Ion Source

T. Kurita, T. Nakagawa, T. Kawaguchi, and S. M. Lee

In recent years, we have constructed a facility for experiments to study the dynamic behaviors of metal clusters such as fission and multifragmentation. One of the main features of this facility is the production of multiply ionized clusters with soft peripheral collisions of highly charged ions with metal clusters. This method allows the multiple ionization of a metal cluster without strong additional excitation.<sup>1)</sup> This offers the possibility to study the dynamic behavior of a metal cluster. To produce an intense beam of highly charged ions for this experiment, we constructed an electron cyclotron resonance (ECR) ion source which consists of liquid-He-free superconducting solenoid coils and a permanent hexapole magnet.<sup>2)</sup>

Solenoid coils are used for axial plasma confinement in an ECR ion source. A superconducting magnet provides a high magnetic field which can't be achieved by room-temperature magnets, and a higher magnetic field makes an ECR ion source deliver highly charged ions.<sup>3,4)</sup> One of the main features of this source is the use of Gifford-McMahon refrigerators for cooling the solenoid coils instead of liquid-He. This feature enables lower cost, lesser complexity and greater compactness than those of conventional superconducting magnets produced using liquid-He. A schematic drawing of our superconducting coil system and the highest axial magnetic field profile are shown in Fig. 1. The magnetic system for the axial magnetic field consists of a set of four solenoid coils divided into three groups. The central one operates in a reverse current to increase the mirror ratio of the axial magnetic field. These superconducting coils have the following characteristics:

- (1) Internal diameter of all coils: 290 mm
- (2) External diameter of the coils other than the central coil: 445 mm
- (3) External diameter of the central coil: 380 mm
- (4) Thickness of the coils other than the inner coil on the injection side: 80 mm
- (5) Thickness of the inner coil on the injection side: 48.1 mm
- (6) Conductor: NbTi/Cu
- (7) Maximum current density: 100 A/mm<sup>2</sup>
- (8) Axial mirror-to-mirror distance: 400 mm

Two refrigerators, a low-power one and a high-power one, are used. The low-power refrigerator cools the current leads and prevents heat invasion of the solenoid coils through the current leads. The high-power refrigerator cools the solenoid coils via a cooling conductor to the temperature of 4 K. The cryostat is enclosed in a 5 cm-thick iron yoke. When using the refrigerators, it is necessary to minimize the unbalanced electromag-

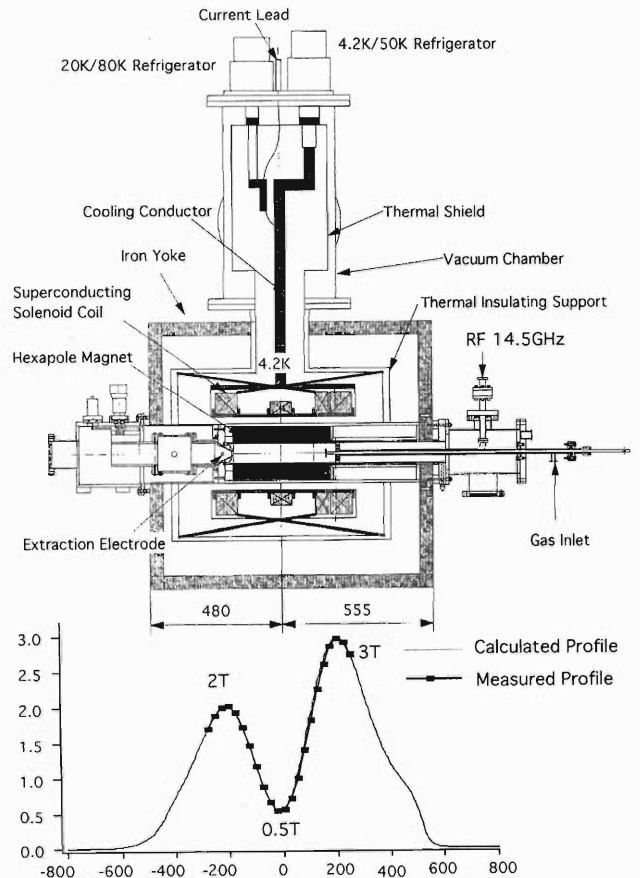


Fig. 1. A schematic drawing of the ECR ion source using liquid-He-free superconducting solenoid coils and axial magnetic profiles. The solid line indicates the calculated profile obtained using code-Opera. The square symbols indicate the measured magnetic profile. The current density of both profiles is 95 A/mm<sup>2</sup>.

netic force which must be supported by thermal insulating supports, because of the associated low cooling power ( $\sim 1$  W at 4.2 K). Our conclusion in the design was that the unbalanced axial force should be less than 15 kN. To minimize the force, we studied the coil arrangement, the axial position of the yoke and the operation conditions using code-OPERA.

Figure 2 shows a cross-sectional view of our superconducting solenoid coils and their electrical connections. The unbalanced electromagnetic force is maximum when some coils are quenched. To reduce the unbalanced electromagnetic force without expanding the iron yoke, the injection-side coils consist of two solenoid coils (Coil 3 and Coil 4), and the extraction-side coil (Coil 1) and Coil 4, i.e., the outer of injection-

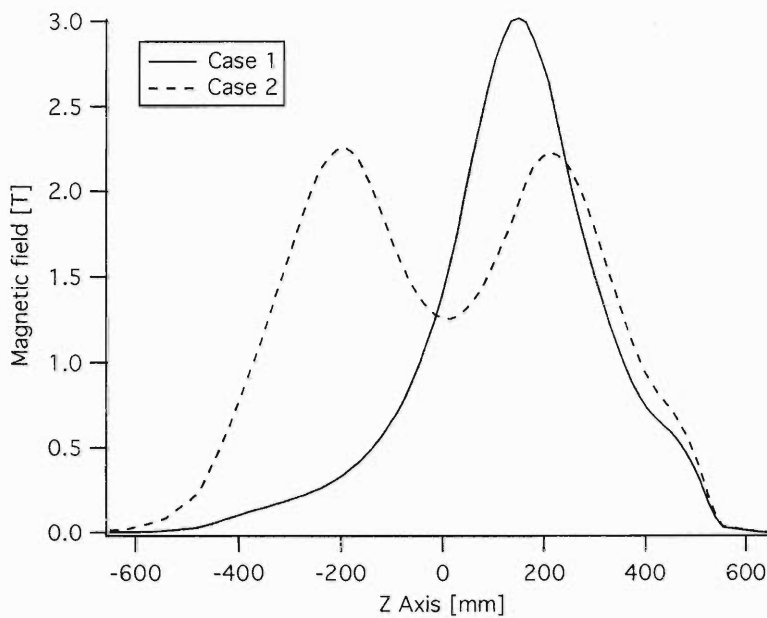


Fig. 2. The injection-side coil is divided and the external aspect of the injection side and the extraction side coil are connected in series. The magnetic field profile and the unbalanced electromagnetic force when the force is maximum are shown in the case of this magnetic configuration.

side coils are connected in series.

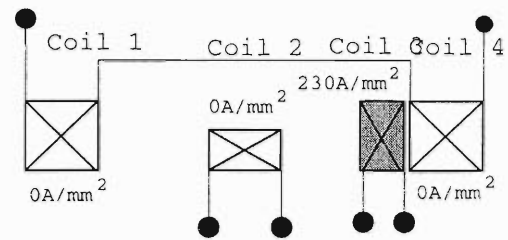
The severest conditions, under which the electromagnetic force becomes maximum are the following configurations:

Case 1: When all coils except Coil 3 are quenched under the condition to yield a maximum axial field, the peak of the magnetic field on the extraction side vanishes. The magnetic field of 3 T generated by the induced current in Coil 3 will remain on the injection side. In this case, the electromagnetic force pushing Coil 3 toward the injection side will become maximum. The magnetic field profile in this case is indicated by the solid line in Fig. 2. Since the position of the peak shifts to the inside, the electromagnetic force will be reduced compared with an undivided coil.

Case 2: When only Coil 1 and Coil 2 are excited with a maximum current, the electromagnetic force toward the extraction side becomes maximum. The magnetic field profile of this case is indicated by the dashed line in Fig. 2. Because Coil 1 and Coil 4 are connected in series, there are always two magnetic field peaks formed on both sides. This property contributes to the reduction of the electromagnetic force between the

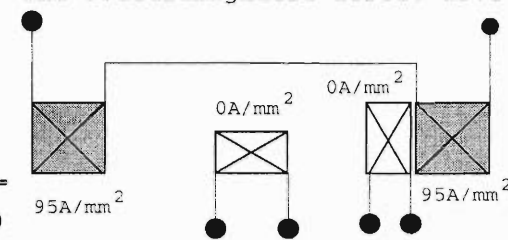
Case 1

The electromagnetic force: 14.4 kN



Case 2

The electromagnetic force: 13.8 kN



iron yoke and the coils.

As an optimized and calculated result, the electromagnetic stress become less than  $\sim 15$  kN, as shown in Fig. 2. With our magnetic configuration, we can successfully reduce the electromagnetic stress without expanding the iron yoke. The measured unbalanced force in Case 2 is  $\sim 13$  kN. This is consistent with the calculated value. If the injection-side coil is not divided, and Coil 1 and Coil 4 are not connected in series, then the electromagnetic force will be greater than 30 kN in some cases. To summarize, it has been demonstrated that we can reduce the electromagnetic force between the iron yoke and the solenoid coils, and we have succeeded in designing a compact magnetic system for an ECR ion source.

#### References

- 1) F. Chandenzon et al.: Phys. Rev. Lett. **74**, 3784 (1995).
- 2) T. Kurita et al.: RIKEN Accel. Prog. Rep. **31**, 156 (1998).
- 3) R. Geller: Annu. Rev. Nucl. Part. Sci. **40**, 15 (1990).
- 4) G. Ciavola and S. Gammino: Rev. Sci. Instrum. **63**, 2881 (1992).

## Automatic $^{18}\text{F}$ Supply System for a Slow Positron Beam

F. Saito, N. Suzuki, J. H. Kim, Y. Nagashima, T. Kurihara, Y. Itoh, T. Hyodo, and A. Goto

The spin-polarized slow positron beam is a promising probe for surface magnetism. A spin-polarized positron beam is conveniently produced using a  $\beta^+$  decay radio-isotope (RI) source. However, the activity of  $^{22}\text{Na}$  which is routinely used, is at most 6 GBq. Recently we have developed a practical way of producing an  $^{18}\text{F}$  (half-life 110 min,  $\beta^+$  endpoint energy 635 keV) positron source for use in materials research. To perform continuous measurements for a few days, however, the process of fabricating the source has to be simple and rapid. In the present paper, we report an automatic system which rapidly supplies an  $^{18}\text{F}$  positron source produced by the AVF cyclotron at RIKEN.

$^{18}\text{F}$  is produced via the  $^{18}\text{O}(p, n)^{18}\text{F}$  reaction. The apparatus used is similar to that used routinely for the production of  $^{18}\text{F}$  as a PET (Positron Emission Tomography) source. A 14-MeV proton beam from the AVF cyclotron is used for the bombardment of liquid  $\text{H}_2^{18}\text{O}$ . The activity of  $^{18}\text{F}$  is about 4 GBq after an hour of proton irradiation at  $2 \mu\text{A}$ . The  $^{18}\text{F}$  solution is automatically transferred by He gas at a pressure of 1.5 atm through a Teflon capillary from the target container in the AVF cyclotron vault to the experiment vault downstairs.

An automated electro deposition and source-supply mechanism, which is controlled by a personal computer, is shown in Fig. 1. It has two rotatable discs. One serves as a turntable which carries 12 electro-deposition cells made of platinum. The cell acts as a cathode as well as a vessel for the  $^{18}\text{F}$  solution. Twelve graphite rod anodes of 3 or 5 mm are installed on the side of the second disc, which is perpendicular to the horizontal turntable, rotatable and movable vertically. When the cell is filled with the  $^{18}\text{F}$  solution, the turntable rotates to set the cell at the position for electro deposition, directly below the source window of the slow positron beam apparatus. Then the second disc descends until the end of a graphite rod dips 0.2 mm below the surface of the solution. The position of the liquid surface is detected by monitoring the electric current passing through the graphite rod. The typical electro-deposition time is about 15 min. After the electro deposition, the vertical disc is raised to the original position and rotated by 180 degrees. It is then raised farther about 7 mm so that the graphite rod is close at 1 mm to the positron incidence Ti window of the beam apparatus. The source is placed outside the beam apparatus so as not to break the vacuum in the apparatus. The entire procedure takes only 20 min including the liquid transfer time and the 15 min of electro-deposition.

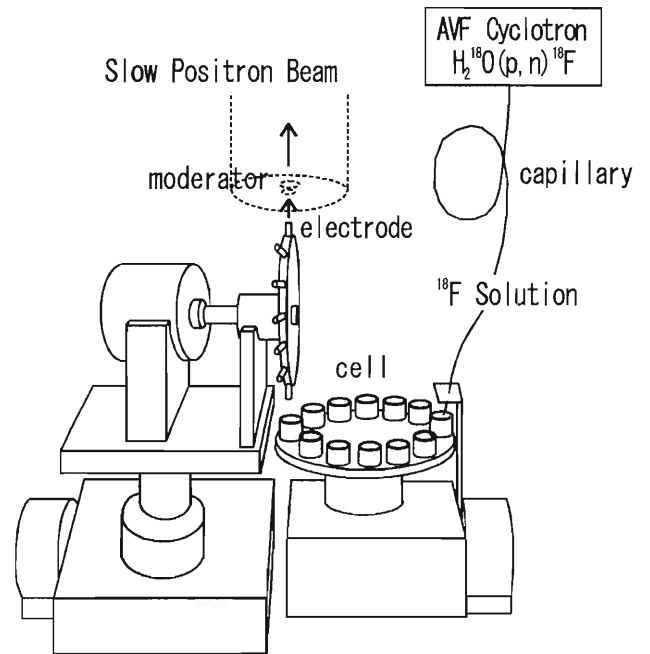


Fig. 1. Figure of automated electro-deposition and source supply system, cells are placed on a turntable. Carbon rods are placed on the side of a vertical rotatable disc.  $^{18}\text{F}$  solution is transferred through the capillary.

While  $^{18}\text{F}$  is being electro deposited and used as a source, the next batch of  $^{18}\text{O}$ -water is loaded in the target container and irradiated by protons. In this way, the  $^{18}\text{F}$  source is supplied continuously throughout the experiments.

The highest efficiency of electro deposition was 97% using 2 GBq  $^{18}\text{F}$  solution deposited on a 5 mm  $\phi$  graphite rod for 30 min. The fraction of the positrons emitted from of the surface was 45%. Thus, as much as 42% of the  $\beta^+$  from the  $^{18}\text{F}$  in the  $^{18}\text{O}$ -water can be used as a source of the slow positron beam.

The maximum activity of  $^{18}\text{F}$  was estimated from the density of the  $^{19}\text{F}$  carrier which was used for electro-deposition. It was three orders of magnitude larger than that of 2 GBq  $^{18}\text{F}$ . Since both  $^{19}\text{F}$  and  $^{18}\text{F}$  are electro deposited with the same efficiency, we expect that an  $^{18}\text{F}$  activity of at least 2 TBq can be electro-deposited on a 5 mm  $\phi$  graphite rod, provided we produce  $^{18}\text{F}$  with such an activity. For example, if a small cyclotron commonly used for PET, having a proton beam current of  $50 \mu\text{A}$ , is available, a positron source of 100 GBq can be easily produced and about  $10^7$  slow positrons per second would be produced with a tungsten moderator.

## Design and Simulation of an Electrostatic Spin-Polarized Positron Beam System for Surface Magnetism Studies

J. H. Kim, N. Suzuki, F. Saito, Y. Nagashima, T. Kurihara, A. Goto, Y. Itoh, and T. Hyodo

Spin-polarized low-energy positrons are considered to be useful as probes for studying electron spin states of both surface and bulk materials. Positrons are polarized along their momentum directions when they are emitted from a radioactive source.<sup>1)</sup> The formation of positronium (Ps, an electron-positron bound system) can be distinguished from the formation of different electron spin states due to the spin-dependent interactions between positrons and electrons on the surface. This method has the advantage of combining spin sensitivity and surface selectivity. Recently, a positron source of  $^{18}\text{F}$  (half-life 110 min,  $E_{max} = 0.635$  MeV) has been developed for a polarized slow positron beam at RIKEN.<sup>2)</sup>

We are in the process of designing an electrostatic positron beam system in combination with a spin rotator that can change the spin direction of the positrons without changing the beam optics. This design of the beam system can will be applied to the investigation of both surface and interface magnetism. Moreover, the beam system may be applicable to studies of polarized low energy positron diffraction or polarized Auger lineshape.

An overview of the positron beam optics is shown in Fig. 1. Positrons from a moderator are extracted and accelerated in a spin rotator, bent  $90^\circ$  by a parallel-plate analyzer, and finally focused onto the target by a series of electrostatic lenses. For the rays of positrons, we have chosen 33 trajectories (ranging from  $-80^\circ$  to  $+80^\circ$ ) which are evenly spaced on the moderator with a diameter of 6 mm in the x-y plane. The distance from the parallel-plate to the sample is about 1500 mm. The spatial separation prevents the  $\gamma$ -rays, emanating from the source region, from reaching the sample.

After spin-polarized positrons are extracted from a moderator (A), they enter the spin rotator (B) where the angle of the positron spin direction rotates along the magnetic field due to Larmor precession, while their path is not changed. The parallel-plate mirror (D) bends the positron beam  $90^\circ$  in order to prevent the fast positrons and  $\gamma$ -rays emitted by the source from reaching the sample. Although the positron's momentum direction is changed, its spin direction remains the same in an electric field. By the combination of the spin rotator and the parallel-plate bender, both longitudinal and transversal spin components of positrons can be adjusted at the sample.

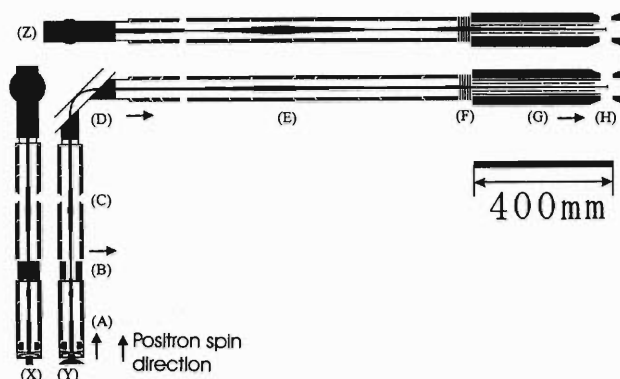


Fig. 1. An overview of the positron beam optics. The positrons were traced through the beam optics using SIMION, which is a charged-particle trajectory program with space charge effects neglected. Positrons from a moderator are extracted and accelerated into a spin rotator, bent  $90^\circ$  by a parallel-plate analyzer, and finally focused onto the target by a series of electrostatic lenses. The arrow indicates the direction of positron spin in the case of  $90^\circ$  rotation at the spin rotator. Three different views are shown: side view (X), front view (Y) and top view (Z).

The source-moderator chamber is insulated from the sample chamber and floats at voltages from 0.1 to 30 kV to accelerate positrons while the sample is maintained at ground potential. The voltages at the end of a linear-type accelerator (F) are adjusted to vary the positron beam energies. The beam diameter at the sample (H) is simulated to be 2–6 mm in the range of beam energy from 0.1 to 30 keV. A set of lenses with a 20 mm inner diameter is used to transport the accelerated positrons onto the sample through the electromagnet (G) that will produce a magnetic field at the sample. The observation of reflections of positrons (lower than 2 keV beam energy) near the sample when 12 KGauss is applied indicates that further consideration of beam design is required for a better positron polarimeter.

### References

- 1) L. A. Page and M. Heinberg: Phys. Rev. **106**, 1220 (1957).
- 2) I. Fujiwara, Y. Itoh, R. Iwata, F. Saito, and A. Goto: Appl. Surf. Sci. **149**, 30 (1999).

# Calibration of Beam-Line Polarimeter at $E_d = 140$ and 200 MeV

T. Uesaka, H. Sakai, H. Okamura, A. Tamii, Y. Satou, T. Ohnishi, K. Sekiguchi, K. Yakou,  
S. Sakoda, N. Sakamoto, T. Wakasa, K. Itoh, and K. Suda

The deuteron polarimeter, which is based on the  $d + p$  elastic scattering, was calibrated at  $E_d = 140$  and 200 MeV.

The  $d + p$  elastic scattering has several advantages in polarimetry for an intermediate-energy deuteron beam: (1) It is expected to have large vector and tensor analyzing powers. (2) A high signal-to-noise ratio is attainable because the coincidence measurement of the scattered deuterons and recoiled protons is applicable. (3) We can use a polyethylene ( $\text{CH}_2$ ) film as a “hydrogen target” because the coincidence measurement described above makes the contribution from carbons in  $\text{CH}_2$  less important. A thin  $\text{CH}_2$  foil ( $\sim 50 \mu\text{m}$ ) is nondestructive to the beam quality, easy to use, and inexpensive, therefore, it is desirable as a target for a beam-line polarimeter.

In the calibration measurement, the polarizations of a deuteron beam were measured using a low-energy polarimeter<sup>1)</sup> before acceleration in the Ring cyclotron. It is assumed that depolarization during the acceleration process is negligible. It should be noted that we have recently carried out the measurement of absolute polarization via the  $^{12}\text{C}(\vec{d}, \alpha)^{10}\text{B}^*(2^+)$  reaction<sup>2)</sup> independent of this assumption. The typical beam polarization was 70–80% of the ideal value.

A 1-mm-thick polyethylene target was bombarded by the polarized deuteron beam. Scattered deuterons and recoiled protons were detected in coincidence with plastic scintillation detectors. A schematic depiction of the detector setup is presented in Fig. 1. Four sets of deuteron and proton detectors, Left, Right, Up, and Down, were used to reduce systematic uncertainties in analyzing powers (only the Left and Right detector sets

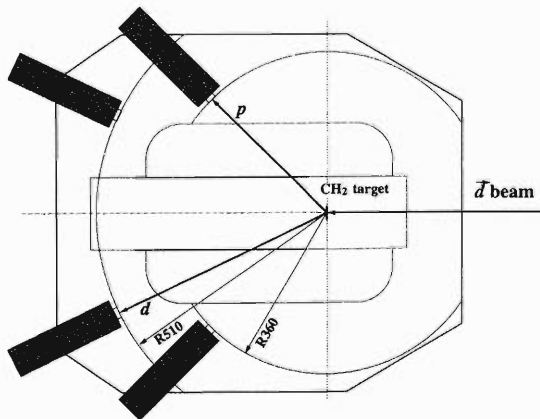


Fig. 1. Detector setup of the deuteron polarimeter. Deuteron and proton detectors (plastic scintillation detectors and photomultipliers) are placed at forward and backward angles, respectively.

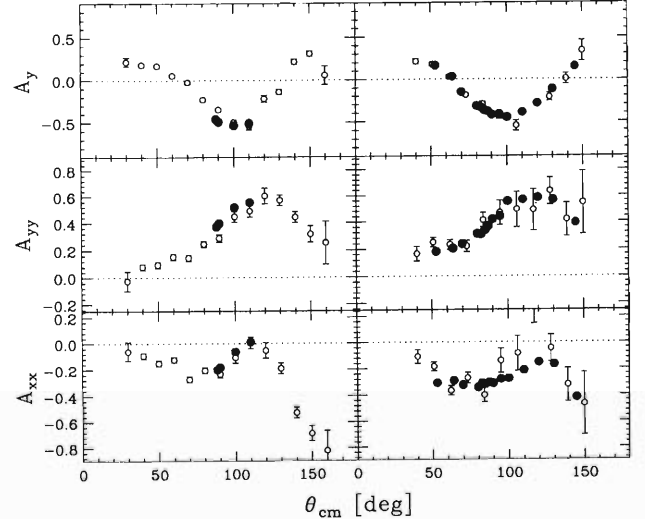


Fig. 2. Analyzing power data ( $\bullet$ ). Left and right panels represent data at  $E_d = 140$  and 200 MeV, respectively. Open circles ( $\circ$ ) represent data at slightly different energies ( $E_d = 144$  and 191 MeV) taken at Saturne.<sup>4)</sup>

Table 1. Analyzing powers used to measure the beam polarization.

	$E_d = 140 \text{ MeV}$	$E_d = 200 \text{ MeV}$
	$\theta_{\text{cm}} = 110^\circ$	$\theta_{\text{cm}} = 82.5^\circ$
$A_y$	$-0.519 \pm 0.005$	$-0.332 \pm 0.005$
$A_{yy}$	$0.541 \pm 0.005$	$0.306 \pm 0.005$
$A_{xx}$	$0.017 \pm 0.007$	$-0.313 \pm 0.006$

are illustrated in Fig. 1). Details of the experimental setup are described in Ref. 3.

In Fig. 2, vector ( $A_y$ ) and tensor ( $A_{yy}$  and  $A_{xx}$ ) analyzing powers for the  $d + p$  elastic scattering are shown. Full and open circles represent the present results and the data taken at Saturne,<sup>4)</sup> respectively.

The angles used in the polarimeter were chosen to be  $\theta_{\text{cm}} = 110^\circ$  and  $82.5^\circ$  at  $E_d = 140$  and 200 MeV, respectively. The analyzing powers at these angles are listed in Table 1.

## References

- 1) T. Uesaka et al.: RIKEN Accel. Prog. Rep. **32**, 161 (1999).
- 2) K. Suda et al.: RIKEN Accel. Prog. Rep. **33**, 154 (2000).
- 3) N. Sakamoto et al.: Phys. Lett. B **367**, 60 (1996).
- 4) W. G. H. Witalla et al.: Few Body Systems **15**, 67 (1993).

# Absolute Calibration of the Deuteron Beam Polarization at an Intermediate Energy via the $^{12}\text{C}(d, \alpha)$ Reaction

K. Suda, H. Okamura, N. Sakamoto, A. Tamii, T. Uesaka, T. Ohnishi, K. Sekiguchi,  
J. Nishikawa, H. Kato, M. Hatano, and H. Sakai

The polarization of the deuteron beam accelerated by AVF and Ring cyclotrons is measured using a polarimeter (high-energy polarimeter), which applies the  $d$ - $p$  elastic scattering as a polarimetry.<sup>1)</sup> The analyzing powers for the reaction were calibrated against the polarization measured using the  $^{12}\text{C}(d, p)^{13}\text{C}$  reaction at the exit of the AVF cyclotron.<sup>1)</sup> However, the analyzing powers calibrated in this manner inevitably have systematic errors because the uncertainty of the analyzing powers for the reference  $^{12}\text{C}(d, p)^{13}\text{C}$  reaction is already significant in amount. Moreover, systematic uncertainty also arises from the long-term instability of the polarization because measurement of the beam polarization and the analyzing powers for the  $d$ - $p$  elastic scattering cannot be carried out simultaneously at RARF. Therefore, it has become necessary to calibrate the high-energy polarimeter directly using nuclear reactions, the absolute values of the analyzing powers of which are unambiguously known. Although such a reaction is not known for the vector analyzing power, a few reactions exist for the tensor analyzing power. One of those is the  $^{16}\text{O}(d, \alpha)^{14}\text{N}(0^-, 4.92 \text{ MeV})$  reaction, and was used at a low energy.<sup>2)</sup> At intermediate energies, however, it is considerably difficult to use the reaction since an energy resolution better than 200 keV is required and the cross section is rather smaller than that at a low energy. As an alternative, we propose to use the  $^{12}\text{C}(d, \alpha)^{10}\text{B}$  reaction for calibrating the absolute value of the polarization. In this reaction at  $0^\circ$ , if the final state of  $^{10}\text{B}$  has natural parity except for  $0^+$ , it can be shown that the tensor analyzing power  $A_{zz}$  is unity due to the parity conservation. Among the levels of  $^{10}\text{B}$ , the  $2^+$  state at 3.59 MeV excitation is advantageous because energy differences between adjacent levels are more than 1 MeV. Moreover, even if the tensor polarized beam has a component of vector polarization, it does not influence on the measurement of the tensor polarization because  $A_y = 0$  at  $0^\circ$ .

The absolute calibration of the high-energy polarimeter using the above reaction was carried out for a 270 MeV deuteron beam. For the measurement of the  $(d, \alpha)$  reaction, we used the spectrometer SMART. A self-supporting natural-carbon foil with a thickness of  $10.94 \text{ mg/cm}^2$  was used as the target. The scattered particles were momentum-analyzed by the SMART and detected using a multiwire drift chamber and three plastic scintillators at the second focal plane. The  $\alpha$  particles were identified using the light output from the plastic scintillators. A typical excitation-energy spectrum is shown in Fig. 1. The cross section for the

$2^+$  state is  $5 \mu\text{b/sr}$  at  $0^\circ$ . In the analysis, we limited the scattering angle to less than  $1^\circ$  in a laboratory system because  $A_{zz}$  for the  $(d, \alpha)$  reaction varies

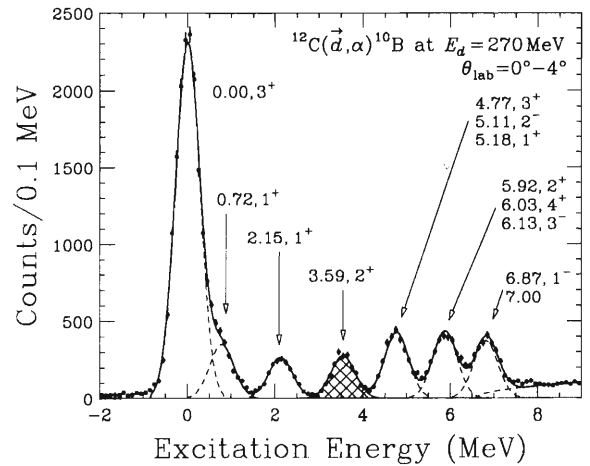


Fig. 1. A typical excitation-energy spectrum for the  $^{12}\text{C}(d, \alpha)^{10}\text{B}$  reaction at  $\theta_{\text{lab}} = 0^\circ\text{--}4^\circ$  is shown with solid circles. The broken line shows the result of a Gaussian fit for each peak. The solid line shows the sum of the fit results. A hatched peak represents the  $2^+$  state of interest at the excitation energy of 3.59 MeV.

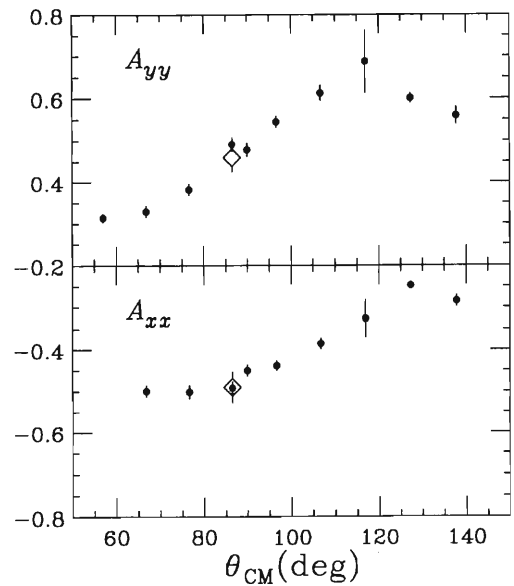


Fig. 2. The analyzing powers  $A_{yy}$  and  $A_{xx}$  for the  $d$ - $p$  elastic scattering. The present data are indicated by open diamonds. The data obtained from Ref. 1 are indicated with solid circles.

considerably near  $0^\circ$ . The horizontal and vertical angular resolutions of the SMART, which are  $0.19^\circ$  and  $0.22^\circ$ , respectively, are sufficiently good. Simultaneously with the measurement of the  $(d, \alpha)$  reaction, the asymmetry of the  $d$ - $p$  elastic scattering was measured using the high-energy polarimeter. With the polarization obtained using the  $(d, \alpha)$  reaction, the analyzing powers  $A_{yy}$  and  $A_{xx}$  for the  $d$ - $p$  elastic scattering were determined. The analyzing powers are compared with the data reported in Ref. 1. The results are in good agreement with the statistical errors, as shown in Fig. 2. The systematic errors are estimated to be equal to or statistical errors.

In the detection of the  $\alpha$  particle, the signal-to-

noise ratio was very low due to the small cross section. The beam intensity was limited to less than 20 nA to prevent the loss of detection efficiency. As a result, the statistical errors of the present data are twice as large as those in Ref. 1. In order to improve the statistical accuracy, we will repeat the experiment again with increased beam intensity and reduced background. Further, we plan to calibrate of the high-energy polarimeter at 140 MeV.

#### References

- 1) N. Sakamoto et al.: Phys. Lett. B **367**, 60 (1996).
- 2) S. Kato et al.: Nucl. Instrum. Methods Phys. Res. A **238**, 453 (1985).

## Calibration of $^3\text{He}$ Polarization Using Electron-Spin-Resonance Method

S. Yamamoto, T. Uesaka, T. Wakui, H. Sakai, and Y. Yano

The RIKEN spin-exchange-type polarized  $^3\text{He}$  target was applied to nuclear physics experiments in 1996<sup>1)</sup> and 1998.<sup>2)</sup> It is important to accurately determine the absolute polarization of  $^3\text{He}$  in such applications. At present, the most common method of  $^3\text{He}$  polarimetry is based on nuclear magnetic resonance (NMR) of adiabatic fast passage (AFP), which we are using. Through this method, however, we can only determine the relative value of polarization.

To calibrate the absolute value of polarization, we measured Boltzmann polarization signals from protons in a sample of water using AFP-NMR (proton NMR) under the same conditions as those used to measure  $^3\text{He}$  polarization. Though it is easy to measure the proton NMR signals, there are considerable systematic errors due to the small strength of proton NMR signals. Thus, we have introduced a method based on the frequency shift of the Rb electron-spin resonance (ESR).<sup>3)</sup>

The frequency shift is proportional to the polarization of  $^3\text{He}$ , the density of  $^3\text{He}$ , and the Rb- $^3\text{He}$  spin-exchange constant  $\kappa_0$ . The value of  $\kappa_0$  is determined accurately as  $4.52 + 0.00934 \times T [^\circ\text{C}]$ .<sup>4)</sup> The uncertainty in  $\kappa_0$  is 1.5% at  $175^\circ\text{C}$ .<sup>4)</sup> Therefore the precision of this calibration depends on the precision of measurements of the Rb ESR frequency shift and the density of  $^3\text{He}$ .

We measured the frequency of Rb ESR in a magnetic field of 30 G as follows: firstly,  $^{85}\text{Rb}$  atoms in the cell, containing 3 amagats<sup>†</sup> of  $^3\text{He}$  gas and a few mg of Rb metal, were optically pumped with circularly polarized light ( $\sigma^+$ ) tuned to the  $D_1$  transition (795 nm) from the ground state  $5^2S_{1/2}$  to the excited state  $5^2P_{1/2}$ . The population of all the Zeeman sub-levels in the ground state was thereby depleted except for the  $m_F = +3$  Zeeman sublevel of the  $F = 3$  hyperfine state. This led to a decreased absorption of the pumping laser light; consequently, the fluorescence intensity was markedly reduced. Secondly, we applied an RF field to repopulate the depleted  $m_F = 2$  level at a frequency corresponding to the ESR transition between  $m_F = +2$  and  $+3$ , and the fluorescence intensity was immediately increased. Therefore, the Rb ESR frequency could be determined as the peak position in the fluorescence spectrum by scanning the RF frequency. In this experiment, the frequency was locked at peak position using a feedback system, and was measured by a frequency counter.

The measurements of the ESR frequencies were performed in the cases where  $^3\text{He}$  nuclear spin  $\mathbf{K}$  is par-

allel ( $\uparrow\mathbf{K} \uparrow\mathbf{B}$ ) and antiparallel ( $\downarrow\mathbf{K} \uparrow\mathbf{B}$ ) to a magnetic field  $\mathbf{B}$ . Figure 1 shows the ESR frequency which was alternately obtained for each case. The frequency shift  $\Delta\nu$  is given with the Rb ESR frequencies  $\nu_{(\uparrow\mathbf{K} \uparrow\mathbf{B})}$  and  $\nu_{(\downarrow\mathbf{K} \uparrow\mathbf{B})}$  as

$$\begin{aligned} \Delta\nu &= \nu_{(\uparrow\mathbf{K} \uparrow\mathbf{B})} - \nu_{(\downarrow\mathbf{K} \uparrow\mathbf{B})} \\ &= \frac{\nu_B g_s}{h(2I+1)} \kappa_0 \frac{8\pi}{3} \nu_{\text{He}} [^3\text{He}] P_{^3\text{He}}, \end{aligned}$$

where  $\nu_B$  is the Bohr magneton,  $g_s$  is the electron  $g$ -factor,  $I$  is the nuclear spin of  $^{85}\text{Rb}$ ,  $[^3\text{He}]$  is the density of  $^3\text{He}$ , and  $P_{^3\text{He}}$  is the polarization of  $^3\text{He}$ . Figure 2 shows the frequency shift and polarization as a function of the NMR signal. In Figs. 1 and 2, error bars are as large as 5 kHz, which indicate an uncertainty in polarization of about 40%. This large uncertainty is due to the instability of the magnetic field. An error

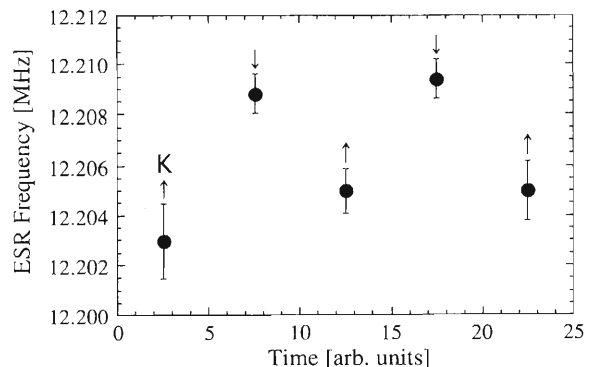


Fig. 1. A typical set of ESR data. We measured the ESR frequencies in the cases where  $^3\text{He}$  nuclear spin  $\mathbf{K}$  is parallel ( $\uparrow\mathbf{K} \uparrow\mathbf{B}$ ) and anti-parallel ( $\downarrow\mathbf{K} \uparrow\mathbf{B}$ ) to a magnetic field  $\mathbf{B}$ .

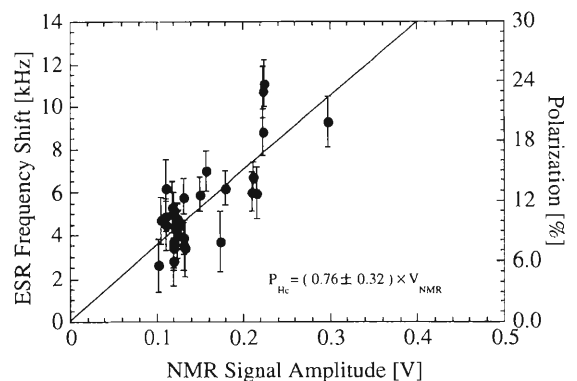


Fig. 2. The relationship between the frequency shift (polarization) and the amplitude of the NMR signal.

<sup>†</sup> An amagat is a unit of density corresponding to 1 atm at  $0^\circ\text{C}$

of 5 kHz corresponds to an instability of 20 mG. To decrease the uncertainty of polarization to less than 5%, we have to decrease the instability to less than 3 mG. We are planning to improve the stability of the magnetic field by introducing a feedback circuit with a magnetometer.

#### References

- 1) T. Uesaka et al.: RIKEN Accel. Prog. Rep. **30**, 139 (1997).
- 2) M. Kurokawa et al.: private communication.
- 3) B. C. Grover et al.: Phys. Rev. Lett. **40**, 391 (1978).
- 4) M. V. Romalis et al.: Phys. Rev. A **58**, 3004 (1998).

## Response of an Imaging Plate for Heavy Particles

S. Gunji, H. Sakurai, N. Sato, K. Morimoto, F. Tokanai, I. Tanihata, Y. Wakasaya, and T. Kato

We are investigating the response of an imaging plate (IP) for heavy particles for use as a detector of ultraheavy cosmic rays.<sup>1,2)</sup> It is well known that photostimulated luminescence (PSL) occurs when the positions injected with heavy particles are illuminated using a laser. By detecting the PSL value using a photomultiplier, we can obtain information about the injection positions of the particles and the deposited energy. However, due to the fading effect, information on the deposited energy of the positions fades as with time.<sup>3)</sup> Therefore, it is very important to detect the PSL in real time. In order to do so, it is necessary to know where the particles are injected. We plan to locate the position using the prompt luminescence<sup>4)</sup> from the IPs. We irradiated the IPs with Bi 10 A MeV and Kr 70 A MeV in the RIKEN cyclotron accelerator, and attempted to detect the prompt luminescence for each particle.

For this experiment, the setup shown in Fig. 1 was used. The four-channel multianode photomultiplier mounted on the side of the IP was used to detect the prompt luminescence, and the plastic scintillator in front of the IP was used to confirm that the heavy particles passed through the IP. The flux of the heavy particles was adjusted to about 1000 counts/sec for an area of 30 cm<sup>2</sup>. The trigger condition was the coincidence of the plastic scintillator with the four channel signals of the multianode photomultiplier. The output signals from each channel of the multianode

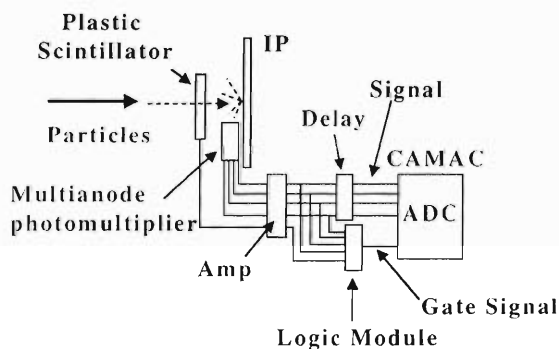


Fig. 1. Experimental setup, consisting of the IP, the plastic scintillator, and the four-channel multianode photomultiplier.

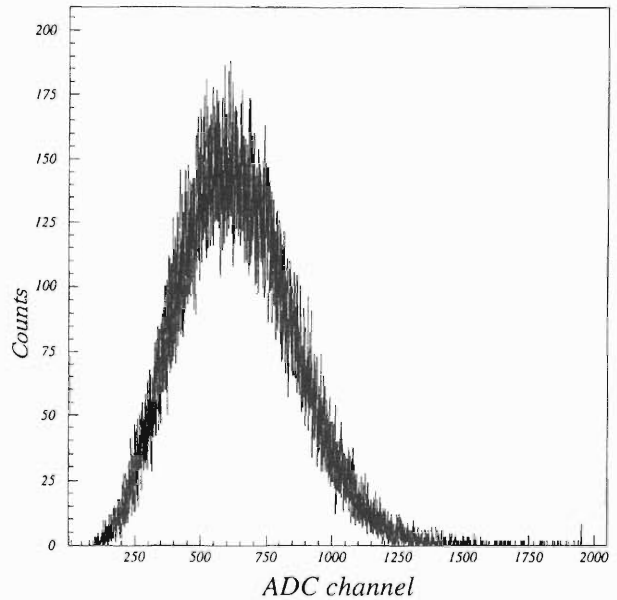


Fig. 2. Summed pulse height distribution for the four channel signals. The clearly observed broad peak is due to the injection of Bi 10 A MeV.

photomultiplier were acquired by the CAMAC system using the trigger condition.

Using this setup, we succeeded in detecting the prompt luminescence of the particles for both Bi 10 A MeV and Kr 70 A MeV. In Fig 2, the summed pulse height distribution for all four channel signals is shown. A broad peak which corresponds to the deposited energy of Bi 10 A MeV, is clearly observed.

In a future work, we will investigate the proportionality of the prompt luminescence to the deposited energy. Moreover, we plan to identify the injection positions by mounting four photomultipliers on the corners of the IP and determining the differences between their signals. We will also investigate the wavelength and the time profile of the prompt luminescence.

### References

- 1) G. Kanase et al.: IEEE Proc., N12-6 (1998).
- 2) S. Gunji et al.: IEEE Proc., N11-4 (1999).
- 3) A. Taniyama et al.: Electron Microsc. 45, 232 (1996).
- 4) K. Sakasai et al.: Proc. 7th Int. Conf. on Nuclear Engineering, Seattle (1999).

## Development of Time-of-Flight Detector with Streak Camera

F. Tokanai, K. Morimoto, M. Kurata-Nishimura, I. Tanihata, and S. Yamada\*

In high-energy physics, time-of-flight (ToF) measurement has commonly been used to determine the mass and energy of heavy ions. One of the main requirements for any ToF detector is good time resolution. A time resolution of up to about 150 ps has been achieved. A time resolution of 150 ps allows for a separation of masses of around 4 amu with an energy of 6.8 GeV for a 1 m flight path. However masses of around 200 amu can be separated only up to 136 MeV.<sup>1)</sup> Recently, construction of the radioactive ion beam facility (RIBF) was begun at RIKEN.<sup>2)</sup> In this facility, heavy ions will be accelerated to energies up to 400A MeV for light nuclei and 150A MeV for the heaviest nuclei. Therefore, if we separate masses of around 200 amu at the energy of 30 GeV, a time resolution of 10 ps is required for a 1 m flight path. For this purpose, we have been developing a novel ToF detector with a 10 ps time resolution, which utilizes a streak camera.

The configuration of the new ToF system is shown schematically in Fig. 1. This system consists of two identical sets of streak cameras (systems 1 and 2). The system 2 streak camera is placed at a distance  $L$  (m) from system 1. These systems are tilted at 45 degrees with respect to the heavy-ion path. Foil is mounted at the center of each system to emit secondary electrons. This foil divides each streak camera system

into a streak-image detector and a center-image detector. An acceleration mesh is mounted on both sides of the foil at a distance of 2.7 mm. In the streak-image detector section, the secondary electrons from the foil are accelerated by the electric field of the mesh and focused by an electronic lens. These electrons are swept by applying a 100 MHz sine wave voltage to the vertical and horizontal diffraction plates. The swept-electrons image appears as a circle of 16 mm diameter on the phosphor screen. In the center-image detector section, the secondary electrons are accelerated, focused by an electric lens, and directly impinge on the phosphor screen (not swept). The position of the electron image on the screen represents the center of the circle from the streak-image-detector section. These light images for both detector sections are recorded by a two-dimensional position-sensitive detector such as an image intensifier.

Since the sweeping electric fields of each system are operated at the same period (angular velocity  $\omega$ ), when a heavy ion passes through this system, we obtain the streak image of  $\theta_0 = \omega t_0$  and  $\theta_1 = \omega(t_0 + \delta t)$  on a circle for system 1 and system 2, respectively. Using the relationship between  $\delta t$  and  $L$ , we can obtain the velocity of a heavy ion. Therefore, this system can be used as a ToF detector.

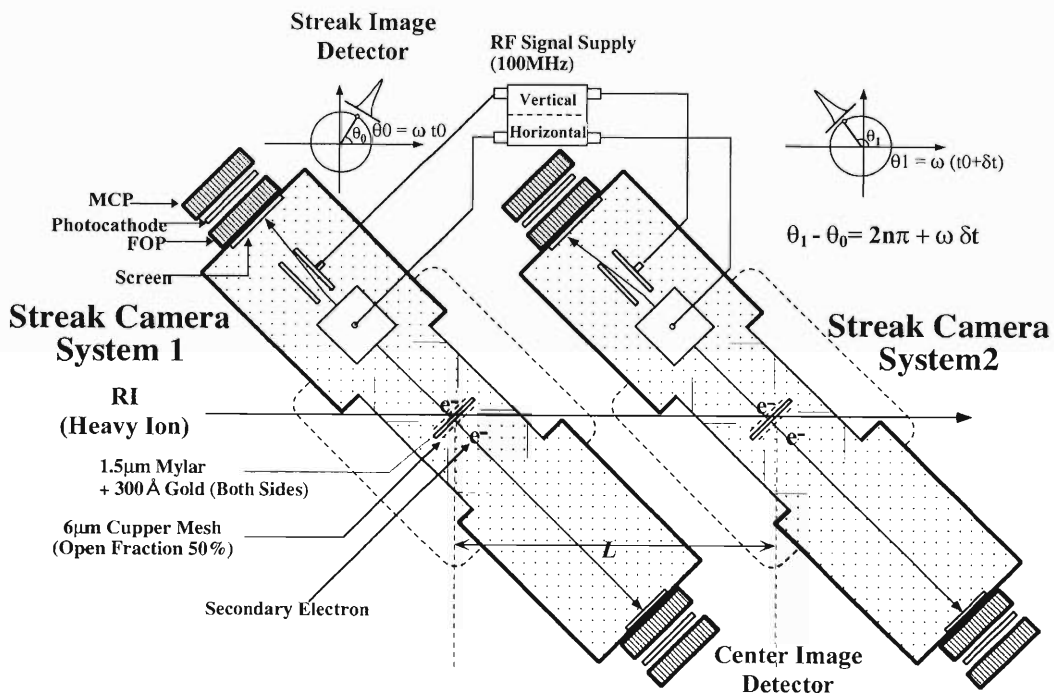


Fig. 1. Schematic view of the new ToF detector system.

\* National Institute of Radiological Sciences

In order to investigate the performance of the ToF system, we carried out test measurements using one streak camera system for the heavy-ion beams. The performance test of the streak camera system was carried out using  $^{10}\text{B}$  and  $^{12}\text{C}$  beams of 2.5A energy MeV from the RIKEN heavy-ion linear accelerator (RILAC). The streak and center images on the phosphor screen were lens-coupled to a CCD camera. Figure 2 shows the streak image obtained for the  $^{10}\text{B}$  beam at 2.5A MeV energy. The center image is also shown in Fig. 3. The beam rate was about  $10^4$  particles/s. We used a gated signal of 111 ms width for the CCD, thus a total of 1110 events was acquired. These images are binned in a  $2 \times 2$  CCD channel ( $13.4 \mu\text{m} \times 13.4 \mu\text{m}$ ). We can see two clusters in the center-position image. The bright cluster was defined as the focused  $^{10}\text{B}$  beam profile with a diameter of about 2 mm and the faint cluster with the effect of the beam attenuator at the beam line. We could not distinguish the two images from the CCD images of the ZnS scintillation light. Therefore,

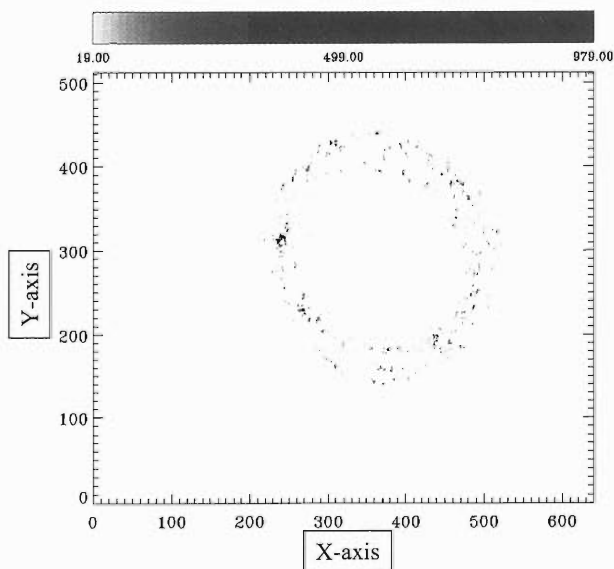


Fig. 2. Streak-position image for  $^{10}\text{B}$  beam at 2.5A MeV energy.

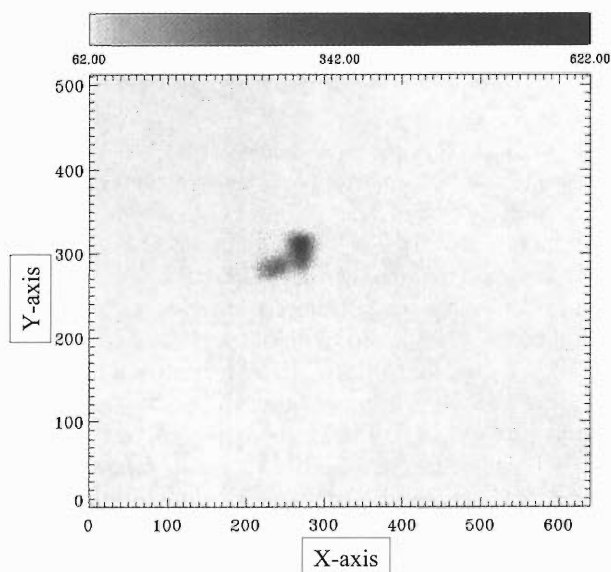


Fig. 3. Center-position image for  $^{10}\text{B}$  beam at 2.5A MeV energy.

the center-image part of this system will be useful for monitoring both the position and the shape of the heavy-ion beam spot. Moreover, the position information of a heavy ion reduces the uncertainty of the flight path between two ToF systems, which is caused by angular straggling in the target. The streak images corresponding to the center-position images are clearly seen in Fig. 2. However, it is not a circular image, but an elliptical one. This is due to the interface between the horizontal and vertical electric fields in the sweep region in the streak image section. This can be fixed by using an electric shield between the horizontal and vertical electrode.

We are currently working on improving the detection efficiency and the event acquisition rate.

#### References

- 1) G. W. Buylter, A. M. Poskanzer, and D. A. Landis: Nucl. Instrum. Methods. **89**, 189 (1970).
- 2) I. Tanihata: J. Phys. G: Nucl. Part Phys. **24**, 1311 (1998).

## Development of a New Photon Detector System for Nuclide Identification

K. Uchiyama, K. Ohta, T. Ishizuka, K. Akimoto,\* S. Aoyagi,\* T. Hirose,\* K. Morita, and N. Sugimoto\*

Over the past few years, several experiments for producing and identifying new isotopes have been performed by the  $\alpha$ - $\alpha$  delayed coincidence method using the RIKEN gas-filled recoil separator (GARIS).<sup>1-3</sup> This method is very useful for identifying new isotopes when the  $\alpha$ -decay of the daughter nucleus is well known. However, there are cases in which this method is not effective, such as when the  $\alpha$ -decay energies of the daughter nucleus are unknown, or when the branching ratio of  $\alpha$ -decay for its daughter nucleus is much smaller than the detection limit. In such cases, additional information, for example, the characteristic X-rays oriented from reaction products, measured around a focal plane detector of the separator, is required for identification.

CdTe and CdZnTe semiconductor detectors are suitable for measurements of rare events such as the production of new isotopes because of the high efficiency per volume due to their large absorption cross section compared with those of conventional X-ray detectors, Ge or Si(Li) detectors. The band gap of CdTe or CdZnTe is sufficiently wide to allow operation at room temperature, so it is expected that low running and maintenance costs will be achieved. However, the CdTe and CdZnTe detectors have several problems, including a low energy resolution compared with Ge or Si(Li) detectors, and difficulty with producing large crystals. As a result of the latter, although the price of one CdTe or CdZnTe crystal is much lower than for a Ge crystal, the size of a commercially available CdTe or CdZnTe crystal is much smaller than that of a Ge crystal. In our experiments, X-ray detectors will be placed around the focal plane detector, so the distance between reaction products which are implanted in the focal plane detector and X-ray detectors will be restricted by the optical condition of the separator. In addition, the detectors should be placed far enough from the focal plane so as not to be damaged by charged particles, and yet close enough to the focal plane to achieve a high detection efficiency. Consequently, the total detection efficiency will be strongly affected by the detector crystal sizes; we must use many crystals set around the focal plane detector in order to cover a sufficiently large solid angle. Thus, the total price of the CdTe or CdZnTe system will become even higher than that of the Ge system; this is the problem which must be solved when the CdTe or CdZnTe detector system is constructed. To find the optimum solution for our new photon detector, we in-

vestigated the basic performance of CdTe and CdZnTe.

First, a Schottky CdTe detector<sup>4)</sup> was tested using the setup shown in Fig. 1. A single crystal of CdTe whose effective area is 10 mm  $\times$  10 mm and thickness is 0.3 mm was mounted on a boron nitride base. The

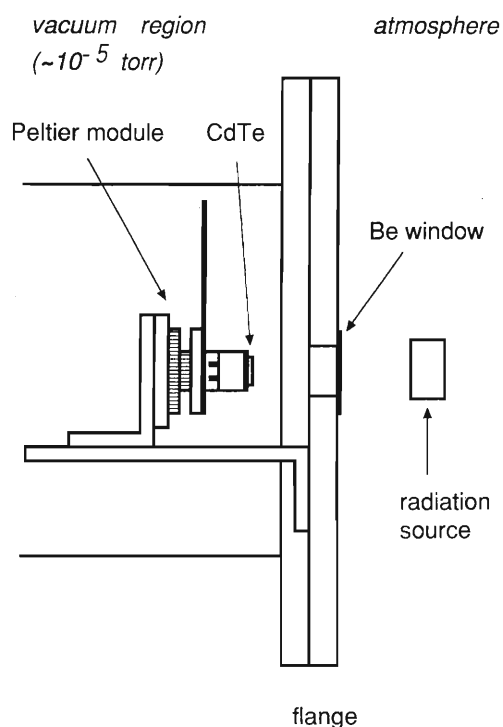


Fig. 1. Schematic diagram of a setup for test experiments of a Schottky CdTe detector.

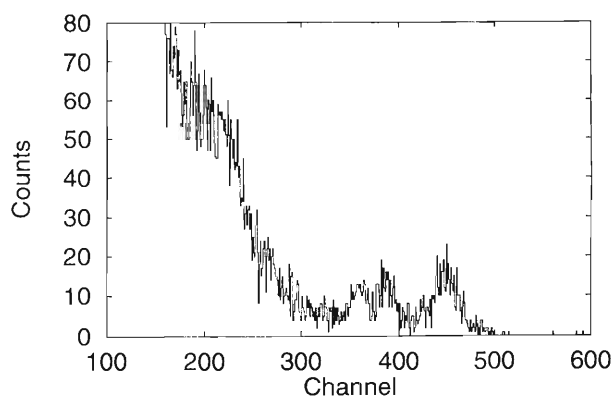


Fig. 2. The  $\gamma$ -ray spectrum of a <sup>133</sup>Ba standard source at room temperature obtained using the Schottky CdTe detector. Positive bias, +100 V, was applied to the indium electrode. The statistics of this spectrum are poor because the radiation sources are weak.

\* Department of Physics, Saitama University

CdTe crystal can be cooled using a Peltier module. The CdTe detector in the vacuum chamber was irradiated by radiation sources through the 0.5-mm-thick metal beryllium window. Figure 2 shows the  $\gamma$ -ray spectrum of a  $^{133}\text{Ba}$  standard source at room temperature. The peaks at 359 channel, 387 channel and 449 channel correspond to 276.4 keV, 302.9 keV and 356.0 keV, respectively. The value of the full-width at half maximum (FWHM) in these energy regions is about 22 keV, and this value is about tenfold that of a sufficient resolution. Although the energy region of characteristic X-rays is lower, we have not yet achieved a sufficient resolution.

The main reason for insufficient resolution is the large electric noise of the preamplifier. It is expected that the photon detectors will be placed in much worse environments with respect to electric noise than the present one. At present, only a standard preamplifier which had been used for our silicon solid-state detectors surrounded by the focal plane detector of the

GARIS is used, so the development of specific preamplifiers may be necessary. On the other hand, the cost of our photon detection system using this CdTe detector may become much higher than that of Ge or Si(Li) detectors if specific preamplifiers which significantly improve the resolution must be used for each crystal. If so, it will be difficult to use the CdTe detector, from an economic point of view. The CdTe detectors discussed above have many merits, and thus the improvement of the resolution and other investigations, including the testing of CdZnTe detectors, are presently in progress.

#### References

- 1) K. Morita et al.: *Z. Physik A* **352**, 7 (1995).
- 2) Y. H. Pu et al.: *Z. Physik A* **357**, 1 (1997).
- 3) Y. Tagaya et al.: *Eur. Phys. J. A* **5**, 123 (1999).
- 4) C. Matsumoto et al.: *IEEE Trans. Nucl. Sci.* **45**, 428 (1998).

## Development of High-Efficiency Delay-Line PPAC for High-Energy Light Ions

H. Kumagai, N. Fukuda, A. Ozawa, K. Sümmerer, and I. Tanihata

The facilities that produce radioactive secondary beams by projectile fragmentation need to routinely measure the positions of a wide range of energetic ions. For position measurements, two-dimensional parallel plate avalanche detectors (PPAC) based on charge-division read-out have been used at the fragment-separator facilities in RIKEN<sup>1)</sup> and NSCL.<sup>2)</sup> The detectors have proven to be highly versatile and reliable. However, signal pileup becomes a serious problem when counting rates are higher than  $5 \text{ k s}^{-1}$  for such detectors. This is a natural limitation in the case of slow ion signals. Thus, we have developed delay-line read-out models. We have successfully achieved reasonable position and timing resolution for counting rates of  $10^6 \text{ s}^{-1}$  for an earlier model.<sup>3)</sup> However, due to a smaller induced signal from the electrons, the previous type was effective only for low energies (less than  $15 \text{ A MeV}$ ) or for large  $Z$  ions at high energies.

In order to improve detection efficiencies for high-energy light ions, we needed to improve the signal-to-noise ratio of the PPAC. Since it is difficult to enhance the signal in the delay-line PPAC, the only way to improve the signal-to-noise ratio is to decrease the noise level in the PPAC. There are two major noise sources; one is the noise from external electronic devices, such as the power supply of pre-amps and turbo-molecular pumps, and the other comes from internal electronics in the PPAC. To decrease external noise, we carefully mounted the PPAC in such a way that it was isolated from the beam-line and its vacuum chamber. The main source of internal noise is the pre-amp. In order to decrease the noise level, we developed a new design for the pre-amp, using a low-noise transistor. We succeeded in decreasing the noise level by a factor of two.

We measured detection efficiencies, position resolution, and time resolution for the newly designed delay-line PPAC at the RIPS in RIKEN and the KAOS facility in GSI.

We produced several types of secondary fragments at the RIPS, namely,  $^{10}\text{Be}$  with  $75 \text{ A MeV}$ ,  $^8\text{Li}$  with  $61\text{--}68 \text{ A MeV}$ , and  $^7\text{Li}$  with  $87\text{--}91 \text{ A MeV}$ . We mounted a plastic scintillator in front of the PPAC to count the number of fragments passing through. In order to measure the position resolution of the PPAC, we mounted a small photomultiplier with three fiber scintillators on the exit window of the PPAC. The distance between fiber scintillators was  $10 \text{ mm}$  and the scintillators were square in shape with a size of  $0.5 \times 0.5 \text{ mm}^2$ . For the PPAC, we used  $\text{C}_3\text{F}_8$  gas at  $30 \text{ Torr}$  and flow rates of about  $6\text{--}10 \text{ l/h}$ . We achieved about  $95\%$  detection effi-

ciency for the above fragments even for a  $10^5 \text{ s}^{-1}$  count rate. To obtain the position resolution, we measured the position spectra of the PPAC coincident with the fiber scintillators. We obtained a  $1.2\text{--}1.5 \text{ mm}$  (FWHM) position resolution for the PPAC, including the size of the scintillators. We also measured the time resolution between the signal of the front plastic scintillator and the anode signal of the PPAC. The measured time resolution was  $1.6\text{--}1.7 \text{ ns}$  (FWHM), including the intrinsic time resolution of the scintillator. It was noted that the flow rate of the gas affects the bias voltage of the PPAC. For a flow rate of  $6 \text{ l/h}$ , we achieved  $96\%$  efficiency at  $1750 \text{ V}$ . On the other hand, for a flow rate of  $10 \text{ l/h}$ , we achieved  $95\%$  at  $1820 \text{ V}$ . The reason for the difference is unclear. Probably, it is due to the purity of the gas and/or the out-gas from materials inside the PPAC chamber. The higher flow rate is preferable for stable PPAC operation.

In one experiment, we applied high count rates (about  $25 \text{ k s}^{-1}$ ) for about 7 hours to check the long-term stability of the PPAC. During the measurements, the PPAC was damaged due to discharges. After the measurements, we compared the damage of the cathodes, with Al and Au platings, due to the discharges. We observed a marked difference in the trace of discharges. The damage in the case of Au plating was greater than at in the case of Al plating. The difference may be due to the different melting points for both metals. Therefore, we chose Al for the final plating. However, the contact between the delay-line and the cathode plate was formed by Au evaporation to maintain a good electronic contact.

We installed two new delay-line PPACs at the KAOS

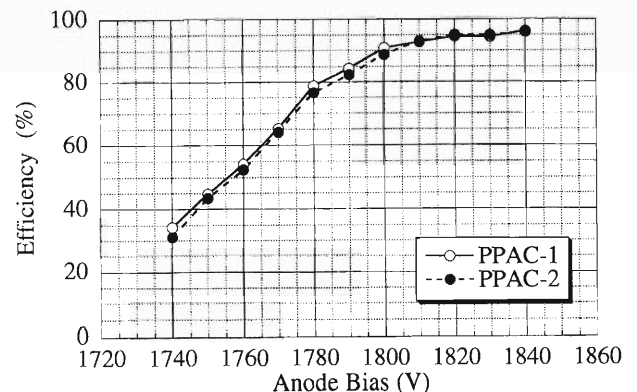


Fig. 1. Bias voltage dependence of the detection efficiency for the newly designed delay-line PPAC measured by the mixed  $^8\text{B}$  beam.

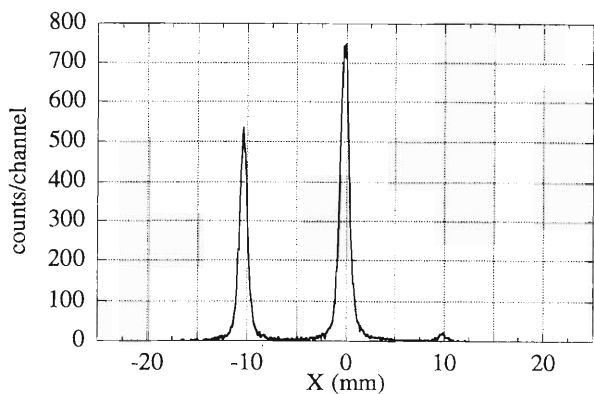


Fig. 2. Position spectra (X-axis) of the newly designed delay-line PPAC coincident with fiber scintillators ( $0.5 \times 0.5 \text{ mm}^2$  size) measured by the mixed  $^8\text{B}$  beam.

facility in GSI in order to check the performance of the detectors at relativistic energies. We produced three types of beams, namely  $^{12}\text{C}$  with 174 A MeV,  $^{12}\text{C}$  with 335 A MeV, and a mixed beam of  $^8\text{B}$  with

254 A MeV and  $^7\text{Be}$  with 216 A MeV, from the FRS facility at GSI. The typical count rate was about  $100 \text{ s}^{-1}$  for the mixed beam. We achieved about 99% detection efficiency for the  $^{12}\text{C}$  beams and about 95% detection efficiency for the mixed  $^8\text{B}$  beam. In Fig. 1, bias voltage dependence of the detection efficiency for the mixed  $^8\text{B}$  beam is observed. To obtain the position resolution, we measured the position spectra of the PPAC coincident with the fiber scintillators. We obtained 1.1–1.2 mm (FWHM) position resolution for the PPAC, as shown in Fig. 2 for the mixed  $^8\text{B}$  beam. We also measured the time resolution between the two PPACs. The measured time resolution was 1.2–1.4 ns (FWHM).

#### References

- 1) H. Kumagai and K. Yoshida: RIKEN Accel. Prog. Rep. **28**, 127 (1995).
- 2) D. Swan, J. Yurkon, and D. J. Morrissey: Nucl. Instrum. Methods Phys. Res. A **348**, 314 (1994).
- 3) H. Kumagai and I. Tanihata: RIKEN Accel. Prog. Rep. **31**, 164 (1998).

## Construction of PHENIX Muon Tracking Chambers

J. Murata, M. L. Brook, D. M. Lee,<sup>\*1</sup> S. Pate,<sup>\*2</sup> N. Saito, T. Shibata,  
W. Sondheim,<sup>\*1</sup> M. Sugioka, and C. Velissaris<sup>\*2</sup>

The PHENIX muon arm consists of a muon identifier (MuID), muon magnets and a muon tracker (MuTr). Muon magnets and MuID panels have been built and installed in the experimental hall.<sup>1)</sup> In May 1999, a RIKEN team joined the MuTr construction team to work mainly on: (1) Chamber quality assurance (QA) system construction, (2) Optical alignment system development, (3) Gas system design and construction, (4) Position resolution evaluation.

Each arm of the MuTr consists of three stations of cathode-strip tracking chambers, which are mounted inside the muon magnets. Each station is now under construction<sup>1)</sup> at factories in BNL, LANL, UNM (University of New Mexico) and NMSU.

(1) The QA test system at the BNL factory, for testing stations 2 and 3 has been built. The QA system consists of a test system for the high anode-voltage supply and a cathode-signal readout system for evaluation using the  $\beta$ -source. A CAMAC-based data acquisition system (DAQ) has been built and checked using signals from scintillators. The 32-octant chambers of stations 2 and 3 are being checked using this system. The total number of channels is 44544 (cathode strips) and 26496 (anode wires).

(2) A real time relative-position monitoring system<sup>2)</sup> has been prepared. The initial placement of the chambers is possible to an accuracy of a few millimeters; however, sufficient resolution can be obtained by measuring the relative alignment of the chambers to within 25  $\mu\text{m}$  using the optical alignment system. The role of this system is not only to measure the initial alignment, but also to monitor the thermal expansion or movements of the chambers. The system comprises an optical fiber connected to a visible-light source, a convex lens and a position-sensing CCD camera. We have developed a DAQ system for CCD utilizing commercially available software. The CCD camera has a sensing area of  $8.8 \times 6.6$  mm with the effective pixels of  $768 \times 493$ . Therefore, the pixel resolution is approximately 12  $\mu\text{m}$  and the centroid resolution is approximately 2  $\mu\text{m}$ . We will use seven alignment monitors per chamber. Preparation for the installation is in progress.

(3) The chamber gas supply and recirculation system design has been completed.<sup>3)</sup> Ar(50%) + CO<sub>2</sub>(30%) + CF<sub>4</sub>(20%) mixed gas was selected with consideration of non-flammability, Lorentz angle, cathode charge distribution, efficiency and so forth. In order to reduce the cost of the expensive CF<sub>4</sub> gas, a system enabling

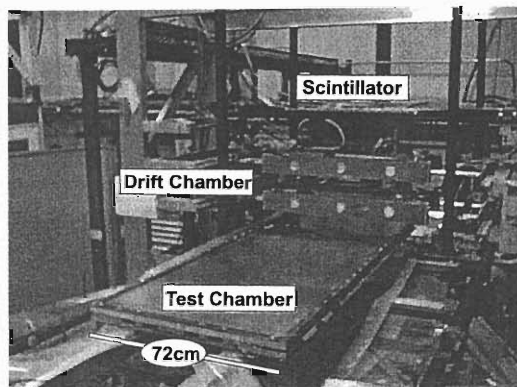


Fig. 1. Experimental setup of the position resolution measurement for the test chamber at LANL. Another two drift chambers and a trigger scintillator are located below the test chamber.

almost complete recirculation has been designed using gas purification filters. Safety precautions with respect to protect against too high and too low pressure have been taken, with particular consideration of the thin gas windows of station 2. The system design has been approved by the RHIC safety review committee and construction will start soon.

(4) The position resolution of a test chamber which has the same strip structure as the real chambers of the MuTr has been measured. The primary purpose for constructing the test chamber is to check the performance of the front end electronics before their mass production. However, this measurement in itself is important because it is the only reference data for the resolution. The cosmic-ray measurement was carried out in October 1999 at LANL using four delay-line drift chambers<sup>4)</sup> as reference chambers (Fig. 1). The drift chambers have the position resolutions in the range of 80–100  $\mu\text{m}$ . Further calibration and analysis is well underway and the position resolution of 100  $\mu\text{m}$  is expected for the test chamber.

### References

- 1) *PHENIX Muon Arms Status, September 1999*, (PHENIX, Brookhaven National Laboratory, New York, 1999).
- 2) M. L. Brooks et al.: *IEEE Trans. Nucl. Sci.* **44**, 683 (1997).
- 3) J. Murata: *Muon Tracker Gas System Design* (1999); <http://spin.riken.bnl.gov/~jiro/mutrgas.html>
- 4) L. G. Atencio et al.: *Nucl. Instrum. Methods Phys. Res.* **187**, 381 (1981).

<sup>\*1</sup> Los Alamos National Laboratory, USA

<sup>\*2</sup> Department of Physics, New Mexico State University, USA

## Status of PHENIX Muon Identifier Mechanics

A. Taketani, V. Cianciolo,<sup>\*1</sup> H. En'yo, N. Hayashi, T. Ichihara, K. Imai, M. Ishihara,  
L. Kotchenda,<sup>\*2</sup> K. Kurita, Z. Li, Y. Mao, K. Read,<sup>\*1,\*3</sup> N. Saito, H. D. Sato,  
T. Shibata, E. Taniguchi, W. Tian,<sup>\*3,\*4</sup> and Y. Watanabe

The installation and testing of the muon identifier (MUID) for the PHENIX detector was completed in 1998. Since then, we have been maintaining the detectors and designing the gas supply system for this large-scale detector. In this article we report on the mechanical maintenance of the MUID, focusing on the recovery procedure following a major accident which happened in Jan. 1999, and the progress of the gas supply system design and construction.

The MUID detector plays an important role in the RHIC spin program<sup>1)</sup> as well as in the heavy ion program. The detector system consists of a range stack formed by the sandwiching of five absorber steel plates and proportional chambers made of plastic larroci tubes.<sup>2)</sup> In order to cover a large acceptance of 10 to 35 degrees in  $\theta$  and 360 degrees in  $\phi$  at 7 m from the reaction point, the area which must be covered is 10 m high and 13 m wide. The detector covers the forward and backward regions, so-called south and north arms, respectively. We segmented a total of 10 gaps. Each gap has 6 of panels which are into 60 which are formed a proportional tube array housed in the aluminum cases. The MUID panels were fabricated<sup>3)</sup> and installed in the fall of 1998.<sup>4,5)</sup>

The PHENIX experimental hall was flooded on Jan. 2, 1999. The rapid increase in temperature melted the accumulated snow on the ground, but did not melt the ground ice. A large amount of muddy water flooded the PHENIX Interaction Region (IR) where all of the MUID panels were installed. All of the water receded the following day, it was observed that the water level had reached about 10 cm above the bottoms of the lower MUID panels. In the following paragraphs, we describe how we recovered the detector following this disaster.

We partially opened one MUID panel and inspected the internal parts. The flood line reached the electronics boards which contain the preamplifier and the high-voltage distributor. However it did not reach the lower end of the larroci tubes, indicating that the chamber volume was not soaked in water. Holes, 6 mm in diameter, were drilled on the side of the bottom rails in order to drain the trapped muddy water. After most of the water was drained, nitrogen gas was introduced into the secondary volumes, which contain the tubes and the electronics, to dry them out until we finished checking all the soaked panels. The electric connec-

tors, which serve as the interface between the MUID panels and external electronics, were cleaned with alcohol. The expected resistance between the terminals of the low- and high-voltage lines was confirmed before applying the operation voltages. Pure CO<sub>2</sub> gas was then introduced into the chamber volume. The high voltage was applied after flow the gas for three volume exchanges. Then, the signal shapes from each tube were checked using an oscilloscope. The signal rates, which are the incidences of cosmic rays, were measured. These data were compared with those which were taken before the disaster. The details of the checking procedure are described in Ref. 4. All the panel tests were completed on Feb. 2, 1999. Two HV channels were found to be newly sparking under the normal operation voltages. We expect that they will recover with further conditioning.

The mud, which was carried along with the water, still remains in the secondary volumes. It cannot be removed since most of the panels are buried in between absorber steel plates, and the secondary volumes of the panels are inaccessible.

To prevent future flooding, permanent drain pumps were set up in the IR and the landscape around the IR was altered to minimize the possible water flow into the IR.

Next, we describe the gas system design and construction. The outstanding requirements of the MUID gas system are as follows.

(1) Large volume of gas (50 m<sup>3</sup>) and high flow rate (17 l/min).

(2) Large number of segmentations of the gas volume.

(3) Widely scattered locations of the panels in the PHENIX IR.

(4) Supply of primary gas (pure CO<sub>2</sub>, CO<sub>2</sub>-iC<sub>4</sub>H<sub>10</sub> mixture which contains a flammable fraction up to 25 percent) and secondary gas (dry air or N<sub>2</sub>).

Figure 1 shows the schematic diagram of our gas system composed of two major parts. One is located in the IR and the other in the mixing house located outside of the building which contains the IR. The mixing house contains the gas supply and recirculation system. A large portion of the gas piping is in the IR.

The CO<sub>2</sub> and iC<sub>4</sub>H<sub>10</sub> gasses are fed to the south and north arm chambers through the mass flow controllers which regulate the mixing and flow rates. Up to half of the chamber gas is recirculated through the compressor and purifier. The remaining portion is exhausted into the atmosphere in a safe manner. The

\*1 Ork Ridge National Laboratory, USA

\*2 Interphysica, Russia

\*3 University of Tennessee, USA

\*4 China Institute of Atomic Energy, China

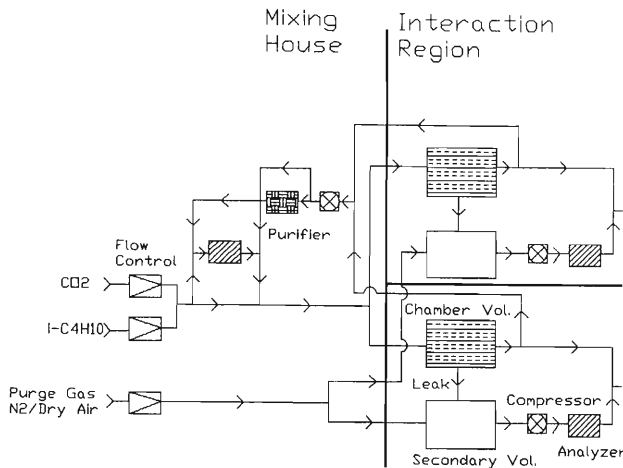


Fig. 1. Schematic view of the MUID gas system.

gas qualities, which reflect the chamber performance, at the inlet and outlet are periodically monitored by the analyzers. When the system detects degradation of the gas quality, a warning signal is triggered. If the degradation is in the fatal level, the system will shut off the HV supplied to the chambers in order to avoid catastrophic failure.

The purpose of having the secondary gas flow is twofold. One is to keep the volume clean and dry. Another is to dilute and purge any leakage of primary flammable gas. The leakage rate from the chamber volume is estimated to be maximum 10 percent of the total flow even without catastrophic failure. Nitrogen gas is sucked from the secondary volume and periodically monitored for its flammability using the nitrogen-sniffing system. If the  $iC_4H_{10}$  fraction in the sucked ni-

trogen exceeds 25 percent of the lowest explosion limit (LEL), the flow of  $iC_4H_{10}$ , as well as the high-voltage and low-voltage power, will be shut off.

The analyzers, pressure gauges, flow meters, and solenoid valves that open/close each gas circuit are remotely controlled by a PC in the mixing house. The PC maintains the system.

The design of the gas supply system was reviewed by the RHIC safety committee. The main concern of the committee was preventive measures against fire accidents. Parts in the flammable gas flow line and those very close to the flammable gas flow line must not provide any possible ignition sources. The time period required for flammability to increase in the secondary volume due to a catastrophic leak was estimated. It takes 70 minutes to reach 25 percent of the LEL. In our design, the nitrogen-sniffing interval for each monitoring point is 30 minutes, so that the system can detect a leak well before it reaches dangerous levels. The gas flow indicators monitor the difference between the inlet and outlet flow rates and are able to trigger the warning signal once leakage is detected. The system is already under construction. The major pipes between the mixing house and IR has been completed.

#### References

- 1) H. En'yo et al.: RIKEN Accel. Prog. Rep. **30**, 34 (1997).
- 2) Y. Mao et al.: RIKEN Accel. Prog. Rep. **30**, 36 (1997).
- 3) A. Taketani et al.: RIKEN Accel. Prog. Rep. **31**, 172 (1998).
- 4) A. Taketani et al.: RIKEN Accel. Prog. Rep. **32**, 50 (1999).
- 5) K. Kurita et al.: RIKEN Accel. Prog. Rep. **32**, 32 (1999).

# High-Energy Beam Test of PHENIX EM Calorimeter at CERN

H. Torii, T. Awes,<sup>\*1</sup> S. Bathe,<sup>\*2</sup> D. Bucher,<sup>\*2</sup> H. Buesching,<sup>\*2</sup> H. En'yo, Y. Goto, K. Imai, M. Ippolitov,<sup>\*3</sup>  
E. Kistenev, V. Mexner,<sup>\*2</sup> U. von Poblitzki,<sup>\*2</sup> T. Peitzmann,<sup>\*2</sup> N. Saito, and S. White

The PHENIX experiment at RHIC<sup>1)</sup> will start soon, first for heavy-ion physics, and next for spin physics. In this experiment, an electromagnetic (EM) calorimeter plays an important role in detecting photons and electrons/positrons. In order to cover topics in both heavy-ion and spin physics, *e.g.*, thermal photon measurement in heavy-ion physics, and prompt photon,  $\pi^0$  and weak boson measurements in spin physics, the EM calorimeter needs to cover a wide energy range from a few hundred MeV to 80 GeV. Spin physics also requires an energy measurement to within 2% accuracy to measure the cross sections of prompt photons and  $\pi^0$ s with less than 10% error, because the cross sections fall steeply as their energy increases.

The EM calorimeter was originally designed for heavy-ion physics. There are two kinds of calorimeters in the PHENIX detector. One is a lead-scintillator sampling calorimeter (PbSc) and the other is a lead glass calorimeter (PbGl). Table 1 shows their basic parameters. A "supermodule" is composed of  $12 \times 12$  channels for PbSc and  $4 \times 6$  channels for PbGl. The total EM calorimeter system in the PHENIX detector consists of these PbSc and PbGl supermodules.

The performance of both calorimeters for accuracy and resolution of energy measurement, and hadron rejection was measured at BNL/AGS up to 7 GeV. In order to measure the performance up to 80 GeV, the high-energy beam test was performed at CERN/SPS.<sup>2)</sup> One PbSc supermodule and four PbGl supermodules were located at the H6 beam line, and all were tested with electron beams from 6 GeV/*c* to 80 GeV/*c* and  $\pi^+$  beams of 40 GeV/*c*. In this report, we present the preliminary results of PbSc.

Figure 1 shows the setup of the beam test. The

Table 1. Basic parameters of the two kinds of PHENIX EM calorimeters.

		PbSc	PbGl
Channel			
cross section	(mm <sup>2</sup> )	52.5 × 52.5	40 × 40
depth	(mm)	375	400
radiation length	(X <sub>0</sub> )	18	14.4
Moliere radius	(mm)	~30	36.8
Supermodule			
number of channels		144 (12 × 12)	24 (4 × 6)
Total system			
number of channels		15552	9216

<sup>\*1</sup> Oak Ridge National Laboratory, USA

<sup>\*2</sup> Institut fuer Kernphysik, University of Muenster, Germany

<sup>\*3</sup> Kurchatov Institute, Russia

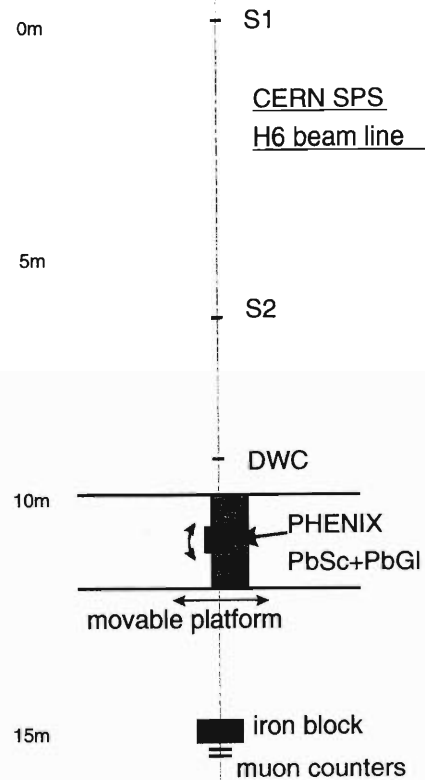


Fig. 1. Setup of the beam test. Each component is described in the text.

EM calorimeters were placed on a movable platform to allow change of the position and angle of the incident beam on the calorimeters. Delay-line wire chambers (DWC) were located just in front of the calorimeters for measurement of the vertical and horizontal beam incident positions. Incident position dependence of the energy deposit was measured and corrected using the DWCs. Two scintillators (S1 and S2) were used as trigger counters, and two other scintillators were set behind iron blocks to identify muons in the beams. We used 10 GeV/*c* muon data for the channel-by-channel gain adjustment of each PbSc channel in addition to the electron-beam data. To correct time-dependent gain drift, we applied a laser monitoring system to the calorimeters.

As a result, we obtained the energy resolution for an electron beam. The result is consistent with the AGS data.<sup>3)</sup> Figure 2 shows all the data points of the energy resolution measured at AGS and CERN. These points are fitted and expressed by the formula

$$\sigma_E/E = 1.9\% \oplus 8.2\%/\sqrt{E},$$

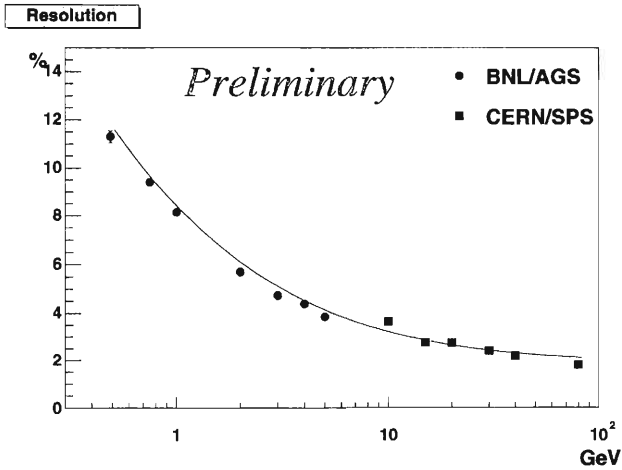


Fig. 2. All data points of the energy resolution measurements at AGS and CERN. The fitting result,  $1.9\% \oplus 8.2\%\sqrt{E}$  is also shown.

where  $\oplus$  represents the quadratic sum. We need more systematic understanding of the correlatoin between the AGS data and the CERN data.

An analysis of the accuracy of the energy

measurement for an electron beam is in progress. In this test, we can investigate the accuracy of energy measurement to within a  $\pm 2\%$  limit. The major limit comes from the remaining error of the channel-by-channel gain adjustment. In this limit, we have found that PbSc has a 2% accuracy of energy measurement in the energy region between 20 GeV and 80 GeV. At 10 GeV/c, we observed a shift of the measured energy larger than 2% of the beam energy. We need to understand the source of this shift, *e.g.*, photo-multiplier tube,<sup>4)</sup> front-end electronics, or accuracy of the beam energy itself.

In the present analysis stage, PbSc almost satisfies the physics requirements to cover both heavy-ion physics and spin physics, although we need greater understanding of its behavior. The PbGl data are also under analysis. We will conclude our analysis for both PbSc and PbGl before the PHENIX experiment starts.

#### References

- 1) Y. Batygin et al.: RIKEN Accel. Prog. Rep. **32**, 44 (1999).
- 2) Y. Goto et al.: RIKEN Accel. Prog. Rep. **32**, 47 (1999).
- 3) A. Bazilevsky: private communication.
- 4) G. David et al.: IEEE Trans. Nucl. Sci. **42**, 306 (1995).

## Feasibility Test of Proton-Carbon CNI Polarimeter for RHIC

I. Alekseev,<sup>\*1</sup> M. Bai,<sup>\*2</sup> B. Bassalleck,<sup>\*3</sup> G. Bunce,<sup>\*2</sup> A. Deshpande,<sup>\*4</sup> J. Doskow,<sup>\*5</sup> S. Eilerts,<sup>\*3</sup> D. E. Fields,<sup>\*3</sup> Y. Goto, H. Huang,<sup>\*2</sup> V. Hughes,<sup>\*4</sup> K. Imai, M. Ishihara, V. Kanavets,<sup>\*1</sup> K. Kurita, K. Kwiatkowski,<sup>\*5</sup> B. Lewis,<sup>\*3</sup> B. Lozowski,<sup>\*5</sup> Y. Makdisi,<sup>\*2</sup> H. O. Meyer,<sup>\*5</sup> M. Nakamura, B. Przewoski,<sup>\*5</sup> T. Rinckel,<sup>\*5</sup> T. Roser,<sup>\*2</sup> A. Rusek,<sup>\*2</sup> N. Saito, B. Smith,<sup>\*3</sup> D. Svirida,<sup>\*1</sup> M. Syphers,<sup>\*2</sup> A. Taketani, T. L. Thomas,<sup>\*3</sup> J. Tojo, D. Underwood,<sup>\*6</sup> D. Wolfe,<sup>\*3</sup> K. Yamamoto,<sup>\*7</sup> and L. Zhu<sup>\*7</sup>

At Brookhaven National Laboratory (BNL) construction of helical dipole magnets for acceleration of polarized proton beams in RHIC rings is under way. Successful commissioning of the helical dipole magnets (what we call “Siberian Snakes”) will enable us to do experiments with polarized protons up to  $\sqrt{s} = 500$  GeV in collider mode for the first time. In the commissioning phase of the polarized proton acceleration, a reliable polarimeter is crucially required. It was proposed in 1997 to use proton-carbon elastic scattering in the Coulomb-nuclear interference (CNI) region for the polarimeter.<sup>1,2)</sup> This polarimeter is called the “pC CNI polarimeter”. In the CNI region, where a range of momentum transfer squared  $t$  ( $\text{GeV}/c$ )<sup>2</sup> is  $10^{-3} < -t < 10^{-2}$ , the theoretically predicted analyzing power  $A_N(t)$ <sup>3,4)</sup> has the maximum value of about 4% at  $-t = 2.3 \times 10^{-3}$  ( $\text{GeV}/c$ )<sup>2</sup> and decreases as  $-t$  increases. This polarimetry has the following advantages: (1) the reaction mechanism is theoretically well understood, (2) the analyzing power weakly depends on beam energy and (3) its figure of merit is large owing to the large cross section.

Experiment BNL-AGS E950 was proposed in August 1998 to test the feasibility of the pC CNI polarimeter for RHIC using a polarized proton beam at the AGS. Our goals are to measure the pC CNI analyzing power  $A_N(t)$  for the first time at the RHIC injection energy and to test experimental devices at the AGS environment. The challenge is in detecting elastic pC scattering in a high background and noise environment inside the AGS ring. The proposed method of identifying pC scattering is detecting only recoil carbons, because the scattering angle of the incident protons in the CNI region is too small to detect. These recoil carbons have a very low energy, ranging from 100 keV to a few MeV, and recoil angles are almost 90 degrees with respect to the beam direction. The experimental setup, consisting of a carbon target and detector arms, is schematically shown in Fig. 1. The entire setup was installed in the AGS ring. The target was a “microribbon carbon target” which had been

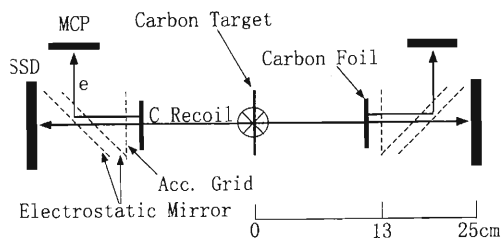


Fig. 1. Schematic layout of the experimental setup (horizontal view upstream of the target).

developed at IUCF<sup>5)</sup>. It was  $6 \mu\text{m}$  wide,  $4 \mu\text{g}/\text{cm}^2$  thick and 3 cm long. This extremely thin target makes it possible to extend its lifetime by reduction of the heating, to suppress the blowup of the beam emittance and to decrease energy loss and multiple scattering of recoil carbons in the target. The silicon strip detector (SSD) had a thickness of  $400 \mu\text{m}$  and was segmented into six strips. Each strip was 4 mm wide and 10 mm long. The surface of the SSD had a special feature of markedly thin Boron implantation with small aluminum wire electrodes so that low-energy recoil carbons could penetrate the surface without being hindered by the electrodes. The microchannel plate (MCP) assembly, consisting of two layers of MCPs and a single anode, had a sensitive area of 27 mm in diameter. It detected secondary electrons emitted from a  $5\text{-}\mu\text{g}/\text{cm}^2$ -thin carbon foil primarily by the passage of recoil carbons. The secondary electrons were accelerated and reflected toward the MCP by both an accelerating grid and an electrostatic mirror. The system in each arm provides the measurements of energy, time-of-flight (TOF) between the MCP and the SSD and particle emission angle to the beam direction event by event.

The experiment was carried out in March 1999. The proton beam transversely polarized in the vertical direction was accelerated to  $21.7 \text{ GeV}/c$ . The polarization sign was flipped each spill in order to reduce systematic errors. The polarization measured by the AGS internal polarimeter was about 40%. The beam had a bunch structure of  $4\text{-}6 \times 10^9$  protons per bunch with a width of 6 ns and a crossing frequency of 370 kHz. The trigger was a coincidence between signals from any of the SSD strips and a beam pulse (RF) from the AGS. The trigger rate was about  $2 \times 10^3$  per spill. ADCs and TDCs of all detectors were obtained with the ADC gate and the TDC start which were generated by the RF.

<sup>\*1</sup> Institute of Theoretical and Experimental Physics, Russia  
<sup>\*2</sup> Brookhaven National Laboratory, USA  
<sup>\*3</sup> Department of Physics and Astronomy, University of New Mexico, USA  
<sup>\*4</sup> Department of Physics, Yale University, USA  
<sup>\*5</sup> Indiana University Cyclotron Facility, USA  
<sup>\*6</sup> Argonne National Laboratory, USA  
<sup>\*7</sup> Department of Physics, Kyoto University

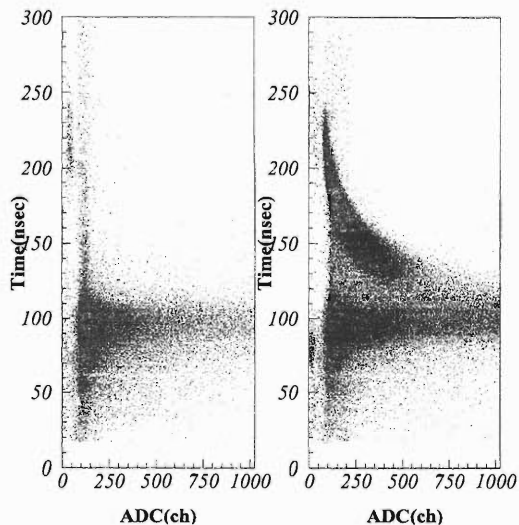


Fig. 2. On-line histograms taken from one of the SSD strips. The left histogram was obtained without the microribbon carbon target whereas the right one was obtained with the target.

The polarization sign and the beam intensity were provided from the AGS. To demonstrate the performance of our detectors, two on-line histograms obtained from one of the SSD strips are shown in Fig. 2. The vertical axis is the timing information obtained from the TDC value and the horizontal axis is the ADC value. The left histogram was obtained without the target whereas the right one was obtained with the target. Signals from recoil carbons are clearly seen in the right histogram.

Off-line data analysis is still under way but preliminary results are reported in this article. The strong correlation between ADC and TDC values of the SSD in the right histogram in Fig. 2 was noted and the values were used to select recoil carbon events. The energy calibration of the SSD was carried out by measuring the energy deposition of 5.48 MeV  $\alpha$  particles from an  $^{241}\text{Am}$  source. The calibration of arrival time from the target to the SSD was performed as follows: (1) TDC data of the SSD are found to be dependent on the pulse height (slewing effect). The dependence was corrected with recoil carbon kinematics using the energy value and TOF between the MCP and the SSD. (2) Time-zero of the arrival time was calculated using the energy value and recoil carbon kinematics. After calibration procedures (1) and (2), the time resolution was defined by the deviation from the center of the carbon locus on the arrival time vs energy plot. The obtained values were 7.3-9.1 ns on each SSD strip. These values were consistent with the width of the AGS beam bunch. To study  $-t$  dependence of raw asymmetry, a 10 ns time bin was defined on the arrival time vs energy plot. Raw asymmetries in each time bin were

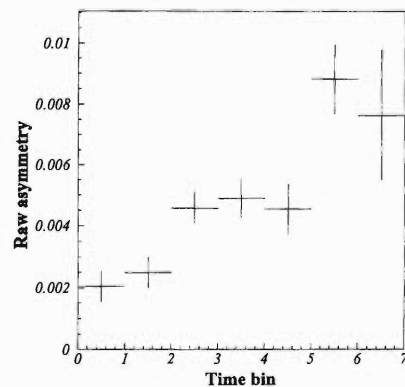


Fig. 3. Preliminary result of the raw asymmetry as a function of time bin on arrival time from the target to the SSD. The error bars are statistical only.

calculated using a so-called square root formula:

$$A_{raw} = \frac{\sqrt{N_L^\uparrow \cdot N_R^\downarrow} - \sqrt{N_L^\downarrow \cdot N_R^\uparrow}}{\sqrt{N_L^\uparrow \cdot N_R^\downarrow} + \sqrt{N_L^\downarrow \cdot N_R^\uparrow}}, \quad (1)$$

where  $N_L^\uparrow(N_R^\downarrow)$  indicates the number of events in the left (right) recoil arm with beam polarization up (down). The result of the raw asymmetry as a function of time bin is shown in Fig. 3. The error bars are statistical only.  $-t$  is a decreasing function of the time bin number; therefore, the measured raw asymmetry decreases as  $-t$  increases. The trend in time bin dependence of the raw asymmetry is consistent with the theory. Further analysis will be conducted to derive the pC CNI analyzing power  $A_N(t)$  from the raw asymmetry and the beam polarization data of the AGS internal polarimeter. We will estimate physics backgrounds which could affect the raw asymmetry and calculate possible systematic errors from them.

In summary, the feasibility of a pC CNI polarimeter was tested using a 21.7 GeV/c polarized proton beam in the AGS environment. Low-energy recoil carbons were detected inside the AGS ring. The preliminary result of the raw asymmetry revealed the behavior as the theory predicts. Based on the success of this experiment, a pC CNI polarimeter for RHIC is under construction at BNL.

#### References

- 1) Proc. Workshop on Hadron Spin-Flip at RHIC Energies, Vol. 3, RIKEN BNL Research Center, July 21–Aug. 22, edited by T. D. Lee (1997).
- 2) J. Tojo et al.: RIKEN Accel. Prog. Rep. **32**, 52 (1999).
- 3) B. Kopeliovich: High-Energy Polarimetry at RHIC, hep-ph/9801414.
- 4) N. H. Buttmore: AIP Conf. Proc., No. 95, p. 634 (1983).
- 5) W. R. Lozowski and J. D. Hudson: Nucl. Instrum. Methods Phys. Res. A **303**, 34 (1991).

## PHENIX Computing Center in Japan (CC-J)

T. Ichihara, Y. Watanabe, N. Hayashi, S. Sawada, S. Yokkaichi,  
A. Taketani, Y. Goto, H. En'yo, and H. Hamagaki

The RHIC experiment is scheduled to start in early 2000. To ensure prompt physics output, we have been preparing to construct the PHENIX Computing Center in Japan (CC-J).<sup>1,2)</sup> R&D for CC-J started in 1998 at the RIKEN BNL Research Center (RBRC). The construction of CC-J at the RIKEN Wako campus, which will extend over a three year period, began in April 1999. CC-J is intended as the principle site of computing for PHENIX simulation, a regional PHENIX Asian computing center, and as a center for the analysis of RHIC spin physics. The planned computing capacity will be sufficient to meet the bulk of the simulation needs of PHENIX. By providing a vital source of regional computing, CC-J will also encourage collaborators from China, Korea, India and Japan to be actively involved in analysis of PHENIX physics data. These capabilities of CC-J are in accord with the research plans of RIKEN and RBRC, which initiated the RHIC spin program and which plan to expand their involvement in the entire PHENIX

program.

Figure 1 shows the concept of the CC-J system. During the RHIC experiment, data acquisition, and raw data recording and monitoring will be performed at the RHIC Computing Facility (RCF) located at the BNL. After the track reconstruction, the data summary tapes (DST) will be produced, duplicated and exported to the CC-J. Data mining will be carried out at CC-J as well as at RCF from the DST to produce micro-DST, filtered by the physics interest. Simulation for the PHENIX experiments will be performed at CC-J and this output will be exported to RCF. Table 1 shows the planned size of CC-J.

Table 1.

	Dec. 1999	Dec. 2000	Dec. 2000
CPU (SPECint95)	2400	5900	10700
Tape Storage (TB)	100	100	100
Disk Storage (TB)	2.0	10	15
Tape I/O (MB/s)	45	90	112

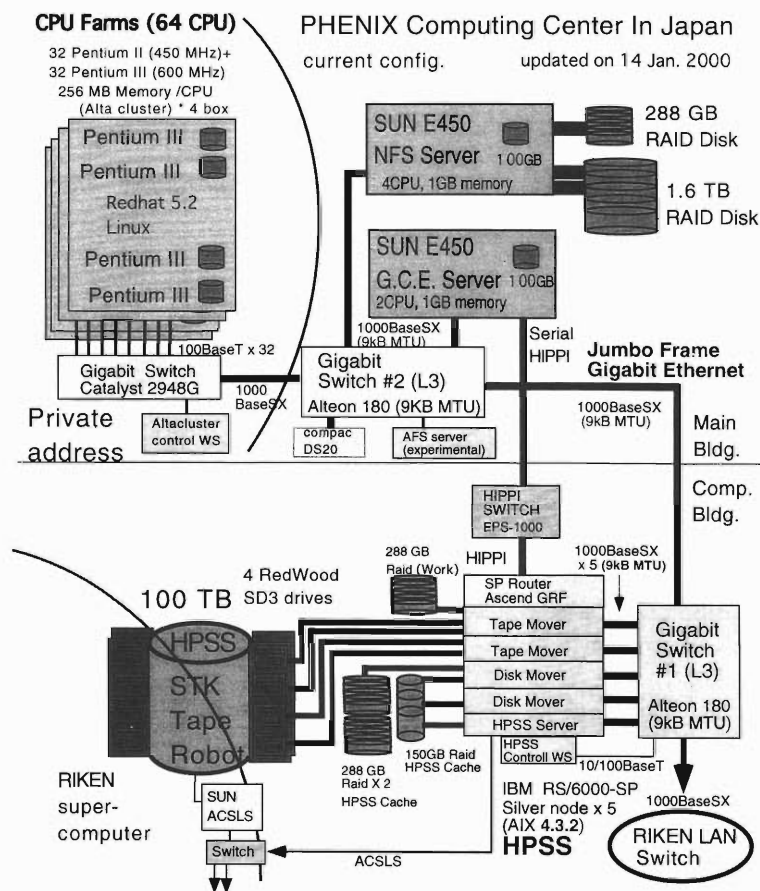


Fig. 1. Concept of the CC-J system.

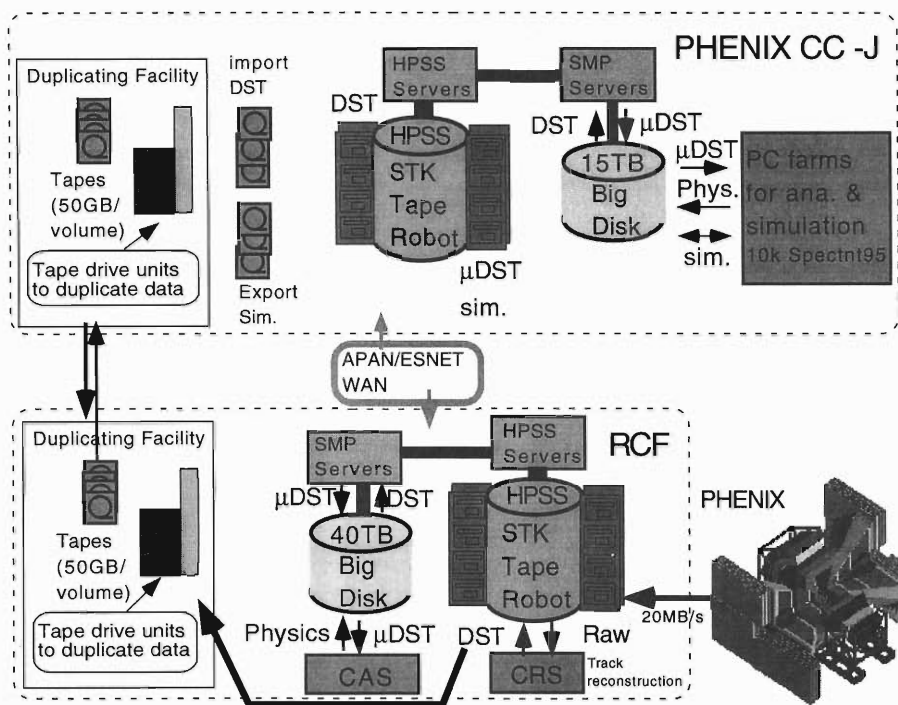


Fig. 2. Configuration of the CC-J system.

Figure 2 shows the configuration of the current CC-J system. A high performance storage system (HPSS) was installed in early 1999 as a hierarchical storage system. The HPSS consists of five nodes of an RS-6000/SP2 server, a cache disk of 720 GB, four Red-Wood tape drivers, and a tape robotic storage of 100 TB. A transfer rate of greater than 50 MB/s has been obtained by parallel ftp (pftp) between HPSS clients and HPSS servers over the Gigabit Ethernet. The test of data exchange between CC-J and RCF using the SD3 tape cartridge has been carried out successfully.

Linux pc's with Intel Pentium II/III processors are used for the CPU farms. Each node is equipped with a dual CPU, 512 MB of memory and a 14-18 GB local disk. Portable batch system (PBS) are used for the batch queueing. The multi router traffic grapher (MRTG) is used for monitoring the network traffic,

CPU load and free memory. The wide network bandwidth between CC-J and RCF has been achieved by the Asia-Pacific Advanced Network (APAN). The file transfer performance of 600 kB/s has been obtained using the large TCP window-size of 256 kB. This enables us to synchronize the data base between CC-J and RCF.

Stress tests for the entire system were carried out successfully in May, July and December 1999. During the tests, the physics simulation outputs were obtained. We plan to start the operation of CC-J in April 2000.

#### References

- 1) <http://ccjsun.riken.go.jp/ccj>
- 2) Y. Watanabe and T. Ichihara: RIKEN Accel. Prog. Rep. **32**, 53 (1999).

## A Workstation Farm Optimized for Monte Carlo Shell Model Calculations: Alphleet

Y. Watanabe, N. Shimizu, S. Haruyama, M. Honma, T. Mizusaki, A. Taketani, Y. Utsuno, and T. Otsuka

We have built a workstation farm named “Alphleet”, which consists of 140 COMPAQ Alpha 21264 CPUs, for Monte Carlo Shell Model (MCSM) calculations. It has achieved a more than 90% scalable performance with 140 CPUs when performing the MCSM calculations using PVM (Parallel Virtual Machine) library and 61.2 Gflops of LINPACK benchmark application.

We have proposed and developed the Quantum Monte Carlo Diagonalization (QMCD) method for solving the many-body problem with a two-body interaction.<sup>1-4)</sup> In the QMCD, the most important basis vectors of the many-body Hilbert space are searched for stochastically, and the Hamiltonian is diagonalized with respect to them. Contrary to the conventional Quantum Monte Carlo (QMC) methods, the minus sign problem is absent, and energy eigenvalues, matrix elements and wave functions can be obtained not only for the ground but also the excited states. In the nuclear shell model, the matrix of the Hamiltonian is diagonalized for a given many-body system where particles are interacting through a two-body system. The dimensions of the Hamiltonian matrix are often too large to carry out the conventional exact diagonalization. On the other hand, the shell model calculations play an indispensable role in going beyond mean field approximations. Thus, an alternative approach is needed in order to solve the shell model. The shell model calculations based on the QMCD are referred to as the Monte Carlo Shell Model (MCSM).

The MCSM is found to be extremely useful for understanding the nuclear shell model, particularly for large systems. Such large systems are of particular significance in the study of nuclei far from the stability line which are being explored by means of radioactive nuclear beams. The MCSM calculation is characterized as the *importance truncation* to the full exact diagonalization of the Hamiltonian matrix,<sup>5)</sup> because it produces a good approximation with a small number (about several tens) of optimally selected important basis vectors.

In the QMCD calculation, it takes almost all the CPU time to calculate each Hamiltonian matrix element with many trial basis vectors to determine the (nearly) optimal transformation. This characteristic is suitable for implementation in a parallel calculation using many CPUs, particularly in a loosely coupled system because the calculation of each matrix element can be divided into individual segments which can be processed in parallel without interacting with each other.

We decided to develop a computer system known as a “cluster” or “farm” because of the absence of a com-

mercially available computer system which realizes this simple parallelism. Every parallel computer available on the market is extremely sophisticated and too costly for our purpose. The performance of floating point calculations is also crucial. However vector CPUs are not suitable for our calculation because our calculation does not produce long enough vector which make vector CPUs work efficiently. We chose the Alpha 21264 which has the highest floating point calculation performance (58.7 SPECfp95 at 500 MHz) in scalar CPUs. It is about fourfold faster than most popular CPUs in the commodity market.

The workstation farm that we have built is named “Alphleet”, which consists of many “Alpha” CPUs in a “Fleet”. Figures 1 and 2 show a schematic diagram and a photograph (half nodes) of the Alphleet, respectively. The Alphleet consists of 71 COMPAQ DS20 s (a server and 70 clients) connected to each other via a high speed network. Each client has two Alpha 21264 CPUs (500 MHz), 512 MB of memory, Myrinet<sup>6)</sup> and 100 BASE-T network interfaces but no hard disks. On the contrary, the server which also functions as a firewall, is well equipped with UPS, 36 GB Disk, Myrinet and four 100 BASE-T network interfaces, but only one CPU and 256 MB of memory. Three NFS groups divided by the 100 BASE-T interfaces of the server (Fig. 1) may relieve the network congestion of NFS. Each client node power supply is connected to a power controller, which enables us to switch the power of each node on/off remotely from the server.

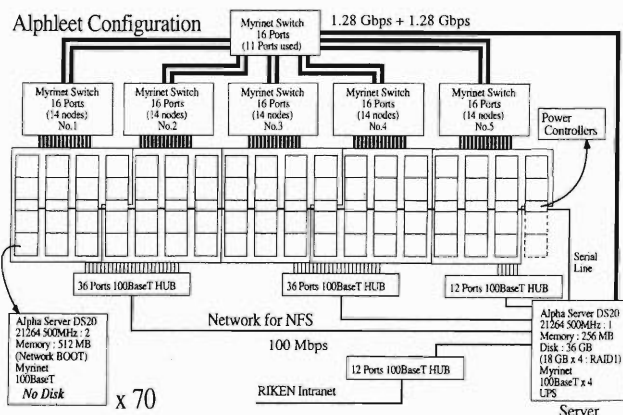


Fig. 1. Schematic diagram of the Alphleet: The Alphleet consists of 71 COMPAQ DS20 s (a server and 70 clients) connected by both Myrinet<sup>6)</sup> and 100 BASE-T to each other. Each client node power supply is connected to a power controller, which enables us to switch the power of each node on/off remotely from the server.



Fig. 2. The Alphleet: This photograph shows the server and half client nodes of the Alphleet.

It is our goal for this system to maximize performance for the MCSM calculation and to minimize management tasks. The latter is desired to enable easy management of such a large scale system for non-professional computer users. Therefore, we decided to design a diskless configuration for clients. We will have almost no reason to service to these clients if they do not have hard disks which are very costly but fragile. This means that each client must be booted up by the server through the network. The power controllers prevent the server from overloading when booting up the entire system by automatically supplying power to each client at 30 sec intervals. Thus the entire system can be booted up within about 40 min. without any difficulties. Moreover, the diskless configuration enables the power to each client node to be switched off with no risk at any time. This feature also enables power to be recycled for each client node from a remote site using power controllers, even if a client has hung up without any response. The lack of local swap space is another difficulty associated with a diskless configuration. Therefore, we added 512 MB memory to each client which is estimated to be sufficient for the MCSM calculation. This approach should be worthwhile for other single purpose computer systems for which the memory consumption can be estimated.

Each node has two types of network interfaces; one is the 100 BASE-T for NFS, also used for booting up, and the other is Myrinet, used only for interprocess communications, which is a 1.28 Gbps + 1.28 Gbps duplex switched network. Because of the Myrinet, the Alphleet achieved a 93% scalable performance when

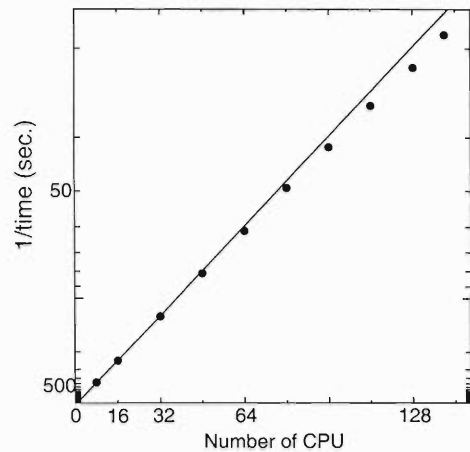


Fig. 3. Scalability of the Alphleet parallel calculation: Filled circles represent measured calculation time of MCSM as a function of number of CPUs. Solid line is a guide for the eyes showing complete scalability. The Alphleet shows a more than 90% scalable performance even with 140 CPUs.

performing the MCSM calculations, with 140 CPUs (Fig. 3). In addition, the Alphleet also achieved the 61.2 Gflops LINPACK benchmark without any precise tuning. It was ranked 169th on the “14 th TOP 500 List”<sup>7)</sup> for the world’s fastest computer systems, published in November 1999.

The Alphleet, which consists of many ready-made components, has achieved superior performance without presenting management difficulties. We demonstrate one sample system which has the advantage of being a single purpose system, in this report. On the other hand, we would like to mention that this technique as a “farm” is useful not only for parallel computing for a few users but also for a more general multipurpose, multiuser system, because job independence of each user should be offered by a loosely-coupled multi-CPU system.

#### References

- 1) M. Honma, T. Mizusaki, and T. Otsuka.: Phys. Rev. Lett. **75**, 1284 (1995).
- 2) T. Mizusaki, M. Honma, and T. Otsuka.: Phys. Rev. C **53**, 2786 (1996).
- 3) M. Honma, T. Mizusaki, and T. Otsuka.: Phys. Rev. Lett. **77**, 3315 (1996).
- 4) T. Otsuka, M. Honma, and T. Mizusaki.: Phys. Rev. Lett. **81**, 1588 (1998).
- 5) T. Otsuka, T. Mizusaki, and M. Honma.: J. Phys. G **25**, 699 (1999).
- 6) <http://www.myri.com/>
- 7) <http://www.top500.org/>

## Development of High-Rate MUSIC

K. Kimura, T. Kato, T. Ohtsubo, A. Ozawa, T. Suzuki, I. Tanihata, and Y. Yamaguchi

At the forthcoming RI beam factory, the high rate particle identification system is expected to be very useful for the experiments using radioactive secondary beams. We have thus constructed a new type of multiple sampling ionization chamber (MUSIC) which can be used stably with high-intensity beams, and tested it by measuring projectile fragments of  $^{40}\text{Ar}$  at  $E/A = 92$  MeV for comparison with the normal type of MUSIC which we had developed previously. The new high-rate MUSIC (HR-MUSIC) has a simple construction as shown in Fig. 1. It consists of multiple anodes and cathodes made of thin foil ( $4\ \mu\text{m}$  thick mylar aluminized on both sides) tilted by  $30^\circ$  toward the center axis. Eight layers of anode and cathode pairs, each separated by a 20 mm space, are stacked together. Thus, the effective length of the HR-MUSIC is 16 cm. The counter was operated using P-10 gas at the pressure of 740 Torr.

Four anode signals were separately amplified using the conventional charge sensitive preamplifier and spectroscopic amplifier systems. Since this IC has no grid, both electrons and slowly moving positive ions contribute to anode signals. Slow positive ion tails could be completely rejected using bipolar signals from the spectroscopic amplifier.

Energy loss of the projectile fragments was measured by the HR-MUSIC and the ordinary MUSIC sharing common gas, located in tandem at the fragment separator course of RIKEN (RIPS). The latter MUSIC is a gridded ionization chamber having five anode pads,

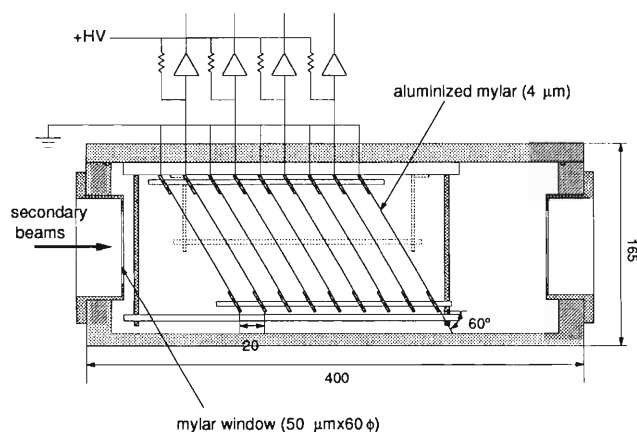


Fig. 1. High-rate multiple sampling ionization chamber (HR-MUSIC).

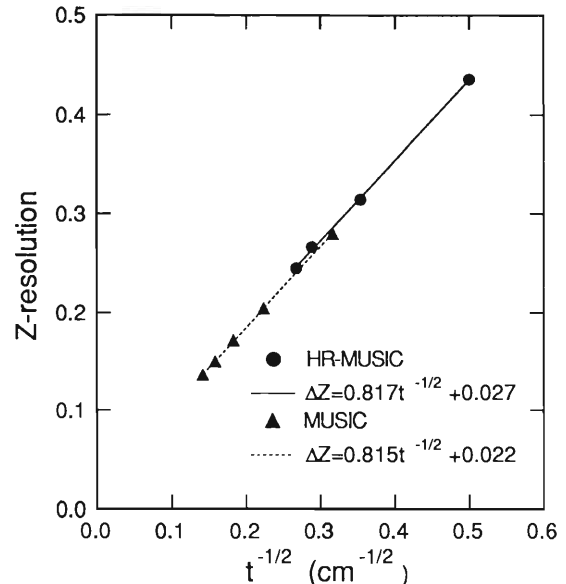


Fig. 2.  $Z$ -resolutions of MUSIC and HR-MUSIC as a function of gas thickness  $t$  in cm.

whose total length is 50 cm. From the energy loss spectra for  $A/Z = 2$  particles, we obtained  $Z$ -resolutions, defined as twice the FWHM of a  $Z$ -peak divided by the difference of peak channels for  $Z + 1$  and  $Z - 1$ . Figure 2 shows the  $Z$ -resolutions of the two MUSICS for  $Z = 14$  as a function of  $t^{-1/2}$ , where  $t$  is gas thickness in cm. They were obtained by plotting the energy loss spectra for the average of various numbers of the multiple anode signals.  $Z$ -resolutions of the two MUSICS fall on a straight line. This dependence indicates that the resolutions are almost entirely determined by the straggling of the energy loss. Contributions from other effects like electronic noise are represented by the offset of the straight line, about 0.02.

As for the rate dependence of  $Z$ -resolutions, we have investigated it under various fragment intensities from 0.4 kcps to 60 kcps and no significant dependence was found. In order to obtain higher rate capabilities of the HR-MUSIC, we have further tested it under higher intensities using a primary  $^{40}\text{Ar}$  beam. It was found that the resolution remains constant up to about 100 kcps and it deteriorates gradually above that. A pileup of the anode pulses appears to be mostly responsible for this effect and not the intrinsic detector performance.

## Calibration of Heavy Ion Telescope on Board MDS-1 Satellite with $^{40}\text{Ar}$ Beam

H. Matsumoto, H. Koshiishi, T. Goka, H. Katoh, and H. Miyasaka

The satellite MDS-1 will be launched into geostationary transfer orbit in 2001 from Tanegashima space center. A heavy ion Telescope (HIT) will be on board this satellite to observe galactic cosmic rays. The geometric factor of the HIT is  $\sim 25 \text{ cm}^2 \cdot \text{sr}$  and the observable energy range is, *e.g.*, 11–83 MeV/nucleon for oxygen.

An  $^{40}\text{Ar}$  beam with an energy of 95 MeV/nucleon was irradiated to examine the particle identification ability of the HIT. The irradiation test was carried out at the E3 of the ring cyclotron of the Institute of Physical and Chemical Research. The energy resolution was tested at four different energies by placing Al moderators of different thickness before in front of the HIT. In the charge discrimination test the secondary particles produced by the nuclear reaction of the  $^{40}\text{Ar}$  beam with acrylic were measured.

Figure 1 shows the test configuration with a cross-

sectional view of the telescope. The HIT consists of two position sensitive detectors (PDS) and sixteen PIN type detectors. The PSD1 has a 62 mm  $\times$  62 mm effective area with a 0.2 mm thickness, PSD2 has a 62 mm  $\times$  62 mm effective area with a 0.4 mm thickness and the PIN type detectors have an 85 mm-diameter circular effective area and a 0.42 mm thickness. The telescope is optically shielded by 0.7 mm-thick aluminum foil.

As a result of the energy resolution test, the peak loss energy of each detector comes within 5% of the theoretical value, and the full-width at half maximum is also about 5%.

In the charge discrimination test, nuclear fragmentation from helium to oxygen were measured. Figure 2 shows the histograms of atomic number resolution obtained by the  $\Delta E$ -E method. This result indicates that the isotope discrimination ability of the HIT is about 0.5 amu (FWHM).

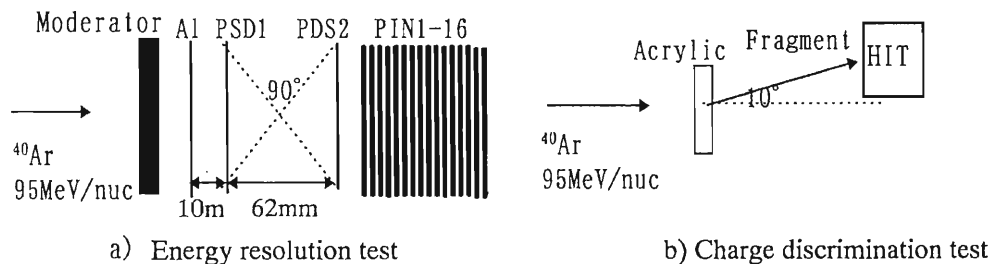


Fig. 1. Cross-sectional view of the telescope and the beam arrangement.

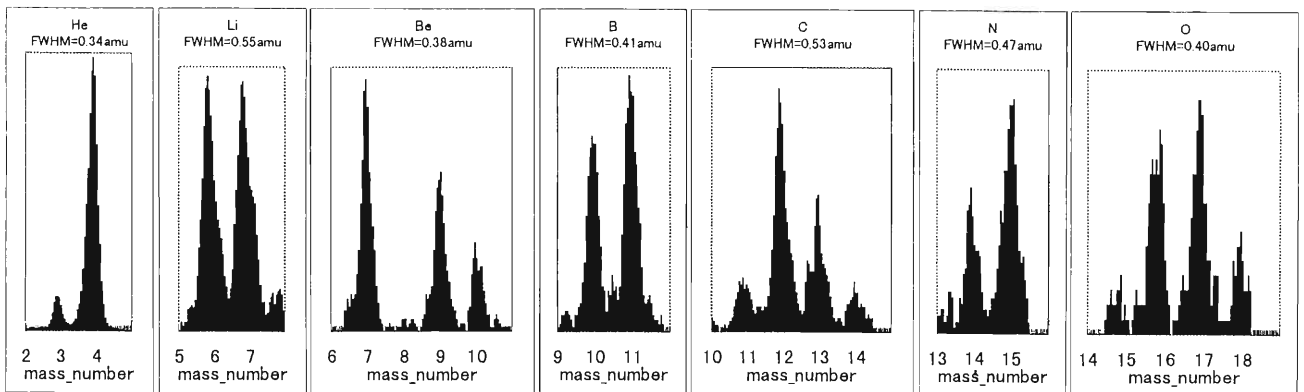


Fig. 2. The atomic number histograms.

## Beam Calibration of Fiber Neutron Monitor onboard the Exposed Facility of the Japanese Experimental Module

K. Koga, T. Goka, H. Matsumoto, H. Kato, H. Miyasaka, and Y. Muraki\*

A new type of neutron detector, the FIB (FIBer neutron monitor), is under development at NASDA (National Space Development Agency of Japan). The FIB uses scintillation fibers and multianode PMTs (photomultiplier tubes). It measures the high-energy neutrons, such as those of solar origin and albedo neutrons, in the energy range from 15 MeV to 100 MeV. The main applications of this detector are to inform the cosmonauts of the arrival of strongly charged particle radiation, and to elucidate the ion acceleration mechanism at the solar surface. This detector will be launched in the JEM (Japanese Experimental Module) exposed facility of the ISS (International Space Station) in the year 2003.

A high-energy neutron undergoes elastic collision with a hydrogen atom in the scintillator and produces a recoil proton. Since the produced recoil proton penetrates two or more scintillators, the energy of an incident neutron can be determined by measuring the path length and the trajectory of the recoil proton using 512 ch outputs of the scintillators which are placed in the two orthogonal directions, X and Y, if only the incident direction of a neutron, e.g., a neutron of solar origin, is known. The light emitted by the scintillator is transported by 15–20 cm-long optical fibers to the PMT. Hamamatsu H4140–20 photomultiplier tubes are used as the multianode (256 ch) photomultiplier tubes in the X and Y directions. The signals from the two PMTs are sent to the electronic equipment, which consists of a charge amplifier, an analog memory and a data-processing board. The circuit was designed using CMOS circuits by the KEK (High Energy Accelerator Research Organization) advanced technology group. Figure 1 shows the structure of the FIB. Figure 2 shows a picture of the FIB sensor.

The EM (engineering model) of this FIB was investigated using an accelerated beam. The EM is devoid of the problems of crosstalk and anticoincidence experienced by the BBM (bread board model). The hydrogen molecular ion beam bombards the sensor after passing through aluminum plates of different thicknesses. Figure 3 shows the irradiation test conditions.

Beam Energy: 120 MeV ( $H_2^+$ )

Beam Intensity:  $1 \times 10^3$ – $1 \times 10^6$  p/sec.

Moderator: 0, 5, 10, 15, 20, 30, 60 mm (Aluminum)

We used aluminum plates (0–60 mm thickness) as both the moderator and the target to obtain a mixed source of protons and neutrons of different energies. The following issues were investigated in this test:

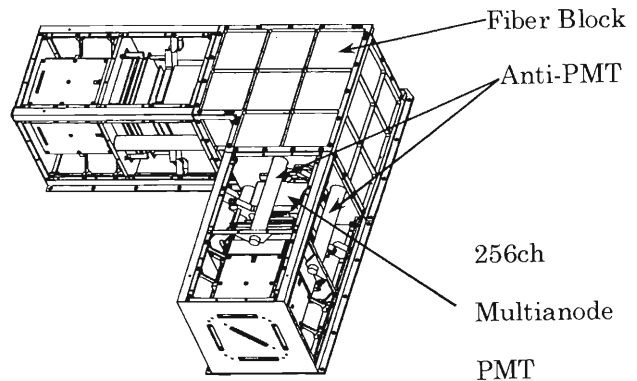


Fig. 1. Structure of the FIB.

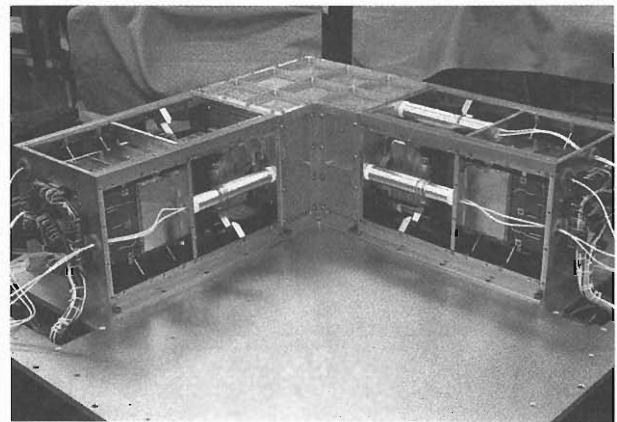


Fig. 2. Picture of the FIB sensor.

- (1) Energy calibration
- (2) Crosstalk between fibers
- (3) Discrimination of neutrons from protons
- (4) Performance of anticoincidence

Figure 4 shows actually obtained typical tracks in the sensor. From these tracks, we can distinguish between neutrons and protons. The track of the proton started from the first layer of the fiber and advanced in the incidence direction. The track of the proton that was recoiled from the neutron started from the optional layer and proceeded at an angle from the incidence direction. The crosstalk between fibers decreased further in the EM than in the BBM. In the case of the BBM, the track was spread out more than three pixels around the exact track. The main modifications to the EM to reduce crosstalk were the shading of each fiber using an aluminum evaporation film, the end-face processing of fibers for use as the reflector and the integrated shaping of the light-guide.

\* Solar-Terrestrial Environment Laboratory, Nagoya University

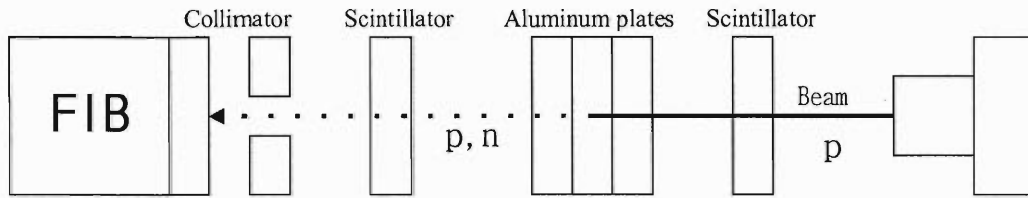


Fig. 3. Irradiation test conditions.

Table 1 shows the energy resolution for protons from the anode and the dynode-sum of a 256 ch PMT. For protons with the energy of 96.84 MeV, the energy resolution is 63% from the anode output and 30% from the dynode-sum output. The realization of an energy resolution in the range better than that for the anode or dynode-sum is under investigation. The performance of anticoincidence is confirmed. The rate of unexpected defeat of protons is from 0.004 to 0.02%.

From irradiation tests of the EM, the performance of the FIB is confirmed. However, there remains some

Table 1. Energy resolution.

The incident energy (MeV)	Energy resolution from output of anode. (FWHM:MeV)	Energy resolution from output of dynode-sum (FWHM:MeV)
33.69	15.82	9.48
48.80	17.16	9.98
60.86	17.95	8.65
71.29	14.80	9.52
80.68	14.69	8.78
96.84	22.68	18.64

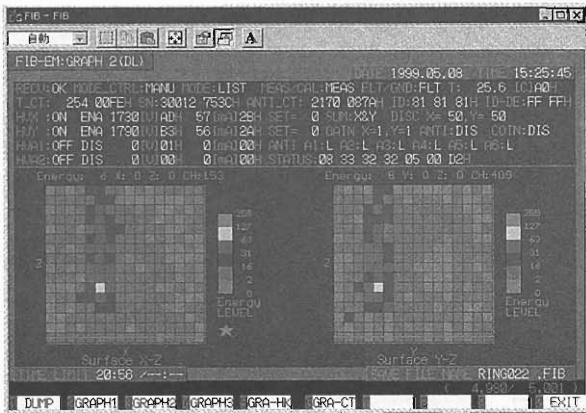


Fig. 4. Actually obtained typical tracks in the sensor.

crosstalk which is caused by the joint between the fibers and the PMT. This problem should be solved before construction of the FM (flight model). Except for this problem, it was almost possible to complete the design of the FM. Manufacture of the FM of the FIB will be started in 2000 and it will be launched in 2003.

#### References

- 1) I. Imaida et al.: Nucl. Instrum. Methods Phys. Res. A **421**, 99 (1999).

## RF Ion-Guide System for Trapping Energetic Radioactive Nuclear Ions from Fragment Separators

M. Wada, I. Katayama, S. Okada, K. Okada, K. Noda,\*<sup>1</sup> H. Kawakami,\*<sup>2</sup> and S. Ohtani

The projectile fragment separator provides a wide variety of radioactive nuclear ions without any restrictions on chemical property or lifetime limit of the ions, which are unavoidable problems in the ordinary ion-source-based ISOL (isotope separator on-line) facilities. The beam energy and quality in terms of the longitudinal and transverse emittance is, however, not adequate for low-energy beam experiments, in particular for trapping experiments.

We have proposed a new scheme to provide low-energy high-quality beams from such fragment separators.<sup>1,2)</sup> The system is comprised of a primary degrader, a large He gas cell and a beam guide. The degrader reduces the beam energy to about 5 MeV/u. If the primary energy of a beam is 100 MeV/u, more than 50% is in the energy range of 0 to 5 MeV/u after passing through a degrader foil of suitable thickness. The medium energy beam thus obtained is then injected into the He gas cell. In order to stop the 5 MeV/u beams, the cell is required to be 2 m in thickness with 0.2 atm of He. The thermalized ions should be extracted from the exit of the cell and then guided to a high vacuum region by the RF sextupole ion beam guide (SPIG) through multiple skimmers.<sup>3,4)</sup>

The main part of the system is the He gas cell. The system is based on the same principle as that of the ion guide ISOL (IGISOL), but a significant difference is in the cell size. In the ordinary IGISOL, a typical cell

size is 1 cm which corresponds to a stopping capability of 10 keV/u. This limits the effective thickness of the target and the corresponding yield. The reason a small cell size is used in the IGISOL is that the transport of the ions in the cell is performed only by the gas flow. If a large cell were used in the ordinary IGISOL, it would take many minutes to extract ions which would cause severe loss of ions due not only to the lifetime limit but also to other processes such as neutralization and diffusion. In the proposed system, on the other hand, ions in the cell are totally under the control of an electric field. Many ring electrodes are placed in the cell, which produces a superposition of a DC field and an RF field (RF ion guide). The DC field gives the ions a relatively high velocity in order to quickly exit the cell and the RF field focuses the ion beam to the small exit hole. This allows the use of a large-size gas cell and a small exit hole.

Numerical simulations were performed for the RF ion-guide system. A single ion motion in the electric field was traced by the Runge-Kutta integration method. The effect of gas collision was taken into account by the Monte Carlo method. The kinematics of each collision was simulated in two different ways. In the simpler one, isotropic scattering at the center of the mass system was assumed and the mean

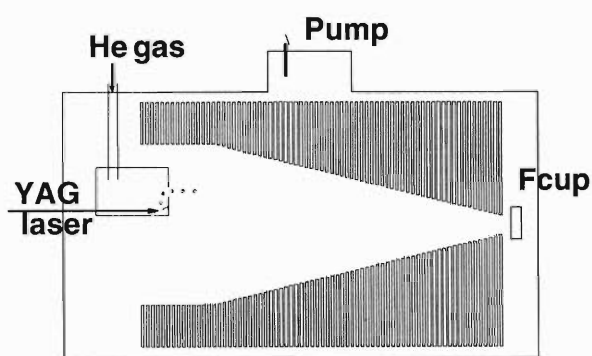


Fig. 1. Schematic diagram of an off-line test. A part of the gas cell which contains 80 ring electrodes with an interval of 2.5 mm is used for the test. RF and DC potentials are applied to the ring electrode. Metallic ions are produced by irradiation of a pulsed YAG laser in a small gas cell. Ions from the small cell are guided by the RF ion guide to a Faraday cup.

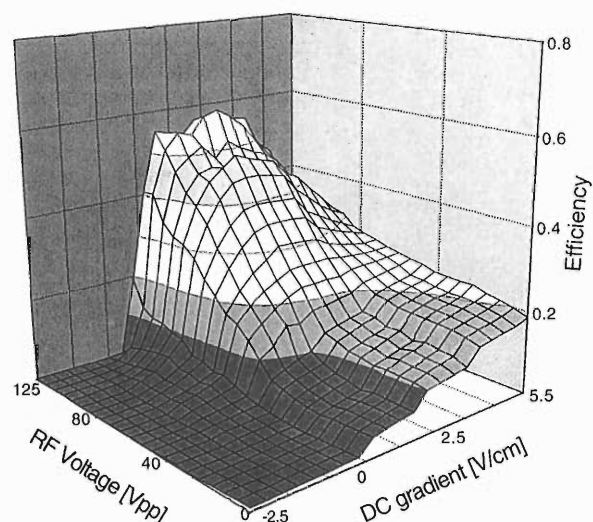


Fig. 2. Preliminary results of an off-line test. Ion current detected at the Faraday cup is plotted as a function of RF voltage and DC electric field of the RF ion guide. Total current was measured at the exit of the small cell for normalization. He pressure of 20 Torr and maximum voltage of 125 Vpp were limited by a discharge problem at the feed through of the present setup.

\*<sup>1</sup> National Institute for Radiological Science

\*<sup>2</sup> Institute of Particle and Nuclear Studies, High Energy Accelerator Research Organization

free path was chosen to emulate the experimental result of the ion mobility in He gas ( $\sim 20 \text{ cm}^2/\text{Vs}$  at 760 Torr). In the more complex one, a classical scattering model in a semi-empirical potential, which was determined by Mason and Schamp from their mobility measurements,<sup>5)</sup> was used. The estimation of the simulation results is under progress.

A test bench for the RF ion-guide system with a gas cell of 60 cm in length has been constructed at KEK-Tanashi. The gas throughput is designed to be 2 Torr l/s which allows the use of turbomolecular pumps and highly pure He gas. The entire cell is capable of baking and a gas purification system (SAES Monotorr) is used to prevent possible losses due to charge exchange with impurities. Off-line tests are under progress using a pulsed ion source. In the present test, pulsed metallic ions were produced in the gas cell by irradiation of a

YAG laser and the transported ions were detected by a Faraday cup which is, for the moment, still located inside the cell. A schematic diagram of the test setup is shown in Fig. 1 and preliminary results are shown in Fig. 2.

On-line test experiments are scheduled to be performed at the RIKEN RIPS facility aiming at the laser spectroscopy experiment of trapped Be isotopes.

#### References

- 1) M. Wada et al.: Int. Workshop on Ion Guide Isotope Separator On-Line (IGISOL-6), Dubna, 1997, unpublished.
- 2) I. Katayama et al.: *Hyperfine Interact.* **115**, 165 (1998).
- 3) H. Xu et al.: *Nucl. Instrum. Methods Phys. Res. A* **333**, 274 (1993).
- 4) S. Fujitaka et al.: *Nucl. Instrum. Methods Phys. Res. B* **126**, 386 (1997).
- 5) E. A. Mason et al.: *Phys. Rev.* **112**, 445 (1958).

## Development of a Polarized Solid Proton Target by Means of the Integrated Solid Effect (ISE)

M. Hatano, H. Sakai, A. Tamii, T. Uesaka, and T. Wakui

We have recently begun developing a polarized proton target system using a single crystal of naphthalene doped with pentacene as the target. The protons in the crystal are polarized by means of the integrated solid effect (ISE).<sup>1-5)</sup> The most significant advantage of this method is its applicability at a high temperature ( $\geq 77$  K) and in a low magnetic field ( $\leq 3$  kG).

The target is appropriate for investigating the structure of unstable nuclei via the inverse kinematics method. In such investigations, it is crucial to be able to detect low momentum recoil protons to achieve high angular and energy resolutions. The polarized proton target is also useful in other experiments, for example, measurement of  $\vec{d} + \vec{p}$  polarization correlation.

The protons are polarized by repeating the following processes (Fig. 1).

- (a) Pentacene molecules are excited to one of higher singlet states by a pulsed laser beam.
- (b) About 2% of the pentacene molecules de-excite to the lowest triplet state ( $T_0$ ), and have large electron population differences among the three Zeeman sub-levels. This indicates that electrons are polarized.
- (c) The polarization of the electrons in the  $T_0$  state is transferred to the protons by irradiation of a microwave and sweeping of the magnetic field (ISE).
- (d) The pentacene molecules de-excite to the ground state ( $S_0$ ).
- (e) The proton polarization is transferred to the neighboring protons by the spin-spin interaction.

In process (b), the population differences among the three Zeeman sublevels are governed by a selection rule in the transition from singlet excited states to the

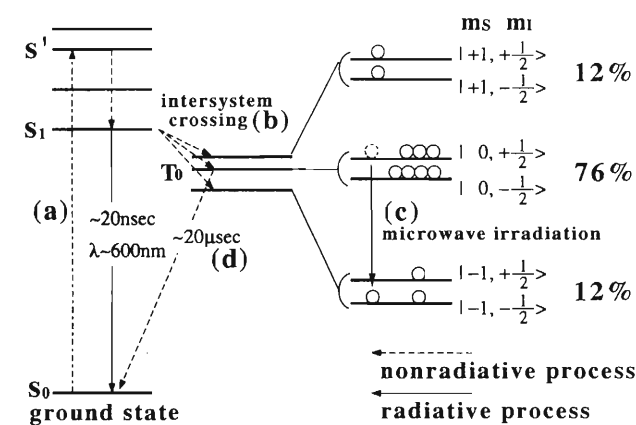


Fig. 1. Energy levels of pentacene.<sup>5)</sup>

triplet state, and therefore have little temperature dependence.

The ISE method, in process (c), is a kind of dynamic nuclear polarization (DNP)<sup>1)</sup> method. In a low magnetic field, the electron spin resonance (ESR) line of the electrons in the  $T_0$  state consists of many narrow and independent ESR lines of spin packets.<sup>1,5)</sup> By the classical DNP method, in which a static magnetic field is applied, the polarization transfer is inefficient in a low magnetic field due to the destructive contribution from many spin packets. However, in the ISE method, the external magnetic field is swept through the ESR line. The polarization is transferred via the following sequence for each spin packet:

$$|0, +\frac{1}{2}\rangle \rightarrow |-1, -\frac{1}{2}\rangle \quad (1)$$

$$|0, +\frac{1}{2}\rangle \rightleftharpoons |-1, +\frac{1}{2}\rangle, \quad |0, -\frac{1}{2}\rangle \rightleftharpoons |-1, -\frac{1}{2}\rangle \quad (2)$$

$$|-1, +\frac{1}{2}\rangle \rightarrow |0, -\frac{1}{2}\rangle. \quad (3)$$

After the magnetic field is swept, the polarizations of electron spin packets are constructively transferred to the protons, even in a low magnetic field.

In process (d), the molecules de-excite to the  $S_0$  state with a lifetime of  $20 \mu\text{sec}$ , which is much shorter than the relaxation time of the electron polarization. Since the  $S_0$  state is diamagnetic, the proton polarization is maintained for a long time, even at a temperature higher than 77 K.

In the actual experiment, we use an  $\text{Ar}^+$  laser beam with a wavelength of 514 nm, which is chopped by an optical chopper with a duty factor of  $1.0 \times 10^{-2}$ . We use an NMR system to measure the proton polarization. A C-type magnet, which achieves a homogeneity of  $10^{-3}$  in a  $3 \times 3 \times 3 \text{ cm}^3$  volume, will be available soon for practical use. A cavity for 9.3 GHz will be ready for mounting in the magnet in a few months. We are now preparing for the manufacturing of single-crystal samples.

### References

- 1) A. Henstra et al.: Ph. D. thesis, Leiden University (1964).
- 2) A. Henstra et al.: Chem. Phys. Lett. **165**, 6 (1990).
- 3) A. Henstra et al.: Phys. Lett. A **134**, 134 (1988).
- 4) D. J. van den Heuvel: Master's thesis, Leiden University (1991) (unpublished).
- 5) M. Iinuma: Ph. D. thesis, Kyoto University (1997).

## 6. Material Analysis



# Development of a Highly Sensitive High-Resolution In-Air Particle-Induced X-Ray Emission (PIXE) System: I

K. Maeda, K. Hasegawa,\* and H. Hamanaka\*

A crystal spectrometer combined with a position-sensitive X-ray detector is demonstrated to be suitable for measuring particle-induced X-ray emission (PIXE) spectra with high energy resolution. Recently, we developed a compact crystal spectrometer system equipped with a position-sensitive proportional counter (PSPC) for a high-resolution PIXE study in air at atmospheric pressure.<sup>1)</sup> The utility of the system for in situ chemical state analysis was demonstrated by measuring the  $K\alpha$  and  $K\beta$  spectra of third period elements.<sup>2,3)</sup> The chemical state analysis was applicable to minor elements down to the order of 0.1%. The system requires a small sample amount (0.1–1 mg), a small target area (1–10 mm<sup>2</sup>) and a short measuring time (<1 h) to obtain a spectrum using a moderate beam current (10–100 nA).

A very low beam current is required for delicate samples. If we intend to use the system for the mapping of chemical states, the measuring time required must be significantly reduced. Therefore, we constructed a prototype of a highly sensitive crystal spectrometer system using a newly developed large-window PSPC<sup>4)</sup> in order to increase the efficiency of X-ray detection by one order of magnitude.

The experimental setup is almost the same as that described in previous papers<sup>1–3)</sup> except for the PSPC. The large-window PSPC used here is a laboratory built, resistance anode type (see Fig. 1 (a)). It employs seven carbon fibers of 7  $\mu\text{m}$  diameter as anodes.

The sensitive area is 44 mm in width and 52 mm in total height. The number of effective analyzing channels is  $310 \times 7$ .

The block diagram of a signal processor for the seven-anode PSPC is shown in Fig. 1 (b). The seven anodes operate independently as a single PSPC. Both ends of each anode wire are connected to charge-sensitive amplifiers (preamplifiers), A and B. After passing through mixing amplifiers with seven inputs, MIX AMP A and B, pulses from the seven anodes are converted into digital signals using a  $512 \times 7$  ch charge-division analyzer and then stored on a computer. A  $512 \times 7$  ch histogram memory is used for 2D measurements. The 7 ch memory address lines correspond to the seven anodes. A set of two output pulses, A and B, of MIX AMP A and B gives information on the absorbed X-ray position. The selection of one of seven lines is carried out with a combination of an ADDER and a 7 ch DISCRIMINATOR. X-rays with undesirable energies are eliminated by the DISCRIMINATOR. We can simultaneously obtain seven spectra.

As an example of test experiments of rapid measurements, phosphorous  $K\alpha$  spectra (2.0 keV) obtained from BP powders are shown in Fig. 2 (a). A proton beam of 2.1 MeV was used for excitation. The proton beam current was 30 nA and the measuring time was 1s. A Ge(111) crystal was used as an analyzing crystal. The conversion of the seven measured spectra into one spectrum was carried out by software. Each

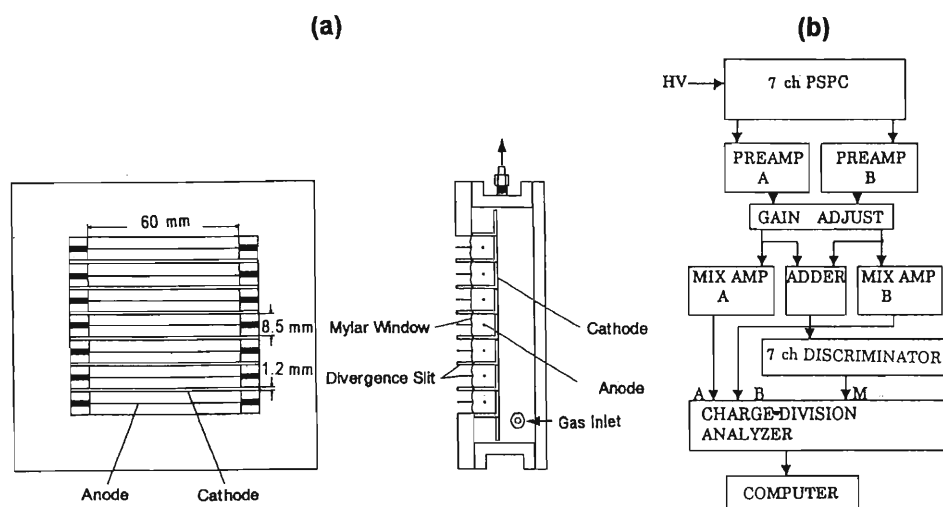


Fig. 1. (a) Schematic illustration of the seven-anode PSPC. (b) Block diagram of the signal processor.

\* College of Engineering, Hosei University

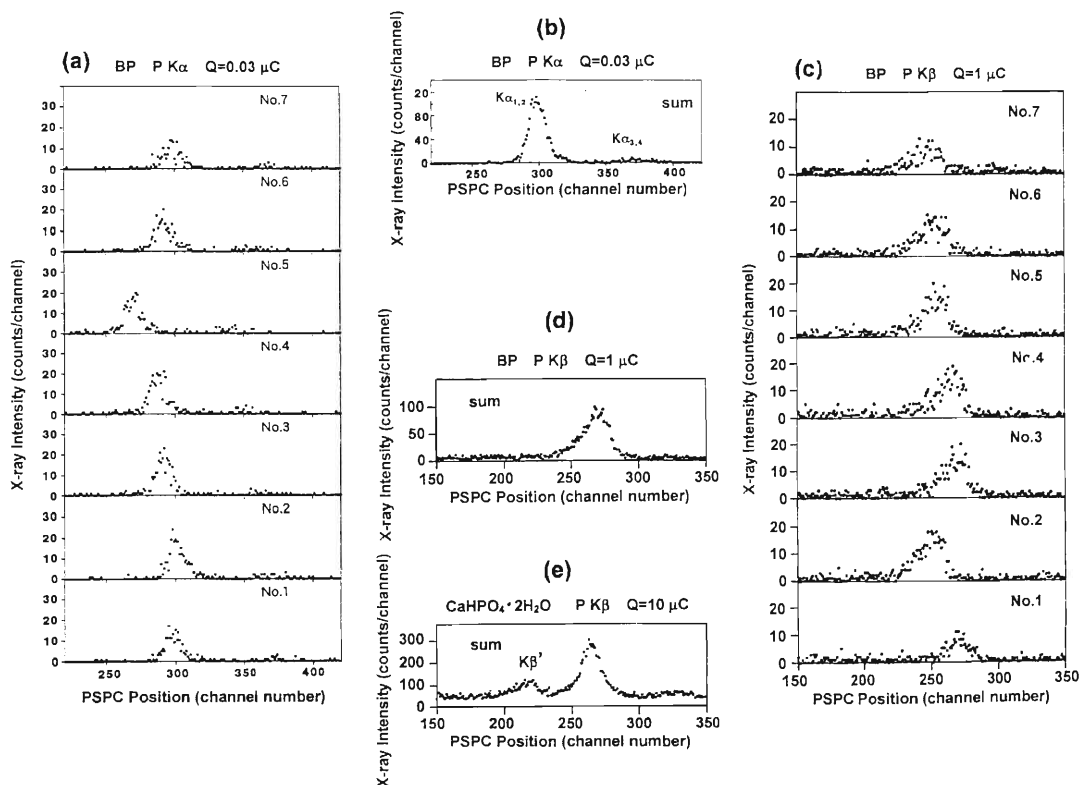


Fig. 2. (a) 7 ch spectra of the P  $K\alpha$  from BP; (b) summed spectra of the P  $K\alpha$  from BP; (c) 7 ch spectra of the P  $K\beta$  from BP; (d) summed spectra of the P  $K\beta$  from BP; (e) summed spectra of the P  $K\beta$  from  $\text{CaHPO}_4 \cdot 2\text{H}_2\text{O}$ . Q is the accumulated projectile charge.

spectrum has its own offset channel and channel-to-position conversion factor. Figure 2 (b) is the sum of spectra No.1–No.7 after correction of the offset and conversion factors. Here, the correction factors were obtained by measuring the peak channel of P  $K\alpha_{1,2}$  at different positions of the PSPC mounted on a sliding stage for a sufficiently long measuring time.

In order to examine the energy resolution of the seven-anode PSPC spectrometer, the full-width at half maximums (FWHMs) of the P  $K\alpha_{1,2}$  lines were measured by a 140 s measurement under the same condition. Line broadening due to aberration of the X-ray flux was observed on the highest (No.7) and lowest (No.1) anodes. However, the effect of line broadening on the summed spectrum is not large: The FWHM of  $K\alpha_{1,2}$  in the summed spectrum (2.8 eV) is 0.4 eV larger than that of the previous single-anode PSPC spectrometer.

Although the  $K\beta$  spectra reflect the chemical bonding nature more prominently than the  $K\alpha$  spectra, the production cross sections of  $K\beta$  X-rays are one or two orders of magnitude smaller than those of  $K\alpha$  X-rays. The seven-anode PSPC spectrometer was applied to measure the P  $K\beta$  spectra (2.1 keV) of BP. Figure 2 (c) is a 7 ch spectra obtained with a 30 s measuring

time. The shape of each spectrum is not clear. However, the asymmetric feature of the P  $K\beta$  of BP<sup>2)</sup> is well reproduced in the summed spectra shown in Fig. 2 (d). The  $K\beta$  spectrum of P in  $\text{CaHPO}_4 \cdot 2\text{H}_2\text{O}$  is also shown in Fig. 2 (e). The low-energy satellite peak  $K\beta'$ , which is evidence of P-O bonding, is clearly observed. The peak-to-background ratio is somewhat poorer than that obtained by the previous spectrometer.<sup>2)</sup>

The high sensitivity of the crystal spectrometer combined with a large-window multianode PSPC was demonstrated. Further improvements of energy resolution and suppression of background noise are required as the next step.

#### References

- 1) K. Maeda, K. Hasegawa, H. Hamanaka, and K. Ogiwara: Nucl. Instrum. Methods Phys. Res. B **134**, 418 (1998).
- 2) K. Maeda, K. Hasegawa, H. Hamanaka, and M. Maeda: Nucl. Instrum. Methods Phys. Res. B **136/138**, 994 (1998).
- 3) K. Maeda, A. Tonomura, H. Hamanaka, and K. Hasegawa: Nucl. Instrum. Methods Phys. Res. B **150**, 124 (1999).
- 4) K. Hasegawa, K. Maeda, S. Nakayama, A. Tonomura, and H. Hamanaka: Int. J. PIXE **8**, 47 (1998).

## PIXE Analysis of Lead in the Feather of a Jungle Crow Living in Tokyo

H. Yoshiki, K. Maeda, A. Tonomura, and H. Higuchi\*

Examination of bird feathers is considered to be valuable for monitoring the environmental pollution of the bird species' habitat.<sup>1)</sup> For evaluation of the pollutants, heavy metals, such as cadmium, lead, and mercury, absorbed by the feathers, are often analyzed by atomic absorption spectrometry. We demonstrated that particle-induced X-ray emission (PIXE) was useful for the analysis of heavy metals in feathers without any pre-treatment.<sup>2)</sup> This method enables the analysis of heavy metals in various parts of the feather. In this report, we describe the PIXE analysis of lead concentrations in different parts of the feather of a jungle crow living in Tokyo. Moreover, we discuss how lead is excreted from the body to the feather.

A feather of an adult jungle crow (*Corvus macrorhynchos*) was collected from Meguro-ku in Tokyo on October 4, 1997. The length of the vane in the feather was approximately 18 cm. The feather was cleansed with an ultrasonic cleaner in a commercial neutral detergent (Iuchi Seieido Co., Clean Ace S) for 1 hr, and then thoroughly washed with deionized water. The feather was bombarded in air with a 1.6-MeV proton beam of 3 mm diameter. X-rays emitted from the feather were detected using a Si(Li) solid-state detector through an 8- $\mu$ m-thick Be window (EG & G Co.). A graphite sheet with a 0.3-mm-diameter pinhole (graphite pinhole absorber) or 74- $\mu$ m-thick Al was used as an absorber to attenuate the X-rays in the low-energy region. The concentration of each trace element was estimated from the sulfur concentration determined by an ion gas chromatograph (Yokogawa Co. IC100), the peak area, and the ratio of the theoretical X-ray yield calculated by the computer program THICK in PIXAN.<sup>3)</sup>

Figure 1 illustrates the relationship between the concentration of the detected trace elements and the distance from the top of the feather. Measurements were carried out at points along the shaft of the feather: 2, 4, 6.5, 9, 11.5, and 15 cm from the top of the vane, and approximately 1 cm away from the shaft. The concentration of lead decreased towards the bottom of the vane. At 2 cm from the top, the lead concentration was 100 ppm, but at 15 cm from the top, it decreased to 9 ppm. A similar trend was observed for zinc which was also detected by the above method; however, the rate of decrease of zinc concentration was lower than that for lead, as shown in Fig. 1. On the other hand, different elemental distributions on the vane were observed for manganese and iron. The concentrations of

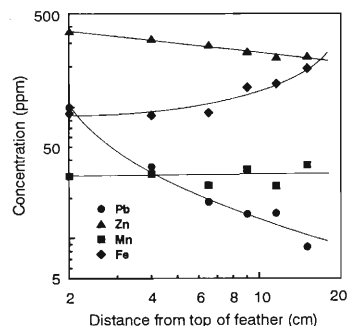


Fig. 1. Concentrations of lead, zinc, manganese, and iron in the feather of a jungle crow living in Tokyo detected by PIXE analysis.

manganese were almost constant throughout the vane. However, the concentrations of iron increased towards the bottom of the vane.

A similar result was obtained from the measurements along the barb. The concentration of lead was 44 ppm at the top of the barb and 19 ppm near the shaft. It is known that feather replacement occurs regularly with change of season. In this replacement, a new feather starts forming from the top of the vane and shaft in the first stage and then grows rapidly towards the bottom of the vane.<sup>4)</sup> Therefore, these results may indicate that lead, as a toxic substance taken into the body of jungle crows, is preferentially excreted into feathers in comparison with other trace elements.

In summary, a PIXE analysis has been carried out on different parts of the feather of a jungle crow living in Tokyo. At 2 cm from the top of the vane, 100 ppm of lead was detected. The amount of lead decreased towards the bottom of the vane. However, this tendency was not observed for either manganese or iron detected in the same vane. Therefore, lead appears to be preferentially excreted from the body to the feather during feather formation. We expect that the PIXE analysis of different parts of feathers will be useful to understand and clarify the process of elimination of heavy metals in birds.

### References

- 1) L. L. Getz, L. B. Best, and M. Prather: *Environ. Pollut.* **12**, 235 (1977).
- 2) H. Yoshiki, K. Maeda, A. Tonomura, T. Tsuruda, and H. Higuchi: *Proc. 4th Asian Symp. on AAWM*, p. 288 (1998).
- 3) E. Clayton: *PIXAN: The Lucas Heights PIXE Analysis Computer Package AAEC/M113* (1986).
- 4) F. B. Gill: in *Ornithology*, (W. H. Freeman and Company, New York, 1990), p. 65.

\* School of Agriculture and Life Sciences, University of Tokyo

## RBS Analysis of Na-Implanted Glassy Carbon

M. Iwaki and A. Nakao

Depth profiles of Na implanted in glassy carbon have been obtained and analyzed using Rutherford backscattering spectrometry (RBS).

Substrates used were glassy carbon (GC) sheets, GC-20 made by Tokai Carbon with a size of  $10 \times 10$  mm<sup>2</sup> and thickness of 1 mm. Before ion implantation, the surfaces were mechanically mirror-polished by using a buffing wheel with diamond slurry. Na ions were implanted at doses of  $1 \times 10^{16}$ ,  $5 \times 10^{16}$  and  $1 \times 10^{17}$  ions/cm<sup>2</sup> and an energy of 150 keV at room temperature. The beam current density was about  $0.5 \mu\text{A}/\text{cm}^2$  to prevent surface heating by the beam itself. RBS measurements were carried out with 1.5 MeV He ions and a fluence of  $10 \mu\text{C}$ , using a Tandem-type accelerator. A He-ion beam was irradiated in the direction normal to the specimen surface and the detector angle was 168 degrees.

Figure 1 shows the RBS spectra for Na-implanted GC at the doses of  $1 \times 10^{16}$ ,  $5 \times 10^{16}$ , and  $1 \times 10^{17}$  ions/cm<sup>2</sup>. Arrows of C, O and Na indicate the positions of C, O and Na atoms at the surface, respectively. The Na depth profiles are Gaussian at the doses of  $1 \times 10^{16}$  and  $5 \times 10^{16}$  ions/cm<sup>2</sup>. The atomic ratio of Na/C is 0.03 at the maximum Na concentration at the dose of  $1 \times 10^{16}$  ions/cm<sup>2</sup>. At the dose of  $1 \times 10^{17}$  ions/cm<sup>2</sup>, the concentration of Na atoms increased at the surface and it remained constant in the implanted layers. The profile is considered to reflect high Na concentrations, generation of high compression and consequent migration of Na atoms toward the surface. High concentrations of

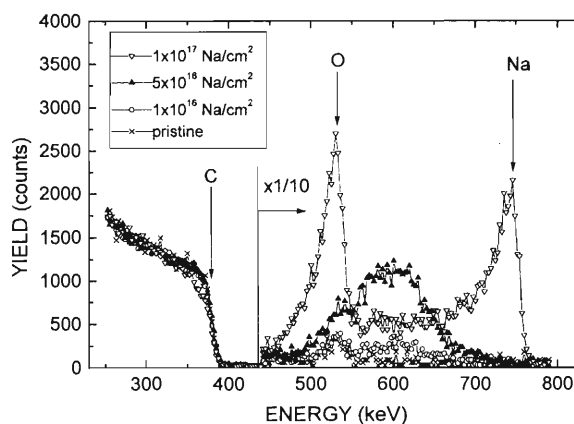


Fig. 1. RBS spectra of Na-implanted glassy carbon.

O-atoms can be seen at the surface. The appearance of O atoms seems to be due to surface migration and oxygenation of Na atoms during and/or after ion implantation. The atomic ratios of Na/C and O/C at the surface are 0.06 and 0.16, respectively. Such phenomena have been observed in the case of Li and K implantation in GC.

The depth at the peaks can be calculated from the energy loss from the surface, assuming the atomic density of implanted layers. However, it is difficult to determine the atomic density because the structure of implanted layers changes from glassy to amorphous; consequently the depth profile of Na could not be obtained.

# Heavy-Ion Irradiation Effects in Bi-2223 Tapes

H. Ikeda, N. Kuroda, A. Iwase, T. Kambara, and R. Yoshizaki\*

We have investigated the effect of columnar defects on the irreversibility line for the point-pin-enriched sample of Bi-2223 tapes.<sup>1)</sup> Since irradiation can introduce defects in a controlled manner, it can be used as a useful tool to probe the response of the a flux line system to the known defect structure. Whether or not columnar defects act cooperatively with point defects to pin vortices is not a trivial question.

Ag-Cu alloy sheathed tapes were prepared by the powder-in-tube method. Ag-Cu alloy sheaths in this study were filled with Cu-poor Bi-2223 powder, since copper atoms were expected to diffuse into the inner oxide core from the outer Ag-Cu alloy sheath. We introduced Hf elements into the Ag-Cu alloy sheathed Bi-2223 tapes. This resulted in the improvement of the transport  $J_c$ . The details of the preparation method and the fundamental properties of the samples have been reported elsewhere.<sup>2)</sup>

Bi-2223 tapes with  $3.0 \times 3.0 \times 0.1 \text{ mm}^3$  dimensions were irradiated with 3.5 GeV  $^{163}\text{Xe}^{31+}$  ions irradiation at the RIKEN ring cyclotron facility to introduce columnar defects perpendicular to the tape surface direction. The total pin density was estimated to be  $7.2 \times 10^{10} \text{ cm}^{-2}$ , which corresponded to a dose-equivalent matching field of  $B_\phi = 1.4 \pm 0.2 \text{ T}$ . This type of irradiation has produced continuous amorphous track with a diameter of  $\approx 6 \text{ nm}$  throughout the thickness of the Bi-2223 sample. We estimated sample qualities using X-ray diffraction measurements and transmission electron microscopy. We confirmed that the Hf atoms were substituted for 0.5–1% of Sr by high-resolution analytical electron microscopy (HRAEM).<sup>3)</sup> The magnetic properties were measured using a superconducting quantum interference device (SQUID) magnetometer. The magnetic field was applied perpendicular to the wide surface of the tape.

Figure 1 shows the magnetic field versus the irreversibility temperature ( $T_{irr}$ ), using by solid symbols for the irradiated Ag and Ag-Cu alloy sheathed Bi-2223 tapes with columnar defects and open symbols for the unirradiated tapes. We can observe that the irreversibility line curve for the irradiated Ag sheathed tapes is located on the higher temperature side of the unirradiated tape samples below 4 T and merges with the line curve for the unirradiated tape samples at a magnetic field of about triplicate of  $B_\phi$ . We found that the irreversibility line curve for the Ag-Cu alloy sheathed tapes was drastically shifted to higher temperatures in the measured magnetic field up to 5 T

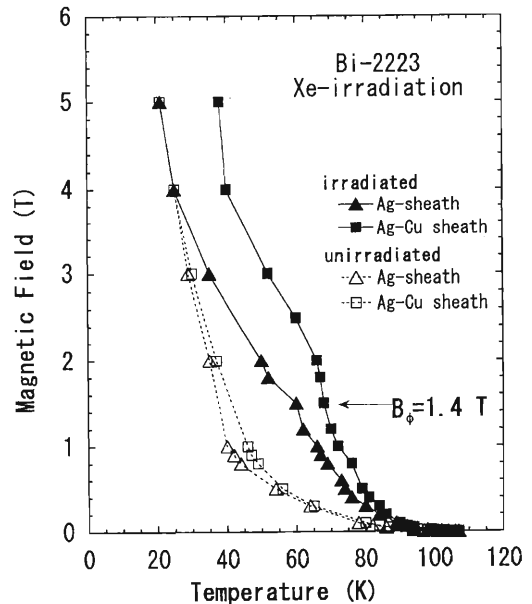


Fig. 1. The irreversibility temperatures are plotted in the H-T plane using by solid symbols for the irradiated Ag and Ag-Cu alloy sheathed Bi-2223 tapes with columnar defects and open symbols for the unirradiated tapes.

following Xe-ion irradiation. This behavior suggests that the pinning force of the irradiated Ag-Cu alloy sheathed tapes is larger than that of the Ag sheathed ones.

In fact, according to the results of the pinning force measurement, the field dependence of  $F_p$  of the Bi-2223 tape samples was improved by the Hf substitution for Sr due to the collective pinning.<sup>3)</sup> Therefore, it is expected that the columnar defects will function as effective pinning centers in cooperation with the point defects induced by Hf doping.

We observed the effect of the columnar defects in the Bi-2223 tapes. We found that the irreversibility curve of the irradiated Ag-Cu alloy sheathed tape sample is located on the higher temperature side of the irradiated Ag sheathed tape sample even in magnetic field higher than the triplicate of the matching field  $B_\phi$ .

## References

- 1) L. Civale et al.: Phys. Rev. Lett. **71**, 4124 (1993).
- 2) M. Ishizuka et al.: Physica C **252**, 239 (1995).
- 3) H. Ikeda et al.: in *Advances in Superconductivity IX*, edited by S. Nakajima and M. Murakami, (Springer-Verlag, Tokyo, 1997), p. 847.

\* Institute of Materials Science, University of Tsukuba

# A New Method for Determining the Vacancy Formation Energy of Metals Using the Positron Age-Momentum Correlation Technique<sup>†</sup>

N. Suzuki, Y. Nagai,\* and T. Hyodo

The positron lifetime spectra for materials containing mono-vacancies consist of two components. The shorter lifetime is the inverse of the sum of the positron annihilation rate in the bulk and the trapping rate into vacancies. Thus it is possible, in principle, to determine the vacancy formation energy from the temperature dependence of the shorter lifetime.

The analysis used to obtain the vacancy formation energy is, however, usually performed using the averaged lifetime, since it is difficult to obtain a reliable value for the short lifetime, which is usually shorter than the instrumental time resolution.<sup>1)</sup>

In this report we present a new method for separating the short-lifetime component using the positron age-momentum correlation (AMOC) technique.<sup>2)</sup>

This method characterizes the AMOC spectrum  $N(p, t)$  (number of counts vs. the momentum of the annihilating electron-positron pairs and the positron lifetime) in terms of the time-dependent line-shape parameter  $S(t)$ .<sup>2)</sup> When the positrons annihilate from two different states which have different  $S$  parameters,  $S(t)$  is written as,

$$S(t) = \frac{S_1 \cdot l_1(t) + S_2 \cdot l_2(t)}{L(t)}, \quad (1)$$

$$L(t) = l_1(t) + l_2(t) = \int N(p, t) dp, \quad (2)$$

where  $l_i(t)$  and  $S_i$  denote the lifetime spectrum and the time-independent specific  $S$  value for the  $i$ -th state, respectively. It then follows that

$$l_1(t) = \frac{S(t) - S_2}{S_1 - S_2} \cdot L(t) \propto (S(t) - S_2) \cdot L(t). \quad (3)$$

If the lifetime of the second component is appreciably longer than that of the first,  $S_2$  is determined by averaging  $S(t)$  in the time range where the second component is dominant. It is then possible to isolate the shorter lifetime component  $l_1(t)$ , apart from the normalization factor, solely from the AMOC data.

The reconstructed short-lifetime spectrum of Zn at 453 K is shown in Fig. 1. The lifetime  $\tau_1$  of this spectrum can be obtained by simply fitting these data to a single-component exponential decay function convoluted with the resolution function. The solid curve represents the result of the fit and reproduces the spectrum very well.

The values of  $\tau_1$  thus obtained are plotted against temperature in Fig. 2. The line represents the result of

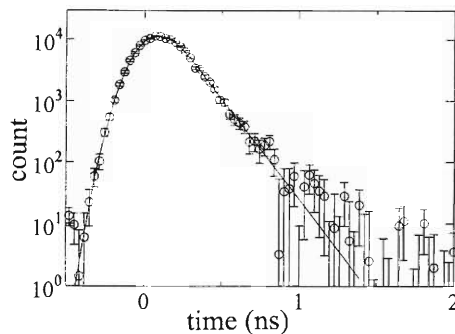


Fig. 1. Reconstructed positron lifetime spectrum for the shorter lifetime component for Zn at 453 K.

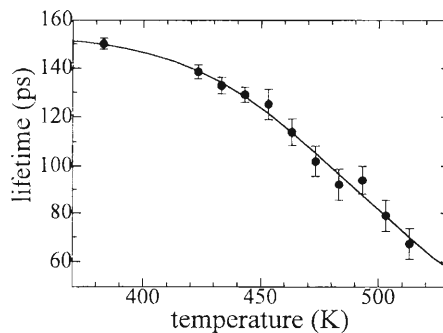


Fig. 2. The shorter lifetime values plotted against the temperature.

fitting using the two-state trapping model.<sup>1)</sup> The fit is satisfactory. The vacancy formation energy  $E_D$  for Zn determined from the fitted curve is  $0.50 \pm 0.06$  (eV). This value is in good agreement with the reported value.

Note that  $E_D$  was determined using only the data for the temperature range 383–513 K, considerably lower than the melting point of Zn (693 K). In the conventional determination of  $E_D$  by positron techniques, it is necessary to perform measurements at temperatures close to the melting point to estimate the parameters for fully trapped positrons.

Utilizing this advantage, we are now planning to determine the vacancy formation energy of alloys that undergo a structural phase transition, which prevent a consistent analysis of the data, at high temperatures.

## References

- 1) See for example, R. N. West: in *Positron in Solids*, edited by P. Hautojärvi, (Springer, Berlin, 1979), p. 89.
- 2) N. Suzuki, Y. Nagai, and T. Hyodo: *Radiat. Phys. Chem.* (to be published).

<sup>†</sup> Condensed from the article in *Phys. Rev. B* **60**, R9893 (1999)

\* Institute for Material Research, Tohoku University

## 7. Miscellaneous



## Neutrino Advanced Generation with Accelerated Muon

K. Nagamine

A neutrino ( $\nu_e, \bar{\nu}_e, \nu_\mu, \bar{\nu}_\mu, \nu_\tau, \bar{\nu}_\tau$ ), a massless elementary particle, if generated in the form of an intense and high-quality energetic beam, can be useful not only for particle-physics experiments such as neutrino oscillation studies, but also for probing the inside of gigantic objects such as the earth itself. Some proposals<sup>1)</sup> suggest using neutrinos to explore the nature of the earth. An intense neutrino beam is proposed to be generated using an intense and high-energy (multi-TeV) proton accelerator. However, because of the limited quality of the neutrino beam, the idea should be considered unrealistic, or at least very difficult to be realized.

Using high-energy proton accelerators which produce energetic pions ( $\pi^+, \pi^-$ ), one can expect two methods for neutrino generation: (1) A pion decay to a neutrino through  $\pi^+ \rightarrow \mu^+ + \nu_\mu$  or  $\pi^- \rightarrow \mu^- + \bar{\nu}_\mu$ , (2) A muon decay to neutrinos through  $\mu^+ \rightarrow e^+ + \nu_e + \bar{\nu}_\mu$  or  $\mu^- \rightarrow e^- + \bar{\nu}_e + \nu_\mu$ . Thus far, most of the accelerator-based neutrino experiments, including the inner-earth studies described above, are considered using an energetic neutrino beam obtained through the decay of energetic pions or muons based upon the decay-kinematics law. The quality of the neutrino beam can be considerably improved once the beam quality of the parent particle, pions or muons, can be improved.

Recently, the concept of ultra slow  $\mu^+$  was proposed<sup>2)</sup> and realized at KEK-MSL.<sup>3,4)</sup> In addition, the possibility of the use of this ultra slow  $\mu^+$  as the ion source for further acceleration towards  $\mu^+\mu^-$  colliders has been emphasized. There are two processes in the

realization of an ultra slow  $\mu^+$  source: (1) Thermal Mu ( $\mu^+e^-$ ) production in vacuum by stopping  $\mu^+$  at the rear side of the selected metallic material, such as hot tungsten, followed by  $\mu^+$  diffusion towards the surface as well as Mu evaporation from the surface of the foil, (2) Efficient muonium ionization using a method such as laser-resonant ionization via  $1s \rightarrow 2p \rightarrow$  unbound excitation utilizing intense pulsed lasers in combination with a pulsed muon beam.

Recently it has been noted that, in combination with the large-solid-angle MeV muon source, an intense ultra-slow  $\mu^+$  source with an intensity of  $10^{12} \mu^+/\text{s}$  and an emittance of better than  $10^{-7} \text{ rad}\cdot\text{m}$  can be generated in the setup shown in Fig. 1. In this setup a thick carbon target with a large-solid-angle pion collector will be installed at the external beam line of medium-energy, such as 1 GeV, protons followed by the pion decay section (super-super muon channel) coupled with the ultra slow  $\mu^+$  generator mentioned above. Preliminary optics design work for the 90-degree muon extraction from the proton beam has been done in strong collaboration with K. Ishida. By adopting a strong superconducting solenoid for pion collection and a reasonable length of a decay solenoid installed at the strongest existing pulsed proton beam line of the ISIS synchrotron at RAL (UK), one can obtain a source with an intensity of greater than  $10^{10} \mu^+/\text{s}$ . The momentum spread of the  $\mu^+$  obtained at the end of the decay solenoid is very large (nearly  $\pm 40\%$ ). However,

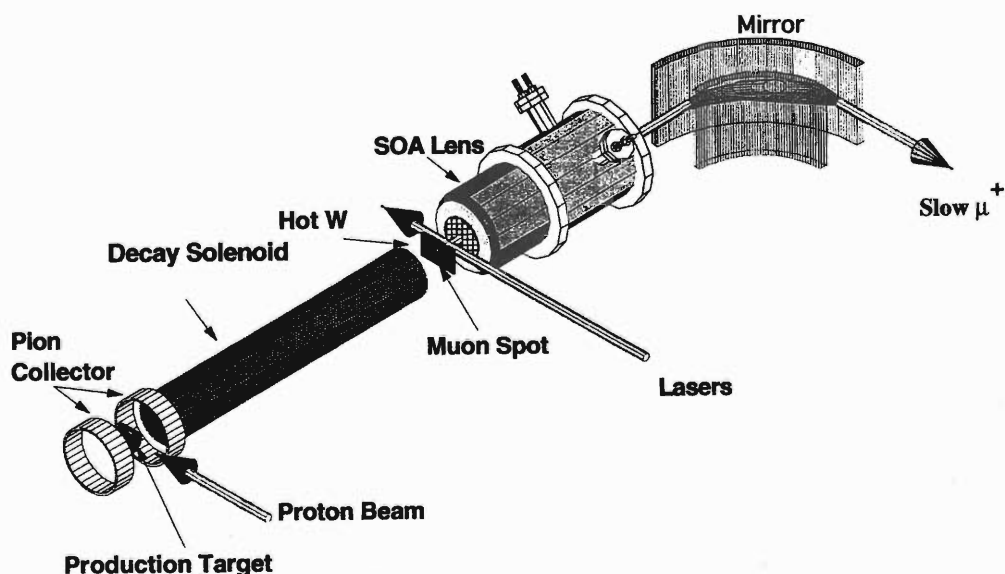


Fig. 1. Intense ultra slow  $\mu^+$  production employing high-intensity muon production via a large acceptance pion collection.

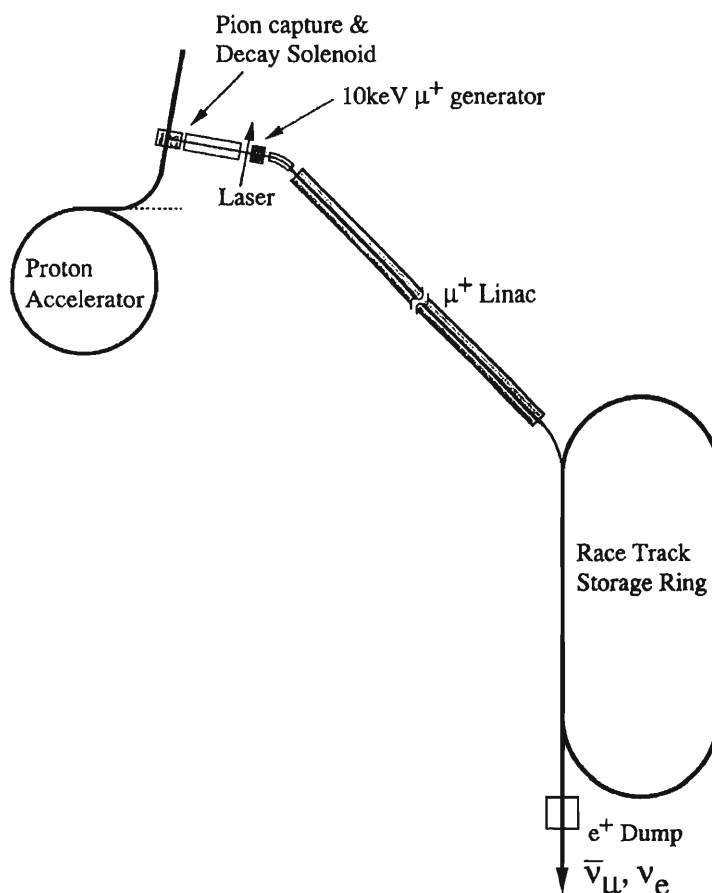


Fig. 2. Proposed scheme of the advanced generation of a neutrino beam based upon a decay of the muon accelerated from the ultra-slow  $\mu^+$  ion-source.

it becomes possible to stop generated  $\mu^+$  inside a multi layer of hot W, so that an intense ultra slow  $\mu^+$  beam can be generated by the method of laser-resonant ionization of thermal muonium emitted from the surface of hot W. Simulation calculations are in progress to confirm the characteristic features of the ultra slow  $\mu^+$  produced after optimization.

The high-intensity ultra slow  $\mu^+$  produced can be applied as an ion source for acceleration, by installing radio frequency quadropole (RFQ) and drift-tube linac (DTL) preaccelerators followed by, e.g., a super-conducting linac. One of the most important applications of the intense low-energy  $\mu^+$  source is as an advanced source of neutrinos ( $\bar{\nu}_\mu, \nu_e$ ) with accelerated  $\mu^+$ . By installing a relevant decay section for the accelerated  $\mu^+$ , intense and high-quality neutrinos would be produced via  $\mu^+ \rightarrow \bar{\nu}_\mu + \nu_e + e^+$ , employing the setup shown in Fig. 2.

The key factors in the realization of this advanced neutrino beam can be summarized as follows.

(1) Quality of the accelerated muons

One can expect a greater than  $10^{10}$   $\mu^+$  source with an extremely small phase space ( $0.2 \text{ eV} \times (\text{cm})^2$ ).

(2) Muon decay section

A race-track-type muon storage ring, as shown in

Fig. 2, is an attractive idea.

(3) Quality of the produced neutrino beam

Regarding the decay cone, the opening half-angle,  $\theta_\mu$ , becomes smaller at higher muon energy ( $E_\mu$ ), with the relationship of  $m_\mu/E_\mu$ .

Using the future intense pulsed proton source (with more than MW-order power) to be available also for a spallation neutron source, an intensity of  $10^{12}$   $\mu^+$ /s can be obtained. A rough estimate for other proton accelerators can be obtained by scaling to the proton beam power.

Helpful discussions with Drs. K. Ishida and Y. Miyake are acknowledged.

References

- 1) A. De Rújula, S. L. Glashow, R. R. Wilson, and G. Charpak: Phys. Rep. **6**, 341 (1983).
- 2) K. Nagamine and A. P. Mills, Jr.: Los Alamos Report LA10714-C, 21 (1986); K. Nagamine: At. Phys. **10**, 225 (1987).
- 3) K. Nagamine, Y. Miyake, K. Shimomura, P. Birrer, J. P. Marangos, M. Iwasaki, P. Strasser, and T. Kuga: Phys. Rev. Lett. **74**, 4811 (1995).
- 4) Y. Miyake, J. P. Marangos, K. Shimomura, P. Birrer, T. Kuga, and K. Nagamine: Nucl. Instrum. Methods Phys. Res. B **95**, 265 (1995).

# Light Hadron Spectrum in Quenched Lattice QCD

S. Kim\* and S. Ohta

Reproducing the known light hadron mass spectrum is the most important test that the numerical lattice quantum chromodynamics (QCD) has yet to pass, in spite of the steady progress<sup>1)</sup> since the pioneering works of Weingarten and Hamber and Parisi.<sup>2)</sup> The main obstacle is the difficulty in including light dynamical quarks, and consequently, the available full-QCD calculations still suffer from a too heavy quark mass, too coarse lattice spacing or too small lattice volume. However, with the quenched approximation in which one neglects dynamical quark loops, recent calculations have used sufficiently fine lattice spacing and sufficiently large lattice volume to allow understanding of the systematic errors arising from them. Indeed, recent quenched-approximation calculations have collectively revealed that both of these errors are smaller than the statistical noise, albeit with rather heavy quarks. Nevertheless these calculations leave three major problems unresolved: The nucleon to  $\rho$ -meson mass ratio is too high, the pion to  $\rho$ -meson mass ratio is too high, and extrapolation to realistically light quark mass values is necessary. Hence quenched-approximation calculations with realistically light quark mass values on a sufficiently large and sufficiently fine lattice such as the one we report here<sup>3)</sup> are desired.

We chose a gauge coupling of  $6/g^2 = 6.5$  and a lattice volume of  $48^3 \times 64$ . These parameters correspond to the lattice spacing of  $a = 0.0544(9)$  fm or the cutoff of  $a^{-1} = 3.63(6)$  GeV and a spatial volume of  $(2.59(5) \text{ fm})^3$ . We use a staggered quark because it is superior to the Wilson one for controlling the quark mass; the quark mass is well defined and protected by the remnant U(1) chiral symmetry in the former, while in the latter, one encounters the intractable problem of defining the critical hopping parameter under the inevitable presence of exceptional gauge configurations.<sup>4)</sup> For the gauge part, we use a single-plaquette Wilson action. This is because our lattice spacing is sufficiently fine and we do not require any help from action improvement to approach the continuum limit.

The main result is summarized in our Edinburgh plot (Fig. 1) where two mass ratios,  $m_N/m_\rho$  and  $m_\pi/m_\rho$ , are plotted against each other. For our lightest bare quark mass of  $m_q a = 0.00125$  (approximately 4.5 MeV), we obtain  $m_N/m_\rho = 1.230 \pm 0.035$  and  $m_\pi/m_\rho = 0.273 \pm 0.006$ . The former is in good agreement with the observed value, although the latter remains approximately 50% larger. The proximity of these results to the continuum limit is measured by the extent of breaking of the flavor symmetry in pion

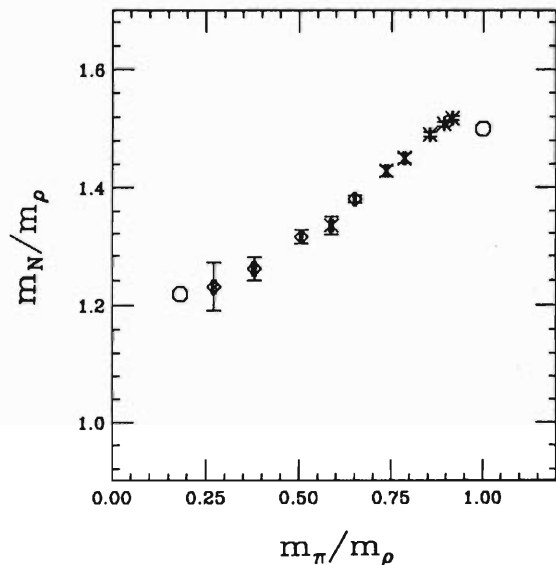


Fig. 1. The nucleon to  $\rho$  mass ratio vs pion to  $\rho$  mass ratio at  $6/g^2 = 6.5$  for  $m_q a = 0.05, 0.04, 0.03, 0.02, 0.015, 0.01, 0.0075, 0.005, 0.0025,$  and  $0.00125$ . The lower circle represents the experimental value and the upper circle represents the nonrelativistic limit.

and  $\rho$  meson channels ( $m_{\pi_2} a - m_\pi a$ ) and ( $m_{\rho_2} a - m_\rho a$ ). These breakings are expected to decrease as  $O(a^2)$ , as the lattice spacing  $a$  approaches the continuum limit value of 0. We can see that they are hidden below statistical errors for sufficiently light quark mass values: The symmetry is restored adequately. In other words, the lattice is sufficiently close to the continuum limit.

In conclusion, we achieved a realistic nucleon to  $\rho$ -meson mass ratio of  $m_N/m_\rho = 1.23 \pm 0.04$  (statistical)  $\pm 0.02$  (systematic) in our quenched lattice QCD numerical calculation with staggered quarks, without relying on any extrapolation. The systematic error is mostly due to the finite-volume effect, and the finite-spacing effect is negligible. The breaking of the flavor symmetry in the pion and  $\rho$  meson is no longer evident.

## References

- 1) See recent "Lattice" Conference Proceedings for the Current Status, e.g., Nucl. Phys. B (Proc. Suppl.) **63** (1998).
- 2) D. Weingarten: Phys. Lett. B **109**, 57 (1982); H. Hamber and G. Parisi: Phys. Rev. Lett. **47**, 1792 (1981).
- 3) S. Kim and S. Ohta: Phys. Rev. D, in press. (hep-lat/9912001) and references therein.
- 4) W. Bardeen et al.: Phys. Rev. D **57**, 1633 (1998); Nucl. Phys. B (Proc. Suppl.) **63**, 141 (1998).

\* Sejong University, Korea

# Monte Carlo Simulation of Supersymmetric Matrix Model

J. Nishimura and T. Hotta

Large  $N$  reduced models are the zero-volume limit of gauge theories. They have been developed for the study of gauge theories at the large  $N$  limit.<sup>1)</sup> Recently there has been a revival of interest in these models in the context of nonperturbative formulations of string theory.<sup>2,3)</sup> An important feature in this context is the presence of supersymmetry. The bosonic counterpart of the model is well understood,<sup>4)</sup> but the inclusion of fermions makes the system far more complicated. In our project, we study such a supersymmetric model numerically. The partition function of the model that we investigate is given by

$$\begin{aligned} Z &= \int dA e^{-S_b} \int d\psi d\psi^* e^{-S_f}, \\ S_b &= -\frac{1}{4g^2} \text{tr}[A_\mu, A_\nu]^2, \\ S_f &= -\frac{1}{g^2} \text{tr}\left(\psi_\alpha^* (\Gamma^\mu)_{\alpha\beta} [A_\mu, \psi_\beta]\right), \end{aligned} \quad (1)$$

where  $A_\mu$  ( $\mu = 1, \dots, 4$ ) are  $N \times N$  traceless Hermitian matrices and  $\psi_\alpha$  ( $\alpha = 1, 2$ ) are traceless  $N \times N$  complex matrices. This model is manifestly invariant under Lorentz transformation, where  $A_\mu$  transforms as a vector and  $\psi_\alpha$  transforms as a Weyl spinor.  $\Gamma^\mu$  are  $2 \times 2$  matrices acting on the spinor components:

$$\Gamma^1 = i\sigma_1, \quad \Gamma^2 = i\sigma_2, \quad \Gamma^3 = i\sigma_3, \quad \Gamma^4 = \Gamma^{\dots} \quad (2)$$

The model can be regarded as the four-dimensional counterpart of the IIB matrix model.<sup>3)</sup>

The integration over fermionic variables can be done explicitly and the result is given by  $\det \mathcal{M}$ ,  $\mathcal{M}$  being a  $2(N^2 - 1) \times 2(N^2 - 1)$  complex matrix. Hence the system we want to simulate can be written in terms of bosonic variables as

$$Z = \frac{1}{N^4} \int dA e^{-S_b} \det \mathcal{M}. \quad (3)$$

The determinant  $\det \mathcal{M}$  is known to be real positive. We therefore introduce a  $2(N^2 - 1) \times 2(N^2 - 1)$  Hermitian positive matrix  $D = \mathcal{M}^\dagger \mathcal{M}$ , so that  $\det \mathcal{M} = \sqrt{\det D}$ , and the effective action of the system takes the form

$$S_{eff} = S_b - \frac{1}{2} \ln \det D. \quad (4)$$

We apply the hybrid R algorithm<sup>5)</sup> to simulate this system. We use the exact result,

$$\langle \text{tr} F^2 \rangle = -\langle \text{tr}([A_\mu, A_\nu]^2) \rangle = 6g^2(N^2 - 1), \quad (5)$$

to check the code and the numerical accuracy.

We first study the space-time structure of the reduced model. In the IIB matrix model, the eigenvalues of the bosonic matrices  $A_\mu$  are interpreted as space-time coordinates.<sup>3,6)</sup> We measure the extent of the eigenvalue distribution and find that it scales as  $\sqrt{g}N^{1/4}$ , which is consistent with the branched-polymer picture based on one-loop expansion.<sup>6)</sup>

We then study the large  $N$  scaling of correlation functions of Wilson loop operators, which correspond to string creation operators in the IIB matrix model.<sup>7)</sup> This issue has been addressed in the two-dimensional Eguchi-Kawai model, where nontrivial large  $N$  scaling has been observed.<sup>8)</sup> We measured the correlation functions up to three-point functions, and found that they scale universally in the large  $N$  limit.

Finally, we also study whether the large  $N$  reduced model is equivalent to the ordinary gauge theory as presented by Eguchi-Kawai.<sup>1)</sup> For this purpose, it is convenient to consider a model without a traceless condition on  $A_\mu$ . Such a model has the  $U(1)^4$  symmetry  $A_\mu \rightarrow A_\mu + \alpha_\mu$ , which is spontaneously broken. Hence the equivalence to ordinary gauge theory is nontrivial, since this equivalence is guaranteed only if the symmetry is *not* broken. However, the breaking is much milder than in the bosonic case; the attractive potential among the eigenvalues of the  $A_\mu$ 's, which induces the spontaneous symmetry breaking, is suppressed by  $1/N$  due to supersymmetry.<sup>6)</sup> We found that in the supersymmetric case, the equivalence does hold in the intermediate scale but not throughout the entire scale, while in the bosonic case, the equivalence does not hold in any range of the scale.

## References

- 1) T. Eguchi and H. Kawai: Phys. Rev. Lett. **48**, 1063 (1982).
- 2) T. Banks, W. Fischler, S. H. Shenker, and L. Susskind: Phys. Rev. D **55**, 5112 (1997).
- 3) N. Ishibashi, H. Kawai, Y. Kitazawa, and A. Tsuchiya: Nucl. Phys. B **498**, 467 (1997).
- 4) T. Hotta, J. Nishimura, and A. Tsuchiya: Nucl. Phys. B **545**, 543 (1999).
- 5) S. Gottlieb, W. Liu, D. Toussaint, R. L. Renken, and R. L. Sugar: Phys. Rev. D **35**, 2531 (1987).
- 6) H. Aoki, S. Iso, H. Kawai, Y. Kitazawa, and T. Tada: Prog. Theor. Phys. **99**, 713 (1998).
- 7) M. Fukuma, H. Kawai, Y. Kitazawa, and A. Tsuchiya: Nucl. Phys. B **510**, 158 (1998).
- 8) T. Nakajima and J. Nishimura: Nucl. Phys. B **528**, 355 (1998).

## New Method for Trace Element Analysis Using the Electron Cyclotron Resonance Ion Source and Heavy-Ion Linac

M. Kidera, T. Nakagawa, K. Takahashi, S. Enomoto, T. Minami,\* M. Fujimaki,  
E. Ikezawa, O. Kamigaito, M. Kase, A. Goto, and Y. Yano

We measured the contamination in an  $\text{Al}_2\text{O}_3$  rod and in composite elements of cinnabar (collected from the Tenjinyama ancient tomb) using the electron cyclotron resonance ion source (ECRIS) and the RIKEN linear accelerator (RILAC) complex. Elements of mass number smaller than 100, such as  $^{50}\text{V}$ ,  $^{55}\text{Mn}$  and  $^{75}\text{As}$ , were mainly identified by the system.

Since the 1960s, the technique of accelerator mass spectrometry (AMS) has been developed in cooperation with an electrostatic-tandem accelerator. A negative ion source is conventionally used for a tandem accelerator, and the development of an ion source is an important research theme. The negative ionization of the element strongly depends on its electron affinity. For the production of negative ions from elements with low electron affinity, great effort is required for sample preparation. In particular, it is impossible to produce negative ions from rare gases, such as Ar and Kr. In many cases, the measurement has a large margin of error due to the effect of the various treatments of the element. These are some of the disadvantages of using a tandem accelerator for AMS. In addition, when using a tandem accelerator to identify impurities in materials, automation for scanning both the analyzing magnet of the injection and extraction side of the accelerator is required, which is quite complicated, leading to uncertainties in the determined amount of impurities. To overcome this, we combined the ECRIS and heavy-ion Linac to conduct experiments of element analysis. The 18 GHz ECRIS<sup>1)</sup> at RIKEN was used as the external ion source of the RIKEN linear accelerator (RILAC).<sup>2)</sup> The production of positive ions does not depend on ionization tendency in the ECR plasma and highly charged positive ions were produced in the ECR plasma for all elements at a high temperature. The acceleration and transportation depends only on the mass-to-charge ratio ( $A/q$ ). Ions with the same  $A/q$  were simultaneously analyzed and detected by this system. With  $A/q = 3, 4,$  and  $5$ , approximately 90% of all elements can be accelerated and analyzed.

The composite elements of cinnabar from the Tenjinyama ancient tomb were measured using the same system. Approximately 100 mg of cinnabar was placed into a 4-mm-diameter, 2-mm-thick Ta tube. The tip of the Ta tube was closed using pliers, and two 1-mm-diameter holes were formed in the upper side of the Ta tube. The powdered sample was heated by ECR plasma. The particles with  $A/q = 5$ , ana-

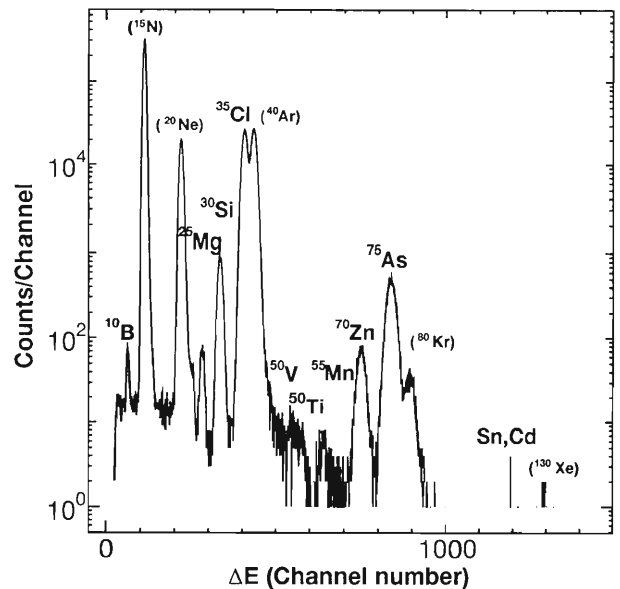


Fig. 1.  $\Delta E$  spectrum for measurement of cinnabar.

lyzed using the first analyzing magnet, were accelerated to 1.0 MeV/u using RILAC and the variable-frequency RFQ (radio-frequency quadrupole linac) pre-accelerator.<sup>3)</sup>

The  $\Delta E$  spectrum is shown in Fig. 1. By fixing the acceleration parameter to  $A/q = 5$ , the mass number of detected elements is a multiple of 5. The accelerator has large ambiguity in terms of mass resolution due to influences such as the fluctuation of the RF phase; however, in the system used in this investigation, the detected elements were almost certain to have  $A/q = 5$ , because elements were reselected by the analyzing magnets.

We established a method for the measurement of the relative abundance of elements in a sample by using ECRIS. Unlike conventional AMS, this system allows the measurement of numerous elements at the same time. The effect of spectroscopic interference is negligible owing to ionization in the high-temperature field by the ECR plasma, implying that the number of elements was increased and the margin of measurement error was decreased.

### References

- 1) T. Nakagawa et al.: Nucl. Instrum. Methods Phys. Res. A **396**, 9 (1997).
- 2) M. Odera et al.: Nucl. Instrum. Methods **227**, 187 (1984).
- 3) O. Kamigaito et al.: Rev. Sci. Instrum. **70**, 4523 (1999).

\* College of Toyooka



## **IV. NUCLEAR DATA**



## Status Report of the Nuclear Data Group

Y. Tendow, A. Yoshida, and K. Kitao

Until now, the RIKEN Nuclear Data Group has continued three kinds of long-term nuclear data activity described below.

### (1) Nuclear reaction cross section data (EXFOR)

Since 1983, our group has been a member of the worldwide network for the compilation of the charged particle nuclear reaction cross sections coordinated by the IAEA Nuclear Data Section (NDS). The tasks of this network are to collect charged particle reaction cross sections and compile them into a special format called EXFOR (EXchange FORmat). The compiled data are incorporated into the master database and provided to clients free of cost upon request.

First we limited data collection to the cross section data of important reactions producing the following twenty typical radioisotopes for medical applications:  $^{11}\text{C}$ ,  $^{13}\text{N}$ ,  $^{15}\text{O}$ ,  $^{18}\text{F}$ ,  $^{28}\text{Mg}$ ,  $^{52}\text{Fe}$ ,  $^{67}\text{Ga}$ ,  $^{68}\text{Ge}$ ,  $^{74}\text{As}$ ,  $^{77}\text{Br}$ ,  $^{82}\text{Br}$ ,  $^{77}\text{Kr}$ ,  $^{81}\text{Rb}$ ,  $^{82\text{m}}\text{Rb}$ ,  $^{111}\text{In}$ ,  $^{123}\text{Xe}$ ,  $^{127}\text{Xe}$ ,  $^{123}\text{I}$ ,  $^{124}\text{I}$ , and  $^{125}\text{I}$ . Subsequently, in order to maintain the completeness of the database, we extended the scope of data collection to the important reaction data not included in the EXFOR master file.

So far, we have added 53 entries, 'R0001' through 'R0053' containing as many as 535 excitation functions in total to the EXFOR database.

### (2) Evaluated Nuclear Structure Data File (ENSDF)

We have been participating in the ENSDF compilation network coordinated by the Brookhaven National Nuclear Data Center (NNDC). The task of the network is to evaluate various existing experimental nuclear structure data to construct and recommend a reliable nuclear data set and level scheme for each nuclide in a mass chain.

We have thus far evaluated nuclear structure data for mass chains  $A = 120$ ,  $121$ ,  $127$  and  $129$ , and the results have been published in the Nuclear Data Sheets.<sup>1-5)</sup>

A draft of a new evaluation of the  $A = 120$  mass chain is now under the author's review prior to the printing. Because much new data on high-spin states for  $A = 129$ , as well as for other neighboring masses, have been accumulating since our last evaluation,

we are planning to make partial update of  $A = 129$  mass chain in the near future.

### (3) Nuclear Science References (NSR)

We are engaged in collecting and compiling the secondary references printed in Japan (unpublished works such as annual reports, conference proceedings, etc.) into the Nuclear Science References (NSR) file format and transmitting them to the NNDC. The NSR data are disseminated through on-line network services and also in print as 'Recent References'.

The compilation of the 1998 annual report containing 150 papers has already been completed and transmitted to the NNDC. The Japanese secondary sources surveyed were as follows (shown in the NSR file code name):

RIKEN (RIKEN Accel. Prog. Rep.),  
 JAERI-TV (JAERI Tandem & V. D. G. Rep.),  
 JAERI-TIARA (JAERI Takasaki Ion Acc. Advanced Rad. Appl.),  
 UTTAC (Univ. Tsukuba Tandem Accel. Center),  
 RCNP (Res. Center Nucl. Phys., Osaka Univ.),  
 OULNS (Osaka Univ. Lab. Nucl. Studies),  
 CYRIC (Cyclo. Radioisot. Center, Tohoku Univ.),  
 KUTL (Kyushu Univ. Tandem Accel. Lab.).

The compilation of works for the 1999 annual report is now in progress.

The RIKEN Nuclear Data Group could not spare the manpower in recent years to carry out other work than the three database activities mentioned above. With the upcoming reorganization of the Radiation Laboratory, we will have to reconsider our activities as a whole.

### References

- 1) A. Hashizume, Y. Tendow, and M. Ohshima: Nucl. Data Sheets **52**, 641 (1987).
- 2) T. Tamura, Z. Matumoto, A. Hashizume, Y. Tendow, K. Miyano, S. Ohya, K. Kitao, and M. Kanbe: Nucl. Data Sheets **26**, 385 (1979).
- 3) A. Hashizume, Y. Tendow, K. Kitao, M. Kanbe, and T. Tamura: Nucl. Data Sheets **35**, 181 (1982).
- 4) K. Kitao and M. Ohshima: Nucl. Data Sheets **77**, 1 (1996).
- 5) Y. Tendow: Nucl. Data Sheets **77**, 631 (1996).



## **V. DEVELOPMENT OF ACCELERATOR FACILITIES**



## Biased Electrode Method for RIKEN 18 GHz ECRIS

Y. Higurashi, T. Nakagawa, M. Kidera, Y. Miyazawa, M. Hemmi, T. Chiba,  
M. Kase, T. Kageyama, A. Goto, and Y. Yano

In order to increase the beam intensity of highly charged heavy ions from ECRIS, several methods have been suggested and successfully applied in many laboratories in the last decade. The installation of an electrode into the plasma chamber is one of the most popular methods. In RIKEN, we have also applied this method and successfully increased the beam intensity of highly charged heavy ions. In spite of the great success of this method, the mechanism is still not completely clear. As a first step toward understanding the mechanism of this method, we measured the beam intensity while changing the electrode position and the biased voltage.

The design and performance of the RIKEN 18 GHz ECRIS without using the biased electrode is described in Ref. 1. Figure 1 shows the cross-sectional view of the RIKEN 18 GHz ECRIS with a stainless steel electrode. The diameter and thickness of the electrode are 18 and 1 mm, respectively. A negative bias voltage is applied between the electrode and plasma chamber as shown in Fig. 1. The electrode can also be used at the floating potential by disconnecting it from the electric power supply. The electrode is placed on the axes of the plasma chamber. The position of electrode (L) is

defined in Fig. 1. The axial position of the electrode is remotely controlled with an accuracy of 0.1 mm.

For all elements heavier than carbon, gas mixing is usually used to obtain a higher intensity of highly charged heavy ions. In the present case, we used oxygen as a mixing gas to produce Xe ions. The plasma

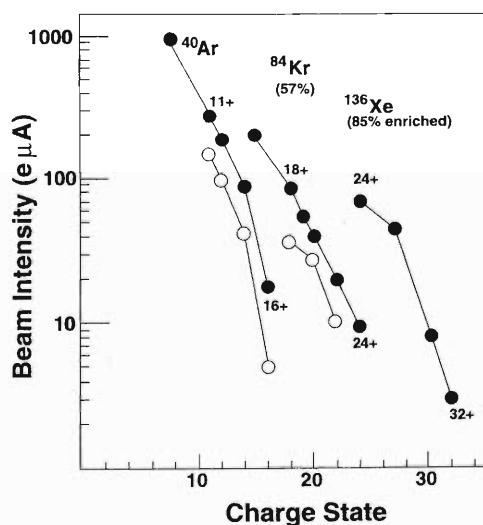


Fig. 2. Beam intensity of highly charged ions from gaseous elements. Open and closed circles are results without using and using the disc, respectively.

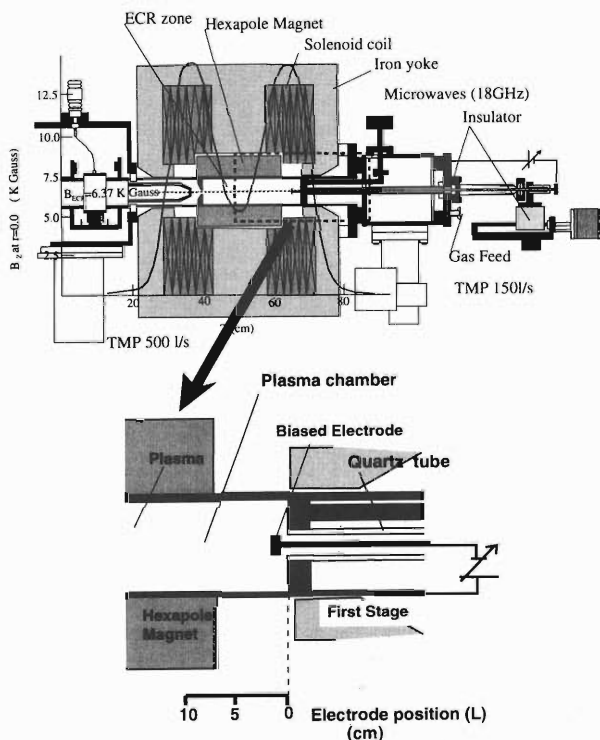


Fig. 1. Cross-sectional view of RIKEN 18 GHz ECRIS.

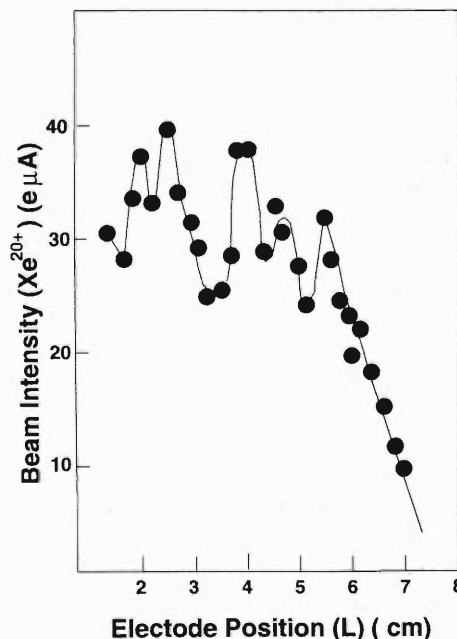


Fig. 3. Beam intensity of Xe<sup>20+</sup> as a function of the electrode position at the RF power of 200 w.

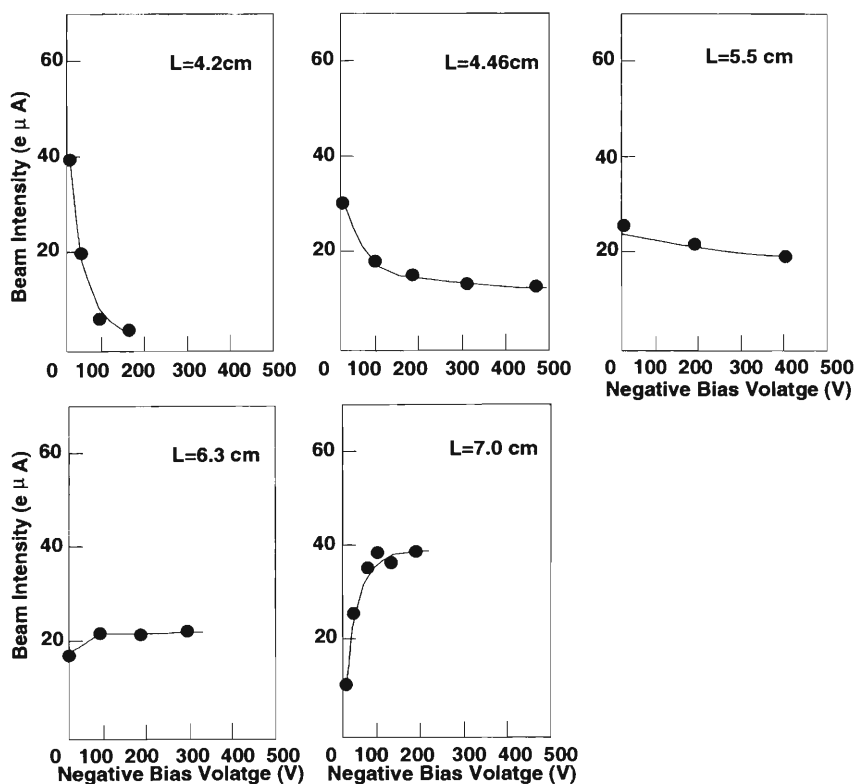


Fig. 4. Beam intensity of  $\text{Xe}^{20+}$  as a function of the negative bias voltage for several electrode positions.

chamber wall is covered with aluminum tubing (of 1 mm thickness). The aluminum oxide surface emits several secondary electrons per primary electron impact, which helps increase the plasma density.<sup>1)</sup>

Figure 2 shows the summary of the beam intensities inclesise of the highest beam intensity of the gaseous elements. The closed and open circles are the results obtained using and without using the electrode, respectively. The beam intensity of highly charged ions was strongly enhanced with the use of the electrode, *e.g.*, the intensity of 300  $e\mu\text{A}$  of  $\text{Ar}^{11+}$  is almost two times higher than that resulting whithout using the electrode.<sup>2,3)</sup>

The measurement was performed under the condition that the ion source was tuned for producing a  $\text{Xe}^{20+}$  beam at the bias voltage of 0 V. The gas pressure of the plasma chamber was  $7 \times 10^{-7}$  Torr. The maximum and minimum magnetic field strength of the mirror magnetic field were 1.4 and 0.47 T, respectively. The extraction voltage was 10 kV. The injected microwave power was 200 W. For the experiment, we did not change these parameters except for the negative bias voltage and position of electrode. Figure 3 shows the beam intensity of  $\text{Xe}^{20+}$  as a function of electrode position at a bias voltage of 0 V. The beam intensity strongly depends on the position of the electrode. It oscillated as the electrode position

changed from  $L = 2$  to 6 cm. We infer this oscillation may be caused by the standing waves of the micro-wave (18 GHz  $\sim$  17 mm),<sup>4)</sup> however its mechanism is still not clear. Additionally, when the electrode position ( $L$ ) is near the ECR plasma ( $L = 6$ –7 cm), the beam intensity decreased as a function of  $L$ .

Figure 4 shows the beam intensity dependence  $L$  and the negative bias voltage. At smaller values of  $L$ , the beam intensity decreases with increasing negative bias voltage. However, the beam intensity increases with negative bias voltage when the electrode is placed far from the chamber wall.

#### References

- 1) T. Nakagawa, Y. Miyazawa, M. Hemmi, T. Chiba, N. Inabe, M. Kase, T. Kageyama, O. Kamigaito, A. Goto, and Y. Yano: *Jpn. J. Appl. Phys.* **35**, 4077 (1996).
- 2) T. Nakagawa, S. Biri, M. Kidera, Y. Miyazawa, M. Hemmi, T. Chiba, N. Inabe, M. Kase, T. Kageyama, O. Kamigaito, A. Goto, and Y. Yano: *Jpn. J. Appl. Phys.* **35**, L1124 (1996).
- 3) S. Biri, T. Nakagawa, M. Kidera, Y. Miyazawa, M. Hemmi, T. Chiba, N. Inabe, M. Kase, T. Kageyama, O. Kamigaito, A. Goto, and Y. Yano: *Nucl. Instrum. Methods Phys. Res. B* **152**, 386 (1999).
- 4) M. Delaunay, B. Jacquot et, and M. Pontonnier: *Nucl. Instrum. Methods Phys. Res. A* **305**, 223 (1991).

## Present Status of 14.5 GHz Caprice in RIKEN

Y. Kanai, Y. Nakai, H. Ohyama, T. Kambara, and Y. Yamazaki

The ECRIS (14.5 GHz Caprice) and the experimental beam lines were built in 1994–1995 in the accelerator research annex for atomic physics experiments.<sup>1)</sup> This year, we moved the ECRIS and all setups to the Nishina building. The ECRIS and the beam transport line (analyzing magnet and triplet quadrupole magnets) were transferred to the ion source room for the AVF cyclotron. The experimental beam line (switching magnet and four beam lines) and experimental setups were transferred to the new experimental hall for low-energy highly charged ions. The beam transport line passes through the wall between the ion source room and the experimental hall. The power supplies for the ECRIS and the beam transport line were situated in the ion source room. The ECRIS and the beam transport system are controlled from the control desk in the experimental hall.

On this movement, we have not changed the configuration of the beam focussing elements.<sup>1)</sup> Due to the 56 cm difference in the floor level between the ion source room and the experimental hall, the height of the beam lines was about 94 cm and 150 cm in the ion source room and in the experimental hall, respectively.

The double-wall plasma chamber made of stainless steel (SUS) with an aluminum sheet was replaced with a single-wall aluminum (Al) chamber, which is expected to provide higher charge state ions.<sup>2)</sup> In the middle of October, we conducted a test of the ECRIS and beam transport system. Typical ion currents before and after the replacement are summarized in Table 1. The extraction voltage was 15 kV and the size of the beam was collimated by the slits to 18 mm × 18 mm before the Faraday cup. The data indicate that the Al single-wall chamber provides higher currents, particularly at higher charges, as expected. We note that by using the Al sheet, the ion currents at a higher charge state were increased as compared to those with the simple SUS chamber, as

Table 1. Typical ion currents from 14.5 GHz Caprice in RIKEN. Extraction voltage is 15 kV. Beam is collimated by slits to 18 mm × 18 mm. *a*: single-wall plasma chamber made of aluminum, *b*: double-wall plasma chamber made of stainless steel with aluminum sheet.

	Ions currents ( $e\mu\text{A}$ )	
O <sup>3+</sup>	740 <sup>a</sup>	464 <sup>b</sup>
O <sup>5+</sup>	232 <sup>a</sup>	370 <sup>b</sup>
O <sup>6+</sup>	330 <sup>a</sup>	350 <sup>b</sup>
O <sup>7+</sup>	60 <sup>a</sup>	37 <sup>b</sup>
Ar <sup>8+</sup>	175 <sup>a</sup>	291 <sup>b</sup>
Ar <sup>11+</sup>	64 <sup>a</sup>	68 <sup>b</sup>
Ar <sup>14+</sup>	5 <sup>a</sup>	3.5 <sup>b</sup>
Ar <sup>16+</sup>	0.3 <sup>a</sup>	0.12 <sup>b</sup>

reported before.<sup>3)</sup> On the basis of the present results, we can put forth that the Al single-wall plasma chamber is more effective than the SUS double wall plasma chamber with the Al sheet to obtain the higher charge state ions. This is due to the difference in the area of the Al surface in the plasma chamber between the Al chamber and the SUS chamber with the Al sheet.<sup>2)</sup>

We will test the deceleration mode of the beam transport to use the very slow highly charged ions at the experimental setups.<sup>4)</sup> Following this test, we will start the experiments using ion beams from the ECRIS.

### References

- 1) Y. Kanai et al.: RIKEN Accel. Prog. Rep. **29**, 208 (1996).
- 2) D. Hitz et al.: Rev. Sci. Instrum. **67**, 883 (1996).
- 3) Y. Kanai et al.: RIKEN Accel. Prog. Rep. **30**, 168 (1997).
- 4) M. Kitajima et al.: RIKEN Accel. Prog. Rep. **31**, 157 (1998).

## Development of Compact High Current Multicharged Ion Source for RIKEN RI Beam Factory

S. Bhattacharjee, T. Nakagawa, M. Kase, A. Goto, and Y. Yano

Ion sources form an integral part of an accelerator facility.<sup>1,2)</sup> High-current multicharged ion beams are one of the major requirements of the RIKEN RI beam factory. Electron cyclotron resonance ion sources (ECRIS) have been successfully applied for several years. However, specific needs such as high-current maximally charged heavy ions and the increasing demand for higher beam intensities<sup>3)</sup> have initiated a quest for new types of ion sources. To address the forthcoming challenges, the development of ion sources using novel concepts is essential.

The performance of an ion source is greatly determined by the characteristics of the source plasma.<sup>3-5)</sup> In order to obtain higher beam intensities and multicharged states, it is imperative to increase the electron density, the electron temperature and the ion and electron confinement times. With such an objective, we attempt to improve upon these plasma parameters using methods that have not been previously explored.

In ECRIS, the bore of the plasma chamber is usually made larger than the cutoff dimension of the fundamental waveguide mode to permit wave propagation and plasma sustenance. The waves are launched with the propagation vector parallel to the axial magnetic field, created by electromagnetic coils. The axial mirror field, although useful for plasma confinement and heating, has a loss cone and instability, such as drift instability. Moreover, the plasma uniformity can become poor and heating can be inefficient when there are large gradients of the magnetic field.<sup>6)</sup>

Studies<sup>7)</sup> have shown that, for waves launched perpendicular to the magnetic field, a peripheral arrangement of permanent magnets in a multicusp geometry around the waveguide (plasma chamber) helps to obviate the geometrical cutoff problem. In this way the launched microwaves can be efficiently guided into the plasma chamber with a cross section even smaller than the cutoff value. The reduced bore diameter increases the microwave power density which aids in the production of a plasma much denser than the cutoff density. Moreover, perpendicular wave launching favors resonance heating such as upper hybrid resonance, which is unexpected for waves launched parallel to the magnetic field. The absence of electromagnetic coils results in a compact device. Experiments with continuous mode (cw) microwaves of 2.45 GHz indicate that the plasma density is  $>10^{11} \text{ cm}^{-3}$ . Good radial and axial uniformity are obtained within a 40 mm diameter and along the length of the chamber ( $\sim 400 \text{ mm}$ ), respectively. The low-energy electron temperature, measurable by a probe, lies in the range of 10–14 eV, which is much higher than for other high-density microwave plasmas such as surface-wave or helicon-wave sources.

To further raise the electron temperature and the plasma density, it is desired to increase the power of the microwaves. Pulsed mode microwaves are useful in this regard because higher powers can be obtained. Moreover, the pulse repetition frequency and the pulse width provide additional control of the plasma and the extracted beam. We have considered the application

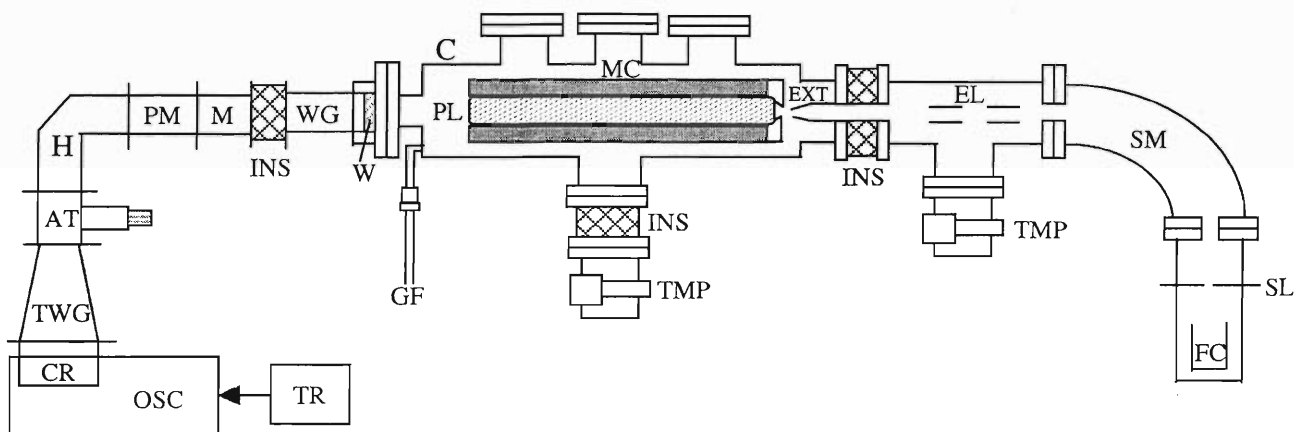


Fig. 1. Schematic of the experimental facility. TR: Trigger signal for pulse initiation, OSC: Magnetron oscillator, CR: Circulator, TWG: Tapered waveguide, AT: Attenuator, H: Rectangular bend, PM: Power monitor, M: E-H tuner, INS: Insulator, WG: Rectangular waveguide, W: Quartz window, PL: Plasma, C: Vacuum chamber, GF: Gas feed, MC: Multicusp, TMP: Turbomolecular pump, EL: Einzel lens, SM: Sector magnet, SL: Slit, FC: Faraday cup.

of high-power short-pulse microwaves. The strong electric fields with a short interval accelerate electrons to high energies during the pulse.<sup>8)</sup> The high electron temperature persists in the interpulse regime with a decay constant much smaller than those of the charged particles. This can be helpful for successive ionization whereby the possibility for obtaining multiply charged states is increased. The increase in power density in the narrow tube leads to nonlinear effects such as ponderomotive force and nonlinear dispersion. These effects, together with the anisotropic diffusion of the plasma, are expected to be favorable for increasing the beam intensity.

The experimental findings in cw and pulsed microwaves are expected to have great implications in applications where collimated, intense and multicharged ion beams are required. We are currently undertaking feasibility studies of the above concepts for ion source applications. Figure 1 shows a schematic of the experimental system. The design of the vacuum chamber, plasma chamber, microwave circuitry and pumping system has been accomplished. The components are currently being assembled and the experimental facility

constructed. Ports have been provided on the vacuum chamber to access the plasma from the radial and axial directions and for beam extraction. Beam intensity and charge states will be measured. There will be provisions for plasma diagnostics such as X-ray, optical, probe and electromagnetic field measurements. Investigations will be carried out to obtain an optimized beam using waves in cw, pulsed or a superposition of the two modes.

We would like to thank Mr. T. Chiba for assisting us with the technical drawings. S. B. thanks Dr. H. Amemiya for his encouragement.

#### References

- 1) T. Nakagawa et al.: *Rev. Sci. Instrum.* **69**, 637 (1998).
- 2) T. Nakagawa et al.: *Jpn. J. Appl. Phys.* **37**, 6215 (1998).
- 3) C. Perret et al.: *Phys. Plasmas* **6**, 3408 (1999).
- 4) A. Girard et al.: *Rev. Sci. Instrum.* **65**, 1714 (1994).
- 5) G. Melin et al.: *Rev. Sci. Instrum.* **61**, 236 (1990).
- 6) H. Koivisto et al.: *Rev. Sci. Instrum.* **70**, 2979 (1999).
- 7) S. Bhattacharjee and H. Amemiya: *Jpn. J. Appl. Phys.* **37**, 5742 (1998).
- 8) S. Bhattacharjee and H. Amemiya: *J. Appl. Phys.* **84**, 115 (1998).

## Laser-Plasma Production for Laser Ion Source at RIKEN

T. Takeuchi, T. Katayama, T. Nakagawa, M. Okamura, K. Yano,  
T. Hattori,<sup>\*1</sup> K. Sasa,<sup>\*2</sup> B. Sharkov,<sup>\*3</sup> and S. Kondrashev<sup>\*3</sup>

In the MUSES project at RIKEN,<sup>1)</sup> a pulsed-ion source for highly charged heavy ions is required. A laser-ion source (LIS)<sup>2)</sup> is expected to satisfy MUSES requirements. A test bench at RIKEN is now being developed to investigate the laser plasma for the pulsed-ion source. A schematic drawing of the test bench is shown in Fig. 1. A TEA CO<sub>2</sub> laser and a YAG laser are used for producing the laser plasma. The maximum energy and the pulse duration of the TEA CO<sub>2</sub> laser ( $\lambda = 10.6 \mu\text{m}$ ) are 10 J and 100 nsec, respectively. A convex BeCu mirror ( $20\phi$ , 5 t, R = 5 m) and a concave BeCu mirror ( $50\phi$ , 10 t, R = 10 m) are used as a resonator system for the CO<sub>2</sub> laser. We have obtained an output energy of 5.7 J using this resonator system under the gas mixture condition (CO<sub>2</sub> : N<sub>2</sub> : He = 1 : 1 : 8). On the other hand, the Nd:YAG laser (INDI-50, Spectra-Physics;  $\lambda = 1.064 \mu\text{m}$ ) has a maximum output energy of 500 mJ and the pulse duration of 6–7 nsec. The repetition rate is up to 10 Hz for both lasers. An aluminum target is located in the center of the vacuum chamber. The focused laser irradiates the target at an incident angle of 36 degrees. The laser plasma expands perpendicular to the target surface. Using a streak camera and CCD camera set, one can obtain data of the plasma expansion as a function of time. We obtained results using the Nd:YAG laser; a laser-produced plasma image using of a 250 mJ laser pulse is presented in Fig. 2. After about 100 pulses, the crater shape became an ellipse with a long axis of 700  $\mu\text{m}$  and a short axis of 500  $\mu\text{m}$ , as shown in Fig. 3.

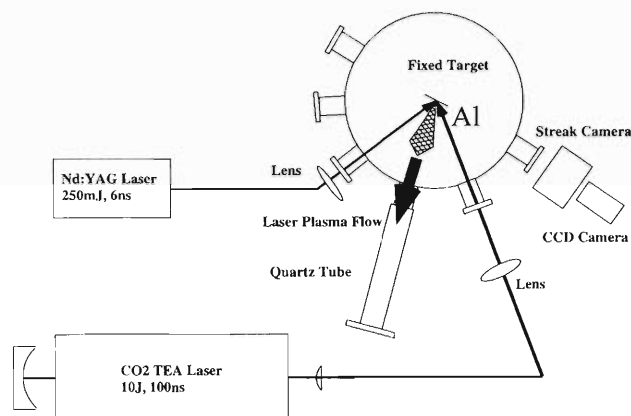


Fig. 1. Schematic of RIKEN LIS test bench.

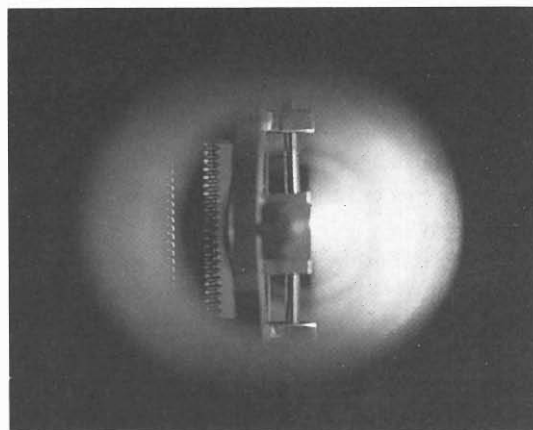


Fig. 2. Photo of laser-produced plasma of the 250 mJ Nd:YAG laser.

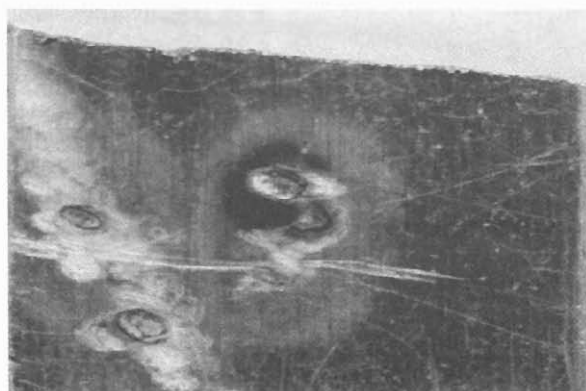


Fig. 3. Target surface for the 250 mJ Nd:YAG laser.

The power density [ $\text{W}/\text{cm}^2$ ] on the target surface can be estimated as  $10^{10} \text{ W}/\text{cm}^2$  from the size of the ellipse, the laser energy (250 mJ) and the laser-pulse duration (100 ns). From this value, it is expected that the charge state of aluminum ions is at least 3–4.<sup>3)</sup>

### References

- 1) T. Katayama et al.: Nucl. Instrum. Methods Phys. Res. A **626**, 545c (1997).
- 2) B. Sharkov et al.: in *Handbook of Ion Sources*, edited by B. Wolf, (CRC Press, Boca Raton, 1995), p. 149.
- 3) R. Scrivens et al.: Rev. Sci. Instrum. **71**, 924 (2000).

<sup>\*1</sup> Research Laboratory for Nuclear Reactors, Tokyo Institute of Technology

<sup>\*2</sup> Tandem Accelerator Center, University of Tsukuba

<sup>\*3</sup> Institute for Theoretical and Experimental Physics, Moscow, Russia

# Generation of Heavy-Ion Pulses with Short Width and Long Interval

A. Yoneda and T. Kambara

A beam chopping and bunching system has been developed for the generation of nearly single-bunch pulses of a heavy-ion beam from the RILAC and RIKEN Ring Cyclotron. With this system, the beam-pulse frequency can be set to any value between DC and 1 MHz. The source timing signals are sent from either the control room of the Ring Cyclotron or an experimental site.

Figure 1 shows the system used to generate and monitor the short pulses. A heavy-ion beam is chopped by electric pulses at a vertical deflector after the 18 GHz ECR ion source. Then the beam is modulated by a subharmonic RF buncher for time focusing and accelerated by the RFQ linac, RILAC and Ring Cyclotron. The microscopic time structure of the beam is monitored by secondary-electron monitors before and after the acceleration by the Ring Cyclotron. In the monitor, the ion beam crosses a tungsten wire which emits secondary electrons. The wire has a 0.3 mm diameter and it negligibly affects the overall beam characteristics. The secondary electrons are collected by an electrostatic field and amplified by a microchannel plate (MCP). A similar monitor, with aluminum foil for the secondary-electron emitter, is also set on the experimental beam line (E5A).

The system has been tested with a Xe-ion beam accelerated up to 26 MeV/u. The accelerators were operated at a frequency of  $f = 28$  MHz. The chopping voltage at the deflector had an amplitude of about 500 V,

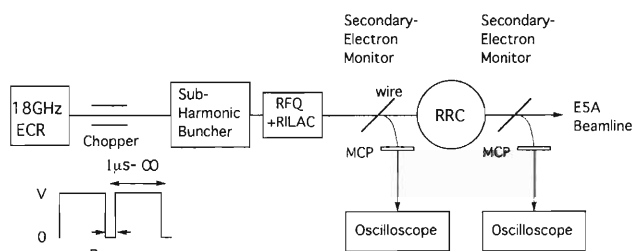


Fig. 1. Generation and measurement systems of short beam pulses.

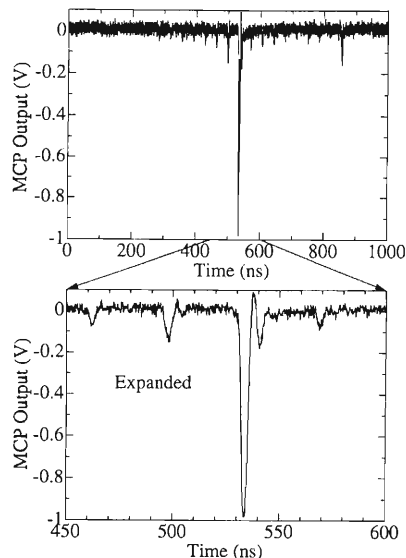


Fig. 2. Time structure of the beam bunch.

width of 250 ns for beam ON and interval of 25 ms. The subharmonic buncher was operated at a frequency of  $f/7$ . The time structure, shown in Fig. 2, was obtained at the E5A beam line. The highest peak had a width of about 3 ns. The additional periodical peaks with an interval of about 35 ns were microbunches, which were not collected by the sub-harmonic buncher. A relatively high peak later than the main peak by about 320 ns ( $9 \times$  microbunch period) was a microbunch extracted from the cyclotron one turn later than the main bunch (the harmonic number of the Ring Cyclotron was 9). The number of ions in a pulse was estimated to be in the range of  $10^4$ . The beam leakage, that is the beam intensity in the OFF status, was lower than  $10^{-4}$  of that in the ON status.

This system has been successfully used in experiments reported elsewhere.<sup>1)</sup>

## References

- 1) T. Kambara et al.: Nucl. Instrum. Methods Phys. Res. B (2000), in press.

## A Plan for a New Control System for the RIKEN Ring Cyclotron Using EPICS

M. Kobayashi-Komiyama, M. Kaji,\*<sup>1</sup> M. Nagase, I. Yokoyama, T. Tanabe, M. Sugimoto,\*<sup>2</sup> and M. Kase

With regard to the control system of the RIKEN RI beam factory (RIBF) project,<sup>1)</sup> it has become necessary to expand the present control system of the RIKEN ring cyclotron (RRC) to maintain compatibility with the RIBF project. Therefore, we are searching for the optimum means of extending the present system to improve its compatibility. In this paper, we report a plan which uses the Experimental Physics and Industrial Control System (EPICS).<sup>2)</sup>

Figure 1 shows a block diagram of the present control system of the RRC. It has been more than 13 years since system operation was started. The main concerns regarding this system are as follows:

(1) A host computer (minicomputers, Mitsubishi M60/500) is the only brain in the present control system. As a result, it plays many roles in the system. These roles include the operator interface, input/output control and data storage (which are the parameters of RRC operation). In order to aid in the tasks of the host computer, intelligent modules are used for the interface between CAMAC modules and control devices. Two types are used: one is a CAMAC module called a communication interface module (CIM), and the other is a terminal module for high-speed local control of accelerator devices, called a device interface module (DIM). Both module types were developed in our laboratory. The details of these modules are given in Refs. 3 and 4. As there is an expansion

limit to the control ability of this system, it is not suited for expansion.

(2) The components of the system have become old. Thus, the system maintenance cost has become high. The age of the touch panel in particular has become a serious problem. Most man-machine interactions are performed using the touch panels: however, sometimes they do not respond during beam operation. Replacing the panels with new ones would require developing new applications; this would not be easy in any respect.

(3) Both control data and logic are written in the same application code. In other words, the current control system does not separate control data and logic. This type of system is not suited for extension.

In order to solve these problems, a plan for an alternative new control system of the RRC using EPICS was proposed last year. We employed part of the alternative system this year as a preliminary test.

The EPICS is the distributed supervisory control system which has many servers (usually on VMEbus). Present and future developments are being carried out cooperatively by the EPICS collaboration, originally developed by ANL and LANL. Currently, the collaboration is expanding and now includes several laboratories around the world (not only in the US). The real-time operating system VxWorks runs on the VME computers. As shown in Fig. 2, the operator interface (OPI) and input/output controllers (IOCs) are connected using Ethernet, and thus the number of IOCs is not limited. Therefore, the EPICS is suited for large

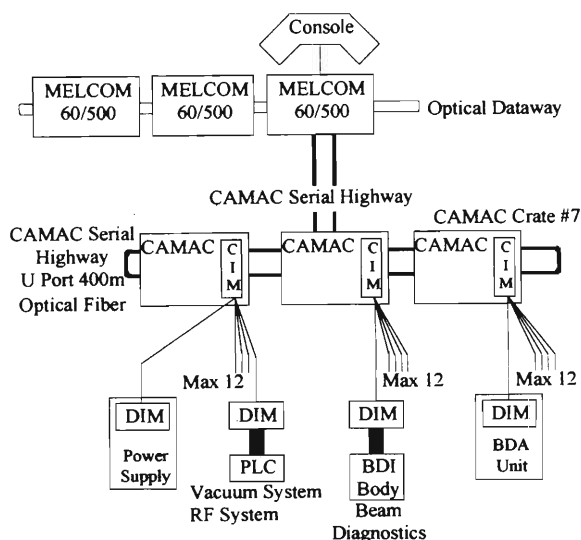


Fig. 1. The present control system of the RRC.

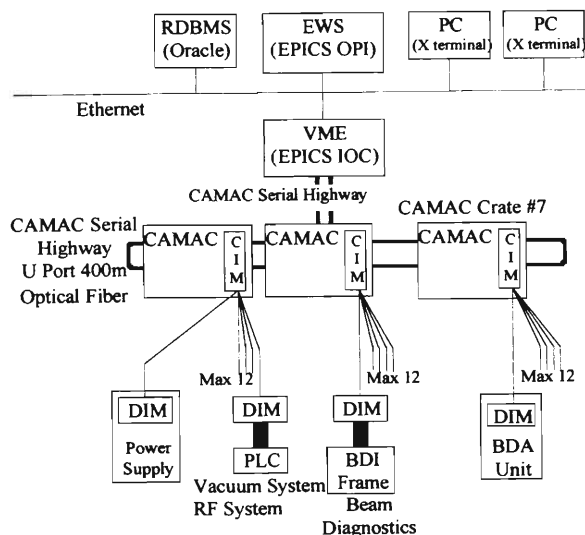


Fig. 2. The new control system using the EPICS.

\*<sup>1</sup> Mitsubishi Electric Corporation

\*<sup>2</sup> Mitsubishi Electric Control Software Corporation

Table 1. Comparison between the M60 computer system and the EPICS.

<Hardware>	Present System	New EPICS
<b>Computer</b>	Minicomputers M60 CAMAC Crate Controllers	VME Computers (for I/O Controller) EWSs (for Operator Interface) CAMAC Crate Controllers
<b>Network</b>	CAMAC Serial Highway (UDP Optical Fiber)	CAMAC Serial Highway (UDP Optical Fiber) Ethernet (between EWS and VME)
<b>Operational Screen</b>	Character-Based Touch Panels	Graphic User Interface (Motif-Based Windows)
<Software>	Present System	New EPICS
<b>OS</b>	M60: OS60/UMX	VME: VxWorks 5.2 (Included by Tornado 1.0) EWS: HP-UX 10.20
<b>Middleware</b>	<i>None</i>	EPICS R3.13, Oracle Workgroup Server 8.0
<b>Control Logic</b>	Fortran Programs	EPICS Device/Driver Supports (Low Level) EPICS Database (Middle Level) EPICS Client Applications (High Level)

projects such as the RIBF when we take into consideration the cooperative development and control of many accelerators. The EPICS has been used at a number of sites not only in particle accelerators and telescopes but in general enterprises at more than 70 sites around the world. Furthermore, use of the EPICS is free for public research institutes.

The replacement plan using the EPICS is shown in Fig. 2. The M60 computer system is removed and VME computers and engineering workstations (EWSs) are installed in its place. Software on the M60 computer system is replaced by the EPICS and an Oracle (a relational database management system)-based software system. In the new control system, we plan to store all accelerator system data using in Oracle. This enables the sharing of data between users and prevents dual storage of the control data. This database manages the properties of the control devices such as device name, control address and specifications. As shown in Fig. 2, the remaining components, including the CAMAC loop, are not replaced. Taking into consideration the fact that the RRC is in operation, we plan to replace the M60 computer system and the man-machine interface components first, so as not to significantly influence the RRC operation. However, by replacing the M60 computer system with EWS and VME computers, the present equipment is expected to realize maximum control ability. A comparison

between the present system and the new system is shown in Table 1.

We have tested the preliminary system for controlling the power supplies, profile monitors and Faraday cups of the RRC. The graphic user interfaces (GUIs) for controlling the above equipment were prepared, and they exhibited the same responses as the current system. Furthermore, the access speed between the OPI and the DIM was 30 times faster (3 ms) for each access in the new system; this speed is very fast and we expect smoother operation because of this. However, the test situations differed between both systems, so an accurate comparison of the two may not be possible.

Therefore, it has been verified that fundamental operations can be performed using the preliminary system. From this point, the development of the control system replacement will continue and the actual replacement will be performed.

#### References

- 1) Y. Yano et al.: Proc. 15th Int. Conf. on Cyclotrons and Their Applications 1998, Caen, p. 696 (1998).
- 2) L. R. Dalesio et al.: Proc. Int. Conf. on Accelerators and Large Experimental Physics Control Systems (ICALPECS' 93), Berlin, p. 179 (1993).
- 3) T. Wada et al.: Proc. 11th Int. Conf. on Cyclotrons and Their Applications, Tokyo, p. 407 (1987).
- 4) T. Wada et al.: IEEE Trans. Nucl. Sci. **NS-32**, 2095 (1984).

## Low Power Test of CSM Resonators

O. Kamigaito, M. Kase, Y. Miyazawa, T. Chiba, N. Sakamoto, M. Hemmi,  
S. Kohara, E. Ikezawa, A. Goto, and Y. Yano

The resonators of the first unit of the Charge-State Multiplier (CSM)<sup>1)</sup> have been constructed and low power tests were carried out.

Table 1 summarizes the design parameters of the first unit. It consists of two acceleration tanks and one deceleration tank, each of which has eight rf-gaps with a maximum gap voltage of 450 kV. The resonant frequency was chosen to be twice the fundamental frequency; it varies from 36.0 to 76.4 MHz. The designed voltage-gain of each tank is about 2.9 MV over the entire frequency range.

The resonator structure of the first unit is illustrated in Fig. 1. It is based on a  $\lambda/4$ -coaxial resonator with a movable shorting plate. By using the computer code MAFIA, the shape of the stems as well as the size of the coaxial part were optimized so that the current density on the sliding contact would be as small as possible. In the final design, the current density is estimated to be 60 A/cm at the maximum gap voltage.

All three resonators have the same dimensions except for the drift tubes and the stems. The rf-power is fed through a capacitive feeder. A capacitive tuner is used for the fine tuning of the resonant frequency. Each resonator is equipped with a cryogenic pump of 4000 l/s and a turbomolecular pump of 500 l/s.

Cooling is one of the most significant problems associated with these resonators. According to the calculation, the maximum power loss in each end-stem amounts to 9 kW. Therefore, the arrangement of the cooling channels has been carefully designed based on the heat analysis. The maximum displacement of the drift tubes due to thermal deformation is estimated to be 0.06 mm in the vertical direction. Taking these analyses into account, the drift tubes have been aligned with an accuracy of  $\pm 0.15$  mm in the transverse direc-

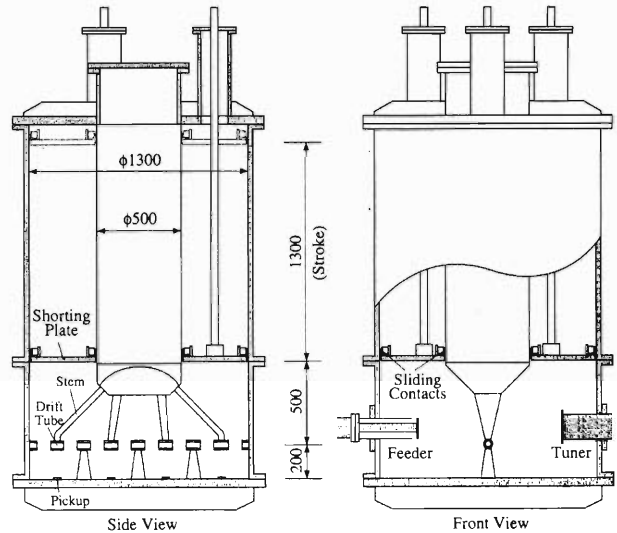


Fig. 1. Schematic diagram of the resonator of the first unit. Dimensions are given in mm. All components of the three resonators are the same size except for the drift tubes and stems.

tion and  $\pm 0.3$  mm in the longitudinal direction.

Figure 2 shows the resonant frequency of the fundamental mode in the first acceleration tank. As shown in the figure, movement of the shorting plate by a stroke of 1300 mm varies the resonant frequency from 34.8 to 81.5 MHz. The measured results are in good agreement with the MAFIA prediction. Similar results have been obtained in the other two resonators. We have also seen that the capacitive tuner changes the reso-

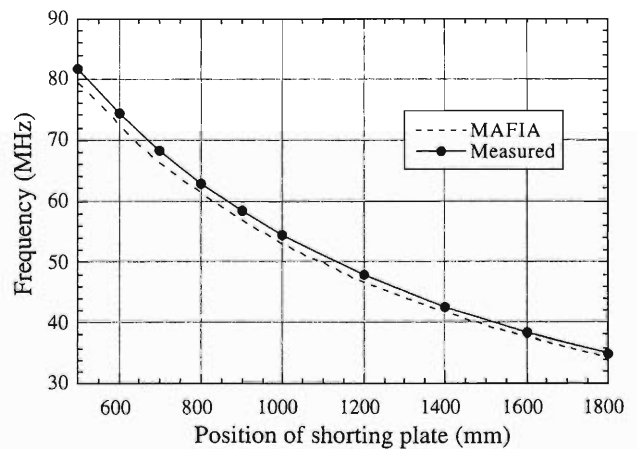


Fig. 2. Measured resonant frequency of the first acceleration tank (solid line) along with the MAFIA calculations (dashed line).

Table 1. Designed parameters of the first unit.

Tank	Accel.1	Accel.2	Decel.
Frequency (MHz)	36.0–76.4	36.0–76.4	36.0–76.4
m/q	24.7 <sup>a</sup> –5.5 <sup>b</sup>	24.7 <sup>a</sup> –5.5 <sup>b</sup>	12.0 <sup>a</sup> –2.7 <sup>b</sup>
$E_{in}$ (MeV/u)	0.65 <sup>a</sup> –2.91 <sup>b</sup>	0.76 <sup>a</sup> –3.43 <sup>b</sup>	0.88 <sup>a</sup> –3.96 <sup>b</sup>
$E_{out}$ (MeV/u)	0.76 <sup>a</sup> –3.43 <sup>b</sup>	0.88 <sup>a</sup> –3.96 <sup>b</sup>	0.65 <sup>a</sup> –2.91 <sup>b</sup>
Number of gaps	8	8	8
Gap voltage (kV)	450	450	450
Synchronous phase	– 25°	– 25°	+ 25°
Bore radius (cm)	1.75	1.75	1.75
Inner length (m)	1.3	1.3	1.3
Power loss (kW) <sup>b,d</sup>	58	61	58
$Z_s$ (M $\Omega$ /m) <sup>c,d</sup>	147	152	146

a: At 36.0 MHz (lowest frequency)

b: At 76.4 MHz (highest frequency)

c: At 54.4 MHz d: MAFIA prediction

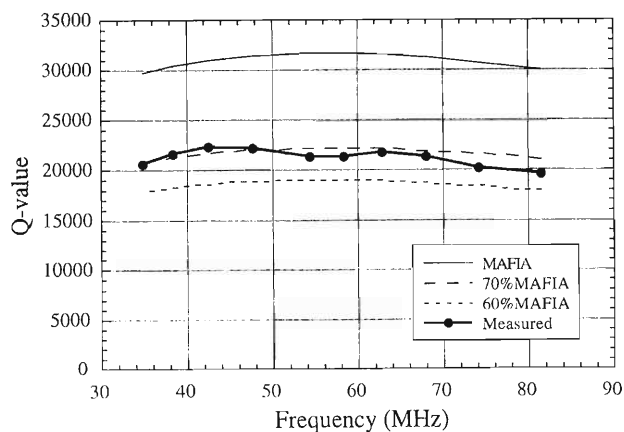


Fig. 3. Measured Q-values of the the first acceleration tank along with the MAFIA calculations. The dashed curves indicate the calculated values scaled by 70 and 60%.

nant frequency more than 0.5% in the whole frequency range.

The second and third higher modes appear around 100 and 150 MHz, respectively. These frequencies are well reproduced by the MAFIA calculation.

The measured Q-values of the first acceleration tank are shown in Fig. 3 along with the MAFIA calculations. As shown in the figure, the measured values are around 20000. They are approximately 63–71% of the calculated ones. The results for the other tanks are quite similar to that observed for the first tank. By comparing these results with the MAFIA calculations, the maximum power loss is estimated to be 90 kW.

We also measured the parallel shunt resistance ( $R_s$ ) of the first tank by using the calibrated pickups of the resonator.  $R_s$  is related to the power loss  $P$  and the gap voltage  $V$  by  $P = V^2/(2R_s)$ . The obtained values are about 1.5 M $\Omega$  over the entire frequency range, which gives the power loss of only 70 kW at the maximum gap voltage. It is known, however, that this measurement overestimates  $R_s$ ; an estimation given by the Q-value above would be more reliable.

Figure 4 shows the electric-field distribution of the

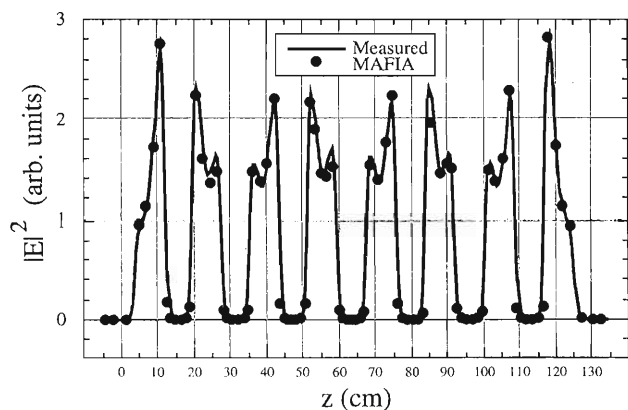


Fig. 4. Electric-field distribution on the acceleration axis measured for the fundamental mode at the lowest frequency (34 MHz). The solid curve indicates the measured data. MAFIA prediction is indicated by closed circles.

fundamental mode on the acceleration axis, which was measured by means of a perturbation method. Since the gap length is long, the field strength is minimum at the center of each gap. Moreover, the strength on the upper drift tubes is larger than that on the lower ones, which reflects the vertical asymmetry of the resonator structure. These results are well reproduced by the MAFIA calculations, as shown in the figure.

The power amplifiers have already been fabricated based on a tetrode tube, SIEMENS RS2058CJ. The output power of 100 kW has been successfully achieved over the entire frequency range required for the operation. Details of the amplifiers are given in Ref. 2.

The three tanks will be installed in the RILAC building within the next year. Acceleration tests will be carried out after high power tests using the amplifier.

#### References

- 1) O. Kamigaito et al.: Proc. 12th Symp. on Accelerator Science and Technology, Wako, p. 233 (1999).
- 2) Y. Murakami et al.: Proc. 12th Symp. on Accelerator Science and Technology, Wako, p. 239 (1999).

## Construction of the IRC for RIKEN RI Beam Factory

T. Mitsumoto, A. Goto, M. Kase, J. Ohnishi, O. Kamigaito, N. Sakamoto, K. Ikegami, K. Sugii, H. Okuno, Y. Miyazawa, T. Hiasa,\* Y. Kumata,\* and Y. Yano

The intermediate ring cyclotron (IRC) is a room-temperature ring cyclotron with four sectors that is utilized for the RIKEN RI-Beam Factory. It will be installed as the intermediate stage between the existing RIKEN Ring Cyclotron (RRC) and the Superconducting Ring Cyclotron (SRC).<sup>1)</sup> The IRC, having a K value of 980 MeV, accelerates the extracted beam from the RRC; The maximum acceleration energy and the maximum magnetic rigidity of the IRC is 126.7 MeV/nucleon and 4.57 Tm, respectively.<sup>2)</sup>

Figure 1 shows a plan view of the IRC, which consists mainly of four sector magnets, two main RF resonators, one flattop resonator, and injection and extraction devices. The main components of the IRC are installed in an area of 14 meters square.

The IRC will be operated at a harmonic value of 7, while that of the RRC is 9. Thus, the injection radius of the IRC is determined to be 7/9 of the extraction radius of the RRC. The main parameters of the IRC are listed in Table 1.

The fundamental structure of the sector magnet of the IRC is similar to that of the RRC. The main coils of the sector magnets are designed to be of a low power consumption type. The maximum power of the main coils is suppressed at 70% of that of the RRC, although the maximum magnetic field is higher than that of the

Table 1. Main parameters of the IRC.

K-value		980 MeV
Number of sectors		4
Harmonics		7
Average radius	Injection	2.77 m
	Extraction	4.15 m
Velocity gain factor		1.5
Number of cavities	Main	2
	Flat-top	1
Cyclotron frequency		2.57-5.45 MHz

RRC. The temperature increase of the cooling water due to the main coils is calculated to be less than 10 degrees.

Manufacturing of the sector magnets is in progress at the Niihama works of Sumitomo Heavy Industries, Ltd. The machining of yoke plates and poles for four sector magnets has already been completed. Figure 2 shows a photograph of the lower yoke of the first sector magnet (E-sector) being assembled. Figure 3 shows the main coil of the sector magnet.

The first sector magnet will be completed in February of year 2000. Magnetic field measurement of the sector magnet will start from March of year 2000. Firstly, measurement for one sector magnet will be performed. After that, two sector magnets will be aligned with a configuration that is the same as the actual one. Then, field mapping of a 180 degrees region will be performed in order to measure the coupling effect of the sector magnets. The field mapper of the IRC is designed to be able to measure 360 degrees mapping

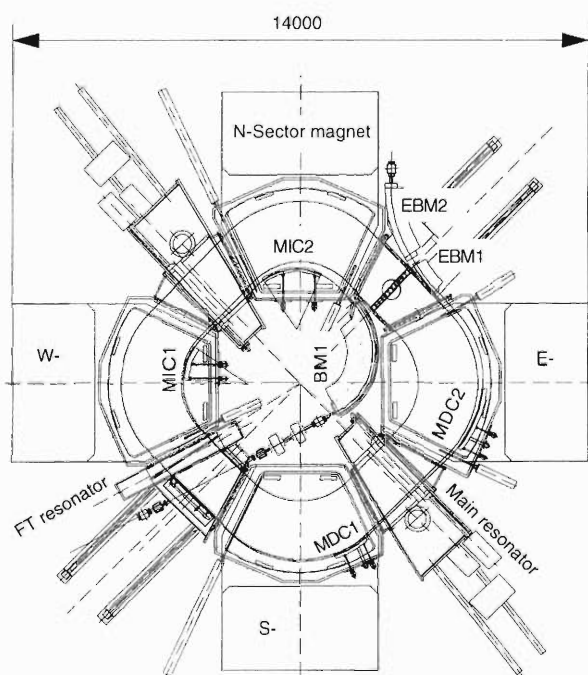


Fig. 1. Plan view of the IRC.

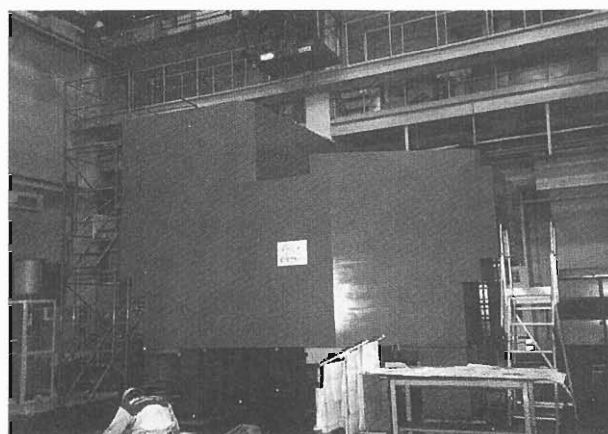


Fig. 2. Lower yoke of the E-sector magnet being assembled at Niihama works, Sumitomo Heavy Industries, Ltd.

\* Sumitomo Heavy Industries, Ltd.

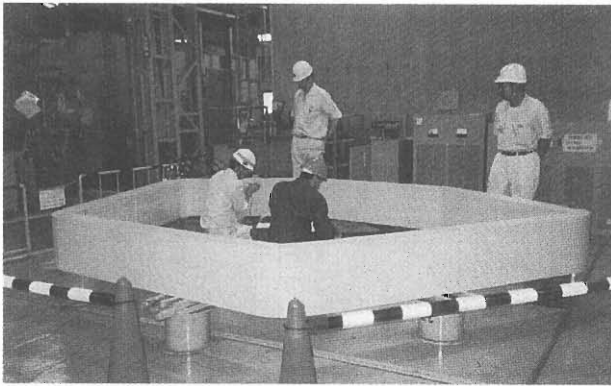


Fig. 3. Main coil for the sector magnet.

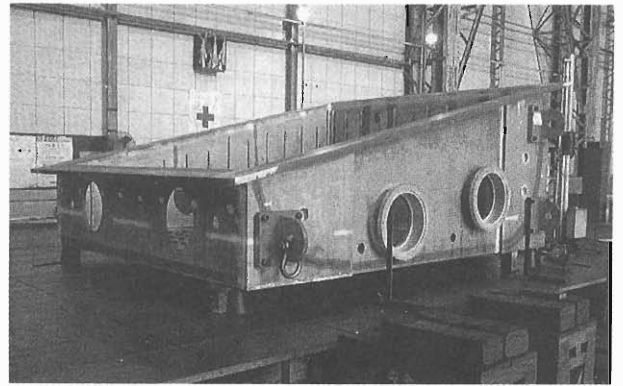


Fig. 4. Main resonator of the IRC.

after installation of the entire sector magnets into the RIKEN site.

Two types of resonators are adopted for the IRC: Two main resonators and one flattop resonator. The main resonators are of a single-gap type with flapping panels for changing the resonant frequency.<sup>3)</sup> Figure 4 shows the stainless steel wall of the main cavity being constructed. The flattop resonator is of a single-gap type with shorting plates. In order to realize ultra-high vacuum, a duplicated-wall structure is adopted.<sup>4)</sup> Manufacturing of the main resonators has been

started and will be completed in the summer of 2000.

#### References

- 1) Y. Yano et al.: Proc. 1997 Particle Accelerator Conf., Vancouver, 1997, p. 930 (1998).
- 2) T. Mitsumoto et al.: RIKEN Accel. Prog. Rep. **32**, 195 (1999).
- 3) N. Sakamoto et al.: Proc. 12th Symp. on Accelerator Science and Technology, Wako, 1999, p. 224 (1999).
- 4) T. Hiasa et al.: Proc. 12th Symp. on Accelerator Science and Technology, Wako, 1999, p. 293 (1999).

## Model Test of the RIKEN-IRC\* Main Resonator

N. Sakamoto, O. Kamigaito, Y. Miyazawa, T. Chiba, A. Goto, and Y. Yano

The intermediate-stage ring cyclotron, IRC, which is the first stage booster in the RIKEN RI beam factory,<sup>1)</sup> consists of four normal conducting sector magnets, two acceleration resonators and one flat-top resonator.<sup>2)</sup> The frequency range of the acceleration resonators is from 18.0 to 38.2 MHz. In order to obtain a sufficient turn separation as large as 6 mm at the extraction orbit, the acceleration voltage is required to be 1.2 MV/turn in the case of 38.2 MHz operation. The acceleration resonator is a single-gap-type resonator whose structure is basically the same as that of the Research Center for Nuclear Physics (RCNP), Osaka University, ring cyclotron. Its geometrical design has been optimized using a three-dimensional rf calculation code, MAFIA.<sup>3)</sup> In order to determine the accuracy of the calculated frequencies and the Q-values in comparison with the theoretical ones, a 1/5 scale model was built and test measurements were performed. A theoretical Q-value of the model is  $1/\sqrt{5}$  that of the actual resonator, while a resonant frequency is five times higher.

A schematic drawing of the model is shown in Fig. 1. A resonant frequency of the resonator is tuned by flapping two panels which are located symmetrically on the median plane. The calculated rf characteristics of the model are shown in Table 1.

In order to evaluate the Q-values accurately in comparison with the calculated ones, the mechanical design of the model was carefully carried out to simulate the structure of the actual resonator. To know the realistic

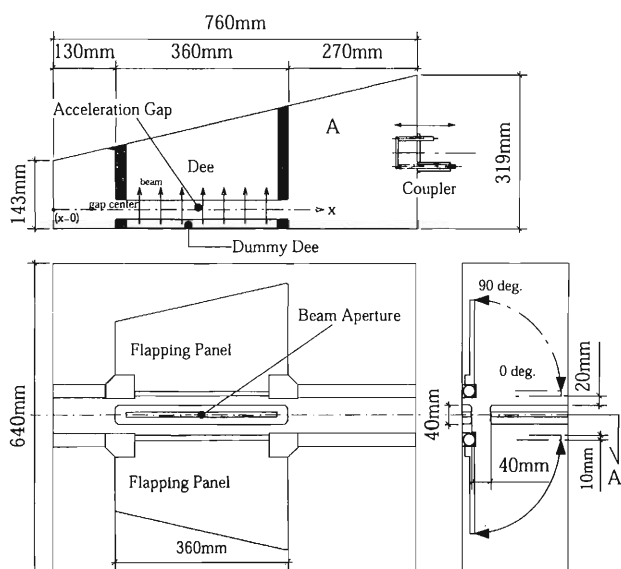


Fig. 1. Schematic drawing of the 1/5 scale model.

Table 1. The calculated resonant frequencies and Q-values using MAFIA.

Flapping panel	0 deg.	90 deg.
Frequency	89.8 MHz	193.6 MHz
Q-value	12970	16550

Q-values is crucial in determining the rf power and the coupler size of the actual resonator.

The conductive parts of the model were made of copper. The contact fingers and contact strips were used to reduce the resistivity between the conductive parts. The overall geometrical misalignment was less than 0.3 mm. The rf power was fed using an inductive coupler which was located at the center of the rear wall, as shown in Fig. 1. The resonant frequencies and the Q-values were measured using a network analyzer with an S-parameter test set (HP8753E). Two pickup loops were used, one for excitation and the other for detection. These loops were identical and were very weakly coupled to the resonator. Figure 2 shows the measured resonant frequencies and Q-values. The measured resonant frequencies were slightly high in comparison with calculated values (compare Tables 1 and 2). The Q-values were as large as 63–71% of the calculated values.

The coupler was an inductive type whose coupling could be varied by changing the cross section of the loop. A schematic drawing of the coupler for the model is shown in Fig. 3. A characteristic impedance of the coaxial part was set to be 50  $\Omega$ . By sliding the coupler position  $l = 14$ –35 mm, the input impedance of the resonator could be matched to 50  $\Omega$  and the

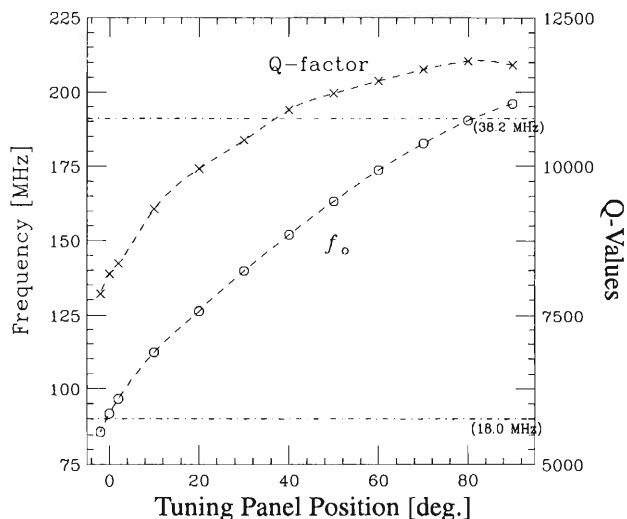


Fig. 2. Measured resonant frequencies and Q-values for the 1/5 scale model.

\* Intermediate-stage Ring Cyclotron

Table 2. Measured resonant frequencies and Q-values at the panel angles of 0 deg. and 90 deg.

Flapping Panel	0 deg.	90 deg.
Frequency	91.69 MHz	196.05 MHz
Q unloaded	8190 (63%)	11710 (71%)
loaded	4190	5840

Numbers in parenthesis indicate the ratio to the theoretical values listed in Table 1.

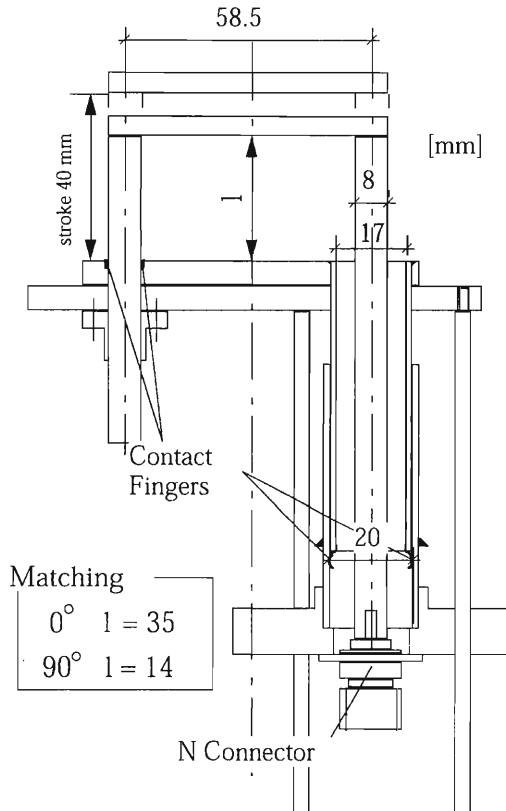


Fig. 3. Schematic drawing of the coupler.

$S_{11}$  was less than  $-50$  dB for the entire frequency range. The loaded Q-values were almost 50% of the unloaded ones (see Table 2). A measurement of the electric field distributions was performed using the perturbation method. A spherical field perturber ( $3/8''\phi$ ) made of Teflon was used. By integrating the field strength distribution along the beam orbit,

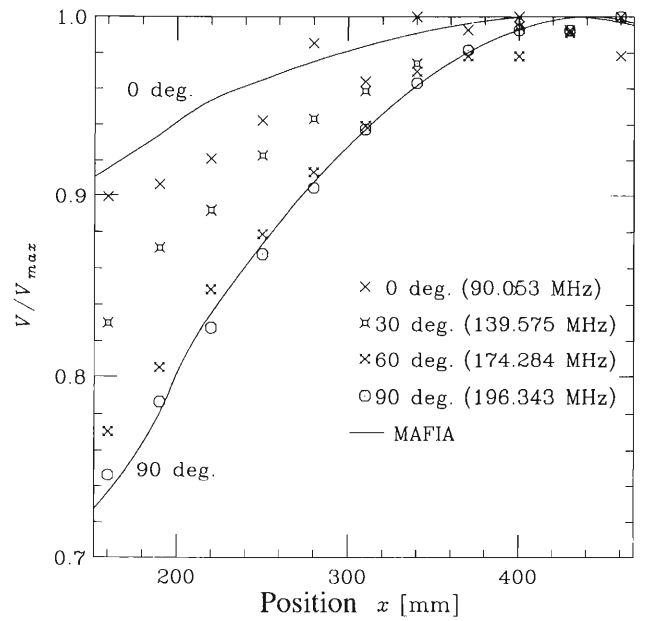


Fig. 4. Gap voltage distribution. Curves were obtained using MAFIA.

gap voltages were obtained, as shown in Fig. 4. The voltage distribution was found to be in good agreement with the MAFIA calculation. According to the result of the frequency measurement, a gap size between the flapping panel and the dee surface at the panel position of 0 deg. was reduced by 5 mm (original 100 mm  $\rightarrow$  new 95 mm) so as to reduce the lowest frequency. The size of the coupler was decided to be five times larger than the model coupler, that is, the margin of the coupling size is about 50%. The results of the model test are being considered in the design of the actual resonator which is now under construction.

#### References

- 1) Y. Yano et al.: Proc. 1997 Particle Accelerator Conf., Vancouver, 1997, p. 930(1998).
- 2) N. Sakamoto et al.: Proc. 15th Int. Conf. on Cyclotrons and Their Applications, Caen, 1998, p. 223(1999).
- 3) The MAFIA Collaboration, User's Guide MAFIA Version 4.0, CST GmbH, Luteschägerstraße 38, D-64289, Darmstadt, Germany.

## Status of the SRC for the RIKEN RI Beam Factory

A. Goto, H. Okuno, T. Kawaguchi, J. Ohnishi, T. Mitsumoto, T. Tominaka, S. Fujishima, J. W. Kim, K. Ikegami, N. Sakamaoto, K. Sugii, Y. Miyazawa, O. Kamigaito, M. Kase, T. Wada, T. Morikawa, T. Chiba, and Y. Yano

The layout of the SRC (Superconducting Ring Cyclotron) has been changed from the previous design, as shown in Fig. 1. The changes are as follows.

(1) Injection and extraction are carried out in the same valley chamber.

(2) An electrostatic inflection channel (EIC) and an electrostatic deflection channel (EDC) are set in opposite valley chambers, so that the injection beam does not pass through holes of both channels but only the hole of EIC.

(3) The flat-top resonator is placed beside one of the four acceleration resonators in the same valley chamber.

Fabrication of the prototype sector magnet is continuing. As of December 1999, both the upper and lower cold masses, including main coils, trim coils and poles, have been completed. Figure 2 shows a photograph of the upper and lower cold masses that have been preliminarily assembled. The cryostat is nearly complete and the assembly of the cold masses in the cryostat is about to start. Lower and side yokes have been installed at the factory test site. Scheduling of a

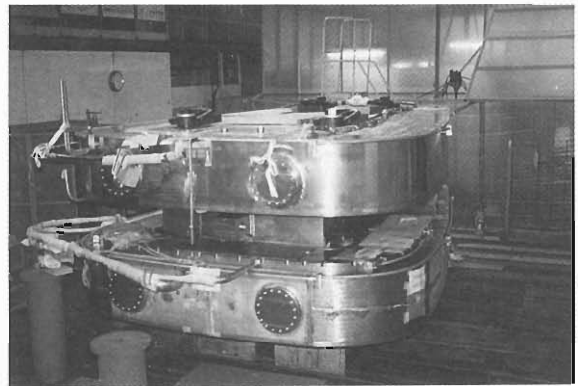


Fig. 2. Photograph of upper and lower cold masses that have been preliminarily assembled.

test of the prototype sector magnet has been delayed due mainly to the electrical shorts in the main coil; a cool-down test of the entire system, as well as the measurement of magnetic fields, has been rescheduled to take place by the summer of 2000.

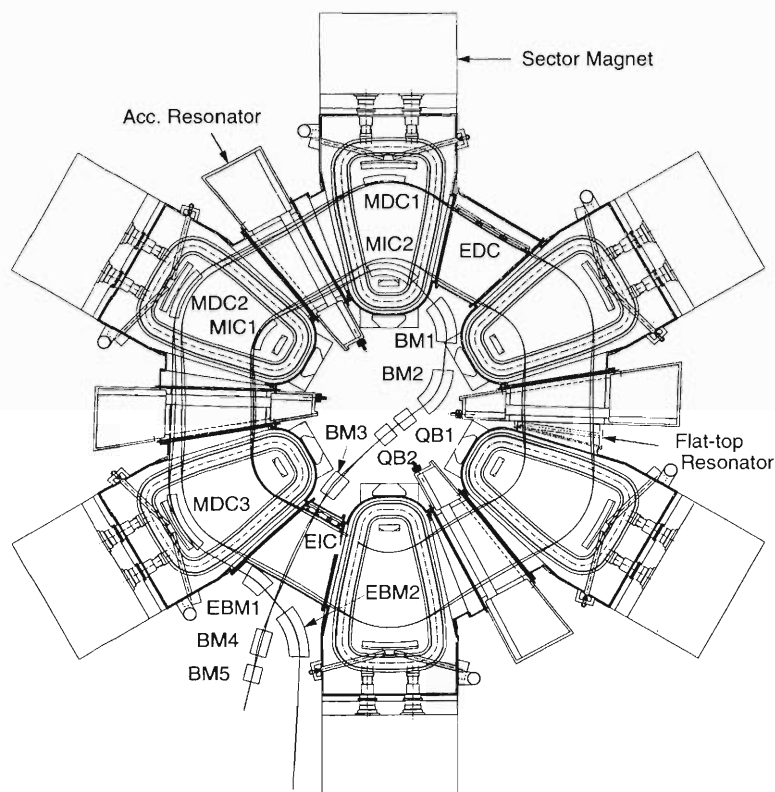


Fig. 1. Plan view of the redesigned SRC.

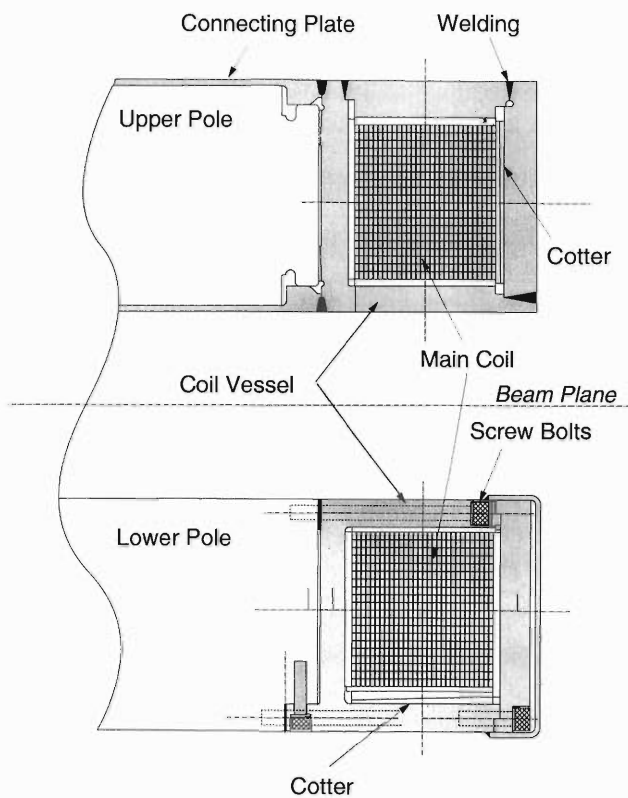


Fig. 3. Cross-sectional view of the main coil, coil vessel and cold pole.

We encountered some serious problem in the course of the fabrication of the prototype sector magnet; electrical shorts were found in both the upper and lower main coils when the coil winding was almost completed, as well as in the trim coil. For details, see Ref. 1. We have made a major change in the method of fixing the main coil vessel to the pole of the prototype sector magnet. The “hooks” anchoring the main coil vessel to the pole in the upper cold mass have been replaced by two connecting plates covering the surfaces of the pole, as shown in Fig. 3.

The second international technical advisory committee (TAC) for the review of the sector magnet was held in May 1999.

Design and/or R&D of other components of the SRC, such as a superconducting injection channel and an rf resonator, are also being carried out. A prototype of superconducting inflection channel MIC2 is being fabricated, and will be tested in the prototype sector magnet. A 1/5-scale model of the resonator for the IRC, which is quite similar to that of the SRC, was fabricated and tested. A coaxial rf resonator has also been produced in order to develop rf contacts that can endure high current density.

#### References

- 1) T. Kawaguchi et al.: RIKEN Accel. Prog. Rep. **33**, 214 (2000).

## Development and Construction of the SRC Sector Magnets

T. Kawaguchi, H. Okuno, A. Goto, J. Ohnishi, T. Tominaka, T. Mitsumoto, and Y. Yano

Six superconducting sector magnets<sup>1)</sup> are to be incorporated into the superconducting ring cyclotron (SRC)<sup>2)</sup> for the RIKEN RI beam factory. A full-scale prototype magnet<sup>3)</sup> is currently under construction. The construction status of the prototype at December 1999 is as follows: Two sets of the superconducting main and trim coils were completed; the vacuum vessel was completed; the 80 K thermal shield is under production; 14 sets of the thermal insulating support rods for fixing the coil position were completed; a group of sliced plates for the yoke, with a total weight of 730 tons, was completed and is now being assembled at a cold test facility. The assembly and the cooling/excitation test of the prototype will be completed in the spring and summer of 2000, respectively.

During prototype construction, we experienced some problems. The first problem was the occurrence of electric turn-shorts in the main coils. In the lower main coil, turn-shorts were found at 12 points after the closing of the bolt-type vessel.<sup>3)</sup> Uncoiling of the shorted lower coil and rewinding using the same superconducting wire were adopted as a remedy. As a result, it took another four months to obtain a satisfactory coil. Upon the uncoiling, all of the turn-shorts were observed in both turn-transition and layer-transition regions shown in Fig. 1. We concluded that the turn-shorts occurred because of the following causes. (1) The transition regions of the wire, initially formed into the designed shape by a forming tool, were stretched and deformed by winding tension. (2) The local coil size at the transition regions became larger than the size at the normal region due to the unmatched transition shape. (3) Coil pressing of the lower coil was carried out so as to obtain the same coil size. Thus, the transition regions were over pressed and some of the transition regions made the turn-shorts. The im-

proved items applied to the lower coil are as follows. (1) The transition regions of the wire were initially over formed with a change of the forming tool shape, so as to be of the designed shape after the application of winding tension. (2) The winding tension was decreased from 260 kg to 170 kg. (3) The electric insulation of the transition regions was reinforced. (4) A continuous electric inspection was performed during the entire winding process. These improvements should be applied to the serial production of the SRC sector magnets.

In addition to those in the main coils, turn-shorts were found at two points in the upper coil after the final welding of the upper coil vessel. The upper coil was wound by a different company than the lower coils. The shorts were also located in the transition regions. The repair of the shorts was carried out by inserting additional insulating film between the shorted turns through two holes which were drilled in the coil vessel for the repair.

The second problem was regarding the structure design of the weld-type upper coil vessel. The maximum stress at the "Hook-connection"<sup>3)</sup> in the cold-pole was calculated to be 370 MPa against the main coil's electromagnetic force. On the other hand, the measured result of the fatigue strength of pure iron which was used as the cold-pole material, showed the minimum strength to be 510 MPa after 10000 cycles of load at 78 K. The safety factor of  $510/370 = 1.34$  was much less than our criterion of 2.0. After some studies and discussions, the connection structure of the prototype was finally changed to the "Connecting-plate" shown in the figure of Ref. 4.

The third problem was again turn-shorts, this time in a trim coil. These shorts were caused by the me-

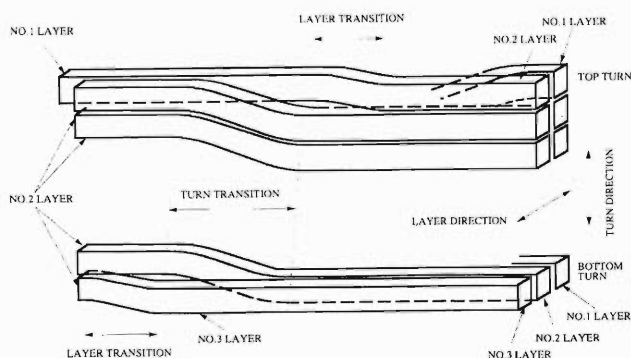


Fig. 1. Schematic drawing of the transition regions in the main coil winding.



Fig. 2. The proto-trim-coil vessel after the closing weld. The numerous circular marks indicate the stay-rod welds.

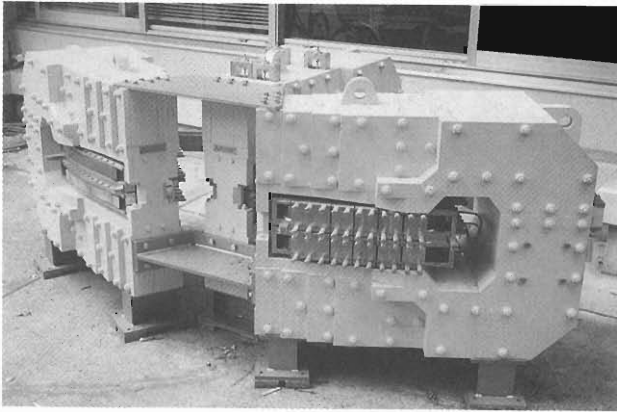


Fig. 3. The three-sector arrangement of the 1/6-scale test magnets for the magnetic force measurement.

chanical deformation of the trim coil vessel due to the stay-rod welds shown in Fig. 2. Many turn-shorts were found in one of the six sub-coils. In the end, this one sub-coil was electrically bypassed to allow the use of the five sound sub-coils. As the basic improvement for this problem has not yet been applied to the proto-trim-coil, the solution should be studied before the manufacture of the SRC sector magnets.

Other R&D works are mainly as follows.

(1) Measurement of the unbalanced magnetic forces  
Three sets of 1/6-scale Cu/iron magnets were fabricated, and the unbalanced magnetic forces between the coil/pole and yoke were measured in both one-sector and three-sector arrangements. Figure 3 shows a photograph of the three-sector arrangement. These test magnets were cooled to 78 K and excited in pulse for 1 to 2 seconds. The maximum magnetic field reached 4.0 T, which corresponds to 90% of the maximum value of the actual superconducting sector magnet. The measured results can be converted to the value for the full-scale magnet by using a scaling law. Table 1 shows the converted values in comparison with the calculated ones.

(2) Estimation of the eddy current loss in the cold-pole  
For the study of the thermal effects on the helium

Table 1. Comparison of the calculated and measured results of the unbalanced magnetic forces at 6 MA/magnet in the case without trim coils.

Direction	Arrangement	Calculated	Measured
Radial	1-sector	-56 tons	-30 at 4.5 MA *1
Radial	3-sector	Not calculated	37 tons
Radial	6-sector	100 tons	72 tons *2
Vertical	1-sector	7 to 12 tons/mm	8 tons/mm *3
Azimuthal	1-sector	Not calculated	-0.8 ton/mm *3
Azimuthal	3-sector	Not calculated	-0.15 ton/mm *3

\*1 The maximum occurred at 4.5 MA in the measurement.

\*2 This is an estimated value from the three-sector measurement.

\*3 Plus indicates decentering and minus recentering force.

cooling system,<sup>1)</sup> the eddy current loss in the cold-pole at the time of magnetic field change was estimated. The electric resistance of pure iron was measured at 4.2 K in 0 to 4 T, and a value of  $1.0 \times 10^{-8}$  to  $1.2 \times 10^{-8}$  Ohm-m was obtained as the specific resistance. Using this resistance number, the eddy current losses under two conditions were calculated. In the case of current ramping from 0 A to 5000 A (corresponding to 4.5 T) in 2 hours, the average eddy current loss was calculated to be 22 W per magnet. Also, in the case of current break with a time constant of 52 seconds for emergency safety operation at the magnet failures such as coil quench, the total loss during the current break was calculated to be 4 MJ per magnet. This value corresponds to 6% of the total magnetic stored energy of 65 MJ. These estimated values are not thought to be a cause of serious problems for the helium cooling system.

#### References

- 1) T. Kawaguchi et al.: RIKEN Accel. Prog. Rep. **32**, 201 (1999).
- 2) A. Goto et al.: RIKEN Accel. Prog. Rep. **32**, 193 (1999).
- 3) T. Kubo et al.: RIKEN Accel. Prog. Rep. **31**, 210 (1998).
- 4) A. Goto et al.: RIKEN Accel. Prog. Rep. **33**, 212 (2000).

## Quench Analysis of Stagnant Normal Zone in the RIKEN Prototype Sector Magnet

J.-W. Kim, A. Goto, and Y. Yano

The prototype sector magnet under construction at RIKEN is designed to be cryostable with cooling by pool boiling. However, a quench may occur when conditions for cryostability is not met in the actual coil vessel. A likely quench scenario in a cryostable coil, besides accidents and unexpected quenches, is that heat generation larger than critical quench energy initiates a quench in a poorly cooled region where a section of conductor is exposed to helium vapor.

The effects of existence of uncooled conductor were studied using the one-dimensional heat diffusion equation. It is assumed that a normal conducting region is initiated in the  $2L$  long section of uncooled conductor, and that the initial normal conducting region has no cooling throughout the quench propagation. The equation has a symmetry point at zero of the  $x$ -coordinate along the conductor length as given by

$$C(T)A \frac{\partial T}{\partial t} = \frac{\partial}{\partial x} \left( K(T)A \frac{\partial T}{\partial x} \right) + i(T)^2 \rho(x, T), \quad x < L, \quad (1)$$

$$C(T)A \frac{\partial T}{\partial t} = \frac{\partial}{\partial x} \left( K(T)A \frac{\partial T}{\partial x} \right) + i(T)^2 \rho(x, T) - h(T)(T - T_b), \quad x > L, \quad (2)$$

where  $C(T)$  is the specific heat of conductor,  $K(T)$  is the thermal conductivity,  $A$  is the cross sectional area,  $\rho(x, T)$  is the resistivity,  $h(T)$  is the heat transfer coefficient between the conductor and LHe, and  $T_b$  is the LHe bath temperature. The temperature distribution corresponding to a normal conducting domain is plotted in Fig. 1. It is prescribed in the ohmic heating term  $i(T)^2 \rho(x, T)$  that the sharing of current in the temperature range between  $T_b$  and conductor critical

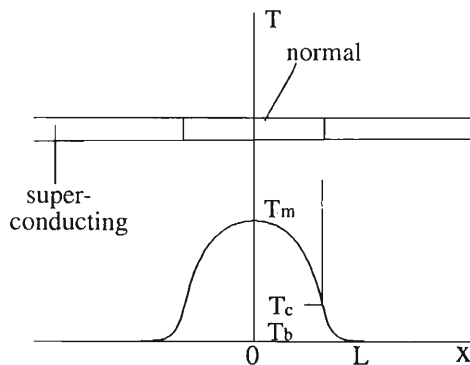


Fig. 1. Temperature distribution in a normal conducting domain used for the heat diffusion equation.

temperature  $T_c$  is linear with temperature.<sup>1)</sup> The heat transfer is thought to be static because of the slow propagation of normal conducting region in the pool-boiling coil.

Because the cooling can deteriorate also in the regions outside the initially uncooled section, degradation of the cooling was taken into account by adapting cooling efficiency ( $\epsilon$ ) to the heat transfer term as  $\epsilon h(T)(T - T_b)$ . The resultant partial differential equations were solved using the NAG Fortran Library employing a finite difference method.

There is a minimum uncooled length of the conductor, beyond which a normal conducting region can propagate at small perturbations, i.e. in the order of  $10^4$  J/m<sup>3</sup> for the conductor of the prototype magnet. Critical lengths of the uncooled conductor ( $L_c$ ) were calculated as a function of  $\epsilon$  at the maximum excitation with a current of 5 kA as shown in Fig. 2. If the uncooled section is shorter than the critical length, minimum quench energies are appreciably high, so that quench is normally unexpected. When  $L$  is shorter than  $L_c$ ,  $T_m$ 's are plotted in Fig. 3 for two given cooling efficiencies 1 and 0.5. The minimum quench energies are in the order of one hundred J, and the energy densities are over  $10^6$  J/m<sup>3</sup>, which are considered sufficiently large for the coil to be cryostable.

Figure 4 shows quench propagation initiated from a section of the uncooled conductor slightly longer than  $L_c$ . The cooling efficiency is set to be 0.5. It is clearly shown that the normal zone propagates slowly, namely a growing stagnant-zone is established. Part of the conductor is then overheated. Quench detection using

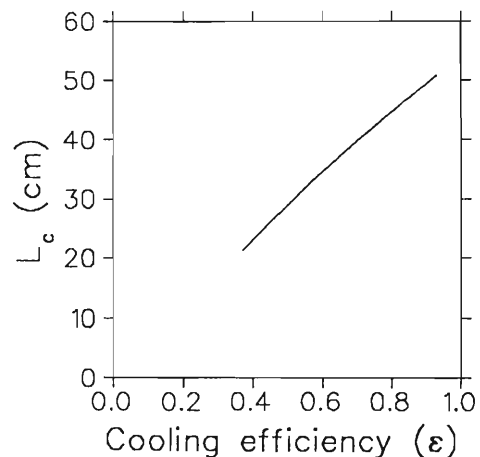


Fig. 2. Critical lengths of the uncooled conductor versus cooling efficiency.

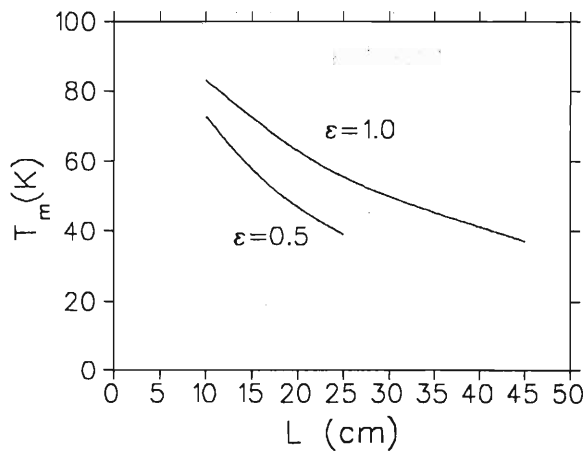


Fig. 3. Temperature at the center of the normal conducting zone as a function of uncooled conductor length, when  $L$  is shorter than  $L_c$ , for two different cooling efficiencies.

voltage taps cannot be facilitated in this case because of low levels of resistive voltage drop. For the prototype it appears that the supports and insulators laid in the coil vessel are configured to avoid a wide-range bubble trap.

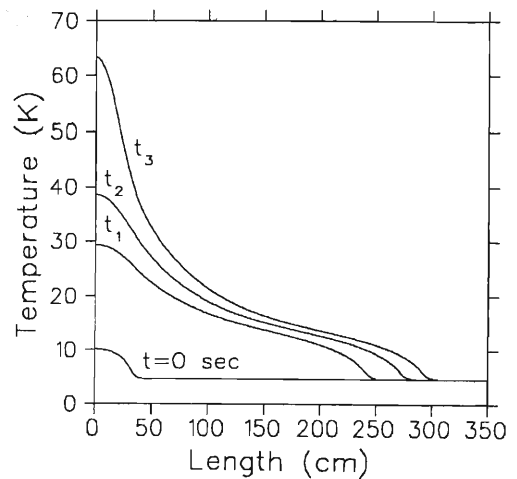


Fig. 4. Propagation of the normal conducting zone when  $L$  is slightly longer than  $L_c$ . Temperature distributions are plotted along the conductor length at different times:  $t_1 = 20$  s,  $t_2 = 40$  s, and  $t_3 = 60$  s.

References

- 1) M. Wilson: *Superconducting Magnets*, (Oxford University Press, 1983).

## Analysis of the Injection and Extraction Systems for the RIKEN Superconducting Ring Cyclotron

S. Fujishima, H. Okuno, A. Goto, and Y. Yano

Design of the injection and extraction systems for the RIKEN Superconducting Ring Cyclotron (SRC) is in progress.<sup>1)</sup> The purpose of the present analysis is the optimization of the layouts and specifications of the injection and extraction elements of the SRC. In the analysis, a lot of care was taken especially to minimize not only the required fields of the elements but also the differences between the trajectories in the elements.

The sector magnets of the SRC generate strong field of 4.3 T at the maximum, and also generate a stray field in the valley originated from saturation of the iron yokes. This stray field gets up to  $-0.6$  T at the maximum and depends non-linearly on the magnetic rigidities of the beams. Thus, the trajectories of various beams differ considerably from each other. Large difference between the trajectories requires wide bore of the element. Besides, the injection and extraction elements should be installed in a small space limited with the vacuum chambers of the sector magnets. Because of the space limitation and high rigidity of the beam, the injection and extraction elements should generate considerably high fields. These difficulties make the design of the injection and extraction systems quite challenging.

Table 1 shows the energies and magnetic rigidities of three typical beams. The beam of  $^{16}\text{O}^{7+}$  (1) has the lowest magnetic rigidity. On the other hand, the beam of  $^{238}\text{U}^{58+}$  has the highest one. Between these two beams, the difference of trajectories is most remarkable. The beam of  $^{16}\text{O}^{7+}$  (2) requires the highest electrostatic fields of the electrostatic channels.

In the first stage of the analysis, magnetic fields of the sector magnets were calculated with a three-dimensional computer code, "TOSCA". However, the design of the normal-conducting trim coils of the sector magnets has not been optimized perfectly, so the calculated fields of the sector magnets include about

Table 1. Energies and magnetic rigidities of typical beams.

	Energy [MeV/u]		$B\rho$ [Tm]	
	Inj.	Ext.	Inj.	Ext.
$^{16}\text{O}^{7+}$ (1)	74.2	200	2.89	4.90
$^{16}\text{O}^{7+}$ (2)	126.7	400	3.83	7.25
$^{238}\text{U}^{58+}$	58.0	150	4.57	7.52

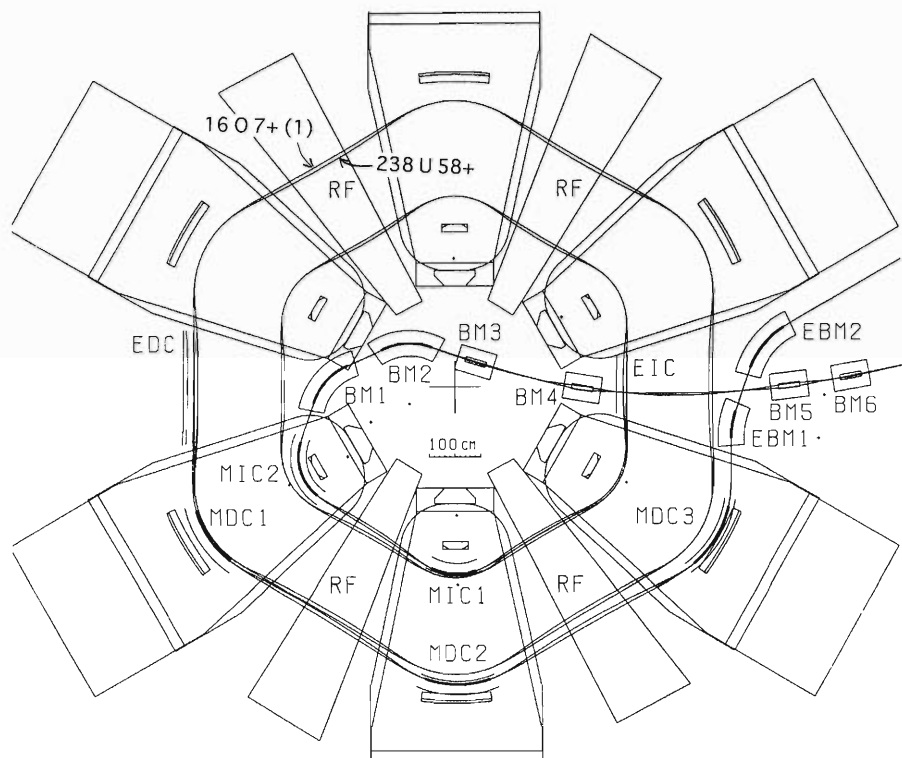


Fig. 1. Schematic layout of the elements and trajectories of two typical beams.

Table 2. Specifications of the injection and extraction elements.

	Radius [cm]	Angle [deg.]	Length [cm]	B or E (max.) [T],[kV/cm]
EIC	928~3217	variable	101.7	100
MIC1	112.7	45.5	89.5	0.30 (Normal)
MIC2	95.6	69.3	115.5	1.12 (Super)
BM1	117.0	49.0	100.1	4.70 (Super)
BM2	117.0	49.0	100.1	4.40 (Super)
BM3	straight	-	49.6	0.25 (Super)
BM4	straight	-	49.6	1.36 (Super)
BM5	straight	-	49.6	0.90 (Super)
BM6	straight	-	49.6	-1.00 (Super)
EDC	1578~3611	variable	212.5	-105
MDC1	185.0	37.0	119.5	-0.15 (Normal)
MDC2	190.0	39.0	129.3	-0.27 (Normal)
MDC3	203.5	36.8	130.7	-0.51 (Normal)
EBM1	169.4	17.7	52.3	-4.00 (Super)
EBM2	152.4	39.1	104.0	-4.54 (Super)

0.3% error. Error of the field causes position error to the injection and extraction trajectories. To correct relative position error of the trajectories, the energies of the injection or extraction beams were slightly changed as the length of the first or the last equilibrium orbits become equal to the design value, respectively. And then, to trace the beam trajectories, the equation of motion was solved with using the Runge-Kutta-Gill method. In the calculation, the electric or magnetic field of each element was superimposed on the field of the sector magnets.

Figure 1 shows a schematic layout of the injection and extraction elements, and shows the trajectories of two typical beams of  $^{16}\text{O}^{7+}$  (1) and  $^{238}\text{U}^{58+}$ . This layout has not been optimized completely, so it may be modified partly. Because of the stray field in the valley, two trajectories differ considerably from each other. The injection system consists of six bending magnets (BM1-BM6), two magnetic inflection channels (MIC1 and MIC2), and an electrostatic inflection channel (EIC). The extraction system consists of two

Table 3. Differences of the trajectories and bores in the elements.

	Difference [mm]	Bore [mm] verti. × horiz.
EIC (movable)	61	12 (horiz.)
MIC1	5	30 × 35
MIC2~BM2	≐ 13	30 × 40
BM3~BM6	≦ 70	30 × 100
EDC (movable)	75	12 (horiz.)
MDC1~EBM2	≐ 13	30 × 40

bending magnets (EBM1 and EBM2), three magnetic deflection channels (MDC1, MDC2 and MDC3), and an electrostatic deflection channel (EDC). All MICs and all MDCs are installed between upper and lower coils of the sector magnets. The injection beams are introduced crossing the EIC, so that the EIC has a hole to pass the beams. To minimize the hole diameter, each trajectory was adjusted to cross at the same point on the electrode of the EIC.

Table 2 shows the specifications of the injection and extraction elements. The MIC1 and all MDCs consist of normal-conducting coils. The MIC2, all BMs and all EBMs consist of superconducting coils. The BM1 and BM2 have identical structure and size to reduce fabrication costs. For the same reason, the BM3, BM4, BM5 and BM6 are identical. Each magnetic element consists of main dipole coils and compensation coils to suppress the fringe field on the first or the last equilibrium orbits. Gradient-field-coils are additionally built in the MIC2, BM1 and BM2 to adjust the injection beam envelopes. The length of each element was determined in consideration of the balance between the difference of the trajectories in the element and the required field of the element. Table 3 shows the differences of the trajectories and bores in the elements.

#### References

- 1) S. Fujishima et al.: Proc. 12th Symp. on Accelerator Science and Technology, Wako, p. 435 (1999).

# Superconducting Magnetic Channel for the RIKEN Superconducting Ring Cyclotron

H. Okuno, S. Fujishima, T. Tominaka, J.-W. Kim, J. Ohnishi, T. Kawaguchi, M. Okamura, A. Goto, and Y. Yano

A six-sectored superconducting ring cyclotron (SRC) is designed to boost the energy of the ion beams available from the Intermediate Ring Cyclotron (IRC).<sup>1)</sup> The extraction energies of the SRC beams will be 400 MeV/nucleon for light ions such as carbon and 150 MeV/nucleon for heavy ions such as uranium with an intensity of 1 pμA. Figure 1 shows the trajectories of injected and extracted beams in the SRC consisting of six sector magnets<sup>2)</sup> and four acceleration resonators.<sup>3)</sup> Among the elements of the injection and extraction systems, the MIC2, BM1-2, EBM1-2 are difficult to design and further research and development are required, because their coils are curved very tightly and the required fields in the coils are as high as 6 T and because the spaces for the installation are limited. In this report, the plan and status of R&D for the MIC2 is described.

The main parameters of the MIC2 are listed in Table 1. It needs to generate a magnetic field of about 1 T on the base field of 4 T of the sector magnet, along the beam trajectory, which is curved with a curvature of about 1 m. Figure 2 shows the proposed cross section and 3D-view of the coil structure. Six current sheets (center coils and half of side coils) located close to the

Table 1. Main specifications of the MIC2.

Item	Value
Type	Iron free, Active shield type
Coil configuration	Center coil, Side coil
Required field	~ 1.12 T
Required gradient field	About 2T/m
Maximum field in the coil	6.12T
Homogeneity	$1 \times 10^{-3}$
Beam bore	40 (H) x 30 (V) mm <sup>2</sup>
Radius	955 mm
Angle	73 degree
Fringe field at the 1 <sup>st</sup> . E.O.	< 100 gauss

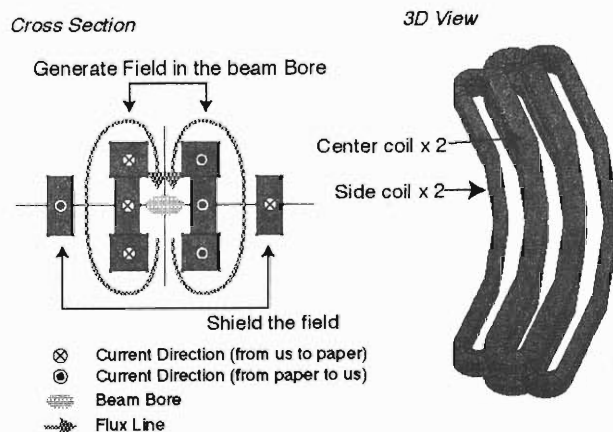


Fig. 2. Coil structure of the MIC2.

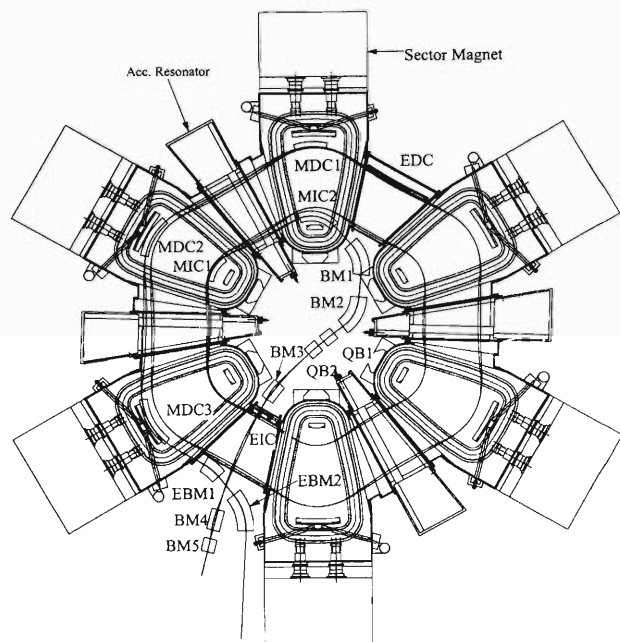


Fig. 1. A schematic layout of injection and extraction elements for the SRC along with trajectories of the injected and extracted beams.

beam axis generate a magnetic field in the beam bore, and the other two current sheets (half of side coils) generate a field that cancels the fringe field from the six current sheets. Such configurations of the current sheets can realise the structure of coils that need not be bent up at the ends of the channel, which makes coil winding and coil supporting easier. The overall current density is required to be about 150 A/mm<sup>2</sup> to achieve the required field for the MIC2. Rectangular monolithic (0.8 mm x 2.4 mm) wire was adopted for well-aligned winding. The conductor was coated with polyimide of 50 μm in thickness for electrical insulation. Polyimide was adopted because of its strength against radiation.

Coil winding is one of the key problems for the MIC2 production because the coils of the MIC2 have negative curvature, which cannot be wound with any tension. The winding method shown in Fig. 3 was adopted. In

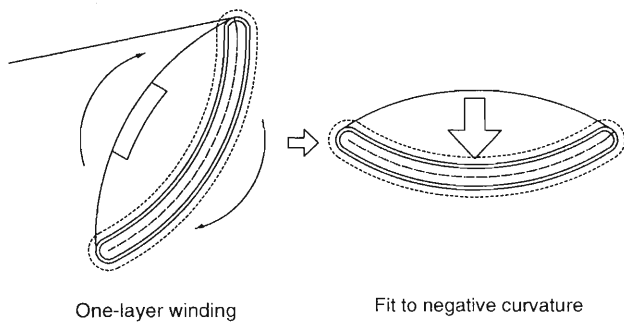


Fig. 3. Concept of the winding.

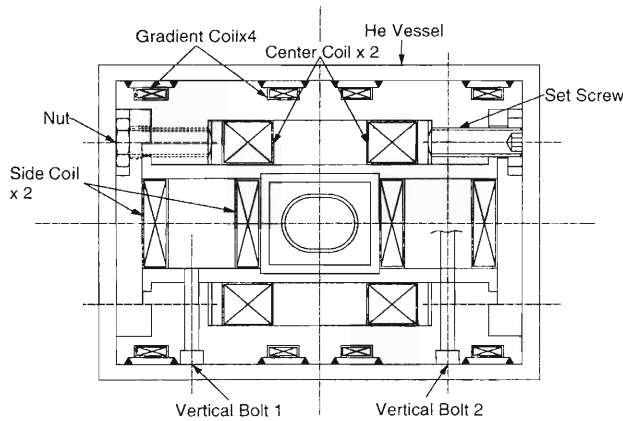


Fig. 4. Coil support of the MIC2.

the first step, the coil is wound into a shape with tension, which has no negative curvature. The circumference of the coil should be the same as that of the final shape of the MIC2 coil. After winding of one layer, the layer is pushed to the mandrel to form the proper shape of the coil. The merit of the method is that the time required for winding can be shortened without a decrease in performance. The coils are mainly supported in the horizontal and vertical directions with a pair of continuous clamps and bolts, respectively. The pre-stress required to maintain the coil compression when the magnet is excited is provided by set-screw bolts, a nut at the end of the set-screw bolt and vertical bolts as shown in Fig. 4. The support structure was adopted since so many zigs are not necessary to press the coils. Ti will be used for the inner mandrel of the center coil to decrease the degradation of the stress of the coil.

Two coils which simulate the center coils of the MIC2 were produced and are being tested. Their coil size, winding method/winding structure, support

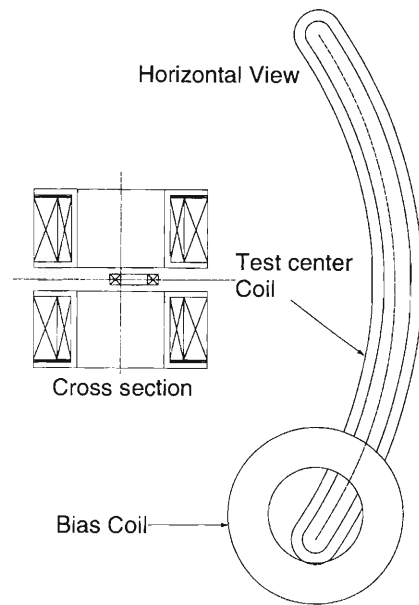


Fig. 5. A coil configuration for the test center coil.

Table 2. Preliminary results of the test of the first test coil for the MIC2. The operational condition is also indicated in the last column.

No.	Bias Field (T)	Current (A)	Field in the Coil (T)	jooverall (A/mm <sup>2</sup> )	Comment
1	0	500	2.7	222	No Quench
2	2	500	4.5	222	No Quench
3	4	460	6.2	204	Quench
4	4	550	6.7	244	No Quench
5	0	800	4.2	356	No Quench
Operation	4	340	6.5	150	

structure were designed to be as close as possible to those of the real one. The coils are tested in the field generated with a bias split coil in order to simulate the real operation as shown in Fig. 5. Table 2 shows a brief preliminary result for the first coil which was already tested. The result is promising because the quench current is fairly larger than the operational current. Fabrication and tests of the other coil are in progress.

#### References

- 1) T. Mitsumoto et al.: RIKEN Accel. Prog. Rep. **33**, 208 (2000).
- 2) T. Kawaguchi et al.: RIKEN Accel. Prog. Rep. **33**, 214 (2000).
- 3) N. Sakamoto et al.: RIKEN Accel. Prog. Rep. **33**, 224 (2000).

# Helium Cooling System of RIKEN Superconducting Ring Cyclotron

K. Ikegami, T. Kawaguchi, H. Okuno, M. Ohtake, A. Goto, and Y. Yano

A superconducting ring cyclotron (SRC) is to be built in the RIKEN RI-Beam Factory Project as one of the post accelerators of the existing K540 ring cyclotron.<sup>1)</sup> The SRC is designed to have a K-value of 2500 MeV, and consist of six superconducting sector magnets. The cold part of each sector magnet consists of superconducting main coils, cold poles and superconducting trim coils, which are installed in a single cryostat. The superconducting active shield coils of a Helmholtz coil type will be installed outside of the SRC to decrease leakage of magnetic fields produced by the SRC.<sup>2)</sup> Figure 1 shows a plane view of the SRC and active shield coils, together with the injection and extraction systems.

The injection system of the SRC consists of five bending magnets (BM1, BM2, BM3, BM4, and BM5), two magnetic inflection channels (MIC1 and MIC2) and an electrostatic inflection channel (EIC). The extraction system consists of two bending magnets (EBM1 and EBM2), three magnetic deflection channels (MDC1, MDC2 and MDC3) and an electrostatic deflection channel (EDC).<sup>3)</sup> Five magnets in the injection system (MIC2, BM1, BM2, BM3, BM4, and BM5) and two magnets in the extraction system (EBM1 and EBM2) are superconducting.

Figure 2 shows a cooling system for the SRC and active shield coils. The cooling system will be a closed-circuit system without liquid nitrogen. It consists of

a refrigerator, the cryostat of the SRC and the active shield coils, three compressors and five buffer tanks.

The refrigerator has a capacity of 850 W for the cooling of cold mass at 4.5 K, and 5000 W for the cooling of thermal shields at 70 K. The cooling capacity

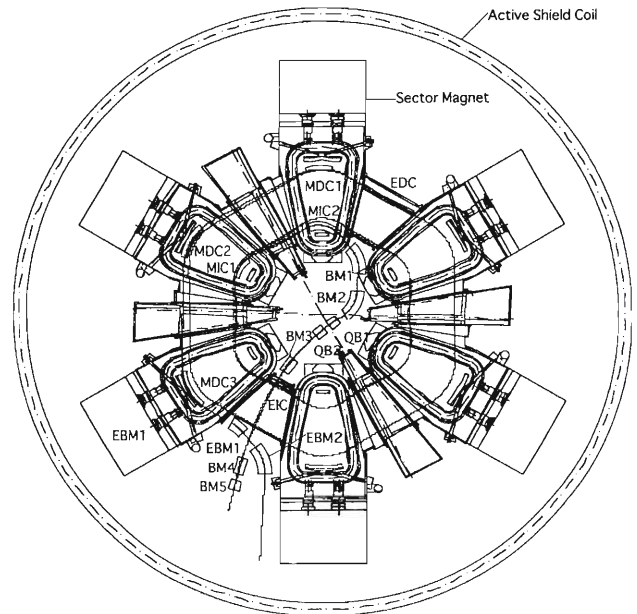


Fig. 1. A plane view of the SRC and active shield coils.

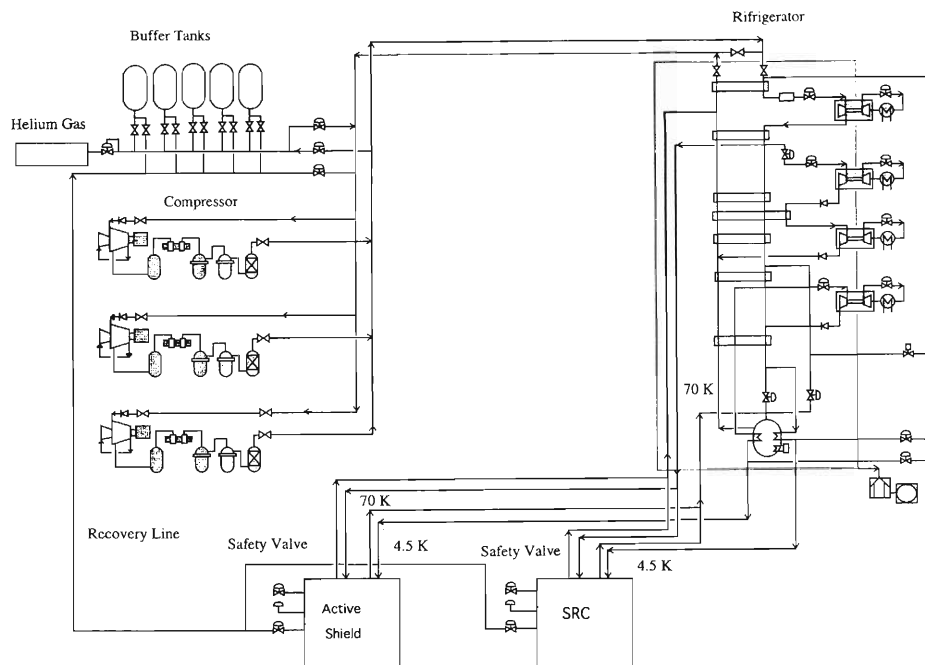


Fig. 2. The cooling system for the SRC with an active shield.

for current leads is 70 l/h. The coil vessels which accommodate the main and trim coils are mechanically designed assuming a maximum pressure of 0.5 MPa. The cold mass weight of the six sector magnets is 360 tons. It will take 45 days to cool them from room temperature to 4.5 K. Three compressors will be operated in this case. After the cooling is finished, one of the three compressors will be stopped and maintained as a standby. Each buffer tank has a volume of 100 m<sup>3</sup> and is connected through air valves to the compressors and the recovery tube line, as shown in Fig. 2. A recovery tube line will be used to introduce evaporated helium gas into the buffer tanks if an electric power failure suddenly happens. The active shield coils will be cooled down to 4.5 K by the forced cooling method, in which supercritical helium with a pressure of 1.2 MPa is used.

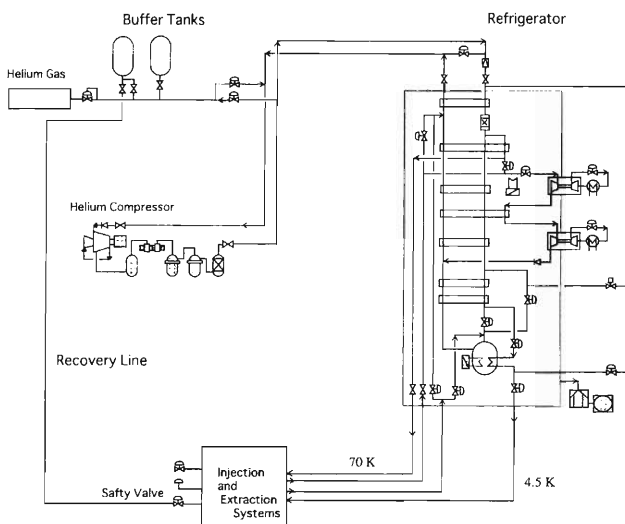


Fig. 3. The cooling system for the injection and extraction systems.

Table 1. Cooling capacities of refrigerators for the sector magnets and active shield coils, and the injection and extraction systems.

Capacity	Sector magnets and active shield coils	Injection and extraction systems
Coils at 4.5 K ( W )	850	160
Thermal shield at 70 K(W)	5000	1000
Current lead ( l/h )	70	12

The coil vessels of superconducting magnets in the injection and extraction systems will be designed assuming a maximum pressure of 0.3 MPa. Because the maximum pressure and the cooled volume of the magnets are small compared with those of the SRC, another cooling system will be used for the injection and extraction systems. Figure 3 shows the cooling system for the injection and extraction systems. The cooling system consists of a refrigerator, the cryostat of the magnets, a compressor and two buffer tanks. The refrigerator has a capacity of 160 W for cooling at 4.5 K, and 1000 W for the cooling of thermal shields at 70 K. The cooling capacity for current leads is 12 l/h. Each buffer tank has a volume of 50 m<sup>3</sup> and is connected through air valves to the compressor and the recovery tube line. The cooling capacities of the refrigerator for the sector magnets and active shield coils, and the injection and extraction systems are listed in Table 1.

#### References

- 1) A. Goto et al.: RIKEN Accel. Prog. Rep. **32**, 193 (1999).
- 2) J. Ohnishi et al.: RIKEN Accel. Prog. Rep. **32**, 205 (1999).
- 3) H. Okuno et al.: Proc. 12th Symp. on Accelerator Science and Technology, Wako, p. 334 (1999).

## Design of the RIKEN-SRC\* RF System

N. Sakamoto, O. Kamigaito, A. Goto, Y. Miyazawa, T. Chiba, H. Okuno, T. Mitsumoto, and Y. Yano

For the RIKEN RI-Beam Factory (RIBF)<sup>1)</sup> the new booster ring cyclotrons, the Intermediate-Stage Ring Cyclotron (IRC) and the superconducting Ring Cyclotron (SRC), are planned to be constructed to boost the energy of heavy-ion beams from the RIKEN Ring Cyclotron (RRC) to the intermediate energy region of 60–400 MeV/u with a beam intensity of 1 pμA.

The SRC<sup>2)</sup> requires acceleration resonators<sup>3)</sup> with a wide frequency range from 18 to 38.2 MHz to suit the condition of the RRC operation.

The maximum magnetic field of the SRC sector magnet is as large as 4.2 T. Because of the strong magnetic field, a high acceleration voltage is also required in order to obtain a large turn separation. A large turn separation at the extraction orbit is crucial to reduce the beam losses at the extraction devices. For example, in the case of <sup>16</sup>O<sup>7+</sup> ion acceleration up to the maximum energy of 400 MeV/u at the rf frequency of 38.2 MHz with a harmonic number  $h = 6$ , an acceleration voltage of 2.4 MV/turn is required to obtain a turn separation larger than 4 mm at the extraction orbit.

A flat-top system is also helpful in reducing the beam losses at the extraction because the energy spread of the accelerated beam can be reduced by flat-top acceleration. The phase acceptance  $\Delta\phi$ , which is defined by  $|V(\Delta\phi)|/V(\phi = 0) \leq 10^{-4}$ , for non-flat-top acceleration and flat-top acceleration are  $\pm 0.81^\circ$  and  $\pm 7.3^\circ$ , respectively.

In order to realize a large turn separation, four acceleration resonators are employed. The peak voltage of the resonators is set to be 600 kVp/gap at the highest frequency operation. One flat-top resonator with the third-harmonic of the acceleration resonator is employed and its peak voltage is set to be about 11% of the acceleration voltage.

The key parameters of the present design of the resonators are listed in Table 1. Since the location of the flat-top resonator has been moved from the center region of the valley chamber to next to the acceleration resonator (see Fig. 1), a new design of the flat-top resonator has been introduced. The dimensions of the accelerator resonator have also been rearranged.

For the flat-top system the third-, fourth-, and fifth-harmonics are used. This is helpful for the mechanical design of the flat-top resonator because the frequency range becomes narrower. The frequency range of the new flat-top resonator is 85.97–114.6 MHz instead of 54.0–114.6 MHz which is for the third-harmonic system. The phase acceptances of the fourth- and the fifth-harmonic flat-top system (Fig. 2) are sufficiently

Table 1. Key parameters of the acceleration and the flat-top resonator for the SRC.

resonators	accel.	flat-top
No. of units	4	1
Frequency [MHz]	18–38.2	85.97–114.6
Acc. gap	single gap	
	250	120
Aperture	60 <sup>H</sup>	60 <sup>H</sup>
[mm × mm]	×2240 <sup>W</sup>	×1975 <sup>W</sup>
Coarse tuner	flapping panel	shorting plate
Tuner stroke	0–90°	500–1100 mm
Trimmer	block tuner	-
Feeder	inductive loop	
Max. V <sub>p</sub> [MV/gap]	0.6	0.36
Voltage stability	10 <sup>-4</sup>	10 <sup>-3</sup>
Phase stability	±0.1°	±0.3°
Max. power [kW]	81	43
Q-values	37000	25000

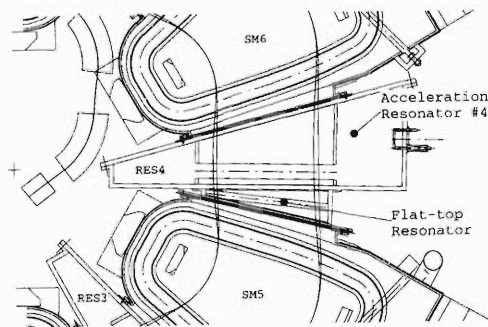


Fig. 1. Top view of acceleration resonator No. 4 and flat-top resonator.

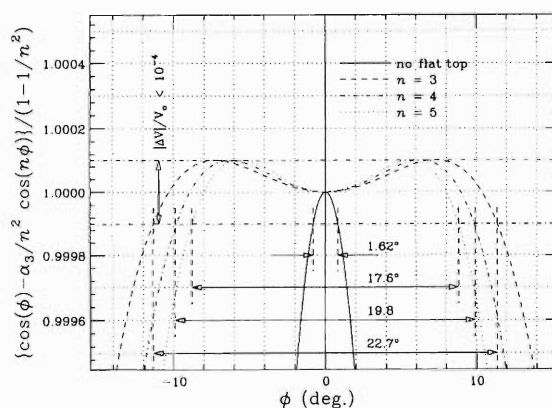


Fig. 2. Acceleration voltage with a flat-top resonator.  $\Delta\phi \equiv |V(\Delta\phi)|/V(\phi = 0) \leq 10^{-4}$

large to accept the beam from the RRC.

The acceleration resonator is a single-gap type whose structure is basically the same as that of the RCNP ring cyclotron (RCNP-RC).<sup>4)</sup> The resonant frequency

\* Superconducting Ring Cyclotron

is tuned by adjusting two flapping panels which are placed symmetrically to the median plane.

The rf characteristics of the acceleration resonator are calculated at the flapping panel positions of  $0^\circ$  and  $90^\circ$  by MAFIA,<sup>5)</sup> as shown in Table 2. Since the Q-value and the shunt-impedance of the actual resonator are expected to be 60–70% of the theoretical values,<sup>6)</sup> the maximum rf power dissipation of the actual resonator is estimated to be 115–135 kW. The calculated current density at the sliding contacts (see Fig. 3) is less than 60 A/cm.

The new design of the flat-top resonator for the SRC is shown in Fig. 2. Resonant frequency tuning is achieved by moving the shorting plates which are placed symmetrically with the median plane. By utilizing the multi-harmonic numbers of 3, 4, and 5, the required frequency range becomes 85.97–114.6 MHz. As shown in Fig. 4, the frequency range is successfully covered by moving the shorting plate from 500 to 100 mm with large Q-values (Fig. 5). The maximum wall loss is estimated to be 85 kW if the Q-value of the actual resonator is 50% of the theoretical value.

The main parameters of the rf amplifiers are listed in Table 3. The design of the final stage amplifier for the acceleration resonator is the same as that of the RRC. Since the transmitter tubes do not function in the strong magnetic field, the amplifiers are to be placed where the leakage field of the SRC sector magnets becomes smaller than 50 Gauss. The length of the power transmission lines is estimated to be 50 m.

Table 2. The calculated rf characteristics of the acceleration resonator obtained by MAFIA.

Flapping Panel	0 deg.	90 deg.
Frequency [MHz]	17.474	38.607
Q-value	28200	36649
Rs [MΩ]	0.63	2.23
Vp [kV]	250	600
P <sub>w.l.</sub> [kW]	50	81

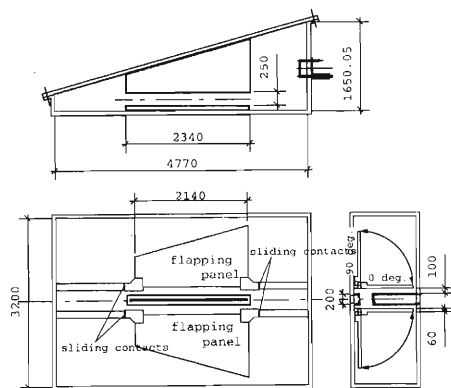


Fig. 3. Schematic view of acceleration resonator. Resonances with the lowest and highest resonant frequencies are obtained when the flapping panel is horizontal ( $0^\circ$ ) and vertical ( $90^\circ$ ), respectively.

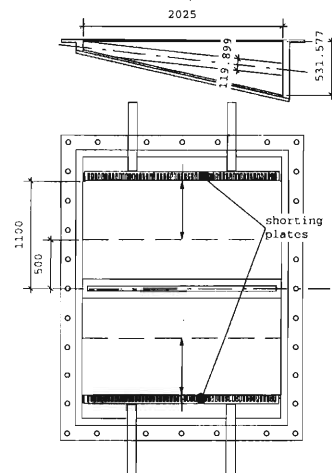


Fig. 4. Schematic view of flat-top resonator.

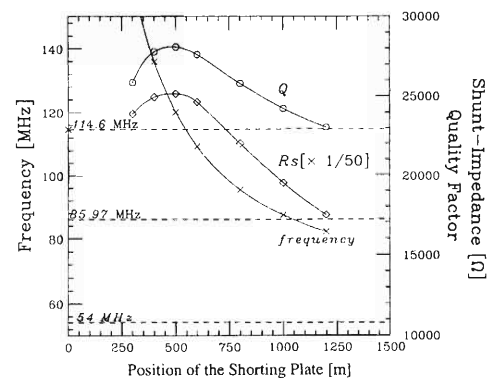


Fig. 5. Calculated rf characteristics of the flat-top resonator obtained by MAFIA.

Table 3. Characteristics of the RF amplifier.

		acceleration	flat-top
Frequency	[MHz]	18.0–38.2	85.97–114.6
Wide band amp.	[kW]	1	1
2nd stage		RS2012CJ	-
Output power	[kW]	15	5
Final stage		RS2042SK	RS2058CJ
Output power	[kW]	300	100
Trans. line		WX152D/50Ω	

#### References

- 1) Y. Yano et al.: Proc. 1997 Particle Accelerator Conf., Vancouver, 1997, p. 930 (1998).
- 2) A. Goto et al.: Proc. 12th Symp. on Accelerator Science and Technology, Wako, 1999, p. 7 (1999).
- 3) N. Sakamoto et al.: Proc. 15th Int. Conf. on Cyclotrons and Their Applications, Caen, 1998, p. 223 (1999).
- 4) T. Saito et al.: Proc. 12th Int. Conf. on Cyclotrons and Their Applications, Berlin, 1989, p. 201 (1990).
- 5) The MAFIA Collaboration, User's Guide MAFIA Version 4.0, CST GmbH, Lanteschägerstraße 38, D-64289, Darmstadt, Germany.
- 6) N. Sakamoto et al.: Proc. 12th Symp. on Accelerator Science and Technology, Wako, 1999, p. 224 (1999).

# Vacuum System for the RIKEN Superconducting Ring Cyclotron

K. Sugii, K. Ikegami, S. Yokouchi, A. Goto, and Y. Yano

Beam transmissions are aimed to be above 99% for all ion beams available in the RIKEN Superconducting Ring Cyclotron (SRC). We have estimated the required pressure of the beam chamber on the basis of the relationships between pressure and beam loss which is caused by a change in the charge state of the beam due to collisions with residual gas. As an example, Fig. 1 shows the beam transmission of  $^{238}\text{U}^{58+}$  ions as a function of pressure of the beam chamber, since the charge-exchange cross section of heavy ions such as  $^{238}\text{U}^{58+}$  is very large. As can be seen from Fig. 1, the required pressure should be below  $1 \times 10^{-5}$  Pa in order to achieve the goal of 99% beam transmission.

The vacuum chamber of the SRC consists of six beam chambers each in the sector magnet, four RF resonators, a flattop resonator, two valley chambers, and beam pipes for injection and extraction (see Fig. 2). Table 1 gives the total volume of the vacuum chamber and the surface areas of the main materials in the vacuum chamber. We plan to use 18 cryopumps with a total pumping speed of  $170 \text{ m}^3/\text{s}$  as the main pumping system in order to achieve the required range of pressure as quickly as possible.

Figure 3 shows the design of the pumping system for the vacuum chamber of the SRC. The pumping system consists of a roughing system, a high-vacuum system, an ultrahigh-vacuum system and a differential pumping system. The surface areas of the RF resonators and the flattop resonator are very large, since the resonators have a duplicated wall structure same as the

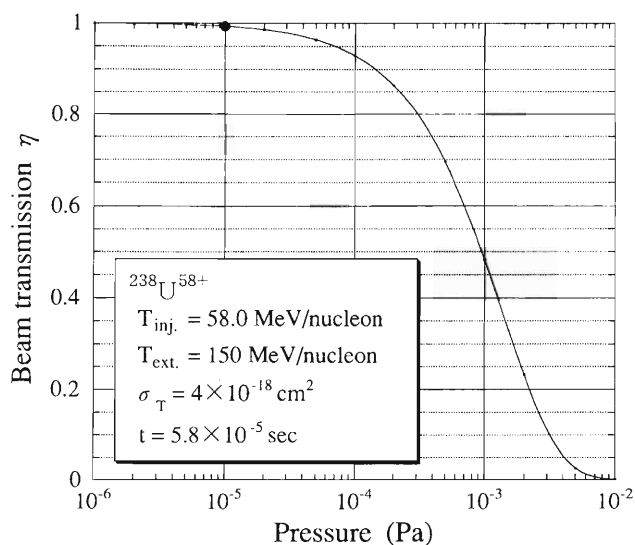


Fig. 1. Beam transmission of  $^{238}\text{U}^{58+}$  ions at the injection energy of 58.0 MeV/nucleon as a function of pressure of the beam chamber.

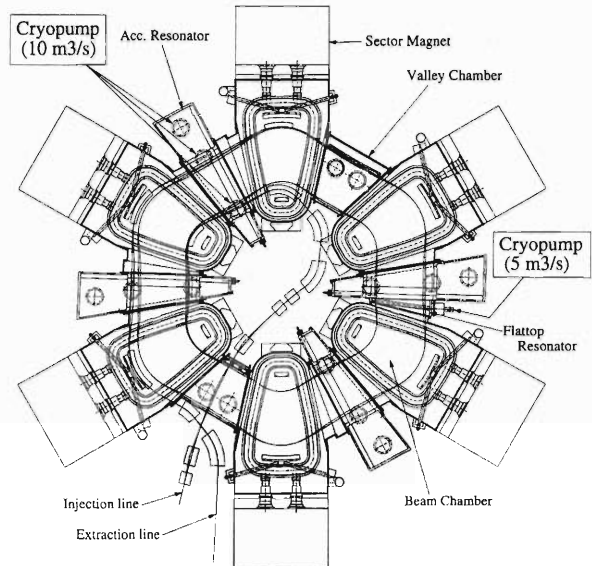


Fig. 2. Plan view of the SRC.

Table 1. Total volume of the vacuum chamber and the surface areas of main materials exposed to ultrahigh vacuum. The values including the extent of subvacuum are shown in parentheses.

Area Stainless steel	197 (442) $\text{m}^2$
Copper	356 (605) $\text{m}^2$
FPM (O-ring)	3.4 (5) $\text{m}^2$
Volume	85 (90) $\text{m}^3$

IRC resonators; copper plates with a thickness of approximately 4 mm are located on 25 mm away from the stainless steel vacuum walls.<sup>1)</sup> We plan to evacuate the gas in the subvacuum space between the vacuum walls and the copper plates by a differential pumping system in order to reduce the gas load for the cryopumps. Therefore, it is necessary to minimize the leak rate from the subvacuum space to the ultrahigh-vacuum space. The roughing system is composed of a roots pump of  $2600 \text{ m}^3/\text{h}$  and a rotary pump of  $290 \text{ m}^3/\text{h}$ , and is installed at each valley chamber. The high-vacuum system is composed of a turbomolecular pump of  $5.5 \text{ m}^3/\text{s}$  and a rotary pump of  $155 \text{ m}^3/\text{h}$ . This high-vacuum system is installed at each RF resonator. The high-throughput-type turbomolecular pump will be used for the following reasons: (1) to shorten the pumping time prior to the ultrahigh-vacuum system by switching from the roughing system to the high-vacuum system at a high pressure (about 70 Pa), and (2) to prevent the contamination in the RF resonator

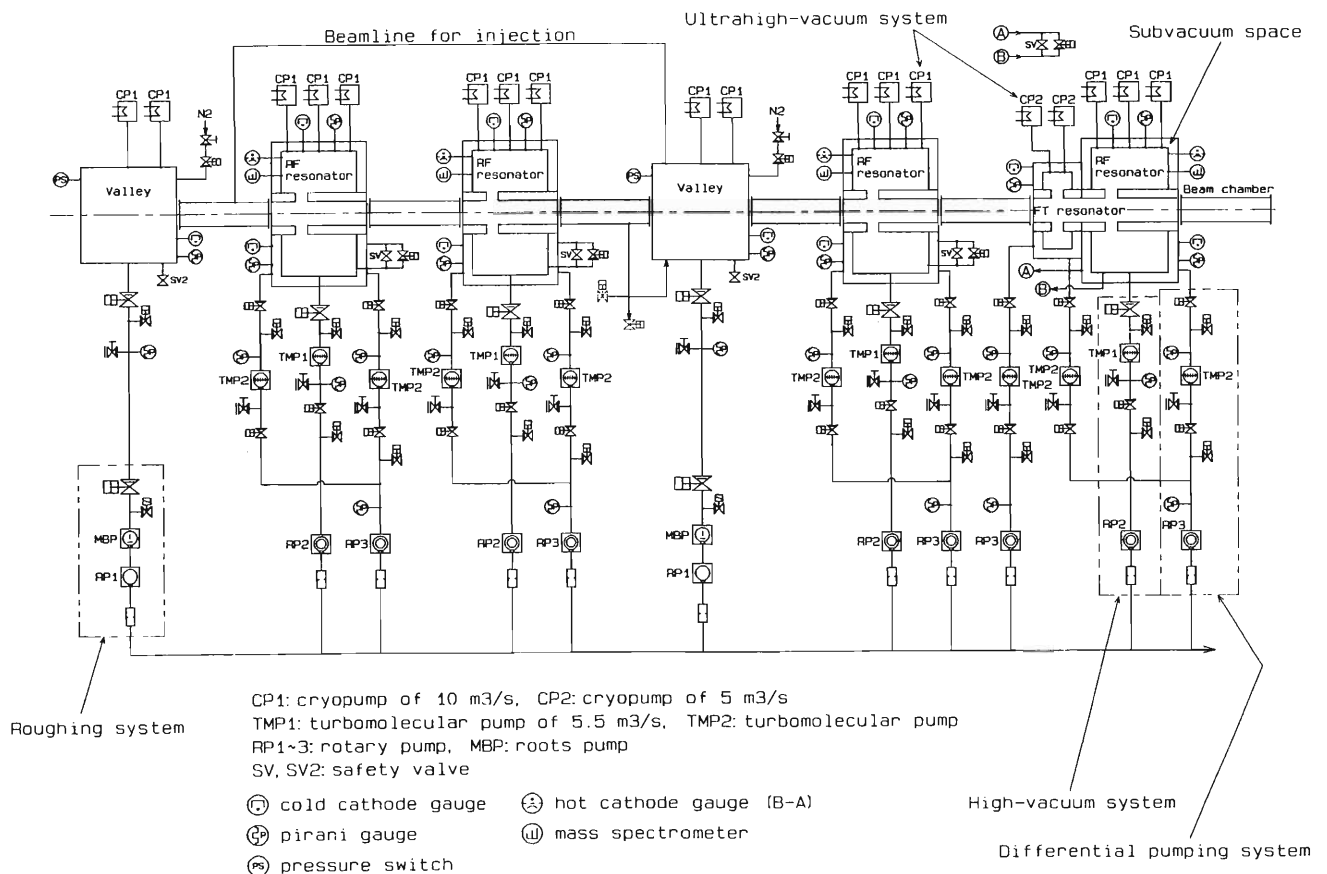


Fig. 3. Pumping system for the vacuum chamber of the SRC.

caused by the backflow of oil vapor from a rotary pump by the same switch. If the ultrahigh-vacuum system with cryopumps starts to operate at a pressure of  $1 \times 10^{-3}$  Pa, the total pumping time required to reduce the atmospheric pressure to  $1 \times 10^{-3}$  Pa using the roughing pump and the turbomolecular pump is calculated to be approximately 22 hrs. The ultrahigh-vacuum system deploys 18 cryopumps: 16 of which are  $10 \text{ m}^3/\text{s}$  and two of which are  $5 \text{ m}^3/\text{s}$ . The  $5 \text{ m}^3/\text{s}$  cryopumps are installed at the flattop resonator and the  $10 \text{ m}^3/\text{s}$  cryopumps are distributed to the two valley chambers and each of the RF resonators. We chose cryopumps as the main pump for the ultrahigh-vacuum system, because they have high pumping speeds against the water vapor and hydrogen gas, both of which are the predominant residual gas components in an unbaked vacuum system. Furthermore, they can be operated even under a large environmental magnetic field. The total effective pumping speed of the cryopumps is approximately  $75 \text{ m}^3/\text{s}$ . Considering this pumping speed and the published data for the outgassing rate of materials, the pumping-down time to achieve the order of  $10^{-6}$  Pa is estimated to be a few hundred hrs.

The pressure in the vacuum chamber of the SRC will be measured with a nude-type hot ionization gauge during a nonoperation period of the SRC. During the SRC operation, a cold cathode gauge will be used, since a hot ionization gauge is impractical use due to a large leakage flux from the sector magnet. A cold cathode gauge is equipped with a permanent magnet, therefore, it is expected to be usable even in an external magnetic field. Measurement of pressure using a cold cathode gauge under an external magnetic field was reported.<sup>2)</sup> However, we also measured the influence of an external magnetic field on cold cathode gauges, because the pressure measurement is limited by a large leakage flux from the SRC magnet.<sup>3)</sup>

#### References

- 1) T. Hiasa et al.: Proc. 12th Symp. on Accelerator Science and Technology, RIKEN, p. 293 (1999).
- 2) N. Yasumitsu: Proc. 8th Meet. on Ultra High Vacuum Techniques for Accelerators and Storage Rings, KEK, p. 75 (1992).
- 3) K. Sugii et al.: RIKEN Accel. Prog. Rep. **33**, 228 (2000).

## Influence of External Magnetic Field on the Performance of Cold Cathode Gauges

K. Sugii, K. Ikegami, M. Otake, S. Yokouchi, A. Goto, and Y. Yano

A Cold Cathode Gauge (CCG) is used to monitor the pressure of a vacuum chamber during the operation of the Superconducting Ring Cyclotron (SRC) sector magnet. To examine the effect of external magnetic fields on the performance of CCGs, an experiment using an electromagnet was carried out. Since the pressure required for the beam chamber of the SRC is estimated to be of the order of  $10^{-6}$  Pa,<sup>1)</sup> the vacuum gauge used in the SRC beam chamber is required to have a minimum measuring range which is one order or more lower than the order of the required pressure. Therefore, we chose two types of CCGs available on the market, that is, (1) Balzers: IKR060 and (2) Leybold: PR36.

A schematic diagram of the experimental setup is shown in Fig. 1. Figure 2 shows a photograph of the CCG set in a magnet gap. Both CCGs were positioned in such a way that the direction of the magnetic fields generated by the permanent magnets coincided with those of the external magnetic fields. For testing in an external magnetic field with a gradient, the CCGs were placed around the pole edge. The gradient of the external magnetic field at that position was estimated to be about  $-0.74$  T/m at a uniform field of 1 T. The measurement was performed under the following four conditions: (1) without a permanent magnet in a uniform external magnetic field, (2) without a permanent magnet in a nonuniform external field, (3) with a permanent magnet in a uniform external field, and (4) with a permanent magnet in a nonuniform external field. For the measurement without a permanent magnet, the pressure at zero field was measured using a permanent magnet.

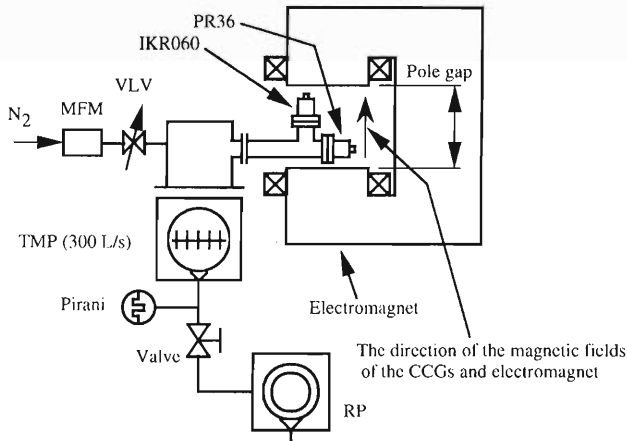


Fig. 1. Schematic diagram of the experimental setup.

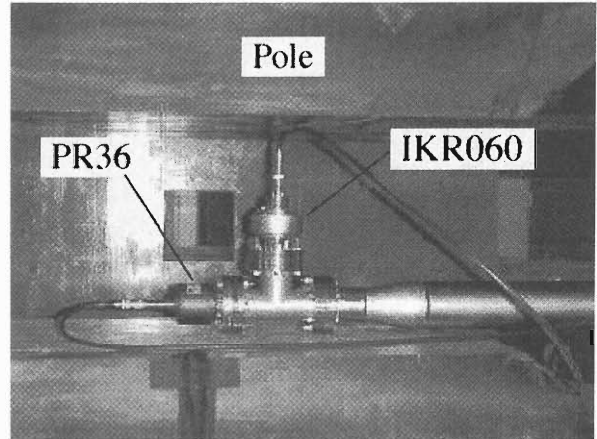


Fig. 2. CCGs in the pole gap.

Figure 3 shows the changes in pressure as a function of the external magnetic field near IKR060 without a permanent magnet when the external field is uniform. The pressure increases as the external field increases in the case of a low initial pressure. Figure 4 shows the changes in pressure without a permanent magnet of both CCGs when the external field is not uniform. In the case of IKR060, the trend of change at pressures above  $3 \times 10^{-5}$  Pa is similar to that in the case of a uni-

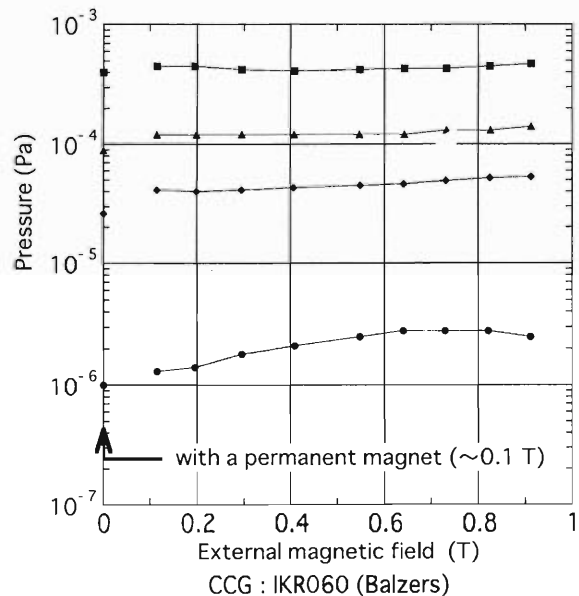


Fig. 3. Changes in pressure as a function of the magnetic field near IKR060 without a permanent magnet when the external field is uniform.

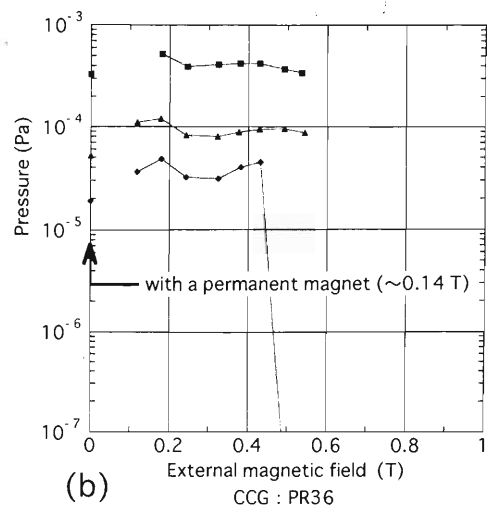
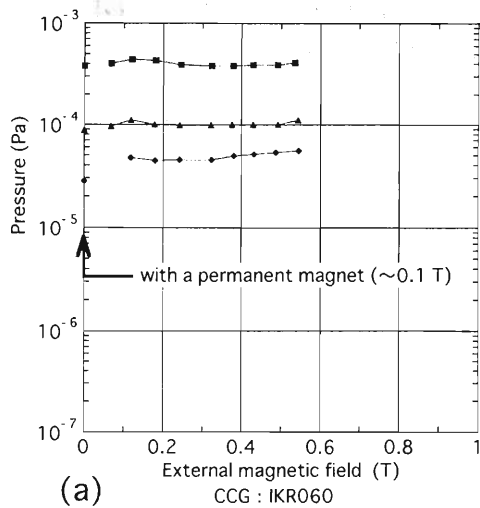


Fig. 4. Changes in pressure as a function of the magnetic field near CCGs without a permanent magnet when the external field is not uniform: (a) IKR060 and (b) PR36.

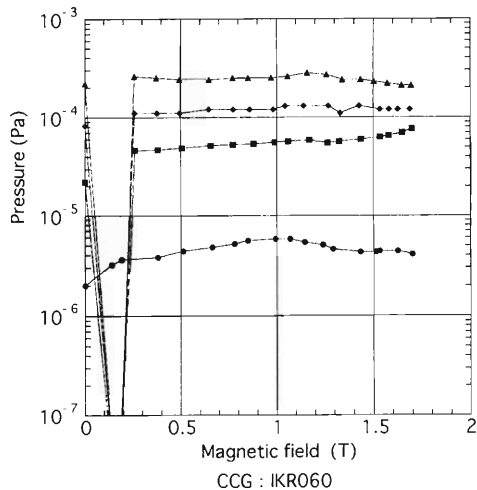


Fig. 5. Changes in pressure as a function of the magnetic field near IKR060 with a permanent magnet when the external field is uniform.

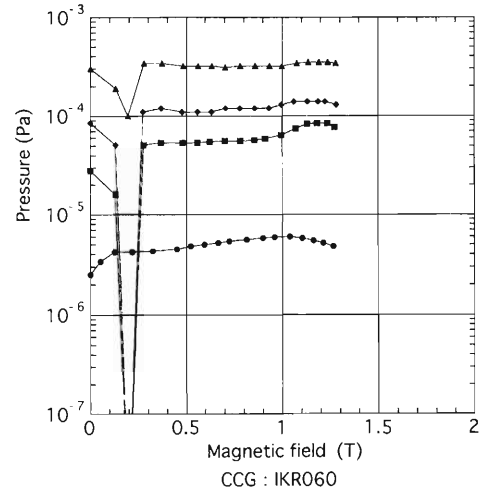


Fig. 6. Changes in pressure as a function of the magnetic field near IKR060 with a permanent magnet when the external field is not uniform.

form magnetic field. In the case of PR36, the change in pressure is larger than that for IKR060. The cause of this instability is thought to be due to the fact that the axis of PR36 was not exactly parallel to the lines of the external field; PR36 was located slightly away from the median plane of the magnet (see Fig. 2). Figures 5 and 6 show the changes in pressure as a function of the magnetic field near IKR060 with a permanent magnet. The results in the case of a uniform field are shown in Fig. 5. It can be seen from this figure that the pressure decreases suddenly in the range of 0–0.25 T and errors in measurement are observed when the pressure at zero field was above  $10^{-5}$  Pa. The results in the case of a nonuniform field are shown in Fig. 6. It can be observed that the pattern of change in pressure is similar to that seen in Fig. 5.

We conclude that we can use CCGs to monitor the pressure of a vacuum chamber in leakage flux of the SRC sector magnet unless we wish to pursue a more precise measurement. It is recommended to use a CCG without a permanent magnet because the external magnetic field during SRC operation is expected to be below 0.3 T, in which range measurement using a CCG with a permanent magnet becomes erroneous for unknown reasons. Moreover, we must determine the cause of errors in measurements using a CCG without a permanent magnet when the external field is very small (0–0.1 T).

#### References

- 1) K. Sugii et al.: RIKEN Accel. Prog. Rep. **33**, 226 (2000).

## Design Studies on Beam Transport System of RIKEN RI Beam Factory

N. Fukunishi, K. Kusaka, H. Sakurai, T. Kubo, T. Nagafuchi, H. Okuno, T. Mitsumoto,  
S. Fujishima, M. Kase, A. Goto, and Y. Yano

The beam transport system in the RI Beam Factory<sup>1)</sup> (RIBF) consists of four parts; one is a beam line from the RRC to the IRC. The maximum magnetic rigidity ( $B\rho$ ) required for the beam line is 2.94 Tm which corresponds to a 24.5-MeV/nucleon  $^{238}\text{U}^{58+}$  beam. The second is a beam line from the IRC to the SRC. The maximum  $B\rho$  is 4.57 Tm corresponding to a 58.0-MeV/nucleon  $^{238}\text{U}^{58+}$  beam. The third is beam lines from the SRC to experimental halls through the Big-RIPS. The last one is a beam line that returns the beams accelerated by the IRC to the RARF. In this report, we will explain the present status of design studies on the beam line from the RRC to the IRC and that from the IRC to the SRC. The layout of the beam lines is illustrated in Fig. 1.

The beam line from the RRC to the IRC mainly consists of five bending magnets, eight quadrupole triplets, two quadrupole doublets and seven quadrupole singlets. In addition, there is another Q-doublet in the injection system of the IRC (QDI3). The functions required for the beam line are the dispersion matching, the matching of phase-space ellipses in the transverse direction (beam shaping) and the RF-phase matching.

For the dispersion matching, the bending magnet (BM1) in the injection system of the IRC is designed to produce the desired dispersion. The actual condition required for the beam line is to make a doubly achromatic beam immediately before the BM1. The

spatial dispersion of the RRC beam is roughly 2.5 m at the Electric Deflection Channel (EDC). The angular dispersion is zero at the EDC. The 90-degree bending magnet (BM90) in the E1 experimental hall makes a doubly achromatic beam (see Fig. 2). In addition, the section from the EDC to the QTE13 is an entirely doubly telescopic system. This enables us to perform an emittance measurement for a beam at the P1 point in the beam line. The momentum analysis will be also performed with the bending magnet BM90.

The beam shaping is carried out using four Q-singlets (QSI2-QSI5). To this end, the beam line is designed to have horizontal waists at the QSI2 and the QSI4, and to have vertical waists at the QSI3 and the QSI5. The section from the BM24-1 to the BM24-2 is doubly achromatic and matches the beam direction to the injection system of the IRC. The section from the BM30-1 to the BM30-2 is also doubly achromatic and lowers the beam line by 3 m. This vertically achromatic feature causes a beam to be defocused in the horizontal direction. To avoid the divergence of the beam, the Q-doublet QDI2 focuses the beam before this section.

We show the results of an ion-optical calculation in Fig. 2. The calculation was performed using the TRANSPORT code.<sup>2)</sup> The emittance of the beam is  $5\pi$  mm mrad and the momentum spread is  $\pm 0.05\%$  in the present calculation. The assumed value of the emittance is based on the observation but depends on the actual beam tuning. For the momentum spread, here we use double the observed half-width. The maximum value of the quadrupole-filling factor is designed to be 50%.

With respect to the beam bunching, detailed investigations are necessary. The RF-phase width of the RRC is 10 degrees. On the contrary, the RF-phase acceptance of the IRC is 20 degrees because a flattop resonator is introduced. The first-order ion-optical calculation with  $\pm 0.05\%$  of the momentum spread predicts that the full width of the beam pulse at the Electric Inflection Channel (EIC) of the IRC is 24 degrees, which nearly corresponds to the RF-phase acceptance. Note that the assumed value of the momentum spread is double the observed half-width.

The functions required for the beam line from the IRC to the SRC are the dispersion matching and the beam shaping. The beam bunching is not necessary because the beam transport system is sufficiently short. The beam line consists of two bending magnets, seven Q-singlets and a Q-doublet. In addition, the injection

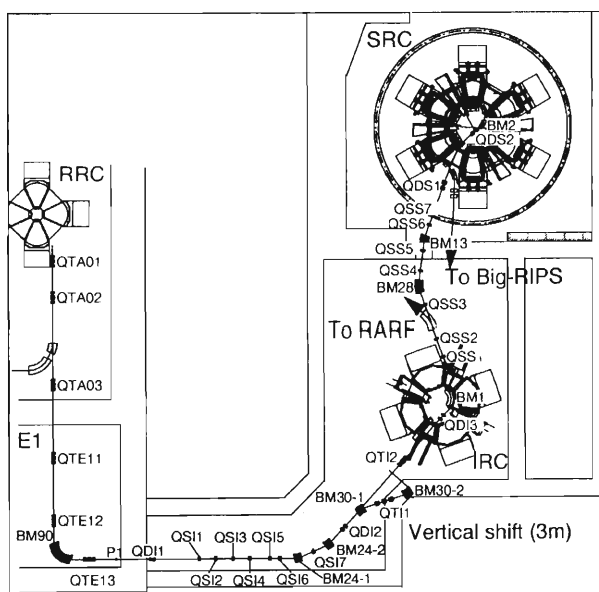


Fig. 1. Layout of the beam transport system of the RIBF.

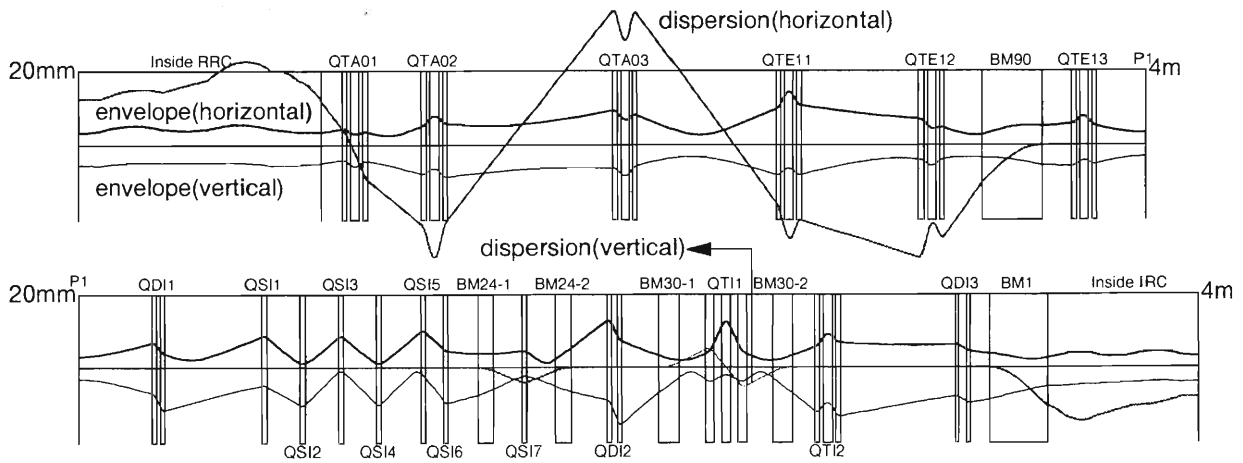


Fig. 2. Beam envelopes and dispersion calculated for the beam line from the RRC to the IRC. Thick and thin lines represent the horizontal and vertical directions, respectively. The full scale is 20 mm for the beam envelope and 4 m for the dispersion.

system of the SRC has another Q-doublet. In the beam line, there are no sections that are doubly achromatic. Hence, the beam shaping and the dispersion matching couples mutually. The roles of the Q-magnets are as follows. The QSS1 changes the beam shape for both horizontal and vertical directions but has little effect on the dispersion. The QSS2 is very sensitive to the beam shaping in the horizontal direction. On the contrary, the QSS3 mainly changes the beam shape in the vertical direction. The QSS4 and the QSS6 are mainly used for the dispersion matching. Moreover, the first magnet of the QSD1 is important for both the beam shaping and the dispersion matching. By adjusting the six Q-magnets as mentioned above, the beam accelerated by the IRC is matched to the conditions in injecting to the SRC.

We show the result of an ion-optical calculation in Fig. 3. In this calculation, the matching conditions are given at the entrance of the BM2 magnet of the injection system of the SRC. From the BM2 to the EIC of the SRC, orbit calculations were performed. The assumed emittance of the beam is  $3.3\pi$  mm mrad and the assumed momentum spread is  $\pm 0.05\%$  in this calculation. The quadrupole-filling factor is less than 50% for this beam line. The dispersion (horizontal) calculated here is also shown in Fig. 3. It should be noted here

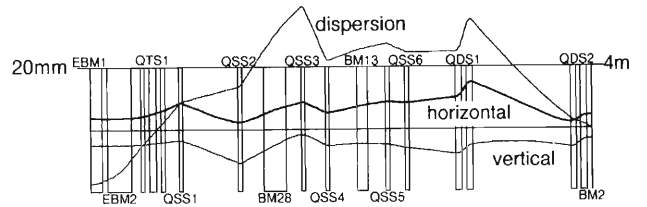


Fig. 3. Beam envelopes and dispersion for the beam line from the IRC to the SRC.

that the matching conditions in the present calculation are given only for a  $^{238}\text{U}^{58+}$  beam that corresponds to the highest magnetic rigidity. In the area near the SRC, there exists the strong stray field from the sector magnets of the SRC that depends nonlinearly on the magnetic rigidity of the beam.<sup>3)</sup> In this sense, we need to study beams with low magnetic rigidity, even though the present design of the beam transport system is designed to match various conditions.

#### References

- 1) Y. Yano et al.: Proc. 1997 Particle Accelerator Conference, 1, 930 (1997).
- 2) K. L. Brown et al.: SLAC91, Rev. 1 (1991).
- 3) S. Fujishima et al.: Proc. 15th Int. Conf. on Cyclotrons and Their Applications 1998, p. 485 (1998).

## Design Study of Beam Transport Lines from SRC to Three Big RIPSs

K. Kusaka and T. Kubo

In the RI-Beam Factory (RIBF) project,<sup>1)</sup> energetic heavy-ion beams from the RIKEN superconducting ring cyclotron (SRC) will be delivered to projectile fragment separators, called Big RIPS,<sup>2)</sup> to produce RI beams. Constructions of three Big RIPSs are being planned. Two of them, called Big RIPS I and II, are dedicated to ordinary RI-beam experiments. The third Big RIPS will be for the Multi-USE Experimental Storage rings (MUSES), in which produced RI-beams are injected into the accumulator cooler ring (ACR). These three separators share the primary beams from SRC by means of time sharing. A design study of beam transport lines from SRC to Big RIPS's has been carried out, taking constraints of building layout and design of magnets into account.

In this design study, we consider the following time sharing system. Since ACR can accept short-pulsed beams with a small duty factor, we consider a kicker magnet (KM) to deliver primary beams to MUSES lines. A strong KM, which bends SRC beams by  $7^\circ$  at an orbit radius of 9 m in a period of  $\sim 50 \mu\text{sec}$ , is under consideration. The time sharing between Big RIPS I and II is designed to be realized by a fast pulse magnet (PM) with a ramping time of less than 50 msec. Its bending angle is  $20^\circ$  and the orbit radius is 5.5 m. R & D studies of these magnets are in progress. A high-field normal conducting bending magnet (HFBM) is also under consideration, since bending magnets with small orbit radii are indispensable for fitting the beam lines in a limited area of the new RIBF building. Although a superconducting magnet is possible, we prefer HFBM from the view point of cost and ease of operations. The maximum field of HFBM is assumed to be 2 T. A design study of HFBM has shown that it is possible to build such a high-field magnet with a good field uniformity of  $10^{-4}$ .<sup>3)</sup>

A possible layout of beam lines together with SRC and Big RIPS I is schematically shown in Fig. 1. Three quadrupole doublets (QDs) transport a primary beam from SRC to a bending magnet (BM). The BM changes the direction of the beam  $30^\circ$  making the beam achromatic together with two QDs, so that the beam focuses at the intermediate focus IF. A  $60^\circ$ -HFBM, together with two quadrupole triplets (QTs), transports the beam from IF to the KM. While the KM is excited, pulsed beams are delivered to the MUSES line. While the KM is off, on the other hand, an unkicked beam is transported to the pulsing magnet (PM). The PM, when excited, steers the beam to the beam line to the target T1 for Big RIPS I. The beam line after PM consists of QD— $70^\circ$ -HFBM—QT—QT. When the

PM is off, the beam is delivered to a branch line to the target T2 for Big RIPS II which consists of QD— $20^\circ$ -BM—QD— $70^\circ$ -HFBM—QT—QT. The last QT pairs focus the beam on the targets T1 and T2. Both beam lines from IF to T1 and to T2 are achromatic point-to-point focusing. For the quadrupole multiplets, we have assumed two types of magnets. One has a 40 cm magnetic length and the others 75 cm. Figure 2 shows an example of calculated first order beam envelopes of these beam lines from the EBM2 exit to T1 and T2. The assumed beam is  $^{238}\text{U}^{59+}$  with an energy of 150 MeV/u, emittance of  $\epsilon_x = \epsilon_y = 5\pi$  mm mrad, and momentum spread of  $\Delta p/p = \pm 0.05\%$ . The calculated field gradients of quadrupoles are typically 10–15 T/m and the beam spot size on the target T1 and T2 is 1.2 mm in this case.

We have demonstrated that primary beams from SRC can be delivered to the three Big RIPSs by time sharing in the present floor-plan of the new RIBF building without introducing any superconducting magnet. Further optimization of the layout and magnet design is in progress.

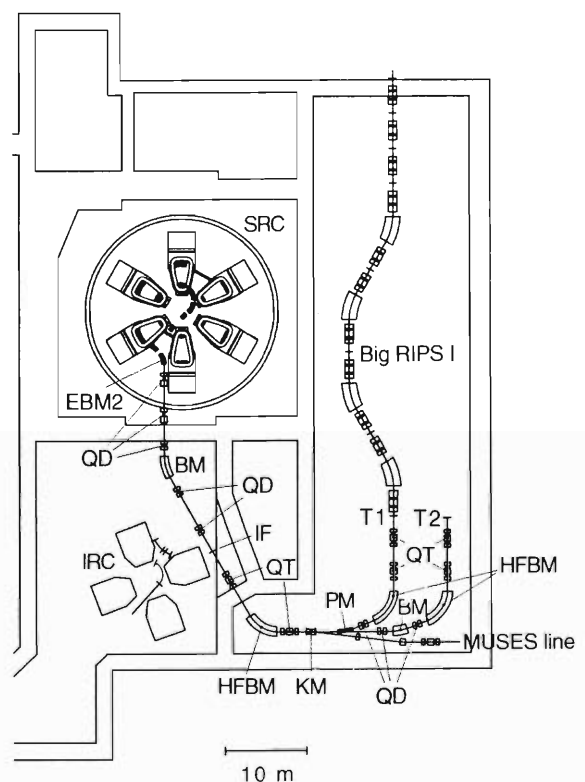


Fig. 1. Schematic layout of the beam transport line from SRC to Big RIPSs.

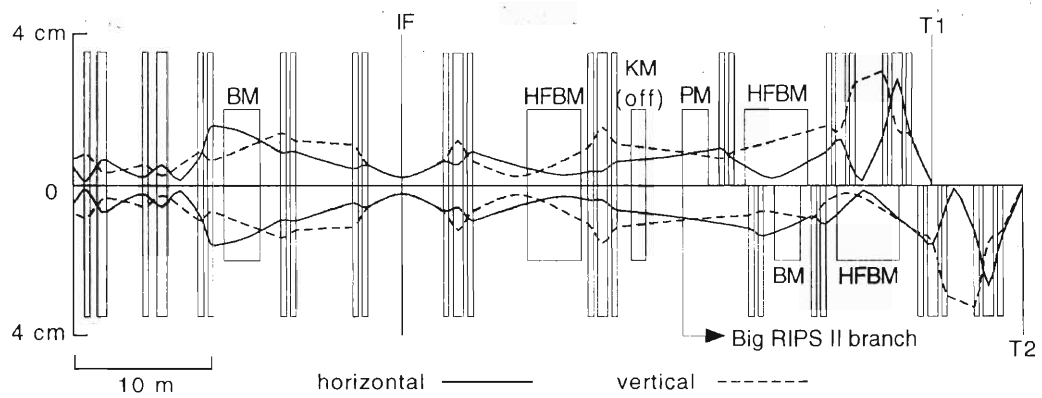


Fig. 2. First-order beam envelope.

References

- 1) Y. Yano et al.: Proc. 15th Int. Conf. on Cyclotrons and Their Applications, p. 696 (1998).
- 2) T. Kubo et al.: RIKEN Accel. Prog. Rep. **33**, 236 (2000).
- 3) T. Nagafuchi et al.: RIKEN Accel. Prog. Rep. **33**, 234 (2000).

## Design of a 2 T Room-Temperature Dipole Magnet for Beam Transport Lines of RIBF Project

T. Nagafuchi, M. Okamura, and T. Kubo

In this report, we describe the design of a high-field room-temperature dipole magnet to be used in the RIKEN RI-beam factory (RIBF) project.<sup>1)</sup>

In the RIBF project, heavy ion beams extracted from the superconducting ring cyclotron (SRC)<sup>2)</sup> are to be delivered to the target positions of BigRIPS (RIKEN projectile fragment separator)<sup>3)</sup> to produce RI beams. The beam transport lines between SRC and BigRIPS are being designed.<sup>4)</sup> According to the building layout for the project, the beam lines must be bent by a total of 150 degrees to reach the target positions. This bend is to be made using two dipole magnets, between which a number of quadrupole magnets, a kicker magnet, and a pulsing magnet are to be placed. The kicker and pulsing magnets are used for the time sharing of a primary beam.<sup>4)</sup> It is found that the limited space in the building makes it difficult to install these magnets, if the dipole magnets are designed to be conventional room-temperature magnets with the field strength of 1.5 to 1.6 T.

One solution to this problem is to build superconducting dipole magnets with high fields such as 3 T. In this case, although the fabrication cost is high, much more space becomes available, since the magnets become much smaller. Another solution is to build room-temperature iron-dominated dipole magnets with high fields. An optics design of the beam lines has shown that sufficient space becomes available if the field strength chosen is 2 T.<sup>4)</sup> The key points to be considered in this case are: (1) sufficiently good uniformity at such high fields, and (2) efficient water-cooling of magnet coils. We decided to examine the second solution, because not only can the room-temperature magnet be designed easily, but also it can be fabricated at a low cost, as compared with superconducting ones.

As for the type of dipole magnet, we chose the modified window-frame type as shown in Figs. 1 and 2, because a large space can be made available for the coils as compared with other types, hence facilitating the cooling, and it was expected that this type might have a good uniformity. We have developed the design by means of a two-dimensional field calculation, taking field uniformity into consideration. The coil cooling was also taken into account simultaneously. The calculation was carried out using the code OPERA-2d.

The modified window-frame-type dipole magnet has an inner coil and an outer coil as shown in Fig. 2. It was found in the course of designing that the field uniformity was sensitive to the coil geometry. Therefore, in

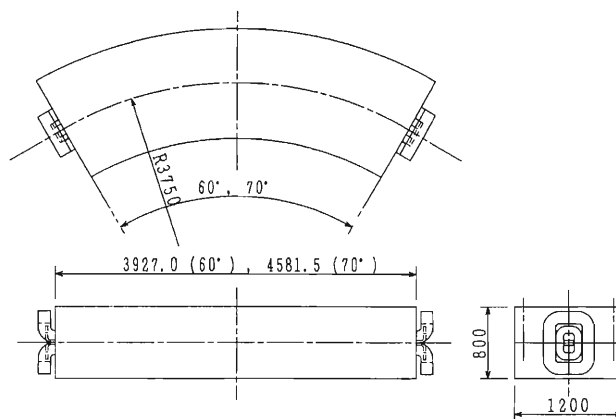


Fig. 1. Schematic diagrams of a 2 T dipole magnet.

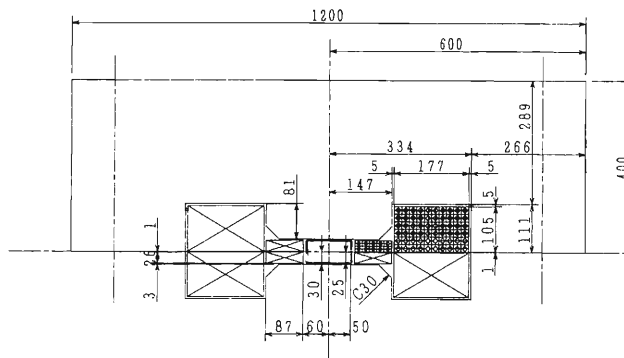


Fig. 2. Cross-sectional view of a 2 T dipole magnet.

the design we optimized the field uniformity by adjusting the horizontal and vertical dimensions of the coils, particularly those of the outer coil. The dimension of the hollow conductor as well as the horizontal and vertical turn numbers were adjusted in the optimization. The geometry of pole pieces such as chamfering of the side edge was also optimized. Figure 2 shows a cross-sectional view of a magnet thus optimized. Some basic parameters of the magnet are listed in Table 1. The inner and outer coils are connected in series, but consist of different conductors whose specifications are given in Table 1. The turn numbers per pole are 10 for the inner coil (horizontally, 5 and vertically, 2), and 60 for the outer coil (horizontally, 10 and vertically, 6). The nominal operation current is 723 A for 2 T. The coil cooling is divided into eight circuits (2 for the inner coil and 6 for the outer coil). The temperature rise of the coil at 2 T is estimated to be about 14 degrees at a cooling-water pressure of 3.5 kg/cm<sup>2</sup>, when the bending angle is 70 degrees.

Table 1. Main parameters of a 2 T dipole magnet.

Magnetic rigidity	7.52 Tm
Bending radius	3.75 m
Bending angle	60, 70 degree
Dipole field strength	2.01 T
Pole gap	60 mm
Turn number per pole	70
Turn number of inner coil per pole	10
Turn number of outer coil per pole	60
Hollow conductor of inner coil	11.5 mmW $\times$ 11.5 mmH- $\phi$ 8 mm
Hollow conductor of outer coil	16 mmW $\times$ 16 mmH- $\phi$ 10 mm
Nominal current	723 A
Good field region	$\pm 50$ mm
Magnetic field uniformity	Better than $2 \times 10^{-4}$

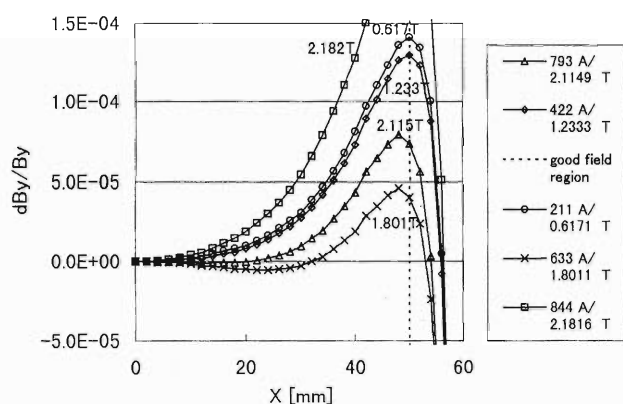


Fig. 3. Midplane field uniformity of a 2 T dipole magnet shown as a function of horizontal position X. X = 0 denotes the center of the magnet.

Figure 3 shows field uniformity as a function of horizontal position on the median plane of the magnet. It is shown that the field uniformity of about  $1 \times 10^{-4}$  has been achieved at the horizontal position of  $\pm 50$  mm up to the field strength of 2 T. It is surprising that an iron-dominated dipole magnet can exhibit such good uniformity at such a high field. It is interpreted that this is because the field distribution generated by the coils cancels well that generated by the iron pole pieces. Note that the field distributions of these two contributions behave in opposite ways: one increases while the other decreases at larger horizontal positions. It was found that suitable coil dimensions had to be selected, so that the two contributions could cancel each other well. For instance, if the turn number of the outer coil is chosen to be

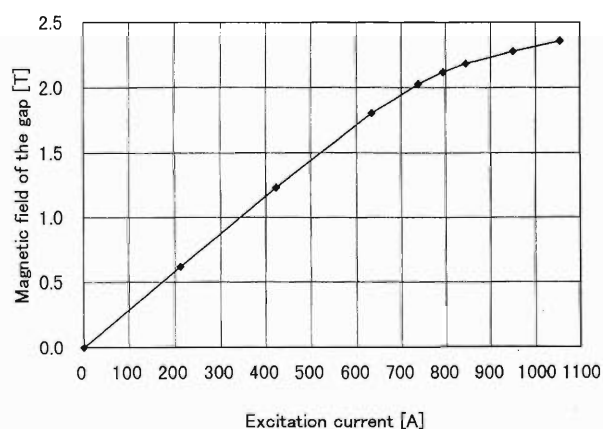


Fig. 4. Excitation curve of a 2 T dipole magnet as function of operation current.

eight both horizontally and vertically, the uniformity becomes about  $1 \times 10^{-3}$ , which is 10 times worse than that shown in Fig. 3.

Figure 4 shows the excitation curve as a function of operation current. The power consumption is estimated to be about 100 kW at a 2 T in case of a bending angle of 70 degrees.

#### References

- 1) Y. Yano et al.: Proc. 15th Int. Conf. on Cyclotrons and Their Applications, Caen, France, 1998, p. 696 (1998).
- 2) A. Goto et al.: Proc. 15th Int. Conf. on Cyclotrons and Their Applications, Caen, France, 1998, p. 148 (1998).
- 3) T. Kubo et al.: RIKEN Accel. Prog. Rep. **33**, 236 (2000).
- 4) K. Kusaka and T. Kubo: RIKEN Accel. Prog. Rep. **33**, 232 (2000).

## Design of the BigRIPS Separator for the RIKEN RI-Beam Factory Project

T. Kubo, H. Sakurai, K. Kusaka, and I. Tanihata

In the RIKEN RI-beam factory project, two new cyclotrons, IRC and SRC, are to be built as post accelerators of the existing cyclotron RRC.<sup>1)</sup> The cascade of these cyclotrons will be able to accelerate heavy ion beams up to *e.g.*, 400 MeV/u for relatively light heavy ions like oxygen, 300 MeV/u for Kr ions, 200 MeV/u for Xe ions, and 150 MeV/u for U ions. The expected beam intensity is as high as 1 pμA. Such capability allows efficient production of radioactive isotope (RI) beams using the projectile fragmentation method,<sup>2)</sup> in which RI beams are produced by a magnetic spectrometer called the projectile-fragment separator. The separator collects and isotopically separates RI beams which are produced in heavy-ion collisions with target nuclei, such as projectile fragmentation of various heavy ions and projectile fission of uranium ions.

Three projectile-fragment separators, which are named BigRIPS separators, are planned to be built in the RI-beam factory project, and to be placed after the SRC cyclotron. The project is divided into two phases called the phase I project and phase II project (or MUSES project). Two BigRIPS separators are intended for use in the phase I project in which ordinary RI-beam experiments are to be carried out. The other BigRIPS separator is for use in the MUSES project in which RI-beam colliding experiments are to be carried out. These three BigRIPS separators are to share a primary heavy-ion beam from the SRC by means of time sharing.<sup>3)</sup> In this report, we describe the design of the BigRIPS separator for the phase I project.

As production reactions for the BigRIPS separator, we are planning to use projectile fission as well as projectile fragmentation, because projectile fission was found to be very powerful for the production of neutron-rich RI beams.<sup>4)</sup> The acceptance of the BigRIPS separator has been determined considering the kinematics of the reactions to be used.

The angular spread of projectile fragments is not very large in the case of projectile fragmentation. The most severe is the case when light projectiles are used to produce RI beams which are far from the projectiles. For instance, the full angular spread is estimated to be about 40 mr when <sup>11</sup>Li beams are produced from <sup>18</sup>O beams at 400 MeV/u. On the other hand, the spread is quite large in the case of projectile fission of U beams. The full angular spread is estimated to be as large as about 200 mr at 150 MeV/u. In designing the BigRIPS separator, we aimed to achieve an angular acceptance of around 100 mr, so that the separator could cover half of the angular spread of fission fragments. The momentum spread of projectile fragments is estimated

to be about 4% for the case mentioned above. The momentum spread of fission fragments is estimated to be as large as about 20%. However, due to the angle and momentum correlation in reaction kinematics, the spread is reduced to a few percent when the angular acceptance is assumed to be 100 mr. In the design, we aimed at achieving momentum acceptance of around 6%, considering the broadening of momentum spread due to energy loss in the production target as well as the momentum spread in the case of projectile fragmentation. Larger momentum acceptance allows the use of a thicker production target. These values of acceptance enable the collection of fission fragments at an efficiency of about 10%.

The maximum magnetic rigidity ( $B\rho$ ) of the separator was set at 9.5 Tm, considering light neutron-rich RI beams produced by projectile fragmentation. This  $B\rho$  value, corresponding to fragments with  $A/Z$  (mass-to-charge ratio) of 3 and energy of 400 MeV/u, is about 26% larger than that of the SRC cyclotron (7.52 Tm). The maximum  $B\rho$  value necessary for projectile fission is estimated to be 5 to 6 Tm.

We chose a mirror-symmetric achromatic system with four bends for the BigRIPS separator. Its schematic diagram is shown in Fig. 1. The configuration may be written as TQ-D-TQ-F-TQ-D-TQ-F-TQ-D-TQ-F-TQ-D-TQ, where TQ, D and F represent quadrupole triplet magnets, a dipole magnet and an intermediate focus, respectively. Not only the configuration but also the first-order optics are mirror-symmetric with respect to the midfocus, where the waist condition should be fulfilled. The wedge-shaped energy degrader is placed at the midfocus for isotope separation. We chose the mirror-symmetric achromatic system with four bends, because (1) two bends allow a high momentum resolution at the midfocus, hence a better isotope separation, (2) some geometrical aberrations disappear because of the symmetry, and (3) the system has high flexibility in terms of its optics design. A large value of image magnification at the midfocus gives rise to the emittance growth of RI

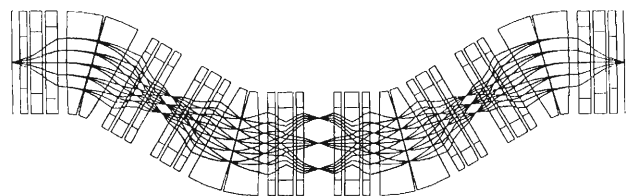


Fig. 1. A schematic diagram of the BigRIPS separator.

beams when the energy degrader is placed. Hence we aimed at small values around 1. The system should have different operation modes, since two kinds of reactions are to be used.

Quadrupole magnets used for the BigRIPS separator should have not only large apertures but also high fields, because large acceptance and high  $B\rho$  values are required. In designing the separator, we assumed the use of the iron-dominated superconducting quadrupole magnets, by which high pole-tip fields such as 2.4 T can be achieved.<sup>5)</sup> Their aperture and length were determined based on the optics design, in which the maximum pole-tip fields were assumed to be 2.4 T. The dipole magnets were assumed to be room-temperature magnets with maximum fields of 1.6 T and a mean radius of 6 m. The bending angle was chosen to be 30 degrees, considering the constraints of the new building.

The optics design of the BigRIPS separator was made using the code GIOS and taking into account the aforementioned considerations and assumptions. The basic parameters of the BigRIPS separator are given in Table 1. The parameters are listed for two different operation modes of the same system, which

Table 1. Basic parameters of the BigRIPS separator.

	High acceptance mode	High resolution mode
$\Delta\theta$ [mr]	80	40
$\Delta\Phi$ [mr]	100	80
$\Delta P/P$ [%]	7	4
$\Delta\Omega$ [msr]	8	3.2
$(x/x)$	1.48	1.02
$(x/\delta)$ [cm/%]	3.52	4.87
$(y/y)$	1.73	1.21
$P/\Delta P^*$	2380	4770
Max. $B\rho$ [Tm]	7.52	9.5
Length[m]	42.8	

\* First-order momentum resolution at the mid focus.

A beam spot size of 1 mm is assumed.

may be called the high acceptance mode and high resolution mode. The high acceptance mode has a first-order momentum resolution of about 2400, almost achieving the desired acceptance for projectile fission. This momentum resolution is satisfactory because the isotope separation power is limited due to the energy straggling effects caused by the degrader. Although it has smaller acceptance values, the high resolution mode has a momentum resolution of about 4800, which is a factor of two better than that of the high acceptance mode. The maximum  $B\rho$  value of high resolution mode is 9.5 Tm, achieving the desired value for projectile fragmentation. Because of the large acceptance value, the correction of optical aberrations is necessary to improve the isotope separation. The important aberrations are the second-order chromatic term ( $x/\theta\delta$ ) and some third-order terms. The aberration correction is in progress using sextupole and octupole magnets.

The superconducting quadrupole magnets of the BigRIPS separator have large apertures. For example, the quadrupole triplets between the first and fourth dipole magnets have a pole-tip radius of 17 cm and a warm-bore radius of 12 cm. These triplets consist of three iron-dominated superconducting quadrupoles with effective lengths of 50, 80 (or 100), and 50 cm. Their maximum pole-tip fields are about 2.4 T as assumed in the optics design. Design studies of the superconducting quadrupoles have been made,<sup>6)</sup> and construction of a prototype triplet is in progress.

#### References

- 1) Y. Yano et al.: Proc. 15th Int. Conf. on Cyclotrons and Their Applications, Caen, France, p. 696 (1998).
- 2) B. M. Sherrill: Proc. 2nd Int. Conf. on Radioactive Nuclear Beams, Louvain-la-neuve, Belgium, p. 3 (1991).
- 3) K. Kusaka and T. Kubo: RIKEN Accel. Prog. Rep. **33**, 232 (2000).
- 4) M. Bernas: Proc. ENAM98 Conf. on Exotic Nuclei and Atomic Masses, Bellaire, Michigan, p. 664 (1998).
- 5) A. F. Zeller et al.: IEEE Transactions on Applications and Superconductivity **9**, 693 (1999).
- 6) T. Hiramachi et al.: Proc. 16th Int. Conf. on Magnet Technology, Florida, 1999, in press; T. Kubo et al.: RIKEN Accel. Prog. Rep. **33**, 238 (2000).

## Design of a Superferric Quadrupole Magnet for the RIKEN RI-Beam Factory Project

T. Kubo, T. Hiramachi, T. Tominaka, H. Sakurai, T. Nagafuchi, K. Kusaka, M. Okamura,  
T. Tsuchihashi,\*<sup>1</sup> O. Ohsaki,\*<sup>1</sup> T. Senba,\*<sup>2</sup> and S. Suzuki\*<sup>2</sup>

In the RIKEN RI-beam factory project,<sup>1)</sup> radioactive isotope (RI) beams are to be produced using projectile fragment separators called BigRIPS.<sup>2)</sup> A BigRIPS separator is designed to be a magnetic spectrometer consisting of dipole, quadrupole, sextupole and octupole magnets. The quadrupoles must have a large aperture and a high field gradient, because a large acceptance as well as high magnetic rigidity are required for the BigRIPS separator. An optics design of the separator led us to conclude that the quadrupoles must be superconducting to meet the requirements. With respect to the type of superconducting quadrupoles, we considered two types: the superferric quadrupole (iron-dominated superconducting quadrupole) which has been developed at NSCL/MSU<sup>3,4)</sup> and the  $\text{COS}(2\theta)$  quadrupole. We have chosen the superferric quadrupole for the BigRIPS separator, considering the liquid helium consumption as well as the fabrication cost. A prototype of the superferric quadrupole will be built for R&D studies. The prototype will be a quadrupole triplet mounted in a single cryostat.

The prototype quadrupole triplet consists of three superferric quadrupoles with identical cross sections. They are installed in a single helium vessel and cooled by the liquid-He bath cooling method. Their schematic depiction is shown in Fig. 1. The quadrupoles have a pole-tip radius of 170 mm and a warm bore radius of 120 mm. The design effective lengths of the quadrupoles are 0.5, 0.8, and 0.5 m. The maximum

pole-tip fields are chosen to be 2.4 T, corresponding to the field gradient of 14.1 T/m, because the uniformity of the field gradient is found to rapidly worsen at higher fields. Correction coils such as sextupole and octupole coils are to be installed in the gap between the pole tip and the inner pipe of the helium vessel.

In designing the prototype superferric quadrupoles, we studied two types which have different quadrupole coils. One is the race-track type (or flat-winding type) whose coils can be wound by ordered winding. The other is the NSCL/MSU type, which is essentially the same as that developed at NSCL/MSU.<sup>3,4)</sup> In this case, the coils are wound by random winding. The reason for choosing to also study the race-track type is that it was expected that ordered coil winding would be more feasible and coil quality could be controlled more easily, as compared with the NSCL/MSU-type random winding. Hereafter, these two types are referred to as type A and type B, respectively.

The uniformity of the field gradient has been optimized by means of a two-dimensional (2D) magnetic field calculation, in which the codes OPERA-2d and OPERA-3d/TOSCA<sup>5)</sup> were used. In order to derive quadrupole fields as well as higher multipole fields such as 12-pole and 20-pole fields, the calculated fields were analyzed by the multipole analysis method, in which the reference radius was chosen to be 120 mm. The cross-sectional shape and position of coils were adjusted looking at the 12-pole fields, since this component was expected to most strongly affect the uniformity. The current density of coils was kept at around



Fig. 1. Schematic depiction of the prototype quadrupole triplet.

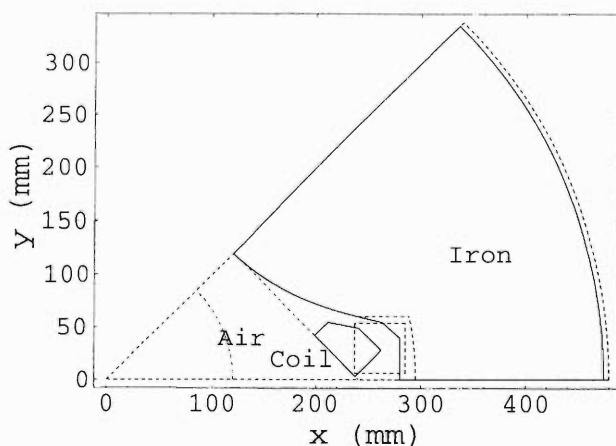


Fig. 2. Octant of optimized cross section for type A (solid line) and type B (dashed line) superferric quadrupoles.

\*<sup>1</sup> Toshiba Corp.

\*<sup>2</sup> Hitachi Ltd.

100 A/mm<sup>2</sup>, considering the quench protection and the superconducting wire to be used. Care was taken to prevent the interference between the correction coils and quadrupole coils at the coil end. The optimized cross sections are shown in Fig. 2 for both type A and type B quadrupoles. It can be seen that ordered coil winding is possible for type A, while it is difficult for type B. Some main parameters for the quadrupoles are listed in Table 1.

Figure 3 shows the 12-pole and 20-pole fields derived from the 2D calculation as a function of quadrupole field gradient. The 12-pole and 20-pole fields are shown as a ratio to the quadrupole fields. It can be seen that the 12-pole fields are the most important. The 12-pole fields of type A and B quadrupoles behave similarly at field gradients larger than 12.5 T/m. However at lower field gradients, the 12-pole fields of type B are much smaller than those of type A. With respect to the 2D calculation, type B has better uniformity than type A.

A three-dimensional (3D) field calculation has been performed, since end effects were expected to be large due to the large aperture and the short magnet length.

Table 1. Main parameters of type A and B quadrupoles (0.5 m).

Type	A	B
Effective magnetic length (m)	≈ 0.54	≈ 0.53
Pole tip radius (mm)	170	170
Winding of coil	orderly	random
Nominal current per pole (kA)	190	240
Nominal current (A)	127	136
Nominal turn number	1500	1760
Nominal current density (A/mm <sup>2</sup> )	111	104
Cross section of coil (mm <sup>2</sup> )	1720	2300
Straight length of coil (mm)	440	450
Total length of coil (mm)	640	626
Length of iron (mm)	440	450
Outer radius of yoke (mm)	475	480

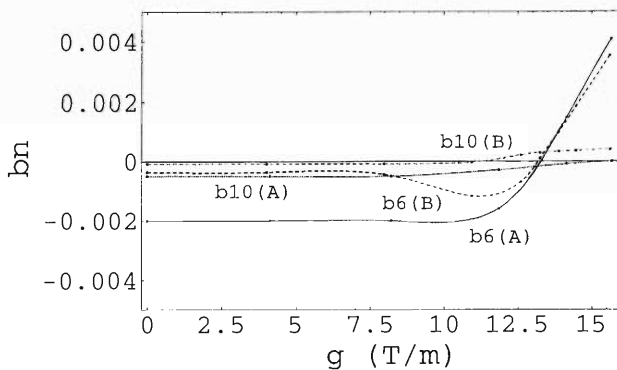


Fig. 3. Twelve-pole (b6) and 20-pole (b10) fields at a radius of 120 mm derived from the 2D calculation. These fields are shown as a ratio to the quadrupole fields, and are plotted as a function of quadrupole field gradient  $g$ . Types A and B are indicated in parentheses.

The calculation was made using the code OPERA-3d/TOSCA. In this case, the multipole analysis was carried out position-by-position along the magnet axis, and then the derived fields were integrated over the axis. Figure 4 shows the integrated 12-pole and 20-pole fields at a radius of 120 mm. The fields are shown as a ratio to the integrated quadrupole fields, and are plotted as a function of quadrupole field gradient at the middle of magnet axis. It can be seen that the 12-pole fields, which make dominant contributions, are much larger in low and high field-gradient regions as compared with those of the 2D calculation. Furthermore, the behavior of type A is very similar to that of type B quadrupoles. The results of the 3D calculation indicate the large end effects, as anticipated. In order to understand the end effects, the calculated fields were decomposed to two components: those generated by coil contributions and those by iron contributions. It was found that the large 12-pole fields in the low field gradient region arose from the effects of the iron pole end, while those in the high field gradient region arose from the effects of the coil end part. Furthermore, it was found that the 12-pole fields in the low field gradient region could be reduced by chamfering the pole ends, and those in the high field gradient region could also be reduced by adjusting the distance between the pole end and the coil end part so that the two contributions could negate each other. The optimization of the magnet end is in progress.

The superconducting wire for the quadrupole coils was chosen mainly based on the requirements of low current operation, hence low helium consumption, and self-protection against quenching. The coils must not break down even if all the stored energy is dissipated into one of four quadrupole coils. Some of the main parameters of the chosen superconducting wire are listed in Table 2, and were determined based on the quench

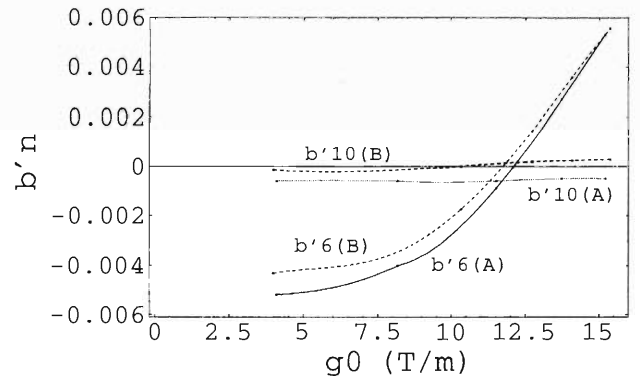


Fig. 4. Integrated 12-pole (b'6) and 20-pole (b'10) fields at a radius of 120 mm derived from the 3D calculation. These fields are shown as a ratio to the integrated quadrupole fields, and are plotted as a function of quadrupole field gradient at the center of magnet axis  $g_0$ . Types A and B are indicated in parentheses.

Table 2. Main parameters of superconducting wire.

Parameter	
Insulated diameter (mm $\phi$ )	1.15
Bare diameter (mm $\phi$ )	1.10
Cu/super Ratio	6.6
RRR of Cu	100 - 150
Filament diameter ( $\mu$ m $\phi$ )	75

Table 3. Calculated results of quench protection.

Quad. Type	I (A)	L (H)	$E_s^a$ (MJ)	$T_{max}$ (K)	$V_{max}$ (V)	$V_{L,max}^b$ (V)	$R_{n,f}^c$ ( $\Omega$ )
A	153	26	0.30	100	670	29	13
B	170	33	0.48	110	880	44	15

<sup>a</sup>  $E_s$ : stored energy, <sup>b</sup>  $V_{L,max}$ : maximum voltage between layers, <sup>c</sup>  $R_{n,f}$ : final resistance of the normal zone.

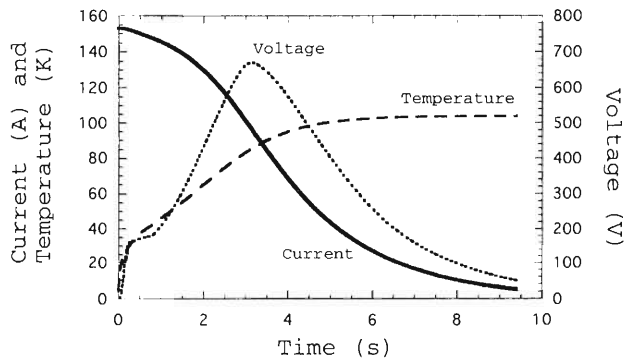


Fig. 5. Current decay, temperature rise and voltage development after quenching of the type A quadrupole whose effective length is 0.8 m.

protection analysis.

The quench protection analysis was carried out for the quadrupole with the effective length of 0.8 m, because it has the largest stored energy. For safety, the excitation current was chosen to be 20% larger than the nominal maximum value. As the worst case, it was assumed that the quenching occurs in one of four coils, while the rest of them remains superconducting. As the design criteria, the maximum allowable voltage and temperature were taken to be 1 kV and 100 K, respectively. The calculated results are listed in Table 3. Quench characteristics such as current decay, temperature rise and voltage development are shown in Fig. 5 for the type A quadrupole. It is shown that the quadrupole coils wound with the chosen wire can be self-protecting.

The basic design of the superferic quadrupoles which produce a maximum field gradient of 14.1 T/m over a 120 mm radius with the uniformity of about 0.5%, has been carried out with 2D and 3D magnetic field calculations. The mechanical design is being studied on the basis of the field calculation.

#### References

- 1) Y. Yano et al.: Proc. 15th Int. Conf. on Cyclotrons and Their Applications, Caen, France, p. 696 (1998).
- 2) T. Kubo et al.: RIKEN Accel. Prog. Rep. **33**, 236 (2000).
- 3) A. F. Zeller et al.: IEEE Transactions on Applications and Superconductivity **9**, 693 (1999).
- 4) B. Zhang: Ph. D. thesis, Michigan State University.
- 5) OPERA-2d and OPERA-3d/TOSCA, Vector Field, Ltd., Oxford, England.

## Estimation of Deposited Heat and Damage by Neutrons on the Downstream Superconducting Magnet of the Target Assembly

T. Mukhopadhyay, T. Kubo, and T. Maruyama

When radioactive ion beams are produced by the Big-RIPS separator, superconducting magnets located immediately after the production target are exposed to intense neutrons with high energy. The cooling capacity of the cryogenic system of the magnet must take into account the heat deposited by the neutrons on the magnet. Theoretical estimations of the power deposited by the neutrons on the magnet, assumed to be a solenoid for simplicity, in a geometrical setup as in Fig. 1, have been performed based on the measured or computed production yield of neutrons for several beam-target combinations. A study of radiation damage, based on the maximum absorbed dose per unit mass on the magnet, leads to estimates of lifetime of operation of the magnet. Similar radiation damage study on the epoxy of the magnet coil has also been carried out using KERMA (kinetic energy released in material) values.

First, the computed or measured differential yield or cross-section for neutron production in heavy ion collisions with the target material is necessary. Let  $\Sigma(E, \theta)$  be the double differential yield of neutrons as a function of neutron energy  $E$  and the angle  $\theta$  of the beam-target combination. Using the  $\Sigma(E, \theta)$  values we calculate the average number of neutrons  $\bar{n}$  per incident ion, the mean neutron energy  $\bar{E}$  and the total neutron power ( $P$ ) released in the region of space occupied by the downstream solenoid.

The average number of neutrons produced per incident beam particle, covering the space at the entrance of the solenoid, is given by

$$\bar{n} = 2\pi \int_{E_i}^{E_f} \int_{\theta_i}^{\theta_f} \Sigma(E, \theta) \sin \theta d\theta dE, \quad (1)$$

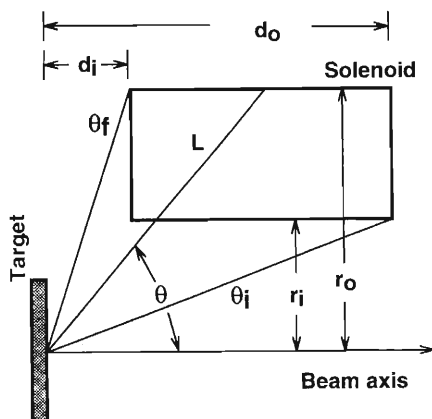


Fig. 1. Cross-sectional view of the target and solenoid setup.

where  $E_i$ - $E_f$  is the total energy range of the neutrons and  $\theta_i$ - $\theta_f$  is the angular space covered by the solenoid with respect to the centre of the target and the beam axis. Similarly, the average energy  $\bar{E}$  of the neutron produced is given by

$$\bar{E} = 2\pi \int \int E \Sigma(E, \theta) \sin \theta d\theta dE / \bar{n}. \quad (2)$$

The total power in the space at the entrance of the solenoid is then given by  $P = CI_0 \bar{n} \bar{E}$ , where  $I_0$  = the primary beam intensity in particles per second and  $C = 1.60217733 * 10^{-13}$  joules/MeV.

We next proceed to calculate the similar quantities,  $\bar{n}'$  and  $\bar{E}'$  in the space at the exit of the solenoid after the neutrons pass through the material of the solenoid. A simple method to carry this out is to assume that while the neutrons traverse through the material of the solenoid, the energy weighted neutron flux is attenuated exponentially with the distance travelled within the material, which is a current technique in accelerator shielding. This means that the quantity  $I_0 \Sigma(E, \theta) E$  at the entrance of the solenoid becomes  $I_0 \Sigma(E, \theta) E \exp(-L(\theta)/\lambda(E))$  at the exit of the solenoid. The distance  $L(\theta)$  traversed within the solenoid by a neutron moving at an angle  $\theta$  with the beam axis can be determined easily from the geometry of the setup. For attenuation length  $\lambda(E)$  as a function of energy  $E$ , we have used a set of  $\lambda(E)$  values calculated with HETC code, which is based on the cascade and evaporation model,<sup>1)</sup> to interpolate the values of  $\lambda$  at required energies. In this method, iron is assumed to be the only constituent material of the magnet. With the transformed variable  $\Sigma'(E, \theta) = \Sigma(E, \theta) \exp(-L(\theta)/\lambda(E))$ , the new average values ( $\bar{n}'$ ,  $\bar{E}'$ ), and the power ( $P'$ ) at the exit of the solenoid can be easily calculated. The power loss within the solenoid is then given by

$$H = \Delta P = CI_0 (\bar{n} \bar{E} - \bar{n}' \bar{E}'). \quad (3)$$

Results are shown in Table 1. Experimental measurements<sup>2)</sup> have demonstrated that such results of deposited neutron power based on the theoretical model are overestimated by a factor of 2.4-4.5. Although inaccurate, such results are useful in determining various scaling factors between theoretical and experimental estimates, between cases of thin and thick targets, and between different geometries. In spite of favorable scaling factors, the high values of deposited heat call for special arrangements for the cold part of the magnet.

We next study the distribution of radiation dose deposited per unit mass of the magnet, called the gray

Table 1. Neutron power absorbed in the solenoid.  $r_i = 20.0$  cm,  $r_o = 48.0$  cm,  $d_i = 50.0$  cm, length = 250.0 cm. The various cases cited are (i) 400 MeV/u  $^{20}\text{Ne}$  beam on a Cu target thick enough to stop the beam. (ii) 400 MeV/u  $^{18}\text{O}$  beam on a thin ( $1 \text{ gm/cm}^2$ )  $^9\text{Be}$  target. (iii) 400 MeV/u  $^{40}\text{Ar}$  beam on a thin ( $1 \text{ gm/cm}^2$ )  $^9\text{Be}$  target. Intensity of the beam was  $I_0 = 6.24 * 10^{12}$  pps ( $\equiv 1 \text{ p}\mu\text{A}$ ) in each case.

Case	$\bar{n}$	$\bar{E}$ (MeV)	$P$ (wt)	$\bar{n}'$	$\bar{E}'$ (MeV)	$P'$ (wt)	$\Delta P$ (wt)
(i)	2.1861	151.21	330.5	0.3546	144.03	51.1	279
(ii)	0.3035	312.06	94.7	0.0383	256.63	9.8	85
(iii)	0.7174	340.77	244.4	0.0732	287.66	21.1	223

value, expressed in Gray ( $\equiv \text{Joules/Kg}$ ). To calculate the gray value distribution, the solenoid is divided into smaller cells along its length and thickness. To calculate energy loss by a neutron in a particular cell, one has to account for the energy loss of the same neutron along its earlier journey in the solenoid. The energy loss in a cell can be calculated from

$$\Delta E = 2\pi I_0 \int \int E \Sigma'(\theta, E) [1 - e^{-l_s(\theta)/\lambda(E)}] \sin \theta d\theta dE, \quad (4)$$

where  $\Sigma'(\theta, E) = \Sigma(\theta, E) * e^{-l_s(\theta)/\lambda(E)}$ ,  $l_s$  = path length in the cell, and  $l_s$  = path length traversed in the solenoid before entering the cell.

Based on the maximum gray value estimate and the radiation damage safety criteria of a maximum allowable dose of  $1 \times 10^7$  Gy/year (1 year of operation time  $\equiv 20\%$  of 4800 hr) on any part of the magnet and associated coil, we estimate the lifetime of operation of the magnet, shown in Table 2.

We have also studied the radiation damage to the epoxy of the superconducting coils of the magnets using KERMA values. The purpose of the epoxy is to restrain coil wire motion, which can result in a quench. Considerable damage resulting in the degradation of the compressive strength of the epoxy can occur with radiation. Earlier studies<sup>3)</sup> have shown a 20% reduction in compression strength of the epoxy with a radiation dose of about  $2 \times 10^7$  Gy. For our calculation we take  $1 \times 10^7$  Gy as the total dose limit for acceptable coil lifetime.

Table 2. Calculations of yearly radiation dose to superconducting magnet.

Case	Av. Gray (wt/Kg)	Max. Gray (wt/Kg)	Av. dose ( $10^4$ Gy/yr)	Max. dose ( $10^7$ Gy/yr)	Lifetime (Years)
(i)	0.024	0.327	8.2944	0.1130	9
(ii)	0.0073	0.0644	2.516	0.0223	45
(iii)	0.0192	0.189	6.6355	0.0653	15

Table 3. Calculations of radiation dose to superconducting coil epoxy (by KERMA). Cross-section set used was that of case (iii) in Table 1.

Target-to-Coil Distance (cm)	Coil angle (Degree)	Yearly Dose ( $10^7$ Gy)	Lifetime (Years)
64	1	0.1705	6
64	10	0.0301	33
64	20	0.0043	231
64	30	0.0010	981
35	10	0.1005	10

The calculation is similar to that of a dose to a tissue in biological applications using KERMA values. The KERMA is defined as the expectation value of the kinetic energy transferred to the charged particles per unit mass at a point in matter, whereas the KERMA factor refers to the KERMA per unit neutron fluence. The partial KERMA factor for a certain secondary charged-particle type is obtained from the product of the cross section [b] and the average energy [MeV], in units of b-MeV/atom which can be converted to the SI unit of  $\text{Gy}\cdot\text{m}^2$ .

Only the main molecular component in stycast epoxy, butyl glycidyl ether,  $(\text{C}_4\text{H}_{10}\text{O}_2\text{N}_2)_n$ , where n is a large number, is considered in estimating the damage. Tables of KERMA factors for H, C, N, and O are available for neutron energies of 1 MeV to 150 MeV from Los Alamos T2 group Information Service.<sup>4)</sup> These factors are weighted by stoichiometric ratios, and then summed to obtain the effective KERMA value for the molecule as a function of neutron energy. For neutrons with energy higher than 150 MeV, these factors are extrapolated.

The energy delivered by neutron collisions to a  $1 \text{ cm}^3$  sample of epoxy placed at a distance and angle from the neutron source can be calculated using

$$D = I_0 \Omega_0 t \rho \times 10^{-3} \int \Sigma(E, \Omega_0) K(E) dE, \quad (5)$$

where  $K(E)$  in  $\text{Gy}\cdot\text{cm}^2$  is the effective KERMA value in epoxy at energy  $E$ ,  $\Omega_0$  is the average solid angle subtended by the sample at the source, t in sec is the effective operation time in a year (960 hr) and  $\rho$  in gm/cc is the density of the epoxy. The results, as shown in Table 3, show reasonably acceptable values.

#### References

- 1) N. Fukunishi: private communication.
- 2) E. Baron, L. Bianchi, J. Dural, and C. Grunberg: Proc. 3rd Europe Particle Accelerator Conf., Berlin, 1992, Vol. 1 (Editions Frontiers), p. 1555 (1992).
- 3) R. Ronningen, B. Mukherjee, and A. Zeller: NSCL Report 1998 (unpublished).
- 4) T2 Information Service: <http://t2.lanl.gov/>

## Shielding Design of RIKEN RI Beam Factory

N. Fukunishi, S. Ito, Y. Uwamino, and Y. Yano

We have studied the radiation shield of the RI Beam Factory for two years. New experimental results were obtained this year, which are very useful for the precision check of our method of estimating the radiation dose. One of these results are from shielding experiments performed with 400-MeV/u <sup>12</sup>C beams accelerated by the HIMAC of the NIRS. Two of the authors (S. I. and Y. U.) contributed to one of these experiments. We summarize in Table 1 the comparison between the experimental results and our estimated results. We find that our method reproduces well the experimental results, except for the 0-degree direction, where we find a large discrepancy between the estimated results and the experimental results. This discrepancy comes from the fact that we neglect

the diffusion effect of neutron flux in the shielding material due to the multiple scattering of neutrons in the present estimation. The diffusion effect is marked when the distance from the source to the shield is small (1.5 meters in the experiment) in the 0-degree-direction shielding. We estimated the reduction of the radiation dose due to the diffusion effect with the HETC-3step code.<sup>3)</sup> The reduction factor is 43% for a 1.5-meter-thick shield of normal concrete. The shielding thickness in the experiment is 2.8 meters. As the numerical simulation for the actual experimental setup is too time-consuming, we did not execute it.

Other useful experimental results were given by Kurosawa *et al.*<sup>4-6)</sup> They measured the double-

Table 1. Comparison of the shielding calculation values with experimental values.<sup>1,2)</sup> The beam intensity is  $3 \times 10^8$  pps except for the first two data ( $1 \times 10^8$  pps). Quantity L is the distance from the source to the point where the radiation dose was measured. Quantity t is the thickness of the shield (normal concrete). Angle  $\theta$  refers to the angle from the beam axis. The unit of effective dose is  $\mu\text{Sv/h}$ . (\* 380-cm-thick normal concrete + 50-cm-thick iron).

L(m)	t(cm)	$\theta(\text{deg.})$	Obs.	Calc.
5.0	280	0.00	66	498
10.0	505*	0.00	1.5	1.26
13.86	286	13.38	16.8	24.9
12.98	268	21.48	13.9	19.7
12.38	256	30.56	6.5	13.6
12.12	250	40.29	3.15	5.66
12.40	256	54.95	0.75	1.02

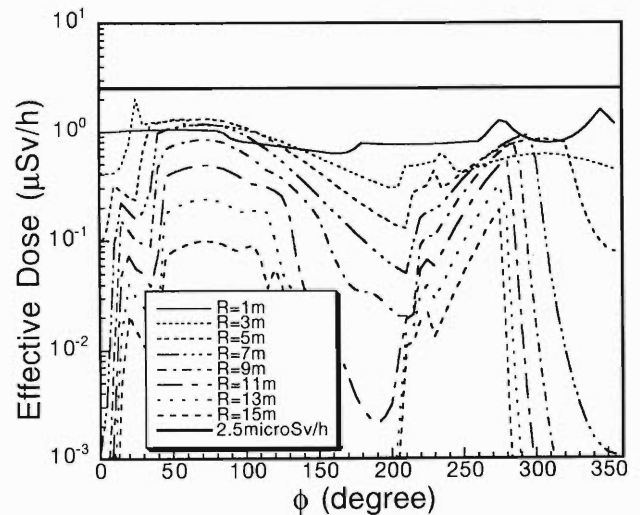


Fig. 1. Effective dose distribution on the SRC roof. The position on the roof is given by the polar coordinates R and  $\phi$ . The origin is just above the machine center of the SRC. At the extraction point, the beam direction is 150 degrees.

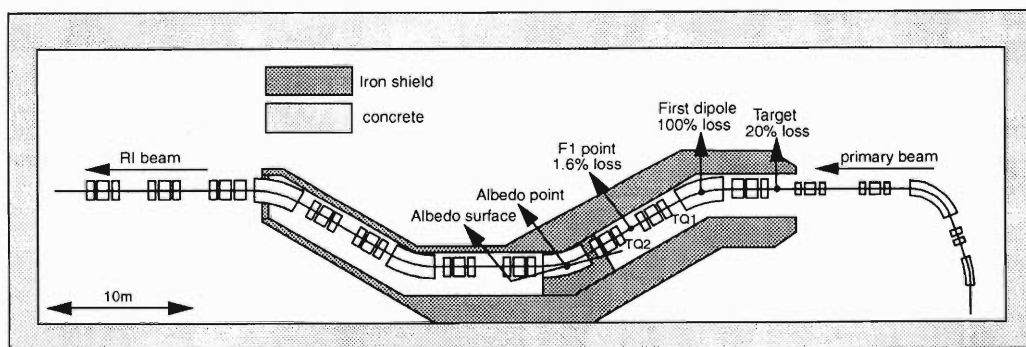


Fig. 2. Plane figure of the radiation shield of the Big-RIPS. We assume that secondary neutrons are produced at the "albedo point". The "albedo surface" determines the injection and scattering angles of the neutrons.

differential neutron yields for various combinations of beams and targets. From these experiments, we can determine how the radiation dose depends on the mass number and the energy of the ion that hits the target. Our speculation was that the effective dose which originated from a heavy-ion beam was proportional to the ion mass and the square of the ion energy per particle. The series of experiments revealed that our speculation was valid. We hence chose a 300-MeV/u-Kr beam as a model beam for the shielding design of the RIBF because the radiation produced by this beam is predicted to be the most serious concern in the RIBF.

Here, we shall explain some results of the shielding calculations. We illustrate in Fig. 1 the effective dose on the roof of the SRC room, which is 3-meter-thick normal concrete. In addition, there also exists a 3-meter-thick local shield of normal concrete placed just above the EDC of the SRC. The EDC is assumed to be the main source of radiation. We found that a 6-meter-thick shield of normal concrete is sufficient for a beam loss of 10 pA. Another example is the shield of the Big-RIPS which is shown in Fig. 2. Downstream from the second bending magnet, secondary neutrons are the most serious radiation. The words "secondary neutrons" indicate the neutrons generated by the neutrons bombarding the iron shield. To estimate the reflection rate of radiation on the iron shield, we calculated double differential albedo functions of the effective dose using the HETC code. Results are shown in Fig. 3 for the case when neutrons are injected into the iron shield at an injection angle of 75 degrees. The design of the local iron shield shown in Fig. 2 was determined taking into account this effect. More detailed aspects of our estimation

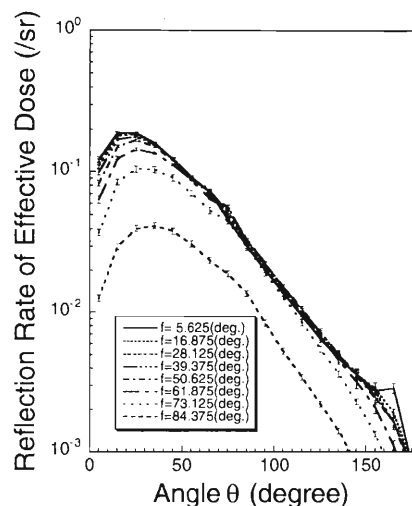


Fig. 3. Double-differential albedo functions of the effective dose. The source neutrons are from the experimental results of a 400 MeV/u  $^{20}\text{Ne}$  beam on a thick Cu target (0 degree). The shielding material is iron in this case.

are summarized in Ref. 7.

#### References

- 1) Two 0-degree data are from Y. Kumamoto: private communication.
- 2) Other data are from S. Ito et al.: private communication.
- 3) P. Cloth et al.: Jül-2203, Kernforschungsanlage, Jülich (1988).
- 4) T. Kurosawa et al.: J. Nucl. Sci. Technol. **36**, 1 (1999).
- 5) T. Kurosawa et al.: Nucl. Sci. Eng. **132**, 30 (1999).
- 6) T. Kurosawa et al.: private communication.
- 7) N. Fukunishi et al.: Proc. SAST99, p. 349 (1999).

# Refinement of Accumulator Cooler Ring Lattice Design

K. Ohtomo and T. Katayama

Preliminary lattice design of the Accumulator Cooler Ring (ACR)<sup>1)</sup> has been focused on the accumulation and cooling of radioactive isotope (RI) beams. Beam momentum spreads of  $\delta p/p = \pm 0.5\%$  after passing through a fragment projectile separator (BigRIPS), will be reduced to  $\delta p/p = \pm 0.15\%$  by a debuncher cavity<sup>2)</sup> located 80 m downstream of the BigRIPS. Devices for multiturn injection and RF stacking are needed to enhance the beam current. Then beam emittance and momentum spreads should be cooled by the electron cooling and stochastic cooling devices in the ACR. The lattice of the ACR should be designed by taking the following device constraints into account:

(1) The electron cooler (EC) requires a long straight dispersion-free space (over 12.0 m long). The horizontal betatron function at an EC should be less than 5 m because an electron beam size covers the RI beam size.

(2) Stochastic cooling devices require a few pairs of dispersion-free spaces for a pickup and a kicker, and the phase advance of the betatron oscillation between them should be nearly  $k\pi/4$  ( $k$ : odd).

(3) Multiturn injection requires sections where the phase advance of the betatron oscillation is nearly  $\pi$ , to arrange kickers and septum magnets.

(4) RF stacking requires a dispersion in the multiturn injection section and a space for a tunable RF cavity.

(5) Accumulation of high current beams requires a large acceptance in the horizontal plane ( $\epsilon_x = 125 \pi \cdot \text{mm} \cdot \text{mrad}$ ) and a large momentum spread ( $\Delta p/p = \pm 2.0\%$ ).

Table 1. Parameters of the ACR.

Circumference	168.4836 m
Max. magnetic rigidity	8 Tm
Max. beam energy ( $A/Z = 2.3$ )	400 MeV/u
Injected beam emittance (Hor./Ver.)	10/10 $\pi \cdot \text{mm} \cdot \text{mrad}$
Injected beam momentum spreads	$\pm 0.15\%$
Stored beam emittance (Hor./Ver.)	125/10 $\pi \cdot \text{mm} \cdot \text{mrad}$
Stored beam momentum spreads	$\pm 2.0\%$
Betatron tune (Hor./Ver.)	3.440/3.540
Transition gamma	4.533
Max. beta functions (Hor./Ver.)	28.58 m/28.04 m
Max. dispersion	3.96 m

Refined design of the lattice is shown in Table 1 and Figs. 1 and 2.

The ACR lattice consists of four arc sections, two long straight sections and two short straight sections, as shown in Fig. 1 and is described as follows:

$$\text{ACR} = \text{STRL-ARC-STRS-ARC-STRL-ARC-STRS-ARC},$$

where STRL denotes a long straight section, STRS a short straight section and ARC an arc section.

An ARC is symmetric and is based on the FODO lattice cell.

$$\text{ARC} = \text{QF-B-QD-QD-B-QF-QF3-QD3-(INJ)-QD3-QF3-QF-B-QD-QD-B-QF},$$

where QF and QD are the main focusing and

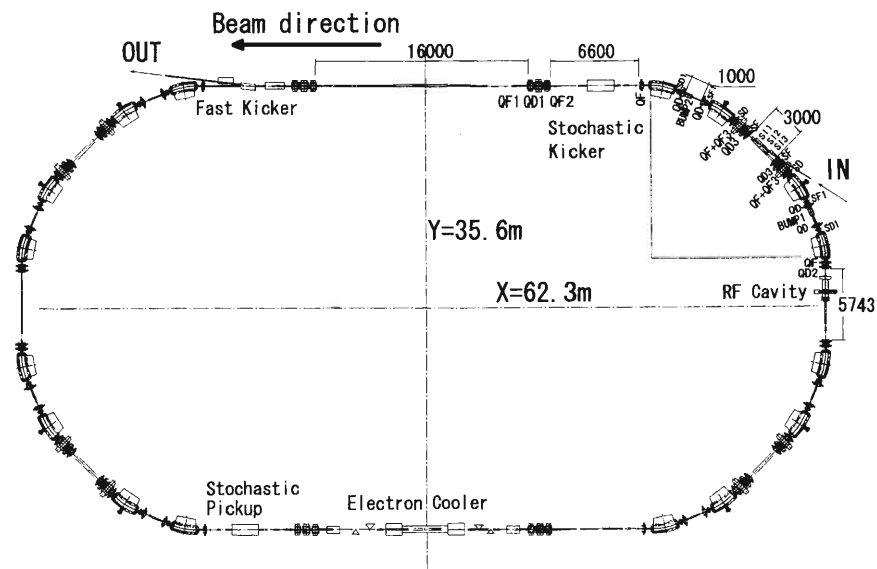


Fig. 1. The layout of the ACR.

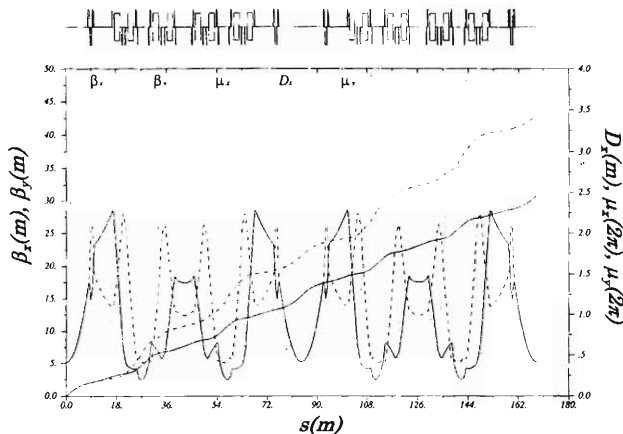


Fig. 2. Twiss parameters. The periodic solid line represents the horizontal betatron function, the periodic dashed line the vertical betatron function, the periodic dotted line the dispersion function, the increasing dashed-dotted line the horizontal phase advance and the increasing solid line the vertical phase advance.

defocusing quadrupoles, respectively, QF3 and QD3 the dispersion adjustable quadrupoles, and the B bending magnets. The drift space between QD3s is assumed as an injection point. The ARC functions are assumed as dispersion suppressers. Four families of sextupoles are installed each drift space for chromaticity correction.

The long straight section is defined as follows:

$$\text{STRL} = -\text{QF2}-\text{QD1}-\text{QF1}-\text{QF1}-\text{QD1}-\text{QF2}-,$$

where QF1, QD1 and QF2 are quadrupoles. The triplets make the horizontal betatron function at the symmetry point less than 5 m. The middle straight section, which has a length of 15 m, is assumed to be the position of the electron cooler or an equipment for experiments. At both end straight sections, of 6 m length, stochastic cooler devices and extraction kickers are installed.

The short straight section is defined as follows:

$$\text{STRS} = -\text{QD2}-\text{QD2}-,$$

where QD2s are quadrupoles to adjust the tune and beta functions' amplitude at STRS. A tunable RF cavity will be located in this section.

Horizontal tune is selected to be nearly a half integer because the betatron tune advance between every opposite pair of straight sections become nearly a quarter integer, i.e., constraint (2) is satisfied (Fig. 3). The large acceptable momentum spread operation makes the half integer stop band large. It causes a betatron modulation with a different momentum. However, the modulation amplitude was turned to be at a tolerable level.

Dynamic aperture of the lattice without a horizontal or vertical orifice has been calculated (Fig. 4).

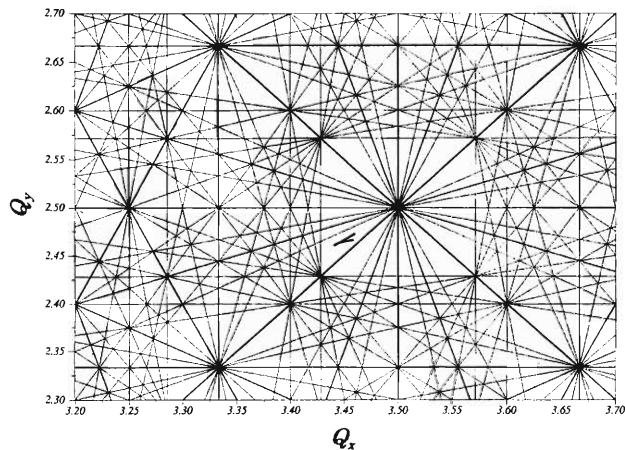


Fig. 3. Tune diagram. Operation points are represented by a thick bent line.

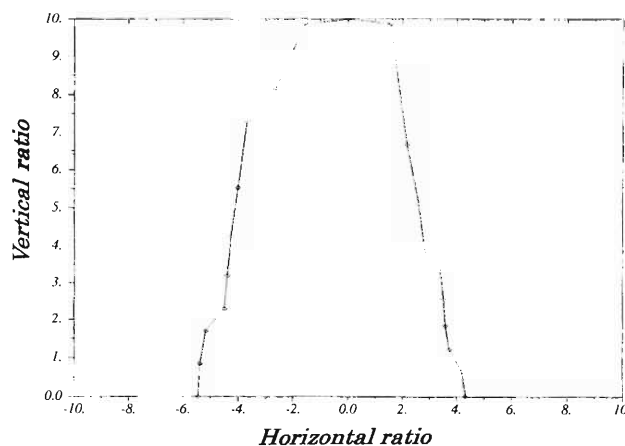


Fig. 4. Dynamic aperture with a bare lattice. Number indicates the ratio of betatron amplitude to normalized horizontal and vertical emittance of 125 and 10  $\pi$ -mm·mrad, respectively.

Solenoids and deflections by troidals of the electron cooler causes the dynamic aperture to shrink but no severe influence is noted under the condition where a first ordered compensation had been added.

Discussion about the momentum compaction factor between stochastic cooler pickup and kickers to shorten stochastic cooling time<sup>3)</sup> is underway. The scalable transition gamma lattice<sup>4)</sup> will be considered in future research.

#### References

- 1) K. Ohtomo et al.: RIKEN Accel. Prog. Rep. **30**, 211 (1997).
- 2) K. Ohtomo and T. Katayama: RIKEN Accel. Prog. Rep. **31**, 225 (1998).
- 3) M. Wakasugi: MUSES Meet.
- 4) A. Dolinskii et al.: Proc. European Particle Accelerator Conf. '96, p. 596 (1996).

## Development of ACR Electron Cooler (2)

T. Tanabe, K. Ohtomo, T. Rizawa, and T. Katayama

The highlight of the cooler design in the accumulator cooler ring (ACR) in MUSES project<sup>1,2)</sup> is the gun section which utilizes a He-free superconducting solenoid with an output of 4 T. To optimize the cost and uniformity of the solenoid field, a smaller gun and an acceleration tube are preferred. However, without the possibility of placing vacuum pumps in the vicinity of the cathode, high-vacuum conductance must be maintained through to ensure ultra-high vacuum (UHV.) Poor vacuum would cause contamination of the cathode surface, lowering of the discharge limit due to a high voltage (HV), and an increase of unnecessary radiation hazard. Both Egun<sup>3)</sup> and SAM<sup>4)</sup> are used to examine the behavior of an electron beam (e-beam) to optimize the design. Figure 1 shows results of EGUN simulation with the current design.

Optimization of the design of the magnetic shield and solenoids is directed toward the uniformity of the field over the acceleration area, the minimization of the shield thickness, and the reduction of the adiabatic parameter, which is defined as

$$\chi = \frac{\lambda_c}{B} \left| \frac{dB}{dz} \right|, \quad (1)$$

where  $B$  is the solenoid magnet field and  $\lambda_c$  is the spiral length of the cyclotron motion

$$\lambda_c = \frac{2\pi\sqrt{2m_e E_e}}{eB}. \quad (2)$$

A cross-sectional view of the design of an electron gun, an acceleration tube, a superconducting solenoid, a warm solenoid, and magnetic shielding are delineated in Fig. 2. The magnetic field distribution and the adiabatic parameter are shown in Fig. 3.

The electrons are further perturbed when they pass through the toroidal sections. This perturbation is observed in electrons which are displaced from the equilibrium axial trajectory. When the electrons pass through a toroidal magnet, additional drift velocity appears which is inversely proportional to the square of the radius of the axial electron trajectory in the toroidal section.<sup>5)</sup> Hence, the discontinuity of the magnetic field at the entrance/exit of toroidal magnets generates additional transverse temperature which can be

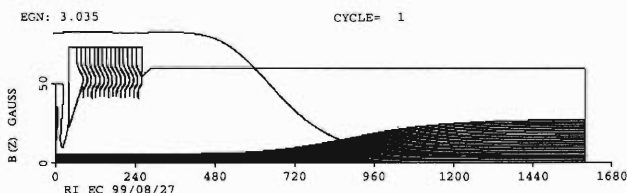


Fig. 1. EGUN simulation of the electron gun section.

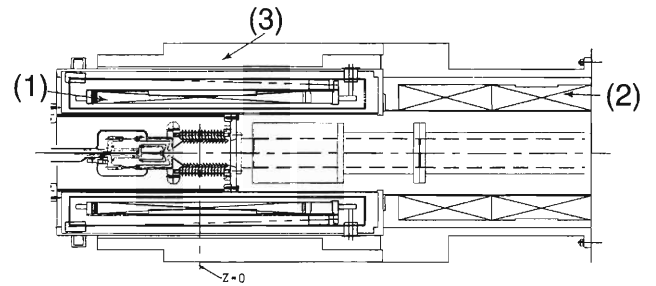


Fig. 2. Layout of (1) a superconducting solenoid, (2) a warm solenoid and (3) magnetic shielding.

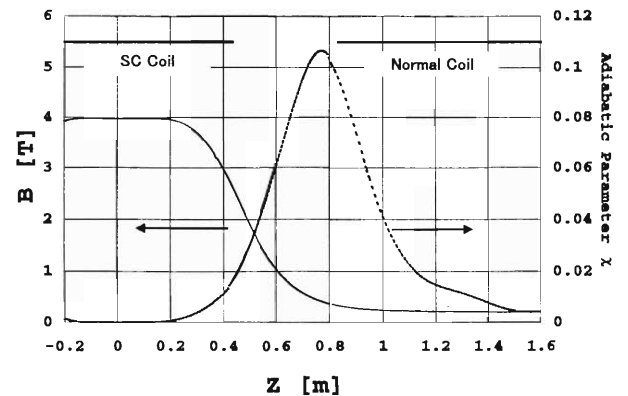


Fig. 3. The longitudinal magnetic distribution and the adiabatic parameter.

reduced by increasing the toroidal radius and decreasing the adiabatic parameter at the entrance/exit of toroidal magnets.

The initial design of the ACR collector was based on the TARN II collector. Various improvements have been incorporated during the past year. The geometry of the new collector section is given in Fig. 4.

The ratio of the current density of the reflected secondary electrons that escape a collector to those of the incoming beam is proportional to<sup>5)</sup>

$$\frac{j_{ref}}{j} \approx \frac{\sigma_e}{\pi} \left( \frac{\phi_{min}}{U_{col}} \right)^2 \frac{B_{col}}{B_{\phi_{min}}}, \quad (3)$$

where  $j$  is the incoming beam current,  $\sigma_e \approx 1$  is the secondary emission coefficient,  $B_{col}$  and  $U_{col}$  is the magnetic field and voltage on the collector surface, respectively,  $\phi_{min}$  is the minimum potential on the axis and  $B_{\phi_{min}}$  is the magnetic field in the region of minimum potential value. The types of modifications applied were as follows:

- (1) The collector diameter was increased to reduce the magnetic field on the collector surface,  $B_{col}$ .
- (2) To increase  $B_{\phi_{min}}$ , a permanent magnet coil was

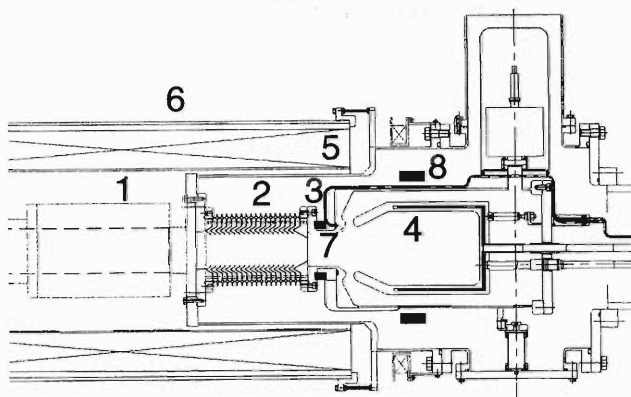


Fig. 4. The design of the collector. 1 indicates the drift chamber, 2 the deceleration tube, 3 the repeller, 4 the collector electrode, 5 the solenoid of electron cooling, 6 magnetic shielding, 7 the permanent magnet coil placed at the collector entrance, and 8 the permanent magnet coil placed on the collector surface.

placed inside the repeller electrode with a magnetic field of 2 kG.

(3) A permanent magnet coil was placed on the collector surface to reduce  $B_{col}$ .

(4) The collector radius was reduced at the entrance to shift the position of the virtual cathode to a region of higher magnetic field.

The collector perveance is estimated as  $P_{col} = I/U_{col}^{3/2} \approx 25 \sim 30 \mu\text{A}/\text{V}^{3/2}$ . The permanent magnets produce a negative radial magnetic field on the collector surface in the region of  $44 \text{ cm} < z < 51 \text{ cm}$  (magnetic-insulated region). Consequently, the current loss was reduced by one order of magnitude compared to the old design.

A diagnostic setup for an e-beam can be separated in two categories of devices: Conventional and special ones. The conventional diagnostic devices measure electrode potential, e-beam current and e-beam loss current. The special devices are used for the measurement of the transverse electron temperature, the parameters of the neutralized electron beam, and the characteristics of the secondary electrons and ions. The details of the designs have yet to be established.

Table 1 shows the latest parameters of the device,

Table 1. Parameters of ACR-EC.

Acceleration Voltage	30 ~ 250 kV
Magnetic Field (gun/cooling)	4 T / 0.2 T
Field Uniformity (gun/cooling)	$1 \times 10^{-4} / 2 \times 10^{-5}$
Cathode Diameter	12.7 mm
Maximum E-Beam Current	4 A
Gun Perveance	$0.79 \mu\text{P}$
Anode-Cathode Voltage	30 kV
Main Solenoid Length	3.6 m
Toroidal Angle / Radius	$90^\circ / 1.5 \text{ m}$
Collector Efficiency	$> 99.98\%$

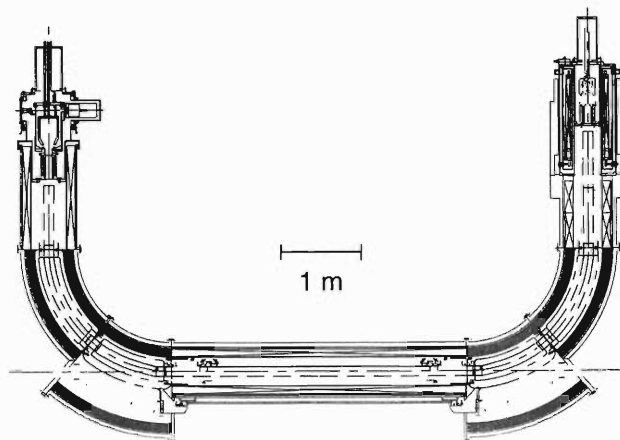


Fig. 5. Cross-sectional view of the MUSES-ACR EC. The gun section is on the right-hand side and the collector section is on the left-hand side.

and the cross-sectional view of the entire EC system is shown in Fig. 5.

#### References

- 1) T. Katayama et al.: Proc. EPAC98, p. 529 (1998).
- 2) T. Tanabe, K. Ohtomo, T. Rizawa, and T. Katayama: RIKEN Accel. Prog. Rep. **32**, 212 (1999).
- 3) B. Herrmansfeld: SLAC 226, NC. 28.
- 4) M. Tiunov, B. Fomel, and V. Yakovlev: Preprint INP, Novosibirsk, p. 85 (1996).
- 5) E. Syresin: Nucl. Instrum. Methods Phys. Res. A **391**, 114 (1997).
- 6) MUSES Conceptual Design Report, RIKEN, Chap. 4 (1997).

## Study of Pickup for Stochastic Cooling

N. Inabe, M. Wakasugi, M. Kanazawa, and T. Katayama

Stochastic cooling<sup>1)</sup> is used for beam cooling of Accumulator Cooler Ring (ACR).<sup>2)</sup> The cooling time in ACR should be short ( $\sim 100$  ms) since fast beam cooling must be realized for Radioactive Isotope (RI) beams with very short intrinsic lifetimes. The stochastic cooling system is composed of pickups, preamplifiers, amplifiers, filters, and kickers; it forms a feedback loop from the pickups to the kickers. In order to obtain a short cooling time a large gain, a low noise and a wide frequency band are required for the system.<sup>3)</sup> To develop such a system we need a highly sensitive pickup, a low-noise preamplifier and a large gain amplifier for a wide frequency region (0.3–2.0 GHz). As the first developmental step, we fabricated a pickup and tested it using a beam from the HIMAC<sup>4)</sup> synchrotron.

Figure 1 depicts a pickup system. The pickup system is composed of 16 pairs of electrodes, a ground box, and a vacuum chamber. Each electrode is a loop typed coupler and its length (50 mm) is chosen so as to be maximally sensitive around 0.5–1 GHz. The electrode width (81 mm) and gap (60 mm) are determined so as not to disturb HIMAC beam. The signal picked up by the electrode is sent to two terminals located at either edge of the electrode through a stripe-line of

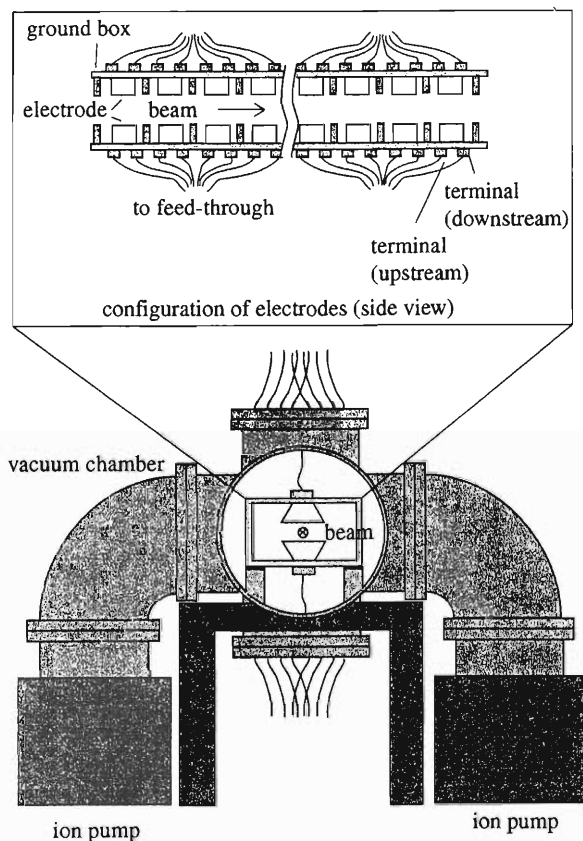


Fig. 1. Schematic depiction of the pickup system.

$50 \Omega$  composed of the electrode and the ground box. Each terminal is connected by a coaxial cable (Dip-sol Co. Ltd.; Cu-s5DDs-08) having a wide frequency band and low outgas and the signal is sent outside the vacuum chamber through an original feed-through connector. Since the voltage of the output signal from the terminal depends on the beam velocity, we prepared two terminals so that we can choose the larger signal of the two terminals. When using the system, the terminal with the smaller signal is terminated by the  $50\text{-}\Omega$  terminator.

In order to have adequate vacuum pressure ( $\sim 10^{-10}$  Torr) in the synchrotron the vacuum chamber has two ion pumps (400 l/s each). Before the pickup system was installed into the synchrotron we backed it. The baking temperature was raised to  $180^\circ\text{C}$  over two days and kept at the temperature for another two days. One week after the end of baking, the vacuum pressure became  $2 \times 10^{-9}$  Torr. One month after installation the pressure was  $5 \times 10^{-10}$  Torr.

A beam test for the pickup system was performed using a carbon beam of 290 MeV/u from the HIMAC synchrotron. The intensity of the beam was  $1.9 \times 10^9$  particles per second and it was very stable. In the test we measured signals picked up by the electrodes for a bunched beam and a coasting beam after acceleration with respect to the time and frequency domains. In the measurement for the coasting beam the RF voltage of the cavity was turned off. Figure 2 shows an electrical circuit for the measurement. A pulse from the synchrotron produced at the finishing time of acceleration was used as a gate signal for the measurement. For the measurement of the bunched beam, an RF signal was used to mark the time origin. The signal from the electrode was sent to a sampling oscilloscope for the time-domain measurement and a spectrum analyzer for the frequency-domain measurement. In the measurement, when the signal from one terminal was

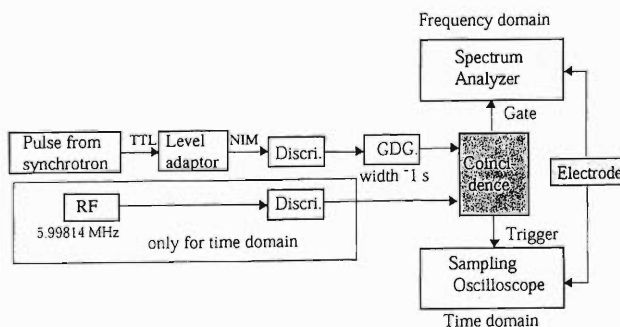


Fig. 2. Electrical circuit for measurement of the pickup signal.

measured, the other terminal was terminated. Since this measurement was the first test of the pickup system, we concentrated on observing any signals and did not use a preamplifier.

Figures 3 and 4 show the time- and frequency-domain signals for the bunched beam. The interval between peaks in Fig. 3 shows the time interval between bunches. The interval between peaks in Fig. 4 shows the RF frequency of the synchrotron. The measured values of 166 ns in Fig. 3 and 6 MHz in Fig. 4 were consistent with RF frequency set for the synchrotron (5.998 MHz). In Fig. 4 one can see that the peak height decreases as the frequency becomes higher. The bunch length of the beam was long and the electromagnetic field produced by this long bunched beam has a strong component in the low-frequency region. The tendency of decreasing peak height results from the long bunch length.

We attempted to reproduce the time-domain signal

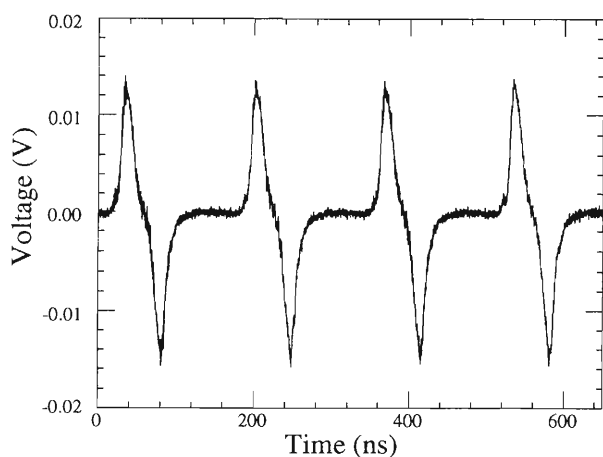


Fig. 3. A time-domain signal from an electrode of the pickup system.

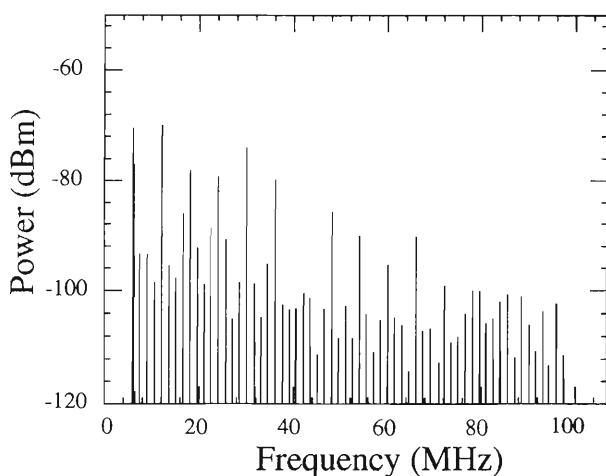


Fig. 4. A frequency spectrum from an electrode of the pickup system.

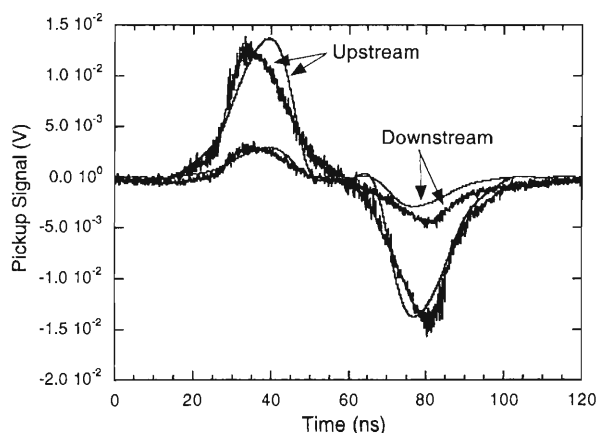


Fig. 5. Calculated and measured time spectra for both terminals of one electrode.

on the basis of theoretical calculation.<sup>5)</sup> In the calculation, the distribution of the bunched beam was assumed to be the Gaussian part plus the flat parts and frequency up to 100 MHz was taken into account from Fig. 4. The widths of the Gaussian and the flat part as well as the sensitivity of the pickup were parameters for the reproduction. Here, sensitivity is a quantity defined by  $V_{out}/I_{beam}$ , where  $V_{out}$  is the output voltage measured in the sampling oscilloscope and  $I_{beam}$  is the average beam current. In Fig. 5, the reproduced spectra for the two terminals of one electrode are shown with measured signals. In the figure, widths of the Gaussian and the flat parts are common for the two curves. The obtained half-width of the Gaussian part is 2.0 m and that of the flat part is 0.85 m. The obtained sensitivity of the pickup around 100 MHz is 5  $\Omega$  for the upstream terminal and 1.5  $\Omega$  for the downstream terminal. These values are rather high compared to the ones from the theoretical calculation.

Unfortunately, we can not measure the frequency spectrum of the coasting beam because the signal is very small. However, this is not inconsistent with the theoretical calculation. In the next experiment scheduled on January in 2000, we will measure the spectrum by using of a preamplifier and obtain a sensitivity up to 2 GHz. Moreover, we will examine how to combine signals from various electrodes using the pickup system.

#### References

- 1) S. van der Meer: CERN Report, CERN/ISR-PO/72-31 (1978).
- 2) K. Ohtomo et al.: Proc. 17th PAC, Vancouver, May, p. 1072 (1997).
- 3) N. Inabe et al.: Proc. 6th EPAC, Stockholm, June, p. 1037 (1997).
- 4) Y. Hirao et al.: Nucl. Phys. A **538**, 541c (1992).
- 5) D. A. Goldberg et al.: LBL Report, LBL-25924 (1989).

## The Ferrite Test Cavity for MUSES (II)

K. Ohtomo, T. Rizawa, and Y. Chiba

We reported on a ferrite test cavity in the last issue of this annual report,<sup>1)</sup> used for measuring the characteristics of ferrite at the same high rf power level as that planned for the booster synchrotron of the Multi-USE Experimental Storage rings (MUSES) project; an accelerating cavity is required to generate 25 kV in the frequency range of 25 to 53 MHz. In this issue, we report on the further improvement and calibration of the system. Figure 1 shows a schematic of the cavity.

Improvement of the system: In the first step of the experiment with the cavity, unstable behavior of the Q value of the cavity itself, without the ferrite, was identified. This behavior was caused by a malfunction of the contact fingers used on the cylindrical surfaces a, b, c, d and e shown in Fig. 1. Improvements were made by replacing the contact fingers with a Helicoflex metal gasket at a and c, a flat face metal-metal contact at b and another type of contact spring at d and e.

Calibration of the system: The system is divided into two parts, as seen Fig. 1, by taking the junction plane at S. The admittance of the upper half with the ferrite is denoted by  $Y_m$  and that of the lower half, by  $Y_c$ . The entire system is formed by the parallel connection of  $Y_m$  and  $Y_c$ .  $Y_m$  is inductive at the resonance frequency and  $Y_c$ , capacitive. Hereafter, G and B denote the real and imaginary parts, respectively, of the admittance Y, e.g.,  $Y_m = G_m + iB_m$  and  $Y_c = G_c + iB_c$ . The resonance condition is given by  $B_m = -B_c$ .

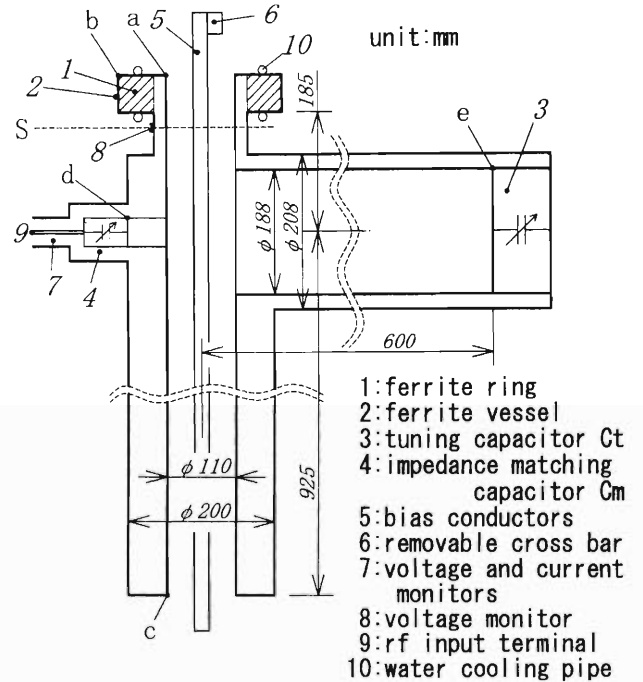


Fig. 1. Schematic diagram of the ferrite test cavity.

The relative permeability,  $\mu$ , and magnetic Q value,  $Q_m$ , of ferrite are determined from  $Y_m$ . This process depends on the electrical model describing the ferrite vessel containing the ferrite. The simplest model is

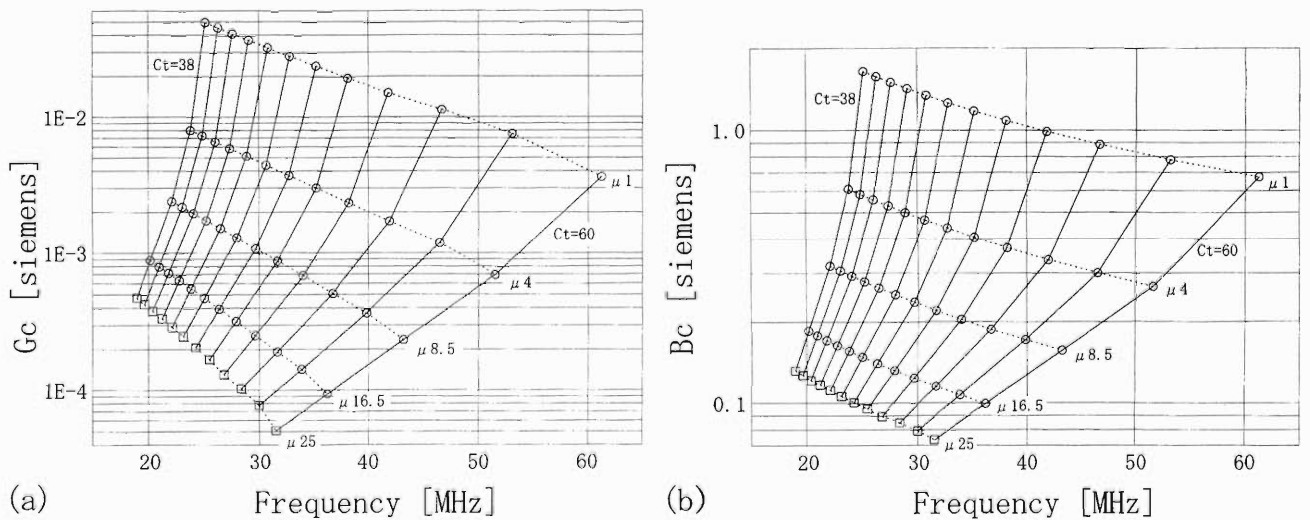


Fig. 2. (a) Real part of  $Y_c$  and (b) imaginary part of  $Y_c$ . Circles indicate calibration points, e.g., points on the dotted line labeled  $\mu_4$  represent measurements with a reference stub corresponding to a  $\mu$  of 4. Points with the same  $C_t$  are connected by a solid line.  $C_t$  varies from 38 to 60 with an interval of 2. Squares indicate points corresponding to a  $\mu$  of 25, which are estimated using the transmission line approximation.

one that ignores the radial dependence of  $\mu$  due to the bias field and assumes a low frequency limit. This yields an effective  $\mu$  by  $(f \cdot B_m \cdot \mu_o \cdot t \cdot \ln(b/a))^{-1}$  and  $Q_m$  by  $|B_m|/G_m$ , where  $f$  is the measuring frequency,  $\mu_o$  is the permeability of vacuum, and  $t$ ,  $b$  and  $a$  are the thickness and the outer and inner radii of the ferrite ring, respectively. We use a model based on the transmission line approximation, in which the vessel is treated as a radial mode transmission line and a radially constant  $\mu$  is assumed. This model is appropriate for the frequency range studied here and can be solved numerically.

With the value of voltage,  $V$ , across  $Y_m$ , and input power,  $P$ , at the resonance frequency,  $G_m$  is directly obtained from  $(P/V^2) \cdot G_c$  using a precalibrated value of  $G_c$ .  $B_c$  is dependent on the frequency and the value of the tuning capacitor,  $C_t$ , while the impedance matching capacitor contributes only a small correction.  $B_c$  can be estimated with reasonable precision on the basis of the transmission line calculation but  $G_c$  must be estimated by measurements, because of the contribution from the resistance of the structural contact surfaces and the loss factors of the tuning capacitor. Therefore, both quantities were estimated using calibration measurements as a function of frequency and division number of the revolution dial

of the tuning capacitor.

Four types of reference admittance are provided. They are nearly equivalent to the admittance of ferrite rings (8" outer diameter, 5" inner diameter and 1" thick) with  $\mu$  equal to 1, 4, 8.5 and 16.5. They consist of simple coaxial stubs whose admittance,  $G_r + iB_r$ , is easily calculated. Replacing the ferrite vessel with a reference stub, the resonance frequency and the conductance of the entire system,  $G_s$ , are measured using an impedance analyzer connected to the junction point on plane S. Thus,  $Y_c$  is determined at the resonance frequency as  $Y_c = (G_s - G_r) - iB_r$ . For each reference stub, calibration is made at 12 positions of the tuning capacitor between the number of dial divisions  $C_t = 38$  to 60, which corresponds to a real capacitance of 642 to 70.5 pF. Results are shown in Fig. 2 (a) for the real part and Fig. 2 (b) for the imaginary part.

$\mu$  and  $Q_m$  are calculated from the measured data by linear interpolation between the calibration points; measured data are  $f$  (MHz),  $C_t$  (division),  $V$  (volt) and  $P$  (watt).

#### References

- 1) K. Ohtomo and Y. Chiba: RIKEN Accel. Prog. Rep. **32**, 218 (1999).

## Development of the Kicker Magnet for BSR

T. Ohkawa, T. Katayama, M. Wakasugi, and Q. You

In the booster synchrotron ring (BSR), kicker magnets are used for ion-beam injection and ion-beam and electron-beam fast extraction. The injection and extraction kicker field must rise and fall from approximately 5% to 95% of full strength during the time interval between bunches (about 50 ns).<sup>1)</sup> The high performance of the kicker magnet is crucial for the efficiency of beam injection and extraction. In this paper, the development of a kicker magnet for BSR is presented.

We have adopted the Pulse Forming Network (PFN)-type kicker magnet which is often used to generate a high magnetic field with a rapid rise and fall time. The characteristic impedance  $Z$  is related to the inductance  $L_0$  and capacitance  $C_0$  of the unit cell by

$$Z = \sqrt{L_0/2C_0} \quad (1)$$

and the transmission time  $\tau_m$  of the total magnet is calculated by

$$\tau_m = N\sqrt{2L_0C_0}, \quad (2)$$

where  $N$  is the cell number. The relationship between  $Z$  and  $\tau_m$  is obtained by Eqs. (1) and (2) as

$$\tau_m = NL_0/Z. \quad (3)$$

Therefore, decreasing the impedance causes an increase of the transmission time. In order to generate a magnetic field of the design value in a core gap of 30 mm, PFN voltage is required up to 100 kV. When the PFN is added with 100 kV, the kicker magnet can produce a magnetic field of 0.084 T with a flat top of 1  $\mu$ s and a rise time of 65 ns. The design parameters are listed in Table 1. The height and width of the kicker magnet aperture are 30 mm and 130 mm, respectively. The kicker magnet has a transmission-line structure of nine cells and the characteristic impedance is 25  $\Omega$ .

Table 1. Design parameters for the kicker magnet.

ITEM	DESIGN VALUE
Gap height	30 mm
Gap width	130 mm
Total core length	225 mm
Cell number	9
Inductance of unit cell	0.136 $\mu$ H
Capacitance of unit cell	108.9 pF
Characteristic impedance	25 $\Omega$
Gap field	0.084 T
Coil current	2000 A
PFN voltage	100 kV
Field rise time	65 ns

The characteristic impedance and the transmission time are measured using a low-voltage short pulse. A schematic of the measurement system is depicted in Fig. 1. The kicker magnet and pulse generator are connected by the 50  $\Omega$  transmission cable. In order to match the impedance, a matched resistor  $R_1$  is installed between the inlet of the magnet and the 50  $\Omega$  transmission cable and the outlet of the magnet is terminated in the matched resistor  $R_2$ . The reflected signal follows the input pulse and can be presented in the same oscilloscope record. The amplitude of the reflected pulse serves as an indicator of the matching. In the ideal case the pulse travels to the matched resistor and there should be no reflected pulse. Figure 2 presents the results of the 0.5 V pulse with a flat top of 1  $\mu$ s and a rise time of 65 ns. Figures 2 (a) and (b) show the reflected voltage pulses when one of the matched resistors  $R_1$  and  $R_2$  is changed while the other

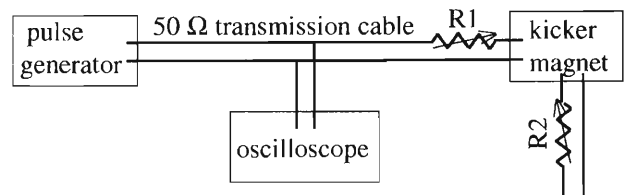
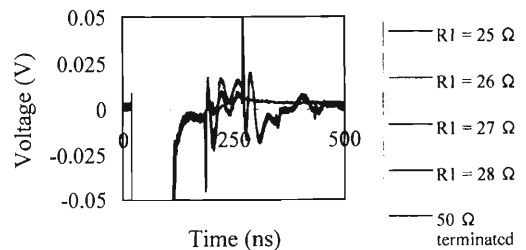
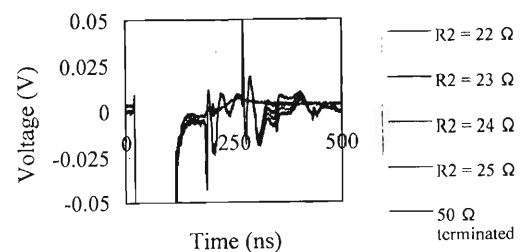


Fig. 1. Schematic of the measurement system.



(a) R1 is changed



(b) R2 is changed

Fig. 2. Low-voltage pulse and reflection. (a) R1 is changed, (b) R2 is changed.

one is kept constant.

The reflected pulse is delayed by approximately 160 ns with respect to the initial signal because we observe both of them on the same oscilloscope. Figure 2 shows that the characteristic impedance of the kicker magnet is  $23 \Omega$ .

The voltage pulses at the electrodes of each cell are shown in Fig. 3.

The measurement shows that the transmission time of the kicker magnet is 59 ns and the field rise time is 69 ns. The calculated results of the inductance  $L_0$  and capacitance  $C_0$  of the unit cell are obtained by Eqs. (1) and (2) as  $L_0 = 0.14 \mu\text{H}$ ,  $C_0 = 136 \text{ pF}$ . The calculated value of the inductance is almost the same as the designed value, but the calculated value of the capacitance is larger than the design value. The reason why the capacitance of the unit cell is larger than the design value is that there is floating capacitance between the electrodes and the housing.

We designed, produced and tested the PFN-type kicker magnet. We determined that the characteristic impedance of the kicker magnet is  $23 \Omega$ , the transmission time of the kicker magnet is 59 ns and the field rise

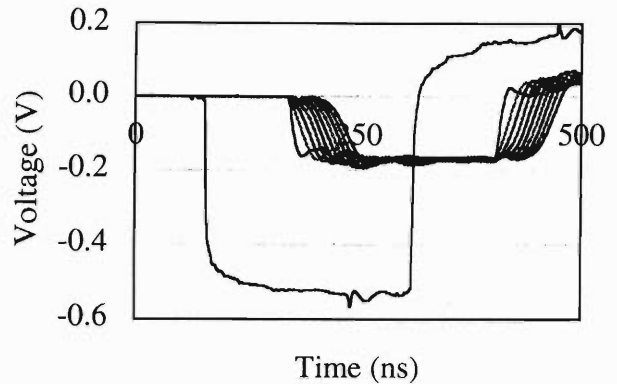


Fig. 3. Voltage pulse at the electrode of each cell.

time is 69 ns. The measurements demonstrate that the design of the kicker magnet for BSR is quite realistic. We intend to perform further tests and study the kick strength and the amplitude stability.

#### References

- 1) T. Ohkawa et al.: Proc. 17th PAC, Vancouver, 1997, p. 1024 (1998).

## Development of a High-Intensity Slow-Positron Source for Cooling of Highly Charged Ions

N. Oshima, D. Dumitriu, T. M. Kojima, A. Mohri, H. Oyama, T. Kambara, Y. Kanai, Y. Nakai, M. Wada, and Y. Yamazaki

We study positron cooling of highly charged ions in an electromagnetic trap in which more than  $10^8$  positrons must be prepared. In order to stack such a large number of positrons at a high accumulation rate, a high-intensity slow-positron source is under development.

Slow positrons are generally produced by moderation of fast positrons which can be obtained by  $\beta^+$  decay of radioisotopes or pair production using an accelerator. Fast positrons injected into a moderator lose their energy via inelastic collisions and a considerable fraction is ejected into vacuum as slow positrons. The energy spread of slow positrons is typically less than 3 eV, hence, slow positrons are controllable as a beam by beam optics.

In our study, rare-gas-solid moderators such as those made from Ne, Ar, and Kr are used. Rare-gas solids are well known to be efficient moderators of positrons.<sup>1)</sup> When the positron energy becomes less than the inelastic threshold of the moderator, the positron energy loss is reduced drastically since phonon excitation becomes the dominant process of the energy loss. Threshold energies are relatively large in rare-gas solids, therefore, positrons can diffuse long distances about  $1 \mu\text{m}$ , and the reemission probability into vacuum increases.

Figure 1 shows a schematic of the slow-positron

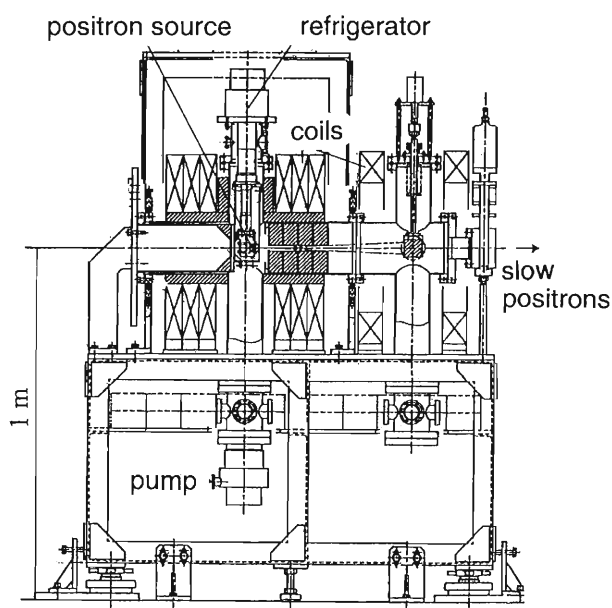


Fig. 1. Design of a slow-positron source.

source. An encapsulated  $^{22}\text{Na}$  positron source is mounted on the top of a refrigerator and is cooled down to 5 K, so that a rare-gas-solid moderator is formed on its front face (see, Fig. 2). Slow positrons are then extracted using an electrostatic field and guided magnetically to an electromagnetic trap.

The trap is set in a superconducting magnet which generates a strong magnetic-field,  $B_T = 5 \text{ T}$ , to achieve a stable confinement of positrons. When positrons are injected into a strong magnetic field, they are subject to a repulsive force. This is called the magnetic mirror effect. Under the assumption that positrons are guided adiabatically into the trap, the positrons must have a kinetic energy of greater more than a threshold energy  $E_a$  to overcome the magnetic mirror effect.  $E_a$  is calculated as  $E_a = E_{\perp} \cdot B_T / B_0$ , where  $B_0$  is the magnetic-

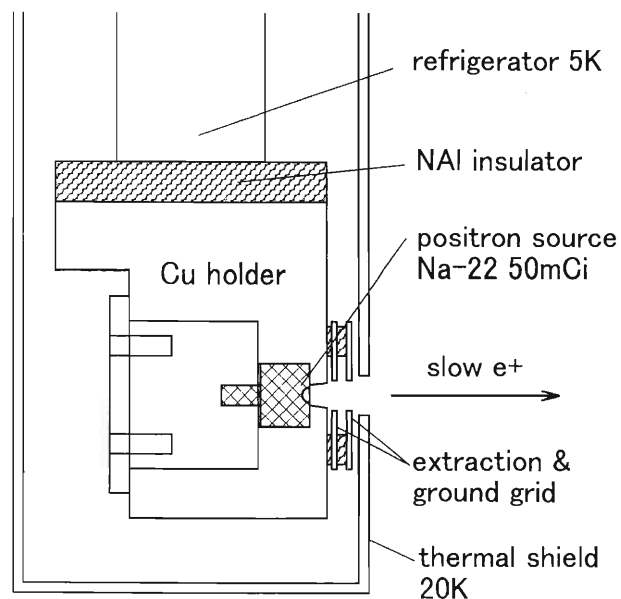


Fig. 2. Positron source and moderator assembly.

Table 1. Expected specifications of the positron source.

positron source	$^{22}\text{Na}$ (50 mCi)
beam intensity	$10^7$ positrons/sec
beam energy	0–500 eV
energy spread	2 eV
beam diameter	5 mm
magnetic field strength at a moderator	0–0.25 T

field strength at the moderator and  $E_{\perp}(= 2 \text{ eV})$  is the positron kinetic energy component perpendicular to the magnetic field at the moderator. We designed coils around the moderator which can form a magnetic field of up to  $B_0 = 0.25 \text{ T}$ ; hence,  $E_a$  is expected to be only 40 eV. Consequently, almost of all of the generated slow positrons can be injected into the trap at an energy of more than 40 eV.

The expected specifications of the new slow-positron

source are listed in Table 1. The high-intensity slow-positron source will be used not only for a positron cooling study but also for other experiments, such as positron-ion collisions and a positronium beam production, and simulations of antihydrogen formation techniques.

#### References

- 1) R. G. Greves et al.: *Can. J. Phys.* **74**, 445 (1996).

## Preliminary Studies on CORBA-based RIBF Control System

T. Tanabe, T. Masuoka, and M. Kase

The common object request broker architecture (CORBA)<sup>1</sup> provides a means of communication between applications regardless of their physical location or design. The object request broker (ORB) allows client objects to invoke methods in a server object without having to know specific information about the machine the server is running on, its programming language, or where it is located. The ORB intercepts method calls and attempts to find an object which can perform the request. The Internet inter-ORB protocol (IIOP), which is used for communication among ORBs, is expected to become one of the next standard communication protocols for the internet.

CORBA would prevent us from becoming vendor dependent because it allows different operating systems (OSes) and platforms to communicate with each other. It would also make integration of legacy controls easier, which is suited for the RIBF project as it is an expansion of existing facilities. There are several accelerators and telescopes currently in operation around the world whose controls are based on CORBA. However, the use of ORBs on real-time operating systems (RTOSes) in VME is just starting and very few examples exist. Therefore, as a part of the R&D work for the RIKEN RIBF control system, we have conducted various tests of ORBs for RTOSes on VME/CPCI.

The main purposes of our R&D are:

- (1) To establish CORBA-based communications among different GUIs (created in C++ and Java) and VME/CPCI running different RTOSes.
- (2) To estimate the total operational overhead due to the use of CORBA.
- (3) To confirm interoperability through IIOP among different ORBs.
- (4) To clarify the deficiencies, if any.

In addition to the interoperability test, the ORB chosen for use in all components was VisiBroker<sup>2</sup> due to the availability of both VxWorks<sup>3</sup> and pSOSystem<sup>4</sup> as well as its widespread use throughout the Netscape browser. Visual C++ 6.0 is used for C/C++ applications and Visual Cafe for Enterprise Edition<sup>5</sup> is used for Java applications. Figure 1 shows the system configuration for this R&D.

A few GUI applications are written using C++ which utilizes conventional socket functions to communicate with VxWorks running on a PowerPC 604 based VME (Motorola MVME 2600). We have installed and tested the function of a variety of VME I/O boards with a VxWorks driver. Then, sources for each layer were modified and compiled with links to CORBA libraries. Using CORBA, one can discard routines for socket functions which require detailed information on the

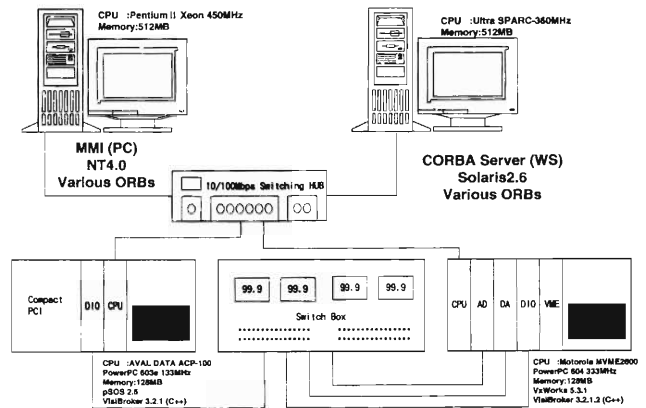


Fig. 1. CORBA test system configuration.

hardware characteristics of both sending and receiving sides. The client, who may not know the details of the server, simply invokes the server object to complete a two-way communication.

Under normal circumstances for accelerator controls, the interface information is known and static. Therefore, static invocation interface (SII) is adequate. Dynamic invocation interface (DII) can be used when the types of parameters used in the programs are unknown. The program of the client using DII will be more complex because operations, such as looking up the argument of the server and returning the value must be carried out dynamically. As far as RIBF controls are concerned, DII is deemed unnecessary. A naming service (NS) is useful in the case one type of ORB is used for the entire system.

For comparison, the response times for various I/O boards have been measured for three different methods. Test routines include the following: (a) Server returns I/O values at the request of a client. (b) Client invokes the object 100 times and the elapsed time is measured. This routine is repeated 10 times to obtain more reliable statistics.

In addition to VisiBroker, a free ORB (for non-commercial use only) such as ORBacus,<sup>6</sup> was used to evaluate the interoperability among different ORBs. The interoperable naming service is not available until CORBA 3.0<sup>1</sup> so one way to pass the object reference across different ORBs is as follows: (1) Interoperable object reference (IOR) is changed into a string, and a server side writes it to the file. (2) A client side reads the file created on the server side, and returns a string to IOR. A file is delivered with FTP, NFS, and so on. The times for two-way calls for different configurations have been measured and compared. The method is as follows: (a) Server returns a random number (float)

when it is called upon by a client. (b) Client invokes the object 10000 times and the elapsed time is measured. This routine is repeated 10 times to obtain more reliable statistics.

One of our goals is to establish a heterogeneous environment for the accelerator controls. Therefore, a RTOS other than VxWorks should be tested. A pSOSystem has been chosen due to the availability of ORBs, particularly VisiBroker. A compact PCI CPU board (AVAL DATA ACP-100)<sup>7)</sup> is used as the main controller. A DIO board by the same manufacturer<sup>8)</sup> is installed for comparison as a corresponding VME board. However, numerous unforeseen problems prevented us from completing this test in time for publication.

For the measurement of response times for various I/O boards, Windows-NT 4.0 is used as the client OS, and Visual C++ 6.0 is used as the compiler. For the server, VxWorks 5.3.1 running on PowerPC 604 and its C++ compiler are employed. VisiBroker is used for both the client and server. Table 1 lists the measurement times in msec for different methods. It seems that the rather large fluctuation in the response for socket communication is due to the use of an event-driven socket library (CAynchSocket). Events not related to this test might have affected the results during transmission. As for the DII cases, this particular test somewhat sacrifices the generality. The server interface definition languages (IDLs) are given a priori so that the time during which the DII searches for the interfaces is shortened.

The results of interoperations among different ORBs and OSES are listed in Table 2. The numbers with an asterisk indicate that a VisiBroker function utilizing interprocess communication is used. So far, only ORBacus for Java has been tested for Java/CORBA implementation. JDK 1.2 has been used for the evaluation. It suggests that Java client implementation for this particular ORB is approximately 2.5-3.5 times slower than C++ implementation for the same task. It is yet not certain whether variations in response among different OSES are due to those in hardware performance or in software design. It appears that VxWorks as a server gives smaller fluctuations in response than other OSES as expected for RTOS.

For comparison, the times using socket programming are shown in Table 3. Instead of the event driven socket library (CAynchSocket), winsock.dll is used to measure

Table 1. Response Times for Various I/O Boards [msec].

	SII		NS		DII (Sv. idls known)		Socket	
	SmartAgent		SmartAgent & NS		SmartAgent & IR		CAynchSocket	
	Av.	Std. Dev.	Av.	Std. Dev.	Av.	Std. Dev.	Av.	Std. Dev.
DI	1.25	0	1.12	0.07	1.25	0.00	1.00	0.91
AI	1.41	0	1.24	0.05	1.25	0.00	1.68	0.34
DO	1.29	0.09	1.19	0.08	1.27	0.05	3.44	1.61
AO	1.27	0.05	1.22	0.07	1.28	0.07	1.89	0.28

Table 2. Response time matrix for various ORBs and OSES (average [std. dev.] in  $\mu$ sec). Asterisked numbers using IPC are 446 and 177  $\mu$ sec, respectively.

Client \ Server		VisiBroker (C++)			ORBacus (C++)	
		Sun	NT	VxWorks	Sun	NT
VisiBroker (C++)	Sun	519*[0.0819]	428 [0.191]	735 [0.0481]	380 [0.0525]	455 [0.178]
	NT	492 [0.191]	317*[0.00876]	664 [0.0154]	413 [0.0838]	321 [0.0115]
ORBacus (C++)	Sun	466 [0.103]	417 [0.269]	768 [0.0467]	351 [0.158]	460 [0.422]
	NT	497 [0.0886]	327 [0.0158]	727[0.00422]	406 [0.179]	328 [0.00738]
ORBacus (Java)	Sun	1340 [0.129]	1237 [0.102]	1635[0.0706]	1243 [0.0953]	1256 [0.0644]
	NT					

Table 3. Response time for socket communication [ $\mu$ sec].

Client \ Server		Socket		
		Sun	NT	VxWorks
Socket	Sun	110 [0.0242]	180 [0.0389]	185 [0.0094]
	NT	180 [0.0283]	121 [0.0135]	165 [0.0080]
	VxWorks			

genuine elapsed time for socket communication.

It is now preferable to create GUIs for OPI in Java because of its portability among different platforms. Sharing codes with other laboratories is one of the most important benefits of using Java/CORBA. Visual Cafe has been tested to create GUIs using Java beans<sup>9)</sup> component. We also plan to test more Java implementation of ORBs both as a client and a server to augment the matrix for interoperation. An object oriented database management system (OODBMS) may replace the relational database management system (RDBMS) for CORBA-based accelerator controls. Objectivity/DB for Linux<sup>10)</sup> is being tested for future application.

It has been shown that replacing socket communication with a CORBA layer significantly improves the manageability of accelerator controls. There appears to be no significant problem associated with VisiBroker on VxWorks. For the pSOS version, there appear to be more problems, but these may also be due to our lack of experience on this OS. Interoperability between ORBacus and VisiBroker is found to be satisfactory and response times do not vary greatly with different combinations. Without using product dependent CORBA services, the flexibility of the system codes can be improved at the expense of finding ways to share the stringified objects.

#### References

- 1) <http://www.omg.org/>
- 2) <http://www.borland.com/visibroker/>
- 3) <http://www.windriver.com/products/html/vxworks.htm>
- 4) <http://www.isi.com/>
- 5) <http://www.microsoft.com/>
- 6) <http://www.ooc.com/>
- 7) <http://www.avaldata.co.jp/jpn/index.html>
- 8) <http://elc.asaka.or.jp/electro/index.html>
- 9) <http://www.javasoft.com/>
- 10) <http://www.objectivity.com/>

# Spin Tracking with “Real” Siberian Snakes in Relativistic Heavy Ion Collider(RHIC)

M. Xiao and T. Katayama

To achieve high-energy polarized proton collision in Relativistic Heavy Ion Collider (RHIC), the polarized protons should be accelerated to a high energy without losing their polarization, which requires an understanding of the evolution of spin during acceleration and the tools to control it. The spin of a polarized proton in external magnetic fields is governed by the Thomas-BMT equation<sup>1)</sup>

$$\frac{d\vec{S}}{dt} = -\left(\frac{e}{\gamma m}\right)[(1 + G\gamma)\vec{B}_\perp + (1 + G)\vec{B}_\parallel] \times \vec{S}, \quad (1)$$

where the polarization vector  $\vec{S}$  is expressed in the frame that moves with the particle.  $\vec{B}_\perp$  and  $\vec{B}_\parallel$  are the magnetic field components perpendicular and parallel to the velocity  $\vec{v}$  of the particle, respectively.  $G$  is the anomalous gyromagnetic g-factor,  $G = 1.7928$  for the proton.  $\gamma = E/m, \gamma mc^2$  is the energy of the moving particle. The orbit motion of the particle is governed by the Lorentz force equation as follows

$$\frac{d\vec{v}}{dt} = -\left(\frac{e}{\gamma m}\right)[\vec{B}_\perp] \times \vec{v}. \quad (2)$$

From the comparison of these two equations it can readily be seen that in a pure vertical field, the spin rotates  $G\gamma$  times faster than the orbital motion. In this case, the factor  $G\gamma$  gives the number of full spin precessions for every full revolution, and we define it as spin tune,  $\nu_{sp}$ .

The polarization of polarized protons can be destroyed at many energies during the acceleration in RHIC, known as the depolarizing resonances with two types, the intrinsic resonances and imperfection resonances. Intrinsic resonances arise from the spin motion coupling with horizontal magnetic fields due to vertical betatron oscillations. Imperfection resonances are caused by orbit distortions due to field errors. The resonance conditions<sup>2)</sup> are  $\nu_{sp} = kP \pm \nu_y$  for intrinsic resonances and  $\nu_{sp} = k$  for imperfection resonances. Here,  $k$  is an integer and  $P$  is the superperiodicity of the accelerator;  $P = 3$  in RHIC.  $\nu_y$  is a vertical betatron tune;  $\nu_y = 29.18$  for RHIC.

The Siberian Snake is a local spin rotator, which is proposed to rotate the spin by  $180^\circ$  around a horizontal axis with no effect on the orbit motion of the particle. Figure 1 shows the rotations of three components of the spin in the ring with two Siberian Snakes installed. It was found that the kick of transverse magnetic field perturbations on spin can be cancelled every two revolutions if the axes of the two Siberian Snakes are perpendicular to each other. Therefore, with the installation of two Siberian Snakes in each ring of the

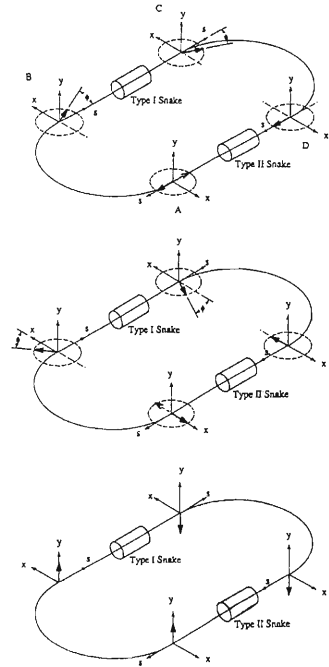


Fig. 1. Rotations of three components of the spin in the ring with two Siberian Snakes.

RHIC, the spin tune becomes one-half and is independent of the beam energy. Clearly, the depolarizing resonance conditions cannot be satisfied anymore, and no depolarization would occur.

The depolarization due to the resonances can be studied by numerically tracking protons with spin. The equations of spin motion are linear, and hence the transformation of the spin variables can be described by a matrix, whose elements depend only on the orbital quantities. The spin rotation matrices of some ordinary magnets such as dipole, quadrupole and sextupole magnets were obtained.<sup>3)</sup> Based on the numerical field map generated by TOSCA, the study of spin precession and orbital motion in a Siberian Snake was completed.<sup>4)</sup> The work gave the energy-dependent numerical symplectic orbital matrices and unitary spin matrices of the snakes and the results were used in spin tracking with “real” Siberian Snakes in RHIC for the entire acceleration and storage period.

The tracking code SPINK<sup>5)</sup> was upgraded for the spin tracking with “real” snakes in RHIC. The general idea is to track one or a certain number of protons, located on the contour of a phase-space ellipse or randomly generated inside a phase-space volume with Gaussian distribution, through the machine lattice. Each proton is characterized by four normalized

transverse canonical variables of phase space, ( $x, p_x = P_x/p_s, y, p_y = P_y/p_s$ ), the longitudinal one pair of canonical variables, ( $-c\Delta t, p_t = \frac{\Delta E}{p_s c}$ ) and three components of a real unitary vector of spin,  $\vec{S} = (s_x, s_y, s_z)$ . The quantities  $P_x$  and  $P_y$  are transverse momenta, and  $p_s$  is the momentum of the particle.  $\Delta E = E - E_o$ , where  $E$  and  $E_o$  are the total and design energies, respectively.  $\delta_s$  is defined as  $\frac{\Delta p}{p_o}$ , and  $\Delta t$  is the relative time respect to synchronous particle. We define  $\hat{y}$  as the vertical coordinate for a horizontal ring.

Orbital tracking is carried out using symplectified first-order “transport” maps provided directly by the optical code MAD.<sup>6)</sup> To study the problems of lattice misalignments and field errors, MAD transmits to SPINK on the errors (measured or randomly assumed) of each machine element and corrected closed orbit distortion. SPINK accordingly displaces and rotates the corresponding orbit transport maps.

The numerical matrices of two types of Siberian Snakes in RHIC are inserted into the lattice as follows

$$M = [D_{L/2}][M_{effect}][D_{L/2}], \quad (3)$$

where  $M$  represents both  $M_T$  and  $M_s$ .  $M_T$  is a 6-D symplectic orbital map of the snakes, and  $D_{L/2}$  is the drift matrix of the half length of the snake. Since both orbital maps and spin matrices of the snakes are energy-dependent, their interpolation is necessary at a certain energy during the acceleration of the polarized proton. Special care has been taken to keep the interpolated orbital map symplectic and the spin matrix unitary. The spin tracking with real Siberian Snakes in RHIC has been completed through the acceleration from the injection energy 25 GeV to the top energy 250 GeV. The momentum gain per turn is  $3 \times 10^{-5}$  GeV/C. Figure 2 gives the single particle tracking results in RHIC with no misalignment in the lattice. The particle is extracted from the contour of phase space, with an emittance of 5  $\pi\text{mm}\cdot\text{mrad}$ , 10  $\pi\text{mm}\cdot\text{mrad}$ , 15  $\pi\text{mm}\cdot\text{mrad}$  and 20  $\pi\text{mm}\cdot\text{mrad}$ , shown in (a)–(d) respectively. The depolarizations of the spin in this figure are only caused by intrinsic resonance. Figure 3 indicates the single particle tracking results in RHIC with the misalignments assigned randomly by a truncated Gaussian distribution, the r.m.s value of 2.5 mm and the standard deviations of 1 mm for the position in  $x$  and  $y$  directions and 1 mrad for the rotation angle around the  $s$ -direction. The corrected closed orbit distortion is 0.2 mm (r.m.s.). The depolarizations of the spin in this figure are caused by both intrinsic and imperfection resonances.

It has been shown that (1) “real” Siberian Snakes can maintain the polarization of the protons through the acceleration of more than 95% in a RHIC machine with no closed orbit distortion, and of more than 88% in a machine with corrected closed orbit distortion of 0.2 mm (r.m.s) if the polarized proton is extracted from a contour of less than 10  $\pi\text{mm}\cdot\text{mrad}$ . (2) symplec-

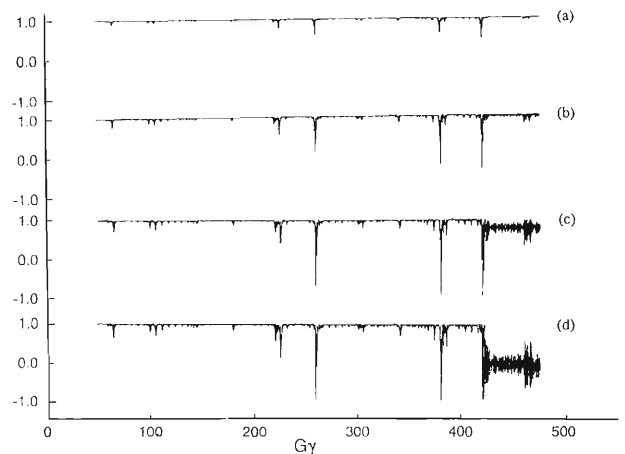


Fig. 2. Spin tracking with Real Snakes in RHIC, ideal machine (a) 5  $\pi\text{mm}\cdot\text{mrad}$ , (b) 10  $\pi\text{mm}\cdot\text{mrad}$ , (c) 15  $\pi\text{mm}\cdot\text{mrad}$ , and (d) 20  $\pi\text{mm}\cdot\text{mrad}$ .

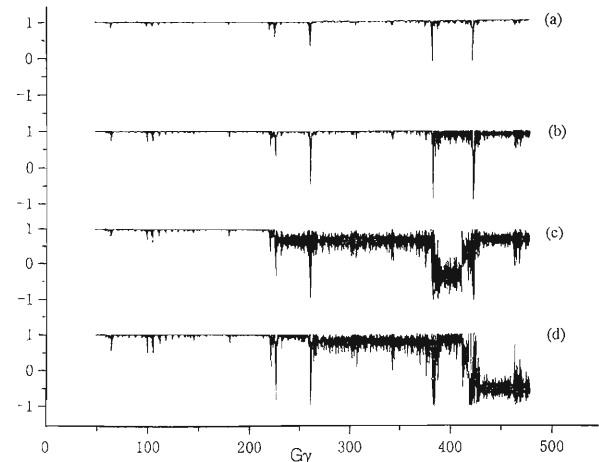


Fig. 3. Spin tracking with Real Snakes in RHIC, misalignment randomly assigned, COD  $\approx$  0.2 mm (a) 5  $\pi\text{mm}\cdot\text{mrad}$ , (b) 10  $\pi\text{mm}\cdot\text{mrad}$ , (c) 15  $\pi\text{mm}\cdot\text{mrad}$ , and (d) 20  $\pi\text{mm}\cdot\text{mrad}$

tic problems on orbital motion are one of the key issues for the spin tracking for over  $10^7$  turns. We solve this problem, and make it possible to predict the “actual” operation conditions in RHIC with real Siberian Snakes.

#### References

- 1) V. Bargmann et al.: Phys. Rev. Lett. **2**, 15 (1959).
- 2) S. Y. Lee: AIP Conf. Proc., No. 223, p. 30 (1990).
- 3) T. Katayama: Basic Theory of Spin Dynamics in RHIC, 1996.
- 4) M. Xiao: Spin note AGS/RHIC/SN, No. 078, BNL Internal Paper, Sept. 10 (1998).
- 5) A. Luccio: Spin note AGS/RHIC/SN, No. 011, BNL Internal Paper, Sept. 14 (1995).
- 6) F. Christoph: The MAD Program Version 8.13 Physical Method Manual., Geneva, Jan., 1994.

## Ion Optics Study of RHIC OPPIS

T. Takeuchi, M. Okamura, and A. Zelenski\*

A new optically pumped polarized ion source (OPPIS)<sup>1</sup> has been developed for the relativistic heavy-ion collider (RHIC) which is now under construction at Brookhaven National Laboratory (BNL), New York, United States of America. In order to achieve a luminosity of  $2 \times 10^{32}/\text{s cm}^2$  in RHIC, the new source is designed to deliver polarized protons of 1.5 mA and 200  $\mu\text{s}$  with a polarization of more than 85%. We have studied the beam optics and depolarization effect of this beam extraction system at this high current.

A schematic view of the OPPIS is shown in Fig. 1. The protons pick up a polarized electron in the Rb cell to become neutral. The neutralized H beam drifts, without being affected from the magnetic fields to the sodium cell, where it picks up an electron to become  $\text{H}^-$ . The  $\text{H}^-$  beam then leaves the OPPIS under the influence of the fringing field of the ionizer solenoid. The beam emittance and the polarization are determined at the ionizer solenoid, which consists of a solenoid magnet and a sodium jet cell.

To investigate the effect of multiple charge exchange processes and the degradation of a longitudinal spin polarization caused by a fringing field of the solenoidal magnet, the optics and the polarization of the particles were tracked by a combination of the Runge Kutta method and the Monte Carlo method. A magnetic field map ( $B_r, B_z$ ) in the Runge Kutta simulation was obtained by OPERA-2D and the Monte Carlo method for the charge exchange processes. Further details on the numerical simulation have already been published.<sup>2)</sup>

In this simulation, 5000 particles of  $\text{H}^0$  atoms, were tracked from 20 cm upstream of the center of the sodium cell ( $[20 \text{ cm}] \times \phi[2.0 \text{ cm}]$ ), to 30 cm downstream of it. The assumed incident  $\text{H}^0$  beam was almost parallel, the phase ellipse of which was ( $\pm 10 \text{ mm}$ : circle)  $\times$  ( $\pm 1 \text{ mrad}$ ). We assumed  $\text{H}^0 \rightarrow \text{H}^-$  and  $\text{H}^- \rightarrow \text{H}^0$  as charge exchange processes (CEP) between hydro-

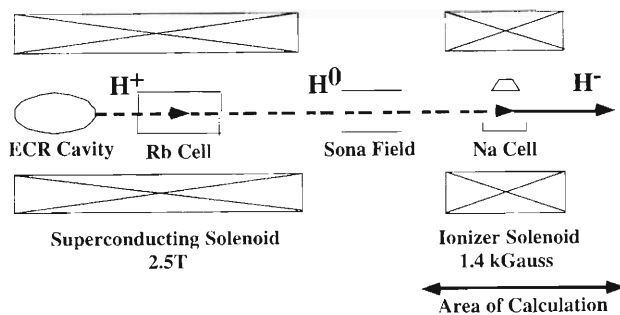


Fig. 1. Schematic view of RHIC OPPIS.

gen and sodium atoms, with cross sections of about  $0.03 \times 10^{-14} \text{ cm}^2$  and  $0.30 \times 10^{-14} \text{ cm}^2$ , respectively, which are obtained from Ref. 3, respectively. At the beam energy of 3.5 keV from the ECR ion source, other cross sections for CEP are some orders of magnitude smaller than the cross sections of the processes mentioned above and are negligible for this calculation. The sodium vapor distribution was assumed to be Gaussian and the total vapor thickness was set to be  $10^{15} \text{ atoms/cm}^2$ . In the spin calculation, it was assumed that the nuclear spin of incident  $\text{H}^0$  atoms has 100% polarization.<sup>4,5)</sup>

Figure 2 shows the calculated results of the beam trajectory. The point  $Z = 0$  is the center of the sodium vapor cell (length = 20.0 cm). In Fig. 2(a), the thick and thin solid lines indicate the magnetic field distribution and the sodium vapor density distribution with  $\sigma = 3.0 \text{ cm}$ , respectively. Figure 2(b) and (c) shows the  $\text{H}^0$  and  $\text{H}^-$  trajectories of the transverse X projection, respectively, where only 100 particles are shown. It is clearly seen that the  $\text{H}^-$  ions diverge from the Z axis due to the existence of the fringing field

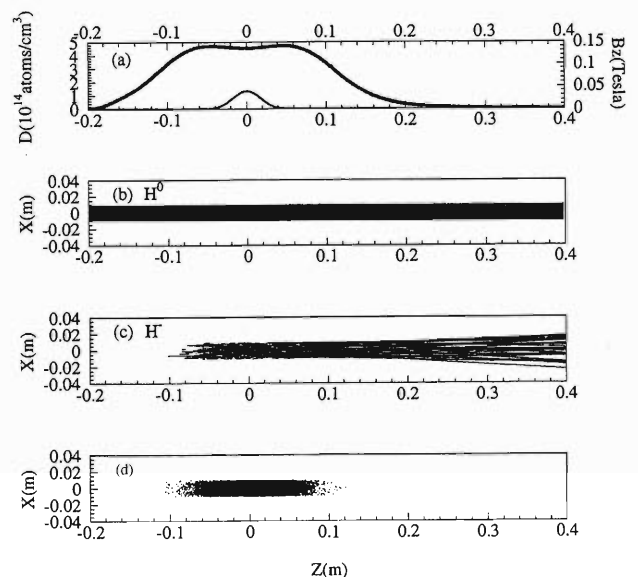


Fig. 2. The beam trajectory and charge exchange points in the case of the sodium vapor density distribution of  $\sigma = 3.0 \text{ cm}$ . The point,  $Z = 0$ , corresponds to the center of the sodium jet cell (length = 20 cm). In (a), the thick and thin lines indicate the magnetic field distribution and the sodium density distribution, respectively; (b) and (c) show  $\text{H}^0$  and  $\text{H}^-$  trajectories of the transverse X projection, respectively, where 100 particles are traced. In (d), the charge exchange points of  $\text{H}^0 \rightarrow \text{H}^-$  and  $\text{H}^- \rightarrow \text{H}^0$  are plotted.

\* TRIUMF, Canada

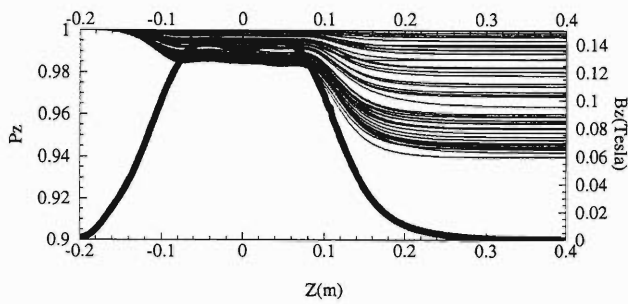


Fig. 3. Motion of the longitudinal spin polarization. The thick line indicates the field strength along the beam axis. Thin lines indicate the longitudinal spin polarizations.

emanating from the solenoid magnet. On the other hand, many of the  $H^0$  atoms pass straight through the sodium jet ionizer cell. The points where the charge exchange of  $H^0 \rightarrow H^-$  or  $H^- \rightarrow H^0$  occurs are plotted in Fig. 2(d). The  $H^-$  ion production yield was estimated

to be 9.0%. The beam radius and the normalized beam emittance for the  $H^-$  ion are about 13 mm and  $2.4 \pi$  mm mrad, respectively. Figure 3 shows the degradation of the nuclear spin polarization. The nuclear spin polarization is 94–100% at 30 cm downstream of the sodium ionizer cell.<sup>5)</sup>

Based on the results of the simulation described above, the beam extraction system and the low energy transport line were optimized and are being fabricated at BNL.

#### References

- 1) A. N. Zelenski et al.: Proc. PAC99, New York.
- 2) T. Takeuchi et al.: Rev. Sci. Instrum. **69**, 412 (1998).
- 3) M. Tanaka et al.: Phys. Rev. A **50**, 1184 (1994).
- 4) T. Takeuchi et al.: Spin Note AGS/RHIC/SN, No. 077, BNL Internal Paper, Sept. 10 (1988).
- 5) T. Takeuchi et al.: Proc. Int. Workshop on Polarized Sources and Targets (PST99), Erlangen, Germany, 1999, to be published.

## Ultraslow Muon Production Using the Resonant Ionization Method

Y. Matsuda, Y. Miyake, K. Shimomura, P. Bakule, R. Scheuermann, P. Strasser,  
S. N. Nakamura, N. Kawamura, K. Ishida, T. Matsuzaki, and K. Nagamine

Muons have been used in numerous research fields, such as muon-catalyzed fusion, material sciences, and fundamental physics. In particular, the use of polarized muons as spin probes in matter ( $\mu$ SR method) has been used by many researchers, and it is widely recognized that the  $\mu$ SR method provides a unique tool for studying various aspects of matter.

The muon beam for  $\mu$ SR is delivered from an accelerator facility, such as ISIS, where the RIKEN-RAL muon facility operates. Certain characteristics of the muon beam, however, may limit its application. For example, the energy of the produced muons is in the MeV range and their energy spread is approximately 10%. In practice, this limits the application of the  $\mu$ SR method to the study of characteristics of bulk matter only. In order to study surface characteristics or different implantation depths in a material, it is essential to use a polarized muon beam with variable energy from a few eV to a few tens of keV, with small energy distribution. The realization of such a muon beam will open new possibilities for  $\mu$ SR studies.

An apparatus for production of ultraslow muons is under construction now at the RIKEN-RAL muon facility.

A muon beam with an energy of approximately 4 MeV is injected into a thin tungsten foil which is heated up to about 2000 K. Muonium atoms with thermal kinetic energy are evaporated from the surface after its formation following electron-capture in the foil.<sup>1)</sup> Then, the electrons of the muonium atoms are removed by irradiation with VUV laser light to produce ultraslow muons (Fig. 1).

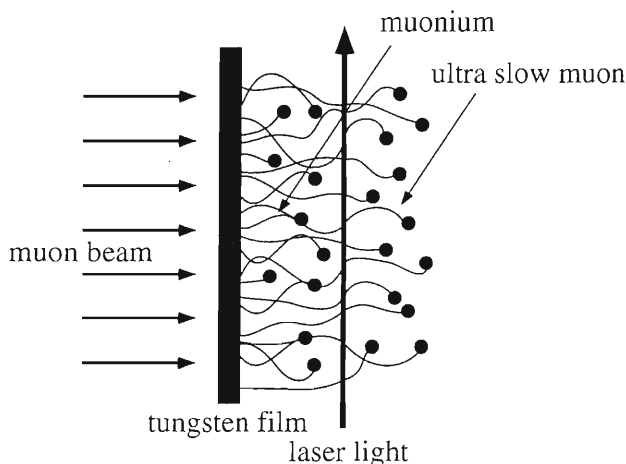


Fig. 1. Schematic diagram of the resonant ionization method to produce ultraslow muons.

This resonant ionization method has been developed at the Meson Science Laboratory of High Energy Accelerator Research Organization (KEK).<sup>2)</sup> Another method using cryogenic moderators has been developed at the Paul Scherrer Institute (PSI)<sup>3)</sup> and is also used on the RAL EC site (DEVA area). Using the cryogenic moderator method at a pulsed muon facility, the time resolution for  $\mu$ SR experiments is determined by the pulse width of the primary muon beam, which is approximately 100 ns (or 450 ns at higher intensities). The laser resonant ionization method offers a much better time resolution since the time structure is determined by the temporal width of the VUV laser pulse, which is approximately 5 ns. That is, by using the resonance ionization method, we can also overcome the current limitation of time resolution of pulsed muon beams.

The experimental apparatus mainly consists of two parts. One is the laser system for generation of the VUV laser light to ionize muonium in the region of the hot tungsten target. The second part is the beam transport system, in which the ultraslow muons are extracted and delivered to the sample region.

We ionize muonium through the  $1S \rightarrow 2P \rightarrow$  unbound transitions. The energy difference between  $1S$  and  $2P$  states is 122.05 nm in the case of muonium atom. To obtain the required 122 nm photon, we adopt the sum-difference frequency mixing method, using two photons of 212.55 nm for two-photon excitation of the  $4P^5_5P[1/2, 0]$  state in krypton, subtracted by a photon of a tunable difference wavelength.<sup>4)</sup>

To generate 212.55 nm light, we first obtain single-mode 850 nm light with an OPO (Optical Parametric Oscillator) system. Then, the 850 nm light is amplified by a Ti:Sapphire crystal which is pumped by frequency-doubled Nd:YAG laser light. The output energy of the amplifier is approximately 230 mJ/pulse with a 25 Hz repetition rate. This beam is split into two light paths. By using  $Ba_2BO_4$  crystals for frequency-quadrupling, two beams, each with a wavelength of 212.55 nm and an energy of 6 mJ/pulse, are generated.

The difference wavelength is generated by a system consisting of OPO and OPA (Optical Parametric Amplifier) crystals which is driven by a frequency-doubled Nd:YAG laser. We obtain 25 mJ/pulse at a wavelength of 820 nm and with a 25 Hz repetition rate.

Another 355 nm of photons from a frequency-tripled Nd:YAG laser are used to remove electron through transition from the  $2P$  state to an unbound state. This scheme is illustrated in Fig. 2.

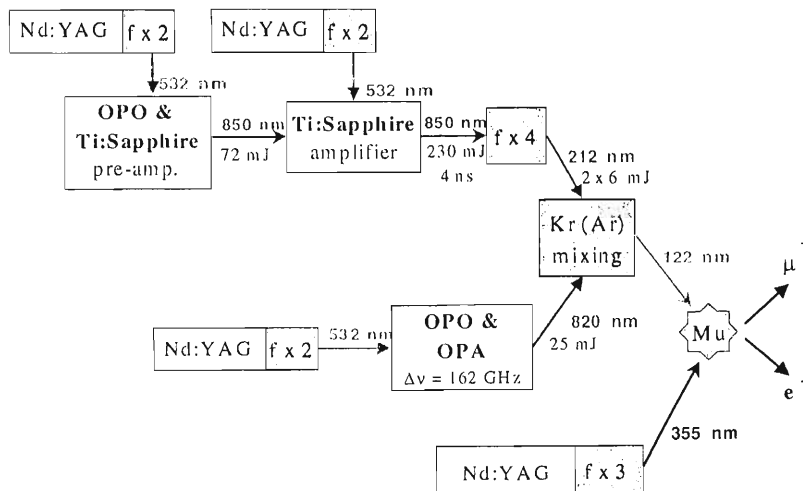


Fig. 2. Diagram of the laser system which is used in the resonant ionization method to obtain 122 nm photons and 355 nm photons for ionizing muonium atoms.

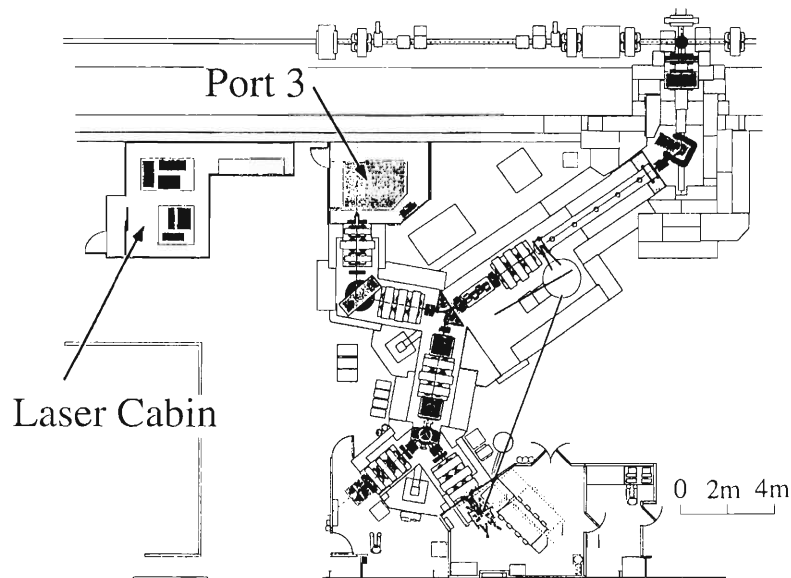


Fig. 3. Layout of the RIKEN-RAL muon facility and the laser cabin constructed for the ultraslow muon generation experiment. The temperature in the cabin is stabilized within 1 K.

The ultraslow muons generated at the production region are accelerated up to 10 keV, and then transported to a microchannel plate (MCP) detector located at the end of the transport system. The muons are identified by their charge( $Q$ )/mass ratio which was selected by adjusting the magnetic field of a bending magnet in the transport system, and by their time-of-flight (TOF) spectrum.

The construction of the apparatus is now underway. The laser cabin was constructed next to the Port 3 experimental area at the RIKEN-RAL muon facility (Fig. 3). Installation of the laser system is now in

progress. The beam transport system is currently being tested in Japan. The installation of the optics will be carried out in spring of year 2000, and we aim to start the experiment in June 2000.

#### References

- 1) A. P. Mills et al.: Phys. Rev. Lett. **56**, 1463 (1986).
- 2) K. Nagamine et al.: Phys. Rev. Lett. **74**, 4811 (1995).
- 3) E. Morenzoni et al.: Hyperfine Interact. **106**, 229 (1997).
- 4) J. P. Marangos et al.: J. Opt. Soc. Am. B **7**, 1254 (1990).

## **VI. RADIATION MONITORING**



## Radiation Safety Control System for the RIKEN Ring Cyclotron

S. Fujita, S. Nakajima, S. Ito, H. Sakamoto,\*<sup>1</sup> A. Fujiwara,\*<sup>2</sup> A. Uchiyama,\*<sup>2</sup>  
M. Kase, and Y. Uwamino

The radiation safety control system<sup>1)</sup> was in operation from 1986 until the first of February 1999. This system, based on a minicomputer MITSUBISHI MX-3000, is now out-of-date and trivial troubles, such as data transfer errors through an optical fiber, often occurred. We replaced the old system with a new

network system when the Ring and AVF cyclotrons were shut down for the relocation of the electric power source. The new system consists of five different sub-systems;

- (1) Radiation monitoring system
- (2) Access control system

The Radiation Safety Control System

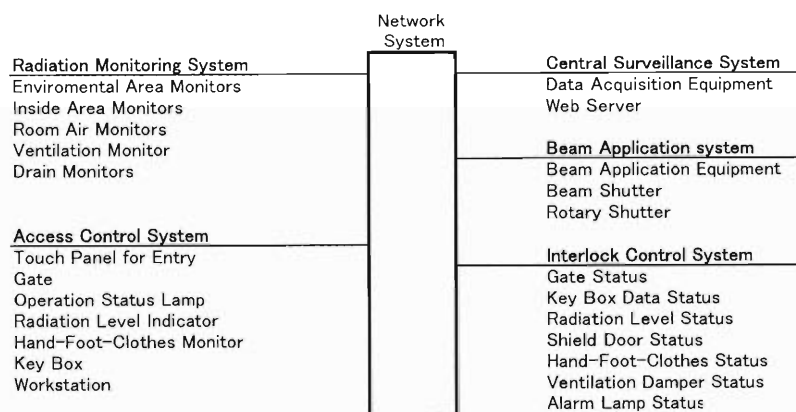


Fig. 1. A block diagram of the new radiation safety control system.

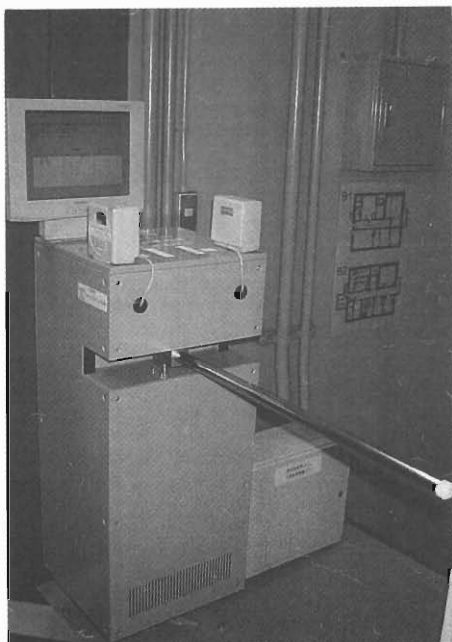


Fig. 2. Names of people in the safety controlled room are displayed on the screen on the gate bar console.

- (3) Beam application system
- (4) Interlock control system
- (5) Central surveillance system.

The subsystems, based on a personal computer and/or UNIX server, are interconnected via a network system. A block diagram of this connection is shown in Fig. 1. The radiation monitoring system observes the status of the radiation monitors and collects the data from them. The collected data can be shown as numerical values or on a graph. These data are transmitted to the central surveillance system through the network, edited and stored on data acquisition equipment.

Several functions have been added to the new system. One of them is the display of names of people staying in the safety controlled room on the monitor screen set on the gate bar console, as is shown in Fig. 2. The new system has been working continuously since the middle of April 1999.

### References

- 1) I. Sakamoto, S. Fujita, T. Wada, and H. Takebe: RIKEN Accel. Prog. Rep. 20, 206 (1986).

\*<sup>1</sup> Sumijyu Accelerator Service, Ltd.

\*<sup>2</sup> Faculty of Science, Science University of Tokyo

# Routine Work for Radiation Safety in the Ring Cyclotron Facility

S. Fujita, S. Nakajima, S. Ito, H. Sakamoto,\*<sup>1</sup> A. Fujiwara,\*<sup>2</sup> A. Uchiyama,\*<sup>2</sup> M. Kase, and Y. Uwamino

## Measurement of Residual Radioactivity

Residual radioactivities in the ring cyclotron facility were measured on the surface at various locations using ionization-chamber survey meters. The measurements were performed during the routine overhaul period as well as after almost every beam experiment.

An experiment was carried out with a <sup>59</sup>Co beam of 80 MeV/nucleon in the E6 experimental vault from July 31 to Aug. 3, 1999, as the last beam experiment of the spring term. The routine overhaul started just after that date. The dose rates in the ring cyclotron and in the AVF cyclotron were measured from Aug. 9 to 31. The results are shown in Figs. 1 and 2 along with the date of measurement.

In the period from Oct. 1, 1998 to Sept. 30, 1999, dose rates were measured along the beam lines. The spots a-z, marked by bullets in Fig. 3, are the places where the dose rates exceeded 50 μSv/h. Table 1 summarizes the observed dose rates and gives the dates when the measurements were performed. The maximum dose rate was found to be 17 mSv/h (17000 μSv/h) at the target chamber, denoted by x in Fig. 3. Whenever we observed a high dose rate, we roped off the area and posted a sign warning that it was dangerous to remain for long a time in that place.

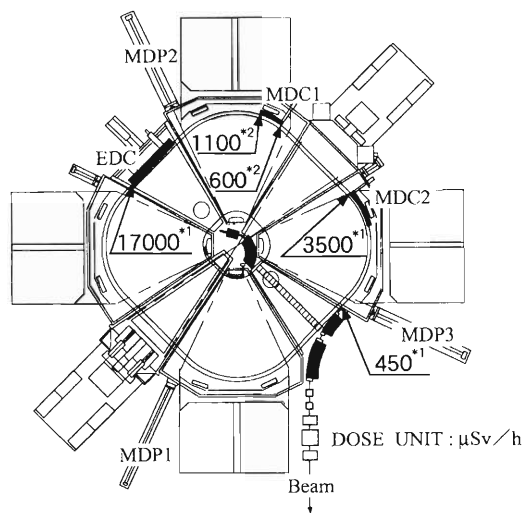


Fig. 1. Measured locations around the RIKEN Ring Cyclotron: EDC, electrostatic deflection channel; MDC1, magnetic deflection channel 1; MDC2, magnetic deflection channel 2; MDP1, main differential probe 1; MDP2, main differential probe 2; and MDP3, main differential probe 3. The numbers are dose rates in units of μSv/h. The measurements were carried out on \*1, Aug. 26 and \*2, Aug. 31 (1999).

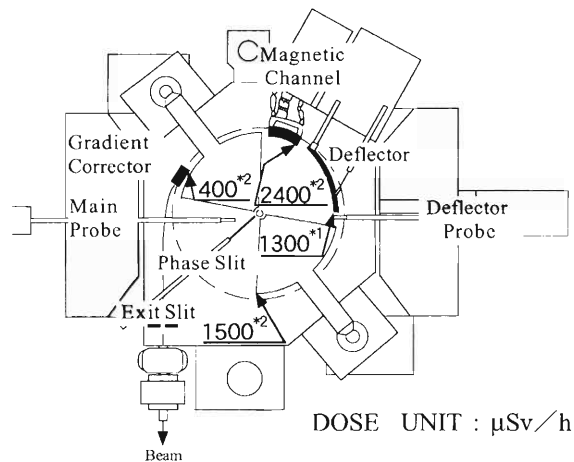


Fig. 2. Dose rates measured inside the injector AVF cyclotron. They are given in units of μSv/h. The measurements were done on \*1, Aug. 9 and \*2, Aug. 11 (1999).

Table 1. Summary of the dose rates measured along the beam lines with ionization-chamber survey meters. The detection points a-z indicate the measured locations shown in Fig. 3.

Detection point	Measured dose rate (μSv/h)	Date	Particle	Energy (MeV/u)	Intensity (enA)	Period (days)
a	100	Jul 9, '99	d	135	100	2
b	110	Jul 9, '99	d	135	100	2
c	75	Jul 9, '99	d	135	100	2
d	240	Apr 15, '99	Ni-58	25	500	2
e	650	Apr 15, '99	Ni-58	25	500	2
f	85	Apr 15, '99	Ni-58	25	500	2
g	140	Sept 24, '99	Ne-20	135	630	1
h	80	Nov 9, '98	Ar-40	95	750	3
i	280	Nov 13, '98	Xe-136	7.6	1000	3
j	150	Jan 5, '99	Co-59	80	250	8
k	1650	Apr 15, '99	Xe-136	7.6	4500	4
l	300	Sept 24, '99	C-12	135	1200	2
m	50	Jun 9, '99	C-13	100	3200	12
n	90	Nov 27, '98	Ne-20	135	1600	1
o	60	Nov 27, '98	Ne-20	135	1600	1
p	55	Nov 13, '98	Kr-84	70	7.5	3
q	90	Nov 26, '98	Ne-20	135	1600	1
r	105	Dec 1, '98	C-12	135	2000	2
s	80	Jul 12, '99	N-14	135	1500	2
t	3500	Jul 12, '99	N-14	135	1500	2
u	1950	Dec 1, '98	C-12	135	2000	2
v	100	Jun 17, '99	d	135	250	3
w	220	Jul 9, '99	d	135	100	2
x	17000	Jun 17, '99	d	135	250	3
y	450	Jul 9, '99	d	135	100	2
z	1100	Jun 21, '99	d	135	250	3

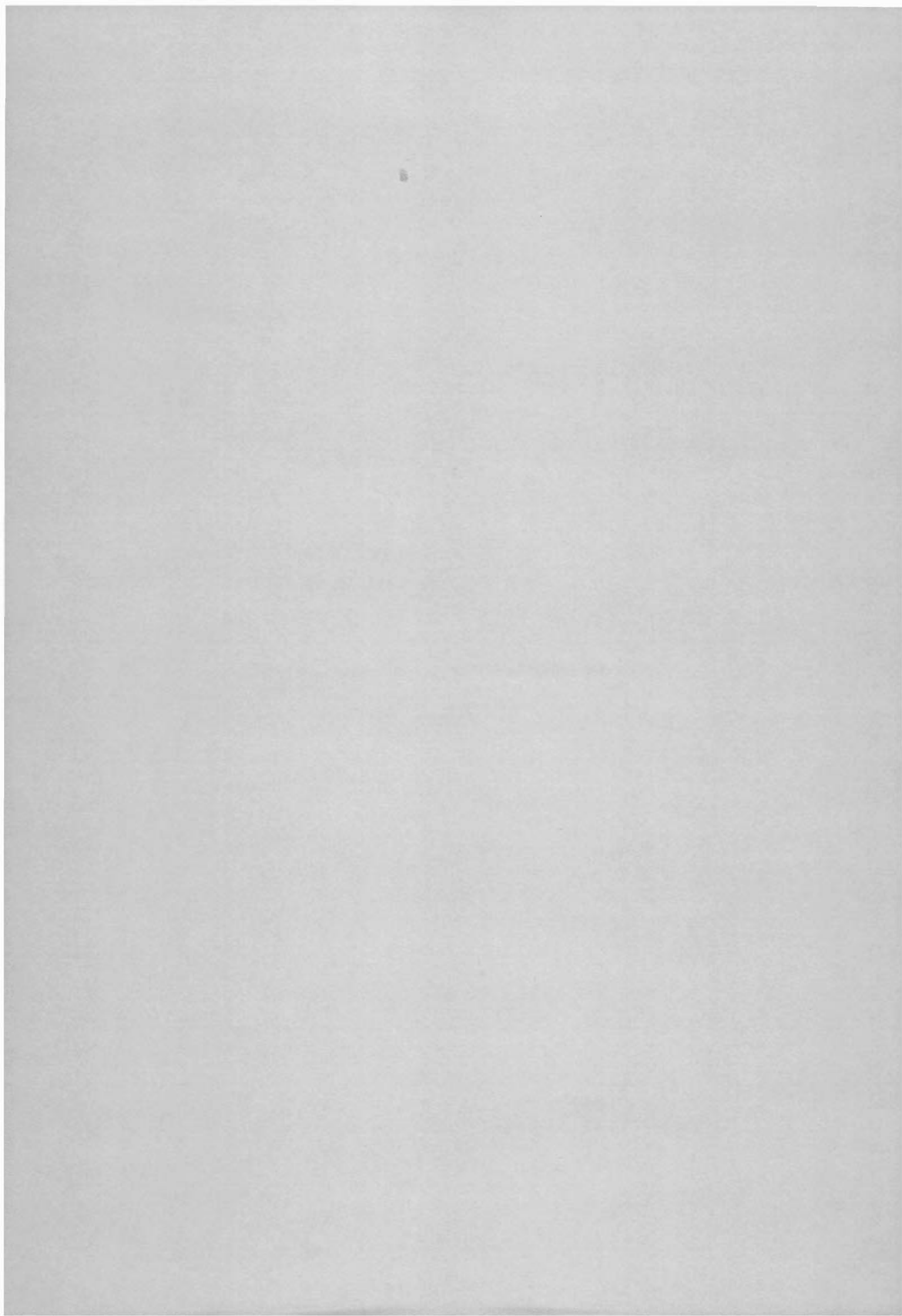
## Measurement of Leakage Radiation Level

Having analyzed the collected data of leakage neutrons, we found that the radiation levels in the controlled area were much less than the allowable dose limit. Leakage of γ-rays and neutrons was below the

\*1 Sumijyu Accelerator Service, Ltd.  
\*2 Faculty of Science, Science University of Tokyo









## VII. LIST OF PUBLICATIONS

### 1. Accelerator development and accelerator physics

- A. Goto, H. Okuno, T. Kawaguchi, T. Mitsumoto, T. Tominaka, S. Fujishima, J.-W. Kim, J. Ohnishi, K. Ikegami, N. Sakamoto, S. Yokouchi, K. Sugii, T. Wada, T. Morikawa, T. Kubo, and Y. Yano: "The K2500 superconducting ring cyclotron of RIKEN RI Beam Factory: Overview and status", Proc. 15th Int. Conf. on Cyclotrons and Their Applications 1998, Caen, France, 1998-06, edited by Eric Baron and Marcel Lieuvin, pp. 148-155 (1998).
- S. Kohara, Y. Miyazawa, O. Kamigaito, T. Chiba, E. Ikezawa, M. Kase, and A. Goto: "Model study of a resonator for a flat-top acceleration system in the RIKEN AVF cyclotron", Proc. 15th Int. Conf. on Cyclotrons and Their Applications 1998, Caen, France, 1998-06, edited by Eric Baron and Marcel Lieuvin, pp. 219-222 (1998).
- H. Okuno, T. Tominaka, S. Fujishima, T. Mitsumoto, T. Kubo, T. Kawaguchi, J.-W. Kim, K. Ikegami, N. Sakamoto, S. Yokouchi, T. Morikawa, Y. Tanaka, A. Goto, and Y. Yano: "Design study of the injection and extraction systems for the RIKEN Superconducting Ring Cyclotron", Proc. 1997 Particle Accelerator Conf. (PAC '97), Vancouver, Canada, 1997-05, edited by Mike Craddock, pp. 21-23 (1998).
- S. Hasegawa, A. Fujiwara, H. Yano, T. Nishimura, S. Sasaki, H. Ohashi, T. Iwai, K. Kobayashi, and H. Shibata: "Design of electrostatic accelerators for the development of microparticle detectors in Japan", Adv. Space Res. **23**, 119-122 (1999).
- S. Bhattacharjee and H. Amemiya: "Characteristics of a plasma produced by high power short pulse microwaves", Bull. Am. Phys. Soc. **44**, 252-253 (1999).
- S. Bhattacharjee and H. Amemiya: "Production of microwave plasma in a waveguide with a dimension below cutoff", J. Tech. Phys. **40**, 213-216 (1999).
- D. Toprek, A. Goto, and Y. Yano: "Beam orbit simulation in the central region of the RIKEN AVF Cyclotron", Nucl. Instrum. Methods Phys. Res. A **425**, 409-414 (1999).
- A. Goto and Y. Yano: "Construction of the RIKEN Superconducting Ring Cyclotron", Proc. 12th Symp. on Accelerator Science and Technology, Wako, 1999-10, edited by Y. Yano, RIKEN, pp. 7-9 (1999).
- T. Takeuchi, T. Katayama, T. Nakagawa, M. Okamura, T. Hattori, K. Sasa, and S. Kondrashev: "Development of laser ion source at RIKEN", Proc. 12th Symp. on Accelerator Science and Technology, Wako, 1999-10, edited by Y. Yano, RIKEN, pp. 203-205 (1999).
- O. Kamigaito, M. Kase, Y. Miyazawa, T. Chiba, M. Hemmi, N. Sakamoto, S. Kohara, E. Ikezawa, A. Goto, and Y. Yano: "Construction of the charge-state multiplier system for the RIKEN RI-beam factory", Proc. 12th Symp. on Accelerator Science and Technology, Wako, 1999-10, edited by Y. Yano, RIKEN, pp. 233-235 (1999).
- S. Fujishima, H. Okuno, A. Goto, and Y. Yano: "Analysis of the injection and extraction systems for the RIKEN Superconducting Ring Cyclotron", Proc. 12th Symp. on Accelerator Science and Technology, Wako, 1999-10, edited by Y. Yano, RIKEN, pp. 435-437 (1999).
- J.-W. Kim, A. Goto, T. Mitsumoto, and Y. Yano: "Studies on single turn extraction for a superconducting cyclotron", Proc. 1999 Particle Accelerator Conf., New York, USA, IEEE, pp. 2268-2270 (1999).
- O. Kamigaito, M. Kase, Y. Miyazawa, T. Chiba, M. Hemmi, S. Kohara, E. Ikezawa, A. Goto, and Y. Yano: "Construction of the first unit of the charge-state multiplier system for the RIKEN RI beam factory", Proc. 24th Linear Accelerator Meet. in Japan, Sapporo, 1999-07, pp. 146-148 (1999).
- S. Bhattacharjee and H. Amemiya: "Production of microwave plasma in narrow cross sectional tubes: Effect of the shape of cross section", Rev. Sci. Instrum. **70**, 3332-3337 (1999).
- O. Kamigaito, A. Goto, Y. Miyazawa, T. Chiba, M. Hemmi, M. Kase, S. Kohara, Y. K. Batygin, E. Ikezawa, T. Nakagawa, and Y. Yano: "Construction of a variable-frequency radio-frequency quadrupole linac for the RIKEN heavy-ion linac", Rev. Sci. Instrum. **70**, 4523-4531 (1999).
- A. Goto: "A superconducting ring cyclotron for the RIKEN RI Beam Factory", Teion Kougaku **34**, 376-384 (1999).
- S. Bhattacharjee and H. Amemiya: "Build up characteristics of a plasma produced by high power short pulse microwaves", XXIV Int. Conf. on Phenomena in Ionized Gases, Proc. Contributed Papers Vol. 1, Warsaw, Poland, 1999-07, edited by P. Pisarczyk, T. Pisarczyk, and J. Wolowski, Space Research Centre, Polish Academy of Sciences, Poland, pp. 133-134 (1999).

### 2. Nuclear physics and nuclear instrumentation

- I. Tanihata: "The new RIB project at RIKEN", Nucl. Instrum. Methods Phys. Res. B **126**, 224-230 (1997).
- K. Varga, Y. Suzuki, K. Arai, and Y. Ogawa: "Microscopic description of light unstable nuclei with the stochastic variational method", Nucl. Phys. A **616**, 383c-391c (1997).
- I. Tanihata: "Planned storage ring facilities in Japan and in China", Nucl. Phys. A **626**, 531c-544c (1997).

- N. Tanaka, Y. Suzuki, and K. Varga: "Exploration of resonances by analytic continuation in the coupling constant", *Phys. Rev. C* **56**, 562–565 (1997).
- Y. Mochizuki and S. Kumagai: "The half-life of titanium 44 and SN 1987A", *The Hot Universe: Proc. 188th Symp. of the Int. Astronomical Union*, edited by K. Koyama, S. Kitamoto, and M. Ito, Kluwer Academic Publishers, The Netherlands, pp. 241–242 (1998).
- Y. Mochizuki, T. Izuyama, I. Tanihata, and K. Oyamatsu: "A microscopic model of neutron star glitches", 1997 Pacific Rim Conf. on Stellar Astrophysics, ASP Conf. Ser., Vol. 138, pp. 245–248 (1998).
- T. Uesaka, H. Sakai, H. Okamura, S. Ishida, N. Sakamoto, H. Otsu, Y. Satou, T. Ohnishi, T. Wakasa, T. Nonaka, G. Yokoyama, K. Itoh, K. Sekiguchi, T. Wakui, and Y. Yano: "Study of deuteron high momentum component via the  ${}^3\bar{\text{H}}e(\vec{d}, p){}^4\text{He}$  reaction at 270 MeV", *Int. Symp. on New Facet of Spin Giant Resonances in Nuclei*, Tokyo, 1997-11, edited by H. Sakai, H. Okamura, and T. Wakasa, World Scientific, Tokyo, pp. 477–479 (1998).
- K. Yoneda, N. Aoi, H. Iwasaki, H. Sakurai, H. Ogawa, T. Nakamura, W. D. Schmidt-Ott, M. Schäfer, M. Notani, N. Fukuda, E. Ideguchi, T. Kishida, S. S. Yamamoto, and M. Ishihara: "Half-life measurements of the neutron drip line nuclei  ${}^{19}\text{B}$ ,  ${}^{22}\text{C}$  and  ${}^{23}\text{N}$ ", *J. Phys. G* **24**, 1395–1398 (1998).
- T. Suzuki, H. Geissel, O. Bochkarev, L. Chulkov, M. Golovkov, N. Fukunishi, D. Hirata, H. Irnich, Z. Janas, H. Keller, T. Kobayashi, G. Kraus, G. Münzenberg, S. Neumaier, F. Nickel, A. Ozawa, A. Piechaczek, E. Roeckl, W. Schwab, K. Sümmerer, K. Yoshida, and I. Tanihata: "Nuclear radii of Na and Mg isotopes", *Nucl. Phys. A* **630**, 661–677 (1998).
- L. Ya. Glozman, Z. Papp, W. Plessas, K. Varga, and R. F. Wagenbrunn: "Light and strange baryons in a chiral quark model with Goldstone-boson-exchange interactions", *Nucl. Phys. A* **631**, 469c–472c (1998).
- T. Uesaka, H. Sakai, H. Okamura, S. Ishida, N. Sakamoto, H. Otsu, Y. Satou, T. Ohnishi, T. Wakasa, T. Nonaka, G. Yokoyama, K. Itoh, K. Sekiguchi, T. Wakui, Y. Yano, and M. Wakasugi: "Measurement of polarization correlation coefficient for the  ${}^3\bar{\text{H}}e(\vec{d}, p){}^4\text{He}$  reaction", *Nuclear Study* **43**, No. 2, pp. 89–98 (1998).
- K. Sumiyoshi and T. Ebisuzaki: "Performance of parallel solution of a block-tridiagonal linear system on Fujitsu VPP500", *Parallel Comput.* **24**, 287–304 (1998).
- N. Dinh Dang, K. Tanabe, and A. Arima: "Damping of hot giant dipole resonance due to complex configuration mixing", *Phys. Lett. B* **445**, 1–7 (1998).
- N. Dinh Dang, K. Tanabe, and A. Arima: "Contribution of higher-order processes to the damping of hot giant dipole resonance", *Phys. Rev. C* **58**, 3374–3387 (1998).
- K. Varga, J. Usukura, and Y. Suzuki: "Second bound state of the positronium molecule and biexcitons", *Phys. Rev. Lett.* **80**, 1876–1879 (1998).
- Y. Mochizuki, S. Kumagai, and I. Tanihata: "The half-life of  ${}^{44}\text{Ti}$  and SN 1987A", *Proc. Int. Symp. on Origin of Matter and Evolution of Galaxies 97*, edited by Kubono et al., pp. 327–334 (1998).
- Y. Mochizuki: "The origin of neutron star glitches", *Astron. Her.* **92**, 19–31 (1999).
- Y. Mochizuki, T. Izuyama, and I. Tanihata: "Dynamics of exotic nuclear rod formation for the origin of neutron star glitches", *Astrophys. J.* **521**, 281–296 (1999).
- H. Miyasaka: "Observation of trapped anomalous cosmic rays with MIDORI satellite", *Cosmic Radiation* **1**, 117–125 (1999).
- Yu. Ts. Oganessian, A. V. Yeremin, G. G. Gulbekian, S. L. Bogomolov, V. I. Chepigin, B. N. Gikal, V. A. Gorshkov, M. G. Itkis, A. P. Kabachenko, V. B. Kutner, A. Yu. Lavrentev, O. N. Malyshev, A. G. Popeko, J. Rohác, R. N. Sagaidak, S. Hofmann, G. Münzenberg, M. Veselsky, S. Saro, N. Iwasa, K. Morita, and V. I. Chepigin: "Search for new isotopes of element 112 by irradiation of  ${}^{238}\text{U}$  with  ${}^{48}\text{Ca}$ ", *Eur. Phys. J. A* **5**, 63–68 (1999).
- N. Dinh Dang, K. Tanabe, and A. Arima: "Temperature dependence of quantal and thermal dampings of giant dipole resonance due to complex configuration mixing", *Highlights of Modern Nuclear Structure*, S. Agata sui due Golfi, Italy, 1998-05, edited by A. Covello, World Scientific, Singapore, pp. 459–466 (1999).
- K. Ishida, K. Nagamine, T. Matsuzaki, S. N. Nakamura, N. Kawamura, S. Sakamoto, M. Iwasaki, M. Tanase, M. Kato, K. Kurosawa, H. Sugai, I. Watanabe, K. Kudo, N. Takeda, and G. H. Eaton: "Measurement of X-rays from muon to alpha sticking and fusion neutrons in solid/liquid D-T mixtures of high tritium concentration", *Hyperfine Interact.* **118**, 203–208 (1999).
- K. Sato, T. Miyake, A. Morishita, K. Matsuta, T. Minamisono, M. Tanigaki, S. Takeda, M. Mihara, M. Fukuda, Y. Nojiri, K. Minamisono, T. Fukao, Y. Matsumoto, T. Ohtsubo, S. Fukuda, S. Momota, K. Yoshida, A. Ozawa, T. Kobayashi, I. Tanihata, H. Sagawa, H. Kitagawa, G. F. Krebs, J. R. Alonso, and T. J. M. Symons: "Hyperfine interactions of  ${}^{19}\text{O}$  in  $\text{TiO}_2$  and quadrupole moments of  ${}^{13,19}\text{O}$ ", *Hyperfine Interact.* **120/121**, 661–665 (1999).
- K. Matsuta, T. Onishi, M. Fukuda, T. Minamisono, H. Akai, M. Sasaki, T. Yamaguchi, T. Miyake, K. Sato, K. Minamisono, F. Ohsumi, Y. Muramoto, S. Oui, C. Ha, K. Tanaka, K. Kidera, A. Morishita, A. Kitagawa, M. Torikoshi, M. Kanazawa, T. Nishio, S. Koda, T. Ohtsubo, S. Fukuda, Y. Nojiri, S. Momota, A. Ozawa, K. Yoshida, T. Suzuki, T. Kobayashi, I.

- Tanihata, S. S. Hanna, J. R. Alonso, G. F. Krebs, and T. J. M. Symons: "Electromagnetic moments of short lived  $\beta$  emitters  $^{21}\text{F}$ ,  $^{23}\text{Mg}$ ,  $^{27}\text{Si}$  and  $^{39}\text{Ca}$ ", *Hyperfine Interact.* **120/121**, 673-677 (1999).
- E. J. Kim, T. Nakamura, Y. Uwamino, N. Nakanishi, M. Imamura, N. Nakao, S. Shibata, and S. Tanaka: "Measurements of activation cross sections on spallation reactions for  $^{59}\text{Co}$  and  $^{\text{nat}}\text{Cu}$  at incident neutron energies of 40 to 120 MeV", *J. Nucl. Sci. Technol.* **36**, 29-40 (1999).
- T. Horibata, M. Oi, and N. Onishi: "Band crossing studied by GCM with 3D-CHFB", *J. Phys. G* **25**, 885-888 (1999).
- N. Nakao, Y. Uwamino, T. Nakamura, T. Shibata, N. Nakanishi, M. Takada, E. Kim, and T. Kurosawa: "Development of a quasi-monoenergetic neutron field using  $^7\text{Li}(p,n)^7\text{Be}$  reaction in the 70-210 MeV energy range at RIKEN", *Nucl. Instrum. Methods Phys. Res. A* **420**, 218-231 (1999).
- T. Kurosawa, T. Nakamura, N. Nakao, T. Shibata, Y. Uwamino, and A. Fukumura: "Spectral measurements of neutrons, protons, deuterons and tritons produced by 100 MeV/nucleon He bombardment", *Nucl. Instrum. Methods Phys. Res. A* **430**, 400-422 (1999).
- Y. Mizoi, T. Fukuda, Y. Matsuyama, T. Miyachi, J. Nakano, N. Fukuda, M. Hirai, H. Kobinata, Y. Watanabe, H. Sakurai, Y. Watanabe, and A. Yoshida: "Multiple-sampling and tracking proportional chamber for nuclear reactions with low-energy radioactive isotope beams", *Nucl. Instrum. Methods Phys. Res. A* **431**, 112-122 (1999).
- N. Dinh Dang, K. Tanabe, and A. Arima: "Shape evolution of the hot giant dipole resonance", *Nucl. Phys. A* **645**, 536-558 (1999).
- T. Horibata, M. Oi, N. Onishi, and A. Ansari: "Band structures of  $^{182}\text{Os}$  studied by GCM based on 3D-CHFB", *Nucl. Phys. A* **646**, 277-295 (1999).
- N. Dinh Dang, K. Tanabe, and A. Arima: "Quantal and thermal damping of the hot giant dipole resonance due to complex configuration mixing", *Nucl. Phys. A* **649**, 201c-204c (1999).
- I. Tanihata: "Reaction with radioactive ion beams", *Nucl. Phys. A* **654**, 235c-251c (1999).
- A. Ansari, M. Oi, N. Onishi, and T. Horibata: "High-spin structure of  $^{182,184}\text{Os}$  in tilted axis cranking approach", *Nucl. Phys. A* **654**, 558-578 (1999).
- Y. Koike: "Twist-3 effects in polarized Drell-Yan and semi-inclusive DIS", *Nucl. Phys. B (Proc. Suppl.)* **79**, 626-628 (1999).
- T. Kurosawa, N. Nakao, T. Nakamura, Y. Uwamino, T. Shibata, N. Nakanishi, A. Fukumura, and K. Murakami: "Measurements of secondary neutrons produced from thick targets bombarded by high-energy helium and carbon ions", *Nucl. Sci. Eng.* **132**, 30-57 (1999).
- H. Sakurai, S. M. Lukyanov, M. Notani, N. Aoi, D. Beaumel, N. Fukuda, M. Hirai, E. Ideguchi, N. Imai, M. Ishihara, H. Iwasaki, T. Kubo, K. Kusaka, H. Kumagai, T. Nakamura, H. Ogawa, Y. E. Penionzhkevich, T. Teranishi, Y. Watanabe, K. Yoneda, and A. Yoshida: "Evidence for particle stability of  $^{31}\text{F}$  and particle instability of  $^{25}\text{N}$  and  $^{28}\text{O}$ ", *Phys. Lett. B* **448**, 180-184 (1999).
- M. H. Smedberg, T. Baumann, T. Aumann, L. Axelsson, U. Bergmann, M. J. G. Borge, D. Cortina-Gil, L. M. Fraile, H. Geissel, L. Grigorenko, M. Hellström, M. Ivanov, N. Iwasa, R. Janik, B. Jonson, H. Lenske, K. Markenroth, G. Münzenberg, T. Nilsson, A. Richter, K. Riisager, C. Scheidenberger, G. Schrieder, W. Schwab, H. Simon, B. Sitar, P. Strmen, K. Sümmerer, M. Winkler, and M. V. Zhukov: "New results on the halo structure of  $^8\text{B}$ ", *Phys. Lett. B* **452**, 1-7 (1999).
- T. Suzuki and H. Sakai: "The Landau-Migdal parameters,  $g'_{\text{NN}}$  and  $g'_{\text{N}\Delta}$ ", *Phys. Lett. B* **455**, 25-29 (1999).
- K. Matsuta, K. Sato, M. Fukuda, M. Mihara, T. Yamaguchi, M. Sasaki, T. Miyake, K. Minamisono, T. Minamisono, M. Tanigaki, T. Ohtsubo, T. Onishi, Y. Nojiri, S. Momota, S. Fukuda, K. Yoshida, A. Ozawa, T. Kobayashi, I. Tanihata, J. R. Alonso, G. F. Krebs, T. J. M. Symons, H. Kitagawa, and H. Sagawa: "Quadrupole moment of the proton drip-line nuclide  $^{13}\text{O}$ ", *Phys. Lett. B* **459**, 81-85 (1999).
- A. Ansari, M. Oi, N. Onishi, and T. Horibata: "High- $K$  exotics in osmium isotopes", *Phys. Lett. B* **460**, 24-30 (1999).
- T. Uesaka, H. Sakai, H. Okamura, T. Ohnishi, Y. Satou, S. Ishida, N. Sakamoto, H. Otsu, T. Wakasa, K. Itoh, K. Sekiguchi, and T. Wakui: "Polarization correlation coefficient for the  $^3\text{He}(\vec{d},p)^4\text{He}$  reaction", *Phys. Lett. B* **467**, 199-204 (1999).
- J. Meng, K. Sugawara-Tanabe, S. Yamaji, and A. Arima: "Pseudospin symmetry in Zr and Sn isotopes from the proton drip line to the neutron drip line", *Phys. Rev. C* **59**, 154-163 (1999).
- M. Sambataro and N. Dinh Dang: "Variational approach to collective excitations", *Phys. Rev. C* **59**, 1422-1431 (1999).
- N. Dinh Dang, K. Tanabe, and A. Arima: "Damping of double giant dipole resonance", *Phys. Rev. C* **59**, 3128-3138 (1999).
- N. Dinh Dang, K. Tanabe, and A. Arima: "Evolution of the hot giant dipole resonance as a manifestation of the order-and-chaos coexistence", *Phys. Rev. C* **60**, 034306-1-034306-7 (1999).
- H. Okamura: "Three-body treatment of the  $(d, ^2\text{He})$  reaction on the basis of the adiabatic approximation", *Phys. Rev. C* **60**, 064602-1-064602-8 (1999).
- A. A. Korshennikov, M. Golovkov, A. Ozawa, E. A. Kuzmin, E. Y. Nikolskii, K. Yoshida, B. G. Novatskii, A. A. Ogloblin, I. Tanihata, Zs. Fülöp, K. Kusaka, K. Morimoto, H. Otsu, H. Petruscu, and F. Tokanai: "Observation of an excited state in  $^7\text{He}$  with unusual structure", *Phys. Rev. Lett.* **82**,

- 3581–3584 (1999).
- N. Iwasa, F. Boué, G. Surówka, K. Sümmerer, T. Baumann, B. Blank, S. Czajkowski, A. Förster, M. Gai, H. Geissel, E. Grosse, M. Hellström, P. Koczon, B. Kohlmeyer, R. Kulesa, F. Laue, C. Marchand, T. Motobayashi, H. Oeschler, A. Ozawa, M. S. Pravikoff, E. Schwab, W. Schwab, P. Senger, J. Speer, C. Sturm, A. Surowiec, T. Teranishi, F. Uhlig, A. Wagner, W. Walus, and C. A. Bertulani: “Measurement of the Coulomb dissociation of  $^8\text{B}$  at 254 MeV/nucleon and the  $^8\text{B}$  solar neutrino flux”, *Phys. Rev. Lett.* **83**, 2910–2913 (1999).
- T. Suzuki, H. Sakai, and T. Tatsumi: “The Landau-Migdal parameters,  $g'_{\text{NN}}$  and  $g'_{\text{N}\Delta}$  and pion condensation”, *Proc. Int. Conf. on Nuclear Responses and Medium Effects*, Osaka, 1998–11, edited by T. Noro, H. Sakaguchi, H. Sakai, and T. Wakasa, Universal Academy Press, Tokyo, pp. 77–85 (1999).
- K. Ishida, T. Matsuzaki, and K. Nagamine: “Recent topics in muonic atom, molecule and muon catalyzed fusion”, *Proc. Workshop on Atomic and Molecular Processes in Space*, Sagamihara, 1998–12, edited by Y. Ichikawa, Institute of Space and Astronautical Science, pp. 37–40 (1999).
- K. Ishida: “Plans of high intensity muon channels at RIKEN-RAL and KEK-MSL”, *Proc. Workshop on High Intensity Secondary Beam with Phase Rotation*, Uji, 1998–09, edited by Y. Kuno and N. Sasao, Kyoto, pp. 128–135 (1999).
- K. Ishida, K. Nagamine, T. Matsuzaki, S. N. Nakamura, N. Kawamura, S. Sakamoto, M. Iwasaki, I. Watanabe, M. Tanase, M. Kato, K. Kurosawa, K. Kudo, N. Takeda, and G. H. Eaton: “Recent  $\mu\text{CF}$  research -  $\mu\text{CF}$  experiment at RIKEN-RAL(1) X-ray and neutron studies on muon to alpha sticking in D-T  $\mu\text{CF}$ ”, *Proc. Workshop on Ultra-high Intensity Muon Beam and Muon Science in the 21st Century*, Tsukuba, 1999–03, edited by S. Sakamoto, High Energy Accelerator Research Organization, Tsukuba, pp. 105–108 (1999).
- K. Ishida, T. Matsuzaki, I. Watanabe, S. N. Nakamura, Y. Matsuda, and K. Nagamine: “Design of an ultra-high intensity muon channel for the second phase of the RIKEN-RAL Muon Facility”, *Proc. Workshop on Ultra-high Intensity Muon Beam and Muon Science in the 21st Century*, Tsukuba, 1999–03, edited by S. Sakamoto, High Energy Accelerator Research Organization, Tsukuba, pp. 61–66 (1999).
- K. Ishida, K. Nagamine, T. Matsuzaki, S. N. Nakamura, N. Kawamura, S. Sakamoto, M. Iwasaki, I. Watanabe, M. Tanase, M. Kato, K. Kurosawa, K. Kudo, N. Takeda, and G. H. Eaton: “X-ray and neutron studies on muon to alpha sticking in D-T muon catalyzed fusion”, *RIKEN Rev.*, No. 20, pp. 3–7 (1999).
- S. N. Nakamura, Y. Matsuda, K. Ishida, T. Matsuzaki, I. Watanabe, K. Nagamine, M. Iwasaki, D. Tomono, S. Sakamoto, and M. Gren: “A new approach to measure the positive muon lifetime and test the exponential decay law”, *RIKEN Rev.*, No. 20, pp. 58–63 (1999).
- T. Suzuki: “ $E1 \times E1$  and  $E1 \times E2$  giant resonances”, *RIKEN Rev.*, No. 23, pp. 119–122 (1999).
- H. Kurasawa, N. Uchiyama, and T. Suzuki: “Giant resonance states of atomic clusters”, *Tohoku LNS Report LNS1011-99*, 181–189 (1999).

### 3. Atomic and solid-state physics

- Y. Kobayashi, J. Nakamura, A. Yoshida, Y. Watanabe, N. Aoi, N. Inabe, M. Kase, A. Goto, Y. Yano, M. Ishihara, F. Ambe, Y. Yoshida, K. Yukihira, K. Hayakawa, M. Miyasaka, S. Hiyama, Y. Kobayashi, and S. Nasu: “In-beam Mössbauer spectroscopy using a  $^{57}\text{Mn}$  beam from RIPS of RIKEN”, *Proc. Specialist Research Meet. on Solid State Physics with Probes of Radiations and Nuclei (I)*, pp. 71–73 (1997).
- T. Kambara: “Atomic physics at the planned new RIKEN facility”, *Hyperfine Interact.* **115**, 101–106 (1998).
- A. Iwase, N. Ishikawa, Y. Chimi, K. Tsuru, H. Wakana, O. Michikami, and T. Kambara: “High energy heavy ion irradiation damage in oxide superconductor  $\text{EuBa}_2\text{Cu}_3\text{O}_y$ ”, *Nucl. Instrum. Methods Phys. Res. B* **146**, 557–564 (1998).
- N. Kuroda, N. Ishikawa, S. Okayasu, A. Iwase, H. Ikeda, R. Yoshizaki, and T. Kambara: “Vortex dynamics in  $\text{Bi}_{2+x}\text{Sr}_{2-(x+y)}\text{La}_y\text{CuO}_{6+\delta}$  and  $\text{Bi}_2\text{Sr}_2\text{CaCu}_2\text{O}_y$  irradiated with heavy-ions: Correlation between the Bose-glass behavior and the coupling of pancake vortices”, *Nucl. Instrum. Methods Phys. Res. B* **146**, 572–576 (1998).
- Y. Yamazaki: “Stabilized multiply excited states produced with highly charged ions passed through microcapillaries”, *Photonic, Electronic and Atomic Collisions*, Vienna, Austria, 1997–07, edited by F. Aumayr and H. Winter, World Scientific, pp. 693–702 (1998).
- S. Okayasu, N. Kuroda, A. Iwase, and T. Kambara: “Recoupling vortices due to columnar defects in 3.5 GeV Xe-irradiated QMG-YBCO”, *Advances in Superconductivity XI (Proc. 11th Int. Symp. on Superconductivity (ISS'98))*, Fukuoka, 1998–11, edited by N. Koshizuka and S. Tajima, Springer-Verlag, Tokyo, Hong Kong, pp. 287–290 (1999).
- H. Ikeda, N. Kuroda, A. Iwase, T. Kambara, and R. Yoshizaki: “Vortex state of heavy ion irradiated Ni-doped Bi-2212”, *Advances in Superconductivity XI (Proc. 11th Int. Symp. on Superconductivity (ISS'98))*, Fukuoka, 1998–11, edited by N. Koshizuka and S. Tajima, Springer-Verlag, Tokyo, Hong Kong, pp. 291–294 (1999).
- Y. Awaya, T. Kambara, and Y. Kanai: “Multiple  $K$ - and  $L$ -shell ionizations of target atoms by collisions

- with high-energy heavy ions”, *Int. J. Mass Spectrom.* **192**, 49–63 (1999).
- Y. Yamazaki: “Beam capillary spectroscopy”, *Int. J. Mass Spectrom.* **192**, 437–444 (1999).
- T. Maruyama, T. Hasegawa, N. Komuro, H. Yamada, W. Ohtsuka, K. Akimoto, Y. Kitajima, K. Maeda, and E. Yagi: “Compensation centers in ZnSeTe”, *J. Appl. Phys.* **86**, 5993–5999 (1999).
- H. Sakairi, E. Yagi, and A. Koyama: “Annealing of Cu<sub>3</sub>Au irradiated with protons,  $\alpha$ -particles and C ions at liquid nitrogen temperature”, *J. Nucl. Mater.* **271/272**, 194–199 (1999).
- S. Uramoto: “Superexcited states of the hydrogen molecule converging to the first excited state of the hydrogen molecular ion”, *J. Phys. Soc. Jpn.* **68**, 1541–1547 (1999).
- E. Yagi, T. Sasahara, T. Joh, M. Hacke, T. Urai, T. Sasamoto, N. Tajima, T. Watanabe, and S. T. Nakagawa: “Xe bubble formation in Xe-implanted Fe as observed by the channelling method”, *J. Phys. Soc. Jpn.* **68**, 4037–4044 (1999).
- Y. Yamazaki: “Production of ultra slow antiprotons, its application to atomic collisions and atomic spectroscopy-ASACUSA project”, *Nucl. Instrum. Methods Phys. Res. B* **154**, 174–184 (1999).
- B. Sulik, K. Tökési, Y. Awaya, T. Kambara, and Y. Kanai: “Single and double K-shell vacancy production in N<sup>7+</sup> + Ti collisions”, *Nucl. Instrum. Methods Phys. Res. B* **154**, 286–290 (1999).
- Y. Zou, R. Hutton, S. Huldt, I. Martinson, K. Ando, T. Kambara, H. Oyama, and Y. Awaya: “Improvement in the reliability of lifetime measurements for highly charged ions in the 0.01–100-ns range”, *Phys. Rev. A* **60**, 982–985 (1999).
- Y. Morishita, S. Ninomiya, Y. Yamazaki, K. Komaki, K. Kuroki, H. Masuda, and M. Sekiguchi: “Visible light emission from slow highly charged ions transmitted through a Ni microcapillary”, *Phys. Scr. T* **80**, 212–214 (1999).
- M. Kitajima, Y. Nakai, Y. Kanai, Y. Yamazaki, and Y. Itoh: “Crossed beam experiment for multi-electron capture in ion-atom collision in the energy range of 10–100 eV/q”, *Phys. Scr. T* **80**, 377–378 (1999).
- K. Tökési, Y. Awaya, T. Kambara, Y. Kanai, and B. Sulik: “Double K-shell vacancy production in N<sup>7+</sup> + Ti collisions”, *Phys. Scr. T* **80**, 408–410 (1999).
- K. Ishii, S. Kawae, T. Nakano, K. Ando, H. Oyama, and T. Kambara: “Beam-foil spectra of highly charged Neon ion in visible region”, *Phys. Scr. T* **80**, 458–459 (1999).
- Y. Zou, R. Hutton, S. Huldt, I. Martinson, K. Ando, H. Oyama, B. Nyström, T. Kambara, and Y. Yamazaki: “Limitations of the beam-foil method in lifetime measurements”, *Phys. Scr. T* **80**, 460–462 (1999).
- R. Hutton, Y. Zou, S. Huldt, I. Martinson, K. Ando, B. Nyström, T. Kambara, H. Oyama, and Y. Awaya: “A CCD detector system for beam-foil spectroscopy”, *Phys. Scr. T* **80**, 532–533 (1999).
- N. Okabayashi, K. Kuroki, Y. Tsuruta, T. Azuma, K. Komaki, and Y. Yamazaki: “Measurements of potential sputtered H<sup>+</sup> with 2D position sensitive detector”, *Phys. Scr. T* **80**, 555–556 (1999).
- K. Kuroki, T. Takahira, Y. Tsuruta, N. Okabayashi, T. Azuma, K. Komaki, and Y. Yamazaki: “Charge state dependence of proton sputtering from solid surfaces with slow highly charged ions”, *Phys. Scr. T* **80**, 557–558 (1999).
- N. Ishikawa, Y. Chimi, N. Kuroda, A. Iwase, and T. Kambara: “Ion-velocity effects on defect production in high-T<sub>c</sub> superconductors and metals irradiated with swift heavy ions”, *Phys. Scr. T* **80**, 559–561 (1999).
- N. Kuroda, N. Ishikawa, Y. Chimi, A. Iwase, S. Okayasu, H. Ikeda, R. Yoshizaki, and T. Kambara: “Vortex dynamics in Bi<sub>2</sub>(Sr,La)<sub>2</sub>CuO<sub>6+ $\delta$</sub>  and Bi<sub>2</sub>Sr<sub>2</sub>CaCu<sub>2</sub>O<sub>8+ $\delta$</sub>  single crystals with columnar defects”, *Physica C* **321**, 143–150 (1999).
- E. Yagi: “Formation of solid krypton bubbles in aluminium as investigated by a channelling method”, *Rad. Eff. Def. Sol.* **148**, 193–211 (1999).
- N. Kawamura, K. Nagamine, T. Matsuzaki, K. Ishida, S. N. Nakamura, S. Sakamoto, I. Watanabe, M. Iwasaki, M. Tanase, M. Kato, K. Kurosawa, K. Kudo, N. Takeda, and G. H. Eaton: “Measurements of He accumulation effect on muon catalyzed fusion in the solid/liquid D-T mixtures”, *RIKEN Rev.*, No. 20, pp. 14–17 (1999).
- I. Shimamura: “Atomic physics of muon-catalyzed fusion”, *Supercomputing, Collision Processes, and Applications*, edited by Bell et al., Kluwer Academic/Plenum Publishers, New York, pp. 269–278 (1999).

#### 4. Radiochemistry, radiation chemistry, and radiation biology

- S. Gouthu, T. Arie, and I. Yamaguchi: “Uptake of <sup>137</sup>Cs and <sup>90</sup>Sr by cucumber in three soil-types”, *Comparative Evaluation of Environmental Toxicants: Health Effects of Environmental Toxicants Derived from Advanced Technology*, edited by J. Inaba and Y. Nakamura, National Institute of Radiological Sciences, pp. 275–276 (1998).
- K. Kimura, W. Hong, J. Kaneko, and N. Itoh: “Extremely fast decay component of UV luminescence from 2-MeV/amu ion irradiated alumina”, *Nucl. Instrum. Methods Phys. Res. B* **141**, 425–430 (1998).
- K. Kimura and W. Hong: “Decay enhancement of self-trapped excitons at high density and low temperature in an ion-irradiated BaF<sub>2</sub> single crystal”, *Phys. Rev. B* **58**, 6081–6089 (1998).
- R. Hirumuma, K. Endo, S. Enomoto, S. Ambe, and F. Ambe: “Study on the distribution of radioactive trace elements in vitamin D-overloaded rats using the multitracer technique”, *Appl. Radiat. Isot.* **50**, 843–849 (1999).

- I. Fujiwara, Y. Itoh, R. Iwata, F. Saito, and A. Goto: “ $^{18}\text{F}$  intense spot positron source for spin polarized positron beam”, *Appl. Surf. Sci.* **149**, 30–33 (1999).
- T. Abe: “A new mutation method for plants using heavy-ion beams”, *Biosci. Ind.* **57**, 39–40 (1999).
- K. Sueki, K. Kikuchi, K. Akiyama, T. Sawa, M. Katada, S. Ambe, F. Ambe, and H. Nakahara: “Formation of metallofullerenes with higher group elements”, *Chem. Phys. Lett.* **300**, 140–144 (1999).
- S. Ambe, T. Shinonaga, T. Ozaki, S. Enomoto, H. Yasuda, and S. Uchida: “Ion competition effects on the selective absorption of radionuclides by komatsuna (*Brassica rapa var. perviridis*)”, *Environ. Exp. Bot.* **41**, 185–194 (1999).
- S. Ambe, T. Ozaki, S. Enomoto, and T. Shinonaga: “Multitracer study on the soil-to-plant transfer of radionuclides in komatsuna at different growth stages”, *Environ. Technol.* **20**, 111–116 (1999).
- S. Gouthu, R. G. Weginwar, T. Arie, S. Ambe, T. Ozaki, S. Enomoto, F. Ambe, and I. Yamaguchi: “Subcellular distribution and translocation of radionuclides in plants”, *Environ. Toxicol. Chem.* **18**, 2023–2027 (1999).
- M. Kikuchi, I. Narumi, S. Kitayama, H. Watanabe, and K. Yamamoto: “Genomic organization of the radioresistant bacterium *Deinococcus radiodurans*: Physical map and evidence for multiple replicons”, *FEMS Microbiol. Lett.* **174**, 151–157 (1999).
- T. Arie, S. Gouthu, H. Hirata, S. Ambe, and I. Yamaguchi: “Plant uptake of radionuclides and rhizosphere factors”, *Final Reports on Nuclear Cross-Over Research (II): Transfer Models and Parameters of Radionuclides in Terrestrial Environment*, edited by Promotion Committee on Nuclear Cross-Over Research, Tokyo, pp. 97–107 (1999).
- K. Ushida, Y. Yoshida, T. Kozawa, S. Tagawa, and A. Kira: “Evidence of oxidation of aromatic hydrocarbons by chloromethyl radicals: Reinvestigation of intersolute hole transfer using pulse radiolysis”, *J. Phys. Chem. A* **103**, 4680–4689 (1999).
- T. Nozaki, Y. Itoh, Z.-L. Peng, N. Nakanishi, A. Goto, Y. Ito, and H. Yoshida: “Preparation of  $^{18}\text{F}$  source for slow positron beam by proton bombardment of  $^{18}\text{O}$ -water”, *J. Radioanal. Nucl. Chem.* **239**, 175–178 (1999).
- R. Hirunuma, N. Sotogaku, K. Endo, S. Enomoto, S. Ambe, and F. Ambe: “Time dependence of distribution of radioactive trace elements in Se-deficient rats: Application of the multitracer technique”, *J. Radioanal. Nucl. Chem.* **239**, 213–215 (1999).
- S. Oishi, R. Amano, A. Ando, S. Enomoto, and F. Ambe: “Simultaneous biobehavior of trace elements, Sc, Mn, Fe, Co, Zn, Se, Rb, and Zr in the brain and other organs of C57BL/6N mice”, *J. Radioanal. Nucl. Chem.* **239**, 411–416 (1999).
- N. Sotogaku, K. Endo, R. Hirunuma, S. Enomoto, S. Ambe, and F. Ambe: “Binding properties of various metals to blood components and serum proteins: A multitracer study”, *J. Trace Elements Med. Biol.* **13**, 1–6 (1999).
- T. Arie, S. Gouthu, H. Hirata, S. Ambe, and I. Yamaguchi: “Plant uptake of radionuclides and rhizosphere factors”, *JAERI-Conf.*, edited by S. Matsumoto, S. Uchida, H. Yamazaki, and H. Amano, Japan Atomic Energy Research Institute, Tokaimura, pp. 202–212 (1999).
- K. Ishioka, K. Ushida, K. G. Nakamura, S. Hishita, and M. Kitajima: “Effect of ion irradiation on coherent phonon dynamics in bismuth”, *Jpn. J. Appl. Phys.* **38**, L446–L447 (1999).
- Y. Kagawa, T. Shimazu, A. Gordon, N. Fukunishi, N. Inabe, M. Suzuki, M. Hirano, T. Kato, M. Watanabe, F. Hanaoka, and F. Yatagai: “Complex *hprt* deletion events are recovered after exposure of human lymphoblastoid cells to high-LET carbon and neon ion beams”, *Mutagenesis* **14**, 199–205 (1999).
- K. Kimura, W. Hong, J. Kaneko, and N. Itoh: “Stimulated emission and exciton complex in some insulator crystals irradiated by heavy ions”, *Nucl. Instrum. Methods Phys. Res. B* **154**, 318–324 (1999).
- K. Kimura, J. Kaneko, S. Sharma, W. Hong, and N. Itoh: “Stimulated emission at 326 nm and an ultrafast 100-ps-lived luminescence component by ion irradiation of  $\alpha$ -alumina”, *Phys. Rev. B* **60**, 12626–12634 (1999).
- H. Iwai, T. Abe, S. Yoshida, H. Kamada, and S. Satoh: “Production of non-organogenic and loosely attached callus in leaf disk cultures of haploid *Nicotiana glauca* by  $^{14}\text{N}$  ion beam irradiation”, *Plant Biotechnol.* **16**, 307–309 (1999).
- T. Shinonaga, G. Pröhl, H. Müller, and S. Ambe: “Experimentally determined mobility of trace elements in soybean plants”, *Sci. Total Environ.* **225**, 241–248 (1999).

## 5. Material analysis

- K. Hasegawa, K. Maeda, S. Nakayama, A. Tonomura, and H. Hamanaka: “Crystal spectrometer PIXE system equipped with a multi-anode PSPC”, *Rep. Res. Cen. Ion Beam Technol., Hosei Univ.*, No. 18, pp. 35–39 (1997).
- K. Hasegawa, K. Maeda, S. Nakayama, A. Tonomura, and H. Hamanaka: “A multianode position-sensitive proportional counter for in-air high-resolution PIXE using a crystal spectrometer”, *Int. J. PIXE* **8**, 47–56 (1998).
- Y. Tokimitsu, K. Maeda, S. Murao, and E. Henseler: “External-PIXE identification of material for popular music pipes during the late Meiji era, Japan”, *Int. J. PIXE* **8**, 155–166 (1998).
- H. Hamanaka, A. Tonomura, K. Hasegawa, K. Maeda, and S. Yumoto: “PIXE analysis of Al compounds using a wavelength-dispersive spectrometer with PSPC(1)”, *Rep. Res. Cen. Ion Beam Technol., Hosei Univ.*, Suppl. No. 16, pp. 87–92 (1998).

- K. Maeda, A. Tonomura, H. Hamanaka, and K. Hasegawa: "Chemical shift measurements of PIXE spectra using a position-sensitive crystal spectrometer", *Nucl. Instrum. Methods Phys. Res. B* **150**, 124–128 (1999).
- H. Hamanaka, A. Tonomura, K. Hasegawa, K. Maeda, and S. Yumoto: "PIXE analysis of Al compounds using a wavelength dispersive spectrometer with PSPC(2)", *Rep. Res. Cent. Ion Beam Technol. Hosei Univ., Suppl. No. 17*, pp. 141–145 (1999).
- W. Hong, S. Hayakawa, K. Maeda, S. Fukuda, and Y. Gohshi: "Light element analysis in steel by high-energy heavy-ion time of flight elastic recoil detection analysis", *Spectrochim. Acta B* **54**, 151–157 (1999).

## VIII. LIST OF PREPRINTS

1999

RIKEN-AF-NP

- 303 V. B. Carlson and D. Hirata: “The Dirac-Hartree-Bogoliubov approximation for finite nuclei”
- 304 H. Ogawa, K. Asahi, K. Sakai, A. Yoshimi, M. Tsuda, Y. Uchiyama, T. Suzuki, K. Suzuki, N. Kurokawa, M. Adachi, H. Izumi, H. Ueno, T. Shimoda, S. Tanimoto, N. Takahashi, W.-D. Schmidt-Ott, M. Schafer, S. Fukuda, A. Yoshida, M. Notani, T. Kubo, H. Okuno, H. Sato, N. Aoi, K. Yoneda, H. Iwasaki, N. Fukuda, N. Fukunishi, M. Ishihara, and H. Miyatake: “Magnetic moment and electric quadrupole moment of the  $^{18}\text{N}$  ground state”
- 305 A. Ansari, M. Oi, N. Onishi, and T. Horibara: “High exotics in osmium isotopes”
- 306 A. Ansari, M. Oi, N. Onishi, and T. Horibara: “High spin structure of  $^{182,184}\text{Os}$  in tilted axis cranking approach”
- 307 Y. Mochizuki, K. Takahashi, H.-Th. Janka, W. Hilenzaki, and R. Diehl: “ $^{44}\text{Ti}$ : Its effective decay rate in young supernova remnants, and its abundance in Cas-A”
- 308 H. Madokoro and M. Matsuzaki: “Relativistic and non-relativistic mean field investigation of the super-deformed bands in  $^{62}\text{Zn}$ ”
- 309 N. Saito: “Measurement of anti-quark polarization in the proton and its flavor decomposition with PHENIX at RHIC”
- 310 Y. Goto: “Gluon polarization measurement with photon detection at PHENIX”
- 311 M. R. Ahmady and E. Kou: “A more careful estimate of the charm content of  $\eta$ ”
- 312 A. A. Korshennikov, M. S. Golovkov, A. Ozawa, E. A. Kuzmin, E. Yu. Nikolskii, K. Yoshida, B. G. Novatskii, A. A. Ogloblin, I. Tanihata, Z. Fülöp, K. Kusaka, K. Morimoto, H. Otsu, H. Petruscu, and H. Tokanai: “Observation of the  $^7\text{He}$  excited state with unusual structure”
- 313 Y. Mochizuki, T. Izuyama, and I. Tanihata: “Dynamics of exotic nuclear rod formation for the origin of neutron star glitches”
- 314 N. Itagaki and S. Okabe: “Nucleon-alpha chain states in  $^{10}\text{Be}$ ”
- 315 N. Dinh Dang, K. Tanabe, and A. Arima: “Evolution of the hot giant dipole resonance as a manifestation of the order-and-chaos coexistence”
- 316 A. Kohama, K. Yazaki, and R. Seki: “Correlation and finite interaction-range effects in high-energy electron inclusive scattering”
- 317 T. Suzuki, H. Sakai, and T. Tatsumi: “The Landau-Migdal parameters,  $g'_{\text{NN}}$  and  $g'_{\text{N}\Delta}$  and pion condensation”
- 318 T. Suzuki: “ $E1 \times E1$  and  $E1 \times E2$  giant resonances\*: Effects of the exchange current on the excitation of double giant resonance states”
- 319 H. Okamura: “Three-body treatment of the  $(d, ^2\text{He})$  reaction on the basis of the adiabatic approximation”
- 320 V. Yu. Denisov and S. Yamaji: “One and double-phonon giant monopole resonances in the nonlinear approach”

- 321 T. Nakamura, N. Fukuda, T. Kobayashi, N. Aoi, H. Iwasaki, T. Kubo, A. Mengoni, M. Notani, H. Otsu, H. Sakurai, S. Shimoura, T. Teranishi, Y. Watanabe, K. Yoneda, and M. Ishihara: “Coulomb dissociation of  $^{19}\text{C}$  and its halo structure”
- 322 Y. Goto: “Sensitivity to gluon polarization at RHIC”
- 323 N. Saito: “RHIC spin physics-status of the polarized collider and spin-flavor structure of the nucleon”
- 324 N. Dinh Dang, K. Eisenman, J. Seitz, and M. Thoennessen: “Statistical analysis of the hot giant dipole resonance with the phonon damping model”
- 325 N. Dinh Dang, K. Tanabe, and A. Arima: “Damping of multiphonon giant resonances”
- 326 A. Ansari, N. Dinh Dang, and A. Arima: “Hot giant dipole resonance in static path approximation”
- 327 H. Kurasawa and T. Suzuki: “Effects of the Dirac sea on the giant monopole states”
- 328 T. Maruyama and S. Chiba: “Isoscalar giant quadrupole resonance state in the relativistic approach with the momentum-dependent self-energies”
- 329 N. Itagaki and S. Aoyama: “Systematic study on He-isotope with antisymmetrized molecular dynamics plus generator coordinate method”
- 330 T. Uesaka, H. Sakai, H. Okamura, T. Ohnishi, Y. Satou, S. Ishida, N. Sakamoto, H. Otsu, T. Wakasa, K. Itoh, K. Sekiguchi, and T. Wakui: “Polarization correlation coefficient for the  $^3\vec{\text{He}}(\vec{d}, p)^4\text{He}$  reaction”
- 331 N. Dinh Dang, T. Suzuki, and A. Arima: “Giant dipole resonance in neutron-rich nuclei within the phonon damping model”
- 332 S. Sugimoto, K. Sumiyoshi, D. Hirata, B. V. Carlson, I. Tanihata, and H. Toki: “Systematic study of triaxial deformation in the relativistic mean field theory”
- 333 N. Itagaki and S. Okabe: “Molecular orbital structures in  $^{10}\text{Be}$ ”
- 334 M. Tanifuji, S. Ishikawa, Y. Iseri, T. Uesaka, N. Sakamoto, Y. Satou, K. Itoh, H. Sakai, A. Tamii, T. Ohnishi, K. Sekiguchi, K. Yako, S. Sakoda, H. Okamura, K. Suda, and T. Wakasa: “Reaction mechanism and characteristics of  $T_{20}$  in  $d+^3\text{He}$  backward elastic scattering at intermediate energies”
- 335 M. Oi, A. Ansari, T. Horibata, and N. Onishi: “Wobbling motion in the multi-bands crossing region”
- 336 K. Tanabe and N. Dinh Dang: “Exact form of the random phase approximation equation at finite temperature including the entropy effect”
- 337 K. Sumiyoshi, H. Suzuki, K. Otsuki, M. Teranishi, and S. Yamada: “Hydrodynamical study of neutrino-driven wind as an r-process site”

#### RIKEN-AF-NC

- 12 S. Biri, T. Nakagawa, M. Kidera, Y. Miyazawa, M. Hemmi, T. Chiba, N. Inabe, M. Kase, T. Kageyama, O. Kamigaito, A. Goto, and Y. Yano: “Production of highly charged ions in the RIKEN 18 GHz ECR ion source using an electrode in two modes”
- 13 G. Shirkov: “Multicomponent consideration of electron fraction of ECR source plasma”
- 14 E. Syresin, T. Tanabe, T. Rizawa, T. Katayama, and I. Mashkov: “Simulation and design of an electron cooling system for ACR”

- 15 S. Kondrashev: "Laser ion source-intense pulsed source of highly-charged ion beams for RIKEN MUSES Project"
- 16 P. Zenkevich and T. Katayama: "Storage of ion beams in ACR by use of charge-exchange injection"

## IX. PAPERS PRESENTED AT MEETINGS

1. Accelerator development and accelerator physics
  - I. Watanabe, T. Tanabe, K. Ohtomo, and T. Katayama: "Electron cooling at ACR in MUSES project", 6th European Particle Accelerator Conf. (EPAC'98), (MSL), Stockholm, Sweden, June (1998).
  - T. Tanabe, Y. Watanabe, and M. Kase: "RIKEN-RIBF control system", 2nd Workshop on PCs and Particle Accelerator Control (PCaPAC '99), (KEK), Tsukuba, Jan. (1999).
  - T. Tanabe, K. Ohtomo, T. Rizawa, and T. Katayama: "Development of MUSES-ACR electron cooler", 1999 Particle Accelerator Conf. (PAC '99), (Brookhaven National Laboratory), New York, USA, Mar. (1999).
  - O. Kamigaito: "A pre-injector RFQ and a 'charge-state multiplier' system of the RIKEN heavy ion linac", 4th Korea-Japan Joint Symp. on Cyclotrons and Nuclear Science, (Korea Cancer Center Hospital), Seoul, Korea, Mar. (1999).
  - T. Tanabe, T. Rizawa, K. Ohtomo, T. Katayama, E. Syresin, I. Meshkov, and A. Yamashita: "Design of an electron cooling device for the accumulator cooler ring in MUSES project", ECOOL '99 Workshop on Electron Cooling and Related Topics Incorporating 5th Workshop on Medium Energy Electron Cooler (MEEC), (Svedberg Laboratory), Uppsala, Sweden, May (1999).
  - M. Kidera, K. Higurashi, T. Nakagawa, S. Biri, G. Shirkov, Y. Miyazawa, M. Hemmi, T. Chiba, T. Kageyama, M. Kase, A. Goto, and Y. Yano: "Effect of biased electrode to high energetic electrons in plasma of RIKEN 18 GHz ECRIS", 14th Int. Workshop on ECR Ion Sources (ECRIS99), (CERN), Geneva, Switzerland, May (1999).
  - T. Tominaka, T. Kawaguchi, J.-W. Kim, H. Okuno, J. Ohnishi, A. Goto, and Y. Yano: "RIKEN Superconducting Ring Cyclotron (III): Quench protection of sector magnet", 60th Meet. on Cryogenics and Superconductivity, (Cryogenics Association of Japan), Sapporo, June (1999).
  - A. Goto and Y. Yano: "RIKEN Superconducting Ring Cyclotron (I): Overview and status", 60th Meet. on Cryogenics and Superconductivity, (Cryogenics Association of Japan), Sapporo, June (1999).
  - A. Goto: "Superconducting ring cyclotron for RIKEN RI Beam Factory", 1999 1st Chou-Dendou Ouyou Kenkyuukai, Tsukuba, July (1999).
  - S. Bhattacharjee and H. Amemiya: "Build up characteristics of a plasma produced by high power short pulse microwaves", 24th Int. Conf. on Phenomena in Ionized Gases (ICPIG), Warsaw, Poland, July (1999).
  - S. Bhattacharjee and H. Amemiya: "Production of microwave plasma in a waveguide with a dimension below cutoff", Int. Symp. PLASMA'99 on Research and Applications of Plasmas, (Polish Academy of Sciences), Warsaw, Poland, July (1999).
  - O. Kamigaito, M. Kase, Y. Miyazawa, T. Chiba, M. Hemmi, S. Kohara, E. Ikezawa, A. Goto, and Y. Yano: "Construction of the first unit of the charge-state multiplier system for the RIKEN RI-Beam Factory", 24th Linear Accelerator Meet. in Japan, (Laboratory of Energy Conversion Engineering, Graduate School of Engineering, Hokkaido University), Sapporo, July (1999).
  - K. Higurashi, T. Nakagawa, M. Kidera, Y. Miyazawa, M. Hemmi, T. Chiba, M. Kase, T. Kageyama, A. Goto, and Y. Yano: "The effect of an electrode in plasma chamber of electron cyclotron resonance ion source (ECRIS)", 1999 Fall Meet. of Physical Society of Japan, Matsue, Sept. (1999).
  - T. Kurita, T. Nakagawa, T. Kawaguchi, and S. M. Lee: "Design of ECR ion source using liquid-helium-free superconducting solenoid coils", 1999 Fall Meet. of Physical Society of Japan, Matsue, Sept. (1999).
  - S. Bhattacharjee and H. Amemiya: "Pulsed microwave plasma production in a conducting tube with a radius below cutoff", 11th Int. School on Vacuum, Electron and Ion Technologies (VEIT'99), (Institute of Electronics at the Bulgarian Academy of Sciences), Varna, Bulgaria, Sept. (1999).
  - M. Kidera: "Status and future plan of RIKEN ECRIS", Int. Workshop on Ion Sources for Producing the Intense Beam of Multi-charged Metallic Ions, Wako, Sept. (1999).
  - T. Takeuchi: "Future plan of laser ion source at RIKEN", Int. Workshop on Ion Sources for Producing the Intense Beam of Multi-charged Metallic Ions, Wako, Sept. (1999).
  - M. Kase, T. Masuoka, J. Ohnishi, T. Tanabe, and Y. Watanabe: "CORBA based control system with RTOS on VME/CPCI", 7th Int. Conf. on Accelerator and Large Experimental Physics Control Systems (ICALEPCS) 99, (Sincrotrone Trieste), Trieste, Italy, Oct. (1999).
  - K. Higurashi, T. Nakagawa, M. Kidera, Y. Miyazawa, M. Hemmi, T. Chiba, M. Kase, T. Kageyama, A. Goto, and Y. Yano: "The effect of an electrode in plasma chamber of RIKEN 18kHz ECRIS (Electron Cyclotron Resonance Ion Source)", 12th Symp. on Accelerator Science and Technology, Wako, Oct. (1999).
  - O. Kamigaito, M. Kase, Y. Miyazawa, T. Chiba, M. Hemmi, N. Sakamoto, S. Kohara, E. Ikezawa, A. Goto, and Y. Yano: "Construction of the charge-state multiplier system for the RIKEN RI-Beam Factory", 12th Symp. on Accelerator Science and Technology, Wako, Oct. (1999).

- T. Rizawa, K. Ohtomo, and T. Katayama: "Electron coolers in MUSES project", 12th Symp. on Accelerator Science and Technology, Wako, Oct. (1999).
- T. Rizawa, A. Yamashita, S. Takama, M. Ushijima, T. Katayama, and T. Tanabe: "Experimental studies of discharge under magnetic field for the electron gun design of the ACR electron cooler", 12th Symp. on Accelerator Science and Technology, Wako, Oct. (1999).
- A. Goto, M. Kase, J. Ohnishi, O. Kamigaito, N. Sakamoto, K. Ikegami, K. Sugii, H. Okuno, Y. Miyazawa, T. Hiasa, Y. Kumata, and Y. Yano: "Construction of the IRC for RIKEN RI-Beam Factory", 12th Symp. on Accelerator Science and Technology, Wako, Oct. (1999).
- S. Bhattacharjee and H. Amemiya: "Characteristics of a plasma produced by high power short pulse microwaves", 41st Ann. Meet. of the Division of Plasma Physics, (American Physical Society), Seattle, USA, Nov. (1999).
- A. Goto: "Non-nuclear physics researchers at RIKEN accelerator research facility", BATAN-JAIF Bilateral Seminar on Accelerator Technology and Its Applications, (Research and Development Centre for Advanced Technology), Yogyakarta, Indonesia, Nov. (1999).
- T. Tominaka, H. Okuno, and T. Kubo: "2D magnetostatic field calculation with mathematica", 61st Meet. on Cryogenics and Superconductivity, (Cryogenics Association of Japan), Hachioji, Nov. (1999).
- ## 2. Nuclear physics and nuclear instrumentation
- I. Tanihata: "The RI Beam Factory and planned experiments related to astrophysics", Int. Conf. on Neutron Stars and Pulsars: Thirty Years after the Discovery, (Rikkyo University), Tokyo, Nov. (1997).
- I. Tanihata: "New horizon in nuclear physics and astrophysics using radioactive nuclear beams", 11th Nishinomiya-Yukawa Memorial Symp., Hyogo, Nov. (1997).
- T. Kishida: "Windowless gas target system for high intensity beam", 53rd Ann. Meet. of Physical Society of Japan, Funabashi, Apr. (1998).
- A. Ozawa, A. A. Korshennikov, Y. Ogawa, I. Tanihata, and K. Yoshida: "Measurements of interaction cross-sections for C-isotopes at relativistic energies", 74th Korean Physical Society Meet., Seoul, Korea, Apr. (1998).
- T. Matsuzaki, K. Nagamine, K. Ishida, S. N. Nakamura, N. Kawamura, M. Tanase, M. Kato, K. Kurosawa, M. Hashimoto, H. Sugai, K. Kudoh, N. Takeda, and G. H. Eaton: "Muon catalyzed fusion and muon to  $^3\text{He}$  transfer in solid  $\text{T}_2$  studied by X-ray and neutron detection", Monte Verità Workshop on Exotic Atoms, Molecules and Muon Catalyzed Fusion, (Paul Scherrer Institute and University of Fribourg), Ascona, Switzerland, July (1998).
- T. Matsuzaki, K. Nagamine, M. Tanase, M. Kato, K. Kurosawa, K. Ishida, S. N. Nakamura, I. Watanabe, and G. H. Eaton: "Tritium gas handling system for muon catalyzed fusion research at RIKEN-RAL muon facility", Monte Verità Workshop on Exotic Atoms, Molecules and Muon Catalyzed Fusion, (Paul Scherrer Institute and University of Fribourg), Ascona, Switzerland, July (1998).
- Y. Mochizuki: "The long half-life of highly ionized  $^{44}\text{Ti}$ ", Nuclei in the Cosmos V, Volos, Greece, July (1998).
- Y. Mochizuki: "A microscopic model of neutron star glitches", Seminar at Max-Planck Institut für Astrophysik, Garching, Germany, July (1998).
- T. Fujita, K. Tsuruta, T. Yagita, H. Okuda, M. Kondo, Y. Tachikawa, H. Urabe, M. Nakamura, K. Shigenaga, H. Nakamura, K. Sagara, T. Nakashima, and H. Akiyoshi: "Precise measurement of  $A_y$  for the nd scattering at 16 MeV", 1998 Fall Meet. of Physical Society of Japan, Akita, Oct. (1998).
- T. Onishi, T. Kawa, K. Matsuta, M. Mihara, M. Fukuda, T. Minamisono, T. Miyake, M. Sasaki, T. Yamaguchi, K. Sato, K. Minamisono, A. Morisita, K. Tanaka, K. Kidera, T. Ohtsubo, S. Momota, Y. Nojiri, A. Kitagawa, M. Torikoshi, S. Kouda, S. Nishio, A. Ozawa, K. Yoshida, I. Tanihata, S. S. Hanna, J. R. Alonso, G. F. Krebs, and T. J. M. Symons: "The quadrupole moments of  $^{27}\text{Si}$  and  $^{39}\text{Ca}$ ", 1998 Fall Meet. of Physical Society of Japan, Akita, Oct. (1998).
- T. Matsuzaki: "Studies on  $\mu\text{CF}$  and muon transfer in pure  $\text{T}_2$  target", RIKEN Symp. on Muon Science '98: New Direction in Muon Catalyzed Fusion  $\mu\text{SR}$  Studies and Fundamental Muon Physics, Wako, Oct. (1998).
- N. Kawai, M. Matsuoka, A. Yoshida, T. Mihara, T. Kotani, H. Negoro, Y. Shirasaki, I. Sakurai, K. Torii, H. Tsunemi, E. Miyata, M. Yamauchi, and K. Yoshida: "MAXI (Monitor of All-sky X-ray Image) for JEM on the space station", Small Missions for Energetic Astrophysics: Ultraviolet through Gamma-Ray, (Los Alamos National Laboratory), Los Alamos, USA, Feb. (1999).
- K. Yoneda, H. Sakurai, N. Aoi, N. Fukuda, T. Gomi, E. Ideguchi, N. Imai, H. Iwasaki, T. Kubo, Z. Liu, S. M. Lukyanov, T. Nakamura, M. Notani, H. Ogawa, Y. E. Penionzhkevich, W. D. Schmidt-Ott, S. Shimoura, E. Sokol, Y. Watanabe, A. Yoshida, X. Zhou, and M. Ishihara: "Measurements of beta decay half lives and betadelayed neutron emission probabilities for nuclei near the neutron drip line ( $Z=12-14$ )", 54th Ann. Meet. of Physical Society of Japan, Higashihiroshima, Mar. (1999).
- F. Tokanai, K. Morimoto, M. Kurata, I. Tanihata, and S. Yamada: "Development of time-of-flight detector with streak camera I", 54th Ann. Meet. of Physical Society of Japan, Higashihiroshima, Mar. (1999).
- H. Madokoro and M. Matsuzaki: "Systematic study of

- the superdeformed bands in the  $A=60$  mass region”, 54th Ann. Meet. of Physical Society of Japan, Higashihiroshima, Mar. (1999).
- T. Matsuzaki, K. Nagamine, K. Ishida, S. N. Nakamura, N. Kawamura, Y. Matsuda, S. Sakamoto, M. Tanase, M. Kato, K. Kurosawa, H. Sugai, K. Kudo, N. Takeda, and G. H. Eaton: “Muon catalyzed D-T fusion experiment at RIKEN-RAL muon facility (12)”, 54th Ann. Meet. of Physical Society of Japan, Higashihiroshima, Mar. (1999).
- K. Sumiyoshi, H. Suzuki, and S. Yamada: “Hydrodynamics of neutrino-driven wind for r-process”, 54th Ann. Meet. of Physical Society of Japan, Higashihiroshima, Mar. (1999).
- A. Ozawa, O. Bochkarev, L. Chulkov, D. Cortina-Gil, H. Geissel, M. Hellsroem, M. Ivanov, R. Janik, K. Kimura, T. Kobayashi, A. A. Korshennikov, G. Muenzenberg, F. Nickel, A. A. Ogloblin, M. Pfutzner, V. Pribora, C. Sheidenberger, H. Simon, B. Sitar, T. Suzuki, P. Strmen, K. Suemmerer, I. Tanihata, M. Winkler, and K. Yoshida: “Measurements of interactions cross-sections for oxygen isotopes”, 54th Ann. Meet. of Physical Society of Japan, Higashihiroshima, Mar. (1999).
- H. M. Shimizu, T. Ikeda, H. Kato, K. Kawai, H. Miyasaka, T. Oku, W. Ootani, C. Otani, H. Sato, Y. Takizawa, and H. Watanabe: “Development of superconducting devices for radiation detection at RIKEN”, CRL(Communications Research Laboratory) Int. Symp., Tokyo, Mar. (1999).
- K. Ishida: “Second phase of RIKEN-RAL”, MSL99 Workshop on Super High-Intensity Muon Beam and Muon Science in 21st Century, (Meson Science Laboratory, High Energy Accelerator Research Organization; RIKEN), Tsukuba, Mar. (1999).
- T. Matsuzaki, K. Ishida, S. N. Nakamura, and N. Kawamura: “Recent  $\mu$ CF research -  $\mu$ CF experiment at RIKEN-RAL”, MSL99 Workshop on Super High-Intensity Muon Beam and Muon Science in 21st Century, (Meson Science Laboratory, High Energy Accelerator Research Organization; RIKEN), Tsukuba, Mar. (1999).
- T. Suzuki: “ $E1 \times E1$  and  $E1 \times E2$  giant resonances”, RIKEN Symp. and Workshop on Selected Topics in Nuclear Collective Excitations, Wako, Mar. (1999).
- S. Yamaji: “Damping of isoscalar monopole resonance at highly excited nuclei”, RIKEN Symp. and Workshop on Selected Topics in Nuclear Collective Excitations, Wako, Mar. (1999).
- Y. Mochizuki: “Seeking mysterious universe with RI”, Tokubetsu-Danwa-Kai, Nagoya University, Nagoya, Mar. (1999).
- K. Ishida: “Muon catalyzed fusion experiments, present status and future plans”, Workshop on Intensity Secondary Beam with Phase Rotation, (Institute of Advanced Energy, Kyoto University), Uji, Mar. (1999).
- K. Ishida: “Super-super muon channel at RAL”, Workshop on Intensity Secondary Beam with Phase Rotation, (Institute of Advanced Energy, Kyoto University), Uji, Mar. (1999).
- T. Suzuki: “Sum rule approach to double giant resonances”, Double Giant Resonances in Nuclei, (European Center for Theoretical Studies in Nuclear Physics and Related Areas), Trento, Italy, May (1999).
- N. Dinh Dang, K. Tanabe, and A. Arima: “Damping of double giant dipole resonance”, Double Giant Resonances in Nuclei, (European Center for Theoretical Studies in Nuclear Physics and Related Areas), Trento, Italy, May (1999).
- N. Dinh Dang, K. Tanabe, and A. Arima: “Shape evolution of the hot giant dipole resonance”, Int. Conf. on Achievements and Perspectives in Nuclear Structure, (Institute of Nuclear Physics NCSR Demokritos), Crete, Greece, July (1999).
- H. Madokoro, J. Meng, M. Matsuzaki, and S. Yamaji: “Relativistic tilted axis cranking”, Int. Symp. on Models and Theories of the Nuclear Mass, Wako, July (1999).
- K. Sumiyoshi: “Unstable nuclei and EOS table for supernova explosion and r-process in relativistic many body approach”, Int. Symp. on Models and Theories of the Nuclear Mass, Wako, July (1999).
- A. Yoshida: “Fusion cross section of neutron-rich Be isotopes  $^{11,10,9}\text{Be}+^{209}\text{Bi}$ ”, Workshop on the Nuclear Sciences of the Heaviest Elements, (JAERI), Tokaimura, July (1999).
- K. Sekiguchi, H. Sakai, H. Okamura, N. Sakamoto, T. Uesaka, A. Tamii, Y. Satou, T. Ohnishi, T. Wakasa, K. Yako, S. Fukusaka, K. Suda, S. Sakoda, H. Kato, Y. Maeda, K. Itoh, and T. Niizeki: “Measurement of cross sections and vector and tensor analyzing powers for  $d$ - $p$  elastic scattering at  $E_d = 270$  MeV”, Asia Pacific Conf. on Few-Body Problems in Physics (APFB 99), (Science University of Tokyo), Chiba, Aug. (1999).
- T. Uesaka, H. Sakai, H. Okamura, J. Tamii, Y. Satou, T. Ohnishi, N. Sakamoto, K. Itoh, K. Sekiguchi, K. Yako, S. Sakoda, K. Suda, and T. Wakasa: “ $^3\text{He}(d,p)^4\text{He}$  reaction at intermediate energies”, Asia Pacific Conf. on Few-Body Problems in Physics (APFB 99), (Science University of Tokyo), Chiba, Aug. (1999).
- K. Naito, T. Umekawa, and M. Oka: “Study of linear sigma model at finite temperature using the non-perturbative renormalization group”, Kiken ‘Thermal Field Theory and Its Application’, (Yukawa Institute for Theoretical Physics, Kyoto University), Kyoto, Aug. (1999).
- T. Uesaka, H. Sakai, H. Okamura, A. Tamii, Y. Satou, T. Ohnishi, N. Sakamoto, K. Itoh, K. Sekiguchi, K. Yako, S. Sakoda, K. Suda, and T. Wakasa: “ $^3\text{He}(d,p)^4\text{He}$  reaction at intermediate energies”, 4th Workshop on Polarized Nuclear Fusion, (Research Center for Nuclear Physics, Osaka University), Os-

- aka, Aug. (1999).
- K. Yoneda, T. Gomi, H. Sakurai, T. Motobayashi, N. Aoi, N. Fukuda, U. Futakami, Z. Gacsi, K. Higurashi, N. Imai, N. Iwasa, H. Iwasaki, M. Kunibu, M. Kurokawa, T. Kubo, Z. Liu, T. Minemura, A. Saito, M. Serata, S. Shimoura, S. Takeuchi, Y. Watanabe, K. Yamada, Y. Yanagisawa, K. Yogo, A. Yoshida, and M. Ishihara: "Spectroscopy of neutron-rich nuclei via the projectile-fragmentation reaction of unstable nuclei  $^{36}\text{Si}$ ", 1999 Fall Meet. of Physical Society of Japan, Matsue, Sept. (1999).
- T. Gomi, K. Yoneda, H. Sakurai, S. Shimoura, T. Motobayashi, N. Aoi, N. Fukuda, U. Futakami, Z. Gacsi, K. Higurashi, N. Imai, N. Iwasa, H. Iwasaki, T. Kubo, M. Kunibu, M. Kurokawa, Z. Liu, T. Minemura, A. Saito, M. Serata, S. Takeuchi, Y. Watanabe, K. Yamada, Y. Yanagisawa, K. Yogo, A. Yoshida, and M. Ishihara: "Production rates of excited unstable nuclei by the projectile fragmentation of  $^{36}\text{Si}$ ", 1999 Fall Meet. of Physical Society of Japan, Matsue, Sept. (1999).
- T. Minemura, T. Motobayashi, S. Shimoura, H. Murakami, Y. Ando, T. Teranishi, N. Aoi, Zs. Fülöp, M. Hirai, H. Iwasaki, N. Imai, N. Iwasa, M. Kurokawa, H. Akiyoshi, Y. Yanagisawa, Y. Iwata, S. Ozawa, S. Takeuchi, K. Higurashi, M. Serata, H. Kobayashi, K. Yamada, T. Gomi, H. Sakurai, K. Yoshida, Z. Liu, and M. Ishihara: "Coulomb dissociation of  $^{12}\text{N}$  and  $^{13}\text{O}$ ", 1999 Fall Meet. of Physical Society of Japan, Matsue, Sept. (1999).
- K. Suda, H. Okamura, N. Sakamoto, A. Tamii, T. Uesaka, T. Ohnishi, K. Sekiguchi, J. Nishikawa, H. Kato, M. Hatano, and H. Sakai: "Absolute calibration of the deuteron beam polarization at intermediate energies via the  $^{12}\text{C}(d, \alpha)$  reaction", 1999 Fall Meet. of Physical Society of Japan, Matsue, Sept. (1999).
- K. Naito, Y. Nemoto, K. Yoshida, M. Takizawa, and M. Oka: "Study of chiral symmetry breaking using the CJT effective potential", 1999 Fall Meet. of Physical Society of Japan, Matsue, Sept. (1999).
- H. Madokoro, J. Meng, M. Matsuzaki, and S. Yamaji: "Relativistic mean field model applied to tilted axis rotation", 1999 Fall Meet. of Physical Society of Japan, Matsue, Sept. (1999).
- K. Sumiyoshi, H. Suzuki, K. Otsuki, M. Terasawa, and S. Yamada: "r-Process condition by simulation of neutron-driven wind", 1999 Fall Meet. of Physical Society of Japan, Matsue, Sept. (1999).
- K. Ishida: "Design of ultra intense muon channel", 1999 Nendo Zenki Kyoudou Riyo Jikken Houkokukai & Meson Science Working Group Workshop, (Meson Science Laboratory, High Energy Accelerator Research Organization; Meson Science Association), Tsukuba, Sept. (1999).
- T. Uesaka, H. Sakai, H. Okamura, J. Tamii, Y. Satou, T. Ohnishi, N. Sakamoto, T. Wakasa, K. Itoh, K. Sekiguchi, K. Yako, S. Sakoda, K. Suda, M. Kurokawa, T. Motobayashi, S. Shimoura, H. Akiyoshi, T. Teranishi, S. Takeuchi, H. Iwasaki, N. Imai, T. Gomi, M. Serata, Y. Yanagisawa, S. Kubono, S. Yamamoto, T. Wakui, and Y. Yano: "Nuclear physics experiments with polarized  $^3\text{He}$  target at RIKEN", Int. Workshop on Polarized Sources and Targets, (Erlangen University), Erlangen, Germany, Sept. (1999).
- F. Tokanai, K. Morimoto, M. Kurata, I. Tanihata, and S. Yamada: "Development of time-of-flight detector with streak camera", 1999 IEEE Nuclear Science Symp. and Medical Imaging Conf., Seattle, USA, Oct. (1999).
- T. Uesaka, H. Sakai, H. Okamura, J. Tamii, Y. Satou, T. Ohnishi, N. Sakamoto, T. Wakasa, K. Itoh, K. Sekiguchi, K. Yako, S. Sakoda, and K. Suda: " $^3\text{He}(d, p)^4\text{He}$  reaction at intermediate energies", RCNP-TMU Symp. on Spins in Nuclear and Hadronic Reactions, (Research Center for Nuclear Physics, Osaka University, and Tokyo Metropolitan University), Tokyo, Oct. (1999).
- K. Sumiyoshi, H. Shen, K. Oyamatsu, Y. Sugahara, M. Terasawa, K. Otsuki, H. Suzuki, S. Yamada, T. Kajino, H. Toki, and I. Tanihata: "Unstable nuclei and EOS for supernova and r-process", RCNP-TMU Symp. on Spins in Nuclear and Hadronic Reactions, (Research Center for Nuclear Physics, Osaka University, and Tokyo Metropolitan University), Tokyo, Oct. (1999).
- H. Madokoro, M. Matsuzaki, and M. Matsuzaki: "Largely deformed states in nuclei close to the  $N=Z$  line", YITP Workshop on Structure and Reaction of Unstable Nuclei, (Yukawa Institute for Theoretical Physics, Kyoto University), Kyoto, Nov. (1999).
- K. Sumiyoshi: "Unstable nuclei and EOS table for supernova and r-process simulations in relativistic many body approach", YITP Workshop on Structure and Reaction of Unstable Nuclei, (Yukawa Institute for Theoretical Physics, Kyoto University), Kyoto, Nov. (1999).
- H. Madokoro, J. Meng, M. Matsuzaki, and S. Yamaji: "Shears bands in the  $A=80$  region", Gammasen Kakubunkou to Tanjumpyoukaku no Furontia, (JAERI), Tokai-mura, Dec. (1999).
- K. Naito, T. Umekawa, and M. Oka: "Study of thermal system using the non-perturbative renormalization group", KEK Tanashi Kenkyukai on QCD and Hadron Physics, Tanashi, Dec. (1999).
- T. Suzuki: "Effects of the Dirac sea on nuclear responses", New Development of the Field Theory for Many-Body System, (Yukawa Institute for Theoretical Physics, Kyoto University), Kyoto, Dec. (1999).
- T. Uesaka: "Study of the short-range structure of light nuclei via the nucleon transfer reactions at intermediate energies", RCNP Workshop on TARN-II, (Research Center for Nuclear Physics, Osaka University), Osaka, Dec. (1999).
- T. Suzuki: "A few topics on giant resonance states",

RIKEN Int. Symp. on Quasiparticle and Phonon Excitations in Nuclei, Wako, Dec. (1999).

### 3. Atomic and solid-state physics

- I. Shimamura: "Hyperspherical close-coupling calculations on the dynamics of three-body systems", Int. Lectures on Atomic and Molecular Physics, Asia Pacific Center for Theoretical Physics (APCTP), Seoul, Korea, Apr. (1998).
- Y. Morishita, S. Ninomiya, Y. Yamazaki, K. Kuroki, K. Komaki, H. Masuda, and M. Sekiguchi: "Visible light emission from slow highly charged ions interacting with micro capillaries", 23rd Ann. Meet. of Society for Atomic Collision Research, Yokohama, Aug. (1998).
- N. Okabayashi, K. Kuroki, T. Azuma, K. Komaki, H. Masuda, and M. Sekiguchi: "Two dimensional velocity distribution of hydrogen ions potential-sputtered by highly charged ions", 23rd Ann. Meet. of Society for Atomic Collision Research, Yokohama, Aug. (1998).
- A. Fukaya, I. Watanabe, M. Hagiwara, and K. Nagamine: "Muon spin resonance of the Haldane-gap systems NENP and  $\text{NiC}_2\text{O}_4 \cdot 2(2\text{-methylimidazole})$ ", 1998 Fall Meet. of Physical Society of Japan, Okinawa, Sept. (1998).
- A. Koyama: "Auger electron spectra induced by heavy ion impact", 15th Int. Conf. on the Application of Accelerators in Research and Industry, (University of North Texas), Denton, USA, Nov. (1998).
- T. Kambara: "Atomic physics experiments at RIKEN Accelerators", Busshitsu Kagaku Symp. on Tandem Ryouiki no Jyuuion Kagaku Kenkyukai, (Japan Atomic Energy Research Institute), Mito, Jan. (1999).
- I. Shimamura: "Photon-impact emission of an electron from two-electron atoms and collision processes involving muonic hydrogen atoms", Workshop on Hyperspherical Harmonic Methods in Atomic, Molecular, and Nuclear Physics, (University of Washington), Seattle, USA, Jan. (1999).
- T. Nishimura: "Elastic scattering of positrons from rare gases and simple polyatomic molecules", Genshibutsurigaku Seminaa, (The Institute of Space and Astronautical Science), Sagami-hara, Feb. (1999).
- T. Kambara: "Acoustic emission from heavy-ion irradiation on solids", RIKEN Symp. on Studies on Condensed Matter Physics, Atomic Physics, Nuclear Chemistry, and Biomedical Science Using RIKEN Accelerators, Wako, Feb. (1999).
- Y. Nakai: "Ionization and dissociation of fullerene by fast heavy ion impact", RIKEN Symp. on Studies on Condensed Matter Physics, Atomic Physics, Nuclear Chemistry, and Biomedical Science Using RIKEN Accelerators, Wako, Feb. (1999).
- N. Ishikawa, A. Iwase, Y. Chimi, N. Kuroda, K. Tsuru, O. Michikami, H. Wakana, and T. Kambara: "Defect production through electronic excitation in oxide superconductors irradiated with swift heavy ions", 54th Ann. Meet. of Physical Society of Japan, Higashihiroshima, Mar. (1999).
- Y. Kanai, T. Kamei, K. Ogura, T. Takayanagi, K. Wakiya, and Y. Nakai: "Angular distribution of Auger electrons from doubly-excited states produced by highly-charged ion-atom collisions", 54th Ann. Meet. of Physical Society of Japan, Higashihiroshima, Mar. (1999).
- Y. Morishita, Y. Yamazaki, K. Kuroki, H. Torii, K. Komaki, H. Masuda, and M. Sekiguchi: "Visible light emission from slow highly charged ions transmitted through Ni microcapillary(2)", 54th Ann. Meet. of Physical Society of Japan, Higashihiroshima, Mar. (1999).
- Y. Iwai, S. Thuriiez, R. Hutton, Y. Kanai, H. Oyama, H. Masuda, T. Azuma, K. Ando, K. Komaki, and Y. Yamazaki: "Study of hollow atom with high resolution soft X-ray spectrometer", 54th Ann. Meet. of Physical Society of Japan, Higashihiroshima, Mar. (1999).
- Y. Nakai, T. Kambara, A. Itoh, H. Tsuchida, and Y. Yamazaki: "Ionization and fragmentation of  $\text{C}_{60}$  by fast ion impact in MeV region-TOF spectrum profile II", 54th Ann. Meet. of Physical Society of Japan, Higashihiroshima, Mar. (1999).
- T. Nishimura and I. Shimamura: "Elastic scattering of positrons from Ar atoms and  $\text{CH}_4$  molecules", 54th Ann. Meet. of Physical Society of Japan, Higashihiroshima, Mar. (1999).
- J. Wang, T. Saito, M. Takahashi, T. Shishido, T. Fukuda, E. Yagi, M. Takeda, and J. Wang: "Measurement of  $^{155}\text{Ga}$  Mössbauer spectra", 76th National Meet. of the Chemical Society of Japan, Yokohama, Mar. (1999).
- T. Nishimura: "Elastic scattering of positrons from rare gaseous atoms and simple polyatomic molecules", Seminars for Theory of Atomic/Molecular Processes, Tokyo, Mar. (1999).
- T. Kambara: "Heavy ion accelerators and atomic physics", 6th Genshi Shototsu Kenkyu Kyokai Seminaa, Wako, Apr. (1999).
- T. Nishimura: "Theoretical study for positron-molecule collisions", Kisobutsurigaku Kenkyukai, (Yukawa Institute for Theoretical Physics, Kyoto University), Kyoto, May (1999).
- J. Kim, F. Saito, Y. Nagashima, A. Goto, Y. Itoh, and T. Hyodo: "Design of an electrostatic positron beam for spin state study", 6th Int. Workshop on Positron and Positronium Chemistry, Tsukuba, June (1999).
- E. Yagi, T. Urai, and S. Koike: "The state of hydrogen in Nb-Mo alloys as observed by a channelling method", 14th Int. Conf. on Ion Beam Analysis, (Forschungszentrum Rossendorf, Institute of Ion Beam Physics and Materials Research), Dresden, Germany, July (1999).
- E. Yagi, T. Sasahara, T. Joh, T. Urai, T. Sasamoto, N.

- Tajima, T. Watanabe, and S. T. Nakagawa: "Channelling studies on the Xe bubble formation in Xe-implanted Fe", 14th Int. Conf. on Ion Beam Analysis, (Forschungszentrum Rossendorf, Institute of Ion Beam Physics and Materials Research), Dresden, Germany, July (1999).
- R. Hutton, S. Thuriel, Y. Iwai, Y. Kanai, H. Oyama, H. Masuda, and Y. Yamazaki: "Cascade filling of hollow atoms produced with micro-capillary targets", 21st Int. Conf. on the Physics of Electronic and Atomic Collisions (XXI-ICPEAC), (Society for Atomic Collision Research, Japan, Physical Society of Japan, and Chemical Society of Japan), Sendai, July (1999).
- S. Thuriel, Y. Iwai, Y. Kanai, H. Oyama, R. Hutton, H. Masuda, and Y. Yamazaki: "High-resolution studies of light hollow atoms created using a micro-capillary target", 21st Int. Conf. on the Physics of Electronic and Atomic Collisions (XXI-ICPEAC), (Society for Atomic Collision Research, Japan, Physical Society of Japan, and Chemical Society of Japan), Sendai, July (1999).
- S. Uramoto, I. Shimamura, and H. Sato: "Superexcited states of the hydrogen molecule lying below the third ionization limit", 21st Int. Conf. on the Physics of Electronic and Atomic Collisions (XXI-ICPEAC), (Society for Atomic Collision Research, Japan, Physical Society of Japan, and Chemical Society of Japan), Sendai, July (1999).
- M. Kimura and I. Shimamura: "Vibrational excitation of CO molecule adsorbed on Ag surfaces", 21st Int. Conf. on the Physics of Electronic and Atomic Collisions (XXI-ICPEAC), (Society for Atomic Collision Research, Japan, Physical Society of Japan, and Chemical Society of Japan), Sendai, July (1999).
- A. Iwase, Y. Chimi, N. Ishikawa, and T. Kambara: "Atomic displacements induced by high density electronic excitation in iron", 21st Int. Conf. on the Physics of Electronic and Atomic Collisions (XXI-ICPEAC), (Society for Atomic Collision Research, Japan, Physical Society of Japan, and Chemical Society of Japan), Sendai, July (1999).
- X. P. Xie, W. Sun, W. Huang, P. Xue, C. B. Xu, X. Xu, J.-Z. Tang, and I. Shimamura: "Photoionization of He up to the threshold of production of He<sup>+</sup> (N=10): Hyperspherical close-coupling calculations", 21st Int. Conf. on the Physics of Electronic and Atomic Collisions (XXI-ICPEAC), (Society for Atomic Collision Research, Japan, Physical Society of Japan, and Chemical Society of Japan), Sendai, July (1999).
- T. Watanabe, X.-M. Tong, S. Ohtani, K. Iemura, Y. Kanai, and H. Suzuki: "Mechanism of doubly excited He by double electron transfer from neutral atoms", 21st Int. Conf. on the Physics of Electronic and Atomic Collisions (XXI-ICPEAC), (Society for Atomic Collision Research, Japan, Physical Society of Japan, and Chemical Society of Japan), Sendai, July (1999).
- Y. Kanai: "Production of doubly-excited He-atoms in collisions of He<sup>2+</sup>-ions with alkaline-earth atoms", 21st Int. Conf. on the Physics of Electronic and Atomic Collisions (XXI-ICPEAC), (Society for Atomic Collision Research, Japan, Physical Society of Japan, and Chemical Society of Japan), Sendai, July (1999).
- Y. Nakai, T. Kambara, A. Itoh, H. Tsuchida, and Y. Yamazaki: "Time-of-flight profile of fullerene-like fragment ions in fast He<sup>2+</sup>-C<sub>60</sub> collision", 21st Int. Conf. on the Physics of Electronic and Atomic Collisions (XXI-ICPEAC), (Society for Atomic Collision Research, Japan, Physical Society of Japan, and Chemical Society of Japan), Sendai, July (1999).
- Y. Nakai, T. Kambara, A. Itoh, H. Tsuchida, and Y. Yamazaki: "Asymmetric fission of multiply charged C<sub>60</sub> ion by fast C<sup>6+</sup> impact", 21st Int. Conf. on the Physics of Electronic and Atomic Collisions (XXI-ICPEAC), (Society for Atomic Collision Research, Japan, Physical Society of Japan, and Chemical Society of Japan), Sendai, July (1999).
- R. J. Whitehead, I. Shimamura, and J. F. McCann: "Protonium formation in p-H collisions", 21st Int. Conf. on the Physics of Electronic and Atomic Collisions (XXI-ICPEAC), (Society for Atomic Collision Research, Japan, Physical Society of Japan, and Chemical Society of Japan), Sendai, July (1999).
- I. Shimamura, M. Kimura, and G. Ya. Korenman: "Formation of metastable antiprotonic lithium", 21st Int. Conf. on the Physics of Electronic and Atomic Collisions (XXI-ICPEAC), (Society for Atomic Collision Research, Japan, Physical Society of Japan, and Chemical Society of Japan), Sendai, July (1999).
- S. Kitazawa, M. Sataka, H. Tawara, M. Imai, H. Shibata, K. Komaki, K. Kawatsura, and Y. Kanai: "Ejected electron spectra from high energy highly charged oxygen ions in collisions with atoms", 21st Int. Conf. on the Physics of Electronic and Atomic Collisions (XXI-ICPEAC), (Society for Atomic Collision Research, Japan, Physical Society of Japan, and Chemical Society of Japan), Sendai, July (1999).
- K. Ogura, M. Okamoto, T. Takayanagi, K. Wakiya, Y. Nakai, and Y. Kanai: "A toroidal-type electron energy analyzer for ion-atom collisions", 21st Int. Conf. on the Physics of Electronic and Atomic Collisions (XXI-ICPEAC), (Society for Atomic Collision Research, Japan, Physical Society of Japan, and Chemical Society of Japan), Sendai, July (1999).
- M. Kitajima, Y. Nakai, Y. Kanai, M. Hoshino, Y. Yamazaki, and Y. Itoh: "The angular dependence of the scattering intensity in double electron capture of C<sup>4+</sup> - He at the collisional energy of 116.8 eV/q", 21st Int. Conf. on the Physics of Electronic and Atomic Collisions (XXI-ICPEAC), (Society for Atomic Collision Research, Japan, Physical Society of Japan, and Chemical Society of Japan), Sendai, July (1999).

- T. Nishimura and I. Shimamura: "Low-energy positron collisions with methane molecules and argon atoms", 21st Int. Conf. on the Physics of Electronic and Atomic Collisions (XXI-ICPEAC), (Society for Atomic Collision Research, Japan, Physical Society of Japan, and Chemical Society of Japan), Sendai, July (1999).
- E. Yagi: "Investigation of the state of hydrogen in crystals by the nuclear-reaction channelling method", Japan Institute of Metals Seminar on the Up-to-date Methods for Hydrogen Detection and the Preventive Measures for the Hydrogen Embrittlement, Tokyo, July (1999).
- I. Shimamura: "Atomic three-body dynamics", RIKEN Symp. on the Theory of Atomic and Molecular Processes, Wako, July (1999).
- T. Nishimura: "Positron scattering by polyatomic molecules", RIKEN Symp. on the Theory of Atomic and Molecular Processes, Wako, July (1999).
- Y. Yamazaki: "Trapping, cooling and extraction of antiprotons, and the ASACUSA project", 1999 Workshop on Nonneutral Plasmas, (Princeton University), Princeton, USA, Aug. (1999).
- N. Kuroda, N. Ishikawa, Y. Chimi, A. Iwase, S. Okayasu, H. Ikeda, R. Yoshizaki, and T. Kambara: "Effect of damage morphology on the pinning and vortex dynamics in  $\text{Bi}_2\text{Sr}_2\text{CaCu}_2\text{O}_{8+\delta}$  irradiated with GeV heavy-ions", 22nd Int. Conf. on Low Temperature Physics, (Low Temperature Laboratory, Helsinki University of Technology), Espoo, Helsinki, Finland, Aug. (1999).
- Y. Yamazaki: "Atomic physics and related field with RIKEN MUSES", CCAST-WL Workshop Series: Vol.101 on New Atomic Physics Opportunities at HIRFL-CSR, (Institute of Modern Physics, Chinese Academy of Sciences), Beijing, China, Aug. (1999).
- Y. Chimi, A. Iwase, N. Ishikawa, N. Kuroda, and T. Kambara: "Radiation annealing induced by electronic excitation in iron", Int. Conf. on Atomic Collisions in Solids (ICACS-18), (Physics Department, Odense University), Odense, Denmark, Aug. (1999).
- T. Kambara, T. M. Kojima, Y. Kanai, Y. Nakai, A. Yoneda, K. Kageyama, and Y. Yamazaki: "Acoustic emission from heavy-ion irradiation", Int. Conf. on Atomic Collisions in Solids (ICACS-18), (Physics Department, Odense University), Odense, Denmark, Aug. (1999).
- A. Fukaya, I. Watanabe, S. Ohira, and K. Nagamine: "Muon spin resonance of Haldane-gap systems,  $\text{Ni}(\text{C}_2\text{H}_8\text{N}_2)_2\text{NO}_2(\text{ClO}_4)$  and  $\text{NiC}_2\text{O}_4 \cdot 2(2\text{-methylimidazole})$ ", 8th Int. Conf. on Muon Spin Rotation, Relaxation and Resonance, (Paul Scherrer Institut, EPS, Universitas Turicensis, ETH), Les Diablerets, Switzerland, Aug. (1999).
- A. Fukaya, W. Higemoto, M. Hagiwara, and K. Nagamine: " $\mu\text{SR}$  study of a spin ladder system  $(\text{Cu}_{1-x}\text{Zn}_x)_2(1,4\text{-diazacycloheptane})_2\text{Cl}_4$ ", 8th Int. Conf. on Muon Spin Rotation, Relaxation and Resonance, (Paul Scherrer Institut, EPS, Universitas Turicensis, ETH), Les Diablerets, Switzerland, Aug. (1999).
- Y. Yamazaki: "Atomic spectroscopy and collisions using slow antiprotons", 18th Int. Conf. on X-ray and Inner-Shell Processes, (Argonne National Laboratory), Chicago, USA, Aug. (1999).
- I. Shimamura: "Application of the hyperspherical coordinate method to atomic processes", Int. Symp. on Atomic Physics (ISAP99), Hanoi, Vietnam, Aug. (1999).
- Y. Chimi, A. Iwase, N. Ishikawa, N. Kuroda, and T. Kambara: "Electronic excitation and atomic displacements induced by high-energy heavy ion irradiation in Fe(II)", 1999 Fall Meet. of Physical Society of Japan, Morioka, Sept. (1999).
- E. Yagi, T. Sasahara, T. Joh, M. Hacke, T. Urai, T. Sasamoto, N. Tajima, T. Watanabe, and S. T. Nakagawa: "Investigation of the bubble formation process in Xe-implanted Fe by means of the channelling method", 1999 Fall Meet. of Physical Society of Japan, Morioka, Sept. (1999).
- Y. Yoshida, Y. Kobayashi, A. Yoshida, F. Ambe, Y. Yano, and F. Shimura: "Studies on jump process and lattice position in Si of  $^{57}\text{Mn}/^{57}\text{Fe}$  atoms produced by projectile-fragmentation reaction", 1999 Fall Meet. of Physical Society of Japan, Morioka, Sept. (1999).
- H. Matsushima, Y. Yamazaki, Y. Nakai, A. Hitachi, N. Kiyoto, T. Hosobuchi, N. Kouchi, and Y. Morishita: "Quenching of long decay components in plastic scintillators", 42nd Symp. on Radiation Chemistry, Hiroshima, Sept. (1999).
- M. Matsuda, K. Katsumata, R. S. Eccleston, S. Brehmer, and H.-J. Mikeska: "Magnetic excitations from the  $S=1/2$  two-leg ladders in  $\text{La}_6\text{Ca}_8\text{Cu}_{24}\text{O}_{41}$ ", 44th Ann. Conf. on Magnetism and Magnetic Materials, (American Institute of Physics), San Jose, USA, Nov. (1999).
- E. Yagi: "Observation of lattice locations of hydrogen dissolved in alloys by means of the nuclear reaction channelling method", 138th Fall Meet. of Ion and Steel Institute of Japan, Kanazawa, Nov. (1999).
- T. Maruyama, H. Yamada, T. Mochizuki, K. Akimoto, and E. Yagi: "Luminescence quenching mechanism in Sm doped ZnS", 9th Int. Conf. on II-VI Compounds(II-VI '99), (Japan Society for the Promotion of Science), Kyoto, Nov. (1999).
- Y. Nakai and T. Kambara: "Application of STJ for molecular-, atomic-physics and ion irradiation", RIKEN Symp. on Application of Superconductor Radiation Detectors, STJ Workshop, Wako, Dec. (1999).
- Y. Yamazaki: "Summary of beam microcapillary spectroscopy", RIKEN Symp. on Production of Ultra Slow Highly-Charged Ions and Its Application, Wako, Dec. (1999).
- Y. Iwai: "Soft X-ray spectroscopy of slow highly

- charged ions through microcapillary”, RIKEN Symp. on Production of Ultra Slow Highly-Charged Ions and Its Application, Wako, Dec. (1999).
- M. Wada: “Slow or trapped RI-beams from projectile fragment separators and their laser”, RIKEN Symp. on Production of Ultra Slow Highly-Charged Ions and Its Application, Wako, Dec. (1999).
- Y. Kanai: “Slow HCI production and facility at Atomic Physics Lab.”, RIKEN Symp. on Production of Ultra Slow Highly-Charged Ions and Its Application, Wako, Dec. (1999).
- N. Oshima: “Development of a new positron accumulator using an electron cooling technique”, RIKEN Symp. on Production of Ultra Slow Highly-Charged Ions and Its Application, Wako, Dec. (1999).
- T. M. Kojima: “MCI cooling with cold positrons in a penning-malmberg trap”, RIKEN Symp. on Production of Ultra Slow Highly-Charged Ions and Its Application, Wako, Dec. (1999).
- Y. Nakai: “Plan of multiple ionization experiment of neutral atom with ultra fast TW-laser in RIKEN”, RIKEN Symp. on Production of Ultra Slow Highly-Charged Ions and Its Application, Wako, Dec. (1999).
- Y. Yamazaki: “Phase II research with slow highly charged ions”, RIKEN Symp. on Production of Ultra Slow Highly-Charged Ions and Its Application, Wako, Dec. (1999).
4. Radiochemistry, radiation chemistry, and radiation biology
- Y. Einaga, O. Sato, T. Iyoda, Y. Kobayashi, F. Ambe, K. Hashimoto, A. Fujishima, and K. Hashimoto: “Characterization of cobalt-iron cyanide by  $^{57}\text{Fe}$  Mössbauer spectroscopy”, Proc. Specialist Research Meet. on Solid State Physics with Probes of Radiations and Nuclei, (Research Reactor Institute, Kyoto University), Kumatori, Nov. (1997).
- Y. Kobayashi, Y. Yoshida, A. Yoshida, Y. Watanabe, N. Aoi, K. Hayakawa, K. Yukihira, J. Nakamura, S. Nasu, and F. Ambe: “In-beam Mössbauer spectroscopy for materials science at RIKEN Accelerator Research Facility”, Specialist Research Meet. on Solid State Physics with Probes of Radiations and Nuclei, (Research Reactor Institute, Kyoto University), Kumatori, Nov. (1997).
- T. Abe, H. Takahashi, S. Kumada, C. H. Bae, T. Matsuyama, and S. Yoshida: “Effective plant-mutation method using heavy-ion beams”, Ann. Meet. of Japan Society for Bioscience, Biotechnology, and Agrochemistry, Nagoya, Mar. (1998).
- S. Enomoto, R. Hirunuma, T. Ozaki, S. Ambe, and F. Ambe: “Dynamics of various trace elements in Se-deficient rats”, 2nd Int. Symp. on Metals and Genetics, Toronto, Canada, May (1998).
- R. Amano, S. Oishi, S. Enomoto, and F. Ambe: “Aging effects on regional cerebral uptakes and concentrations of some trace elements in normal mice”, 2nd Int. Symp. on Metals and Genetics, Toronto, Canada, May (1998).
- S. Enomoto, R. Hirunuma, J. Chou, S. Ambe, and F. Ambe: “Transfers of trace elements from the placenta to the rat fetus”, 42nd Symp. on Radiochemistry, Sendai, Sept. (1998).
- S. Enomoto and F. Ambe: “The multitracer technique in bio-trace element research”, Int. Conf. on Nuclear Analytical Methods in the Life Sciences (NAMLS), (China Institute of Atomic Energy), Beijing, China, Oct. (1998).
- S. Sharma, K. Kimura, and J. Kaneko: “New 100 ps-lived luminescence from ion-irradiated RbI”, 41st Symp. on Radiation Chemistry, (Japanese Society of Radiation Chemistry), Kobe, Oct. (1998).
- T. Abe: “Biological effects of heavy-ion beam on plants”, 8th Chromosome Colloq., Tsukuba, Nov. (1998).
- S. Kitayama, I. Narumi, M. Kikuchi, K. Sato, T. Funayama, and H. Watanabe: “*uvrC* gene and its mutation in *Deinococcus radiodurans*”, 41st Ann. Meet. of Japan Radiation Research Society, Nagasaki, Dec. (1998).
- K. Satoh, I. Narumi, M. Kikuchi, T. Funayama, T. Yanagisawa, S. Kitayama, and H. Watanabe: “Cloning of *recA* gene of a radioresistant bacterium, *Deinococcus radiodurans* and its expression in *E. coli*.”, 41st Ann. Meet. of Japan Radiation Research Society, Nagasaki, Dec. (1998).
- T. Funayama, I. Narumi, K. Satoh, O. Kou, S. Kitayama, H. Watanabe, and K. Yamamoto: “DNA repair gene deletion mutants of radioresistant bacteria by the insertion of drug-resistant gene cassette”, 41st Ann. Meet. of Japan Radiation Research Society, Nagasaki, Dec. (1998).
- S. Kitayama, I. Narumi, M. Kikuchi, K. Sato, T. Funayama, H. Watanabe, and K. Sato: “Nucleotide excision repair in a radioresistant bacterium, *Deinococcus radiodurans*”, 21st Ann. Meet. of Japanese Society of Molecular Biology, Yokohama, Dec. (1998).
- R. Amano, S. Oishi, and S. Enomoto: “Regional uptake behaviors of radioactive Rb, Zn, Se, Mn, Sc and Zr tracers in brain of young and aged C57BL/6N mice”, 5th Internet World Congr. on Biomedical Science '98, (McMaster University), Hamilton, Canada, Dec. (1998).
- S. Enomoto: “Distribution of vanadium in various disease animals”, Symp. on Vanadium, (Kyoto Pharmaceutical University), Kyoto, Dec. (1998).
- S. Sharma and J. Kaneko: “Extremely short lived-luminescence components in ionic crystals excited at high density by heavy-ion irradiation”, 54th Ann. Meet. of Physical Society of Japan, Hiroshima, Jan. (1999).
- K. Ushida, K. Ishioka, and M. Kitajima: “Coherent phonon spectroscopy applied to the surface

- modification by ion beams", 22nd Hyomen-Kagaku Kenkyukai, Tsukuba, Feb. (1999).
- C. H. Bae, T. Abe, T. Nakano, T. Matsuyama, N. Nagata, and S. Yoshida: "A novel albino mutant, *alth* deficient in chloroplast gene expression", 1999 Ann. Meet. of Japanese Society of Plant Physiologists, Sendai, Mar. (1999).
- C. H. Bae, T. Abe, T. Nakano, T. Matsuyama, N. Nagata, and S. Yoshida: "A novel albino mutant, *alth* deficient in chloroplast gene expression", Ann. Meet. of Japan Society for Bioscience, Biotechnology, and Agrochemistry, Fukuoka, Mar. (1999).
- H. Takahashi, T. Abe, K. Sekino, C. H. Bae, T. Andoh, and S. Yoshida: "Effect of clomazone on carotenogenesis of tobacco", 24th Ann. Meet. of Pesticide Science Society of Japan, Utsunomiya, Mar. (1999).
- F. Saito, J. Kim, Y. Itoh, A. Goto, I. Fujiwara, T. Kurihara, N. Suzuki, Y. Nagashima, and T. Hyodo: "Development of intense  $^{18}\text{F}$  positron source electro-deposited on graphite", 54th Ann. Meet. of Physical Society of Japan, Higashihiroshima, Mar. (1999).
- R. Hirunuma, S. Enomoto, and K. Endo: "Behavior of radioactive trace elements in Se-deficient rats using the multitracer technique", 119th Ann. Meet. of the Pharmaceutical Society of Japan, Tokushima, Mar. (1999).
- T. Yanagiya, S. Himeno, N. Imura, Y. Kondo, R. Hirunuma, and S. Enomoto: "Alteration in metal transport in cadmium-resistant metallothionein null cells", 119th Ann. Meet. of the Pharmaceutical Society of Japan, Tokushima, Mar. (1999).
- R. Hirunuma, S. Enomoto, K. Endo, S. Ambe, and F. Ambe: "Behavior of multitracer in Se-deficient rats", RIKEN Symp. on Bio-Trace Elements '99, Wako, Mar. (1999).
- K. Matsumoto, K. Endo, R. Hirunuma, S. Enomoto, S. Ambe, and F. Ambe: "Distribution of various elements in cell fraction of liver of Se-deficient rats", RIKEN Symp. on Bio-Trace Elements '99, Wako, Mar. (1999).
- T. Oyama, T. Yoshida, M. Iwama, M. Yanaga, S. Enomoto, R. Hirunuma, M. Noguchi, and T. Omori: "Uptake of various elements in Zn-deficient mice", RIKEN Symp. on Bio-Trace Elements '99, Wako, Mar. (1999).
- H. Suzuki, H. Kumagaya, K. Oohashi, K. Sakamoto, K. Inubushi, S. Enomoto, and F. Ambe: "Uptake of various elements into Arbuscular Mycorrhizal Marigold", RIKEN Symp. on Bio-Trace Elements '99, Wako, Mar. (1999).
- T. Yanagiya, S. Himeno, N. Imura, Y. Kondo, R. Hirunuma, and S. Enomoto: "Study on metal transport pathway using cadmium-resistant metallothionein null fibroblasts", RIKEN Symp. on Bio-Trace Elements '99, Wako, Mar. (1999).
- T. Ozaki, S. Enomoto, Y. Minai, and Y. Makide: "Study on the uptake mechanism and behavior of rare earth elements in plants", RIKEN Symp. on Bio-Trace Elements '99, Wako, Mar. (1999).
- M. Kusakabe, T. Tsukada, N. Hiraiwa, C. Poirier, F. Ike, Y. Yoda, N. Fukunishi, M. Kase, Y. Yano, and A. Yoshiki: "Heavy ion beams: An application to mouse mutagenesis", 32nd Ann. Meet. of the Japanese Society of Developmental Biologists, Kobe, May (1999).
- R. Hirunuma, S. Enomoto, S. Ambe, and F. Ambe: "Distribution of selenium, arsenic, iron, and scandium in selenium-deficient rats using the multitracer technique", 10th Int. Symp. on Trace Elements in Man and Animal, (Joseph Fourier University), Evian, France, May (1999).
- S. Enomoto, R. Hirunuma, T. Ozaki, S. Ambe, and F. Ambe: "Transfers of trace elements from the placenta to the fetus of pregnant rat by using the multitracer technique", 10th Int. Symp. on Trace Elements in Man and Animal, (Joseph Fourier University), Evian, France, May (1999).
- R. Hirunuma, S. Enomoto, F. Ambe, and H. Sakurai: "Behavior of trace elements in Se-deficient rats", 16th Symp. on Trace Nutrients Research, Kyoto, May (1999).
- F. Yatagai, A. Gordon, S. Morimoto, N. Fukunishi, M. Honma, T. Sofuni, and F. Hanaoka: "Hprt mutation induction in human cells by heavy-ion irradiation", 10th Ann. Space Radiation Health Investigator's Workshop, (NASA), New York, USA, June (1999).
- F. Saito, Y. Itoh, A. Goto, I. Fujiwara, T. Kurihara, N. Suzuki, Y. Nagashima, and T. Hyodo: "Preparation of  $^{18}\text{F}$  source for slow positron beam by proton bombardment of  $^{18}\text{O}$ -water", 6th Int. Workshop on Positron and Positronium Chemistry, Tsukuba, June (1999).
- M. Takahashi, K. Sasaki, and S. Enomoto: "Metal uptake by a transgenic tobacco with Mdp1 gene that is expressed in Mn-depleted tomato root", Ann. Meet. of Japanese Society of Soil Science and Plant Nutrition, Sapporo, July (1999).
- H. Suzuki, H. Kumagaya, K. Oohashi, K. Sakamoto, K. Inubushi, S. Enomoto, and F. Ambe: "Analysis of the uptake of trace elements in arbuscular-mycorrhizal plant using multitracer technique (1)", Ann. Meet. of Japanese Society of Soil Science and Plant Nutrition, Sapporo, July (1999).
- F. Saito, N. Suzuki, Y. Itoh, A. Goto, I. Fujiwara, T. Kurihara, Y. Nagashima, and T. Hyodo: " $^{18}\text{F}$  for positron beam source produced by AVF cyclotron", 36th Ann. Meet. on Radioisotopes in the Physical Science and Industries, (Japan Radioisotope Association), Tokyo, July (1999).
- F. Saito, N. Suzuki, Y. Itoh, A. Goto, I. Fujiwara, T. Kurihara, Y. Nagashima, and T. Hyodo: "Development of intense  $^{18}\text{F}$  source for slow positron beam by AVF cyclotron", 21st Int. Conf. on the Physics of Electronic and Atomic Collisions (XXI-ICPEAC), Sendai, July (1999).

- Y. Furusawa, M. Saitou, T. Kanai, F. Yatagai, M. E. Vazquez, and T. C. Yang: "LET-RBE spectra for cell survival upon V79 cells exposed to accelerated silicon-, argon-, and iron-ion beams", 11th Int. Congr. of Radiation Research, Dublin, Ireland, July (1999).
- F. Yatagai, A. Gordon, S. Morimoto, N. Fukunishi, M. Honma, T. Sofuni, and F. Hanaoka: "Nature of hprt mutations induced by heavy-ion irradiation", 11th Int. Congr. of Radiation Research, Dublin, Ireland, July (1999).
- F. Saito, N. Suzuki, Y. Itoh, A. Goto, I. Fujiwara, T. Kurihara, Y. Nagashima, and T. Hyodo: "Development of intense  $^{18}\text{F}$  source for slow positron beam", 10th Workshop on Low-Energy Positron and Positronium Physics, Tsukuba, July (1999).
- Y. Kobayashi: "Experiments of  $^{106}\text{Sg}$  element with long half-life in Dubna (Russia)", Workshop on Nuclear Science of Heavy Elements, (Japan Atomic Energy Research Institute), Tokaimura, July (1999).
- M. Kusakabe, A. Yoshiki, N. Hiraiwa, T. Tsukada, F. Ike, C. Poirier, and Y. Yano: "Novel methodology for mouse mutagenesis by heavy ion irradiation", Research Meet. on SMXA Mice, (Institute for Laboratory Animal Research, Nagoya University School of Medicine), Nagoya, Aug. (1999).
- K. Ushida, H. Sato, K. Ando, T. Kozawa, and A. Kira: "Instability of dimer radical anion of aromatic hydrocarbons", 1999 Bunshi Kouzou Sougou Touronkai, (Chemical Society of Japan), Osaka, Sept. (1999).
- K. Kimura, S. Sharma, and J. Kaneko: "Abnormally short lived-luminescence of alkali halides and metal oxides excited using heavy ions", 1999 Fall Meet. of Physical Society of Japan, Morioka, Sept. (1999).
- K. Kimura, S. Sharma, and J. Kaneko: "Extremely short lived-luminescence of ion-excited wide-band-gap crystals", 1999 Fall Meet. of Physical Society of Japan, Morioka, Sept. (1999).
- K. Ushida, M. Hase, K. Ishioka, M. Kitajima, and K. G. Nakamura: "Application of coherent phonon spectroscopy to probing the distribution of lattice disorders", 1999 Fall Meet. of Physical Society of Japan, Morioka, Sept. (1999).
- M. Hase, K. Ishioka, K. Ushida, S. Hishita, and M. Kitajima: "Dynamical effect of ion irradiation on Bi crystal lattices by coherent phonon spectroscopy", 1999 Fall Meet. of Physical Society of Japan, Morioka, Sept. (1999).
- P. Mehnati, F. Yatagai, Y. Kobayashi, F. Hanaoka, T. Tsuzuki, and H. Sasaki: "Recognition of hit-sites within the cells exposed to accelerated iron-ions (using CR-39 plastics)", 42nd Ann. Meet. of Japan Radiation Research Society, Hiroshima, Sept. (1999).
- S. Morimoto, G. Alasdair, N. Fukunishi, F. Hanaoka, and F. Yatagai: "Effect of pre-irradiation by small dose heavy-ions in human-cells", 42nd Ann. Meet. of Japan Radiation Research Society, Hiroshima, Sept. (1999).
- A. Gordon, S. Morimoto, N. Fukunishi, F. Hanaoka, and F. Yatagai: "P53 and p21 protein induction in TK6 and NS human lymphoblastoid cells after X-ray and heavy-ion irradiations", 42nd Ann. Meet. of Japan Radiation Research Society, Hiroshima, Sept. (1999).
- S. Sharma and J. Kaneko: "New 100 ps lived UV luminescence of ion track in wide band-gap crystals", 42nd Symp. on Radiation Chemistry, (Japanese Society of Radiation Chemistry), Higashihiroshima, Sept. (1999).
- S. Sharma and K. Kimura: "Ion-induced luminescence in alkali iodides: A new 100 ps-lived component", 42nd Symp. on Radiation Chemistry, (Japanese Society of Radiation Chemistry), Higashihiroshima, Sept. (1999).
- Y. Yoshida, A. Saeki, T. Kozawa, M. Miki, K. Ushida, and S. Tagawa: "Study of geminate ion recombination by means of laser-synchronized picosecond and subpicosecond pulse radiolysis", 42nd Symp. on Radiation Chemistry, (Japanese Society of Radiation Chemistry), Higashihiroshima, Sept. (1999).
- K. Ushida, H. Sato, K. Ando, T. Kozawa, and A. Kira: "Why does the dimer radical anion of aromatic hydrocarbons not form?", 42nd Symp. on Radiation Chemistry, (Japanese Society of Radiation Chemistry), Higashihiroshima, Sept. (1999).
- M. Hase, K. Ishioka, K. Ushida, and M. Kitajima: "Phonon dynamics in ion-implanted bismuth as probed by femtosecond laser spectroscopy", 42nd Symp. on Radiation Chemistry, (Japanese Society of Radiation Chemistry), Higashihiroshima, Sept. (1999).
- S. Morimoto, G. Alasdair, N. Fukunishi, F. Hanaoka, and F. Yatagai: "Adaptive response in human cultured cells by the heavy-ion irradiation with a small dose", 13th Ann. Meet. of Japanese Society for Biological Sciences in Space, Tokyo, Sept. (1999).
- T. Kitaura, Y. Hara, T. Abe, K. Miyoshi, and S. Yoshida: "Effect of heavy-ion beam irradiation on shoot elongation in garden roses", 96th Congr. of Breeding Society of Japan, Okayama, Sept. (1999).
- H. Tamano, S. Enomoto, E. Igasaki, N. Oku, N. Itoh, K. Tanaka, and A. Takeda: "Tumor growth after subcutaneous transplantation is affected by hepatic metallothionein level", 2nd Int. Workshop on Metallothionein, (Institute for Reference and Measurements), Geel, Belgium, Oct. (1999).
- T. Abe, J.-M. Wang, T. Asami, and S. Yoshida: "Herbicide resistant mutation using heavy-ion beams", 2nd Pan Pacific Conf. on Pesticide Science, (The Agrochemicals Division of the American Chemical Society), Honolulu, USA, Oct. (1999).
- Y. Kawamura, S. Enomoto, R. Amano, and T. Ozaki: "Synthesis of labeled organometallic chelating agent using multitracer technique", 43rd Symp. on Radiochemistry, Tsukuba, Oct. (1999).
- T. Matsuyama, T. Abe, R. Kiuchi, T. Nakano, T.

- Asami, and S. Yoshida: "RLGS (Restriction Landmark Genomic Scanning) analysis in plant genomes", 63rd Ann. Meet. of the Botanical Society of Japan, Akita, Oct. (1999).
- H. Takahashi, T. Abe, K. Sekino, T. Andoh, and S. Yoshida: "Effect of clomazone on carotenogenesis of tobacco", 34th Ann. Meet. of the Society for the Chemical Regulation of Plants, Tottori, Oct. (1999).
- A. Yoshiki, N. Hiraiwa, T. Tsukada, Y. Yoda, C. Poirier, F. Ike, N. Fukunishi, M. Kase, Y. Yano, and M. Kusakabe: "Heavy ion beams: An application to mouse mutagenesis", 13th Int. Mouse Genome Conf., Philadelphia, USA, Oct. (1999).
- T. Tsukada, M. Furutsu, A. Kogiso, H. Yamaguchi, Y. Kitasaka, M. Kojima, N. Hiraiwa, A. Yoshiki, and M. Kusakabe: "Mouse mutagenesis by heavy ion beams: Detection of mutant mice by random amplified polymorphic DNA (RAPD)", 13th Int. Mouse Genome Conf., Philadelphia, USA, Oct. (1999).
- F. Yatagai, G. Alasdair, S. Morimoto, T. Mizuno, T. Kurobe, N. Fukunishi, and F. Hanaoka: "Heavy-ion exposure effects in human cultured cells and their response at the molecular level", 22nd Ann. Meet. of Japanese Society of Molecular Biology, Fukuoka, Dec. (1999).
- M. Yoshimasu, T. Abe, S. Yoshida, T. Inoue, F. Ling, and T. Shibata: "Analysis of the biological effects of heavy-ion beam on budding yeast cells", 22nd Ann. Meet. of Japanese Society of Molecular Biology, Fukuoka, Dec. (1999).
- S. Morimoto, G. Alasdair, T. Kurobe, N. Fukunishi, M. Honma, T. Kato, F. Hanaoka, and F. Yatagai: "Adaptive response in human cultured cells by the heavy-ion irradiation with a small dose", 28th Ann. Meet. of the Japan Environmental Mutagen Research Society, Gifu, Dec. (1999).
- F. Yatagai, G. Alasdair, S. Morimoto, T. Mizuno, N. Fukunishi, and F. Hanaoka: "Induction of p53 and its related proteins in human cultured cells by the heavy-ion irradiation", 28th Ann. Meet. of the Japan Environmental Mutagen Research Society, Gifu, Dec. (1999).
- S. Enomoto, R. Amano, and Y. Kawamura: "The Multitracer: Production and application to chemistry and biology", 16th Int. Symp. on Separation Chemistry, (National Institute for Research in Inorganic Materials), Tsukuba, Dec. (1999).
- K. Ushida, M. Hase, K. Ishioka, and M. Kitajima: "Use of coherent phonon spectroscopy as a probe for distribution of defects in solids", Int. Workshop on Molecular Design of Photonic Materials, (Osaka National Research Institute (ONRI), Science and Technology Agency (STA)), Takarazuka, Dec. (1999).
- Y. Kawamura, S. Enomoto, and R. Amano: "Synthesis of labeled organometallic chelating agent using multitracer technique", RIKEN Symp. on Bio-Trace Elements '99.12, Wako, Dec. (1999).
- T. Soshi, T. Arie, Y. Nose, and I. Yamaguchi: "Influence of endophyte on radionuclide-uptake by perennial ryegrass", RIKEN Symp. on Bio-Trace Elements '99.12, Wako, Dec. (1999).
- K. Ushida, M. Hase, K. Ishioka, and M. Kitajima: "A new probing method for lattice defects generated by ion beam irradiation: Coherent phonon spectroscopy", 8th Symp. of Research Center for Nuclear Science and Technology, University of Tokyo, Tokyo, Dec. (1999).

## 5. Material analysis

- I. Watanabe, S. Nakajima, K. Nagase, T. Matsuzaki, K. Ishida, and K. Nagamine: " $\mu$ SR on the magnetically ordered and superconducting states of  $TlBa_2Y_{1-x}Ca_xCu_2O_y$ ", 1996 Fall Meet. of Physical Society of Japan, Yamaguchi, Sept. (1996).
- I. Watanabe, N. Wada, H. Yano, A. Yamaguchi, T. Okuno, K. Awaga, S. Ohira, K. Nishiyama, and K. Nagamine: "Ground state of 2-dimensional organic magnet,  $m$ -MPYNN $\cdot$ BF<sub>4</sub>, observed by  $\mu$ SR", 52nd Ann. Meet. of Physical Society of Japan, Nagoya, Mar. (1997).
- S. Ohira, N. Ishida, T. Nogami, I. Watanabe, and K. Nagamine: " $\mu$ SR study on magnetic properties of the organic radical ferromagnet, Ar-CH=N-TEMPO", 1997 Fall Meet. of Physical Society of Japan, Kobe, Oct. (1997).
- I. Watanabe, S. Ohira, K. Nagamine, N. Wada, H. Yano, A. Yamaguchi, and K. Awaga: " $\mu$ SR study on magnetic properties of the 2-dimensional anti-ferromagnet,  $m$ -MPYNN $\cdot$ BF<sub>4</sub>", 1997 Fall Meet. of Physical Society of Japan, Kobe, Oct. (1997).
- Y. Yamamoto, Y. Miyako, K. Nishiyama, I. Watanabe, and K. Nagamine: "Long-range ordering and spin fluctuations of Ce(Ru<sub>1-x</sub>Rh<sub>x</sub>)<sub>2</sub>Si<sub>2</sub>", 1997 Fall Meet. of Physical Society of Japan, Kobe, Oct. (1997).
- I. Watanabe, K. Asai, Y. Kobayashi, N. Yamada, and K. Nagamine: "Magnetic properties of LaCoO<sub>3</sub> studied by  $\mu^+$ SR", 53rd Ann. Meet. of Physical Society of Japan, Funabashi, Apr. (1998).
- S. Ohira, I. Watanabe, K. Nakayama, N. Ishida, T. Nogami, and K. Nagamine: " $\mu$ SR study of the magnetic properties of the organic ferromagnet, ph-CH=N-TEMPO", 53rd Ann. Meet. of Physical Society of Japan, Funabashi, Apr. (1998).
- J. Arai, T. Ishiguro, M. Ariyama, K. Ozawa, K. Nakai, I. Watanabe, and K. Nagamine: "Muon spin relaxation in (La<sub>1-x</sub>Sr<sub>x</sub>)<sub>2</sub>Cu<sub>0.99</sub>Fe<sub>0.01</sub>", 53rd Ann. Meet. of Physical Society of Japan, Funabashi, Apr. (1998).
- M. Akoshima, H. Noji, Y. Ono, Y. Koike, I. Watanabe, and K. Nagamine: "Anomalous electronic properties in Bi2212 phase around  $p \sim \frac{1}{8}$ ", 53rd Ann. Meet. of Physical Society of Japan, Funabashi, Apr. (1998).
- K. Hasegawa, K. Maeda, S. Nakayama, A. Tonomura, and H. Hamanaka: "In-air high-resolution PIXE system with a multiwire proportional chamber", 8th

- Int. Conf. on PIXE and Its Analytical Applications, Lund, Sweden, June (1998).
- K. Maeda, A. Tonomura, H. Hamanaka, and K. Hasegawa: "Chemical shift measurements of PIXE spectra using a position-sensitive crystal spectrometer", 8th Int. Conf. on PIXE and Its Analytical Applications, Lund, Sweden, June (1998).
- M. Akoshima, H. Noji, Y. Ono, Y. Koike, T. Nishizaki, N. Kobayashi, I. Watanabe, and K. Nagamine: " $\frac{1}{8}$  problem in Bi- and Y-systems", Dai36kai Choudendou Magunetikus Kenkyuukai, Tokyo, July (1998).
- I. Watanabe, M. Akoshima, Y. Koike, and K. Nagamine: "Muon-spin relaxation anomaly in Bi-2212 system around the hole concentration of  $\frac{1}{8}$ ", 1998 Fall Meet. of Physical Society of Japan, Naha, Sept. (1998).
- I. Watanabe, S. Ohira, K. Nagamine, N. Wada, H. Yano, and K. Awaga: " $\mu^+$ SR study on the spin fluctuation of the 2-dimensional organic antiferromagnet, *m*-MPYNN·BF<sub>4</sub>", 1998 Fall Meet. of Physical Society of Japan, Naha, Sept. (1998).
- N. Wada, K. Awaga, and I. Watanabe: " $\mu$ SR and 2-dimensional spin-gap state in the Kagomé organic antiferromagnet", 1998 Fall Meet. of Physical Society of Japan, Naha, Sept. (1998).
- S. Ohira, Y. Akui, T. Ise, N. Ishida, T. Nogami, I. Watanabe, and K. Nagamine: " $\mu$ SR study on magnetic properties of the organic ferromagnet, Ar-CH=N-TEMPO", 1998 Fall Meet. of Physical Society of Japan, Naha, Sept. (1998).
- M. Akoshima, H. Noji, Y. Ono, Y. Koike, T. Nishizaki, N. Kobayashi, I. Watanabe, and K. Nagamine: "Anomalous electronic state in the Bi-2212 phase at  $p \sim \frac{1}{8}$  II", 1998 Fall Meet. of Physical Society of Japan, Naha, Sept. (1998).
- T. Takabatake, A. Kratzer, I. Watanabe, D. T. Adroja, K. Umeo, G. M. Kalvius, and K. Nagamine: " $\mu$ SR study on the spin fluctuations in Ce<sub>7</sub>Ni<sub>3</sub>", 1998 Fall Meet. of Physical Society of Japan, Naha, Sept. (1998).
- J. Arai, T. Ishiguro, K. Nakai, I. Watanabe, and K. Nagamine: "Muon spin relaxation in La<sub>2-x</sub>Sr<sub>x</sub>CuO<sub>4</sub> around  $x = \frac{1}{8}$ ", 1998 Fall Meet. of Physical Society of Japan, Naha, Sept. (1998).
- K. Hasegawa and K. Maeda: "Development of a crystal spectrometer for PIXE using a multianode PSPC", Technical Meet. on Nuclear Energy (NE-98), IEE Japan, Tokyo, Sept. (1998).
- M. Akoshima, H. Noji, Y. Koike, T. Nishizaki, N. Kobayashi, I. Watanabe, and K. Nagamine: "Suppression of the superconductivity around the hole concentration of  $p \sim \frac{1}{8}$  in Bi-2212 and Y-123 phases", Ouyoubutsurigakkai Touhokushibu Dai53kai Gakujutsukouenkai, Sendai, Dec. (1998).
- I. Watanabe, M. Akoshima, Y. Koike, and K. Nagamine: " $\mu$ SR study on the  $\frac{1}{8}$  problem of the Bi-2212 system", 54th Ann. Meet. of Physical Society of Japan, Higashihiroshima, Mar. (1999).
- J. Arai, T. Ishiguro, K. Nakai, I. Amamiya, I. Watanabe, and K. Nagamine: "Muon spin relaxation of La<sub>2-x</sub>Sr<sub>x</sub>Cu<sub>1-y</sub>Zn<sub>y</sub>O<sub>4</sub> around  $x=0.115$ ", 54th Ann. Meet. of Physical Society of Japan, Higashihiroshima, Mar. (1999).
- M. Akoshima, K. Nishimaki, H. Noji, Y. Koike, I. Watanabe, and K. Nagamine: "Anomalous electronic properties in the Bi-2212 phase around  $p \sim \frac{1}{8}$  III", 54th Ann. Meet. of Physical Society of Japan, Higashihiroshima, Mar. (1999).
- Y. Yamamoto, Y. Miyako, I. Watanabe, and K. Nagamine: " $\mu$ SR study on the non-Fermi liquid: Ce(Ru<sub>1-x</sub>Rh<sub>x</sub>)<sub>2</sub>Si<sub>2</sub>", 54th Ann. Meet. of Physical Society of Japan, Higashihiroshima, Mar. (1999).
- S. Ohira, I. Watanabe, N. Ishida, T. Nogami, and K. Nagamine: " $\mu$ SR study on the magnetic properties of the organic ferromagnet Ar-CH=N-TEMPO II", 54th Ann. Meet. of Physical Society of Japan, Higashihiroshima, Mar. (1999).
- I. Watanabe, N. Wada, K. Awaga, S. Ohira, and K. Nagamine: " $\mu$ SR study of the quantum spin fluctuation of the ferromagnetic dimer with  $S=1$ ", 1999 Fall Meet. of Physical Society of Japan, Morioka, Sept. (1999).
- I. Watanabe, N. Wada, K. Awaga, S. Ohira, and K. Nagamine: " $\mu$ SR study on the 2-dimensional organic antiferromagnet, *m*-MPYNN·(BF<sub>4</sub>, ClO<sub>4</sub>)", 1999 Fall Meet. of Physical Society of Japan, Morioka, Sept. (1999).
- M. Mekata, K. M. Kojima, H. Ikeda, I. Watanabe, and K. Nagamine: " $\mu$ SR on 2-dimensional Ising-spin antiferromagnet Rb<sub>2</sub>Co<sub>1-x</sub>Mg<sub>x</sub>F<sub>4</sub>", 1999 Fall Meet. of Physical Society of Japan, Morioka, Sept. (1999).
- S. Ohira, Y. Akui, T. Katayama, T. Miyake, N. Ishida, T. Nogami, and K. Nagamine: " $\mu$ SR study on the organic magnet 4-Pr-CH=N-TEMPO", 1999 Fall Meet. of Physical Society of Japan, Morioka, Sept. (1999).
- T. Ishiguro, H. Shinmen, M. Hirai, J. Arai, I. Watanabe, and K. Nagamine: " $\mu$ SR study on La<sub>2-x</sub>Sr<sub>x</sub>Cu<sub>1-y</sub>Zn<sub>y</sub>O<sub>4</sub> in an underdoped region", 1999 Fall Meet. of Physical Society of Japan, Morioka, Sept. (1999).
- I. Watanabe, M. Akoshima, Y. Koike, S. Ohira, W. Higemoto, and K. Nagamine: " $\mu$ SR study on the  $\frac{1}{8}$  problem in Bi-, Y- and La-systems", 1999 Fall Meet. of Physical Society of Japan, Morioka, Sept. (1999).
- M. Akoshima, K. Nishimaki, H. Noji, Y. Koike, I. Watanabe, S. Ohira, W. Higemoto, and K. Nagamine: "The  $\frac{1}{8}$  problem in Bi-, Y-systems studies by transport measurements and  $\mu$ SR", 1999 Fall Meet. of Physical Society of Japan, Morioka, Sept. (1999).
- J. Arai, T. Ishiguro, I. Watanabe, and K. Nagamine: "The Zn-substitution and the stripe structure in La<sub>2-x</sub>Sr<sub>x</sub>Cu<sub>1-y</sub>Zn<sub>y</sub>O<sub>4</sub> studied by  $\mu$ SR", 1999 Fall Meet. of Physical Society of Japan, Morioka, Sept. (1999).

- M. Kidera, T. Nakagawa, K. Takahashi, S. Enomoto, T. Minami, M. Fujimaki, E. Ikezawa, O. Kamigaito, M. Kase, A. Goto, and Y. Yano: "Measurements of  $^{26}\text{Al}$  using high-performance ECR ion source plus heavy ion linac", 8th Int. Conf. on Accelerator Mass Spectrometry, (VERA Laboratory, University of Vienna), Vienna, Austria, Sept. (1999).
- I. Watanabe, M. Akoshima, Y. Koike, S. Ohira, W. Higemoto, and K. Nagamine: " $\frac{1}{8}$  problems in high- $T_c$  oxides", RIKEN Symp. on Frontiers of Magnetism Studies with Microscopic Probes: Space-Time Correlation of Spins, Kofu, Oct. (1999).
- K. Maeda, K. Hasegawa, H. Hamanaka, A. Tonomura, and M. Maeda: "Chemical specification by in-air high-resolution PIXE", 3rd Int. Symp. on Bio-PIXE, (Kyoto University), Kyoto, Nov. (1999).
- H. Hamanaka, T. Hasegawa, K. Hasegawa, K. Maeda, and S. Yumoto: "PIXE analyses of Al compounds by means of wavelength dispersive spectrometer", 3rd Int. Symp. on Bio-PIXE, (Kyoto University), Kyoto, Nov. (1999).
- H. Hamanaka, T. Hasegawa, K. Hasegawa, K. Maeda, and S. Yumoto: "Chemical state analysis of Al compounds by crystal spectrometer PIXE (3)", 18th Symp. on Materials Science and Engineering Research Center of Ion Beam Technology, Hosei University, Koganei, Dec. (1999).

## X. LIST OF SYMPOSIA

(Jan.–Dec. 1999)

- 1) Symp. on Studies on Condensed Matter Physics, Atomic Physics, Nuclear Chemistry, and Biomedical Science Using RIKEN Accelerators  
2 Feb., Wako, Cellular Physiology Lab., RIKEN
- 2) RBRC Workshop on Hard Parton Physics in High-Energy Nuclear Collisions  
1–5 Mar., New York, USA, RIKEN BNL Research Center
- 3) RBRC Workshop on Event Generator for RHIC Spin Physics  
15–19 Mar., New York, USA, RIKEN BNL Research Center
- 4) RIKEN Symp. and Workshop on Selected Topics in Nuclear Collective Excitations  
20–24 Mar., Wako, Cyclotron Lab., RIKEN
- 5) RBRC Workshop on Numerical Algorithm at Non-Zero Chemical Potential  
27 Apr.–1 May, New York, USA, RIKEN BNL Research Center
- 6) RBRC Workshop on Gauge-Invariant Variables in Gauge Theories  
27–29 May, New York, USA, RIKEN BNL Research Center
- 7) Int. Workshop on Space Factory on JEM/ISS  
7–9 June, Tsukuba, Computational Science Div., Advanced Computing Center, RIKEN
- 8) RBRC Workshop on OSCAR II: Predictions for RHIC  
9–16 July, New York, USA, RIKEN BNL Research Center
- 9) Int. Workshop on Atomic Collisions and Atomic Spectroscopy with Slow Antiprotons  
19–21 July, Yokohama, Atomic Physics Lab., RIKEN
- 10) RIKEN Int. Symp. on Models and Theories of the Nuclear Mass  
19–23 July, Wako, RIBF Project Office, Cyclotron Center, RIKEN
- 11) 15th Symp. on Academic Activities for Waste Management  
22–23 July, Wako, Safety Center, RIKEN
- 12) RIKEN Symp. on the Theory of Atomic and Molecular Processes (VII)  
31 July–1 Aug., Wako, Atomic Physics Lab., RIKEN
- 13) RIKEN Int. Conf. on Astrophysics High T and Low Tau  
8–14 Aug., Sedona, USA, RI Beam Science Lab., RIKEN
- 14) RBRC Workshop on Coulomb and Pion Asymmetry Polarimetry and Hadronic Spin Dependence at RHIC Energies  
18 Aug., New York, USA, RIKEN BNL Research Center
- 15) 7th RIKEN Workshop for RI-Beam Physics  
23 Aug., Wako, RI Beam Science Lab., RIKEN
- 16) 8th RIKEN Workshop for RI-Beam Physics on Unstable/Hyper Nuclei  
2–3 Sept., Wako, RI Beam Science Lab., RIKEN
- 17) RBRC Workshop on RHIC Spin Physics  
6–8 Oct., New York, USA, RIKEN BNL Research Center
- 18) 12th Symp. of Accelerator Science and Technology

27–29 Oct., Wako, RIKEN Accelerator Research Facility

- 19) RIKEN Symp. on Frontiers of Magnetism Studies with Microscopic Probes: Space-Time Correlation of Spins  
29–30 Oct., Kofu, Muon Science Lab., RIKEN
- 20) RIBF Workshop on Physics on eA collider at MUSES  
1–2 Nov., Wako, RI Beam Science Lab., RIKEN
- 21) RIKEN Symp. on Large Scale Calculation of Electronic States: Exploring Dynamical Properties of Materials  
4–5 Nov., Wako, Computational Science Div., Advanced Computing Center, RIKEN
- 22) 9th RIKEN Workshop for RI-Beam Physics  
23–24 Nov., Wako, RI Beam Science Lab., RIKEN
- 23) RIKEN Symp. on Production of Ultra Slow Highly-Charged Ions and Its Application  
2–3 Dec., Wako, Atomic Physics Lab., RIKEN
- 24) Int. Symp. on Quasiparticle and Phonon Excitations in Nuclei in Memory of Professor Vadim Soloviev (Soloviev 99)  
4–7 Dec., Wako, Cyclotron Center, RIKEN

## XI. LIST OF SEMINARS

(Jan.–Dec. 1999)

Radiation Lab., RI Beam Science Lab., and  
Beam Technology Div.

- 1) K. Turner, BNL (USA), 12 Jan.  
“W charge asymmetry at the tevatron”
- 2) S. N. White, BNL (USA), 19 Jan.  
“Luminosity measurement”
- 3) N. Saito, RIKEN (Saitama) and RBRC (USA), 26  
Jan.  
“Report of hadron collider physics XIII in India”
- 4) B. A. Brown, Michigan State University, NSCL  
(USA), 1 Feb.  
“Single-nucleon knock out from halo nuclei”
- 5) V. Yu. Denisov, Institute for Nuclear Research,  
Kiev (Ukraine), 2 Feb.  
“Subbarrier heavy ions fusion enhanced by sub-  
barrier nucleons transfer and subbarrier fusion of  
nuclei far from the beta-stability line. Formation  
of superheavy elements (SHEs) in cold fusion re-  
actions”
- 6) L. C. Bland, Indiana University (USA), 4 Feb.  
“Determining the gluon contribution to the pro-  
ton’s spin with STAR”
- 7) J. Symons, Lawrence Berkeley National Labora-  
tory (USA), 9 Feb.  
“Photon detection with the STAR detector at  
RHIC”
- 8) J. Moss, Los Alamos National Laboratory (USA),  
9 Feb.  
“Spin-flavor structure of the nucleon”
- 9) V. Rykov, Wayne State University (USA), 9 Feb.  
“CP-odd single and double spin asymmetries in  
W/Z-production by polarized hadrons and lep-  
tons”
- 10) N. Itagaki, Graduate School of Science, Hokkaido  
University (Hokkaido), 10 Feb.  
“Development of cluster structure in neutron rich  
nuclei”
- 11) K. Goeke, University of Bochum (Germany), 16  
Feb.  
“Deeply virtual compton scattering: Skewed par-  
ton distributions and their theory”
- 12) W. Vogelsang, State University of New York,  
Stoney Brook (USA), 16 Feb.  
“Spin asymmetries in drell-yan production of lep-  
ton pairs”
- 13) P. Moller, Los Alamos National Laboratory  
(USA), 17 Feb.  
“Topology of 1000000 grid-point fission potential-  
energy surfaces”
- 14) A. de Roeck, DESY (Germany), 18 Feb.  
“The polarized HERA project: Machine aspects  
and physics program”
- 15) L. N. Satpathy, Institute of Physics, Bhubaneswar  
(India), 23 Feb.  
“How to go from finite nuclei to infinite nuclear  
matter”
- 16) E. Shuryak, State University of New York, Stoney  
Brook (USA), 23 Feb.  
“Why and how the nucleon spin penetrates into  
the glue and the sea quarks”
- 17) K. Otsuki, National Astronomical Observatory of  
Japan (Tokyo), 25 Feb.  
“Effect of neutrino-driven wind during a super-  
nova explosion on nucleosynthesis through the r-  
process ”
- 18) M. Perdekamp, RBRC (USA), 2 Mar.  
“Determination of  $\Delta G$  in compass”
- 19) T. Blum, RBRC (USA), 9 Mar.  
“Spin on lattice”
- 20) R. L. Jaffe, MIT (USA), 16 Mar.  
“Transversity and interference fragmentation  
functions”
- 21) N. Makins, University of Illinois (USA), 18 Mar.  
“Spin measurements from HERMES”
- 22) S. Ohta, KEK (Tsukuba), 23 Mar.  
“Spin on lattice II”
- 23) A. Deshpande, Yale University (USA), 30 Mar.  
“Bj sum,  $\Delta G$ , and  $\alpha_S(Q^2)$  using pQCD analysis  
of  $g_1$ ”
- 24) B. Ibrahin, Cairo University (Egypt), 5 Apr.  
“A method for calculating the complete expansion  
of the Glauber amplitude and its application to  
 $p+{}^6\text{He}$  scattering”
- 25) M. Tannenbaum, BNL (USA), 6 Apr.  
“kT issues”
- 26) D. Kharzeev, RBRC (USA), 13 Apr.

- “Onia and  $\Delta G$ ”
- 27) T. Nakatsukasa, RIKEN (Saitama), 19 Apr.  
“Self-consistent determination of collective coordinates”
- 28) M. Perdekamp, RBRC (USA) et al., 27 Apr.  
“Report from DIS99”
- 29) W. Vogelsang, State University of New York, Stony Brook (USA), 4 May  
“Further discussions on DIS99 and on the HERMES measurement of two-hadron production”
- 30) J. Meng, Peking University (China), 10 May  
“The surface diffuseness and the spin-orbital splitting in relativistic continuum Hartree-Bogoliubov theory”
- 31) M. Perdekamp, RBRC (USA), 11 May  
“More news from DIS99”
- 32) S. Pittel, Bartol Research Institute, University of Delaware (USA), 12 May  
“An improved single-particle basis for nuclear structure studies far from stability”
- 33) J. Pretz, BNL (USA), 18 May  
“SMC’s semi-inclusive measurements”
- 34) H. Spinka, Argonne National Laboratory (USA), 25 May  
“Polarimetry/luminosity issues”
- 35) G. Schrieder, Technische Universität Darmstadt (Germany), 27 May  
“1) Fragment-neutron correlation in fragmentation of Halo Nuclei; 2) Tentative plans for a HI-Electron-Photon Collider at GSI”
- 36) G. Roepke, University of Rostock (Germany), 28 May  
“Clusters in dense nuclear matter”
- 37) A. Deshpande, Yale University (USA) and G. Bunce, BNL and RBRC (USA), 1 June  
“Highlights of the Hamburg meeting on polarization at HERA”
- 38) T. Roser, BNL (USA), 8 June  
“Machine aspect of HERA-spin workshop”
- 39) W. Vogelsang, State University of New York, Stony Brook (USA), 15 June  
“Prompt photons”
- 40) A. Ogawa, Pennsylvania State University (USA), 22 June  
“Transversity at STAR”
- 41) A. Bruell, MIT (USA), 29 June  
“HERMES results”
- 42) D. A. Kosower, Saclay (France), 29 June  
“Parton distribution with errors”
- 43) S. Xu, Institute of Modern Physics, Chinese Academy of Sciences (China), 13 July  
“Beta-delayed proton decay near the proton-drip line”
- 44) E. J. Stephenson, Indiana University (USA), 13 July  
“Spin dependence in charge exchange scattering”
- 45) S. Nagataki, University of Tokyo (Tokyo), 26 July  
“Explosive nucleosynthesis in SN 1987A: Jet-like explosion inferred from the observations of  $^{44}\text{Ti}$  and Fe”
- 46) M. Anselmino, Torino University (Italy), 10 Aug.  
“Single transverse spin asymmetries”
- 47) K. Imai, Kyoto University (Kyoto), 17 Aug.  
“Polarimetry at collision point”
- 48) Y. H. Zhang, JAERI and IMP (China), 20 Aug.  
“Rotational band structures in odd-odd  $^{178,180}\text{Ir}$ ”
- 49) J. Tostevin, University of Surrey (UK), 23 Aug.  
“Theoretical methods for reactions of composite nuclei”
- 50) J. Tostevin, University of Surrey (UK), 23 Aug.  
“Exotic nucleus spectroscopy using nuclear reactions”
- 51) E. Leader, University of London (UK), 24 Aug.  
“How well do we understand the spin structure of the nucleon?”
- 52) A. Ansari, Institute of Physics, Bhubaneswar (India), 27 Aug.  
“A microscopic study of giant dipole resonances in hot and rotating nuclei”
- 53) E. Leader, University of London (UK), 31 Aug.  
“Collins effect”
- 54) M. Matsuzaki, Fukuoka University of Education (Fukuoka), 1 Sept.  
“Constructing relativistic effective nucleon-nucleon interaction for superfluid gap equation”
- 55) J. Meng, Peking University (China), 1 Sept.

- “The structure of superheavy elements newly discovered in the reaction of  $^{86}\text{Kr}$  with  $^{208}\text{Pb}$ ”
- 56) S. Sasaki, RBRC (USA), 7 Sept.  
“Spin on lattice III”
- 57) A. Contogouris, Athens University (Greece), 21 Sept.  
“Determinations of the polarized gluon distribution”
- 58) N. Buttimore, University of Dublin (Ireland), 28 Sept.  
“Spin flip in proton-carbon polarimetry”
- 59) E. Stein, Regensburg University (Germany), 15 Oct.  
“Higher twist effects for  $g_1$ ”
- 60) J. Q. Chen, Nanjing University (China), 18 Oct.  
“Nucleon-pair shell model calculations of the even-even Xe and Ba nuclei”
- 61) K. Yabana, Institute of Physics, University of Tsukuba (Ibaraki), 19 Oct.  
“Time-dependent mean-field theory applied to finite electronic systems”
- 62) Z. Feng-Shou, Institute of Modern Physics, Chinese Academy of Sciences (China), 26 Oct.  
“Chemical instability and nuclear multifragmentation in heavy ion collisions”
- 63) S. Kretzer, Dortmund University (Germany), 26 Oct.  
“Charm production in charged current DIS”
- 64) R. Johnson, Surrey University, (UK), 29 Oct.  
“Applications of the adiabatic approximation to transfer reactions, break-up and scattering of halo nuclei”
- 65) G. Baur, IKP, FZ, Julich (Germany), 29 Oct.  
“New possibilities for Coulomb dissociation”
- 66) Y. Chen, China Institute of Atomic Energy (China), 8 Nov.  
“The axial symmetry break in superdeformed nuclei”
- 67) T. Blum, RBRC (USA), 16 Nov.  
“Spin on lattice IV”
- 68) T. Roser, BNL (USA), 16 Nov.  
“New idea to operate snake at RHIC”
- 69) K. Kaneko, Kyushu Sangyo University (Fukuoka), 19 Nov.
- “Proton-neutron interactions in an extended P+QQ force model”
- 70) G. Levai, Institute of Nuclear Research of the Hungarian Academy of Sciences (Hungary), 22 Nov.  
“Symmetry aspects of nuclear cluster systems”
- 71) H. Sato, Kyoto University (Kyoto), 23 Nov.  
“Open heavy flavor production”
- 72) M. Wiescher, Notre Dame University (USA), 24 Nov.  
“Trigger and endpoint of the rp-process”
- 73) Y. Zhuo, China Institute of Atomic Energy (China), 24 Nov.  
“Brownian motors driven by non-equilibrium fluctuations”
- 74) P. Bonche, Saclay (France), 24 Nov.  
“Survey of mean-field theories and beyond, from Hartree-Fock to projected configuration mixing”
- 75) R. Seki, California State University, Northridge, and Kellogg Radiation Laboratory, Caltech (USA), 30 Nov.  
“Nuclear physics in atmospheric neutrino oscillation”
- 76) D. Boer, RBRC (USA), 30 Nov.  
“Transverse spin effects: Theory”
- 77) M. Perdekamp, RBRC (USA), 7 Dec.  
“Transverse spin effects: Experiment”
- 78) M. Junker, Laboratori Nazionali del Gran Sasso (Italy), 10 Dec.  
“LUNA: An underground accelerator facility for nuclear astrophysics”
- 79) E. Lomon, MIT/KEK-Tanashi (Tokyo), 13 Dec.  
“Hadronic and quark/gluon degrees of freedom in hadron interactions”
- 80) D. T. Khoa, Institute for Nuclear Science and Technique, Vietnam Atomic Energy Commission (Vietnam), 14 Dec.  
“Consistent study of asymmetric nuclear matter and interaction potential between neutron-rich nuclei”
- 81) F. Ivanyuk, Institute for Nuclear Research, Kiev (Ukraine), 20 Dec.  
“The pairing and shell effects in the transport coefficients of collective motion”

## Atomic Physics Lab.

- 1) M. Kawai, T. Yoneda, and H. Okuyama, RIKEN (Saitama), 26 Jan.  
“Behavior of hydrogen on surfaces”
- 2) S. Hultdt, Lund University (Sweden), 29 June  
“Instrumentation and applications for optical spectroscopy”
- 3) B. Zygelman, University Nevada (USA), 5 Feb.  
“Spin exchange in cold collision of hydrogen atoms”
- 4) P. C. Stancil, Oak Ridge National Laboratory (USA), 26 Mar.  
“Atomic and molecular processes in the early universe”
- 5) M. Wada, RIKEN (Saitama), 19 Apr.  
“Trapping unstable nuclear ions from RIPS and their applications”
- 6) C. Guet, CEA-Grenoble (France), 20 Apr.  
“Theoretical approaches to collisions of metal clusters with ions and electrons”
- 7) T. Miura, University of Tsukuba (Ibaraki), 21 Mar.  
“Modified interatomic potential in atom-C<sub>60</sub> collisions”
- 8) N. Cherepkov, State University of Aerospace Instrument (Russia), 4 June  
“Photoionization of fixed-in-space molecules, or complete photoionization experiments with diatomic molecules”
- 9) K. Yamanouchi, University of Tokyo (Tokyo), 10 June  
“Chemistry in intense laser field”
- 10) Y. Yoshida, Shizuoka Institute of Science and Technology (Shizuoka), 11 June  
“Material science with Mössbauer spectroscopy at RI Beam Factory”
- 11) T. Suda, RIKEN (Saitama), 18 June  
“Production of linearly polarized photons by coherent bremsstrahlung, and a pair polarimeter”
- 12) M. Inokuti, Argonne National Laboratory (USA), 25 June  
“Topics of my current and unfinished research”
- 13) S. J. Buckman, Australian National University (Australia), 8 July  
“Cooling and trapping of metastable helium”
- 14) A. Kheifets, Australian National University (Australia), 8 July  
“Determination of energy-momentum distribution of electron in solids by electron momentum spectroscopy”
- 15) J. Sanderson, University College London (UK), 12 July  
“Coulomb explosions of simple molecules in intense femtosecond laser pulses”
- 16) F. A. Gianturco, University of Rome (Italy), 13 July  
“Molecular physics at the millikelvins: Do Efimov states exist in He clusters?”
- 17) R. Janev, Research Center for Energy Macedonian Academy of Sciences and Arts (Macedonia), 15 Oct.  
“Atomic and molecular processes in fusion plasmas”
- 18) Y. Iwata, Cluster Science Laboratory, ETL (Ibaraki), 12 Nov.  
“New cluster beam source developed for nanometer scale patterned media technologies”
- 19) I. Sakurai, RIKEN (Saitama), 26 Nov.  
“Anomalous gas amplification of Xe + CO<sub>2</sub> proportional counter”
- 20) H. Shiromaru, Tokyo Metropolitan University (Tokyo), 20 Dec.  
“Molecular structure and equilibrium nuclear configuration revealed by Coulomb explosion”

## RIBF Project Office

- 1) Y. Mori, KEK (Ibaraki), 12 Jan.  
“High-gradient RF cavity”
- 2) Y. Batygin, A. Goto, and J. Kim, RIKEN (Saitama), 27 Jan.  
“High current beam dynamics problems in RIBF project”
- 3) T. Satow, NIFS (Chiba), 18 Mar.  
“The first excitation of the Large Helical Device (LHD)”
- 4) M. Kaji, Mitsubishi (Tokyo), 23 Apr.  
“EPIC”
- 5) S. Kato, KEK (Ibaraki), 23 Apr.  
“How to wash surfaces of vacuum chambers”
- 6) J. Hasegawa, Tokyo Institute of Technology (Tokyo), 23 Aug.

“Development of a high brightness laser ion source”

- 7) S. Runkel, Frankfurt University (Germany), 16 Sept.  
“The Frankfurt ECR- (ve) RFQ-Facility”
- 8) T. Mukhopadhyay, VECC (India), 15 Oct.  
“Calculation of neutron heat loads and damages to superconducting magnets”
- 9) K. Chouffani, Hiroshima University (Hiroshima), 22 Oct.  
“Parametric X radiation and diffracted transition radiation at REFER electron ring”

#### Radioisotope Technology Div.

- 1) K. Komatsu, Hiroshima University (Hiroshima), 4 Oct.  
“Cloning and protein function of DNA double-strand break repair gene NBS1”
- 2) A. Grosovsky, University of California (USA), 12 Nov.  
“Radiation-induced genomic instability”

#### Computational Science Div.

- 1) R. Osman, Mount Sinai Medical University (USA), 18 Mar.  
“MD simulation of biopolymer”
- 2) M. Payne, University of Cambridge (UK), 19 Mar.  
“Finite temperature simulations of metal surfaces and zeolites”
- 3) Y. Kobayashi, Soka University (Tokyo), 25 Mar.  
“Physicochemical mechanism of protein folding”
- 4) H. Iwamori, University of Tokyo (Tokyo), 1 Apr.

“Material circulation in subduction zones”

- 5) T. Yamamoto, RIKEN (Saitama), 13 May  
“Application of the molecular orbital calculation to the atomic spectroscopy of low-Z elements”
- 6) K. Ohguchi, RIKEN (Saitama), 20 May  
“Molecular mechanism of binary nucleation in vapor phase”
- 7) M. Matsui, Kyusyu University (Fukuoka), 11 June  
“Molecular dynamics simulation of mantle minerals”
- 8) F. Phicherri, RIKEN (Saitama), 17 June  
“Probing DNA modifications by means of quantum-chemistry”
- 9) Y. Hamahata, Tohoku University (Miyagi), 22 June  
“Molecular Dynamics (MD) estimation of the elastic wave velocity and anisotropy of MgO and MgSiO<sub>3</sub> perovskite under the lower mantle conditions”
- 10) T. Narumi, RIKEN (Saitama), 29 June  
“Progress report on the development of MDM: Special-purpose computer for molecular dynamics simulations”
- 11) Y. Oono, RIKEN (Saitama), 8 July  
“TOMBO Project performance of prototype”
- 12) R. Susukita, RIKEN (Saitama), 26 Aug.  
“MDGRAPE-2: A special-purpose computer for molecular dynamics”
- 13) K. Sato, RIKEN (Saitama), 15 Sept.  
“The effect of quasi-liquid layer in the unstable growth of snow crystals”

## XII. LIST OF PERSONNEL

### RIKEN ACCELERATOR RESEARCH FACILITY

TANIHATA Isao 谷畑勇夫 (Facility Director)  
YANO Yasushige 矢野安重 (Vice Facility Director)

#### Linac Division

IKEZAWA Eiji 池沢英二  
KOHARA Shigeo 小原重夫  
KASE Masayuki 加瀬昌之\*<sup>1</sup>

#### Ring Cyclotron Division

FUJITA Jiro 藤田二郎  
INABE Naohito 稲辺尚人  
KAMIGAITO Osamu 上垣外修一  
KOHARA Shigeo 小原重夫  
NAGASE Makoto 長瀬誠  
OGIWARA Kiyoshi 荻原清  
IKEGAMI Kumio 池上九三男  
KAGEYAMA Tadashi 影山正  
KASE Masayuki 加瀬昌之\*<sup>1</sup>  
KUBO Toshiyuki 久保敏幸  
NAKAGAWA Takahide 中川孝秀  
OKUNO Hiroki 奥野広樹

#### Experimental Support Division

ICHIHARA Takashi 市原卓  
KANAI Yasuyuki 金井保之  
MATSUZAKI Teiichiro 松崎禎市郎  
WATANABE Yasushi 渡邊康  
KAMBARA Tadashi 神原正\*<sup>1</sup>  
KUMAGAI Hidekazu 熊谷秀和  
MORITA Kosuke 森田浩介  
YATAGAI Fumio 谷田貝文夫

#### Radioisotope Facilities Division

KOBAYASHI Yoshio 小林義男  
YATAGAI Fumio 谷田貝文夫\*<sup>1</sup>

#### Radiation Protection Group

FUJITA Shin 藤田新\*<sup>1</sup>  
NAKAJIMA Shunji 中島諄二  
ITO Sachiko 伊藤祥子  
OGIWARA Kiyoshi 荻原清

#### Administration Division

NAKAMURA Toshiko 中村とし子  
TAKEYAMA Ken-ichi 武山謙一\*<sup>2</sup>  
NUMATA Shigeo 沼田茂男

#### Steering Committee

ASAHI Koichiro 旭耕一郎  
HANAOKA Fumio 花岡文雄  
ISHIHARA Masayasu 石原正泰  
KASE Masayuki 加瀬昌之  
KATSUMATA Koichi 勝又紘一  
NAGAMINE Kanetada 永嶺謙忠  
TAKEYAMA Ken-ichi 武山謙一  
YAGI Eiichi 八木栄一  
YANO Yasushige 矢野安重  
YOSHIDA Shigeo 吉田茂男  
GOTO Akira 後藤彰  
ICHIHARA Takashi 市原卓  
KAMBARA Tadashi 神原正  
KATAYAMA Takeshi 片山武司  
MATSUZAKI Teiichiro 松崎禎市郎  
SAWA Hiroshi 澤宏  
TANIHATA Isao 谷畑勇夫  
YAMAZAKI Yasunori 山崎泰規\*<sup>3</sup>  
YATAGAI Fumio 谷田貝文夫

\*<sup>1</sup> Group Leader, \*<sup>2</sup> Manager, \*<sup>3</sup> Chairperson

## Cosmic Radiation Laboratory

### Members

KATO Hiroshi 加藤 博 YOSHIDA Atsumasa 吉田 篤正

### Visiting Members and Postdoctoral Fellows

GOKA Tateo 五家建夫 (NASDA)  
KATO Chihiro 加藤千尋 (Fac. Sci., Shinshu Univ.)  
KOGA Kiyokazu 古賀清一 (NASDA)  
KOSHIISHI Hideki 越石英樹 (NASDA)  
MATSUMOTO Haruhisa 松本晴久 (NASDA)  
MUNAKATA Kazuoki 宗像一起 (Fac. Sci., Shinshu Univ.)

### Trainees

MIYASAKA Hiromasa 宮坂浩正 (Grad. Sch. Sci. Eng., Saitama Univ.)

## Radiation Laboratory

### Head

ISHIHARA Masayasu 石原正泰

### Members

ICHIHARA Takashi 市原 卓 KISHIDA Takashi 岸田 隆  
SAITO Naohito 齊藤直人 SAKURAI Hiroyoshi 櫻井博儀  
TAKETANI Atsushi 竹谷 篤 WATANABE Yasushi 渡邊 康  
YOSHIDA Atsushi 吉田 敦

### Visiting Members and Postdoctoral Fellows

ABE Yasuhisa 阿部恭久 (YITP, Kyoto Univ.)  
ANDO Yoshiaki 安藤嘉章 (Coll. Sci., Rikkyo Univ.)  
AOI Nori 青井 考 (Dept. Phys., Grad. Sch. Sci., Univ. Tokyo)  
ASAI Masato 浅井雅人 (JAERI)  
AWAYA Yoko 粟屋容子 (Musashino Art Univ.)  
BECK F. A. (CRN, France)  
BENTZ Wolfgang (Dept. Phys., Grad. Sch. Sci., Univ. Tokyo)  
BROGLIA R. (Univ. Milano, Italy)  
BROOKS Melynda L. (LANL, USA)  
CASTEN Rick (Phys. Dept., BNL, USA)  
CRIST Norman (Columbia Univ., USA)  
DOOI Makoto 堂井 真 (Inst. Phys., Univ. Tsukuba)  
EN'YO Hideto 延與秀人 (Fac. Sci., Kyoto Univ.)  
FLOCARD Hubert (Div. Phys. Theor. IPN, Inst. Phys. Nucl., France)  
FUCHI Yoshihide 渕好秀 (KEK, Tanashi)  
FUJII Hirotsugu 藤井宏次 (Grad. Sch. Arts Sci., Univ. Tokyo)  
FUJIKAWA Kazuo 藤川和男 (Fac. Sci., Univ. Tokyo)  
FUKUDA Mitsunori 福田光順 (Grad. Sch. Sci., Osaka Univ.)  
FUKUDA Tomokazu 福田共和 (KEK)  
FUKUDA Naoki 福田直樹 (Dept. Phys., Grad. Sch. Sci., Univ. Tokyo)  
FURUTAKA Kazuyoshi 古高和禎 (JAERI)  
GELBERG Adrian (Koln Univ., Germany)  
GONO Yasuyuki 郷農靖之 (Fac. Sci., Kyushu Univ.)  
GOTO Yuji 後藤雄二  
HAMAGAKI Hideki 浜垣秀樹 (Cen. Nucl. Study, Univ. Tokyo)  
HAMAMOTO Ikuko 浜本育子 (Lund Inst. Technol., Univ. Lund, Sweden)  
HATSUDA Tetsuo 初田哲男 (Fac. Sci., Kyoto Univ.)  
HAYASHI Naoki 林 直樹  
HAYASHIGAKI Arata 林垣新 (YITP, Kyoto Univ.)

HIRAI Masaaki 平井正明  
 HORIUCHI Hisashi 堀内 昶 (Fac. Integr. Human Studies, Dept. Fundamental Sci., Kyoto Univ.)  
 HOSAKA Masahito 保坂将人 (KEK, Tanashi)  
 HOTTA Tomohiro 堀田智洋 (Grad. Sch. Arts Sci., Univ. Tokyo)  
 ICHIMURA Munetake 市村宗武 (Grad. Sch. Arts Sci., Univ. Tokyo)  
 IDEGUCHI Eiji 井手口栄治 (Phys. Dept. Frescati, Royal Inst. Technol., Sweden)  
 IEKI Kazuo 家城和夫 (Coll. Sci., Rikkyo Univ.)  
 IMAI Kenichi 今井憲一 (Fac. Sci., Kyoto Univ.)  
 IMOTO Michiko 井本道子 (Lab. Phys., Coll. Sci. Technol., Nihon Univ.)  
 ISHII Tetsuro 石井哲朗 (JAERI)  
 ITAKURA Kazunori 板倉和記 (YITP, Kyoto Univ.)  
 IWASAKI Hironori 岩崎弘典 (Dept. Phys., Grad. Sch. Sci., Univ. Tokyo)  
 IZUMI Hideaki 出水秀明 (Grad. Sch. Sci., Osaka Univ.)  
 JIN Genming 靳根明 (Inst. Modern Phys., Chinese Acad. Sci., China)  
 KAKI Kaori 嘉規香織 (Fac. Sci., Shizuoka Univ.)  
 KAMAE Tsuneyoshi 釜江常好 (Fac. Sci., Univ. Tokyo)  
 KASAGI Jirota 笠木治郎太 (Lab. Nucl. Sci., Tohoku Univ.)  
 KATAYAMA Ichiro 片山一郎 (Cen. Nucl. Study, Univ. Tokyo)  
 KATO Seigo 加藤静吾 (Fac. Ed., Yamagata Univ.)  
 KATORI Kenji 鹿取謙二 (Lab. Nucl. Studies, Fac. Sci., Osaka Univ.)  
 KAWASHIMA Hideo 川島英雄 (KEK, Tanashi)  
 KIM Jong Chan 金鐘賛 (Dept. Phys., Seoul Natl. Univ., Korea)  
 KISTENEV Edouard (Phys. Dept., BNL, USA)  
 KITAO Kensuke 喜多尾憲助 (Data Eng. Inc.)  
 KODAIRA Jirou 小平治郎 (Fac. Sci., Hiroshima Univ.)  
 KOHAMA Akihisa 小濱洋央 (Fac. Sci., Univ. Tokyo)  
 KOIKE Yuji 小池裕司 (Fac. Sci., Niigata Univ.)  
 KUBONO Shigeru 久保野茂 (Cen. Nucl. Study, Univ. Tokyo)  
 KUMANO Shunzo 熊野俊三 (Fac. Sci. Eng., Saga Univ.)  
 KUNIHIRO Teiji 國弘悌二 (Ryukoku Univ.)  
 KURITA Kazuyoshi 栗田和好  
 KUSAKARI Hideshige 草刈英榮 (Fac. Ed., Chiba Univ.)  
 LIU Guanhua 劉冠華 (Inst. Modern Phys., Chinese Acad. Sci., China)  
 LIU Zhong (Inst. Modern Phys., Chinese Acad. Sci., China)  
 LOMON Earle (Massachusetts Inst. Technol., USA)  
 LUCCIO Alfredo (Phys. Dept., BNL, USA)  
 MAO Yajun (Phys. Dept., BNL, USA)  
 MATSUDA Satoshi 松田哲 (Fac. Integr. Human Studies, Dept. Fundamental Sci., Kyoto Univ.)  
 MATSUI Tetsuo 松井哲男 (YITP, Kyoto Univ.)  
 MATSUYANAGI Kenichi 松柳研一 (Fac. Sci., Kyoto Univ.)  
 MENGONI Alberto (Phys. Div., ENEA, Italy)  
 MIN Byung-Joo 閔丙珠 (Korea Atom. Energy Res. Inst., Korea)  
 MITARAI Shiro 御手洗志郎 (Fac. Sci., Kyushu Univ.)  
 MIYAMA Masanori 深山正紀 (Fac. Sci. Eng., Saga Univ.)  
 MIYATAKE Hiroari 宮武宇也 (KEK, Tanashi)  
 MIZOI Yutaka 溝井浩  
 MORII Toshiyuki 森井俊行 (Fac. Human Dev., Kobe Univ.)  
 MORIKAWA Tsuneyasu 森川恒安 (Fac. Sci., Kyushu Univ.)  
 MORINOBU Shunpei 森信俊平 (Fac. Sci., Kyushu Univ.)  
 MOTOBAYASHI Tohru 本林透 (Coll. Sci., Rikkyo Univ.)  
 MOTTELSON Ben R. (Nordita; Nordisk Inst. Theoretisk Fysik, Denmark)  
 MUELLER Ludwig (Phys. Dept., Univ. Padoba, Italy)  
 MURAKAMI Takeshi 村上健 (Natl. Inst. Radiol. Sci.)  
 MURATA Jiro 村田次郎  
 NAGAI Yasuki 永井泰樹 (RCNP, Osaka Univ.)  
 NAGAMIYA Shoji 永宮正治 (KEK)  
 NAITO Kenichi 内藤謙一

NAKAJIMA Mitsuo 中島充夫 (Grad. Sch. at Nagatsuta, Tokyo Inst. Technol.)  
 NAKAMURA Shogo 中村正吾 (Fac. Ed., Yokohama Natl. Univ.)  
 NAKAMURA Takashi 中村隆司 (Natl. Supercond. Cycl. Lab., Michigan State Univ., USA)  
 NAKAMURA Masanobu 中村正信 (Fac. Sci., Kyoto Univ.)  
 NAKAYAMA Shintaro 中山信太郎 (Fac. Integr. Arts Sci., Univ. Tokushima)  
 NEMOTO Yukio 根本幸雄 (RCNP, Osaka Univ.)  
 NIIZEKI Takashi 新関隆 (Fac. Sci., Tokyo Inst. Technol.)  
 NISHIMURA Jun 西村淳 (Cen. Integr. Res. Sci. Eng., Nagoya Univ.)  
 NISHIMURA Syunji 西村俊二 (Cen. Nucl. Study, Univ. Tokyo)  
 NORO Tetsuo 野呂哲夫 (RCNP, Osaka Univ.)  
 NOTANI Masahiro 野谷将広  
 ODAHARA Atsuko 小田原厚子 (Nishinippon Inst. Technol.)  
 OGAWA Masao 小川雅生 (Tokyo Inst. Technol.)  
 OHTA Shigemi 太田滋生 (KEK)  
 OI Makito 大井万紀人 (Cen. Nucl. Study, Univ. Tokyo)  
 OKAMURA Hiroyuki 岡村弘之 (Dept. Phys., Grad. Sch. Sci., Univ. Tokyo)  
 OOISHI Ryutarō 大石竜太郎 (Inst. Phys., Univ. Tsukuba)  
 OYAMA Ken 大山健  
 ORIHARA Hikonojyo 織原彦之丞 (Cycl. Radioisot. Cen., Tohoku Univ.)  
 OSHIMA Masumi 大島真澄 (JAERI)  
 OTSUKA Takaharu 大塚孝治 (Fac. Sci., Univ. Tokyo)  
 PENIONZHKEVICH Iouri (Flerov Lab. Nucl. React., Joint Inst. Nucl. Res., Russia)  
 PIERROUTSAKOU Dimitra (Sez. Napoli (INFN), Italy)  
 REN Zhongzhou 任中洲 (Nanjing Univ., China)  
 SAGAWA Hiroyuki 佐川弘幸 (Cen. Math. Sci., Univ. Aizu)  
 SAKAGUCHI Harutaka 坂口治隆 (Fac. Sci., Kyoto Univ.)  
 SAKAI Kenji 酒井健二 (Tokyo Inst. Technol.)  
 SAKURAGI Hiroyuki 櫻木弘之 (Fac. Sci., Osaka City Univ.)  
 SATO Hikaru 佐藤皓 (KEK)  
 SATO Hiroki D. 佐藤博紀 (Fac. Sci., Kyoto Univ.)  
 SAWADA Shinya 澤田真也 (KEK)  
 SCHAEFER Markus (Phys. Inst., Univ. Goettingen, Germany)  
 SCHMIDT-OTT Wolf-Dieter (Phys. Inst., Univ. Goettingen, Germany)  
 SEDERWALL Bo (Royal Inst. Technol., Sweden)  
 SHIBATA Toshi-Aki 柴田利明 (Tokyo Inst. Technol.)  
 SHIMIZU Hajime 清水肇 (Fac. Ed., Yamagata Univ.)  
 SHIMIZU Yoshifumi 清水良文 (Fac. Sci., Kyushu Univ.)  
 SHIMODA Tadashi 下田正 (Grad. Sch. Sci., Osaka Univ.)  
 SHIMOURA Susumu 下浦享 (Coll. Sci., Rikkyo Univ.)  
 SIGNORINI Cosimo I. (Phys. Dept., Univ. Padoba, Italy)  
 STROE Lucian (Phys. Dept., Univ. Padoba, Italy)  
 SUGAWARA Masahiko 菅原昌彦 (Chiba Inst. Technol.)  
 SUGIOKA Makoto 杉岡誠  
 SUN Zuxun (China Inst. Atom. Energy, China)  
 SUZUKI Yasuyuki 鈴木宜之 (Fac. Sci., Niigata Univ.)  
 SUZUKI Katsuhiko 鈴木克彦 (RCNP, Osaka Univ.)  
 SUZUKI Toshio 鈴木敏男 (Fac. Eng., Fukui Univ.)  
 TAJIMA Yasuhisa 田島靖久 (Cycl. Radioisot. Cen., Tohoku Univ.)  
 TAKADA Eiichi 高田栄一 (Natl. Inst. Radiol. Sci.)  
 TAKAHASHI Tadayuki 高橋忠幸 (Inst. Space Astro. Sci.)  
 TAKAKU Seisaku 高久清作 (KEK, Tanashi)  
 TAKIGAWA Noboru 滝川昇 (Grad. Sch. Sci., Tohoku Univ.)  
 TAKIZAWA Makoto 瀧澤誠 (Showa Coll. Pharm. Sci.)  
 TAMII Atsushi 民井淳 (Fac. Sci., Univ. Tokyo)  
 TANAKA Masahiko 田中雅彦 (KEK, Tanashi)  
 TANOKURA Atsushi 田野倉敦 (Fac. Sci. Technol., Sophia Univ.)  
 TENDOW Yoshihiko 天道芳彦

TERAOKAWA Atsuki 寺川貴樹 (Cycl. Radioisot. Cen., Tohoku Univ.)  
 TERANISHI Takashi 寺西高 (Cen. Nucl. Study, Univ. Tokyo)  
 TORII Hisayuki 鳥井久行 (Fac. Sci., Kyoto Univ.)  
 TOYAMA Takeshi 外山毅 (KEK)  
 TOYOKAWA Hidenori 豊川秀訓  
 UEMATSU Tsuneo 植松恒夫 (Fac. Integr. Human Studies, Dept. Fundamental Sci., Kyoto Univ.)  
 UENO Hideki 上野秀樹 (Lab. Nucl. Studies, Fac. Sci., Osaka Univ.)  
 UNO Masahiro 宇野正宏 (Min. Ed. Sci. Sports Culture)  
 WAKAMATSU Masashi 若松正志 (Lab. Nucl. Studies, Fac. Sci., Osaka Univ.)  
 WAKASA Tomotsugu 若狭智嗣 (RCNP, Osaka Univ.)  
 WATANABE Yutaka 渡辺裕  
 WATANABE Hiroshi 渡邊寛 (Fac. Sci., Kyushu Univ.)  
 WHITE Sebastian (Phys. Dept., BNL, USA)  
 XU Shuwei 徐樹威 (Inst. Modern Phys., Chinese Acad. Sci., China)  
 YAMAMOTO Sukeyasu 山本祐靖 (Fac. Sci. Technol., Sophia Univ.)  
 YAMANISHI Teruya 山西輝也 (Fac. Eng., Fukui Univ. Technol.)  
 YAMASHITA Yoshiki 山下芳樹 (Hirosaki Univ.)  
 YANAGISAWA Yoshiyuki 柳沢善行 (Cen. Nucl. Study, Univ. Tokyo)  
 YAZAKI Koichi 矢崎紘一 (Tokyo Woman's Chr. Univ.)  
 YOKKAICHI Satoshi 四日市悟 (Fac. Sci., Kyoto Univ.)  
 YOSHIMURA Koji 吉村浩司 (Int. Cen. Element. Part. Phys., Univ. Tokyo)  
 YOSHINAGA Naotaka 吉永尚孝 (Fac. Sci., Saitama Univ.)  
 YOSOI Masaru 與曾井優 (Fac. Sci., Kyoto Univ.)  
 ZHANG Yu-Hu 張玉虎 (Inst. Modern Phys., Chinese Acad. Sci., China)  
 ZHU Lihua (China Inst. Atom. Energy, China)

#### *Trainees*

BABA Hidetada 馬場秀忠 (Coll. Sci., Rikkyo Univ.)  
 FUKUCHI Tomonori 福地知則 (Fac. Sci., Kyushu Univ.)  
 FUKUSAKA Shouichi 福坂将一 (Dept. Phys., Grad. Sch. Sci., Univ. Tokyo)  
 FUTAKAMI Udai 二上宇内 (Coll. Sci., Rikkyo Univ.)  
 GOMI Tomoko 五味朋子 (Coll. Sci., Rikkyo Univ.)  
 HATANI Michio 波田野道夫 (Dept. Phys., Grad. Sch. Sci., Univ. Tokyo)  
 HIRAI Masanori 平井正紀 (Fac. Sci. Eng., Saga Univ.)  
 IMAI Nobuaki 今井伸明 (Dept. Phys., Grad. Sch. Sci., Univ. Tokyo)  
 KASHIYAMA Osamu 樫山修 (Fac. Sci., Kyushu Univ.)  
 KATO Hiromitsu 加藤裕充 (Dept. Phys., Grad. Sch. Sci., Univ. Tokyo)  
 KINUGAWA Hiroto 衣川裕人 (Coll. Sci., Rikkyo Univ.)  
 KOBAYASHI Hiroshi 小林寛 (Coll. Sci., Rikkyo Univ.)  
 KUNIBU Makoto 國分誠 (Coll. Sci., Rikkyo Univ.)  
 MAEDA Yukie 前田幸重 (Dept. Phys., Grad. Sch. Sci., Univ. Tokyo)  
 MICHIMASA Shinichiro 道正新一郎 (Fac. Sci., Univ. Tokyo)  
 MINEMURA Toshiyuki 峯村俊行 (Coll. Sci., Rikkyo Univ.)  
 MITSUHASHI Toshiya 三橋利也 (Dept. Phys., Grad. Sch. Sci., Univ. Tokyo)  
 MIYAKAWA Takahiko 宮川貴彦 (Fac. Sci., Tokyo Metrop. Univ.)  
 MOTOMURA Shinji 本村信治 (Fac. Sci., Kyushu Univ.)  
 MUTO Ryotaro 武藤亮太郎 (Fac. Sci., Kyoto Univ.)  
 NAKAJIMA Noriaki 中島典昭 (RCNP, Osaka Univ.)  
 NAKANO Eiji 仲野英司 (Fac. Sci., Tokyo Metrop. Univ.)  
 NAKANO Jo 中野讓 (Cen. Nucl. Study, Univ. Tokyo)  
 OHKUMA Kazumasa 大熊一正 (Fac. Human Dev., Kobe Univ.)  
 SAHA Pranab (KEK)  
 SAITO Koji 齋藤浩司 (Fac. Sci., Kyushu Univ.)  
 SAITOU Akito 齋藤明登 (Coll. Sci., Rikkyo Univ.)  
 SAKODA Seitaro 迫田誠太郎 (Dept. Phys., Grad. Sch. Sci., Univ. Tokyo)  
 SERATA Masaki 世良田真来 (Coll. Sci., Rikkyo Univ.)  
 SUDOH Kazutaka 須藤和敬 (Fac. Human Dev., Kobe Univ.)

SUETSUGU Kentaro 末次健太郎 (Tokyo Inst. Technol.)  
TANIGUCHI Etsuji 谷口悦史 (Tokyo Inst. Technol.)  
TOJO Junji 東城順治 (Fac. Sci., Kyoto Univ.)  
WATANABE Eitoku 渡辺英徳 (Dept. Phys., Grad. Sch. Sci., Univ. Tokyo)  
YAKO Kentaro 矢向謙太郎 (Dept. Phys., Grad. Sch. Sci., Univ. Tokyo)  
YAMADA Kazunari 山田一成 (Coll. Sci., Rikkyo Univ.)  
YONEDA Kenichiro 米田健一郎 (Dept. Phys., Grad. Sch. Sci., Univ. Tokyo)

## RI Beam Science Laboratory

### Head

TANIHATA Isao 谷畑勇夫

### Members

KORSHENINNIKOV Alexei A. KUMAGAI Hidekazu 熊谷秀和  
MATSUO Yukari 松尾由賀利 MORIMOTO Koji 森本幸司  
OZAWA Akira 小沢 顕 SUDA Toshimi 須田利美  
SUMIYOSHI Kohsuke 住吉光介 TONUMA Tadao 戸沼正雄  
YOSHIDA Koichi 吉田光一

### Visiting Members and Postdoctoral Fellows

AOYAMA Shigeyoshi 青山茂義 (Kitami Inst. Tech.)  
ADACHI Shizuko 安達静子 (ICFD)  
AHMADY Mohammad (Western Ontario Univ., Canada)  
ARATANI Michi 荒谷美智 (Inst. Environ. Sci.)  
BOLBOT Michael (Notre Dame Univ., USA)  
BORDEANU Cristina (Horia Hul. Natl. Inst., Romania)  
BOYD Richard (Ohio Univ., USA)  
BROCKMANN Roff (Inst. Phys., Univ. Mainz, Germany)  
CRUCCERU Ilie (Horia Inst. Eng., Romania)  
DATAR Vivek (Bhabha Atom. Res. Cen., India)  
DAVID Dean J. (CALTEC, USA)  
DEMYANOVA Alla S. (Kurchatov Inst. Atom. Energy, Russia)  
DOKE Tadayoshi 道家忠義 (Adv. Res. Inst. Sci. Eng., Waseda Univ.)  
ENYO Yoshiko 延與佳子 (Cen. Nucl. Study, Univ. Tokyo)  
FUJIWARA Mamoru 藤原 守 (RCNP, Osaka Univ.)  
FÜLÖP Zsolt (ATOMIKI, Hungary)  
GACSI Zoltan (ATOMIKI, Hungary)  
GEISSEL Hans (GSI, Germany)  
GIURGIU Mircea (Horia Inst. Nucl. Eng., Romania)  
GOLOVKOV Mkheil S. (Kurchatov Inst., Russia)  
GONCHAROV Sergei A. (Kurchatov Inst., Russia)  
GOSWAMI Ranjana (Variable Energy Cycl. Cen. Calcutta, India)  
GUNJI Shuichi 郡司修一 (Fac. Sci., Yamagata Univ.)  
HASEBE Nobuyuki 長谷部伸行 (Fac. Sci. Eng., Waseda Univ.)  
HIRENZAKI Satoru 比連崎 悟 (Fac. Sci., Nara Women's Univ.)  
HORIUCHI Hisashi 堀内 昶 (Fac. Sci., Kyoto Univ.)  
ISHIMOTO Shigeru 石元 茂 (KEK)  
ITAGAKI Naoyuki 板垣直之  
IWAMOTO Akira 岩本 昭 (JAERI, Tokai Res. Estab.)  
IZUYAMA Takeo 伊豆山健夫 (Fac. Sci., Toho Univ.)  
KANEKO Kazuya 金子 和也 (Kyushu Sangyo Univ.)  
KANUNGO Rituparna (Saha Inst. Nucl. Phys., Calcutta, India)  
KATORI Kenji 鹿取謙二  
KIKUCHI Jun 菊池 順 (Sci. Eng. Res. Lab., Waseda Univ.)  
KIMURA Kikuo 木村喜久雄 (Fac. Eng., Nagasaki Inst. Appl. Sci.)

KOBAYASHI Toshio 小林俊雄 (Fac. Sci., Tohoku Univ.)  
 KOLATA James (Notre Dame Univ., USA)  
 KUMARU, Suresh (Bhabha Atom. Res. Cen., India)  
 KUSAKA Kensuke 日下健祐  
 LE Hong Khiem (Inst. Phys., Natl. Cen. Sci. Technol., Vietnam)  
 LIU Xin (Inst. Nucl. Study, Univ. Tokyo)  
 MARUYAMA Koichi 丸山浩一 (Inst. Nucl. Study, Univ. Tokyo)  
 MARUYAMA Tomoyuki 丸山智幸 (Nihon Univ.)  
 MATSUOKA Nobuyuki 松岡伸行 (RCNP, Osaka Univ.)  
 MATSUTA Kensaku 松多健策 (Fac. Sci., Osaka Univ.)  
 MATSUYAMA Yoshitaka 松山芳孝 (Inst. Nucl. Study, Univ. Tokyo)  
 MINAMISONO Tadanori 南園忠則 (Fac. Sci., Osaka Univ.)  
 MITTING M. (GANIL, France)  
 MIYAKE Yasuo 三明康朗 (Fac. Sci., Univ. Tsukuba)  
 MIYAMURA Osamu 宮村修 (Fac. Sci., Hiroshima Univ.)  
 MOCHIZUKI Yuko 望月優子  
 MOMOTA Sadao 百田佐多生 (Kochi Univ. Technol.)  
 MURAOKA Mitsuo 村岡光男 (Fac. Eng., Aomori Univ.)  
 NAKATSUKASA Takashi 中務孝  
 NOJIRI Yoichi 野尻洋一 (Kochi Univ. Technol.)  
 OGAWA Kengo 小川健吾 (Coll. Arts. Sci., Chiba Univ.)  
 OGAWA Yoko 小川洋子 (Fac. Sci., Osaka Univ.)  
 OGLOBLIN Alexei A. (Kurchatov. Inst., Russia)  
 OHTSU Hideaki 大津秀暁 (Fac. Sci., Tohoku Univ.)  
 OHTSUBO Takashi 大坪隆 (Fac. Sci., Niigata Univ.)  
 OMATA Kazuo 小俣和夫 (Inst. Nucl. Study, Univ. Tokyo)  
 ONISHI Takashi 大西崇  
 ORYU Shinsho 尾立晋祥 (Fac. Sci. Technol., Sci. Univ. Tokyo)  
 OYAMATSU Kazuhiro 親松和浩 (Aichi Shukutoku Univ.)  
 PETRASCU Horia (Horia Inst. Phys. Nucl. Eng., Romania)  
 PETRASCU Marius (Horia Inst. Phys. Nucl. Eng., Romania)  
 SAGAWA Hiroyuki 佐川弘幸 (Cen. Math. Sci., Univ. Aizu)  
 SAKAI Hideyuki 酒井英行 (Fac. Sci., Univ. Tokyo)  
 SAKURAI Hirohisa 櫻井敬久 (Fac. Sci., Yamagata Univ.)  
 SATO Kazuhiro 佐藤和洋 (Tokyo Fire Dept.)  
 SEKI Ryoichi 関亮一 (California Univ., USA)  
 SHERRIL B. (Michigan State Univ., USA)  
 SHIBATA Mitihiro 柴田理尋 (Dept. Energy Eng. Sci., Nagoya Univ.)  
 SHIBATA Toru 柴田徹 (Sci. Eng., Aoyama Gakuin Univ.)  
 SUGANUMA Hideo 菅沼秀夫 (RCNP, Osaka Univ.)  
 SUGAWARA Masahiko 菅原昌彦 (Fundam. Sci., Chiba Inst. Technol.)  
 SÜMMERER Klaus (GSI, Germany)  
 SUZUKI Hideyuki 鈴木英之 (KEK)  
 SUZUKI Takeshi 鈴木健 (Fac. Sci., Niigata Univ.)  
 SUZUKI Tsuneo 鈴木恒雄 (Fac. Sci., Kanazawa Univ.)  
 SUZUKI Yasuyuki 鈴木宣之 (Fac. Sci., Niigata Univ.)  
 TACHIBANA Takahiro 橋高博 (Sen. High Sch., Waseda Univ.)  
 TAKAHASHI Yoshiyuki 高橋義幸 (Alabama Univ., USA)  
 TAKAHASHI Yutaka 高橋豊 (Fac. Sci., Osaka Univ.)  
 TAKANO Masatoshi 鷹野正利 (Fac. Sci. Eng., Waseda Univ.)  
 TOKANAI Fuyuki 門叶冬樹 (JST)  
 TOKI Hiroshi 土岐博 (RCNP, Osaka Univ.)  
 TORBJOEN Baeck (Stockholm Univ., Sweden)  
 TOSTEVIN Jeffrey A. (Univ. Surry, India)  
 UCHIHORI Yukio 内掘幸夫 (Inst. Rad. Sci.)  
 VARGA Kalman (Inst. Nucl., Hungarian Acad. Sci., Hungary)  
 WADA Takahiro 和田隆宏 (Fac. Sci., Konan Univ.)

WINKLER Martin (GEI, Germany)  
YAGI Hirosuke 八木浩輔 (Fac. Sci., Univ. Tsukuba)  
YAMADA Shoichi 山田章一 (Fac. Sci., Univ. Tokyo)  
YAMAGUCHI Takayuki 山口貴之  
YORANN Alhassid (Yale Univ., USA)  
YUZUKI Akira 柚木 彰 (Toshiba Corp.)  
ZAHAR Mohamed (Dept. Phys., Notre Dam Univ., USA)  
ZHENG Tao (Fac. Sci. Technol., Sci., Univ. Tokyo)

#### *Trainees*

AOKI Yuka 青木由香 (Fac. Sci., Tohoku Univ.)  
FUZIMURA Takeshi 藤村 岳 (Sci. Eng., Aoyama Gakuin Univ.)  
HARA Kenichiro 原 健一朗 (Fac. Sci. Eng., Waseda Univ.)  
HIBINO Masaru 日比野 優 (Fac. Sci. Eng., Waseda Univ.)  
IHARA Akifumi 井原亜紀史 (Fac. Sci. Eng., Waseda Univ.)  
KATO Tomomi 加藤智美 (Fac. Sci., Niigata Univ.)  
KATO Toshiyuki 加藤俊幸 (Fac. Sci. Eng., Waseda Univ.)  
KAWA Tadahisa 河 忠久 (Fac. Sci., Osaka Univ.)  
KIHIRA Eiichi 吉平栄一 (Fac. Sci. Eng., Waseda Univ.)  
KITANI Takao 木谷貴雄 (Fac. Sci. Eng., Waseda Univ.)  
KIYAMU Atushi 喜谷武篤史 (Fac. Sci. Eng., Ibaraki Univ.)  
KURIYAMA Koji 栗山幸治 (Sci. Eng., Aoyama Gakuin Univ.)  
MASUMURA Takahiro 増村考洋 (Fac. Sci. Eng., Waseda Univ.)  
MINAMISONO Kei 南園 啓 (Fac. Sci., Osaka Univ.)  
MUTO Nobuo 武藤信雄 (Fac. Eng., Aoyama Gakuin Univ.)  
OHZEKI Kazuki 大関和貴 (Fac. Sci., Tohoku Univ.)  
NISHIKIDO Humihiko 錦戸文彦 (Fac. Sci. Eng., Waseda Univ.)  
OKUDA Takashi 奥田貴志 (Fac. Sci., Tohoku Univ.)  
OKUDAIRA Osamu 奥平 修 (Fac. Sci. Eng., Waseda Univ.)  
OZAKI Kiminori 尾崎公教 (Fac. Sci. Eng., Waseda Univ.)  
SAKAGUCHI Takao 坂口貴男 (Fac. Sci. Eng., Waseda Univ.)  
SASAKI Makoto 佐々木 誠 (Fac. Sci., Osaka Univ.)  
SATO Kazunori 佐藤和則 (Fac. Sci., Osaka Univ.)  
SEKIGUCHI Masatugu 関口昌嗣 (Fac. Sci., Tohoku Univ.)  
SHIMIZU Noritaka 清水則孝 (Fac. Sci., Univ. Tokyo)  
SUGIMOTO Satoshi 杉本 聡 (RCNP, Osaka Univ.)  
TAKEMURA Haruyuki 竹村春礼 (Fac. Sci. Eng., Waseda Univ.)  
TAKENAKA Sunao 竹中 直 (Fac. Sci. Eng., Waseda Univ.)  
TAKENOUCHI Masatoshi 竹之内正俊 (Fac. Sci. Eng., Waseda Univ.)  
TAKEUCHI Satoshi 武内 聡 (Fac. Sci., Rikkyo Univ.)  
TANAKA Motoyuki 田中基之 (Fac. Sci., Waseda Univ.)  
TAZAWA Shinya 田沢伸也 (Fac. Sci., Tohoku Univ.)  
TERASAWA Kazuhiro 寺沢和洋 (Fac. Sci. Eng., Waseda Univ.)  
TERASAWA Mariko 寺澤真理子 (Fac. Sci., Univ. Tokyo)  
TERUHI Shigeru 照日 繁 (Fac. Sci. Eng., Waseda Univ.)  
UMEMURA Tomohiro 梅村朋弘 (Fac. Sci. Eng., Waseda Univ.)  
UZHIE Toru 氏家 徹 (Fac. Sci., Tohoku Univ.)  
WAKASAYA Yoshiaki 若狭谷義朗 (Fac. Sci. Technol., Sci. Univ. Tokyo)  
WANG Haiming 王 海鳴 (Fac. Sci., Univ. Tokyo)  
YAMAGUCHI Yoshitaka 山口由高 (Fac. Sci., Niigata Univ.)  
YAMASHITA Masaki 山下雅樹 (Adv. Res. Inst. Sci. Eng., Waseda Univ.)  
YAMASHITA Naoyuki 山下直之 (Fac. Sci. Eng., Waseda Univ.)  
YASHIRO Junichi 矢代淳一 (Fac. Sci. Eng., Waseda Univ.)

## Applied Nuclear Physics Laboratory

### Head

ASAHI Koichiro 旭 耕一郎

### Members

KOBAYASHI Yoshio 小林 義男

### Visiting Members and Postdoctoral Fellows

EINAGA Yasuaki 栄長 泰明 (Fac. Sci., Univ. Tokyo)  
KUBO Kenya 久保 謙哉 (Fac. Sci., Univ. Tokyo)  
OGAWA Hiroshi 小川 博嗣 (Fac. Sci., Tokyo Inst. Technol.)  
SAKAI Kenji 酒井 健二 (Fac. Sci., Tokyo Inst. Technol.)  
UENO Hideki 上野 秀樹 (Fac. Sci., Osaka Univ.)  
YAMADA Yasuhiro 山田 康洋 (Fac. Sci., Sci. Univ. Tokyo)

### Trainees

GOTO Atsushi 五島 敦 (Fac. Sci., Tokyo Inst. Technol.)  
HONDA Toshiki 本多 俊樹 (Fac. Sci., Tokyo Inst. Technol.)  
HORI Kentaro 堀 健太郎 (Fac. Sci., Sci. Univ. Tokyo)  
KATSUMATA Keiichi 勝又 啓一 (Fac. Sci., Sci. Univ. Tokyo)  
MIYAZAKI Junn 宮崎 淳 (Fac. Sci., Sci. Univ. Tokyo)  
MIYOSHI Hisanori 三好 永哲 (Fac. Sci., Tokyo Inst. Technol.)  
NAGAKURA Masaki 長倉 正樹 (Fac. Sci., Tokyo Inst. Technol.)  
OGAWA Shigeru 小川 茂 (Fac. Sci., Shizuoka Inst. Sci. Tech.)  
ONO Yuuki 小野 祐樹 (Fac. Sci., Sci. Univ. Tokyo)  
SHIMAZAKI Hideo 島崎 秀生 (Fac. Sci., Sci. Univ. Tokyo)  
SHIMIZU Yasunori 清水 康功 (Fac. Sci., Shizuoka Inst. Sci. Tech.)  
SUGA Toshitaka 須賀 敏孝 (Fac. Sci., Tokyo Inst. Technol.)  
SUZUKI Takayuki 鈴木 孝幸 (Fac. Sci., Tokyo Inst. Technol.)  
YOGO Katsumori 余語 克紀 (Fac. Sci., Tokyo Inst. Technol.)  
YOSHIMI Akihiro 吉見 彰洋 (Fac. Sci., Tokyo Inst. Technol.)

## Atomic Physics Laboratory

### Head

YAMAZAKI Yasunori 山崎 泰規

### Members

KAMBARA Tadashi 神原 正	KANAI Yasuyuki 金井 保之
KOJIMA Takao M. 小島 隆夫	NAKAI Yoichi 中井 陽一
NISHIDA Masami 西田 雅美	OURA Masaki 大浦 正樹
OYAMA Hitoshi 大山 等	SHIMAMURA Isao 島村 勲
WADA Michiharu 和田 道治	

### Visiting Members and Postdoctoral Fellows

ANDO Kozo 安藤 剛三  
AZUMA Toshiyuki 東 俊行 (Inst. Appl. Phys., Univ. Tsukuba)  
BRAGE Tomas (Dept. Phys., Univ. Lund, Sweden)  
CHIMI Yasuhiro 知見 康弘 (JAERI, Tokai Res. Estab.)  
CIORTEA Constantin (Natl. Inst. Phys. Nucl. Eng., Romania)  
DATZ Sheldon (Oak Ridge Natl. Lab., USA)  
DEPAOLA Brett (Dept. Phys. Kansas State Univ., USA)  
DUMITRIU Dana (Natl. Inst. Phys. Nucl. Eng., Romania)  
EICHLER Jörg (Hahn-Meitner Inst. Berlin, Germany)  
FAIFMAN Mark (Russian Res. Cent., Kurchatov Inst., Russia)  
FUJIMA Kazumi 藤間 一美 (Fac. Eng., Yamanashi Univ.)

HARA Shunsuke 原 俊介 (Dept. Gen. Ed., Tsukuba Coll. Technol.)  
 HATTORI Toshiyuki 服部俊幸 (Res. Lab. Nucl. React., Tokyo Inst. Technol.)  
 HINO Ken-ichi 日野健一 (Inst. Appl. Phys., Univ. Tsukuba)  
 HITACHI Akira 月出章 (Kochi Med. Sch.)  
 HULDT Sven (Lund Univ., Sweden)  
 HUTTON Roger  
 ICHIMURA Atsushi 市村 淳 (Inst. Space Astr. Sci.)  
 ICHIOKA Toshiyasu 市岡利康 (Grad. Sch. Arts Sci., Univ. Tokyo)  
 IGARASHI Akinori 五十嵐明則 (Fac. Eng., Miyazaki Univ.)  
 IKEDA Hiroshi 池田 博 (Univ. Tsukuba)  
 ISHII Keishi 石井慶之 (Fac. Sci. Eng., Ritsumeikan Univ.)  
 ISHIKAWA Norito 石川法人 (JAERI, Tokai Res. Estab.)  
 ITOH Akio 伊藤秋男 (Fac. Eng., Kyoto Univ.)  
 ITOH Yoh 伊藤 陽 (Fac. Sci., Josai Univ.)  
 IWAI Yoshio 岩井良夫 (Grad. Sch. Arts Sci., Univ. Tokyo)  
 IWASE Akihiro 岩瀬彰宏 (JAERI, Tokai Res. Estab.)  
 KAGEYAMA Kensuke 蔭山健介 (Fac. Eng., Saitama Univ.)  
 KANEKO Shinichi 金子真一 (Fac. Sci., Tokyo Inst. Technol.)  
 KAWATSURA Kiyoshi 川面 澄 (Fac. Eng. Design, Kyoto Inst. Technol.)  
 KHEIFETS Anatoli (Australian Natl. Univ., Australia)  
 KIMURA Kenji 木村健二 (Fac. Eng., Kyoto Univ.)  
 KIMURA Mineo 季村峯生 (Sch. Allied Health Sci., Yamaguchi Univ.)  
 KITAJIMA Masashi 北島昌史 (Fac. Sci. Technol., Sophia Univ.)  
 KOBAYASHI Nobuo 小林信夫 (Dept. Phys., Tokyo Metropol. Univ.)  
 KOIKE Fumihito 小池文博 (Sch. Med., Kitasato Univ.)  
 KOIZUMI Tetsuo 小泉哲夫 (Dept. Phys., Rikkyo Univ.)  
 KOMAKI Ken-ichiro 小牧研一郎 (Grad. Sch. Arts Sci., Univ. Tokyo)  
 KOWARI Kenichi 小割健一 (Dept. Appl. Phys. Chem., Univ. Electro-Commun.)  
 KURODA Naoshi 黒田直志 (JAERI, Tokai Res. Estab.)  
 KUROKI Kenro 黒木健郎 (Natl. Res. Inst. Police Sci.)  
 MANN Ady (Phys. Dept., Israel Inst. Technol., Israel)  
 MARTINSON Indrek (Dept. Phys., Univ. Lund, Sweden)  
 MATSUO Takashi 松尾 崇 (Dept. Pathol., Tokyo Med. Dent. Univ.)  
 MATSUZAWA Michio 松澤通生 (Dept. Appl. Phys. Chem., Univ. Electro-Commun.)  
 MITAMURA Tohru 三田村 徹 (Fac. Eng., Himeji Inst. Technol.)  
 MITSUKE Koichiro 見附孝一郎 (Inst. Mol. Sci.)  
 MIZOGAWA Tatsumi 溝川辰巳 (Nagaoka Coll. Technol.)  
 MOHRI Akihiro 毛利明博  
 MUKOYAMA Takeshi 向山 毅 (Inst. Chem. Res., Kyoto Univ.)  
 NISHIDA Nobuhiko 西田信彦 (Fac. Sci., Tokyo Inst. Technol.)  
 NISHIMURA Tamio 西村民男  
 OHTANI Shunsuke 大谷俊介 (Inst. Laser Sci., Univ. Electro-Commun.)  
 OKADA Kunihiro 岡田邦宏 (Fac. Sci. Tech., Sophia Univ.)  
 OKAYASU Satoru 岡安 悟 (JAERI, Tokai Res. Estab.)  
 OKUNO Kazuhiko 奥野和彦 (Dept. Phys., Tokyo Metropol. Univ.)  
 ONO Fumihisa 小野文久 (Dept. Phys., Okayama Univ.)  
 OSHIMA Nagayasu 大島永康  
 SAKAI Akio 坂井昭夫 (Vacuum Products Co.)  
 SAKATA Hideaki 坂田英明 (Fac. Sci., Tokyo Inst. Technol.)  
 SATO Hiroshi 佐藤浩史 (Fac. Sci., Ochanomizu Univ.)  
 SATOH Kazuhiko 佐藤一彦 (Fac. Sci., Tokyo Inst. Technol.)  
 SHIMA Kunihiro 島 邦博 (Tandem Accel. Cen., Univ. Tsukuba)  
 SHIMAKURA Noriyuki 島倉紀之 (Fac. Sci., Niigata Univ.)  
 SOEJIMA Kouichi 副島浩一 (Fac. Sci., Niigata Univ.)  
 TAKEKAWA Michiya 竹川道也  
 TERANISHI Yoshiaki 寺西慶哲  
 TERASAWA Mititaka 寺澤倫孝 (Fac. Eng., Himeji Inst. Technol.)

THURIEZ Sebastien  
TONUMA Tadao 戸沼正雄 (Adv. Res. Inst. Sci. Eng., Waseda Univ.)  
TOSHIMA Nobuyuki 戸嶋信幸 (Inst. Appl. Phys., Univ. Tsukuba)  
TRIKALINOS Christos (Univ. Athens, Greece)  
TSUCHIDA Hidetsugu 土田秀次 (Fac. Sci., Nara Women's Univ.)  
UEDA Kiyoshi 上田 潔 (Res. Inst. Sci. Meas., Tohoku Univ.)  
WAKIYA Kazuyoshi 脇谷一義 (Fac. Sci. Technol., Sophia Univ.)  
WATANABE Shinichi 渡辺信一 (Dept. Appl. Phys. Chem., Univ. Electro-Commun.)  
YAGISHITA Akira 柳下 明 (KEK)  
ZOU Yaming (Shanghai Jiao Tong Univ., China)

#### *Trainees*

BOYD Micah (Dept. Phys., Univ. Lund, Sweden)  
ENDO Atsumi 遠藤厚身 (Dept. Phys., Grad. Sch. Sci., Univ. Tokyo)  
HASEGAWA Tadayuki 長谷川忠之 (Grad. Sch. Eng., Tokai Univ.)  
HORI Masaki 堀 正樹 (Dept. Phys., Grad. Sch. Sci., Univ. Tokyo)  
HOSHINO Masamitsu 星野正光 (Fac. Sci. Technol., Sophia Univ.)  
IIDA Ryouichi 飯田竜一 (Univ. Electro-Commun.)  
ITO Akira 伊藤 聡 (Dept. Phys., Rikkyo Univ.)  
ITO Takaomi 伊藤高臣 (Grad. Sch. Arts Sci., Univ. Tokyo)  
KAMEI Takehito 亀井武仁 (Fac. Sci. Technol., Sophia Univ.)  
MAJIMA Takuya 間嶋拓也 (Fac. Eng., Kyoto Univ.)  
MATSUSHIMA Hiroshi 松島 広 (Dept. Phys., Grad. Sch. Sci., Univ. Tokyo)  
MORISHITA Yuichiro 森下雄一郎 (Dept. Phys., Grad. Sch. Sci., Univ. Tokyo)  
MURAKOSHI Dai 村越 大 (Grad. Sch. Arts Sci., Univ. Tokyo)  
NAKAMURA Takashi 中村貴志 (Univ. Electro-Commun.)  
OGURA Kunihiro 小倉都宏 (Fac. Sci. Technol., Sophia Univ.)  
OKABAYASHI Norio 岡林則夫 (Grad. Sch. Arts Sci., Univ. Tokyo)  
OKADA Shinichi 岡田晋一 (Fac. Sci. Technol., Sophia Univ.)  
OONO Takayuki 大野隆之 (Fac. Sci. Technol., Sophia Univ.)  
TAGUCHI Yoshio 田口義雄 (Fac. Sci., Tokyo Inst. Technol.)  
TAKABAYASHI Yuichi 高林雄一 (Dept. Phys., Grad. Sch. Sci., Univ. Tokyo)  
TAKAHASHI Takehisa 高橋武寿 (Dept. Phys., Rikkyo Univ.)  
YAMASHITA Kenya 山下賢哉 (Dept. Phys., Grad. Sch. Sci., Univ. Tokyo)

### **Muon Science Laboratory**

#### *Head*

NAGAMINE Kanetada 永嶺謙忠

#### *Members*

ISHIDA Katsuhiko 石田勝彦  
MATSUDA Yasuyuki 松田恭幸  
NAKAMURA Satoshi N. 中村 哲  
YAGI Eiichi 八木栄一  
KOYAMA Akio 小山昭雄  
MATSUZAKI Teiichiro 松崎禎市郎  
WATANABE Isao 渡邊功雄

#### *Visiting Members and Postdoctoral Fellows*

AKIMITSU Jun 秋光 純 (Coll. Sci. Eng., Aoyama Gakuin Univ.)  
AKIMOTO Katsuhiko 秋本克洋 (Inst. Mater., Univ. Tsukuba)  
ARAI Juichiro 新井重一郎 (Sci. Univ. Tokyo)  
ASAI Kichizo 浅井吉蔵 (Univ. Electro-Commun.)  
BAKULE Pavel  
DAS Prasad Tara (Dept. Phys., State Univ. New York, Albany, USA)  
FUKAYA Atsuko 深谷敦子  
HASHI Kenjiro 端 健二郎  
HASHIMOTO Masashi 橋本雅史 (JAERI, Tokai Res. Estab.)

HIGEMOTO Wataru 髭本 亘 (KEK)  
 HIYAMA Emiko 肥山詠美子  
 ITO Atsuko 伊藤厚子  
 IWASAKI Masahiko 岩崎雅彦 (Dept. Phys., Tokyo Inst. Technol.)  
 KADONO Ryosuke 門野良典 (KEK)  
 KATO Mineo 加藤岑生 (JAERI, Tokai Res. Estab.)  
 KAWAMURA Naritoshi 河村成肇  
 KINO Yasushi 木野康志 (Fac. Sci., Tohoku Univ.)  
 KOIKE Youji 小池洋二 (Fac. Eng., Tohoku Univ.)  
 KRISHNAMURTHY Vemuru  
 KUNO Yoshitaka 久野良孝 (KEK)  
 KUROSAWA Kiyoyuki 黒沢清行 (JAERI, Tokai Res. Estab.)  
 MACRAE Roderick M.  
 MARUYAMA Takahiro 丸山隆浩 (Inst. Mater., Univ. Tsukuba)  
 MATSUSHITA Akira 松下 明  
 MEKATA Mamoru 目方 守 (Fac. Eng., Fukui Univ.)  
 MIYAKE Yasuhiro 三宅康博 (KEK)  
 MIYAKO Yoshihito 都 福仁 (Fac. Sci., Osaka Univ.)  
 MOCHIKU Takashi 茂筑高士 (Natl. Res. Inst. Metals)  
 MORITA Masato 森田正人 (Fac. Sci., Josai Univ.)  
 MORITA Reiko 森田玲子 (Josai Jr. Coll. Women)  
 NISHIDA Nobuhiko 西田信彦 (Fac. Sci., Tokyo Inst. Technol.)  
 NISHIYAMA Kusuo 西山樟生 (KEK)  
 PRATT Francis L.  
 SAKAMOTO Shinichi 坂元真一 (KEK)  
 SATO Kazuhiko 佐藤一彦 (Fac. Sci., Saitama Univ.)  
 SCHEUERMAN Robert  
 SHIMOMURA Koichiro 下村浩一郎 (KEK)  
 STRASSER Patrick  
 SUGAI Hiroyuki 須貝宏行 (JAERI, Tokai Res. Estab.)  
 TAKABATAKE Toshiro 高島敏郎 (Grad. Sch. Adv. Sci. Matter, Hiroshima Univ.)  
 TAKIGAWA Masashi 瀧川 仁 (Inst. Solid State Phys.)  
 TANASE Masakazu 棚瀬正和 (JAERI, Tokai Res. Estab.)  
 TORIKAI Eiko 鳥養映子 (Fac. Eng., Yamanashi Univ.)  
 UEDA Kazuo 上田和夫 (Inst. Solid State Phys.)  
 UMEO Kazunori 梅尾和則 (Fac. Sci., Hiroshima Univ.)  
 WADA Nobuo 和田信雄 (Grad. Sch. Arts Sci., Univ. Tokyo)  
 WATANABE Tsutomu 渡部 力 (Int. Chr. Univ.)

#### *Trainees*

OHIRA Seiko 大平聖子 (Grad. Sch., Univ. Tokyo)  
 TANAKA Hiroyuki 田中宏幸 (Grad. Sch., Nagoya Univ.)  
 TOYODA Akihisa 豊田晃久 (Grad. Sch., Univ. Tokyo)

### **Magnetic Materials Laboratory**

#### *Head*

KATSUMATA Koichi 勝又 紘一

#### *Members*

HAGIWARA Masayuki 萩原政幸                      MATSUDA Masaaki 松田雅昌

## Beam Physics and Engineering Laboratory

### *Head*

KATAYAMA Takeshi 片山武司

### *Members*

AMEMIYA Hiroshi 雨宮 宏

NAKAMURA Masato 中村仁音

TAMBA Moritake 丹波護武

HAMAGAKI Manabu 浜垣 学

OKAZAKI Kiyohiko 岡崎清比古

YANO Katsuki 矢野勝喜

### *Visiting Members and Postdoctoral Fellows*

CHOUFFANI Khalid

TAKEUCHI Takeshi 竹内 猛

YUN Chong-Cheoul 尹 鍾哲

## Cellular and Molecular Biology Laboratory

### *Head*

SHIBATA Takehiko 柴田武彦

### *Members*

LING Feng 凌 楓

### *Visiting Members and Postdoctoral Fellows*

YOSHIMASU Masatoshi 吉益雅俊

## Cellular Physiology Laboratory

### *Head*

HANAOKA Fumio 花岡文雄

### *Members*

KITAYAMA Shigeru 北山 滋

YATAGAI Fumio 谷田貝文夫

### *Visiting Members and Postdoctoral Fellows*

ANDO Koichi 安藤興一 (Natl. Inst. Radiol. Sci.)

FURUSAWA Yoshiya 古澤佳也 (Natl. Inst. Radiol. Sci.)

HAMA Yoshimasa 浜 義昌 (Sci. Eng. Res. Lab., Waseda Univ.)

HASE Yoshihiro 長谷純宏 (JAERI, Takasaki Rad. Chem. Res. Estab.)

HOSHINO Kazuo 星野一雄 (Natl. Inst. Radiol. Sci.)

ITO Hisao 伊東久夫 (Sch. Med., Chiba Univ.)

ITSUKAICHI Hiromi 五日市ひろみ (Natl. Inst. Radiol. Sci.)

KANAI Tatsuki 金井達明 (Natl. Inst. Radiol. Sci.)

KASAI Kiyomi 笠井清美 (Natl. Inst. Radiol. Sci.)

KAWACHI Kiyomitsu 河内清光 (Natl. Inst. Radiol. Sci.)

KOBAYASHI Yasuhiko 小林泰彦 (JAERI, Takasaki Rad. Chem. Res. Estab.)

MATSUFUJI Naruhiro 松藤成弘 (Natl. Inst. Radiol. Sci.)

MINOHARA Shinichi 箕原伸一 (Natl. Inst. Radiol. Sci.)

MURAKAMI Masahiro 村上正弘 (Natl. Inst. Radiol. Sci.)

SAITO Mizuho 斉藤瑞穂 (Natl. Inst. Radiol. Sci.)

SASAKI Hiroshi 佐々木 弘 (Fac. Med., Kyushu Univ.)

SHIKAZONO Naoya 鹿園直哉 (JAERI, Takasaki Rad. Chem. Res. Estab.)

SOGA Fuminori 曾我文宣 (Inst. Nucl. Study, Univ. Tokyo)

TANAKA Atsushi 田中 淳 (JAERI, Takasaki Rad. Chem. Res. Estab.)

TOMURA Hiromi 外村浩美 (Natl. Inst. Radiol. Sci.)

WATANABE Masami 渡辺正己 (Fac. Pharm., Nagasaki Univ.)

YAMASHITA Shoji 山下昌次 (Natl. Saitama Hospital)

*Trainees*

LI Ryonpha 李 玲華 (Natl. Inst. Radiol. Sci.)

**Plant Functions Laboratory**

*Head*

YOSHIDA Shigeo 吉田茂男

*Members*

ABE Tomoko 阿部知子

MATSUYAMA Tomoki 松山知樹

*Visiting Members and Postdoctoral Fellows*

HARA Yasuhide 原 靖英 (Kanagawa Inst. Agric. Sci.)

HASHIMOTO Takashi 橋本 隆 (Dept. Biosci., NAIST)

KITAURA Takeo 北浦健生 (Kanagawa Inst. Agric. Sci.)

KIUCHI Reiko 木内玲子

MIYAGAI Mashu 宮外麻周

MIYOSHI Kazumitsu 三吉一光 (Fac. Bioresource Sci., Akita Pref. Univ.)

SATO Fumihiko 佐藤文彦 (Dept. Agric. Chem., Kyoto Univ.)

SATO Shinobu 佐藤忍 (Inst. Biol. Sci., Tsukuba Univ.)

SUZUKI Kenichi 鈴木賢一 (Suntory Ltd.)

*Trainees*

KOMOMI Yuki 許斐佑紀 (Fac. Sci. Tech., Sci. Univ. Tokyo)

TAKAHASHI Hideki 高橋英樹 (Coll. Agric. Vet. Med., Nihon Univ.)

**Microbial Toxicology Laboratory**

*Head*

YAMAGUCHI Isamu 山口 勇

*Members*

ARIE Tsutomu 有江 力

*Visiting Members and Postdoctoral Fellows*

NOSE Yasuhiro 能勢泰寛

SOSHI Takayuki 曾雌隆行

**CYCLOTRON CENTER**

*Chief Scientist*

YANO Yasushige 矢野安重

**RIBF Project Office**

*Head*

YANO Yasushige 矢野安重

*Members*

IKEGAMI Kumio 池上九三男

KAMIGAITO Osamu 上垣外修一

OHNISHI Jun-ichi 大西純一

OTAKE Masao 大竹政雄

TANABE Toshiya 田辺敏也

INABE Naohito 稲辺尚人

KUBO Toshiyuki 久保敏幸

OKUNO Hiroki 奥野広樹

SAKAMOTO Naruhiko 坂本成彦

WAKASUGI Masanori 若杉昌徳

*Visiting Members and Postdoctoral Fellows*

AKIYOSHI Hiromichi 秋吉啓充

AMANO Ryohei 天野良平 (Fac. Med., Kanazawa Univ.)  
 ARAKAWA Kazuo 荒川和夫 (JAERI, Takasaki Rad. Chem. Res. Estab.)  
 BATYGIN Yuri  
 BHATTACHARJEE Sudeep  
 CHATTOPADHYAY Subrata (Variable Energy Cycl. Cen., India)  
 CHIBA Toshiya 千葉利哉  
 CHIBA Yoshiaki 千葉好明  
 DIAO Xungang  
 DINH DANG Nguyen  
 ENDO Kazutoyo 遠藤和豊 (Showa Coll. Pharm. Sci.)  
 FUJINAWA Tadashi 藤縄雅 (Mitsubishi Electric Co., Ltd.)  
 FUJIOKA Tsutomu 藤岡勉 (Toshiba Corp.)  
 FUJISAWA Takashi 藤沢高志 (N.I.R.S.)  
 FUJISHIMA Shiro 藤島史郎 (I.H.I.)  
 FUKUDA Mitsuhiro 福田光宏 (JAERI, Takasaki Rad. Chem. Res. Estab.)  
 FUKUNISHI Nobuhisa 福西暢尚  
 HEMMI Masatake 逸見政武  
 HIMENO Seiichiro 姫野誠一郎 (Sch. Pharm. Sci., Kitasato Univ.)  
 HIRUMACHI Tamiko 蛭町多美子 (Toshiba Corp.)  
 HONMA Toshihiro 本間寿広 (N.I.R.S.)  
 INAGE Hiroko 稲毛寛子 (Int. Life Sci. Inst., Showa Women's Univ.)  
 INAMURA Takashi T. 稲村卓  
 IWASA Naohito 岩佐直仁  
 KAWAGUCHI Takeo 川口武男 (Mitsubishi Electric Co., Ltd.)  
 KIDERA Masanori 木寺正憲  
 KIM Jong-Won  
 KOHAMA Akihisa 小濱洋央  
 KOZU Hideo 神津英雄 (Toshiba Corp.)  
 MADOKORO Hideki 間所秀樹  
 MASUOKA Toshikatu 益岡俊勝 (Hitachi Zosen Corp.)  
 MATSUMOTO Ken-ichiro 松本謙一郎 (Showa Coll. Pharm. Sci.)  
 MATSUSHITA Akira 松下明 (NASDA)  
 MINAI Yoshitaka 葉袋佳孝 (Cen. Art. Sci., Musashi Univ.)  
 MINAMI Takeshi 南武志 (Dept. Living Sci., Kinki Univ., Toyo-Oka Jr. Coll.)  
 MIRONOV Vladmir (J.I.N.R., Dubna, Russia)  
 MITSUMOTO Toshinori 密本俊典 (Sumitomo Heavy Ind., Ltd.)  
 MIYAZAWA Yoshitoshi 宮沢佳敏  
 MORIKAWA Tetsuya 森川鐵也  
 MOTONAGA Shoushichi 元永昭七  
 NAGAFUCHI Teruyasu 永渕照康 (Toshiba Corp.)  
 NAKANISHI Yukiko 中西由季子 (Int. Life Sci. Inst., Showa Women's Univ.)  
 NIIMURA Masanobu 新村正信  
 NODA Koji 野田耕司 (N.I.R.S.)  
 OGURA Yasumitsu 小椋康光 (Fac. Pharm. Sci., Chiba Univ.)  
 OHKAWA Tomohiro 大川智宏 (Mitsubishi Res. Inst., Inc.)  
 OHTOMO Kiyotaka 大友清隆 (Sumitomo Heavy Ind., Ltd.)  
 OKAMOTO Youichi 岡本洋一 (Showa Coll. Pharm. Sci.)  
 OKAMURA Masahiro 岡村昌宏  
 OKUMURA Susumu 奥村進 (JAERI, Takasaki Rad. Chem. Res. Estab.)  
 RIZAWA Takahito 利沢隆人 (Toshiba Corp.)  
 SAITO Fuminori 齊藤文修  
 SAKURAI Hiromu 桜井弘 (Kyoto Pharmaceutical Univ.)  
 SATOU Yoshiteru 佐藤義輝  
 SEKINE Hirotaka 関根弘隆  
 SHINOHARA Atsushi 篠原厚 (Res. Reactor Inst., Kyoto Univ.)  
 SIDORIN Anatoly (J.I.N.R., Dubna, Russia)  
 SUGII Kazuo 杉井一生 (Osaka Vacuum, Ltd.)

SUZUKI Hiroyuki 鈴木弘行 (RI Res. Cen., Chiba Univ.)  
 SUZUKI Kazuo 鈴木和夫 (Fac. Pharm. Sci., Chiba Univ.)  
 SUZUKI Naoki 鈴木直毅  
 TAKAHASHI Masaaki 高橋正昭 (Coll. Agric., Osaka Pref. Univ.)  
 TAKAHASHI Yoshio 高橋嘉夫 (Fac. Sci., Hiroshima Univ.)  
 TAKANAKA Masao 高仲政雄  
 TAKEDA Atsushi 武田厚司 (Sch. Pharm. Sci., Shizuoka Univ.)  
 TAKEUCHI Suehiro 竹内末広 (JAERI, Tokai Res. Estab.)  
 TANAKA Yasushi 田中保志 (Kyokuto Boeki Kaisha, Ltd.)  
 TOMIMASU Takio 富增多喜夫 (Free Electrons Laser Res. Inst.)  
 TOMINAKA Toshiharu 富中利治 (Hitachi, Ltd.)  
 TOMIZAWA Masahito 富沢正人 (KEK)  
 UESAKA Meiko 上坂明子  
 UESAKA Tomohiro 上坂友洋  
 WATANABE Ikuo 渡辺郁男 (Toshiba Corp.)  
 WATANABE Shin-ichi 渡辺伸一 (Cen. Nucl. Study, Grad. Sch. Sci., Univ. Tokyo)  
 WU Dezhong (Scintia Sinica, China)  
 XIA Jia-Wen 夏佳文 (Inst. Modern Phys., Academia Sinica, China)  
 YAMASAKI Mineo 山崎峰夫 (Nara Med. Univ.)  
 YANAGA Makoto 矢永誠人 (Fac. Sci., Shizuoka Univ.)  
 YANG Youg Feng (Scintia Sinica, China)  
 YASUI Hiroyuki 安井裕之 (Kyoto Pharmaceutical Univ.)  
 YOKOUCHI Shigeru 横内茂 (Osaka Vacuum, Ltd.)  
 YOKOYAMA Ichiro 横山一郎  
 YONEDA Akira 米田晃  
 YOSHIDA Yutaka 吉田豊 (Shizuoka Inst. Sci. Tech.)

#### *Trainees*

ARIGA Takehiro 有賀健博 (Fac. Sci., Toho Univ.)  
 FUGONO Jun 畚野純 (Kyoto Pharm. Univ.)  
 IGARASHI Kaori 五十嵐香織 (Int. Life Sci. Inst., Showa Women's Univ.)  
 IWAMA Motonori 岩間基訓 (Fac. Sci., Shizuoka Univ.)  
 KOIZUMI Miwako 小泉美和子 (Int. Life Sci. Inst., Showa Women's Univ.)  
 KURITA Tetsuro 栗田哲郎 (Inst. Phys., Univ. Tsukuba)  
 MAETSU Hitomi 前津仁美 (Fac. Sci., Shizuoka Univ.)  
 OHNISHI Tetsuya 大西哲哉 (Fac. Sci., Univ. Tokyo)  
 OHYAMA Takuya 大山拓也 (Fac. Sci., Shizuoka Univ.)  
 OZAWA Shuichi 小澤修一 (Coll. Sci., Rikkyo Univ.)  
 SEKIGUCHI Kimiko 関口仁子 (Dept. Phys., Grad. Sch. Sci., Univ. Tokyo)  
 SHIOBARA Yamato 塩原大和 (Fac. Pharm. Sci., Chiba Univ.)  
 TAKINO Toshikazu 滝野俊和 (Kyoto Pharm. Univ.)  
 UCHIYAMA Koji 内山浩志 (Inst. Phys., Univ. Tsukuba)  
 XIAO Meiqin 肖美琴 (Cen. Nucl. Study, Grad. Sch. Sci., Univ. Tokyo)  
 YOSHIDA Shozo 吉田昭三 (Nara Med. Univ.)  
 YOSHIDA Tsutomu 吉田努 (Fac. Sci., Shizuoka Univ.)

### **Beam Technology Division**

#### *Head*

YANO Yasushige 矢野安重

#### *Members*

FUJIMAKI Masaki 藤卷正樹	FUJITA Jiro 藤田二郎
FUJITA Shin 藤田新	GOTO Akira 後藤彰
IKEZAWA Eiji 池沢英二	ITO Sachiko 伊藤祥子
KAGEYAMA Masashi 影山正	KASE Masayuki 加瀬昌之
KIMURA Kazuie 木村一宇	KOHARA Shigeo 小原重夫

MAEDA Kuniko 前田邦子  
NAGASE Makoto 長瀬 誠  
NAKAJIMA Shunji 中島 諄二  
USHIDA Kiminori 丑田公規  
YAMAJI Shuhei 山路修平

MORITA Kosuke 森田浩介  
NAKAGAWA Takahide 中川孝秀  
OGIWARA Kiyoshi 荻原清  
WADA Takeshi 和田雄  
YOKOYAMA Ichiro 横山一郎

*Visiting Members and Postdoctoral Fellows*

ABE Yasuhisa 阿部恭久 (Yukawa Inst. Theor. Phys., Kyoto Univ.)  
ABURAYA Takashi 油谷崇志 (NASDA)  
ANZAWA Osamu 安沢 修 (NASDA)  
AOKI Jiro 青木司郎 (NASDA)  
AOYAMA Kazuhiro 青山和広 (NASDA)  
ARIMA Akito 有馬朗人 (Former President, RIKEN)  
ARITOMO Yoshihiro 有友嘉浩 (J.I.N.R., Dubna, Russia)  
BABA Shinji 馬場信次 (NASDA)  
BAN Syuichi 伴 秀一 (KEK)  
BHATTACHARYA Sankar (Variable Energy Cycl. Cen., India)  
CHAKRABARTI Alok (Variable Energy Cycl. Cen., India)  
DATE Schin 伊達 伸 (JASRI)  
DENISOV Vitali (J.I.N.R., Dubna, Russia)  
EJIRI Hiroyasu 江尻宏泰 (RCNP, Osaka Univ.)  
FUJIOKA Manabu 藤岡 学 (Cycl. Radioisot. Cen., Tohoku Univ.)  
FUJITA Yoshitaka 藤田佳孝 (Fac. Sci., Osaka Univ.)  
FUJIWARA Ichiro 藤原一郎 (Dept. Economy, Otomon Gakuin)  
FUJIWARA Mamoru 藤原 守 (RCNP, Osaka Univ.)  
FURUNO Kohei 古野興平 (Inst. Phys., Univ. Tsukuba)  
FURUSE Kaoru 古瀬 馨 (NASDA)  
FUTAMI Yasuyuki 二見康之 (N.I.R.S.)  
GOKA Tateo 五家建夫 (NASDA)  
HAMA Hiroyuki 浜 広幸 (I.M.S.)  
HARADA Toru 原田 融 (Fac. Social Inf., Sapporo Gakuin Univ.)  
HASHIMOTO Osamu 橋本 治 (Fac. Sci., Tohoku Univ.)  
HATANAKA Kichiji 畑中吉治 (RCNP, Osaka Univ.)  
HATSUKAWA Yuichi 初川雄一 (JAERI, Tokai Res. Estab.)  
HATTORI Toshiyuki 服部俊幸 (Res. Lab. Nucl. React., T.I.T.)  
HAYANO Ryugo S. 早野龍五 (Fac. Sci., Univ. Tokyo)  
HIEDA Kohtaro 檜枝光太郎 (Coll. Sci., Rikkyo Univ.)  
HIGUCHI Tatsuro 樋口達郎 (NASDA)  
HIRAO Yasuo 平尾泰男 (N.I.R.S.)  
HIROSE Takayuki 広瀬孝幸 (NASDA)  
HONMA Michio 本間道雄 (Cen. Mathe. Sci., Univ. Aizu)  
HORIBATA Takatoshi 堀端孝俊 (Fac. Eng., Aomori Univ.)  
HORIGUCHI Takayoshi 堀口隆良 (Dept. Clinical Rad., Hiroshima Int. Univ.)  
HORIUCHI Hisashi 堀内 昶 (Grad. Sch. Sci., Kyoto Univ.)  
HOSONO Kazuhiko 細野和彦 (Dept. Eng. Sci., Himeji Inst. Tech.)  
HYODO Toshio 兵頭俊夫 (Grad. Sch. Arts Sci., Univ. Tokyo)  
IDESAWA Masanori 出澤正徳 (Univ. Electro-Commun.)  
IGARASHI Toshio 五十嵐敏雄 (NASDA)  
IKEDA Akitsu 池田秋津 (Shizuoka Inst. Sci. Tech.)  
IKEDA Nobuo 池田伸夫 (Fac. Sci., Kyushu Univ.)  
IKEZOE Hiroshi 池添 博 (JAERI, Tokai Res. Estab.)  
IMAI Kenichi 今井憲一 (Fac. Sci., Kyoto Univ.)  
IMAMURA Mineo 今村峯雄 (National Museum of Japanese History)  
INOUE Makoto 井上 信 (Res. Reactor Inst., Kyoto Univ.)  
ISHIZUKA Takeo 石塚武男 (Fac. Sci., Saitama Univ.)  
ITO Yasuo 伊藤泰男 (Atomic Energy Res. Cen., Univ. Tokyo)  
ITOH Kazuya 伊藤和也 (Tandem Accel. Cen., Univ. Tsukuba)

ITOH Yoshiko 伊東芳子 (Adv. Res. Inst. Sci. Eng., Waseda Univ.)  
 ITOH Yutaka 伊藤寛 (KEK)  
 IVANYUK Fedir (Inst. Nucl. Res., Ukraine)  
 IWAI Satoshi 岩井敏 (Nuclear Development Co., Ltd)  
 IWAMOTO Akira 岩本昭 (JAERI, Tokai Res. Estab.)  
 IWASHITA Yoshihisa 岩下芳久 (Inst. Chem. Res., Kyoto Univ.)  
 IWATA Ren 岩田錬 (Cycl. Radioisot. Cen., Tohoku Univ.)  
 IZUMOTO Toshiaki 泉本利章 (Coll. Tourism., Rikkyo Univ.)  
 JEONG S. C. 鄭淳讚 (KEK)  
 KAMIMURA Masayasu 上村正康 (Fac. Sci., Kyushu Univ.)  
 KANAZAWA Mitsutaka 金沢光隆 (N.I.R.S.)  
 KANEKO Junichi 金子純一 (JAERI, Takasaki Rad. Chem. Res. Estab.)  
 KATO Kiyoshi 加藤幾芳 (Fac. Sci., Hokkaido Univ.)  
 KATSURAGAWA Hidetsugu 桂川秀嗣 (Fac. Sci., Toho Univ.)  
 KAWAZU Akira 河津璋 (Techno Riken Co., Ltd.)  
 KIM Eun Joo (Fac. Eng., Tohoku Univ.)  
 KIM Jaehong  
 KOBAYASHI-KOMIYAMA Misaki 込山美咲  
 KUBOYAMA Satoshi 久保山智司 (NASDA)  
 KUDO Hisaaki 工藤久昭 (Fac. Sci., Niigata Univ.)  
 KUMADA Masayuki 熊田雅之 (N.I.R.S.)  
 KURIHARA Toshikazu 栗原俊一 (KEK)  
 LEE San-Mu 李相茂 (Inst. Phys., Univ. Tsukuba)  
 LI Hongling (RCAST, Univ. Tokyo)  
 MATSUDA Sumio 松田純夫 (NASDA)  
 MATSUKI Seishi 松木征史 (Inst. Chem. Res., Kyoto Univ.)  
 MATSUMOTO Akihiro 松本暁洋 (NASDA)  
 MATSUSE Takehiro 松瀬丈浩 (Fac. Textile Sci. Tech., Shinshu Univ.)  
 MATSUYANAGI Kenichi 松柳研一 (Grad. Sch. Sci., Kyoto Univ.)  
 MATSUZAKI Kazuhiro 松崎一浩 (NASDA)  
 MATSUZAKI Masayuki 松崎昌之 (Fac. Ed., Fukuoka Univ.)  
 MENG Jie (Peking Univ., China)  
 MINAMISONO Tadanori 南園忠則 (Grad. Sch. Sci., Osaka Univ.)  
 MIYATAKE Hiroari 宮武宇也 (KEK)  
 MIZUNO Yoshiyuki 水野義之 (RCNP, Osaka Univ.)  
 MIZUSAKI Takahiro 水崎高浩 (Fac. Sci., Univ. Tokyo)  
 MORI Yoshiharu 森義治 (KEK)  
 MUKHOPADHYAY Tapan (Variable Energy Cycl. Cen., India)  
 MURAKAMI Hideoki 村上英興 (Fac. Ed., Tokyo Gakugei Univ.)  
 MURAKAMI Tetsuya 村上哲也 (Grad. Sch. Sci., Kyoto Univ.)  
 MUTA Atsushi 牟田淳 (Inst. Phys., Univ. Tsukuba)  
 MUTO Kazuo 武藤一雄 (Fac. Sci., T.I.T.)  
 NAGAI Yasuki 永井泰樹 (RCNP, Osaka Univ.)  
 NAGAI Yuki 永井由紀 (NASDA)  
 NAGASHIMA Yasuyuki 長嶋泰之 (Grad. Sch. Arts Sci., Univ. Tokyo)  
 NAKADA Hitoshi 中田仁 (Fac. Sci., Chiba Univ.)  
 NAKAJIMA Hiroshi 中島宏 (JAERI, Takasaki Rad. Chem. Res. Estab.)  
 NAKAMURA Hiroyuki 中村裕之 (Kitakyushu Natl. Coll. Technol.)  
 NAKAMURA Ichiro 中村市郎 (Fac. Sci., Saitama Univ.)  
 NAKAMURA Takashi 中村尚司 (Cycl. Radioisot. Cen., Tohoku Univ.)  
 NAKAO Noriaki 中尾徳晶 (KEK)  
 NEMOTO Norio 根本規生 (NASDA)  
 NODA Akira 野田章 (Inst. Chem. Res., Kyoto Univ.)  
 NOMURA Toru 野村亨 (KEK, Tanashi)  
 NOZAKI Tadashi 野崎正 (Purex Co.)  
 OGAWA Kengo 小川建吾 (Fac. Sci., Chiba Univ.)  
 OHIRA Hideharu 大平秀春 (NASDA)

OHTA Kiyoshi 太田 清 (Fac. Sci., Saitama Univ.)  
 OHTSUKI Tsutomu 大槻 勤 (Lab. Nucl. Sci., Tohoku Univ.)  
 OHYA Jiro 大矢次郎 (NASDA)  
 OI Makito 大井万紀人 (Dept. Phys., Grad. Sch. Sci., Univ. Tokyo)  
 OKAMOTO Hiromi 岡本宏巳 (Grad. Sch. Adv. Sci. Matter, Hiroshima Univ.)  
 OKAMURA Hiroyuki 岡村弘之 (Fac. Sci., Saitama Univ.)  
 ONISHI Naoki 大西直毅 (Fac. Eng., Yamanashi Univ.)  
 OOTOMO Hiromitsu 大友洋光 (NASDA)  
 OTSUKA Takaharu 大塚孝治 (Fac. Sci., Univ. Tokyo)  
 SAGARA Kenshi 相良建至 (Fac. Sci., Kyushu Univ.)  
 SAITO Motozo 齋藤始三  
 SAKAI Hideyuki 酒井英行 (Dept. Phys., Grad. Sch. Sci., Univ. Tokyo)  
 SATO Ken-ichi 佐藤憲一 (Dept. Phys., Tohoku Coll. Pharm.)  
 SATO Kenji 佐藤健次 (RCNP, Osaka Univ.)  
 SATO Osamu 佐藤理 (Mitsubishi Res. Inst., Inc.)  
 SATO Yukio 佐藤幸夫 (N.I.R.S.)  
 SEKINE Toshiaki 関根俊明 (JAERI, Takasaki Rad. Chem. Res. Estab.)  
 SHARMA Sumit (Pune Univ., India)  
 SHENG Yeng Ching (Shanghai Inst. Nucl. Res., China)  
 SHIBATA Tokushi 柴田徳思 (KEK)  
 SHIMADA Osamu 島田修 (NASDA)  
 SHIMIZU Akira 清水昭 (RCNP, Osaka Univ.)  
 SHIMOMURA Koichiro 下村浩一郎 (KEK)  
 SHIN Kazuo 秦和夫 (Fac. Eng., Kyoto Univ.)  
 SHINDO Hiroyuki 新藤浩之 (NASDA)  
 SHINOZUKA Tsutomu 篠塚勉 (Cycl. Radioisot. Cen., Tohoku Univ.)  
 SHIRAI Toshiyuki 白井敏之 (Inst. Chem. Res., Kyoto Univ.)  
 SHUGYOU Shinichi 修行新一 (NASDA)  
 SUEKI Keisuke 末木啓介 (Fac. Sci., Tokyo Metrop. Univ.)  
 SUGAI Isao 菅井勲 (KEK)  
 SUGAWARA-TANABE Kazuko 田辺和子 (Otsuma Women's Coll.)  
 SUGIYAMA Hiroki 杉山大樹 (NASDA)  
 SUMIYOSHI Hiroyuki 住吉広行 (Matsusho-Gakuen Jr. Coll.)  
 SUZUKI Takahiro 鈴木隆博 (NASDA)  
 SUZUKI Toshio 鈴木俊夫 (Coll. Hum. Sci., Nihon Univ.)  
 SUZUKI Toshio 鈴木敏男 (Fac. Eng., Fukui Univ.)  
 SYRESSINE Evgueni (J.I.N.R., Dubna, Russia)  
 TAGISHI Yoshihiro 田岸義宏 (Inst. Phys., Univ. Tsukuba)  
 TAJIMA Naoki 田嶋直樹 (Fac. Eng., Fukui Univ.)  
 TAKADA Masashi 高田真志 (N.I.R.S.)  
 TAKADA Norio 高田憲生 (NASDA)  
 TAKAGI Syunji 高木俊治 (Mitsubishi Res. Inst., Inc.)  
 TAKAHASHI Takehide 高橋丈英 (NASDA)  
 TAKEMASA Tadashi 武政尹士 (Kyoto Univ. Ed.)  
 TAKIGAWA Noboru 滝川昇 (Fac. Sci., Tohoku Univ.)  
 TAKIZAWA Yoshiyuki 滝澤慶之  
 TANABE Kosai 田辺孝哉 (Fac. Sci., Saitama Univ.)  
 TANAKA Jinichi 田中仁市 (KEK)  
 TANAKA Kazuhiro 田中和廣 (Dept. Phys., Sch. Med., Jyuntendo Univ.)  
 TANIKAWA Masashi 谷川勝至 (Fac. Sci., Univ. Tokyo)  
 TEZUKA Hirokazu 手塚洋一 (Dept. Liberal Arts, Fac. Literature, Toyo Univ.)  
 TOHYAMA Mitsuru 遠山満 (Kyorin Univ.)  
 TOMITANI Takehiro 富谷武浩 (N.I.R.S.)  
 TOMODA Toshiaki 友田敏章 (Fac. Eng., Aomori Univ.)  
 TORIYAMA Tamotsu 鳥山保 (Dept. Phys., Musashi Inst. Technol.)  
 TOYOKAWA Hiroyuki 豊川弘之 (Electrotechnical Lab., Agency Ind. Sci. Tech.)  
 TSUBAKI Noriyuki 椿則幸 (NASDA)

UEHARA Takashi 上原 丘 (Nuclear Development Co., Ltd.)  
URITANI Akira 瓜谷 章 (Dept. Phys., Grad. Sch. Sci., Nagoya Univ.)  
UTSUNOMIYA Hiroaki 宇都宮弘章 (Fac. Sci., Konan Univ.)  
VUONG Kim-Au (Inst. Physics-Hanoi-Vietnam, Vietnam)  
WADA Ryoichi 和田良一 (Texas A & M Univ., USA)  
WADA Takahiro 和田隆宏 (Fac. Sci., Konan Univ.)  
WAKAI Masamiti 若井正道 (Grad. Sch. Sci., Osaka Univ.)  
YABANA Kazuhiro 矢花一浩 (Fac. Sci., Niigata Univ.)  
YAMAZAKI Hirohito 山崎寛仁 (Lab. Nucl. Sci., Tohoku Univ.)  
YOSHIDA Nobuaki 吉田宣章 (Fac. Informatics, Kansai Univ.)  
YOSHINAGA Naotaka 吉永尚孝 (Fac. Sci., Saitama Univ.)  
YOSHIOKA Yasuhiro 吉岡康弘 (NASDA)  
ZHAO Yuliang (Fac. Sci., Tokyo Metrop. Univ.)  
ZHAO Yu Min  
ZHOU Shan-Gui (Peking Univ., China)

#### *Trainees*

AOKI Yuka 青木由香 (Fac. Sci., Tohoku Univ.)  
ARIGA Takehiro 有賀健博 (Fac. Sci., Toho Univ.)  
FUJISAKI Takashi 藤崎貴之 (Coll. Sci., Rikkyo Univ.)  
FUJITA Tatsuru 藤田 建 (Fac. Sci., Kyushu Univ.)  
HARUYAMA Seigo 春山征吾 (Dept. Phys., Grad. Sch. Sci., Univ. Tokyo)  
HIGURASHI Yoshihide 日暮祥英 (Coll. Sci., Rikkyo Univ.)  
IWASE Hiroshi 岩瀬 広 (Fac. Sci., Tohoku Univ.)  
KIM Eun Joo (Fac. Eng., Tohoku Univ.)  
KOBORI Tomohiro 小堀智弘 (Fac. Sci., Saitama Univ.)  
KURITA Tetsuro 栗田哲郎 (Inst. Phys., Univ. Tsukuba)  
KUROSAWA Tadahiro 黒澤忠弘 (Grad. Sch. Sci., Tohoku Univ.)  
NISHIKAWA Jun 西川 純 (Fac. Sci., Saitama Univ.)  
NUNOMIYA Tomoya 布宮智也 (Fac. Sci., Tohoku Univ.)  
OHNISHI Tetsuya 大西哲哉 (Fac. Sci., Univ. Tokyo)  
OKAMOTO Tomoko 岡本知子 (Fac. Sci. Tech., Sci. Univ. Tokyo)  
OKUDA Hikaru 奥田 光 (Fac. Sci., Kyushu Univ.)  
OZAWA Shuichi 小澤修一 (Coll. Sci., Rikkyo Univ.)  
SASAKI Michiya 佐々木道也 (Grad. Sch. Sci., Tohoku Univ.)  
SATO Hisaki 佐藤寿樹 (Fac. Eng., Tohoku Univ.)  
SEKIGUCHI Kimiko 関口仁子 (Dept. Phys., Grad. Sch. Sci., Univ. Tokyo)  
SHIOMI Tomoyuki 潮見大志 (Fac. Eng., Tohoku Univ.)  
SUDA Kenji 須田健嗣 (Fac. Sci., Saitama Univ.)  
TAGAYA Yu 多加谷 祐 (Fac. Sci., Univ. Tokyo)  
TANIGUCHI Shingo 谷口真吾 (Grad. Sch. Sci., Tohoku Univ.)  
TOKUNAGA Youji 徳永洋治 (Grad. Sch. Eng., Osaka Univ.)  
TSURUTA Kaoru 鶴田 薫 (Interdisciplinary Grad. Sch. Eng. Sci., Kyushu Univ.)  
UCHIYAMA Koji 内山浩志 (Inst. Phys., Univ. Tsukuba)  
UTSUNO Yutaka 宇都野 穰 (Fac. Sci., Univ. Tokyo)  
WAKUI Takashi 涌井崇志 (Fac. Sci., Tohoku Univ.)  
XIAO Meiqin (Cen. Nucl. Study, Grad. Sch. Sci., Univ. Tokyo)  
YAGITA Takanori 八木田貴典 (Interdisciplinary Grad. Sch. Eng. Sci., Kyushu Univ.)  
YAMAMOTO Sumiko 山本純子 (Fac. Sci., Toho Univ.)  
YASHIMA Hiroshi 八島 浩 (Fac. Eng., Tohoku Univ.)

### **Radioisotope Technology Division**

#### *Head*

YATAGAI Fumio 谷田貝文夫

*Visiting Members and Postdoctoral Fellows*

ENOMOTO Shuichi 榎本秀一  
GORDON Alasdair  
HIRUNUMA Rieko 蛭沼利江子  
KAGAWA Yasuhiro 香川康浩 (Toray Res. Cen. Inc.)  
KATO Takesi 加藤武司  
KAWAMURA Yoshihiro 川村昌寛  
MAEZAWA Hiroshi 前澤博 (Fac. Med. Technol., Tokushima Univ.)  
MORIMOTO Shigeko 森本茂子  
OGURA Koichi 小倉紘一 (Coll. Ind. Technol., Nihon Univ.)  
OZAKI Takuo 尾崎卓郎  
TAMANO Haruna 玉野春南  
YANAGIYA Takahiro 柳谷隆宏

*Trainees*

INOUE Kensuke 井上憲介 (Fac. Sci. Eng., Waseda Univ.)  
KITO Masatoshi 鬼頭昌利 (Fac. Sci. Eng., Waseda Univ.)  
KUROBE Toshihiro 黒部利博 (Fac. Sci. Eng., Waseda Univ.)  
OKA Toshitaka 岡壽崇 (Fac. Sci. Eng., Waseda Univ.)

**ADVANCED ENGINEERING CENTER**

**Research Instruments Development Division**

*Head*

SENOO Katsumi 妹尾克己

*Members*

IKEGAMI Yuji 池上祐司	KITSUNAI Tokuji 橋内徳司
NOMIYA Yoshio 野宮芳雄	SHIGA Tsunenobu 志賀常信
SHIMODA Susumu 霜田進	SHIRAISHI Akira 白石明
SUGAHARA Seigo 菅原正吾	TAJIMA Norio 田島典夫
TAKAHASHI Norikazu 高橋則一	URAI Teruo 浦井輝夫
WATANABE Tokuji 渡辺徳治	YAMADA Shogo 山田正吾
YAMADA Yutaka 山田豊	

*Contracting Members*

KANEKO Naoe 金子直恵  
KUBO Ushizo 久保丑蔵  
MATSUMOTO Akira 松本昭  
NIIOKA Yuzo 新岡勇三  
SASAMOTO Tetsuji 笹本哲司  
TAKAHASHI Kiyoji 高橋清二  
TOKIWA Saburo 常盤三郎  
YAMAMOTO Sumio 山本澄雄

**CHARACTERIZATION CENTER**

**Surface Characterization Division**

*Head*

IWAKI Masaya 岩木正哉

*Members*

NAKAO Aiko 中尾愛子	WATANABE Kowashi 渡辺剛
YAGI Ei-ichi 八木栄一	

*Visiting Members and Postdoctoral Fellows*  
KOBAYASHI Tomohiro 小林知洋

## ADVANCED COMPUTING CENTER

### Computational Science Division

*Head*

EBISUZAKI Toshikazu 戎崎俊一

*Members*

IITAKA Toshiaki 飯高敏晃

SUNOUCHI Kei 洲之内 啓

*Visiting Members and Postdoctoral Fellows*

MAKINO Yuko 牧野祐子

MIURA Hitoshi 三浦均

SHIMIZU Tetsuya 清水鉄也

## BIOGENIC RESOURCES CENTER

### Experimental Animal Research Division

*Head*

KUSAKABE Moriaki 日下部守昭

*Members*

HIRAIWA Noriko 平岩典子

TSUKADA Teruyo 塚田晃代

IKE Fumio 池 郁生

YOSHIKI Atsush 吉木 淳

*Visiting Members and Postdoctoral Fellows*

KOGISO Aya 小木曾 彩

KOJIMA Masayo 小島雅代

KUBOTA Yukihiko 久保田幸彦

NORO Chikako 野呂知加子

POIRIER Christophe

YAMAGUCHI Hirotake 山口弘毅

YAMANOUCHI Jyun 山之内 淳

YODA Yoshika 依田賀香 (Japan Sci. Technol. Corp.)

## Safety Center

*Members*

CHIBA Shigeo 千葉茂夫

HARASAWA Kaoru 原沢 薫

MATSUZAWA Yasuhide 松澤安秀

SHINOHARA Shigemi 篠原茂己

YOSHIKI Hajime 吉識 肇

FUKAZAWA Kunio 深沢国雄

KAGAYA Satoru 加賀屋 悟

MIYAGAWA Makoto 宮川真言

UWAMINO Yoshitomo 上 袁義朋

## AUTHOR INDEX

- ABE Ryo 阿部 亮 4  
 ABE Tomoko 阿部知子 139, 140, 141  
 AIHARA Toshimitsu 藍原利光 6  
 AKAGI Hiroyasu 赤木宏安 4  
 AKIMOTO Keiji 秋本圭司 161  
 AKIYAMA Kazuhiko 秋山和彦 129  
 AKIYOSHI Hiromichi 秋吉啓充 60, 63, 65, 66, 67  
 AKOSHIMA Megumi 阿子島めぐみ 101  
 ALEKSEEV Igor 41, 170  
 ALLGOWER Chris 43  
 AMANO Ryohei 天野良平 120, 128  
 AMBE Fumitoshi 安部文敏 93, 109, 129  
 AMBE Shizuko 安部静子 129  
 ANDO Kozo 安藤剛三 81, 82, 83  
 ANDO Yoshiaki 安藤嘉章 60, 63, 65, 66  
 ANSARI Ahmad 22, 27  
 AOI Nori 青井 考 63, 65, 66, 67, 68, 69, 70  
 AOKI Yuka 青木由香 57, 58  
 AOYAGI Shigenori 青柳重徳 161  
 ARIE Tsutomu 有江 力 138  
 ARIGA Takehiro 有賀健博 80  
 ARIMA Akito 有馬朗人 13, 18, 20, 22, 23, 24  
 AWAGA Kunio 阿波賀邦夫 104  
 AWES Terry 41, 168  
 AZUMA Toshiyuki 東 俊行 78  
 BAI Mei 41, 43, 170  
 BAKULE Pavel 263  
 BASSALLECK Bernd 41, 170  
 BATHE Stefan 41, 168  
 BATURINE Vitaly 43  
 BAZILEVSKY Alexander 41, 44  
 BELIKOV Nikolai 43  
 BENTZ Wolfgang 39  
 BHATTACHARJEE Sudeep 200  
 BOCHKAREV Oleg 74  
 BORDEANU Cristina 72  
 BOYD Richard N. 72  
 BREHMER Sven 100  
 BROOKS Melynda L. 41, 165  
 BROWN B. Alex 16  
 BUCHER Damian 41, 168  
 BUESCHING Henner 41, 168  
 BUNCE Gerry 41, 43, 170  
 CHIBA Toshiya 千葉利哉 197, 206, 210, 212, 224  
 CHIBA Yoshiaki 千葉好明 251  
 CHIMI Yasuhiro 知見康弘 87, 89  
 CHULKOV Leonid 74  
 CIANCIOLO Vince 41, 166  
 CORTINA Dolores 74  
 DEREVSCHIKOV Anatoly 43  
 DESHPANDE Abhay 41, 170  
 DIAO Xungang 90, 93, 94  
 DIEHL Roland 32  
 DINH DANG Nguyen 廷燈 阮 20, 21, 22, 23, 24  
 DO DANG Giu 25  
 DOSKOW Jack 41, 170  
 DUMITRIU Dana 255  
 EATON Gordon H. 51  
 ECCLESTON Roger S. 100  
 EGUCHI-KASAI Kiyomi 江口-笠井清美 145  
 EILERTS Scott 41, 170  
 EISENMAN Kaury 21  
 EN'YO Hideto 延與秀人 41, 43, 44, 166, 168, 172  
 ENDO Kazutoyo 遠藤和豊 114, 116  
 ENOMOTO Shuichi 榎本秀一 111, 112, 113, 114, 116,  
 117, 118, 119, 120, 121,  
 122, 123, 125, 127, 128,  
 129, 130, 193  
 FIELDS Douglas E. 41, 170  
 FUGONO Jun 畚野 純 113  
 FUJIMAKI Masaki 藤卷正樹 6, 193  
 FUJISHIMA Shiro 藤島史郎 212, 218, 220, 230  
 FUJITA Jiro 藤田二郎 4  
 FUJITA Shin 藤田 新 265, 266  
 FUJIWARA Atsushi 藤原篤史 265, 266  
 FUJIWARA Hideki 藤原英樹 60  
 FUKAYA Atsuko 深谷敦子 105  
 FUKUDA Naoki 福田直樹 60, 68, 69, 70, 163  
 FUKUNISHI Nobuhisa 福西暢尚 131, 142, 148, 230, 243  
 FUKUSAKA Shoichi 福坂将一 53, 54, 56  
 FÜLÖP Zsolt 60, 63, 65, 66, 67, 68, 72  
 FURUNO Kohei 古野興平 73  
 FURUSAWA Yoshiya 古澤佳也 144  
 FUTAKAMI Udai 二上宇内 68, 69, 70  
 GACSI Zoltan 68, 69, 70  
 GEISSEL Hans 74  
 GHAZIKHANIAN Vahe 43  
 GOKA Tateo 五家建夫 177, 178  
 GOLOVKOV Mikhail 72  
 GOMI Tomoko 五味朋子 60, 63, 65, 66, 67, 68, 69, 70  
 GONO Yasuyuki 郷農靖之 130  
 GORDON Alasdair 131, 142  
 GOSWAMI Ransana 72  
 GOTO Akira 後藤 彰 4, 151, 152, 193, 197, 200, 206,

- 208, 210, 212, 214, 216, 218,  
220, 222, 224, 226, 228, 230
- GOTO Yuji 後藤雄二 33, 41, 43, 44, 168, 170, 172
- GROSSE PERDEKAMP Matthias 43
- GUNJI Shuichi 郡司修一 158
- HACKE Marcus 97
- HAHN Kevin Inshik 60
- HAMA Yoshimasa 浜 義昌 147
- HAMADA Akira 浜田 亮 76
- HAMAGAKI Hideki 浜垣秀樹 41, 172
- HAMANAKA Hiromi 浜中廣見 183
- HANAOKA Fumio 花岡文雄 131, 142, 146
- HARA Yasuhide 原 靖英 141
- HARUYAMA Seigo 春山征吾 10, 174
- HASEBE Hiroo 長谷部裕雄 6
- HASEGAWA Kenichi 長谷川賢一 183
- HATANAKA Kichiji 畑中吉治 56
- HATANO Michio 波田野道夫 53, 154, 182
- HATTORI Toshiyuki 服部俊幸 202
- HAYAKAWA Kazuo 早川一生 90, 93, 94, 109
- HAYASHI Naoki 林 直樹 33, 41, 43, 44, 46, 166, 172
- HELLSTRÖM Margaret 74
- HEMMI Masatake 逸見政武 197, 206
- HIASA Toshikazu 日朝俊一 208
- HIGEMOTO Wataru 髭本 亘 49, 102, 103
- HIGUCHI Hiroyoshi 樋口広芳 185
- HIGURASHI Yoshihide 日暮祥英 60, 63, 65, 66, 67, 68,  
69, 70, 197
- HILLEBRANDT Wolfgang 32
- HIMENO Seiichiro 姫野誠一郎 119
- HIRAI Masaaki 平井正明 60, 63, 65, 66
- HIRAI Masanori 平井正紀 33
- HIRAIWA Noriko 平岩典子 148
- HIRATA Kazuto 平田和人 102
- HIROSE Takayuki 広瀬孝幸 91
- HIROSE Toshiro 広瀬敏朗 161
- HIRUMACHI Tamiko 蛭町多美子 238
- HIRUNUMA Rieko 蛭沼利江子 111, 113, 114, 116, 117,  
118, 121
- HISANAGA Isamu 久永 勇 60
- HOMMA Takayuki 本間隆之 4
- HONMA Michio 本間道雄 15, 16, 17, 174
- HORIBATA Takatoshi 堀端孝俊 27
- HORIKAWA Hirotugu 堀川博嗣 33
- HOSHINO Masamitsu 星野正光 85
- HOTTA Tomohiro 堀田智洋 192
- HUANG Haixin 41, 43, 170
- HUGHES Vernon 41, 170
- HUI Qin 惠 秦 99
- HULDT Sven 81, 82, 83
- HUTTON Roger 81, 82, 83, 84
- HYODO Toshio 兵頭俊夫 95, 151, 152, 188
- ICHIHARA Takashi 市原 卓 41, 43, 56, 166, 172
- IEKI Kazuo 家城和夫 65
- IGARASHI Kaori 五十嵐香織 121
- IGO George 43
- IHARA Noriko 井原寛子 144
- IKE Fumio 池 郁夫 148
- IKEDA Hiroshi 池田 博 88, 187
- IKEDA Kiyomi 池田清美 11
- IKEGAMI Kumio 池上九三男 4, 208, 212, 222, 226, 228
- IKEZAWA Eiji 池沢英二 6, 193, 206
- IMAI Ken'ichi 今井憲一 41, 44, 166, 168, 170
- IMAI Nobuaki 今井伸明 63, 65, 67, 68, 69, 70
- IMURA Nobumasa 井村伸正 119
- INABE Naohito 稲辺尚人 4, 80, 249
- IPPOLITOV Mikhail 41, 168
- ISERI Yasunori 井芹康統 9
- ISHIDA Katsuhiko 石田勝彦 48, 49, 51, 107, 263
- ISHIDA Satoru 石田 悟 56
- ISHIDA Takayuki 石田尚行 106
- ISHIHARA Masayasu 石原正泰 41, 60, 63, 65, 66, 67,  
68, 69, 70, 166, 170
- ISHIKAWA Norito 石川法人 87, 88, 89
- ISHIKAWA Souichi 石川壮一 9
- ISHIZUKA Takeo 石塚武男 161
- ISSHIKI Hiroshi 一色 博 4
- ITAGAKI Naoyuki 板垣直之 11
- ITO Hisao 伊東久夫 144
- ITO Sachiko 伊藤祥子 243, 265, 266
- ITO Takaomi 伊藤高臣 78
- ITOH Akio 伊藤秋男 79
- ITOH Kazuya S. 伊藤和也 9, 53, 54, 55, 56, 153
- ITOH Yoshiko 伊東芳子 95, 151, 152
- ITSUKAICHI Hiromi 五日市ひろみ 145
- IVANOV Marian 74
- IWAI Yoshio 岩井良夫 84
- IWAKI Masaya 岩木正哉 186
- IWAMA Motonori 岩間基訓 118
- IWASA Naohito 岩佐直仁 59, 60, 63, 65, 66, 67, 68, 69,  
70
- IWASAKI Hironori 岩崎弘典 60, 63, 65, 66, 67, 68, 69,  
70
- IWASAKI Masahiko 岩崎雅彦 48
- IWASE Akihiro 岩瀬彰宏 87, 88, 89, 90, 187
- IWATA Yoshiyuki 岩田佳之 60, 63, 65, 66, 67
- JANIK Rudo 74
- JANKA Hans-Thomas 32

- JOH Tetsuo 城 哲男 97
- KADONO Ryosuke 門野良典 102
- KAGEYAMA Kensuke 蔭山健介 86
- KAGEYAMA Tadashi 影山 正 4, 197
- KAJI Masahiro 梶 正弘 204
- KAJINO Toshitaka 梶野敏貴 29
- KAMBARA Tadashi 神原 正 78, 79, 86, 87, 88, 89, 90,  
187, 199, 203, 255
- KAMIGAITO Osamu 上垣外修一 4, 193, 206, 208, 210,  
212, 224
- KANAI Tatsuki 金井達明 144, 145
- KANAI Yasuyuki 金井保之 78, 84, 85, 86, 199, 255
- KANAVETS Vadim 41, 170
- KANAZAWA Mitsutaka 金沢光隆 249
- KANEKO Junichi 金子純一 133, 134, 135
- KANUNGO Rituparna 59
- KASAGI Jirohta 笠木治郎太 57, 58
- KASE Masayuki 加瀬昌之 4, 6, 80, 91, 148, 193, 197,  
200, 204, 206, 208, 212,  
230, 257, 265, 266
- KASPRZYK Thomas 43
- KATAYAMA Ichirou 片山一郎 180
- KATAYAMA Takeshi 片山武司 202, 245, 247, 249, 253,  
259
- KATO Hiromitsu 加藤裕充 53, 54, 154
- KATO Hiroshi 加藤 博 177, 178
- KATO Mineo 加藤岑生 51
- KATO Tomomi 加藤智美 176
- KATO Toshiyuki 加藤俊幸 59, 72, 158
- KATORI Kenji 鹿取謙二 59, 61
- KATSUMATA Koichi 勝又紘一 100
- KAWAGUCHI Osamu 川口 修 144
- KAWAGUCHI Takeo 川口武男 149, 212, 214, 220, 222
- KAWAKAMI Hirokane 川上宏金 180
- KAWAMURA Naritoshi 河村成肇 51, 263
- KAWAMURA Yoshihiro 川村昌寛 111, 123, 125, 128
- KAWATA Tetsuya 川田哲也 144
- KIDERA Masanori 木寺正憲 4, 193, 197
- KIJIMA Takeshi 鬼島 丈 60
- KIKUCHI Koichi 菊地耕一 129
- KIM Jae Hong 金 宰弘 95, 151, 152
- KIM Jong-Won 金 鍾元 212, 216, 220
- KIM Seyong 金 世容 191
- KIMURA Kazuie 木村一宇 133, 134, 135
- KIMURA Kikuo 木村喜久雄 72, 74, 176
- KIMURA Mineo 季村峯生 76
- KIMURA Shuichi 木村修一 121
- KISTENEV Edouard 41, 168
- KITAJIMA Masashi 北島昌史 85
- KITANO Takahiro 北野高寛 125
- KITAO Kensuke 喜多尾憲助 195
- KITAURA Takeo 北浦健生 141
- KOBAYASHI Hiroshi 小林 寛 63, 65, 66, 67
- KOBAYASHI Kiyoshi 小林清志 4
- KOBAYASHI Toshio 小林俊雄 74
- KOBAYASHI Yoshio 小林義男 93, 94, 109
- KOBAYASHI-KOMIYAMA Misaki 小林-込山美咲 4,  
204
- KOCHELEV Nikolai I. 35
- KOGA Kiyokazu 古賀清一 178
- KOHAMA Akihisa 小濱洋央 13
- KOHARA Shigeo 小原重夫 4, 6, 206
- KOIKE Yoji 小池洋二 101
- KOJIMA Takao M. 小島隆夫 78, 86, 255
- KOMAKI Ken-ichiro 小牧研一郎 78
- KONDO Yasuhiro 近藤恭弘 43
- KONDO Yukihiro 近藤幸尋 119
- KONDRASHEV Sergei 202
- KORSHENINNIKOV Alexei A. 74
- KOSHIISHI Hideki 越石英樹 177
- KOTCHENDA Leonid 41, 166
- KRASZNAHORKAY Attila 72
- KRUEGER Keith 43
- KUBO Atsushi 久保敦司 144
- KUBO Toshiyuki 久保敏幸 68, 69, 70, 230, 232, 234,  
236, 238, 241
- KUBONO Shigeru 久保野 茂 60
- KUBOYAMA Satoshi 久保山智司 91
- KUDO Hisaaki 工藤久昭 59, 72
- KUDO Katsuhisa 工藤勝久 51
- KUMAGAI Hidekazu 熊谷秀和 163
- KUMAGAI Hiroshi 熊谷 宏 122
- KUMANO Shunzo 熊野俊三 33, 38
- KUMATA Yukio 熊田幸生 208
- KUNIBU Makoto 國分 誠 68, 69, 70
- KURASAWA Haruki 倉沢治樹 19
- KURATA-NISHIMURA Mizuki 西村美月 159
- KURIHARA Toshikazu 栗原俊一 151, 152
- KURITA Kazuyoshi 栗田和好 41, 44, 46, 166, 170
- KURITA Tetsuro 栗田哲郎 149
- KUROBE Toshihiro 黒部利博 131, 142
- KURODA Naoshi 黒田直志 87, 88, 89, 187
- KURODA Shinji 黒田眞司 103
- KUROKAWA Meiko 黒川明子 63, 65, 66, 67, 68, 69, 70
- KUROSAWA Kiyoyuki 黒沢清行 51
- KUSAKA Kensuke 日下健祐 230, 232, 236, 238
- KUSAKABE Moriaki 日下部守昭 148
- KWIATKOWSKI Kris 41, 170

- LEE David M. 41, 165  
 LEE Sang Moo 李 相茂 149  
 LEE Shyh-Yuan 43  
 LEWIS Benji 41, 170  
 LI Zihong 41, 166  
 LING Feng 凌 楓 139  
 LIU Zhong 刘 忠 63, 65, 66, 67, 68, 69, 70  
 LOZOWSKI Bill 41, 170  
 MADOKORO Hideki 間所秀樹 26  
 MAEDA Kuniko 前田邦子 183, 185  
 MAEDA Yukie 前田幸重 53, 54  
 MAIE Takeshi 真家武士 4  
 MAKDISI Yousef 41, 43, 170  
 MAO Yajun 冒 巫軍 41, 44, 46, 166  
 MARTINSON Indrek 81, 82, 83  
 MARUYAMA Ko-ichi 丸山浩一 52  
 MARUYAMA Tomoyuki 丸山智幸 241  
 MASON Gren 48  
 MASUDA Hideki 益田秀樹 84  
 MASUOKA Toshikatsu 益岡俊勝 257  
 MATSUDA Masaaki 松田雅昌 100  
 MATSUDA Sumio 松田純夫 91  
 MATSUDA Yasuyuki 松田恭幸 48, 49, 51, 263  
 MATSUMOTO Haruhisa 松本晴久 177, 178  
 MATSUMOTO Ken-ichiro 松本謙一郎 116  
 MATSUO Yukari 松尾由賀利 99  
 MATSUZAKI Masayuki 松崎昌之 26  
 MATSUZAKI Teichiro 松崎禎市郎 48, 49, 51, 107, 263  
 MATULENKO Yuri 43  
 MEHNATI Parinaz 146  
 MENG Jie 26  
 MEXNER Vanessa 41, 168  
 MEYER Haus-Otto 41, 170  
 MICHIKAMI Osamu 道上 修 87  
 MIKESKA Hans-Jürgen 100  
 MINAI Yoshitaka 藥袋佳孝 127  
 MINAMI Takeshi 南 武志 193  
 MINEMURA Toshiyuki 峯村俊行 60, 63, 65, 66, 67, 68, 69, 70  
 MINEO Hirofumi 峯尾浩文 39  
 MITSUMOTO Toshinori 密本俊典 208, 212, 214, 224, 230  
 MIYAGAI Mashu 宮外麻周 140  
 MIYAKE Yasuhiro 三宅康博 263  
 MIYAMA Masanori 深山正紀 33, 38  
 MIYASAKA Hiromasa 宮坂浩正 177, 178  
 MIYAZAWA Yoshitoshi 宮沢佳敏 197, 206, 208, 210, 212, 224  
 MIYOSHI Kazumitsu 三吉一光 141  
 MIZUNO Takeshi 水野 武 131  
 MIZUSAKI Takahiro 水崎高浩 10, 14, 15, 16, 17, 174  
 MOCHIKU Takashi 茂筑高士 102  
 MOCHIZUKI Yuko 望月優子 32, 72  
 MOHRI Akihiro 毛利明博 255  
 MORII Toshiyuki 森井俊行 33, 34, 35, 36, 37  
 MORIKAWA Tetsuya 森川鐵也 212  
 MORIMOTO Kouji 森本幸司 59, 158, 159  
 MORIMOTO Shigeko 森本茂子 131, 142  
 MORITA Kosuke 森田浩介 59, 161  
 MOTOBAYASHI Tohru 本林 透 60, 63, 65, 66, 67, 68, 69, 70  
 MOTOMURA Shinji 本村信治 130  
 MUKHOPADHYAY Tapan 241  
 MÜNZENBERG Gottfried 74  
 MURAKAMI Hiroyuki 村上浩之 63, 65  
 MURAKAMI Masahiro 村上正弘 145  
 MURAKI Yasushi 村木 綏 178  
 MURATA Jiro 村田次郎 41, 46, 165  
 NAGAFUCHI Teruyasu 永渕照康 230, 234, 238  
 NAGAI Yasuyoshi 永井康介 95, 188  
 NAGAI Yuki 永井由紀 91  
 NAGAMINE Kanetada 永嶺謙忠 48, 49, 51, 101, 102, 103, 104, 105, 106, 107, 189, 263  
 NAGASE Makoto 長瀬 誠 4, 204  
 NAGASHIMA Yasuyuki 長嶋泰之 95, 151, 152  
 NAITO Kenichi 内藤謙一 40  
 NAKADA Yoko 中田陽子 43  
 NAKAGAWA Keiko 中川恵子 57, 58  
 NAKAGAWA Sachiko T. 中川幸子 97  
 NAKAGAWA Takahide 中川孝秀 4, 57, 58, 149, 193, 197, 200, 202  
 NAKAHARA Hiromichi 中原弘道 129  
 NAKAI Yoichi 中井陽一 78, 79, 85, 86, 199, 255  
 NAKAJIMA Shunji 中島諄二 265, 266  
 NAKAMURA Masanobu 中村正信 41, 43, 170  
 NAKAMURA Satoshi N. 中村 哲 48, 49, 51, 107, 263  
 NAKAMURA Takashi 中村隆司 60  
 NAKANISHI Yukiko 中西由季子 121  
 NAKAO Aiko 中尾愛子 186  
 NAKATSUKASA Takashi 中務 孝 25  
 NEMOTO Yukio 根本幸雄 40  
 NICKEL Frank 74  
 NIIZEKI Takashi 新関 隆 54, 56  
 NISHIDA Nobuhiko 西田信彦 102  
 NISHIKAWA Jun 西川 純 154  
 NISHIMURA Jun 西村 淳 192  
 NISHIMURA Tamio 西村民男 75

- NODA Koji 野田耕司 180  
 NOGACH Larisa 43  
 NOGAMI Takashi 野上 隆 106  
 NOGUCHI Motoko 野口基子 118  
 NONAKA Takamasa 野中敬正 56  
 NOSE Yasuhiro 能勢泰寛 137, 138  
 NOTANI Masahiro 野谷将広 60  
 NURUSHEV Sergei 43  
 OGAWA Akio 小川暁生 43  
 OGIWARA Kiyoshi 荻原 清 3  
 OGLOBLIN Alexei A. 74  
 OGRA Yasumitsu 小椋康光 117  
 OHIRA Hideharu 大平秀春 91  
 OHIRA Seiko 大平聖子 104, 105, 106, 107  
 OHKAWA Tomohiro 大川智宏 253  
 OHKI Tomonori 大木智則 6  
 OHKUMA Kazumasa 大熊一正 34  
 OHNISHI Jun-ichi 大西純一 208, 212, 214, 220  
 OHNISHI Tetsuya 大西哲哉 9, 53, 54, 55, 56, 153, 154  
 OHSAKI Osamu 大崎 治 238  
 OHTA Kiyoshi 太田 清 161  
 OHTA Ryuichi 太田隆一 4  
 OHTA Shigemi 太田滋生 191  
 OHTAKE Masao 大竹政雄 222  
 OHTANI Shunsuke 大谷俊介 180  
 OHTOMO Kiyotaka 大友清隆 245, 247, 251  
 OHTSUBO Takashi 大坪 隆 176  
 OHYAMA Hitoshi 大山 等 199  
 OHYAMA Takuya 大山拓也 118  
 OI Makito 大井万紀人 27  
 OKA Makoto 岡 真 40  
 OKA Toshitaka 岡 壽崇 147  
 OKABE Shigeto 岡部成玄 11  
 OKADA Kunihiro 岡田邦宏 180  
 OKADA Shin'ichi 岡田晋一 180  
 OKAMURA Hiroyuki 岡村弘之 9, 53, 54, 55, 56, 153, 154  
 OKAMURA Masahiro 岡村昌宏 43, 202, 220, 234, 238, 261  
 OKAYASU Satoru 岡安 悟 88  
 OKUNO Hiroki 奥野広樹 208, 212, 214, 218, 220, 222, 224, 230  
 OMORI Takashi 大森 巍 118  
 ONISHI Naoki 大西直毅 27  
 ONISHI Takashi 大西 崇 61  
 ONOGI Toshiyuki 小野木敏之 102  
 OOHASHI Kunio 大橋國雄 122  
 OSHIMA Nagayasu 大島永康 255  
 OTAKE Masao 大竹政雄 228  
 OTSU Hideaki 大津秀暁 56, 72  
 OTSUKA Takaharu 大塚孝治 10, 15, 16, 17, 174  
 OYAMA Hitoshi 大山 等 81, 82, 83, 84, 255  
 OYAMA Satoshi 大山 聡 35  
 OYAMATSU Kazuhiro 親松和浩 31  
 OZAKI Takuo 尾崎卓郎 123  
 OZAWA Akira 小沢 顕 72, 74, 163, 176  
 OZAWA Shuichi 小澤修一 60, 63, 65, 66, 67, 80  
 PATE Stephen 41, 165  
 PAVLINOV Alexei 43  
 PEITZMANN Thomas 41, 168  
 PETRASCU Horia 72  
 PFÜTZNER Marek 74  
 POPE Kyle 41, 46  
 PRATT Francis L. 107  
 PRIBORA Vacili 74  
 PRZEWOSKI Barbara 41, 170  
 READ Ken 41, 46, 166  
 RINCKEL Tom 41, 170  
 RIZAWA Takahito 利沢隆人 247, 251  
 ROSER Thomas 41, 43, 170  
 RUSEK Adam 41, 170  
 SAITO Akito 齋藤明登 68, 69, 70  
 SAITO Fuminori 斎藤文修 151, 152  
 SAITO Naohito 齊藤直人 33, 41, 43, 44, 46, 165, 166, 168, 170  
 SAKAI Hideyuki 酒井英行 9, 43, 53, 54, 55, 56, 153, 154, 156, 182  
 SAKAMOTO Hideo 坂本秀生 73  
 SAKAMOTO Hisao 坂本久雄 265, 266  
 SAKAMOTO Koh 坂本 浩 120  
 SAKAMOTO Naruhiko 坂本成彦 9, 53, 54, 55, 56, 153, 154, 206, 208, 210, 212, 224  
 SAKAMOTO Shinichi 坂元真一 48, 51  
 SAKODA Seitaro 迫田誠太郎 9, 53, 54, 55, 153  
 SAKUMA Tai 佐久間 泰 41, 44  
 SAKURAI Hirohisa 櫻井敬久 158  
 SAKURAI Hiromu 桜井 弘 113  
 SAKURAI Hiroyoshi 櫻井博儀 63, 65, 66, 67, 68, 69, 70, 72, 230, 236, 238  
 SASA Kimikazu 笹 公和 202  
 SASAHARA Takafumi 笹原孝文 97  
 SASAKI Hiroshi 佐々木 弘 146  
 SASAKI Kohji 佐々木康二 125  
 SASAMOTO Tetsuji 笹本哲司 97  
 SATO Hiroki D. 佐藤博紀 41, 43, 44, 46, 166  
 SATO Nobuhiko 佐藤修彦 158  
 SATOU Yoshiteru 佐藤義輝 9, 53, 54, 55, 56, 153

- SAWADA Shin'ya 澤田真也 41, 172  
SCHEUERMANN Robert 263  
SEITZ Jeremy 21  
SEKI Ryoichi 関 亮一 13  
SEKIGUCHI Kimiko 関口仁子 9, 53, 54, 55, 56, 153, 154  
SENBA Tomoaki 仙波智行 238  
SERATA Masaki 世良田真来 63, 65, 66, 67, 68, 69, 70  
SHARKOV Boris 202  
SHARMA Sumit 133, 134, 135  
SHEN Hong 申 虹 31  
SHEN Wen Qing 57  
SHIBATA Takehiko 柴田武彦 139  
SHIBATA Toshi-Aki 柴田利明 33, 41, 44, 165, 166  
SHIGEMATSU Naoyuki 茂松直之 144  
SHIMAMURA Isao 島村 勲 75, 76  
SHIMIZU Noritaka 清水則孝 17, 174  
SHIMOMURA Koichiro 下村浩一郎 49, 263  
SHIMOOKA Masaaki 下岡正明 57  
SHIMOURA Susumu 下浦 享 60, 63, 65, 66, 67, 68, 69, 70  
SHIMURA Fumio 志村史夫 90, 93, 94, 109  
SHIOBARA Yamato 塩原大和 117  
SIMON Haik 74  
SITAR Brano 74  
SMITH Brauner 41, 170  
SOMORJAI Endre 72  
SONDHEIM Walter 41, 165  
SORENSEN Soren 41, 46  
SOSHI Takayuki 曾雌隆行 138  
SPINKA Harold 43  
STRASSER Patrick 263  
STRMEN Peter 74  
SUDA Kenji 須田健嗣 9, 53, 54, 55, 153, 154  
SUDA Toshimi 須田利美 52, 59  
SUDOH Kazutaka 須藤和敬 34, 37  
SUEKI Keisuke 末木啓介 129  
SUEOKA Osamu 末岡 修 76  
SUGAI Hiroyuki 須貝宏行 51  
SUGANO Ryoko 菅野量子 102  
SUGII Kazuo 杉井一生 208, 212, 226, 228  
SUGIMOTO Makoto 杉本 誠 204  
SUGIMOTO Naohiro 杉本尚宏 161  
SUGIMOTO Satoru 杉本 聡 28  
SUGIOKA Makoto 杉岡 誠 41, 165  
SUMIYOSHI Kohsuke 住吉光介 28, 29, 31  
SÜMMERER Klaus 74  
SUZUKI Hideyuki 鈴木英之 31  
SUZUKI Hiroyuki 鈴木弘行 122  
SUZUKI Kazuo T. 鈴木和夫 117  
SUZUKI Naoki 鈴木直毅 151, 152, 188  
SUZUKI Shohei 鈴木昌平 238  
SUZUKI Takahiro 鈴木隆博 91  
SUZUKI Takeshi 鈴木 健 72, 74, 176  
SUZUKI Toshio 鈴木俊夫 24  
SUZUKI Toshio 鈴木敏男 19  
SVIRIDA Dmitry 41, 170  
SYPHERS Michael 41, 43, 170  
TAJIMA Norio 田島典夫 97  
TAKABAYASHI Yuichi 高林雄一 78  
TAKAHASHI Katsuhiko 高橋克彦 4  
TAKAHASHI Kazuya 高橋和也 193  
TAKAHASHI Kohji 高橋耕士 32  
TAKAHASHI Masaaki 高橋正昭 125  
TAKAHASHI Takehide 高橋丈英 91  
TAKEDA Atsushi 武田厚司 112  
TAKEDA Naoto 武田直人 51  
TAKETANI Atsushi 竹谷 篤 41, 43, 44, 46, 166, 170, 172, 174  
TAKEUCHI Satoshi 武内 聡 59, 60, 63, 65, 66, 67, 68, 69, 70  
TAKEUCHI Takeshi 竹内 猛 202, 261  
TAKINO Toshikazu 滝野俊和 113  
TAKITA Koki 滝田宏樹 103  
TAKIZAWA Makoto 滝沢 誠 40  
TAMANO Haruna 玉野春南 111, 112  
TAMII Atsushi 民井 淳 9, 53, 54, 55, 153, 154, 182  
TANABE Kosai 田辺孝哉 20, 23  
TANABE Toshiya 田辺敏也 204, 247, 257  
TANASE Masakazu 棚瀬正和 51  
TANIFUJI Makoto 谷藤 悃 9  
TANIGUCHI Etsuji 谷口悦史 33, 41, 166  
TANIHATA Isao 谷畑勇夫 29, 52, 57, 59, 61, 72, 74, 80, 158, 159, 163, 176, 236  
TAROHDA Tohru 太郎田 融 120  
TENDOW Yoshihiko 天道芳彦 195  
TERANISHI Takashi 寺西 高 60, 63, 65, 66, 67  
TERASAWA Mariko 寺澤真理子 29, 31  
THOENNESSEN Michael 21  
THOMAS Timothy L. 41, 170  
THURIEZ Sebastien 84  
TIAN Wei 41, 166  
TOJO Junji 東城順治 41, 170  
TOKANAI Fuyuki 門叶冬樹 59, 158, 159  
TOKI Hiroshi 土岐 博 28, 31  
TOMINAKA Toshiharu 冨中利治 212, 214, 220, 238  
TOMONO Dai 友野 大 48  
TONOMURA Atsuro 殿村淳朗 185

- TORII Hisayuki 鳥井久行 41, 168  
 TOYODA Akihisa 豊田晃久 49  
 TRENTALANGE Stephen 43  
 TSUCHIDA Hidetsugu 土田秀次 79  
 TSUCHIHASHI Takahiro 土橋隆博 238  
 TSUKADA Teruyo 塚田晃代 148  
 TSUKIORI Noritoshi 月居憲俊 4  
 UCHIYAMA Akito 内山暁仁 265, 266  
 UCHIYAMA Koji 内山浩志 59, 73, 161  
 UEDA Yukiyo 上田幸代 116  
 UESAKA Tomohiro 上坂友洋 9, 53, 54, 55, 56, 153, 154, 156, 182  
 UNDERWOOD David 41, 43, 170  
 URAI Teruo 浦井輝夫 3, 97  
 UTSUNO Yutaka 宇都野 穰 15, 174  
 UWAMINO Yoshitomo 上藁義朋 243, 265, 266  
 VARGA Kalman 10  
 VASILIEV Alexander 43  
 VELISSARIS Christos 41, 165  
 von POBLOTZKI Ullrich 41, 168  
 WADA Michiharu 和田道治 180, 255  
 WADA Nobuo 和田信雄 104  
 WADA Ryoichi 和田良一 57  
 WADA Takeshi 和田 雄 212  
 WAKANA Hironori 若菜裕紀 87  
 WAKASA Tomotsugu 若狭智嗣 9, 43, 53, 54, 55, 56, 153  
 WAKASAYA Yoshiaki 若狭谷義朗 59, 72, 158  
 WAKASUGI Masanori 若杉昌徳 61, 80, 249, 253  
 WAKUI Takashi 涌井崇志 156, 182  
 WALET Niels R. 25  
 WANG Haiming 王 海鳴 61  
 WATANABE Isao 渡邊功雄 48, 101, 102, 103, 104, 105, 106, 107  
 WATANABE Tokuji 渡辺徳治 97  
 WATANABE Yasushi 渡邊 康 41, 93, 109, 166, 172, 174  
 WATANABE Yutaka X. 渡辺 裕 68, 69, 70  
 WHITE Sebastian 41, 168  
 WHITTEN Charles 43  
 WINKLER Martin 74  
 WOLFE David 41, 170  
 XIAO Meiqin 肖 美琴 259  
 YAGI Eiichi 八木栄一 3, 97  
 YAKOU Kentaro 矢向謙太郎 9, 43, 53, 54, 55, 56, 153  
 YAMADA Kazunari 山田一成 63, 65, 66, 67, 68, 69, 70  
 YAMADA Satoru 山田 聡 159  
 YAMADA Shoichi 山田章一 31  
 YAMAGUCHI Isamu 山口 勇 137, 138  
 YAMAGUCHI Takayuki 山口貴之 59  
 YAMAGUCHI Yoshitaka 山口由高 176  
 YAMAJI Shuhei 山路修平 13, 18, 26  
 YAMAMOTO Kazuhiro 山本和弘 41, 170  
 YAMAMOTO Sumiko 山本純子 156  
 YAMANISHI Teruya 山西輝也 33, 36  
 YAMASHITA Shoji 山下昌次 144  
 YAMAUCHI Hiromoto 山内啓資 6  
 YAMAZAKI Yasunori 山崎泰規 78, 79, 84, 85, 86, 199, 255  
 YANAGA Makoto 矢永誠人 118  
 YANAGISAWA Yoshiyuki 柳澤善行 60, 63, 65, 66, 67, 68, 69, 70  
 YANAGIYA Takahiro 柳谷隆宏 119  
 YANG Yougfeng 楊 永峰 130  
 YANO Katsuki 矢野勝喜 202  
 YANO Yasushige 矢野安重 4, 80, 90, 93, 94, 130, 148, 156, 193, 197, 200, 206, 208, 210, 212, 214, 216, 218, 220, 222, 224, 226, 228, 230, 243  
 YASUI Hiroyuki 安井裕之 113  
 YATAGAI Fumio 谷田貝文夫 131, 142, 144, 145, 146, 147  
 YAZAKI Koichi 矢崎紘一 39  
 YOGO Katsunori 余語克紀 69, 70  
 YOKKAICHI Satoshi 四日市 悟 41, 172  
 YOKOSAWA Aki 43  
 YOKOUCHI Shigeru 横内 茂 226, 228  
 YOKOYAMA Go 横山 剛 56  
 YOKOYAMA Ichiro 横山一郎 4, 204  
 YONEDA Akira 米田 晃 4, 59, 203  
 YONEDA Ken-ichiro 米田健一郎 68, 69, 70  
 YOSHIDA Atsushi 吉田 敦 59, 69, 70, 93, 94, 109, 195  
 YOSHIDA Kazuhiro 吉田和弘 40  
 YOSHIDA Koichi 吉田光一 57, 58, 63, 65, 67, 72, 74  
 YOSHIDA Shigeo 吉田茂男 139, 140, 141  
 YOSHIDA Tsutomu 吉田 努 118  
 YOSHIDA Yutaka 吉田 豊 90, 93, 94, 109  
 YOSHIKI Atsushi 吉木 淳 148  
 YOSHIKI Hajime 吉識 肇 185  
 YOSHIMASU Masatoshi 吉益雅俊 139  
 YOSHINAGA Naotaka 吉永尚孝 18  
 YOSHIZAKI Ryozo 吉崎亮造 88, 187  
 YOU Qubo 游 曲波 253  
 YUKIHIRA Kenichi 行平憲一 93, 109  
 ZELENSKI Anatoli 261  
 ZHAO Yu Min 趙 玉民 18  
 ZHU Lihua 41, 43, 170



## **RIKEN Accelerator Progress Report Vol. 33**

理化学研究所加速器年次報告 第33巻 (2000)

---

印刷 平成12年(2000)3月21日  
発行 平成12年(2000)3月31日

発行者 理化学研究所  
代表者 小林 俊一  
〒351-0198 埼玉県和光市広沢2番1号  
電話 (048) 462-1111

編集者 理化学研究所加速器研究施設  
運営委員会

印刷所 株式会社ユニバーサル・アカデミー・プレス  
〒113-0033 東京都文京区本郷6丁目16番2号BR本郷5ビル

---

定価5,000円  
(消費税別)



理化学研究所

埼玉県 和光市 広沢